STRUCTURAL PERFORMANCE OF PERFORATED STEEL BEAMS WITH NOVEL WEB OPENINGS AND WITH PARTIAL CONCRETE ENCASEMENT

by

Konstantinos-Daniel Tsavdaridis

BEng (Honours), MSc, DIC

Dissertation submitted in fulfilment of the requirement for the award of

PhD

in

Civil Engineering

School of Engineering and Mathematical Sciences

City University

London

March 2010

ABSTRACT

The research covered in this thesis is concerned with the effects of the behaviour and load carrying capacities of classes of steel beam structures with various shapes of web openings. A comprehensive investigation on non-composite and partially concrete encased perforated steel I-sections with large web openings positioned along the centre-line of the beams was undertaken. This thesis enhances the current knowledge on these classes of perforated beams, as previous research has shown that these beams are susceptible to various failure modes, due to the existence of large web openings.

Currently, perforated steel beams with large web openings are utilised in most engineering applications such as infrastructure, ship building and aeronautical engineering. The most significant benefits of using such beams are the achievement of reductions in weight and accommodation of services within their structural depth of floor systems. Specifically, in building applications, service integration eliminates the internal columns and supports, produces lighter structures which leading to reduced construction and installation time and results in cost effective structural forms and uses. However, many uncertainties are associated with perforated beams as well as non-standard methodology is used for their assessment.

Perforated beams with standard circular, hexagonal and elongated web openings are most widely used nowadays, whilst various non-standard web opening shapes, such as 'elliptical', are introduced through this thesis for first time. These new pioneering web opening shapes improve the structural performance of the perforated beams when examined under two critical failure modes (i.e. shear-'Vierendeel' mechanism and web-post buckling). Moreover, the manufacturing procedure of the 'elliptical' web openings show great advantage in comparison with the manufacturing way of the more popular perforated beams with circular web openings (i.e. cellular beams). Also, other web opening shapes are reported and examined in this thesis. Furthermore, the novelty of the work seems to consist of the treatment of web openings of somewhat greater web opening depth than those usually considered and the introduction of a new class of composite concrete-steel beam.

Despite the abundant experimental work on perforated steel beams that has been conducted by researchers throughout the years, the results are not comprehensive, due to the complexity of the beam configuration and the large number of variable parameters. Therefore, using commercially available finite element (FE) software, numerical analyses were verified by comparison to a new experimental programme designed to test each of the new structural forms. The numerical programme was then used to undertake extensive parametric studies to isolate some of the geometric and material properties that influence the failure modes associated with each of the new forms of structural systems. The main parameters under consideration are the web opening depth (noted usually as diameter), the critical opening length of the top and bottom tee-sections, the web opening spacing, the steel flange and web thicknesses, the concrete strength and contact properties between the steel and concrete of the newly formed composite beams. Detailed study of plastic hinges formation (i.e. high stress concentrations) was also employed in the vicinity of the web openings, by conducting both experimental and finite element (FE) investigation.

This research study should now lead to better management of the use of perforated beams with large web openings as the profound difference between the novel and the conventional perforated beams is demonstrated. Useful practical applications of the so-called structural forms would be of particular interest in the general engineering, not just because of their superior structural performance, but also because of their low cost in manufacturing and usage. Another contribution is the investigation of the partial steel encasement with the concrete in-fill, on the percentage of enhancement of the steel perforated beams with web openings under high shear forces as well as on the distinction which is drawn between the conventional and the new composite beams. Finally, a further indirect outcome of this research thesis is the excellent agreement between the experimental and FE analyses as well as the data that can be used by future researchers to widen the above research to various engineering applications.

ACKNOWLEDGEMENTS

Dr C. D'Mello	City University	For his supervision, patience, continuous support and valuable advices throughout the period required for the completion of this dissertation
Dr B. McKinley	City University – Pell Frischmann	For the proof reading of the thesis and his extensive valuable advices
Mr M. Hawes Mr K. Wilson	ASD Westok Ltd.	For the supplement of the steel perforated beams
Prof. K. Virdi	City University – Aarhus University	For the valuable amendments on the transfer-MPhil report
Dr K. Grigoriadis	City University	For his guidance on the research approach
Miss M. Komeilli Miss H.A. Hadjiyianni Ms M.C. Preziosi	City University	For assisting with the English language
Mr P. Beckwith Mr J. Hooker	City University	For their technical assistance
Mr B. Yu Huo Mr S. Chidavaenzi	City University	For their technical support
My parents: Onoufrios and Eleni and my sister: Vassiliki		For their continuous encouragement, care and tremendous support all these years of my studies in the United Kingdom

DECLARATION

I grant powers of discretion to the University Librarian to allow this dissertation to be copied in whole or in part without further reference to me. This permission covers only single copies made for study purposes, subject to normal conditions of acknowledgements.

VOLUME 1:

TABLE OF CONTENTS

VOLUME 2:

APPENDICES

NOTATION

LATIN ALPHABET

A_{ec}	Effective shear area of concrete
A_{tee}	Cross sectional area of the tee-section
A_v	Shear area of the un-perforated section
$A_{vf}(A_{VZ})$	Equivalent shear area of a flange
A_{vo}	Reduced shear area of perforated section
b_e	Effective width of the strut
$b_f(b)$	Width of the top flange of steel beam
c	Critical opening length
d	Displacement vector corresponding to the buckling mode shape
d_o	Web opening diameter
d_T, d_t	Depth of the stem of the tee-section
E	Young's Modulus of the steel
e	Characteristic cut depth in profile cutting manufacturing procedure **(Appendix 2)**
E_c	Young's Modulus of the concrete
f_c	Compressive strength of concrete
f_t	Tensile strength of concrete
$f_{ult.}$	Tensile steel strength
f_v	Shear strength of the steel $\left(\frac{0.577 f_y}{\gamma_{Mo}}\right)$
f_y	Design yield steel strength
f_1	Stress at strain ε_1
G_f	Fracture energy parameter
h	Overall depth of the steel beam
h_c	Distance between the centroids of the top and the bottom tee sections
h_w	Depth of the web

I	Second moment of area of un-perforated steel beam
I_N	Second moment of area of the perforated section
I_T	Second moment of area tee-section
k	Factor affects the bend of the *V/M* interaction curve effectively at x-axis **(Table 3.7, 3.8** and **3.9)**
K	Stiffness matrix
K_g	Stress stiffness matrix
L	Span of the beam
l_e	Effective length of the strut
l_{cr}	Eigenvalue for buckling mode
l_o	Equal to opening length, *c*, for square and rectangular web openings
L_s	Distance between free end and the web opening (**Figure 2.20**)
m	Moment utilization ratio $\left(\frac{M_{Sd}}{M_{o,Rd}}\right)$
$\overline{m}$	Coupled moment capacity ratio $\left(\frac{M_{o,Sd(FEA)}}{M_{o,Rd}}\right)$
M	Global bending moment (**Figure 2.18**)
M_e	Ultimate elastic moment at this section (**Figure 2.18**)
$M_{el,\,Rd}$	Elastic bending resistance
M_{max}	Bending capacity of critical web tee-section
$M_{o,Rd}$	Moment capacity of the perforated section
$M_{o,Sd}$	Bending moment under pure bending moment case
$M_{o,Sd(FEA)}$	Bending moment at the centre-line of the web opening (obtained from FEA)
M_{pt}	Plastic moment capacity of the top tee-section
M_{Sd}	Global bending moment at centre-line of the web opening
$M_{T,Rd}$	Basic shear capacity of the tee-sections under zero axial and shear forces
M_φ	Local bending moment at an angle φ
$M_{\varphi,Sd}$	Local bending moment due to the transfer of shear force across the opening (Bending moment acting at the centroids of the tee-section at an angle φ)
$N_{o,Sd}$	Axial force under pure bending moment case
$N_{v\varphi,Sd}$	Axial force $N_{\varphi,Sd}$ in the presence of high shear force

$N_{\varphi,Sd}$	Axial force acting at the centroids of the tee-section at an angle φ due to the global bending moment, M_{Sd}
p_c	Cylinder compressive strength of the concrete (MPa)
P_{Con}	Contact pressure
$P_{cr.}$	Critical load
P_{max}	Axial capacity of the critical web tee-section
$P_{ult.}$	Ultimate load
P_v	Shear capacity of steel un-perforated sections
q	Factor is used in order to move the x-intercept to smaller values (**Table 3.7** and **3.9**)
R	Radius of the of the semi-circles at the top and bottom tee-sections at the novel non-standard elliptical web openings
R	Radius of web opening (**Figure 2.18**)
r	Root radius of steel UB section
r	Radius of fillet at the mid-depth of circular web openings (i.e. filleted circular web openings)
S	Web opening spacing (opening pitch)
s_o	Web-post width (weld length)
THETA	Angle of the strain lines at the novel non-standard elliptical web openings
t_w *(t)*	Web thickness
u	Horizontal distance between the centroids of the two cross sections (**Figure 2.14**)
v	Vertical distance between the centroids of the two cross sections (**Figure 2.14**)
ν	Poisson's Ratio for steel (i.e. 0.3)
v	Shear utilization ratio $\left(\frac{V_{Sd}}{V_{o,Rd}}\right)$
$\bar{v}$	Coupled shear utilization ratio $\left(\frac{V_{o,Sd(FEA)}}{V_{o,Rd}}\right)$
$\bar{\bar{v}}$	Design 'coupled' shear capacity ratio
V	Global shear force
$V_{b,Rd}$	Shear buckling resistance

$V_{bw,Rd}$	Shear buckling resistance of a web with an isolated web opening
v_c	Poisson's Ratio for concrete
V_c	Nominal shear strength (contribution of the concrete to the vertical shear strength)
V_h	Horizontal shear force on the web-post
$V_{h,Rd}$	Horizontal shear resistance of the web-post
v_i	Vierendeel parameter
V_o	Shear strength of the beam in pure shear (with zero degree of shear connection)
$V_{o,pl,Rd}$	Shear resistance for perforated beams
$V_{o,Rd}$	Shear capacity of the perforated section
$V_{o,Sd}$	Shear force under pure bending moment case
$V_{o,Sd(FEA)}$	Shear force at the centre-line of the web opening (obtained from FEA)
$V_{pl,Rd}$	Plastic shear resistance
V_S	Shear capacity of the web of the steel beam to the vertical shear strength
V_{Sd}	Global shear force at centre-line of web opening
V_{uo}	Ultimate shear strength of the composite beam in pure shear
V_v	Vertical shear resistance due to web-post buckling
$V_{v\varphi,Sd}$	Shear force $V_{\varphi,Sd}$ in the presence of high shear force
$V_{\varphi,Sd}$	Shear force acting at the centroids of the tee-section at an angle φ due to the global shear force, V_{Sd}
w	Load carrying capacity taken from FEA
W_{pl}	Plastic modulus of the overall section
x	Position of the web opening along the beam length (**Table 3.2**)
y	*h/2* for symmetrical I-beam section
z	Factor affects the bend of the *V/M* interaction curve effectively at y-axis (**Table 3.7, 3.8** and **3.9**)
Z_e	Elastic section modulus

GREEK ALPHABET

β	Degree of shear connection between steel and concrete in composite beams (k in **BS** and η in **EC**)
$\beta_{1,2}$	Shear transfer coefficients for open and closed cracks (i.e. shear retention factors)
γ_{Mo}	Partial safety factor taken as unity for conservative design purposes
γ_{Ml}	Partial safety factor taken as to 1.1
δ_v	Additional deflection at the free end which is at a distance l_s from the web opening (**Figure 2.20**)
Δ_x	Length of the tee-section above and below the web opening (**Figure 2.11**)
ε_o	Strain at the ultimate cylinder compressive strength f_c ($f_c = 0.8f_{cu}$)
ε_y	2D Plane vertical strain
ε_x	2D Plane horizontal strain
ε_{xy}	2D Plane shear strain
η	Factor (taken as 1.2)
λ	Slenderness of the web-post
μ	Coefficient of friction
σ_v	Von-Mises stress
σ_{bs}	Maximum shear stress acting on the web-post
σ_{hs}	Horizontal stress acting on the web-post
σ_y	Vertical stress
σ_x	Horizontal stress
σ_{xy}	Plane shear stress
$\sigma_{1,}\ \sigma_{2,}\ \sigma_3$	Principal stresses
τ_{xy}	Shear stress
φ	Angle from the vertical centre line of the opening, at the LMS of the web opening
φ_p	Formation of a plastic hinge at a cross-section announces that the actions on this section are large while the capacities not

ABBREVIATION

ANSI	American National Standards Institute
AISI	American Iron and Steel Institute
ASTM	American Society for Testing Materials
BRE	Building Research Establishment
BS	British Standard
BS EN	British Standard European Norm
CEM	Cement Marked
CFS	Cold Formed Steel
CSR	Specification of the Cohesion Sliding Resistance
EC	Eurocode
ECCS	European Convention for Constructional Steelwork
ENV	European pre-Standard
ISO	International Organization for Standardization
LTB	Lateral Torsional Buckling
OPC	Ordinary Portland Cement
SCF	Stress Concentration Factor
SLS	Serviceability Limit State
UB	Universal Beam
ULS	Ultimate Limit State
USFB	Ultra Shallow Floor Beam
V/M	Shear – Moment Ratio
w/c	Water – Cement Ratio
WPB	Web-post Buckling

CHAPTER 1

INTRODUCTION

1.1 HISTORY

Since the Second World War many attempts have been made by structural engineers to find new ways to decrease the cost of steel structures. Due to limitations on maximum allowable deflections (i.e. beam's self-weight), the high strength properties of structural steel cannot always be utilised to the best advantage. As a result, several new methods have been aimed at increasing the stiffness of steel members without any increase in weight of steel required. Then castellated beams and perforated beams with circular web openings have been used.

It is known that the ease of integration of services as well as their accommodation within the structural depth of the I-sections is a major benefit of perforated beams. Using perforated beams allows the overall height of every floor to be reduced compared to the case of using simple plain beams where the services are supported beneath the I-sections. Typically savings could be up to 500mm per floor. In other words, for every six floors one more floor is gained in height.

1.2 INTEGRATION IN BUILDING STRUCTURES

Perforated beams are becoming increasingly popular as an efficient structural form. The sophisticated design and profiling process affords greater flexibility in beam proportioning for strength, depth, size and position of web openings.

There have been significant improvements in the structural design of commercial multi-storey buildings in recent years, based on the development of long-span composite systems. Long span beams have the advantage of flexibility of internal planning by minimizing the number of columns resulting in savings in the number of foundations and in speed and cost of erection. Long span beams are more competitive in the industry, mainly when they are manufactured for car parking structures (e.g. an application of pre-camber beams), curved

roof beams or stadium cantilever roof tapered beams. A composite beam with perforated steel section may also offer a similar advantage by using its web openings.

Perforated beams with regular web openings are more often used for long span secondary beams, whose design is generally controlled by serviceability requirements. Whereas fabricated beams with isolated web openings are mainly used for long span primary beams, whose design is more controlled by the higher shear forces acting on these beams. Perforated beams are utilised in high risk commercial and industrial projects in terms of the time, budget and quality against the public and the particular company.

The most significant benefits using perforated sections are listed as follows:

- Service integration, hence floor-to-floor depth is decreased.
- Internal columns are eliminated, leading to more efficient use of internal space. Hence, less foundation cost and less seismic loading.
- Architectural flexibility to fit local requirements.
- Fewer components are required (typically 30% fewer beams) leading to reduced construction and installation time.
- Minimum delivery of materials to thin inner city site.
- Protect the beam-to-column connections from high stresses because of the low weight.
- 50% lighter than pre-stressed concrete construction.
- Good acoustic insulation of composite floors and infill walls.
- Fire protection cost can be reduced due to the long span members and minimize the number of connections.
- 25% to 30% less initial cost to construct.

As for the traditional production line for perforated beams with circular web openings an approximate 15% increase of the steel material was considered. This resulted in a 4% increase of the cost in terms of fabrication and erection. Hence, a 1% increase of the total cost at every budget was obtained. After thorough examination, it was found that by lightening the structure by 30%, a saving of 10% on the budget of the structure would be obtained.

1.3 STRUCTURAL BEHAVIOUR

Structurally, web openings cause a significant reduction on the shear resistance of beams, due to the loss of a major proportion of the web, but they cause a smaller reduction in the bending resistance of beams. The shear transfer across sections with large web openings is an important design requirement. Vierendeel bending results in the formation of four plastic hinges above and below the web opening (**Figure 2.12(b)** and **2.13**). This is a result of transferring shear forces across the web opening. The Vierendeel bending resistance

depends on the local bending resistances of the web-flange sections. As the global shear forces cause both shear failure and Vierendeel mechanism in perforated sections, the effect of local Vierendeel moments acting onto the tee-sections above and below the web openings may be incorporated through a reduction to the global shear capacities of the perforated sections. For web openings with large opening lengths under high shear force, Vierendeel mechanism is dominant in the perforated section. In the case of perforated beams with web openings placed next to each other, the combination of forces acting on the edges of the web openings is more complex and a theoretical model is necessary to define their effects.

1.4 AIM OF THE PROJECT

The aim of this research is to develop and investigate the structural behaviour of perforated beams with various non-standard web openings with either large or narrow opening lengths and to compare them with the typical perforated beams with circular and hexagonal web opening shapes. The structural performance in regularly and closely spaced composite and non-composite perforated beams is also of great interest. Simultaneously, the manufacturing procedure of some perforated steel beams with non-standard web openings is to be examined and modified in order to develop a cost effective product for the industry.

The wide variety of long-span steel structures with perforated beams has economic benefits due to fast, light-weight and accurate construction, and also allows the potential advantage of maximising flexibility in internal layout eliminating the number of the columns and creating large open spaces. This is one of the major trends in modern commercial buildings.

1.5 LIST OF OBJECTIVES

To accomplish the aims of this research programme the following objectives should be accomplished:

- To overview the manufacturing procedures for perforated steel beams with standard and non-standard web openings.
- To review all the failure modes for perforated beams and study the most significant ones.
- To conduct a preliminary FE study of perforated beams with non-standard web opening shapes based on combinations of typical geometrical shapes and to describe their main characteristics.
- To establish the shear-moment interaction curves based on a current design method and to compare these with the theoretical curves at the low moment side (LMS) and the high moment side (HMS) of a web opening.

- To investigate the Vierendeel mechanism of unreinforced perforated beams with various standard and non-standard web opening shapes and sizes by using non-linear FE analyses.
- To evaluate the influence of geometric parameters and investigate the contribution of the web opening shape and particularly the opening length of the top tee-section to the shear capacity of perforated beams.
- To present the yield patterns of the perforated beams with various web opening shapes and sizes and investigate the location and movement of the plastic hinges as well as the main characteristics of such beams.
- To develop a simple design method with generalized shear-moment interaction curves for practical design of steel perforated beams with various standard and non-standard web opening shapes and sizes.
- To further conduct a parametric FE investigation on perforated beams with large isolated novel non-standard web openings subjected under high shear forces and bending moments.
- To evaluate the influence of geometric parameters and investigate the contribution of such novel web opening shapes to the structural behaviour of perforated steel beams.
- To investigate the web-post buckling behaviour of unreinforced perforated beams with standard and novel non-standard closely spaced web opening shapes by conducting experimental tests.
- To carry out a parametric FE investigation on perforated beams with closely spaced web openings, simulating the experimental structural behaviour, for validation purposes.
- To also conduct a parametric local FE investigation on the structural behaviour of the web-posts within two closely and regularly spaced novel web openings.
- To demonstrate the enhancement of the vertical shear capacity of non-composite beams due to the concrete in-fill. To experimentally test an Ultra Shallow Floor Beam (USFB).
- To establish a sensitivity FE study of the USFB model, investigating the effects of the material model parameters. To further examine various constitutive relationships modelling the concrete materials and to compare the results.
- To compare various theoretical approaches based on a modified design method with the FE results and propose a theoretical approach which closely predicts the real behaviour of the USFB.

1.6 MANUFACTURING

There are two main types of beams with web openings that are directly related to the method of manufacture of the beams, as follows:

1. Regular circular or hexagonal web openings (sometimes with elongated openings) in which the interaction between the web openings is included in the analysis; these are known generically as 'cellular' or 'castellated' beams, respectively.
2. Isolated (single) circular or rectangular openings cut-out of the web at positions where the interaction between the web openings is minimized.

There are three methods of manufacture:

1. Hot rolled I-sections which are cut to a profile along the web and re-welded to form a deeper beam with a series of regular circular or hexagonal web openings. These beams can be asymmetric in cross-section, when the tee-sections are cut from different I-sections (**Figure 1.1(a)**).
2. Hot rolled I-sections with individually cut web opening, in which the steel section is symmetric shape. This method is mainly used for beams with isolated web openings (**Figure 1.1(b)**).
3. Fabricated sections, which are formed from three plates that are welded together to form an I-section. The section can be asymmetric (for example, with a larger bottom flange) and the beams can be tapered in depth along their length (**Figure 1.1(c)**).

The use of one or more of these methods of construction depends on the number and size of the service ducts and pipes that are required to be integrated in the structural zone, also taking into account the requirements for future re-servicing and change of use of the space. Web openings can be designed either for specific applications or to minimize the weight of the structure, which means that only some web openings are used for service distribution. (Steel Industry Guidance SN 07/2009, 2009)

Figure 1.1: Hot rolled sections (left (a) and right (b))

Figure 1.1(c): Fabricated section

When hot rolled or fabricated beams with various shapes and sizes of cut-outs at different positions are investigated, the following parameters are considered:

- Scrap steel (i.e. waste material) – web opening area
- Load capacity to weight ratio

On the other hand, when perforated beams are manufactured with profile cutting, engineers increasingly utilise open web sections in their design, due to their design and construction advantages. Such design advantages include a reduced weight per unit length of beam and an increased stiffness (larger section modulus) resulting from the increased depth of the final beam compared to the parent (original) un-perforated beam. Therefore, a higher load carrying capacity and lower displacements are achieved. The manufacturing parameters are considered as follows:

- Length of welding line
- Scrap steel (i.e. waste material) after profile cutting (**Appendix 2**)
- Load capacity to weight ratio
- Moment of inertia to weight ratio
- Depth of perforated beam to depth of parent beam ratio

1.7 STRUCTURE OF THE THESIS

The work in this thesis is divided into five main chapters. Following a brief introduction to the failure modes of perforated steel beams with reference to previous research, available work on testing and analysis of perforated beams and composite beams with the use of perforated beams subjected to high shear forces is reviewed in **Chapter 2**. Emphasis is given to the theoretical background that this research study is based upon and the particular necessary checks.

In **Chapter 3**, a comprehensive FE investigation is presented on perforated beams with various standard and non-standard shapes and sizes of web openings. Initially, a FE model is presented and validated against an experimental work found in the literature and then the

same FE model is used to conduct the FE parametric study. An analytical study of four mid-range UB perforated sections with web openings of depth, d_o, equal to the 80% of the beams' final depth is examined. A range of parameters are investigated and non-dimensional shear-moment interaction curves as well as contour stress plots are presented. The location and movement of the plastic hinges in the vicinity of the web openings is of great interest. The outcome of this chapter is a proposed design method based on generalized shear-moment interaction FEM curves.

Following the previous FE investigation on perforated beams with various web opening shapes, the optimization of two novel non-standard web opening configurations is established in **Chapter 4**. The behaviour of a short span (1.5m) beam with large web openings under high shear forces is investigated. An experimental as well as parametric FE study is conducted, while local FE analyses are performed to assure that the results of the specific web opening configurations are well monitored under these boundary conditions. The influence of each geometric parameter is presented and the beam deflections and stresses are plotted against the web opening area of the corresponding web opening shape.

Chapter 5 presents a comprehensive study of perforated beams with closely spaced circular and novel web openings as they are introduced in **Chapter 4**. Web-post buckling is considered while seven specimens (span of 1.7m) are experimentally tested as well as modelled in the FE software. Following that, a local FE parametric study is carried out to demonstrate the stiffness of the web-posts, the modified strut analogy and the failure modes governed. Two categories of tests are designated. The first one consists of perforated beams with filleted circular web openings, where the spacing is constant. The second one consists of various elliptical web openings, where the web-post width is constant. However, for all seven beams the position of the web-post is the same in relation to the load and the support points, so the shear-moment ratio is the same. Furthermore, a parametric local FE study is conducted for a range of parameters, including the web slenderness of I-sections. A new design model for this complex failure mode is developed for perforated beams with the particular novel web opening shapes.

An experimental work is performed for the same beam as in **Chapter 4**, where concrete is entrapped between its steel flanges and passes through the web openings (USFB). The percentage of enhancement of its vertical shear capacity due to the concrete in-fill is examined. Moreover, a sensitivity FE study with various material models, constitutive relationships modelling the concrete and other parameters is conducted to clarify the results from the experimental work. Finally, various theoretical approaches are compared to the FE predictions, and the most effective design model is proposed.

In **Chapter 7** the objectives are repeated together with the corresponding work which has been done on every particular part of the thesis and its findings. Furthermore, the design standards used in this thesis as well as the design recommendations of **EC3 Annex N** and

BS5950 Part 1: 2000 are provided. As this project is only at the first stages of a wide research area, recommendations for future research and developments are listed.

1.8 METHODOLOGY

1.8.1 Experimental studies

The experimental work conducted in this thesis is separated into: i) bare steel perforated beams with standard and non-standard web openings which consists of eight beams and ii) perforated steel beams with partial concrete encasement which consists of four similar beams. In the second case, neither steel reinforcement nor mechanical shear connectors are provided, as they investigate a theoretical beam model and the percentage of the shear enhancement of perforated steel beams due to the concrete infill through the web openings.

In all tests the web openings are subjected to constant high shear forces and so the 'Vierendeel' mechanism and the web-post buckling failure are studied.

Various standard web opening shapes such as the typical circular web openings and non-standard web opening shapes with emphasis on the elliptical forms are experimentally tested, while all the perforations are cut-outs. Neither of the beams is a fabricated steel section or manufactured beam by profile cutting procedure. The purpose is to keep a minimum of parameters so as to be able to accurately evaluate the comparisons and draw clear conclusions. Instead, universal beam (UB) hot rolled symmetric I-sections with isolated web openings cut-outs are used.

1.8.2 Necessity of FE Studies

Experimental based testing has been widely used and this is a method that produces real life response of the structural components. However, this method is extremely time consuming and the use of materials can be quite costly. In recent years, the use of finite element analysis has increased due to progress knowledge and capabilities of computer software and hardware. It has now become the preferred method for this research programme to analyze steel structural components with various geometric parameters, while the web opening shapes can be very complicated. The use of computer software to model these structural components is much faster and extremely cost effective.

To fully understand the capabilities of finite element computer software, one must look back to experimental data and simple analysis. Data obtained from a finite element analysis package is not useful unless the necessary steps are taken to understand what is happening within the model that is created using the software. This is the reason that validation checks of the FE models against experimental work are carried out in every chapter of this thesis.

Furthermore, numerous global and local parametric studies on perforated beams with various web opening shapes are implemented in this research programme using finite element analysis, to demonstrate the response of such beams under different geometric and loading arrangements.

The commercial finite element software packages ANSYS versions 10.0 and 11.0 are used. Mesh refinement study is always carried out to determine the appropriate finite element size. Because of high stress concentration in the vicinity of the web openings, very small finite element sizes are required. Also, the effects of shear locking and hourglass effect are carefully considered.

1.9 CONTRIBUTION TO SCIENCE

A further indirect scope of this research study is to provide future researchers with a comprehensive work on perforated steel beams with various web opening shapes. Abundant experimental tests on mainly typical perforated beams with hexagonal and circular web openings have been found in the literature. Hence, following the validation of the FE models against experimental tests from the literature as well as from this research programme, extensive parametric FE studies are carried out to widen the area of their application. On the other hand, very few experimental tests and limited FE analyses have been found in the literature regarding the web-post buckling behaviour of perforated steel beams. Therefore, an experimental programme is carried out for perforated steel beams with standard and non-standard web opening shapes regularly and closely spaced, followed by a FE investigation and a parametric study, in order to validate and extent the results, providing useful material and conclusions to future researchers.

CHAPTER 2

LITERATURE REVIEW

2.1 INTRODUCTION

A literature review on experimental work and finite element analyses for non-composite and composite perforated, mainly steel beams is carried out. The literature review consists of three sequential sub-chapters; study on non-composite beams with isolated web openings, non-composite beams with closely spaced web openings and study on composite (i.e. perforated steel I-sections with concrete infill) beams. Experimental and finite element analyses reviews are categorized and described in reverse chronological order for each sub-chapter, separately.

2.2 FAILURE MODES OF PERFORATED STEEL BEAMS

2.2.1 Introduction

To date, experimental and finite element studies on perforated beams have reported six main different modes of failure (Redwood and McCutcheon 1968, Kerdar and Nethercot 1984). These modes are closely associated with beam geometry, web opening configuration, web slenderness, type of loading, and provision of lateral supports. Under given applied transverse or 'coupling' forces, failure is likely to occur by one of the following modes:

- 'Vierendeel' or Shear Mechanism
- Flexural Mechanism
- Lateral Torsional Buckling (LTB)
- Rupture of Welded Joints
- Web-post Buckling in Shear
- Compression Buckling

2.2.2 'Vierendeel' or Shear Mechanism

This mode of failure is associated with high shear forces acting on the beam. Formation of plastic hinges at the edges of the web opening shapes (φ_p angles) or at the corners of particular web opening shapes deforms the tee-sections above the web openings to a stretched shape as shown in **Figure 2.1** for castellated and cellular beams, respectively. This mode of failure was first reported by Altifillisch (1957), Toprac and Cook (1959) regarding castellated beams and Redwood and McCutcheon (1968) regarding cellular beams. Beams with relatively short spans, with shallow tee-sections, and longer weld lengths are susceptible to this mode of failure. Shorter spans can carry higher loads leading to shear becoming the governing load. When a perforated steel beam is subjected to shear, the tee-sections above and below the web openings must carry the applied shear as well as the primary and secondary moments. The primary moment is the convectional bending moment on the beams cross-section. The secondary moment, also known as the Vierendeel moment, results from the action of shear force in the tee-sections over the horizontal length of the web opening. Therefore, the horizontal length of the tee web opening directly affects the secondary moment, and the smaller the web opening (i.e. narrower web opening) the better it is. Failure is occurred at the web opening under the maximum shearing force, or if several web openings are subjected to the same high shear, then failure will be occurred at the one with the greatest moment too.

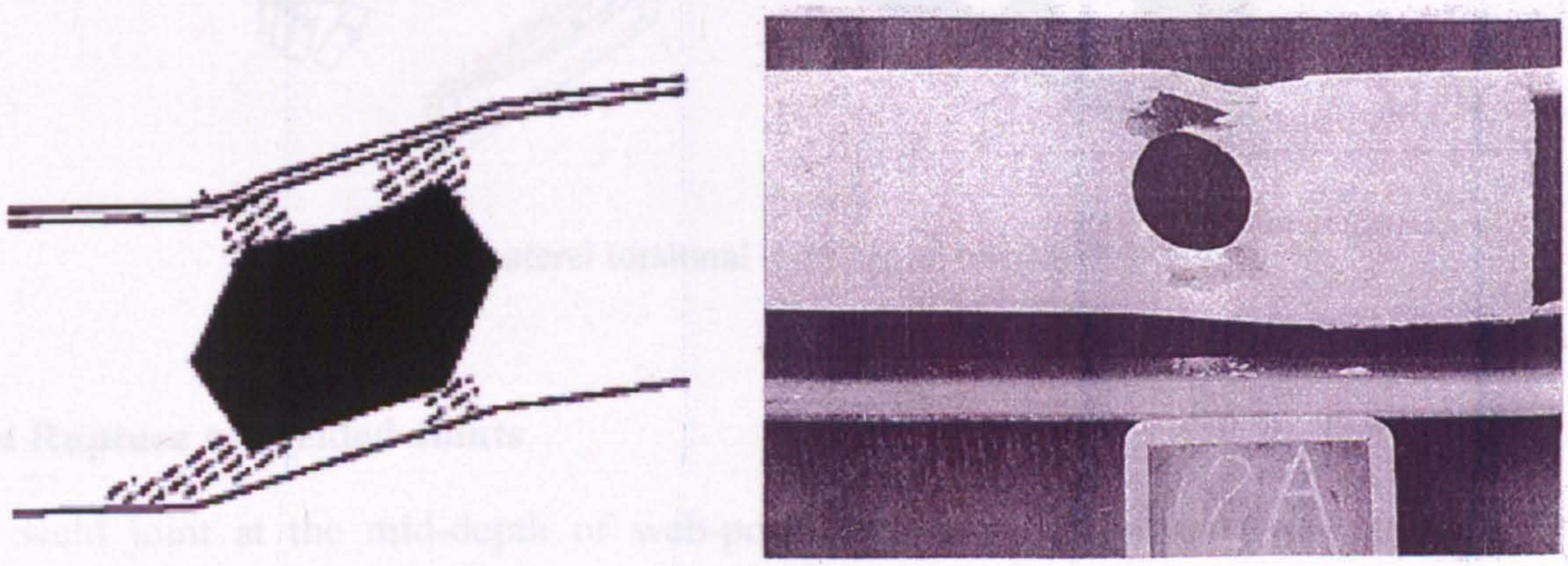

Figure 2.1: Four plastic hinges at rectangular web opening parallelogram mechanism (left) and circular web opening subjected to bending and shear (Redwood, 1969)

2.2.3 Flexural Mechanism

Under pure bending, provided the section is compact (at least Class 2), the tee-sections above and below the web openings are yielded in tension and compression until they become fully plastic.

2.2.3 Lateral Torsional Buckling (LTB)

As in the un-perforated beams, out-of-plane movement of the beam without any web distortions describes this mode of failure. LTB as shown in **Figure 2.2** is usually associated with longer span beams with inadequate lateral support. The reduced torsional stiffness of the web, as a result of relatively deeper and slender section properties, contributes to this buckling mode. Nethercot and Kerdal (1982) examined this mode of failure related to perforated beams. They concluded that web openings had negligible effects on the overall lateral torsional buckling behaviour of the beams they tested. Furthermore, it is suggested that the design procedures that determine the lateral buckling strength of solid webbed beams could be used for perforated beams provided that the reduced cross sectional properties are going to be used.

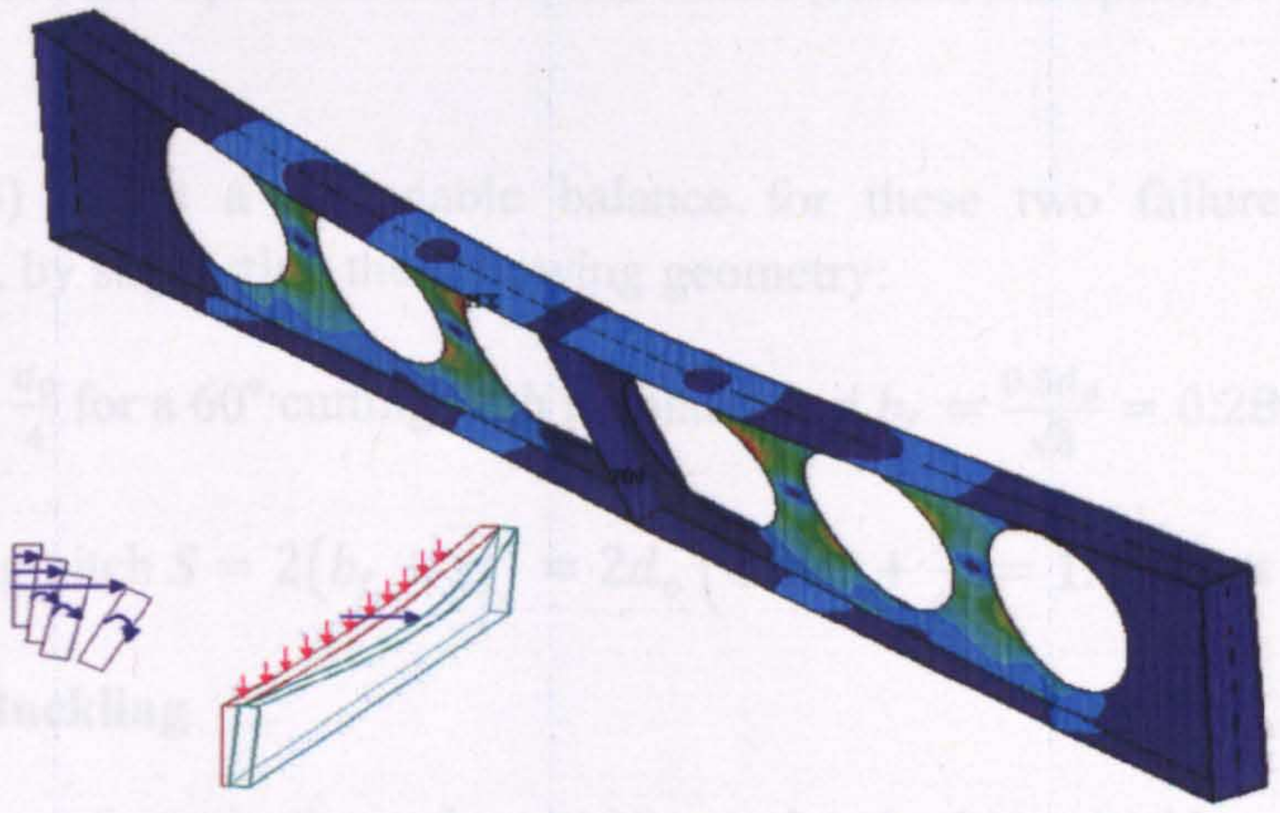

Figure 2.2: Lateral torsional buckling at long span beams

2.2.4 Rupture of Welded Joints

The weld joint at the mid-depth of web-post between two adjacent web openings, in perforated beams that have been manufactured by profile cutting, may ruptures when the horizontal shear stress exceeds the yield strength of the welded joint, as shown in **Figure 2.3**. Hosain and Speirs (1971) investigated this failure mode by testing six beams with short welded joints. This mode of failure depended upon the length of the welded joint s_o. Usually when profile cutting, the critical opening length is directly related to the weld length between the web openings, and if the opening length is reduced to decrease the secondary moments, the welded throat of the web-post becomes weak. As mentioned earlier, formation of a Vierendeel mechanism is likely to occur in beams with large opening lengths and so large weld lengths. On the other hand, short weld lengths are prone to cause failure of the welded joints as the horizontal yield stress is exceeded before the formation of the four plastic hinges in the vicinity of the web openings (**Figure 2.3**).

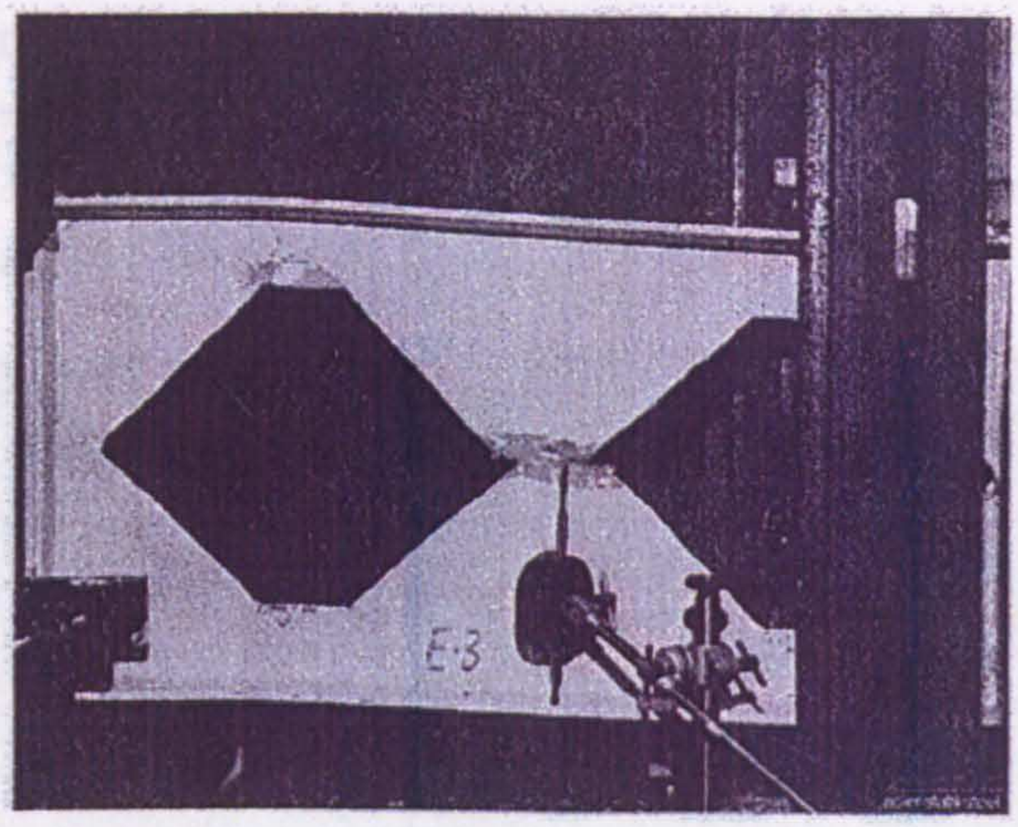

Figure 2.3: Specimen after rupture failure (Hosain and Speirs, 1971)

Dougherty (1993) found a reasonable balance for these two failure modes for the castellated beams, by suggesting the following geometry:

Weld length $s_o = \frac{d_0}{4}$ for a 60° cutting with no plates and $b_f = \frac{0.5d_o}{\sqrt{3}} = 0.289d_o$

Therefore, opening pitch $S = 2(b_f + s_o) = 2d_o\left(0.289 + \frac{1}{4}\right) = 1.08d_o \cong 1.1d_o$

2.2.5 Web-Post Buckling

The horizontal shear force in the web-post is associated with a double curvature bending over the height of the web-post. As shown in **Figure 2.4**, one inclined edge of the web opening will be stressed in tension, and the opposite edge in compression and so buckling will cause a twisting effect of the web-post along its height. Several cases of web-post buckling have been reported in the literature as Sherbourne (1966), Halleux (1967), Bazile and Texier (1968).

Many analytical studies on web-post buckling have also been reported to predict the web-post buckling load due to shearing force. Based on a finite difference approximation for an ideally elasto-plastic hardening material Aglan and Redwood (1976) produced some graphical design approximations for a wide range of beams and web opening geometries. Also, some correlations between experimental and non-linear finite element analysis estimations were done by Zaarour and Redwood (1996). Delesque (1968) used an energy method to solve an elastic buckling problem by treating the web-post as a variable section rectangular beam in double curvature bending, susceptible to LTB. However, Zaarour and Redwood (1996) found large differences in the results obtained from Blodgett's method in comparison to their test results and finite element approximations. Later on, Redwood and Demirdjian (1998) derived approximations of buckling loads based on elastic finite element

analyses and good correlations between experimental and theoretical estimations were found. This work showed that the results of Aglan and Redwood (1976) should not be used for very thin webs. The effect of the web thickness is considered as significant and discussed in greater detail in **Chapter 5**.

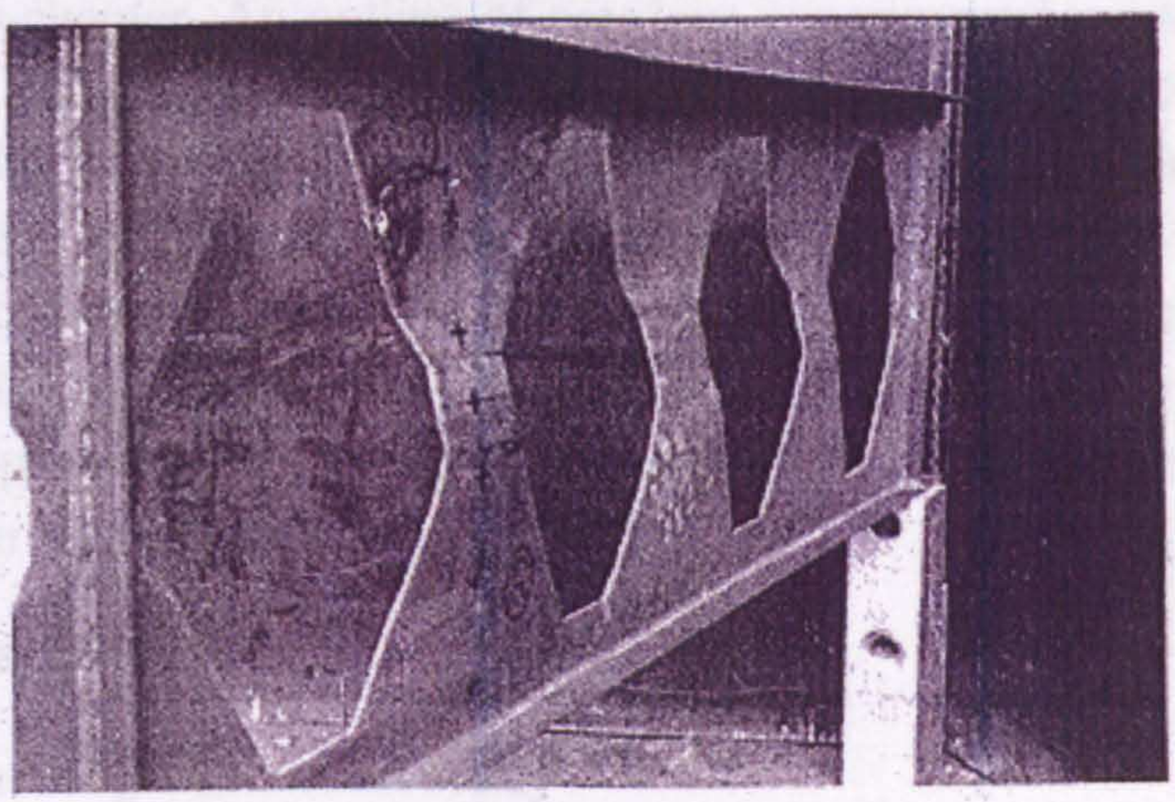

Figure 2.4: Specimen after test (Zaarour and Redwood, 1996)

2.2.6 Web-Post Buckling due to Compression

A concentrated load or a reaction point applied directly over a web-post caused the failure mode, presented in **Figure 2.5**. This mode was reported in the experiments conducted by Toprac and Cook (1959) and Husain and Speirs (1973). Buckling of the web-post under large compression forces is not accompanied by twisting of the post, as it would be under shearing force. Such a failure can be prevented if adequate web reinforcing stiffeners are provided. A 'strut' approach proposed by Dougherty (1993) which suggested that standard column equations could be used to determine the strength of the web-post located at a point load or a reaction load.

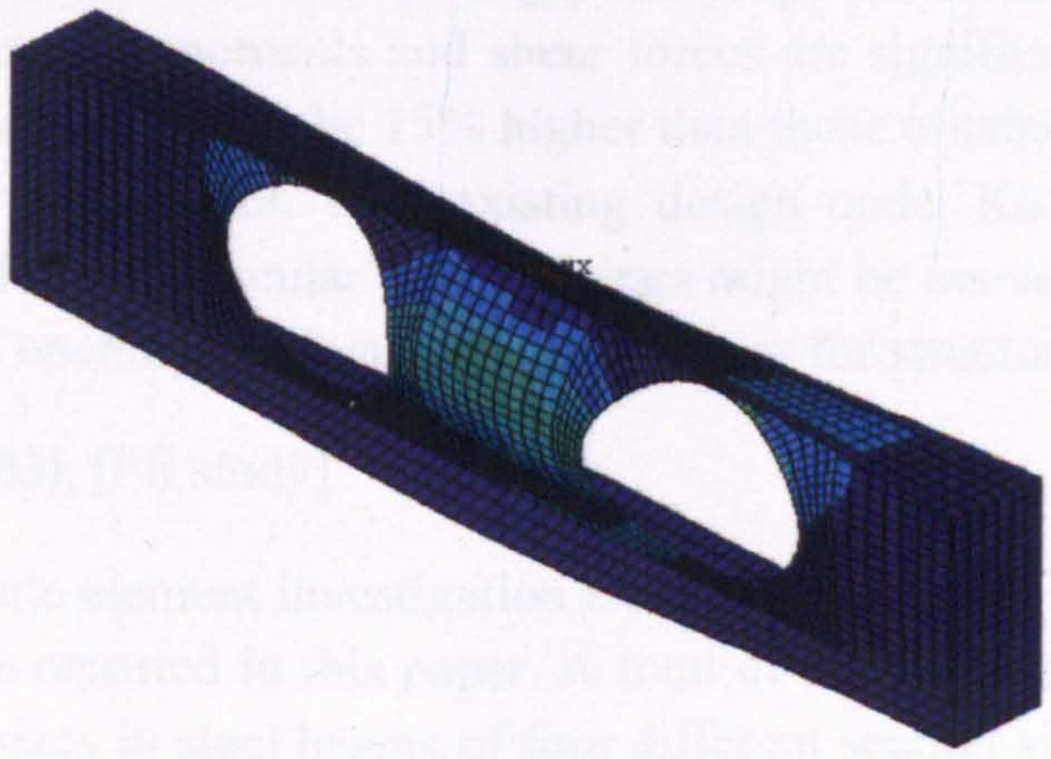

Figure 2.5: Web buckling due to compression

2.3 REVIEW OF NON-COMPOSITE PERFORATED BEAMS

2.3.1 Introduction

Literature reviews on non-composite perforated beams with steel sections are extensively reported in this sub-chapter. An outline of previous experimental work, FE and analytical studies are reported describing the main features of each investigation. Some of the test and finite element results described herein are the subject of detailed analysis in subsequent chapters of this thesis. A literature review is separately reported for every author given in chronological order beginning with the most recent research. It should be noted that in some cases other failure modes are obtained, not directly related to either Vierendeel mechanism or web-post buckling, as an overall reaction to the combination of global forces on the specific beam configuration.

2.3.2 Steel perforated beams

2.3.2.1 Papers regarding Vierendeel study

Chung, Liu and Ko (2003), [FE study]

Following the previous extensive parametric study (Liu and Chung, 2003), a global 'coupled' Vierendeel shear capacity was established and capacity ratios for web openings of various shapes and sizes were obtained directly from the finite element investigation. Moreover, an indicative parameter, the Vierendeel parameter, was established to assess the performance of the Vierendeel mechanism in perforated beams. Through comparison among the moment and the shear capacity ratios and also the 'Vierendeel' parameter, the critical modes of failure in perforated beams under different shear-moment ratios may be readily assessed.

Empirical shear-moment interaction curves at the perforated sections were then suggested for practical design of steel beams with medium to large web openings. However, for perforated sections with small web openings, the proposed curve is slightly conservative when interactions between moments and shear forces are significant. The resulting design capacities were found to typically be 15% higher than those obtained from the convectional design methods. By comparison with existing design code, Ko and Chung (December 2000) also suggested that as circular web openings might be conveniently transformed into equivalent octagonal openings with suitable dimensions for structural assessment.

Liu and Chung (2003), [FE study]

A comprehensive finite element investigation on steel beams with web openings of various shapes and sizes was reported in this paper. A total of eight different web opening shapes with three different sizes in steel beams of four different section sizes were covered with a total of 960 non-linear finite element runs. In this research study, all steel beams were hot

rolled steel I-sections class 1 or 2 (plastic or compact). All web openings were concentric to the mid-height of the sections with diameters, d_o, between *0.5h* and *0.75h*. For perforated beams with these geometrical dimensions, it was generally considered that local buckling in the tee-sections at the perforated beams was not critical. However, for class 3 or semi-compact sections with small web openings, the unsupported webs in the tee-sections could become very slender and hence local buckling could occur.

The results presented in this paper were related to a simply supported beam of UB457x152x52 S275 with a span of 12m under uniformly distributed load. While the web openings of various shapes were located at different positions along the beams length, three specific locations were considered in detail. The perforated beam at location 1 is under pure shear without any global moment, while interaction between global shear force and global moment at positions 2 and 3 were significant.

It was found that all steel beams with large web openings of various shapes behave similarly under a wide range of applied moments and shear forces. The failure modes were common in all beams, and the yield patterns of those perforated beams at failure were also similar to one on other. Comparison on the global shear-moment interaction curves of those steel beams showed that they were of similar shape and thus, it is possible to derive empirical shear-moment interaction curves to assess the load capacities of all steel beams with web openings of various shapes and sizes. Furthermore, it was shown that the most important parameter in assessing the structural behaviour of perforated beams is the length of the tee-sections above and below the web opening, as it controls the magnitude of the local Vierendeel moments acting on the tee-sections.

Chung, Liu and Ko (2000), [FE study]

This paper presents an investigation of the Vierendeel mechanism in steel beams with circular web openings based on analytical and numerical studies. An empirical shear-moment interaction curve at the perforated beam was also suggested for practical designs of steel beams with circular web openings against the Vierendeel mechanism.

In order to provide information for a practical design, a parametric study was performed to assess the structural performance of simply supported steel beams with circular web openings of different sizes at different locations along the beams. For a steel beam of UB457x152x52 S275, the FEM shear-moment curves for web openings of d_o equal to *0.5h* and *0.75h* were examined.

In addition to these, the load carrying capacities of simply supported beams of different spans, namely 5, 6, 7.5 and 10 m, under uniformly distributed loads, was examined (**Figure 3.6**). It was found that the reduction of the load carrying capacity was largely due to reduced moment capacity at perforated sections near the mid-span of the beams while the Vierendeel mechanism was generally not critical. In common, full load carrying capacities

of the beams may be attained even in the presence of large circular web openings, especially in long span beams when the web openings are located within one-third of the span.

Ito, Fujiwara and Okazaki (1991), [Experimental work, FE and Analytical study]

The elastic-plastic behaviour and ultimate strength of steel beams with U-shaped web openings in the top part of the web were experimentally investigated. Nine welded, built-up, simply supported beams were tested with one concentrated load. The beams were classified as follows: type A (*h=300mm*), type B (*h=230mm*), and type C (*h=160mm*). The dimensions of the U-shaped web openings were determined so that they would permit passage of U-shaped ribs of the standard size of 300x200mm, as specified in the Japan Society of Steel Construction provision. The slit depth (20mm) under the rib was included in the U-shaped web opening. The form of the U-shaped web openings was kept as simple as possible. The web depth h_w was selected as follows: Three types were chosen, based on the ratio of the web depth h_w and the height d_o of the U-shaped web openings: (1) $h_w/d_o = 3$ (A type); (2) $h_w/d_o = 2.3$ (B type); and (3) $h_w/d_o = 1.6$ (C type). The height of d_o (100mm) of the U-shaped holes was a constant.

The test results were compared with analytical results based on the finite element method, the beam theory and the ultimate strength method, taking into account the Vierendeel action. The predictions of the bending stresses, the shear stresses and the ultimate strength for such beams were obtained with comparatively good accuracy. Generally, the bending stress distributions of the beam with U-shaped web openings could be accounted for by beam theory. Also, the horizontal shear stresses acting on the web sections between the U-shaped web openings can be predicted by a given formula in this paper. Finally, it was found that local yielding of the corner of U-shaped web openings was not directly related to the ultimate strength of beams.

Dougherty (1980), [Analytical study]

In this paper a theory was presented for determining the elastic deformation of I-beams containing rectangular web openings. Such a theory was a prerequisite for the development of a general method of calculating the elasto-plastic deformation of perforated beams.

It was found that the deflection at any point of a perforated beam is a combination of the primary and Vierendeel deflections. The former was calculated in the same way as an un-perforated beam. In determining the Vierendeel deflections both bending and shear deformations of the tee-sections were taken into account. The analyses also took into account the slope incompatibility that develops at the junction of the perforated and un-perforated beams when only simple Vierendeel action was considered.

Finally, theoretical deflections which were obtained from the analysis were found to be in good agreement with experimental values for both concentric and eccentric web openings. It is worth noting, that the proposed analysis in this paper, provided a suitable means of determining the deformations of perforated beams at working loads.

Redwood (1969), [Experimental work]

Relations were derived for the shear and moment acting together at a section of a beam containing a circular or rectangular web opening. The method was designed to enable shear-moment interaction diagrams to be predicted very rapidly. Circular and rectangular web openings centred at mid-depth of the beam. The theory showed agreement with experimental results when the shear-moment ratio is low, and is conservative when the shear-moment ratio is high. For the purpose of this study experimental tests in which beams containing rectangular and 'extended' circular web openings were loaded up to failure. They are also given in another study by Redwood and McCutcheon (1968).

Redwood and McCutcheon (1968), [Experimental work]

This paper reported tests of wide flange steel beams containing one or two unreinforced web openings of various shapes, under several different shear-moment ratios. The beams used in this investigation consisted of approximately 6m (8W17 sections of A36 steel). Essentially, four different values of the shear-moment ratio at the web openings were tested; one of these being pure bending. Most of the beams were tested elastically to measure flexibilities. Flange reinforcement was required in the region of the applied load, and web stiffeners were attached at load and support positions. In all cases the reinforcement was adequate; hence the failure in every case occurred at the web opening.

The ratios of measured and estimated plastic moments indicated that sometimes there are significant reductions in strength. In some cases the experimental value was as low as 40% of the plastic moment for the gross section. Final failure of the beams occurred when either the flange or the web buckled, or when cracks developed in the web at the web opening boundaries. Flange buckling was in every case a local buckling and did not involve an overall instability of the tee-shaped section comprising the flange and that part of the web above the web opening. Local flange instability would not normally be expected in these 8WF17 sections since A36 steel are compact. However, the sections were in fact non-compact and thus were consistent with the buckling failures. The cracks which developed in the webs were always accompanied by rapidly increasing deflections, at which point loading was discontinued.

Bower (1968), [Analytical study]

This study presents a theoretical approach on the general topic of web openings in steel beams. The information given was intended to be a first step toward providing the design engineer with data on the need for reinforcing web openings in beams.

It was concluded that beams could be designed from either an elastic or plastic design criterion. Concerning the elastic design beams with web openings should be designed using the same basic factors of safety against yielding as in the AISC Specification. Only the maximum allowable bending and shear stresses should be computed using the actual stresses causing yielding at the web opening rather than nominal beam stresses. Because the stresses causing yielding vary with size, shape and location of the web openings, shear-moment interaction design charts should be used to simplify determining the allowable stresses. Concerning the plastic design beams with web openings should be designed using the *C* load factor of 1.7. Only the maximum allowable loads should be computed using the actual ultimate strength of the beam at the web opening, rather than the strength of the gross beam. Shear-moment interaction design charts should also be used to simplify determining the allowable loads.

Toprac and Cooke (1959), [Experimental work]

Nine castellated beams fabricated from 8B10 rolled sections were tested to destruction. The objectives of the investigation were to study the structural behaviour in elastic and plastic ranges, to study load carrying capacity and modes of failure, to compare observed results with theoretical calculations, and to determine an optimum expansion ratio for such beams. Loads were applied at four concentrated points and failure loads were reported as the ultimate loads. Well defined yield stress values were obtained through coupon tests and adequate bearing stiffeners were provided under reaction points.

Specimens A and C failed through excessive lateral buckling and were omitted from further study. The ultimate load of specimen B was recorded, but no further details were given. As for specimen D which had a class 2 web tee-stem-section, web throat, tee-section and compression flange yielding progressed in the shear span. As the maximum load was reached, yield at the top low moment web opening corner and at mid-depth web-post was evident. Yielding and buckling of the compression flange in the pure bending region was the failure mode of beam E. Local buckling of the compression flange in the constant moment region was also the observed failure mode of specimen F; however, as the load was further increased, the beam buckled laterally. A Vierendeel mechanism in the region of highest shear was the mode of failure of specimen G. Specimen H, with a class 2 flange section, failed through buckling of the compression flange in the constant moment region. Specimen I, with a class 1 web tee-stem-section failed through a Vierendeel mechanism at the highest shear region.

Altfillisch, Cooke and Toprac (1957), [Experimental work]

The objective of the investigation was to study the structural behaviour of castellated beams both in the elastic and plastic ranges, and to study their strength and failure mode. Three joists fabricated from 10B11.5 shapes with equal spans and simple supports and with varying positions of two symmetrical concentrated loads were used. Varying expansion ratio, beam depths, web openings and web-post geometries were studied for each of these tests. Test loads were reported as the ultimate loads obtained during the experiments.

Beam A was provided with full bearing stiffeners under each load. It failed through extensive yielding of the tee-section and local compression flange buckling in the region of constant moment. The flange to width ratio of beam A corresponded to a class 2 section.

Beam B consisted of three tests. In the first two, B1 and B2, loads were in the elastic range in order to verify the theoretical stress and deflection analyses. The third test, B3, involved loading to destruction, but was omitted from further study because of the inadequacy of the lateral bracing system. Beam C was provided with short bearing stiffeners, (approximately half beam depth) below the load points. The first two sets were in the elastic range and the third was loaded to destruction. The failure mode of this beam involved yielding the web at the top low-moment corner of the web opening in the shear span nearest the load application point. This was followed by a local buckling of the compression flange at the other end of the web opening. The flange had class 2 section properties. Yielding of the throat was also noticed.

2.3.2.2 Papers regarding web-post buckling study

Dervinis and Kvedaras (2008), [Experimental work and Analytical study]

An algorithm for selecting the rational dimensions of the castellated beams was presented in this paper, and it may be adopted and used for design. Long beams 12m, web thickness 6-12mm and web depth 500-1000mm, were analyzed. Web opening size was varied form half of the web to the total web depth minus 100m. The chosen cross sectional area of two flanges was equal to the cross-sectional area of the web. The thickness of the flanges was twice as big as the thickness of the web. A uniformly distributed load was applied in the FE model while the upper flanges of the beams were restrained out-of-plane.

It was found that the higher the web, the more efficiently the beam material was used. However, the bigger the web slenderness, the greater the influence is on the local buckling on the web.

Lawson, Oshatogbe and Newman (2006), [FE study]

The behaviour of web-posts between regularly spaced circular and rectangular openings in the webs of fabricated steel beams was investigated using the finite element method. FE

analysis was carried out for a range of parameters, including the proportionate depth of the web openings and the web slenderness.

The FEA was carried out using the software package ANSYS. Material non-linearity (i.e. plastic behaviour) as well as geometrical non-linearity (buckling) was utilised. The model used in FEA consisted of a short section of beam between the centre-line of adjacent web openings. The model used in this study was based on a 610mm deep section with a web opening diameter/opening depth, d_o, of 406mm, given a beam depth/opening ratio D/d_o of 1.5. Seven S/d_o ratios in the range of 1.2 to 1.8 were studied with four web thicknesses of 5, 6.4, 7.8 and 10mm, giving d_o/t ratios which vary from 40.6 to 81.2. The main area of interest was the stability of the web-post under the combined effect of shear and compression, especially at the edge of the web opening, where the stabilizing effect of the tension-field action is less than at the centre of the web-post.

As an outcome, a design model was developed based on a 'strut' analogy in which the stability of the web was checked using buckling curves to **BS 59590 Part1**. This 'strut' analogy was presented in terms of the effective width and effective length of the strut, which were derived to give the best fit over the range of web opening parameters.

Lagaros, Psarras, Paradrakakis and Panagiotou (2008) &
Psarras, Lagaros and Paradrakakis (2005), [FE and Analytical study]

The objective of these two pieces of research was to obtain the optimum design of 3D steel framed buildings with perforated I-section beams. The optimization was considered as a combined optimization problem in terms of size, shape and topology. Moreover, the size of the columns and the beams of the structures of each storey constitute the sizing design variables, while the number and the size of the web openings of the beams constitute the topology and shape design variables respectively.

Two distinctive formulations of the optimization problem were considered depending on the finite element simulations used, with beam and shell discretization. The two formulations were compared in terms of the optimum design achieved. A characteristic test example was considered and showed that a quantifiable reduction on the weight of the structure was accomplished by allowing web openings in the beams of the structure without reducing structural strength or serviceability requirements. Evolutionary Algorithms have proved to be a robust and efficient tool for economically design optimization of steel 3D framed building with web openings.

Demirdjian (1999), [FE and Analytical study]

A comprehensive study on the web-post buckling behaviour of castellated beams was described. Both elastic and plastic methods of analysis were utilised to predict the failure modes of these beams. Interaction diagrams of the formation of plastic hinges (i.e.

mechanism), yield of the horizontal web length and elastic buckling analysis using the FE method were correlated with a number of experimental test results from previous studies.

Forty-two test beams ranging from 45° to 60° web openings were computed with the plastic and elastic methods of analysis. A parametric study covering a wide range of 60° castellated beam geometries was performed to derive elastic buckling coefficients under pure shear and bending forces. An elastic buckling interaction diagram was then defined, which along with the diagrams utilised in the plastic analysis, could be used to predict the elastic buckling and plastic failure loads under any given shear-moment ratio.

The effect of plasticity associated with buckling and expressions was derived to improve the previous theoretical models used, by combining elastic and plastic results. This caused the coefficient of variation of the test-to-predicted ratios to be decreased.

Redwood and Demirdjian (1998), [Experimental work]

Four castellated beams, two identical ones with four web openings 10-5(a), 10-5(b), a third with six web openings (10-6) and a fourth with eight web openings (10-7), all with identical cross sectional properties, were tested. The main focus of the experiment was to investigate the buckling of the web-post between web openings and to study any effects of the shear-moment ratio on the mode of failure. Simple supports and a central single concentrated load were used for all specimens. All beams were provided with bearing stiffeners at support and at load points. Mean flange and web yield stress values were obtained from tensile coupon tests.

Based on the experimental ultimate loads, except beam 10-7 which failed by lateral torsional buckling, buckling of the web-post was the observed mode of failure of all these beams. Beam 10-7 was omitted from further consideration in this project, since interest is in web-post buckling only. Ultimate load values were given as the peak test loads. Test conditions were then simulated by elastic finite element analysis, and good predictions of the buckling loads were reported (4% to 14% variations).

Zaarour and Redwood (1996), [Experimental work and FE study]

This paper is based on the previous research conducted by Zaarour (1995). Twelve castellated beams were loaded to failure in order to study the buckling of the web-post between web openings. In 10 cases web-post buckling occurred. FE analysis of the web-post, taking into account inelastic action, was used to predict the buckling loads. Also, graphical results were obtained, in which the web-post was treated as a beam and the finite difference method was used to obtain the buckling loads.

Results showed that the possibility of web-post buckling as a governing design criterion increases significantly if an intermediate web plate is used to deepen the beam. The

strength is continuously reduced from the plastic mechanism value as the ratio of intermediate plate height to web opening height increases.

Both methods show very good correlation with the maximum test loads. Either of these methods provides a satisfactory basis for design, although the FE results were superior because of the lower variability in the predictions. The graphical results provide general solutions covering a practical range of geometries, and could be considered suitable until the results of the FE parametric studies become available.

Zaarour (1995), [Experimental work and FE study]

Fourteen castellated beams fabricated from 8, 10, 12 and 14 inch light beams (Bantam sections manufactured by Chaparral Steel Company) were tested. Six of these had 2 in. (50.8 mm) high plates welded between the top and bottom tee-sections at the mid-depth of the web-post. The objective of the experiments was to study the buckling of the web-post between web openings. Both simple supports and a central single concentrated load were used for all specimens. All beams were provided with bearing stiffeners at support and at load points. Average flange and web yield stresses were obtained from tensile coupon tests for each size of beam.

The reported ultimate strengths were based on peak load capacities of the beams. Web-post buckling was observed in the failure of 10 cases, while in two cases, local buckling of the tee-section above the web openings occurred as subjected to greatest bending moments. Two lateral torsional buckling modes were also observed; these have been omitted from further consideration since interest is in web buckling only. FEM analysis was also used to predict web-post buckling load. There was some bias in the FEM results, leading to slight over-estimates of strength for more slender web-posts, particularly those with intermediate plates.

Galambos, Hosain and Speirs (1975), [Experimental work]

Four castellated beams fabricated from W10x15 sections (10 in. deep, 15 pounds per foot) were tested to validate a numerical analysis approach to determine the optimum expansion ratio based on both elastic and plastic methods of analysis. All beams were simply supported and were subjected to a concentrated load at mid-span. The span and weld lengths were kept constant, but the depths were varied based on different expansion ratios. The ultimate loads were recorded, but no further discussion about the modes of failure were given.

Hosain and Speirs (1973), [Experimental work]

Beams fabricated from twelve 10B15 beams (alternative designation for W10x15) were tested to investigate the effect of web opening geometry on the mode of failure and ultimate strength of castellated beams. Specimens A-2, B-1, C and D were subjected to two

concentrated point loads, and the remainder of the beams had a single concentrated load at mid-span. All beams were simply supported while adequate lateral bracing and full depth bearing stiffeners were provided. The exceptions were beams C and D, where partial depth stiffeners were used. The loads based on the ultimate load values were obtained during the experiments.

Specimens A-1, A-2 and B-3 failed by the formation of plastic hinges at the corners of the web openings, where both shear and moment forces were acting. As for specimens G-1, G-2 with flanges of Canadian Standard S16.1-94 class 1 section properties and G-3, a class 2 section, yielding of the flanges in the region of high bending moment led to flexural failure. The class section properties were calculated for beams in an attempt to investigate if any local buckling possibilities were present. Beams B-2, C and D failed prematurely due to web buckling directly under the point of load application. A similar failure was exhibited by Beam B-1. This failed by web buckling under the concentrated load before a Vierendeel mechanism had formed. Thus, beams B-1, B-2, C and D were obtained from further study.

Hosain and Speirs (1971), [Experimental work]

The main focus of this experiment was to study the yielding and rupture of welded joints of castellated beams. The experimental investigation consisted of testing six simply supported beams under various load systems. A single concentrated point load was applied to beams E-2, E-3, F-1 and F-3 and two concentrated loads were used for beams E-1and F-2. Full depth-bearing stiffeners and sufficient lateral bracings were provided to prevent premature buckling. The final reported results were calculated on the basis of directly measured yield and ultimate shear stress values. The measured shear stresses were higher than theoretical values which would have been anticipated from tensile coupon tests, as a result of strain hardening. The prediction of ultimate strength based on web-post yield, could therefore be expected to be very conservative. Sudden weld rupture accompanied by violent strain energy release was the common mode of failure for all beams.

Bazile and Texier (1968), [Experimental work]

Two series of beams, four HEA360 and three IPE270 sections were tested to failure. The objective of the experiment was to develop a further understanding of different beam characteristics and properties as well as geometries of castellated beams. The simply supported beams were tested under eight uniformly distributed concentrated loads. Three test loads, P1, P2 and P3 were reported to describe the different phases of the load-deflection diagram of each beam. Loads P1 and P2 defined sudden changes in slope and P3 was the ultimate load. Flange and weld yield stresses were obtained from beam coupon tests and full depth stiffeners were provided at support reaction points. Beams A, B and E failed under web buckling in the zone of maximum shear. The beams F and G failed by lateral torsional buckling and were thus omitted from further study herein. Beams C and D

had deep (200mm) plates at mid-depth and were reported as failing by web-post buckling. Estimated strengths of the posts of these two beams, using the column strength formula of CSA (1994) assuming widths were equal to the maximum and minimum actual widths, bracket the ultimate test value of the concentrated load. It was therefore evident that these were compression buckling failures under the action of the concentrated loads acting directly above the un-stiffened web-posts. Since this mode was not being studied, these two beams were not considered further.

Halleux (1967), [Experimental work]

Five types of beams with different geometrical properties, all fabricated from the IPE300 rolled steel sections, were tested to destruction under two equal concentrated loads applied as the third-span points. The experimental failure load was based on the intersection of the tangent to the linear part of the load against a deflection diagram with the tangent to the almost horizontal part of the curve. Measured yield stresses were not reported. Calculations in the reference were based on the yield stress of the material, that is, 24 kg/mm^2 (235 MPa), and it was later stated that yield stresses determined from un-reported tensile tests were significantly higher than the above mentioned value. Therefore, due to the uncertainty in the yield stresses the reported results must be treated circumspectly.

Sherbourne (1966), [Experimental work]

This test program was designed to investigate the interaction of shear and moment forces on the behaviour of castellated beams under varying load conditions. The test arrangement consisted of simply supported beams with full depth bearing stiffeners under load and reaction points. Seven tests were performed which ranged from pure shear to pure bending loading conditions. Load against deflection curves were given in the paper. From these the ultimate loads and loads obtained from the intersection of tangents to the initial linear part and to the almost linear post-yield part were obtained. Beam E1, subjected to a single concentrated load at mid-span, failed through extensive yielding of the throat at mid-depth of the web-post between the first and the second web opening. Beam E2 was designed to investigate the effect of pure moment and was subjected to two concentrated point loads. The failure of this beam occurred outside the central control section and was associated with extensive yielding in the end zones experiencing both shear and moment forces. The web opening closest to the load was the most severely damaged. Web buckling was the mode of failure of specimen E3 in the zone of maximum shear, under the two point loading system. Specimen E4 was designed to study the effect of pure shear across the central web opening. The deflection curve demonstrates considerable strain-hardening, and web buckling was the observed mode of failure. Beams L1, L2 and L3 were tested under pure bending moments. The first two were reported to fail by flexural mechanisms. L3 was also reported to fail by flexural mechanism; however, lateral torsional buckling was also associated with the failure mode.

2.3.3 Perforated beams of other materials

In this sub-chapter, a literature review on non-composite perforated non-steel beams is conducted. Such beams are commonly used as wall studs, floor joists and components for roof trusses in both commercial and residential construction as well as in other applications such as aeronautical, mechanical and shipbuilding engineering. Calibrations against finite element tests are presented in some cases.

Elhajj, Fuller and Crandell (1999), [Experimental work]

In this comprehensive research, a total of 67 cold formed steel (CFS) joist specimens were tested, including 15 for pure bending, 15 for pure shear, 16 for combined bending and shear, and 21 for web crippling. Design recommendations were based on full-scale C-section beams having web height-to-thickness ratios as high as 200 and web opening depth-to-web depth ratios as high as 0.8. The test program considered rectangular and circular web openings. Three web opening diameters were studied: 5.1cm and 10.2cm web openings in 15.2cm deep C-section beams and 15.2cm web openings in 20.3cm deep C-section beams. All steel materials had a minimum specified tensile strength of 228 and 345MPa. The total load was applied at one or two points equidistant from the reactions.

When thin steel bending members with web openings were subjected to loads, three failure modes had occurred: (a) bending, (b) shear, or (c) web crippling. Test results have shown that the equations of the American Iron and Steel Institute (AISI) Design Specification could be used to conservatively predict the moment capacity, shear strength, web crippling strength, and combined bending and shear strength of CFS joist members (C-sections) with folded web openings. Based on the findings of this study, the following conclusions were made regarding the behaviour of CFS floor joists with relatively large, stiffened web openings (i.e. folded edges) under gravity loads:

- The presence of web openings with folded edges did not reduce the ultimate shear and bending.
- The presence of web openings did not promulgate any failure.
- Shear strength was not a controlling factor in the design of CFS joists with folded openings as identified in this report.

Shan, LaBoube and Yu (1996), [Experimental work]

In this paper, the behaviour of standard industrial cold formed steel C-shaped members with web openings subjected to combined bending moment and shear force was studied. In total, sixty-eight beam tests having three different elongated web opening sizes (3.81x10.16cm, 1.91x10.16cm, and 1.91x5.08cm); located at the mid-height of the web,

were examined. Also, two common standard C-section depths of 6.35 and 9.21cm were used. Each beam specimen was tested as a simply supported beam subjected to a concentrated load at mid-span. Particularly, this study included the loading conditions of bending, shear, web crippling, and the combination of these.

It was noticed that, for each test specimen the failure shear load for each web was ¼ of the maximum mid-span load. The corresponding mid-span bending moment was computed on the basis of the failure shear load and the member's span length. It is worth mentioning, that for these test specimens which failed by the combined bending and shear behaviour, the failure pattern was defined by a bending failure at mid-span and a diagonal shear failure around the corners of the web opening. These two failure patterns occurred simultaneously as the ultimate load was achieved.

Based on the outcome of this investigation, it was concluded that the interaction equation employed by the AISI specification, provided an adequate prediction, when the shear and bending capacities were modified to account the influence of the web opening.

2.3.4 Recommendations for research on non-composite perforated beams

Many researchers have experimentally studied perforated beams with various standard web opening shapes. Web opening shapes mainly found in the literature are hexagonal (in some cases with an extra mid-depth plate which then creates an octagonal shape), circular; rectangular; square or elongated (i.e. 'extended').

It was remarkable to note that octagonal web openings behave better than hexagonal ones and they also manufactured easier than circular web openings. From local FE studies it is also seen that web opening cut-outs with rhomboidal shapes lead to lower stresses than circular cut-outs, due to the very narrow opening length at the top and bottom tee-sections.

The majority of the latter studies were based on global analyses with a combination of forces acting on the perforated beams. Therefore, many parameters were included simultaneously and so unpredicted failure modes were obtained without a way to really tell which parameter affects the results in every particular case. The advantage is that there are plenty of real life test results, and so the FE models can be validated against them and then create local FE parametric studies which will non-dimensionalised the results and resolve the complex problems.

Also, the web opening size limits in this research programme will be generally increased to 80% of the beams' final depth instead of 75%; which was the maximum size found in the past. The purpose of this is to either lighten the beam or to increase their final depth after profile cutting manufacturing procedure.

FE research has only been established in the last decade, and it is concerned with various standard web openings. After reviewing the literature research on non-composite perforated

beams, it is believed that various standard as well as non-standard web openings need to be further investigated. In addition, all geometric parameters defining the web opening shapes as well as the beam section sizes are going to be examined separately. Besides, all experimental and FE studies in this research are going to be conducted on UB sections, for direct use from practical engineers in UK.

2.4 REVIEW OF COMPOSITE BEAMS

2.4.1 Introduction

Many research papers with experimental, analytical and FE work found in the literature review regarding conventional composite flooring systems, as shown in **Figure 2.8(a)** below. Conventional composite flooring systems have been already incorporated by many design code procedures (**EC4 Part 1.1: 2004, ANSI/AISC 360-05: 2005** and **PR NBR 8800: 2007**).

For conventional composite construction, with the slab connected on top of the flange of the perforated beam (**Figure 2.9**), research has shown that the concrete slab contributes significantly to the vertical shear strength. Tests on short-span composite plate girders with web openings are initially carried out by Narayanan et al. (1989) and Roberts and Al-Amery (1991). These tests showed that the shear strength of a composite plate girder is significantly higher than that of a steel plate girder alone, if adequate shear connectors (i.e. shear studs, etc.) are provided in the composite girder. In addition, the composite action under predominantly shear loading depends on the tensile or pullout strength of the shear connectors. Also, a limited shear connection between the slab and steel beam within the length of the web opening was found. Therefore, the low level compressive stress due to high shear forces in the concrete slab was the main problem. Analytical models including a contribution from the slab are proposed for determining the shear strength of composite plate girders. Experiments conducted by Clawson and Darwin (1982) and Donahey and Darwin (1988) indicated that the behaviour of composite beams with web openings is largely controlled by the shear-moment ratio at the opening. Darwin and Donahey (1988) proposed an equation to express the ultimate shear-moment relationship for composite beams with web openings.

However, structures such as high-rise residential buildings need shallow flooring systems, since the floor-to-floor height is a significant factor; especially in restricted city areas (Mullett and Lawson, 1993). The fact that a conventional composite beam is deeper than a reinforced concrete beam is a strong disadvantage. Hence, in several situations it was important to reduce the overall depth of the floor using partially encased composite beams such as in **Figure 2.8(b), (c)** and **(e)**. The entrapped concrete between the flanges of the beam also has other advantages, such as increased fire resistance, load carrying capacity,

local buckling stiffness and dramatic increase in the bending stiffness compared to conventional beams. Also, these composite beams with thin steel decks lying on the bottom steel flange are commonly used in steel structures. A lower construction cost compared to the reinforced concrete or the steel frame systems is obtained by using encased beams and hence eliminating the construction time and number of formworks and scaffoldings (Bernuzzi et al., 1996, Viest and Colaco, 1997, Hegger and Goralski, 2005 and Dipaola et al., 2006).

Comparing conventional composite flooring systems (**Figure 2.8(a)** and **2.9**) and partially encased composite beams (**Figure 2.8(b)**, **(c)** and **(e)**), it is seen that the concrete between flanges in the latter case increases the bending stiffness and reduces the vertical displacements. Despite the advantages in terms of structural behaviour and cost, the encased beam is a constructive solution not totally understood yet. In addition, the disadvantage of such partially encased composite beams is that their span is limited to less than 12m (ECCS, 1995) mainly because of its increased weight. Also, the beam-to-column connection is commonly pinned and is not suitable for moment resisting frames.

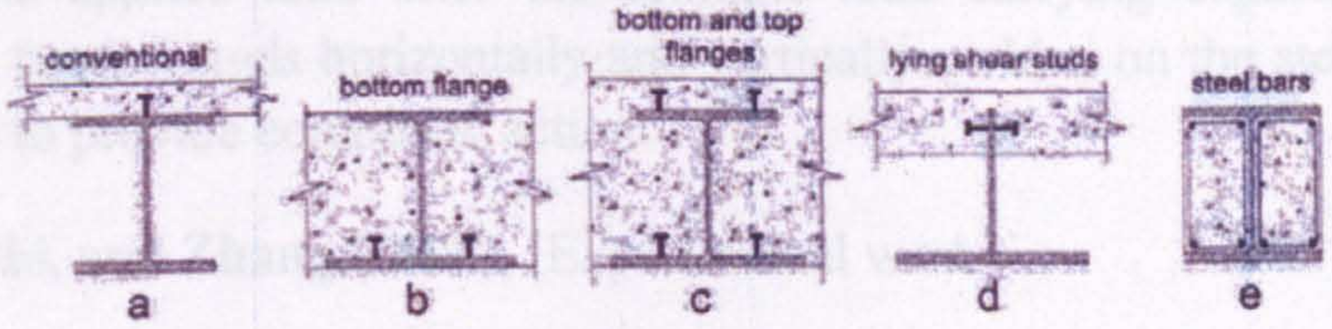

Figure 2.8: Examples of composite beams

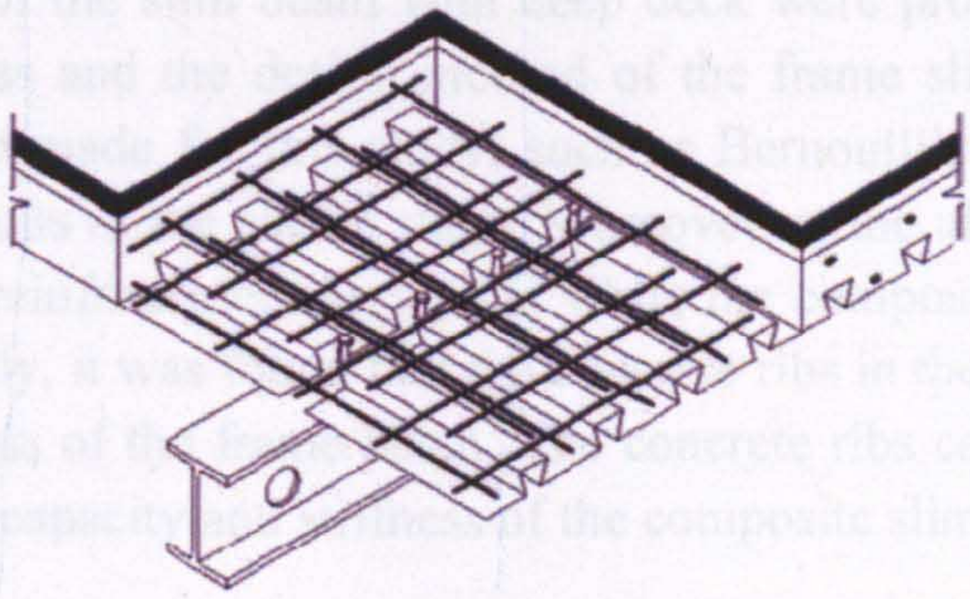

Figure 2.9: Conventional composite construction (Corus)

2.4.2 Partially encased steel perforated beams with concrete in-fill

While numerous research papers were found in the literature review regarding conventional composite flooring systems with the use of plane and perforated steel beams and partially

encased composite beams with the use of plain steel sections, only recently has very limited study been established on partially encased composite beams with the use of perforated steel sections. This allows for lighter construction as well as improved shear connection systems to be achieved as a result of the concrete pass through the web openings. In some cases shear reinforcement or other mechanical shear connectors pass through the steel web openings to enhance the composite shear connection.

2.4.2.1 Papers regarding composite action study

De Nardin and El Debs (2009), [Experimental work]

Investigation on the static behaviour of three partially encased composite beams with the use of perforated steel sections under flexural condition in the context of studying some alternative positions for the headed studs is conducted (**Figure 2.8**). Experimental results showed that the headed studs provide the composite action and increase the bending strength. Analytically, the specimens with headed studs can be considered ductile and the behaviour is almost elasto-plastic, while the specimen without shear connectors slightly decreased in the applied load after the ultimate load carrying capacity was reached. Therefore, both headed studs horizontally and vertically welded on the steel profile can be effectively used to provide composite action.

Wang, Yang, Shi, and Zhang (2009), [Experimental work]

Experimental investigation on the flexural behaviour of two specimens of composite slim frame beam with deep deck under monotonic loading was established. Based on the experimental results; formulas calculating the bending capacity and flexural stiffness in the hogging moment region of the slim beam with deep deck were proposed. Also, formulas for the equivalent stiffness and the design method of the frame slim beams were given. Important conclusions are made for this study, such as Bernoulli's principle is consisted with the experimental results in the elastic stage. Moreover, at the ultimate limit state steel flanges, webs as well as reinforcement bars yield while the composite beam demonstrates significant ductility. Finally, it was found that the concrete ribs in the deep deck make little contribution to the stiffness of the frame beam. The concrete ribs can be neglected during the calculation of loading capacity and stiffness of the composite slim beam.

Ju, Chun and Kim (2009), [Experimental work]

Newly developed partially encased composite beams using asymmetric steel sections with semi-hexagonal (trapezoidal) web openings were proposed and experimentally explored. Shear connectors were not used for the proposed composite beam. Instead, longitudinal shear strength was obtained through the bond strength of the interface between concrete and steel, and the bearing strength of the opened web area. In this paper, the flexural behaviour of the proposed beams was assessed using the simple beam test. For comparison,

a slim floor beam was tested. A bare steel beam was also tested to evaluate resistance under construction loads.

It was found that the ultimate strength of the proposed system exceeded the design value. Beams were failed due to concrete crushing in the compression zone without bond or local failure. Complete composite action before yield and partial composite action after yield is the design objective. Therefore, the proposed system was enabled to develop sufficient ductility, strength and consequently effective composite behaviour, without causing serviceability problems. In addition, the longitudinal shear strength of the proposed system consisted of the bond strength between the steel and the concrete and the bearing strength of the web opening area. Furthermore, the non-composite steel beam failed because of buckling at the upper flange.

2.4.3 Recommendations for research on partially encased perforated steel beams

In order to minimize the structural depth of the composite sections, steel perforated beams are designed to act compositely with floor slabs lying within the steel flanges (**Figure 2.10**). This is part of a wider research programme which takes place at City University, London and investigates the vertical shear strength due to the entrapped concrete between the steel flanges and the longitudinal shear strength due to the innovative shear connectors (i.e. shear studs on the web of the I-section, reinforcing tie-bars or service ducting passing through the web openings). The composite beams are called Ultra Shallow Floor Beams (USFB) and they are designed by ASD Westok Ltd.

The steel section is fabricated by welding two highly asymmetric cellular tee-sections together along the webs resulting in a large bottom flange. Either precast concrete floor units or profiled steel decking rest on the bottom flange of the USFB creating a very shallow floor beam construction system, thus minimising the overall structural depth. A special end diaphragm is used for deep decking floor applications so that the concrete fully surrounds the steel section, apart from the bottom flange. In-situ concrete fills the web openings as the floor slabs are cast.

Up to the present, there has been very limited information on this topic; even though this construction method has already been used in a few projects. More test data are needed for the rational development of an appropriate design method. In addition to that, advanced FE models are necessary to investigate composite beams with different material properties as well as to study in detail the effect of the shear bond between the steel and the concrete. Based on this model, different practical constructional features, such as composite beams with various web opening shapes and sizes, composite beams with asymmetric steel sections, as well as eccentric web openings would be easier investigated in the future. Moreover, currently engineers are strongly encouraged to examine the USFBs while full

structural advantages are offered by composite construction, such as providing some service integration.

In this research project, only the effect from the bond strength of the interface between the steel and the concrete as well as the bearing strength of the opened web area is explored and presented.

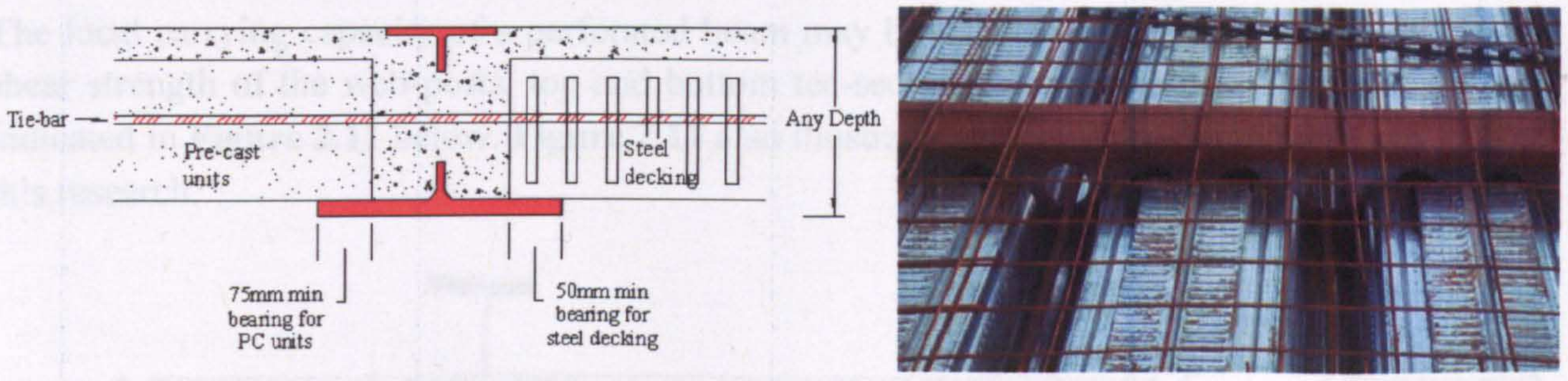

Figure 2.10: Cross-section configuration of the USFB (left) and deep decking floor application (right)

2.5 THEORETICAL BACKGROUND FOR THIS RESEARCH STUDY

2.5.1 Introduction

The load carrying capacity of a perforated beam is the smaller between its overall strength in flexure and lateral buckling, and the smaller among its local strength of the web-posts, top and bottom tee-sections. In practical applications, the beams are laterally restrained, causing local effects in the vicinity of the web openings to control the design. Therefore, a beam should be checked for both its overall and local strength for ultimate and serviceability limit states.

2.5.2 Overall strength

The overall beam behaviour should be checked for:

- Beam flexural capacity
- Beam shear capacity and
- Overall beam buckling

The overall flexural capacity is assessed by considering the plastic moment capacity of the cross section through the centre-line of the web opening.

The vertical shear capacity of the beam is also governed by the cross section through the centre-line of the web opening. The shear capacity is equal to the sum of the shear capacities of the top and bottom tee-sections. The horizontal shear capacity depends on the minimum cross sectional area of the web-post.

Beams without lateral restraint are likely to fail by lateral torsional buckling. In comparison to their parent solid (i.e. plain) web sections, perforated beams are more prone to buckle laterally because of the relatively deep and slender section and the reduced torsional stiffness of the web.

2.5.3 Local strength

The local carrying capacity of a perforated beam may be limited by the local bending and shear strength of the web-posts, top and bottom tee-sections. These likely weak areas are indicated in **Figure 2.11** below. **Figure 2.11** also illustrates the key parameters presented in this research.

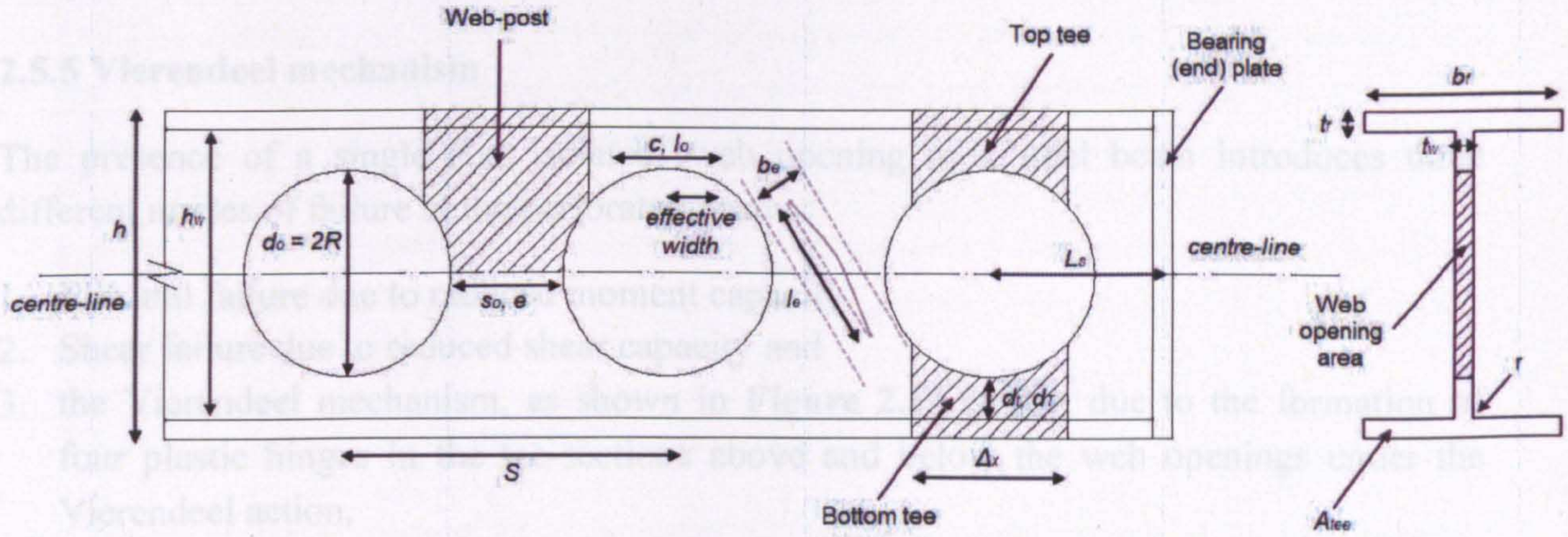

Figure 2.11: Cellular beam (key parameters)

2.5.4 Bending modes

Vierendeel bending is caused by the need to transfer the shear force across the web openings to be consistent with the rate of change of the bending moment along the beam. The flexural capacity of the top and bottom tee-sections under Vierendeel bending is critical. In the absence of local or overall instability, perforated beams with standard web openings have two basic modes of collapse, which depend upon the geometry and the position of the web opening. They are:

- Plastic tension and compression stress blocks in the top and bottom tee-sections in regions of high overall buckling (**Figure 2.12(a)**).
- Parallelogram or Vierendeel action due to the formation of plastic hinges at the four corners or at specific angles around the web opening, in regions of high shear (**Figure 2.12(b)**).

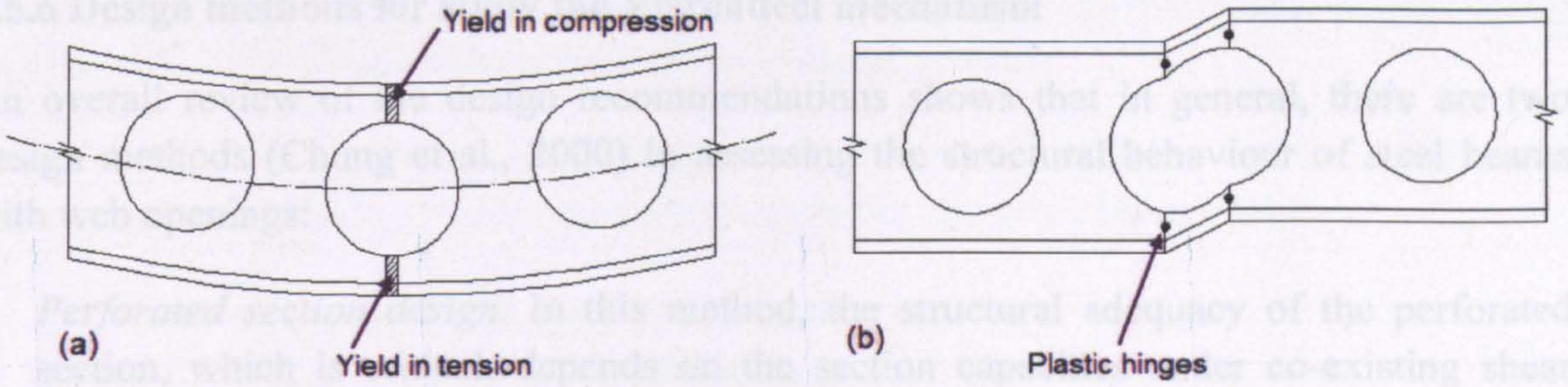

Figure 2.12: (a) Yielding due to high bending and (b) Yielding due to high shear (SCI publication 100, 1990)

2.5.5 Vierendeel mechanism

The presence of a single (i.e. isolated) web opening in a steel beam introduces three different modes of failure at the perforated beams:

1. Flexural failure due to reduced moment capacity
2. Shear failure due to reduced shear capacity and
3. the Vierendeel mechanism, as shown in **Figure 2.13** below, due to the formation of four plastic hinges in the tee-sections above and below the web openings under the Vierendeel action.

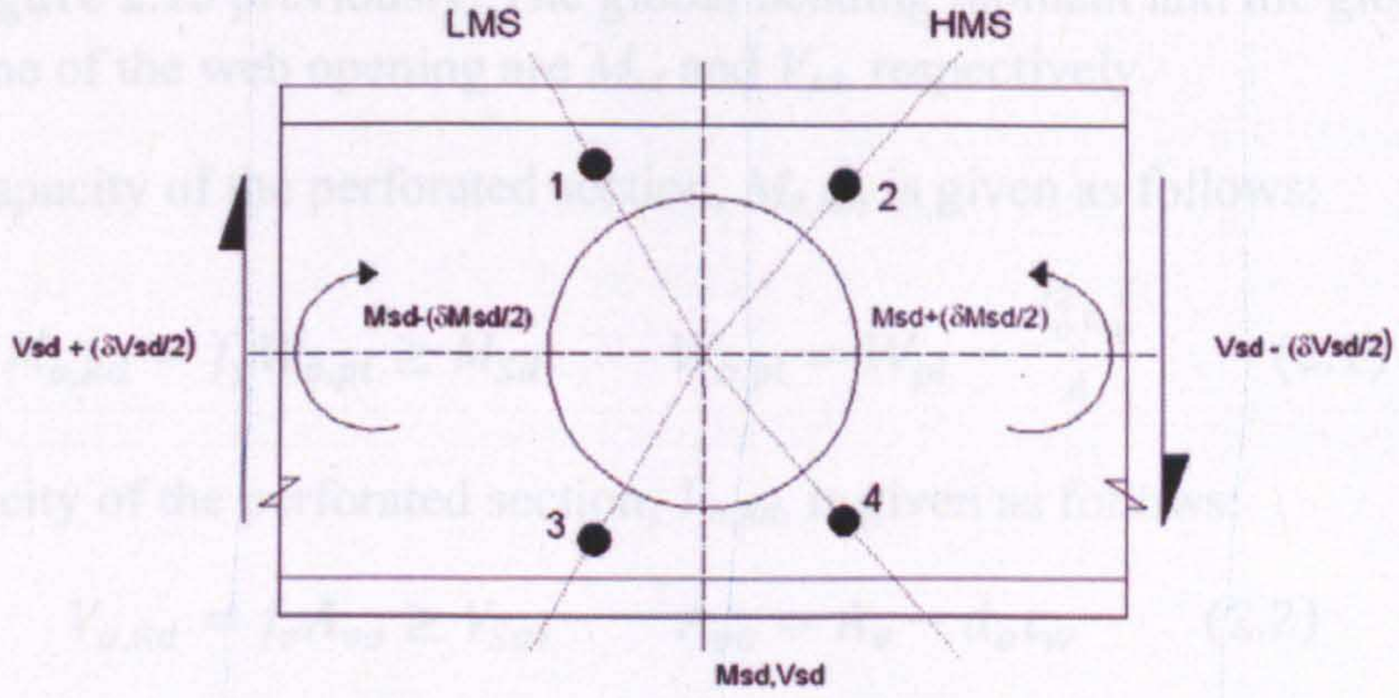

Figure 2.13: Vierendeel mechanism around the circular web opening and location of plastic hinges (Chung et al., 2000)

A failure mode due to a general Vierendeel bending may normally result in the formation of four plastic hinges in the vicinity of the web openings, following load redistribution after the initial plastic hinge formation at the low moment side (LMS) of the top tee-section (**Figure 2.13**). For particular web opening shapes, these critical positions can be found at the sharp-edged corners.

2.5.6 Design methods for study the Vierendeel mechanism

An overall review of the design recommendations shows that in general, there are two design methods (Chung et al., 2000) in assessing the structural behaviour of steel beams with web openings:

- *Perforated section design.* In this method, the structural adequacy of the perforated section, which is critical, depends on the section capacities under co-existing shear force and bending moment due to global actions. Shear-moment interaction curves can be used simply but the results are often considered as very conservative.
- *Tee-section design.* In contrast to the previous method, the perforated section is considered to be made up of two top or bottom tee-sections which are separated by a distance according to the height of the web opening (**Figure 2.14**). In this method all the global actions are represented as local forces and moments and the structural adequacy of the steel beams depends on the section capacities of the tee-sections under co-existing axial forces, shear forces and local moments. However, because of the complexity of the problems in this method, approximate design expressions could be presented and used in order to minimize the calculation effort, even if they are leading to conservative results.

2.5.7 Analytical study of Vierendeel mechanism

Consider a circular web opening of diameter d_o formed in a steel beam of overall depth h, as shown in **Figure 2.13** previously. The global bending moment and the global shear force at the centre-line of the web opening are M_{sd} and V_{sd}, respectively.

The moment capacity of the perforated section, $M_{o,Rd}$, is given as follows:

$$M_{o,Rd} = f_y W_{o,pl} \geq M_{Sd}, \qquad W_{o,pl} = W_{pl} - \frac{d_o^2 t_w}{4} \qquad (2.1)$$

The shear capacity of the perforated section, $V_{o,Rd}$, is given as follows:

$$V_{o,Rd} = f_v A_{vo} \geq V_{Sd}, \qquad A_{vo} = A_v - d_o t_w \qquad (2.2)$$

Where f_v taken as $\frac{0.577 f_y}{\gamma_{Mo}}$ and A_v is equal to ht_w conservatively according to **BS5950 Part 1.**

The value of material partial safety factor γ_{Mo} is mainly lying between 1 and 1.15 as it is indicated in the literature (Kala, 2007). In cases of using higher values than unity an overestimated approach is obtained.

It is worth mentioning, from the demonstration of the above formulas, that the reduction in the shear capacity is more pronounced when compared to the reduction in the moment

capacity, as the presence of the opening in the web reduces the shear area of the section significantly but the reduction to the section modulus is small.

Global actions on perforated sections result the tee-sections above and below the web opening to be subjected to three co-existing actions as shown in **Figure 2.14**:

- Axial force $N_{\varphi,Sd}$ due to the global bending moment, M_{Sd}
- Shear force $V_{\varphi,Sd}$ due to the global shear force, V_{Sd} and
- Local bending moment $M_{\varphi,Sd}$ due to the transfer of shear force across the opening.

When the perforated section is subjected under large M_{sd} and V_{sd} at the centre-line of the web opening, the formation of four plastic hinges at critical locations of the tee-sections under the co-existing $V_{\varphi,Sd}$, $N_{\varphi,Sd}$ and $M_{\varphi,Sd}$ takes place, as a result of the Vierendeel action. These forces are depicted in **Figure 2.14**.

At the cross-section with φ is equal to zero (pure bending moment case), the shear force $V_{o,Sd}$, the axial force $N_{o,Sd}$, and the bending moment $M_{o,Sd}$, could be evaluated as follows:

$$V_{o,Sd} = {}^{1}/_{2}\, V_{Sd} \qquad (2.3(a))$$

$$N_{o,Sd} = \frac{I_N - 2I_T}{I_N h_c} M_{Sd} \qquad (2.3(b))$$

$$M_{o,Sd} = \frac{I_T}{I_N} M_{Sd} \qquad (2.3(c))$$

It is assumed that the global shear force V_{Sd} is equally resisted by the top and the bottom tee-sections, in cases where the web opening is located away from any support or any concentrated load by a distance of at least twice the section depth. On the other hand, the bending moment M_{Sd} is assessed according to the deformation compatibility between the un-perforated section and the tee-sections under the global bending action (Liu and Chung, 1999).

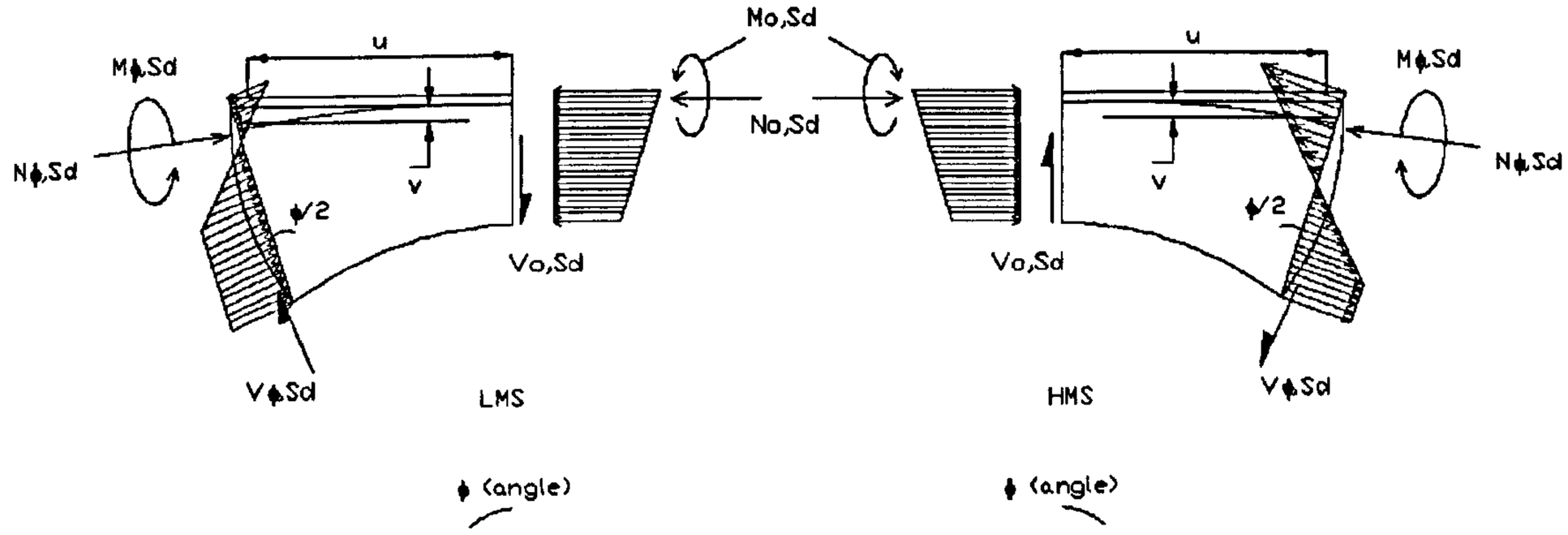

Figure 2.14: Local forces acting at the incline cross-section (Chung et al., 2000)

2.5.7.1 Plastic hinge formation at the low moment side (LMS) of the web opening

According to the geometry of a cross section, at a point of an angle φ from the vertical centre-line of the web opening, at the LMS of the web opening, the shear force $V_{\varphi,Sd}$, the axial force $N_{\varphi,Sd}$, and the bending moment $M_{\varphi,Sd}$ acting at the centroids of the tee-section are given as follows:

$$N_{\varphi,Sd} = N_{o,Sd}\cos\left(\frac{\varphi}{2}\right) + V_{o,Sd}\sin\left(\frac{\varphi}{2}\right) \qquad (2.4(a))$$

$$V_{\varphi,Sd} = N_{o,Sd}\sin\left(\frac{\varphi}{2}\right) - V_{o,Sd}\cos\left(\frac{\varphi}{2}\right) \qquad (2.4(b))$$

$$M_{\varphi,Sd} = V_{o,Sd}\mathrm{u} - N_{o,Sd}\mathrm{v} - M_{o,Sd} \quad (hogging) \qquad (2.4(c))$$

The resultant stress distribution under the co-existing actions is also depicted in **Figure 2.14**.

The increase in the angle φ results from the variation of the stress distribution from elastic to plastic under the increased local bending moment M_{φ} and hence the stress in the web of the top tee-section to be more compressive than that in the flange. However, usually cross sections with large φ are elastic due to large web depth. Particularly, the formation of a plastic hinge at a cross section announces that the actions on this section are large while the capacities are not. In this case the value of φ is designated as φ_p. The same concept also fits the bottom tee-section.

The local moment capacity of the tee-sections may be evaluated according to a linear interaction formula as follows:

$$\frac{N_{\varphi,Sd}}{N_{\varphi,Rd}} + \frac{M_{\varphi,Sd}}{M_{\varphi,Rd}} \leq 1.0 \qquad (2.5)$$

According to **Eurocode 3: Part 1.1**, in the presence of high shear force $V_{\varphi,Sd}$, both the axial force $N_{\varphi,Sd}$ and the moment capacity $M_{\varphi,Sd}$, will be reduced and re-designed as $N_{v\varphi,Sd}$ and $V_{v\varphi,Sd}$, respectively. Particularly, the position of the plastic hinges is dependent on the presence of high axial and shear forces. Moreover, during the evaluation of the moment capacities of the tee-sections against the Vierendeel action, the depth of the web depends on the positions of the plastic hinges.

2.5.7.2 Plastic hinge formation at the high moment side (HMS) of the web opening

In **Figure 2.14** above, the top tee-section at the HMS of the web opening is also illustrated. On that side in contrast with the LMS, as the direction of the shear force is reversed, the flange of the top tee-section has a higher compressive stress than that in the web. Hence,

the co-existing forces at cross-sections of the plane with an angle φ from the vertical are given as follows:

$$N_{\varphi,Sd} = N_{o,Sd}\cos\left(\frac{\varphi}{2}\right) - V_{o,Sd}\sin\left(\frac{\varphi}{2}\right) \qquad (2.6(a))$$

$$V_{\varphi,Sd} = N_{o,Sd}\sin\left(\frac{\varphi}{2}\right) + V_{o,Sd}\cos\left(\frac{\varphi}{2}\right) \qquad (2.6(b))$$

$$M_{\varphi,Sd} = V_{o,Sd}\mathrm{u} + N_{o,Sd}\mathrm{v} + M_{o,Sd} \quad (sagging) \qquad (2.6(c))$$

Due to the axial force on the moment capacity of the tee-section, when the stress in the web is smaller than that in the flange, the HMS plastic hinges will form at a higher load level of V_{Sd} and M_{Sd} than those at the LMS. Therefore, the interaction curves for the formation of the LMS and HMS at cross sections become apparent when there are large co-existing moment and shear forces, i.e. $\frac{V_{Sd}}{V_{o,Rd}} \approx \frac{M_{Sd}}{M_{o,Rd}}$, due to the Vierendeel action. However, there is little difference between LMS and HMS curves at cross-sections under pure shear or bending.

2.5.7.3 Comparison between LMS and HMS

In order to demonstrate the structural performance of perforated steel beams with circular web openings, a shear-moment interaction curve under global actions was developed by Chung et. al (2000). For a global bending moment M_{Sd}, a global shear force V_{Sd} always corresponds, which causes failure of the perforated section.

A typical interaction curve relating the shear utilization ratio $\frac{V_{Sd}}{V_{o,Rd}}$ and the moment utilization ratio $\frac{M_{Sd}}{M_{o,Rd}}$ is plotted in **Figure 2.15**. This refers to a simply supported beam with a web opening at various different positions along the beam span every time. The steel beam is UB 457x152x52 (S275) and the diameter of the circular web opening d_o, is equal to $0.75h$.

It was noticed that the angle φ_p varied from 0° for cross sections under pure moment to approximately 28° for cross sections under pure shear. The typical value of φ_p was taken as 25° conservatively. **Figure 2.15** showed that the simplified method (i.e. φ_p equal to 25°) match very well with the curve LMS. Therefore, it was considered as an effective and conservative simplification for the formation of the LMS plastic hinges. Moreover, comparing the curves it was found that the LMS plastic hinges always form before the HMS plastic hinges. However, after the formation of the LMS plastic hinges, there was load redistribution across the web opening and the HMS plastic hinges were formed in a slightly different way, as it was anticipated.

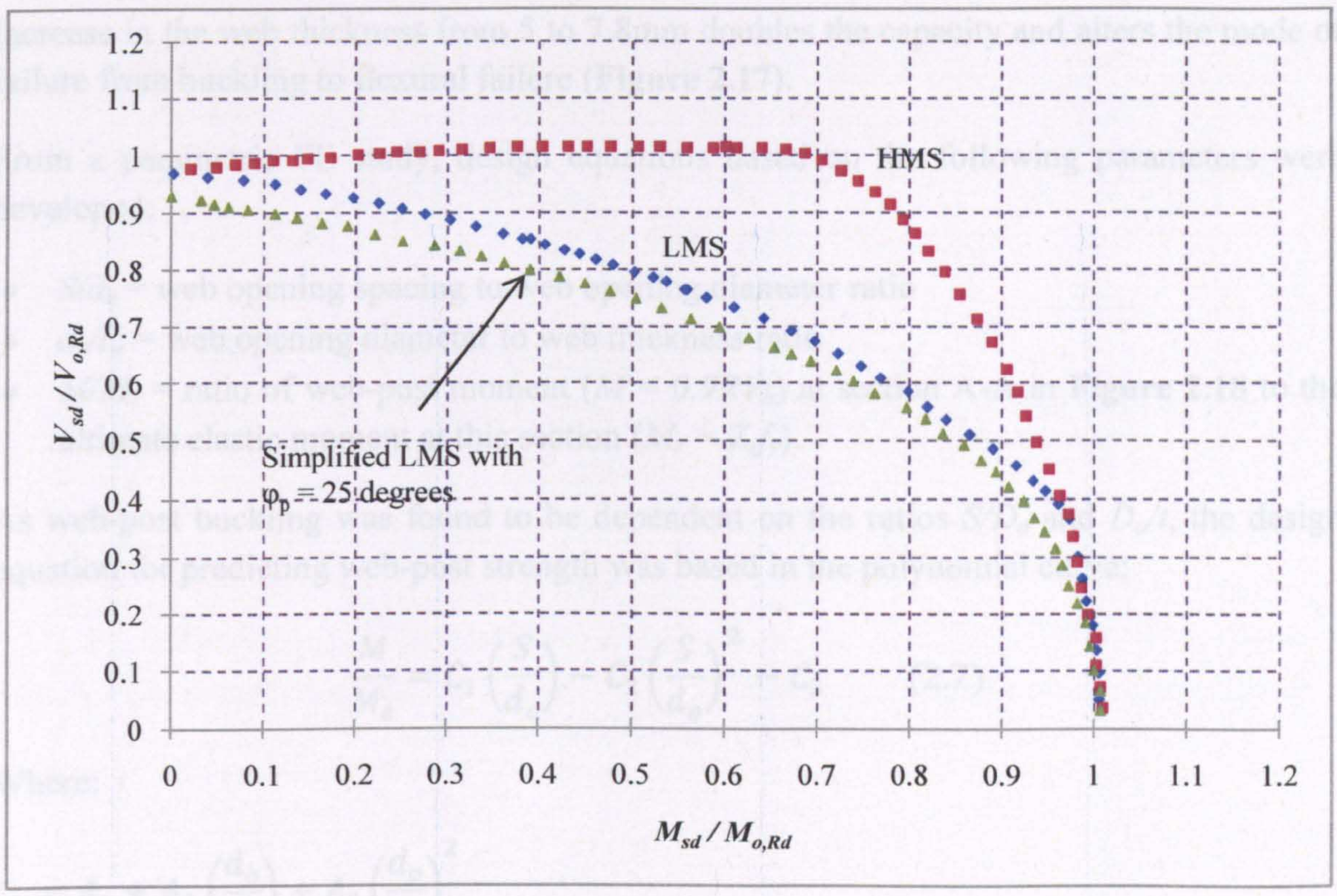

Figure 2.15: Comparison of LMS and HMS curves (Chung et. al, 2000)

2.5.8 Web-post strength

The ultimate strength of a web-post is governed by either a flexural failure caused by the development of a plastic hinge in the web-post, or a buckling failure of the web-post. The failure mode depends on the geometry of the web-post, as governed by the web thickness and the ratio S/d_o (web opening spacing to web opening diameter ratio).

The web-post between adjacent web openings is subject to high stresses due to:

- Horizontal shear on its narrowest width
- Compression due to transfer of vertical shear and
- Bending due to Vierendeel action.

The interaction is more complex because of the possibility of buckling due to combinations of all these effects.

A series of non-linear finite element analyses were undertaken to develop design curves (Ward; SCI P-100, 1990). Assuming elasto-plastic behaviour and using a substructure comprising a web-post and tee-sections, the design capacity was examined. The analytical results for a full model of one-half of the symmetrical beam, and a substructure comprising a web-post and tee-sections were in close agreement (**Figure 2.16**). It was found that an

increase in the web thickness from 5 to 7.8mm doubles the capacity and alters the mode of failure from buckling to flexural failure (**Figure 2.17**).

From a parametric FE study, design equations based on the following parameters were developed:

- S/d_o = web opening spacing to web opening diameter ratio
- d_o/t_w = web opening diameter to web thickness ratio
- M/M_e = ratio of web-post moment ($M = 0.9RV_h$) at section A-A in **Figure 2.18** to the ultimate elastic moment at this section ($M_e = Z_e f_y$).

As web-post buckling was found to be dependent on the ratios S/D_o and D_o/t, the design equation for predicting web-post strength was based in the polynomial curve:

$$\frac{M}{M_e} = C_1\left(\frac{S}{d_o}\right) - C_2\left(\frac{S}{d_o}\right)^2 - C_3 \qquad (2.7)$$

Where:

$$C_1 = A_1 + A_2\left(\frac{d_o}{t_w}\right) + A_3\left(\frac{d_o}{t_w}\right)^2$$

$$C_1 = A_4 + A_5\left(\frac{d_o}{t_w}\right) + A_6\left(\frac{d_o}{t_w}\right)^2$$

$$C_1 = A_7 + A_8\left(\frac{d_o}{t_w}\right) + A_9\left(\frac{d_o}{t_w}\right)^2$$

By using the latter design equations and the analytical finite element results, strength curves were generated and used for the web-post flexural and buckling strength check. In SCI publication 100, these equations are presented and are valid only for $1.08 < S/D_o < 1.5$.

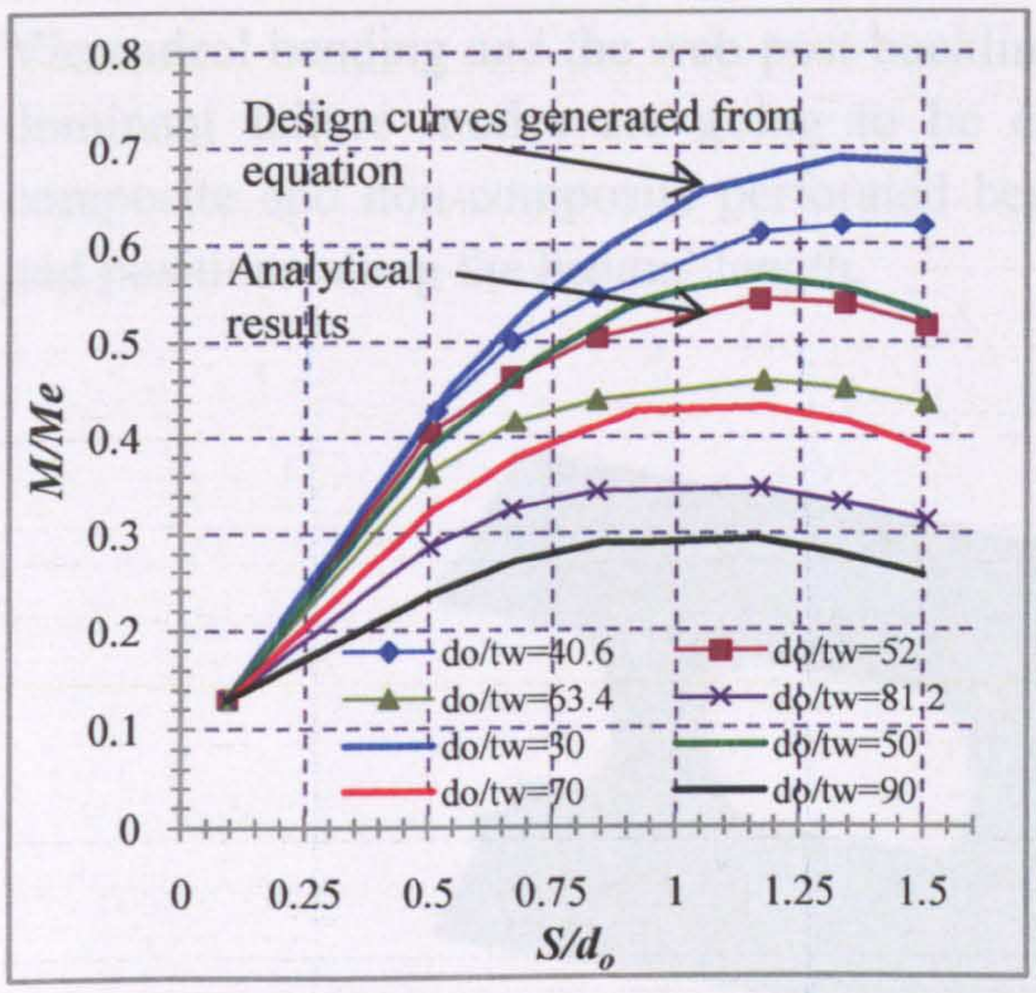

Figure 2.16: Analytical results and Curves (SCI publication 100, 1990)

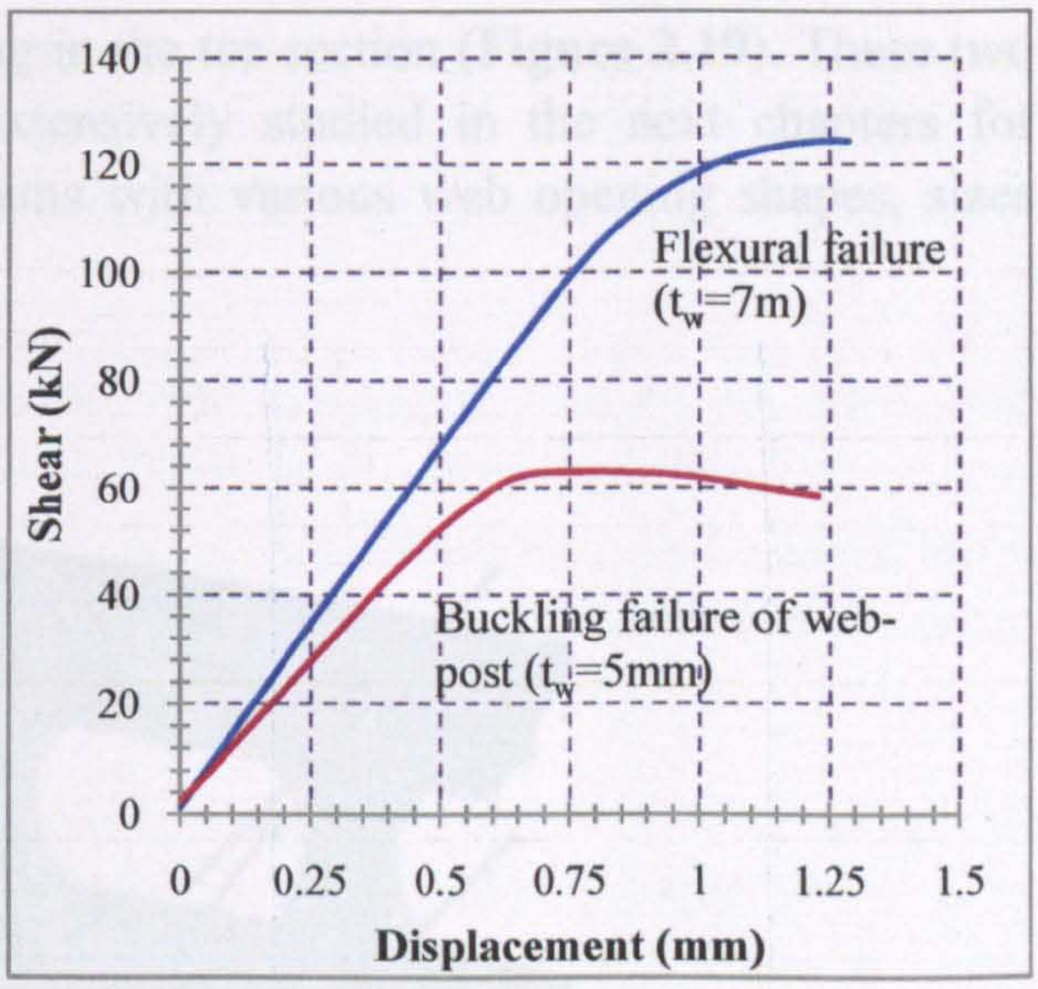

Figure 2.17: Load-Deflection plots Design

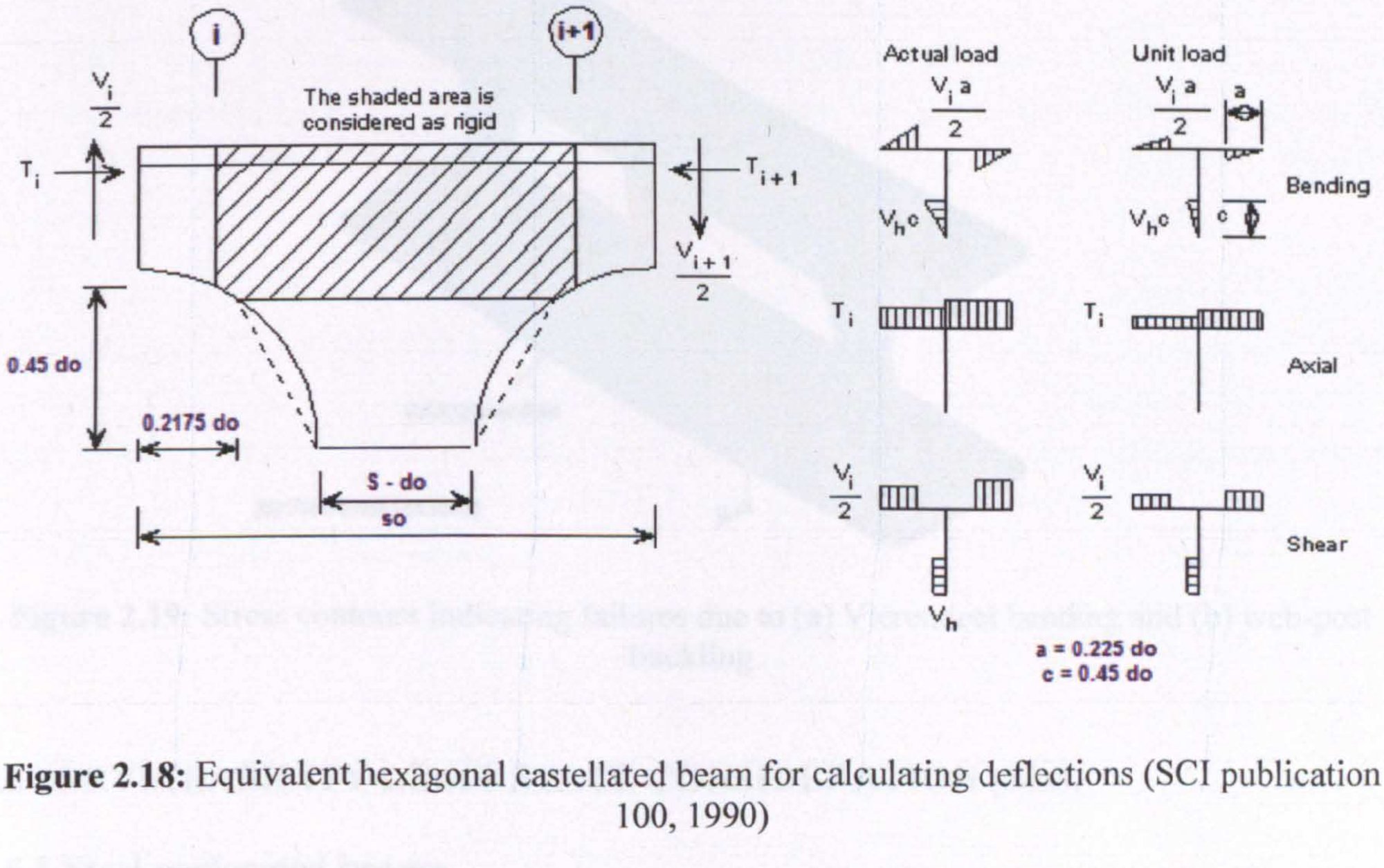

Figure 2.18: Equivalent hexagonal castellated beam for calculating deflections (SCI publication 100, 1990)

2.5.9 Summary

To summarize, it is shown that final failure is dominated by Vierendeel failure for high axial force in the tee-section, and web-post failure for low axial force in the tee-section. This is confirmed by Von-Mises stress patterns, which indicate the critical positions of the

Vierendeel bending and the web-post buckling in the tee-section (**Figure 2.19**). These two dominant failure modes are going to be extensively studied in the next chapters for composite and non-composite perforated beams with various web opening shapes, sizes and positions along the beams' length.

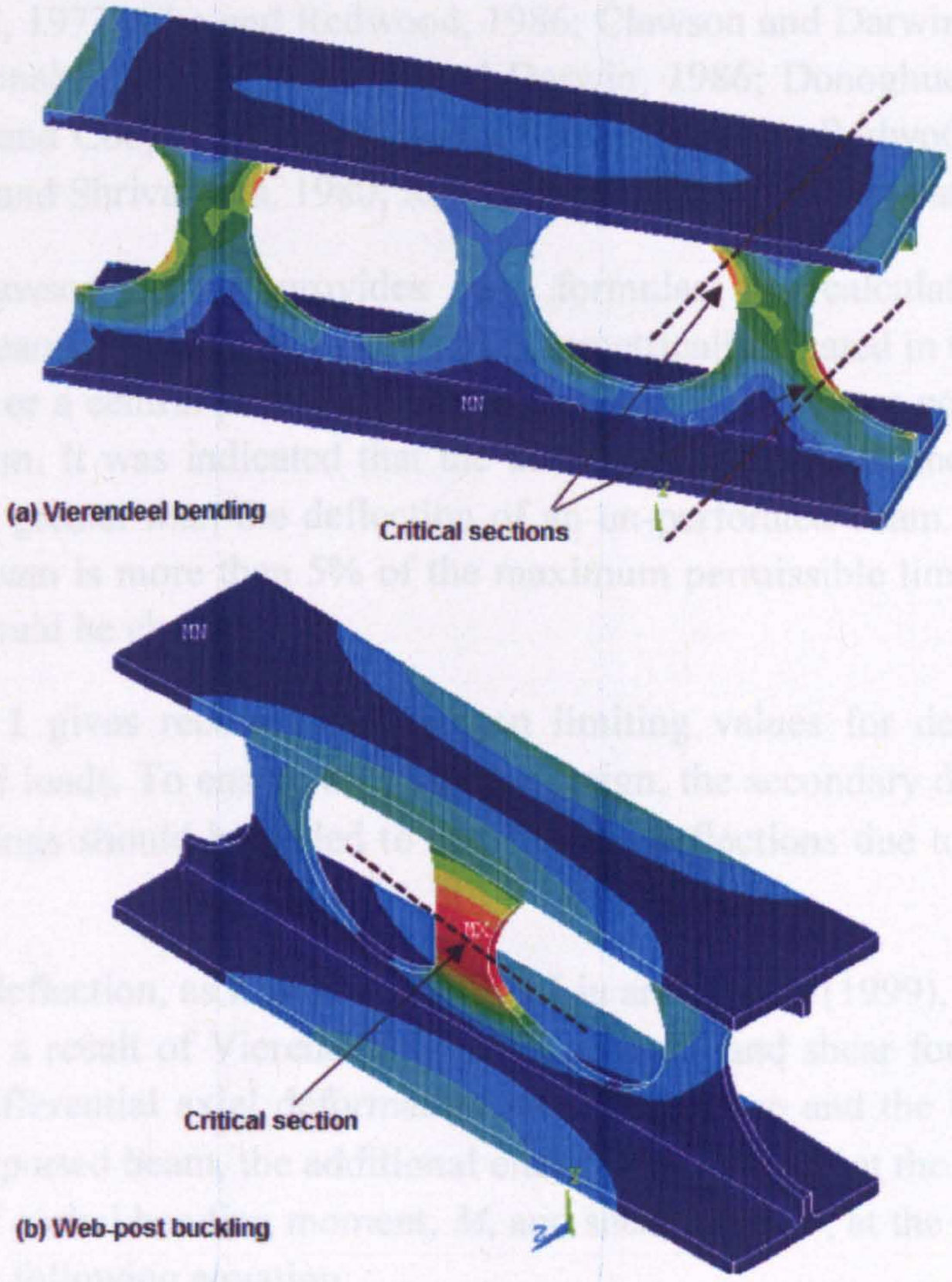

Figure 2.19: Stress contours indicating failures due to (a) Vierendeel bending and (b) web-post buckling

2.6 SERVICEABILITY LIMIT STATE CONSIDERATION (SLS)

2.6.1 Steel perforated beams

The web openings contribute to increased deflections due to elastic effects caused by the local variations in bending and shear stiffness along the beam. The existence of web openings reduce the local moment of inertia of beams which results in an increase in the maximum deflection. Also, web openings result in a local decrease of the shear stiffness which leads to high deflections at the length of the web openings. The first effect is often

greatest when the web opening is located in a region of high moment, while the latter when the web opening is in a region of high shear. It is not necessary to check for local stresses in the vicinity of the web openings at the serviceability limit state because local yielding has a negligible effect on deflections.

Several design procedures have been developed for structural steel beams with web openings (ASCE, 1973; Cho and Redwood, 1986; Clawson and Darwin, 1980; Darwin and Lucas, 1990; Donahey, 1987; Donahey and Darwin, 1986; Donoghue, 1982; Dougherty, 1980; Kussman and Cooper, 1976; Redwood, 1968 and 1971; Redwood and Poumbouras, 1984; Redwood and Shrivastava, 1980; Redwood and Wong, 1982; Wang et al., 1975).

CIRIA/SCI (Lawson, 1987) provides two formulas for calculating the additional deflections for beams with two web openings symmetrically located in the span; either with uniform loading or a central point load, while the web openings are positioned at the mid-depth of the beam. It was indicated that the additional deflections under these conditions are only slightly greater than the deflection of an un-perforated beam. If the deflection of the perforated beam is more than 5% of the maximum permissible limit, then a heavier or deeper section could be chosen.

BS 5950: Part 1 gives recommendations on limiting values for deflections under un-factored imposed loads. To ensure an adequate design, the secondary deflections occurring at the web openings should be added to the primary deflections due to overall bending of the beam.

The increase in deflection, as it was found from Liu and Chung (1999), is mainly due to the local bending as a result of Vierendeel bending moment and shear force, and the rotation caused by the differential axial deformation between the top and the bottom tee-sections. For a simply supported beam, the additional elastic deflection δ_v at the web opening due to a combination of global bending moment, M, and shear force, V, at the web opening can be calculated by the following equation:

$$\delta_v = \frac{M}{EI_N}\left(L_s\Delta x - \frac{\Delta x^2}{2}\right) + \frac{V\Delta x^3}{24EI_T} \qquad (2.8)$$

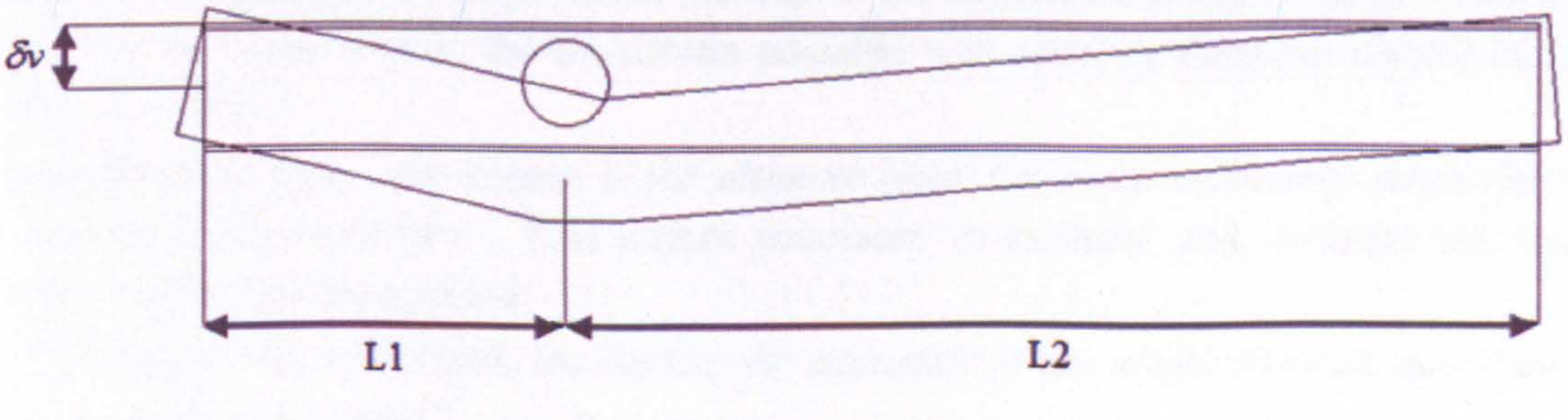

Figure 2.20: Additional deflection due to web opening (Liu and Chung, 1999)

2.6.2 Composite beams

When composite beams with perforated steel sections (conventional composite flooring systems) are considered, engineers need to know the magnitude of additional shear and bending deflections due to each web opening existence. SCI (2008) has suggested that 3% additional imposed load deflection should be allowed for each web opening, provided that the composite section at these web openings also satisfies the resistance criteria for shear, overall bending and local (or Vierendeel) bending. This extra deflection value was based on observations from analyses, and from a series of composite beam tests with stiffened and un-stiffened large rectangular web openings, carried out by Lawson et al. (1992). However, this approach is very conservative where circular web openings are used. Also, it was noticed that additional deflections could be neglected when web openings with diameters smaller than *0.7h* are used, whereas the anticipated extra deflection for web openings with diameters equal to *0.8h* is 2.5 times greater than the ones with diameters equal to *0.7h*. Moreover, when a series of web openings along the beam is considered, the additional deflection is typically evaluated to be between 5 and 15%.

In **BS5950**, deflections are calculated using an appropriate modular ratio, depending on the proportion of variable loads considered as permanent. Deflections are also increased due to slip. According to **EC3** the deflection limits in SLS are taken as: (i) *span/300* for imposed load and (ii) *span/250* for total load.

2.7 RECOMMENDATIONS FOR SPECIMEN CHOICE

In the literature by Lagaros et al. (2008) was found that the 'maximum diameter of a circular opening should not exceed 0.75 times the final depth of the beam. An investigation of rational depths of castellated steel I-beams has recently been conducted (Dervinis and Kvedaras, 2008) and the following conclusions have been made:

- *"When the web thickness is 6mm and the web depth increases, the ultimate load remains almost the same. This happens due to local stability of the web. However, when the web thickness increases, the influence of the web depth is larger."*
- *"When the diameter of perforation increases, the ultimate load decreases."* Hence, in order to be conservative, the maximum possible web opening diameter should be used (e.g. d_o=*0.8h*).
- In addition to that, *"the bigger is the ultimate load, the more it declines when the web opening depth increases"*. This makes necessary to evaluate and compare the results when high loads are applied.
- *"The bigger the web depth, the higher the influence of the perforation diameter on the load carrying capacity"*.

2.8 CONCLUSIONS

Non-composite beams:

The above review has demonstrated the structural behaviour of non-composite perforated steel beams with standard typical and elongated web openings of circular, hexagonal and rectangular shapes. Nevertheless, a non-significant amount of work has been conducted on perforated steel beams with non-standard web openings such as elliptical web openings shapes, combination of web opening shapes, and rotated axes of the web openings that provide an eccentricity to the top and bottom tee-sections. Such web openings could be useful for architecturally pleasing structures and special applications with constructional and cost impact. Moreover, non emphasis was given to the manufacturing procedure of such beams and their improvement in terms of cost. In this research programme the manufacturing procedure will be directly related to the structural performance of the perforated beams.

In the literature review the discussion was mainly focused on perforated beams with large web openings, however the maximum web opening depth found was 75% of the beam's final depth. In this research programme the maximum web opening size will be increased to 80% in order to integrate a higher number of services, lighten the structural form and lower the cost of manufacture, transportation and erection. Also, low weight structures are always of great interest in other engineering applications for various purposes.

Although in the above review global analyses of non-composite perforated beams have been extensively reported and the results were somehow reliable, the combination of forces acting in the vicinity of the web openings, with many parameters included simultaneously, lead to unpredicted failure modes without a way to determine which parameter affects the results in every particular case. Hence, generally accepted design methods have not been established due to complexity of perforated beams and their associated modes of failure. This abundant experimental work on perforated beams with standard web openings can be used to compare and validate the new FE models. Numerous FE studies with an increased number of geometric and material parameters will provide non-dimensionalised results that resolve the complex problems. All experimental and FE studies in this research programme are going to be conducted on UB sections, for direct use from practical engineers in the UK, while for most of the experimental work undertaken in the review, American steel section properties were used.

Composite beams:

In regard to the review with studies of composite beams, conventional composite flooring systems (**Figure 2.8**) have been examined in the past. However, when perforated steel beams were used, they were lying under the concrete slab. Very limited studies have been found in regard to the partially encasement of perforated steel beams. On the other hand, in

this research programme a new structural form of composite beams will be introduced. Such beams allow for lighter construction. Also, improved shear connection systems will be achieved as a result of the concrete pass through the web openings. In addition, the structural depth of these composite sections is minimized as the steel perforated beams are designed to act compositely with floor slabs lying within the steel flanges (**Figure 2.10**). In real applications shear reinforcement and mechanical shear connectors such as either shear studs on the web, anchorage tie-bars, or ducting will pass through the steel web openings to enhance the steel-concrete shear connection. However, shear reinforcement and mechanical shear connectors are not going to be used in this thesis. The percentage of the vertical shear enhancement of the perforated steel beams due to the concrete infill is only under investigation. Until now, there has been very limited information on this topic, even though this construction method has already been used in a number of projects. More test data are needed for the rational development of an appropriate design method. In addition, advanced FE models are necessary to investigate composite beams in order to study in detail the effect of the shear bond between the steel and the concrete. Based on this model, different practical constructional features, such as composite beams with various web opening shapes and sizes and composite beams with asymmetric steel sections would be easier to investigate in the future. In this research project, only the effect from the bond strength of the interface between the steel and the concrete as well as the bearing strength of the opened web area will be explored and presented.

In general, experimental work and FEM studies are necessary to widen the research on non-composite and composite perforated steel beams, providing data and test results to future researchers. Furthermore, non-dimensionalised results and empirical design methods will be proposed for the ease of use from practical engineers.

CHAPTER 3

VIERENDEEL STUDY ON NON-COMPOSITE PERFORATED BEAMS

3.1 INTRODUCTION

Investigation of the Vierendeel mechanism in steel perforated beams with various standard and novel non-standard web openings is presented in this chapter. As it is aforementioned in **sub-chapter 1.8.2** the application of the FE methodology is beneficial in this research programme. Numerous beam models need to be examined in order to obtain accurate results as there is very narrow research on such perforated beams with non-standard web opening shapes. Also, various parameters need to be isolated and investigated in order to understand the significance of their effects and in turn enhance the performance of perforated beams. FE solution provides a fast and cheap method of investigating structural forms in depth mainly looking at stresses and deflections and the results can be reliable after validation. The validation of the FE model is carried out through comparison with experimental work conducted in the past. An elaborated FE model is then established, with both material and geometrical non-linearity so that load redistribution across the web openings and formation of Vierendeel mechanism (i.e. four plastic hinges in the vicinity of the web openings) is taking place. The overall shear force and overall bending moment is also investigated by the effect of the interaction.

Furthermore, the load carrying capacities of Universal steel beams of various mid-range section sizes are examined. The latter beams are of steel grade S275, for the ease of comparison with literature as well as for conservative reasons. However, the results are non-dimensionalised. Only one web opening at each side (i.e. half-span) of the beam is provided, while its position is changed in order to obtain different shear-moment interactions at the centre-lines of the web openings for every case. It should be noted that the web openings are formed by cut-out manufacturing procedures.

In addition to the introduction of the non-standard web opening shapes, the maximum web opening size is now 80% of the final beam's depth; instead of 75% which was the maximum found in the literature. Also, in contrast to the previous studies; a bilinear material model is used to record the structural behaviour and the development of plasticity in tension or compression at a higher load level. The exact position (angles) of

the plastic hinges is also under consideration and consequently empirical design formulas are going to be developed for practical engineers. In conclusion, the geometrical factors which influence the structural behaviour of the perforated beams are going to be thoroughly assessed.

The investigation is divided into the following parts:

1. *Validation of the FE model with an experimental work from literature:*

The construction of the finite element model which is appropriate for the Vierendeel study is described. The mesh refinement study follows in order to find an optimum element size for such analyses, in regards to the accuracy of the results and the time of the analysis. The FE model is then compared with the experimental work conducted in the literature (Redwood and McCutcheon, 1968), to validate the modelling technique and ensure the reliability of the results. Input data, boundary conditions and type of analysis, are provided. The FE software package ANSYS v11.0 is used for modelling.

2. *Validation of the FE model with a FE work from literature:*

A FE model of a steel perforated beam with circular web openings found in the literature (Chung et. al, 2000) and modelled according to part 1 above. Once again the results are compared and validated, while important recommendations are followed for part 3.

3. *Parametric FE study of the Vierendeel mechanism in perforated sections:*

After validation against the experimental work from the literature, a non-dimensional shear-moment interaction curve, namely FEM curve, is established for steel beams with various web opening shapes and sizes as well as mid-range section sizes.

4. *A simple design method:*

A proposed simple shear-moment interaction curve is then developed for practical design of steel perforated beams; based on the general design theoretical model found in the literature (Chung et. al, 2000).

3.2 VALIDATION OF FE MODEL WITH AN EXPERIMENTAL WORK

3.2.1 FE model

The finite element model is validated against the test data of two steel I-section beams with single circular web openings, reported by Redwood and McCutcheon (1968). In **Figure 3.1**, test specimens with their geometrical details are depicted.

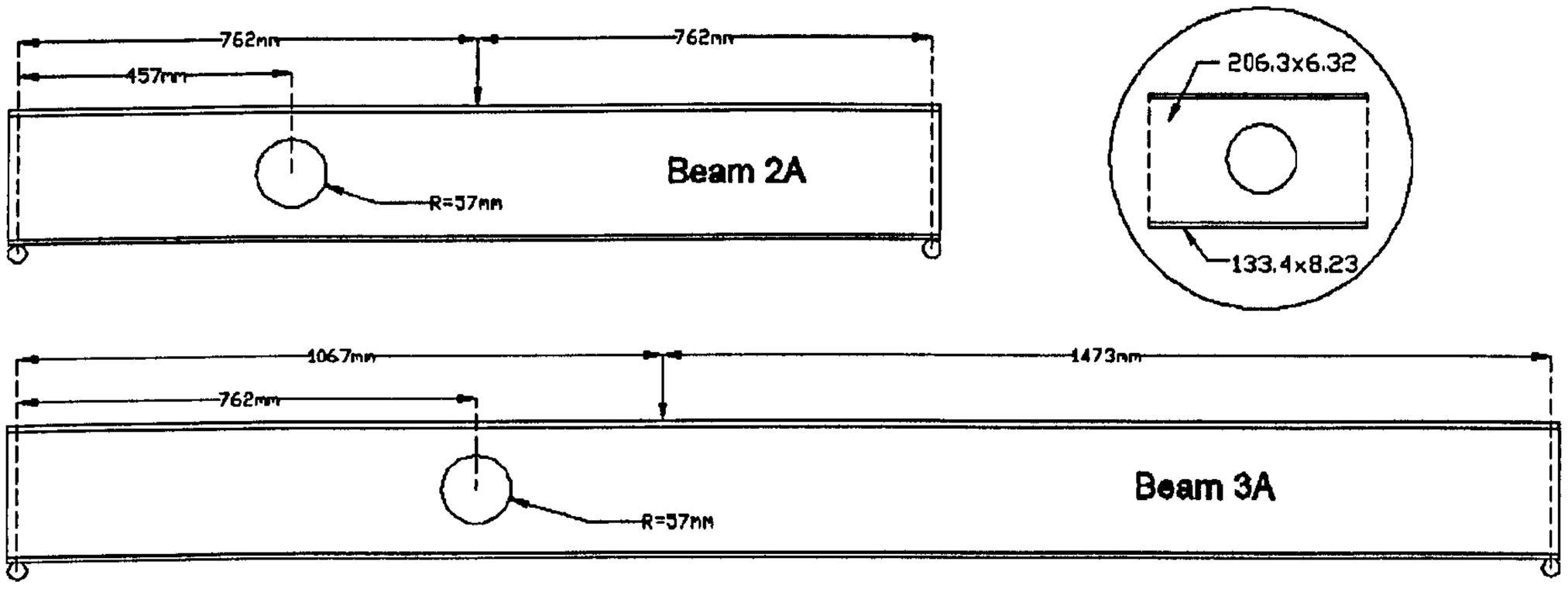

Figure 3.1: Geometrical properties of the test specimens

In order to simulate the structural behaviour of the above steel beams with circular web openings, a finite element model is established as follows:

- With material non-linearity incorporated into the finite element model, it is capable of fully mobilizing the moment capacities of the tee-sections under co-existing axial and shear forces due to global action. The elastic modulus, *E*, assumed to be 200GPa. A bi-linear stress-strain curve is adopted in the material modelling of steel together with Von-Mises yield criterion (**Appendix 3**) and the kinematic hardening rule which is suitable for most metals, including steel.

- Moreover, when geometric non-linearity is incorporated into the finite element model, large deformation in the model is accurately predicted, allowing load redistribution in the web across the web opening after initial yielding. Thus, the Vierendeel mechanism with the formation of four plastic hinges in both the tee-sections above and below the web openings can be investigated in detail.

3.2.2 Material properties

The material properties of the steel beams as reported by McCutcheon (1968) are presented in **Table 3.1** below.

Measured Material Strengths		Beam 2A	Beam 3A
Flanges	Yield Strength, f_y (MPa)	352	311
	Tensile Strength, $f_{ult.}$ (MPa)	503	576
Web	Yield Strength, f_y (MPa)	376	361
	Tensile Strength, $f_{ult.}$ (MPa)	512	492

Table 3.1: Material properties of the steel beams taken from coupon tests

3.2.3 Mesh refinement

Convergence is one of the most overlooked issues that affect accuracy, namely; mesh refinement. This refers to the size of the elements required in a model to ensure that the results of an analysis are .not affected by changing the size of the mesh.

The rate of change of stress is dictated by the rate of change of load or geometry in the region of interest. Areas at which the load or geometry change; will require a more detailed mesh to give the same level of accuracy as a coarse mesh in a region of more uniform stress. In the subsequent models, the most interesting areas are the vicinity of the web openings. The convergence curve for this model is shown below, **Figure 3.2**.

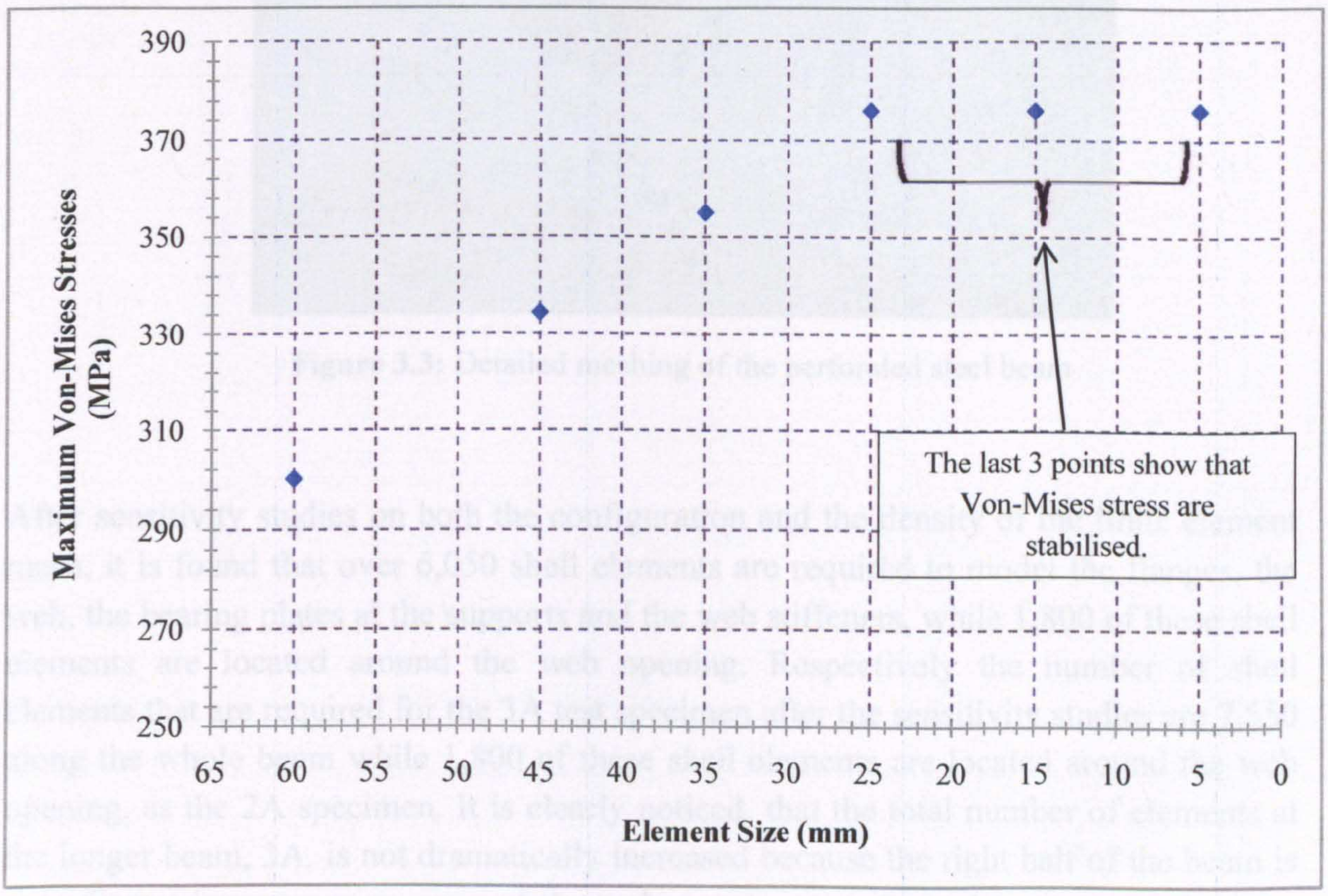

Figure 3.2: Local mesh refinement with a "six-point convergence curve"

An element size of 25mm is chosen for the meshing of the area in the vicinity of the web opening. No attempt to use a finer element is made, because this will result in a time consuming study and a transition region will be necessary.

It is worth mentioning that the error estimation for the displacements is satisfied easier with mesh refinement compared to the error of the stresses, since a 4-noded element is used, as is shown below.

3.2.4 Meshing

In **Figure 3.3** the FE model of a 2A test is illustrated, where the flanges and the web of the steel beam are modelled with an iso-parametric 4-noded quadrilateral plastic shell

element, SHELL181. A circular web opening is formed in the web with refined mesh configuration in order to avoid discontinuities in stress contours across element boundaries. The same element size and type is used for the 3A test specimen, as well.

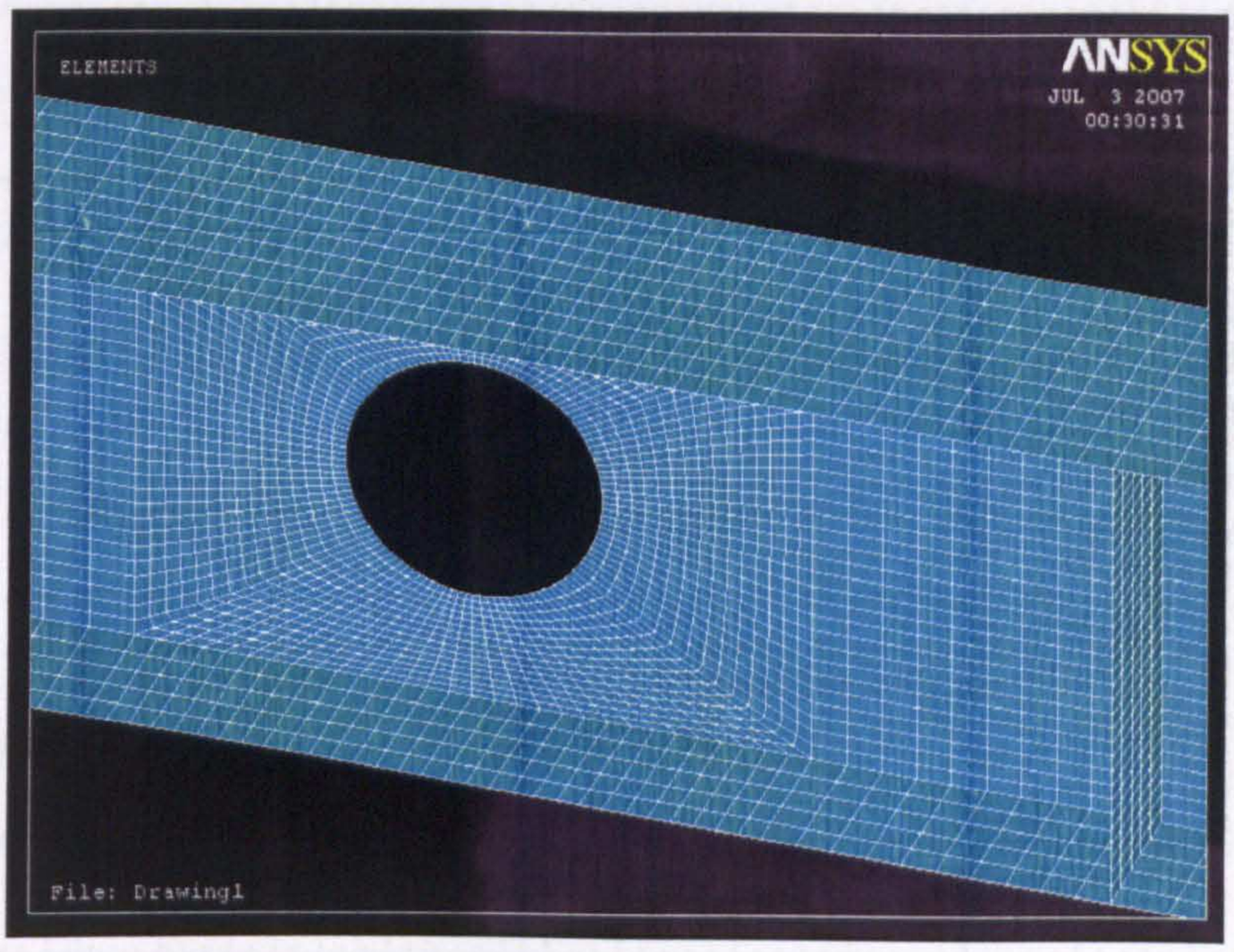

Figure 3.3: Detailed meshing of the perforated steel beam

After sensitivity studies on both the configuration and the density of the finite element mesh, it is found that over 6,050 shell elements are required to model the flanges, the web, the bearing plates at the supports and the web stiffeners, while 1,800 of these shell elements are located around the web opening. Respectively the number of shell elements that are required for the 3A test specimen after the sensitivity studies are 7,550 along the whole beam while 1,800 of these shell elements are located around the web opening, as the 2A specimen. It is clearly noticed, that the total number of elements at the longer beam, 3A, is not dramatically increased because the right half of the beam is not of great importance as none of the web openings are formed; so coarser elements are utilised. The full Newton-Raphson solution procedure is used to analyze the beam during the entire deformation history.

During the numerical investigation, it is necessary to ensure that the finite element models fail only at the perforated sections, similar to the corresponding real tests, and failure in other parts of the beam including overall instability is prohibited. Moreover, the web openings are free from any boundary effects or point loads.

3.2.5 FE Results

For both tests, the bending moment against mid-span deflection curves obtained from the finite element modelling are plotted in **Figure 3.4** together with the measured test data from the literature for a direct comparison. It is shown that both the maximum moment capacities of the perforated sections and the deformation characteristics of the

beams are modelled satisfactorily. This provides confidence in the use of the developed FE model.

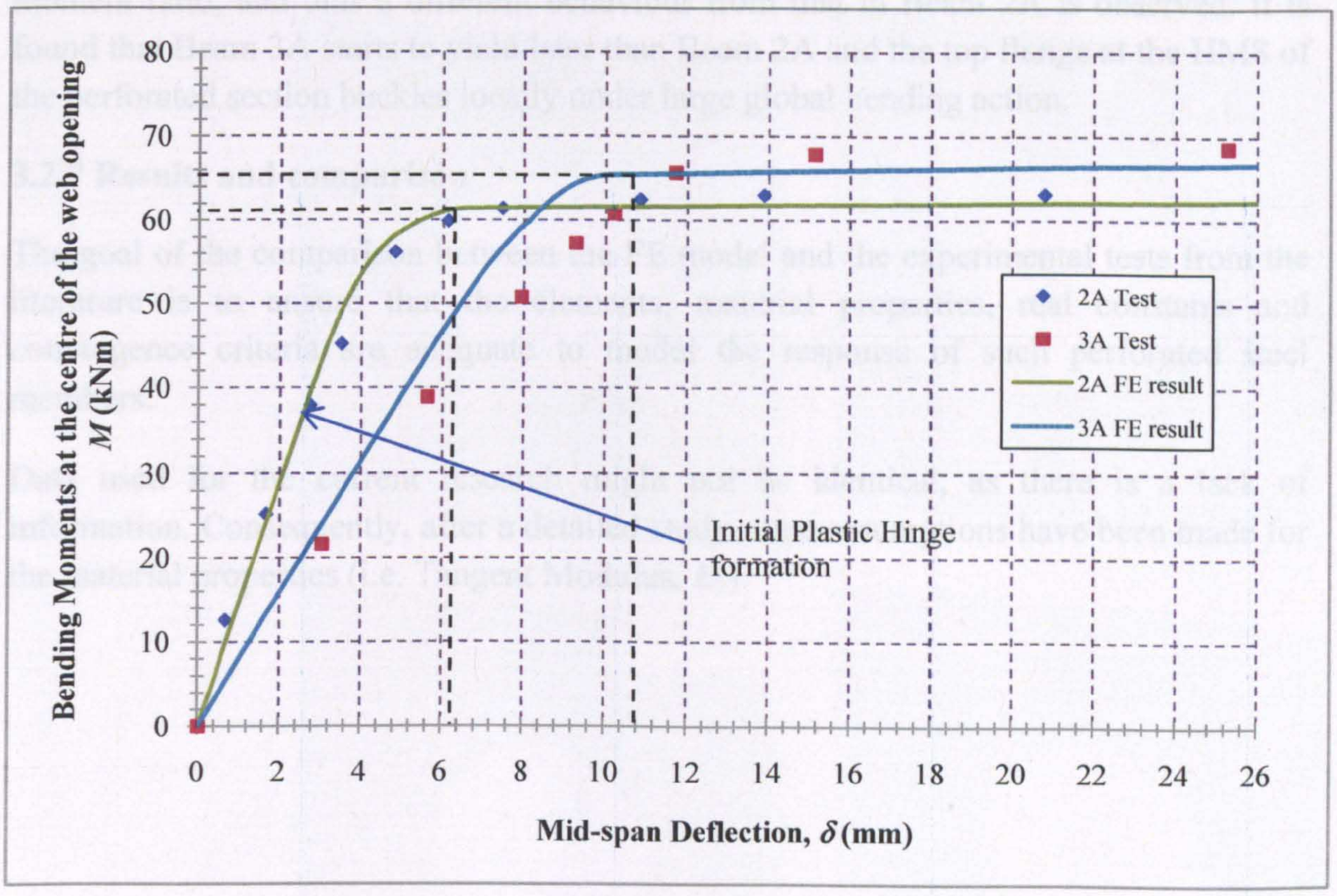

Figure 3.4: Comparison of load-deflection curves for tests 2A and 3A

3.2.6 Yielding under Vierendeel mechanism

After the non-linear (material and geometric) analysis, it is interesting to examine the stress distribution of the perforated beams at both first yield and failure conditions for instance of Beam 2A, as shown in **Figure 3.5**.

As is depicted in **Figure 3.5**, the first yield approximately appeared in the web of the tee-sections at cross sections with $\varphi=30^o$ and $\varphi=45^o$. At the same time, a small amount of shear yielding is also slightly depicted in the web of the tee-sections at cross sections with $\varphi=0^o$. However, this does not create a collapse mechanism and the beam continues to carry additional loading until Vierendeel moment is large enough to cause extensive yielding in the tee-sections.

As it is clearly seen in **Figure 3.5** and Von-Misses stresses at failure point both the webs and the flanges of the tee-sections at the HMS are extensively yielded. However, at the LMS, only the webs of the tee-sections are yielded while the stress level of the flanges reaches around 70% of the yield strength of the HMS. Finally, as it is shown, Beam 2A failed with the formation of four plastic hinges, two of them fully at HMS and another two partially at LMS.

Regarding test Beam 3A; while the beam section and the web opening are similar to those in Beam 2A, the location of the web opening gives rise to a different shear-moment ratio, and thus a different behaviour from that in Beam 2A is observed. It is found that Beam 3A starts to yield later than Beam 2A and the top flange at the HMS of the perforated section buckles locally under large global bending action.

3.2.7 Results and comparison

The goal of the comparison between the FE model and the experimental tests from the literature is to ensure that the elements, material properties, real constants and convergence criteria are adequate to model the response of such perforated steel members.

Data used for the current research might not be identical, as there is a lack of information. Consequently, after a detailed study some assumptions have been made for the material properties (i.e. Tangent Modulus, E_T).

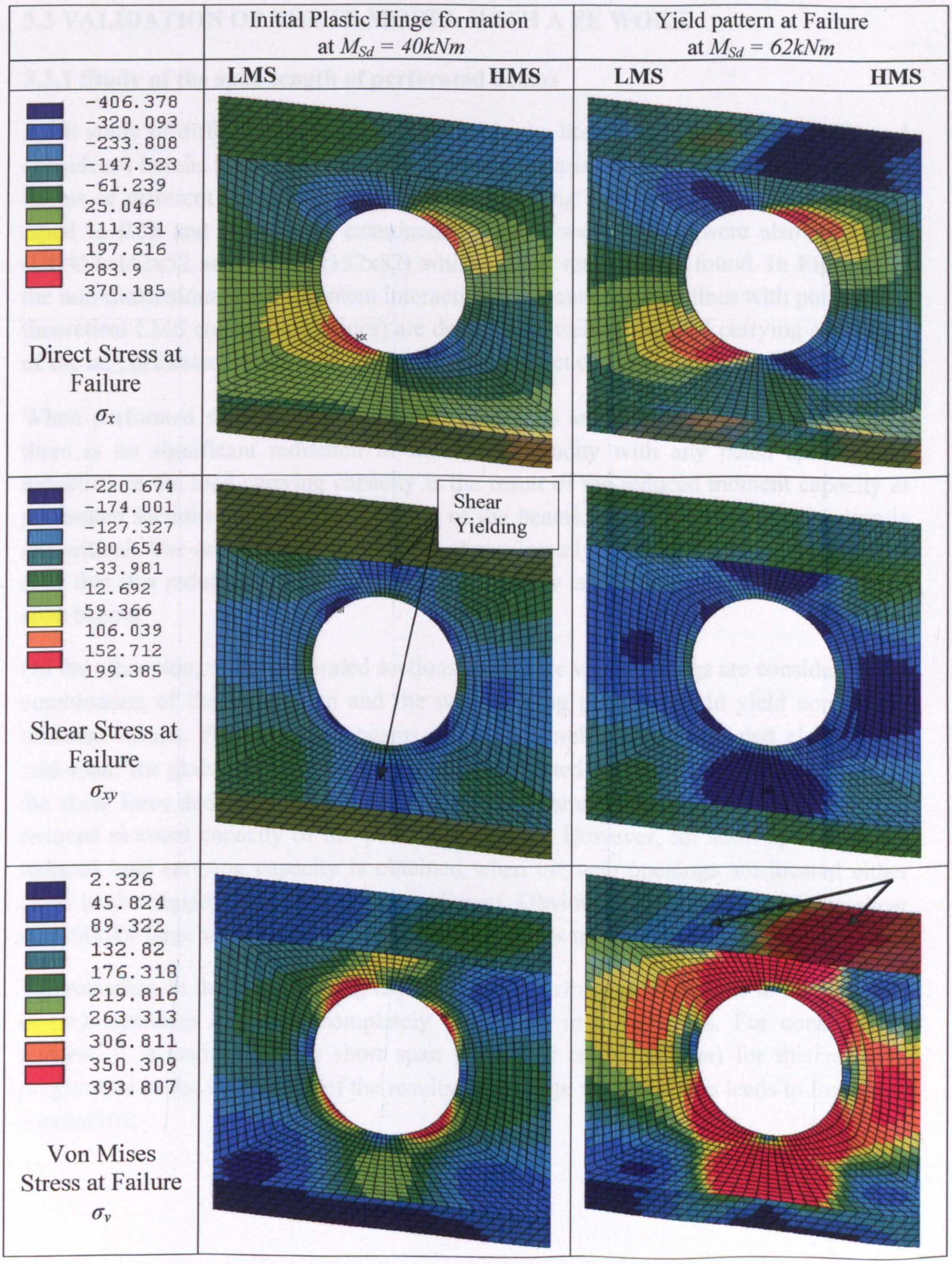

Figure 3.5: Stress distribution at perforated section in Beam 2A

3.3 VALIDATION OF THE FE MODEL WITH A FE WORK

3.3.1 Study of the span length of perforated beams

A FE study of different spans was conducted in the literature (Chung et. al, 2000) and considered herein. The load carrying capacity comparisons of perforated sections with beams of different spans (5, 6, 7.5 and 10m), having various web openings sizes (d_o equal to *0.5h* and *0.75h*) was examined. Different section sizes were also examined (UB457x152x52 and UB457x152x82) while similar results were found. In **Figure 3.6** the non-dimensional shear-moment interaction FEM curves (solid lines with points) and theoretical LMS curves (dotty lines) are depicted as well as the load carrying capacities of the un-perforated sections (dashed lines) for a direct comparison.

When perforated sections with small web openings are considered, it is noticed that there is no significant reduction in the shear capacity with any beam span. Some reduction in the load carrying capacity is the result of the reduced moment capacity at perforated sections close to the mid-span of the beams, where the Vierendeel action is not critical. The area of this reduction is approximately $1/3^{rd}$ of the beam's span. It is seen that this reduction in the load carrying capacity is of a higher magnitude in short span beams.

On the other side, when perforated sections with large web openings are considered, the combination of the beam span and the web opening position could yield completely different results. For long span beams (>7m) and web openings located close to the mid-span; the global bending moment at the perforated section increases quickly while the shear force decreases steadily. Therefore, the beams tend to fail in flexure due to a reduced moment capacity of the perforated section. However, for short span beams a reduced load carrying capacity is obtained when the web openings are located either close to the supports or close to the mid-span. Obviously, the reduction of the shear capacity for large web openings close to the support is more severe.

The reduction in the load carrying capacity of the perforated beams due to the presence of web openings might be completely eliminated in some cases. For conservative reasons, it is decided to use short span perforated beams ($L=5m$) for this research programme as the fluctuation of the results using large web openings leads to important conclusions.

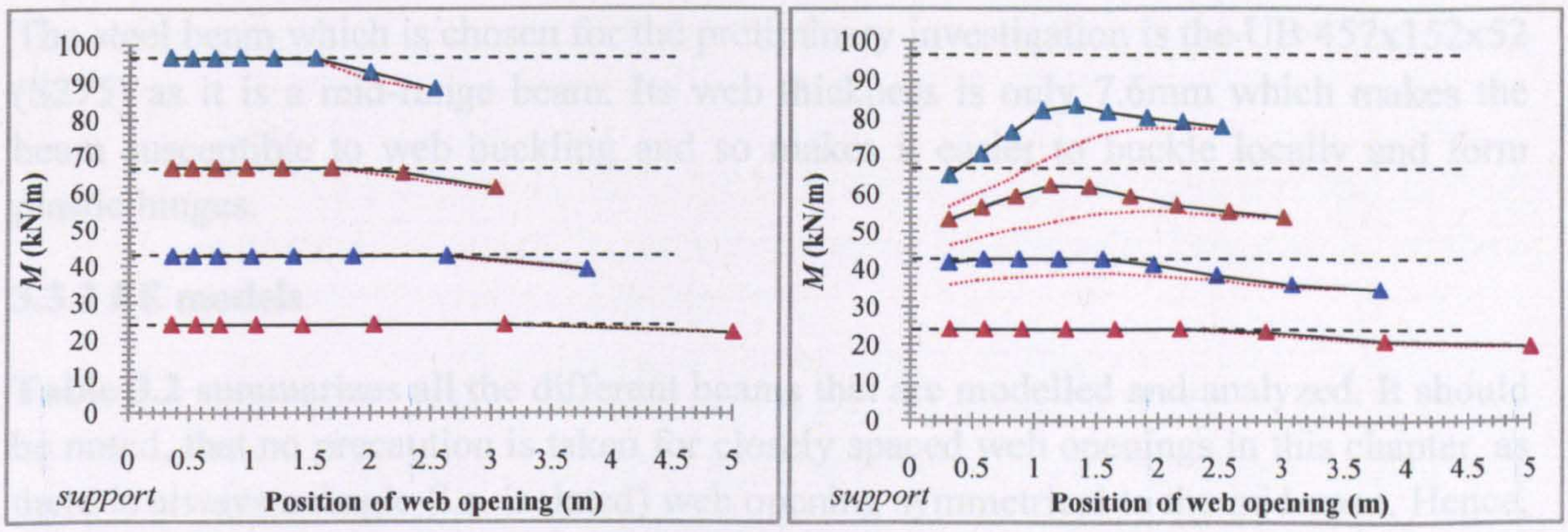

(a) UB457x152x52 S275 with d_o=*0.5h* (left) and d_o=*0.75h* (right)

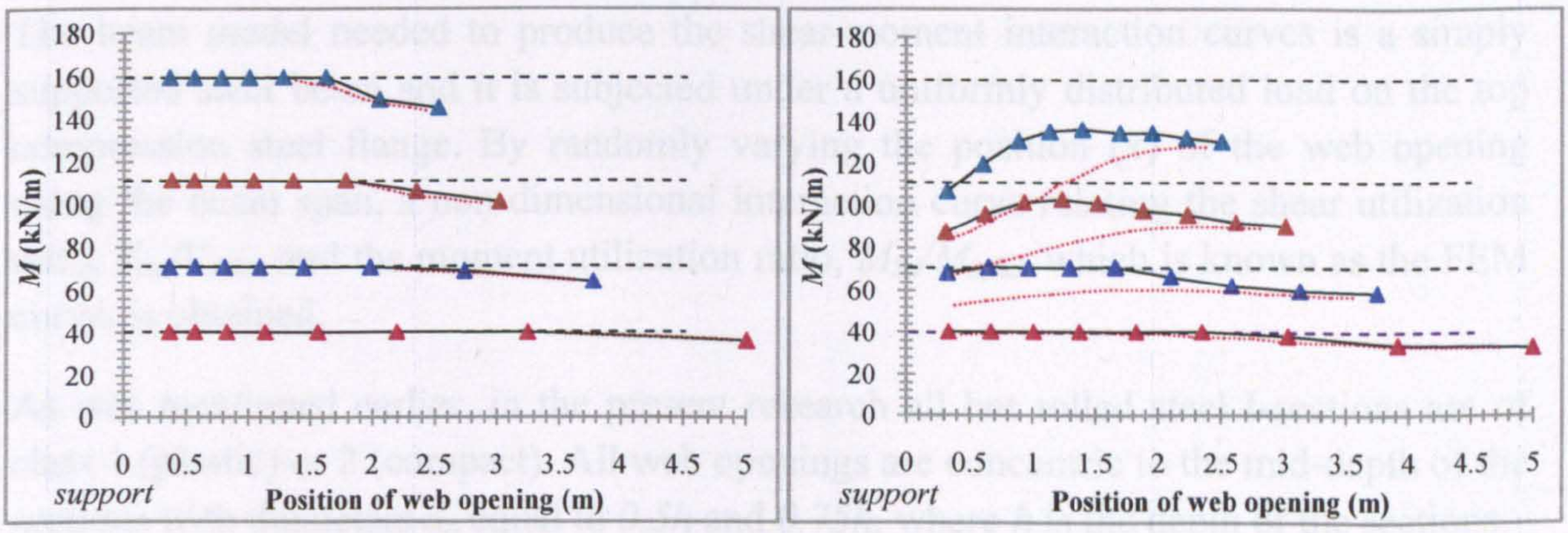

(b) UB457x152x82 S275 with d_o=*0.5h* (left) and d_o=*0.75h* (right)

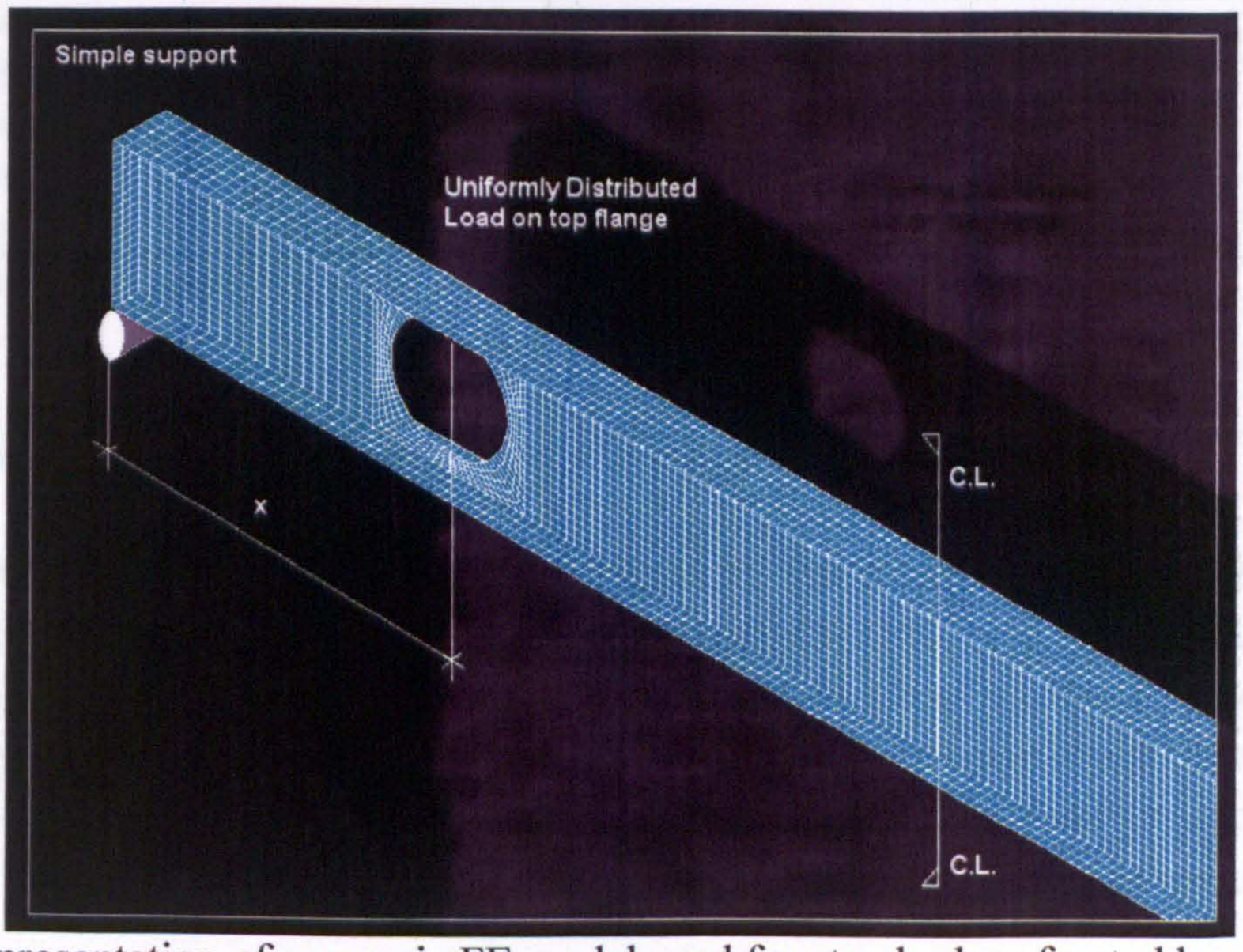

(c) Representation of a generic FE model used for standard perforated beams

Figure 3.6: Moment capacity versus web opening position (Chung et.al, 2000)

The steel beam which is chosen for the preliminary investigation is the UB 457x152x52 (S275) as it is a mid-range beam. Its web thickness is only 7.6mm which makes the beam susceptible to web buckling and so makes it easier to buckle locally and form plastic hinges.

3.3.2 FE models

Table 3.2 summarizes all the different beams that are modelled and analyzed. It should be noted, that no precaution is taken for closely spaced web openings in this chapter, as there is always a single (i.e. isolated) web opening symmetrical to the mid-span. Hence, they are located well away from each other and the effects of the forces are generated only due to the existence of the one web opening.

The beam model needed to produce the shear-moment interaction curves is a simply supported steel beam and it is subjected under a uniformly distributed load on the top compression steel flange. By randomly varying the position (x) of the web opening along the beam span, a non-dimensional interaction curve relating the shear utilization ratio, $V_{Sd}/V_{o,Rd}$, and the moment utilization ratio, $M_{Sd}/M_{o,Rd}$, which is known as the FEM curve, is obtained.

As was mentioned earlier, in the present research all hot rolled steel I-sections are of class 1 (plastic) or 2 (compact). All web openings are concentric to the mid-depth of the sections with diameters d_o equal to $0.5h$ and $0.75h$, where h is the depth of the sections.

Positions (x) no.	Steel Beams	Position of opening from support, (x) (mm)	Positions (x) no.	Steel Beams	Position of opening from support, (x) (mm)
1	inter1	0	**6**	inter6	1299
2	inter2	284	**7**	inter7	1573
3	inter3	537	**8**	inter8	1866
4	inter4	788	**9**	inter9	2177
5	inter5	1039	**10**	inter10	2500

Table 3.2: Identification of all steel beams studied in FEA (span of 5m)

3.3.3 Verification of FE procedure

Automatic solution control in ANSYS uses a norm force (and when the rotational degrees of freedom are active, moment) tolerance equal to 0.5% (or 0.1% for automatic time stepping option *OFF*), as the convergence criteria. A check on the displacement with a tolerance equal to 5% is also used in addition to the force norm check. The check that the displacements are loosely set serves as a double-check on convergence. The same element type and size is used for all beams, which made the results comparable.

A sensitivity study of the solution control factors is established. The input factors are the automatic time stepping option from the FE software (*ON* or *OFF*); the Tangent Modulus evaluation (*0* or *1000*) and the number of sub-steps (i.e. loading increments)

for the load steps (either *10*, *30* or *100*). The description of the latter factors is given as follows:

- Automatic load stepping is the most common convergence enhancement method which attempts to optimize the iteration process by assigning load step increments that will help the solution to converge.
- By varying the Tangent Modulus, different tangent stiffness matrices are generated causing convergence of the model. The Tangent Modulus is useful in describing the behaviour of materials that have been stressed beyond the elastic region and quantifies the 'softening' of material that generally occurs when it begins to yield. The tangent modulus assumption shown below (E_T=*1000MPa*) is found after a detailed study of the test data taken from Redwood and McCutcheon (1968).
- Finally, the number of sub-steps is responsible for the gradual loading which helps the solution to converge. Large sub-steps might cause an abrupt change in behaviour including the onset buckling or sudden changes in stress-strain behaviour, especially when bilinear models are used. It is obvious that the first sub-step should not cause yielding to occur.

The sensitivity study is carried out on a perforated UB457x152x52 (S275) section with circular web openings of diameter d_o equal to *0.65h* at position (x) no.2. The variation of the results is presented by load against displacement curves and maximum Von-Mises stresses at failure (i.e. convergence point), as it is indicated in **Figure 3.7** and **Table 3.3.**

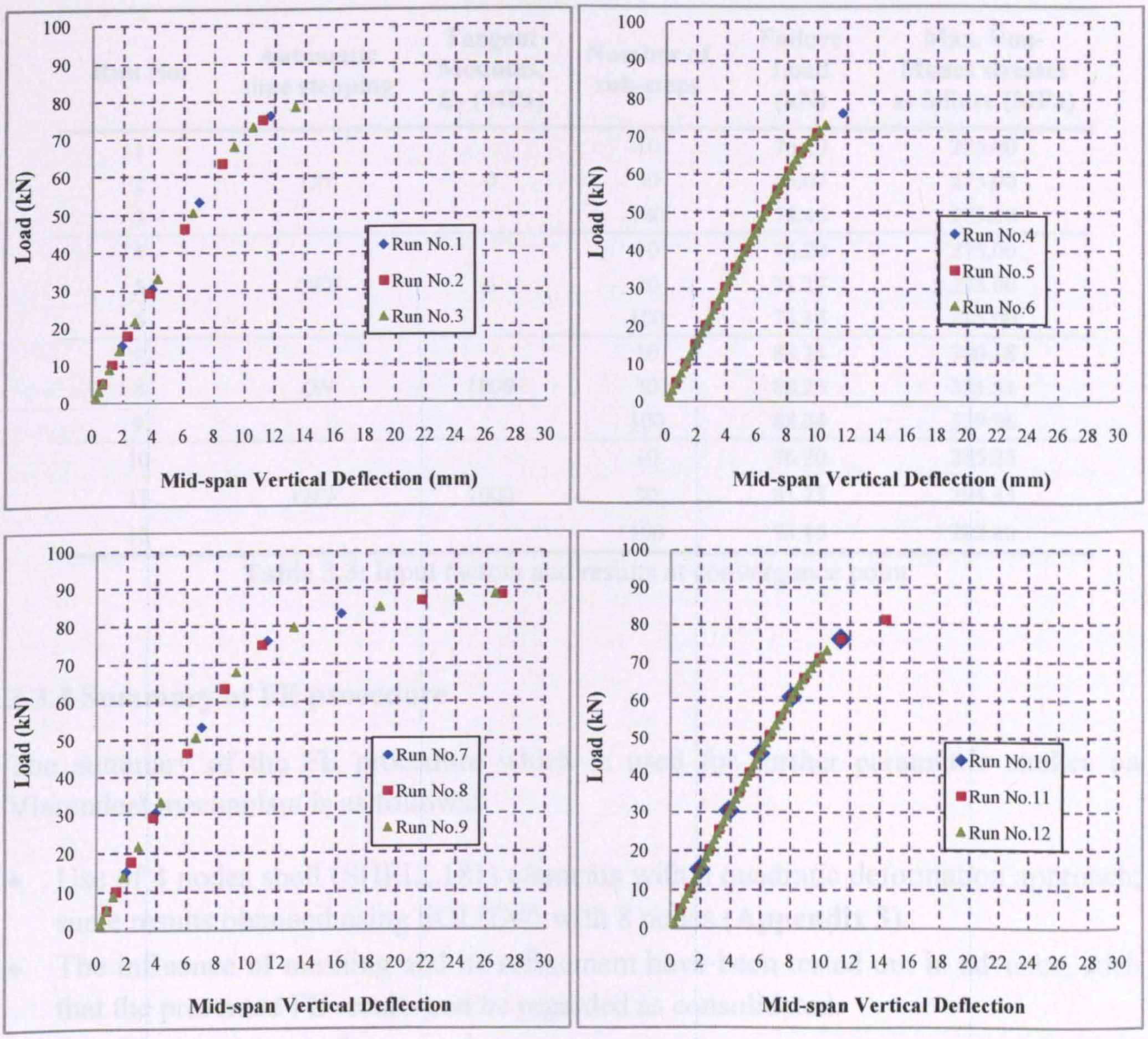

Figure 3.7: Convergence results of the factorial analysis study for a perforated section UB457x152x52 with circular web openings of d_o equal to *0.65h*

From **Figure 3.7** it is seen that run no.8 and 9 represent well the structural behaviour of such perforated beams. However, replacing automatic time stepping *OFF*; instead of *ON* (run no.11), some other benefits are obtained as follows:

- The tolerance in the convergence criteria is smaller.
- The analysis is manually controlled by constant load steps; similar to the experimental tests.
- There are no very high stresses after initial yielding (i.e. easy to monitor).
- The maximum stresses are conservative close to yield strength of the steel, based on the Von-Misses criterion.

Therefore, the factors similar to run no.11 are used for the parametric FE study as follows. As long as there is consistency of the input factors for all FE models, the comparison is valid and the results can be seriously considered. Also, the load increments and the number of sub-steps are preliminarily studied to conform to the convergence criteria.

Run No.	Automatic time stepping	Tangent Modulus, E_T (MPa)	Number of sub-steps	Failure Load (kN)	Max. Von-Misses stresses at failure (MPa)
1			10	76.20	275.00
2	*ON*	0	30	75.07	275.00
3			100	78.46	275.00
4			10	76.20	275.00
5	*OFF*	0	30	71.17	275.00
6			100	73.15	275.00
7			10	83.14	300.18
8	*ON*	1000	30	88.23	331.51
9			100	88.34	329.96
10			10	76.20	285.25
11	*OFF*	1000	30	81.23	294.45
12			100	73.15	282.80

Table 3.3: Input factors and results at convergence point

3.3.4 Summary of FE procedure

The summary of the FE procedure which is used for further parametric studies on Vierendeel mechanism is as follows:

- Use of 4 nodes shell (SHELL181) elements with a quadratic deformation approach; same results obtained using SOLID45 with 8 nodes (**Appendix 3**).
- The influence of meshing and its refinement have been tested out in advance, such that the presented FE results can be regarded as consolidated.
- Big distortion approach.
- Geometrically as well as material non-linear interaction.
- Nominal material properties used.
- Solver by iterations according to Newton-Raphson.
- Ideal elasto-plastic material behaviour using actual (measured) values.
- The full (real) stress-strain curve is not included. However, the error that is induced by this simplification (Bi-Linear with Kinematic Hardening approach) is negligible.
- The beam geometry is based on the Advanced UB sections.
- Bearing plates at the two ends of the beam are modelled and the pressure is directly applied on the compression flange of the beam.
- The load is applied stepwise as pressure.

More information on the FE input data is given in **Appendix 4**.

3.3.5 Results of perforated beams with circular web openings

3.3.5.1 Shear forces and moments at position x

The shear forces and moments at positions x are given according to the formulas below for simply supported beams under a uniformly distributed load.

$$V_{Sd} = w\left(\frac{L}{2} - x\right) \qquad (3.1)$$

$$M_{Sd} = w\mathrm{x}\frac{(L - \mathrm{x})}{2} \qquad (3.2)$$

3.3.5.2 Non-dimensional shear-moment (*V/M*) interaction curves

Non-dimensional shear-moment interaction (FEM) curves are produced by an elasto-plastic non-linear FE analysis of perforated beams with a span of 5m and with web openings of d_o equal to *0.5h* and *0.75h*, as shown in **Figure 3.8**. All beams have two similar and symmetrically positioned web openings which are located at ten different positions along the half-length of the 5m span beam. It should be noted that when the web openings are placed at the mid-span of the beams with $V_{Sd}/V_{o,Rd}=0$, all beams fail in flexure at a bending moment very close to their $M_{o,Rd}$, as given in **Formula 2.1**. This is not the case when the web openings are placed at the supports of the beams. In general, when the shear ratio is decreased, the load carrying capacity is also reduced. Hence, it is easy to conclude that the interaction curve for a circular web opening of d_o equal to *0.75h* is more critical than the one for d_o equal to *0.5h*, with a maximum percentage difference for the particular section size at the pure shear ratio. From FEA it is shown that $V_{o,Rd}$ is dependent on both the relative thickness and area of the web and the flange. Hence, the value of $V_{o,Rd}$ may be increased by a percentage using the finite element model, when compared to the shear capacities obtained from **Formula 2.2**.

The analytical data of the latter interaction curves together with the load carrying capacities, *w*, obtained; are presented in **Appendix 5**.

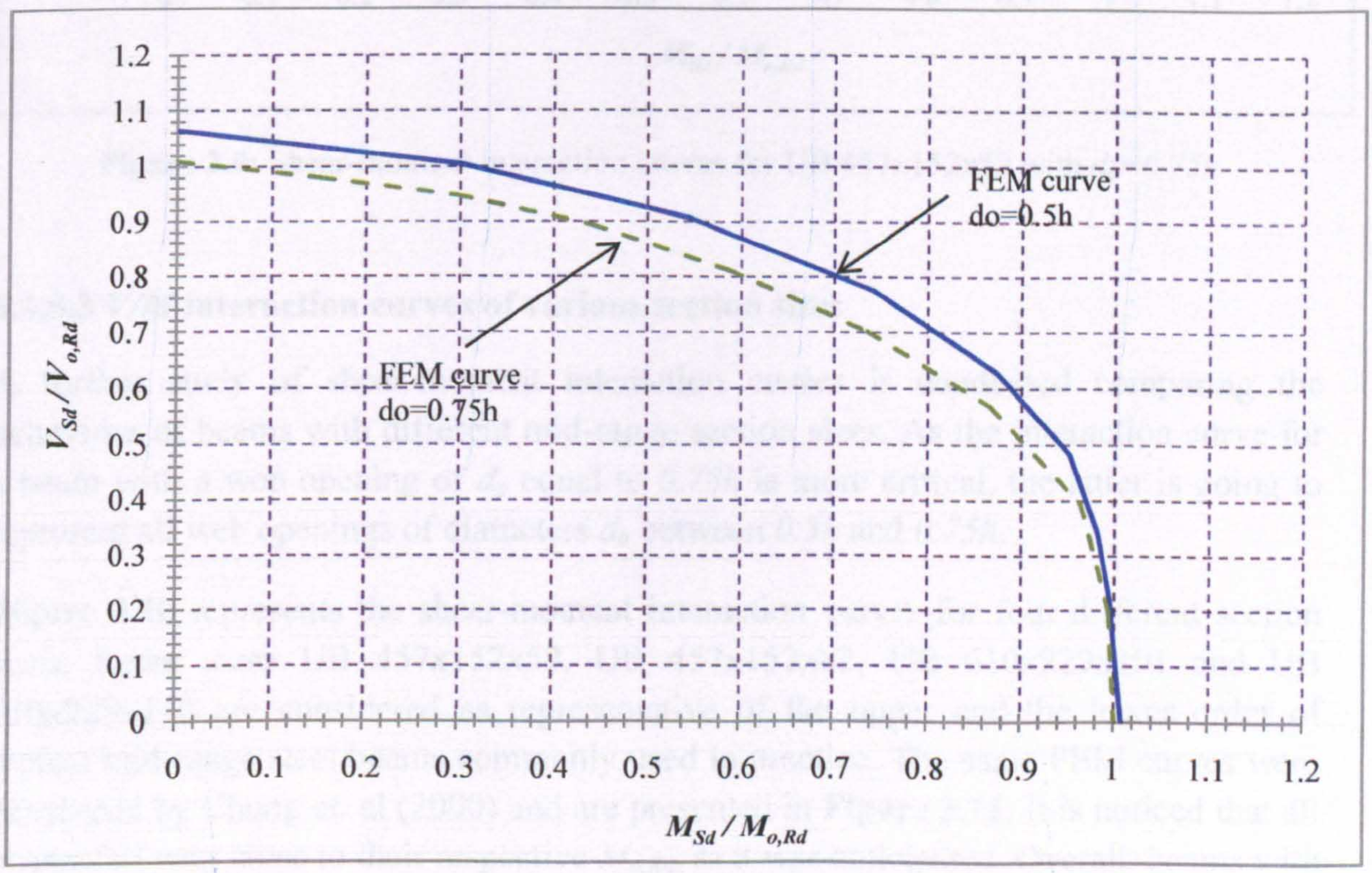

Figure 3.8: Non-dimensional shear-moment interaction (FEM) curves for UB 457x152x52

The above shear-moment interaction curve for perforated beams with large web openings is plotted against the simplified method (i.e. $\varphi_p=25^o$) and the theoretical curves LMS and HMS, as shown in **Figure 3.9**. FEM lies between theoretical curves LMS and HMS. A FEM curve is found to provide a conservative and economical design with an increase in strength up to 15% when compared with curve LMS. In general, it is demonstrated that the load carrying capacity of steel beams with circular web openings may be increased significantly using the shear-moment interaction curve derived from the FE model.

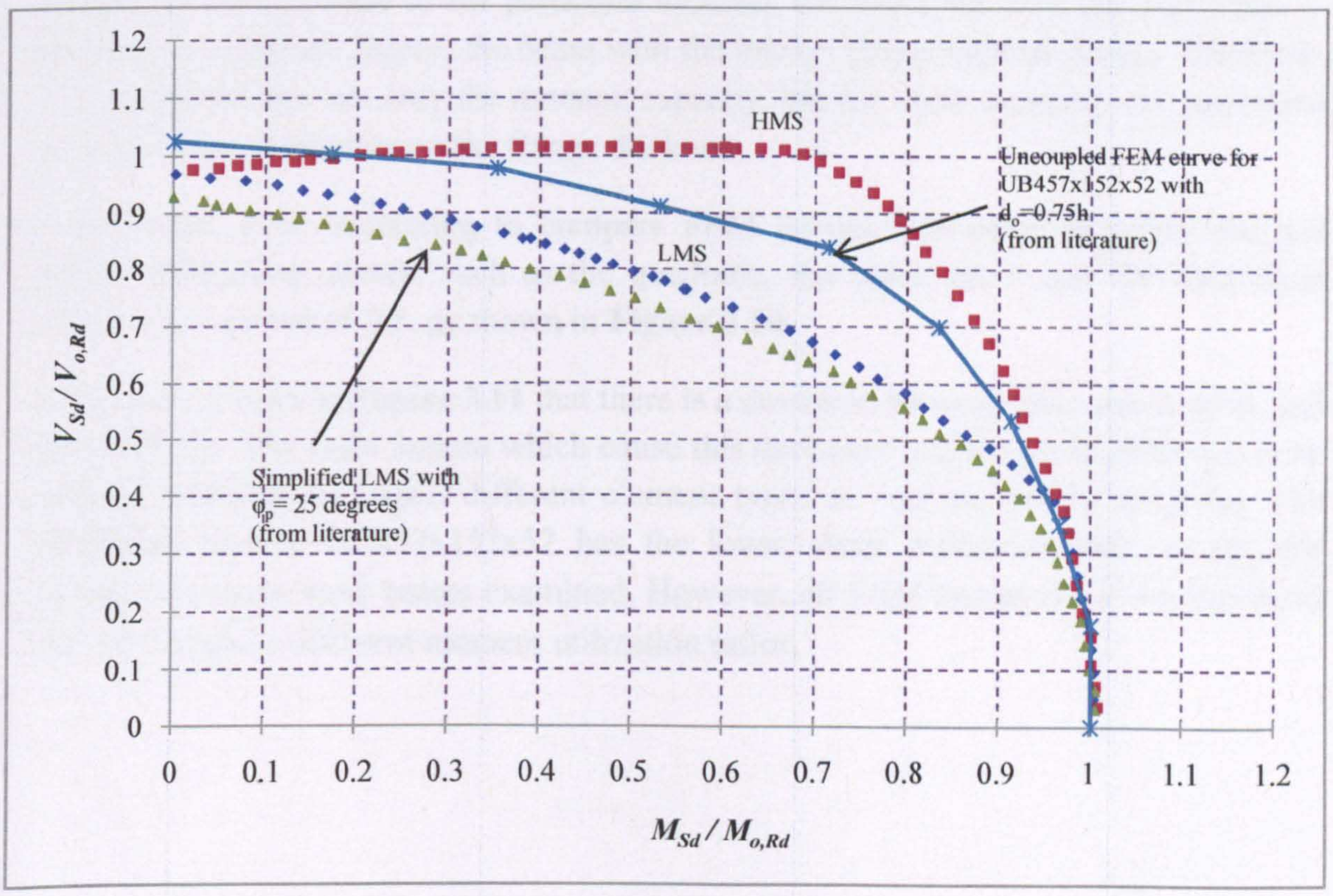

Figure 3.9: Shear-moment interaction curves for UB 457x152x52 with $d_o=0.75h$

3.3.5.3 *V/M* interaction curves of various section sizes

A further study of shear-moment interaction curves is conducted comparing the behaviour of beams with different mid-range section sizes. As the interaction curve for a beam with a web opening of d_o equal to $0.75h$ is more critical, the latter is going to represent all web openings of diameters d_o between $0.5h$ and $0.75h$.

Figure 3.10 represents the shear-moment interaction curves for four different section sizes. Beam sizes UB 457x152x52, UB 457x152x82, UB 610x229x101 and UB 610x229x140 are considered as representative of the upper and the lower order of typical mid-range steel beams commonly used in practice. The same FEM curves were developed by Chung et. al (2000) and are presented in **Figure 3.11**. It is noticed that all beams fail very close to their respective $M_{o,Rd}$, as it was anticipated. Overall, beams with different weights per unit length have curves of similar shape, but with different y-

intercepts; in other words different shear utilization ratios $V_{Sd}/V_{o,Rd}$. This phenomenon is a result of underestimation of the shear capacities of the perforated sections with thick flanges, given by **Formula 2.2**, when compared with the FE model. This underestimation takes place due to the assumption of the shear area of an un-perforated section, A_v, which is taken as ht_w for practical reasons. An easy comparison is between the UB 610x229x101 and UB 457x152x82; that while they have the same web thickness, the beam with the thicker flanges (UB 457x152x82) has a higher y-intercept value even if it has a shallower beam depth. As it can be seen from **Figure 3.10**, comparing the t_w/t_f ratio of the particular sections, the lower the ratio the higher the y-intercept is obtained. Hence, the beam with the thicker flange behaves better. Therefore, it is concluded that not only the moment capacity, but the shear capacity of a perforated section is also dependent on the flange thickness.

Furthermore, it is interesting to compare FEM curves with other empirical but yet simple interaction curves, such as the quadratic, the cubic curve and the theoretical curve with a power of 2.5, as shown in **Figure 3.10**.

It is clearly shown in **Figure 3.11** that there is a deviation between the current study and the literature. The main factors which cause this deviation are the use of different finite element software packages, different element types as well as type of meshing. The perforated section UB457x152x52 has the lower shear utilization ratio among the typical mid-range steel beams examined. However, all FEM curves are of similar trend and have slightly different moment utilization ratios.

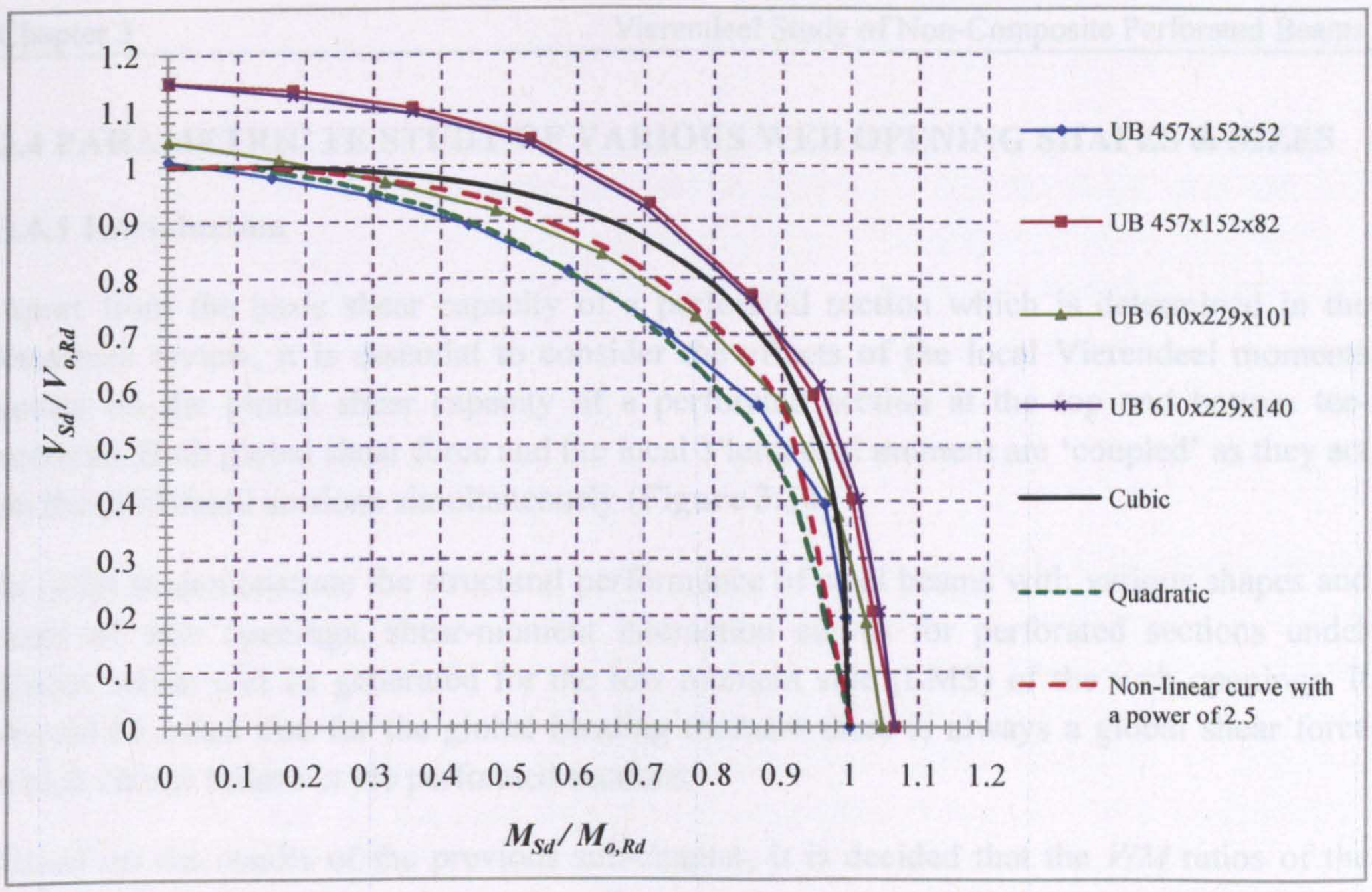

Figure 3.10: Shear-moment interaction FEM curves for web openings $d_o=0.75h$

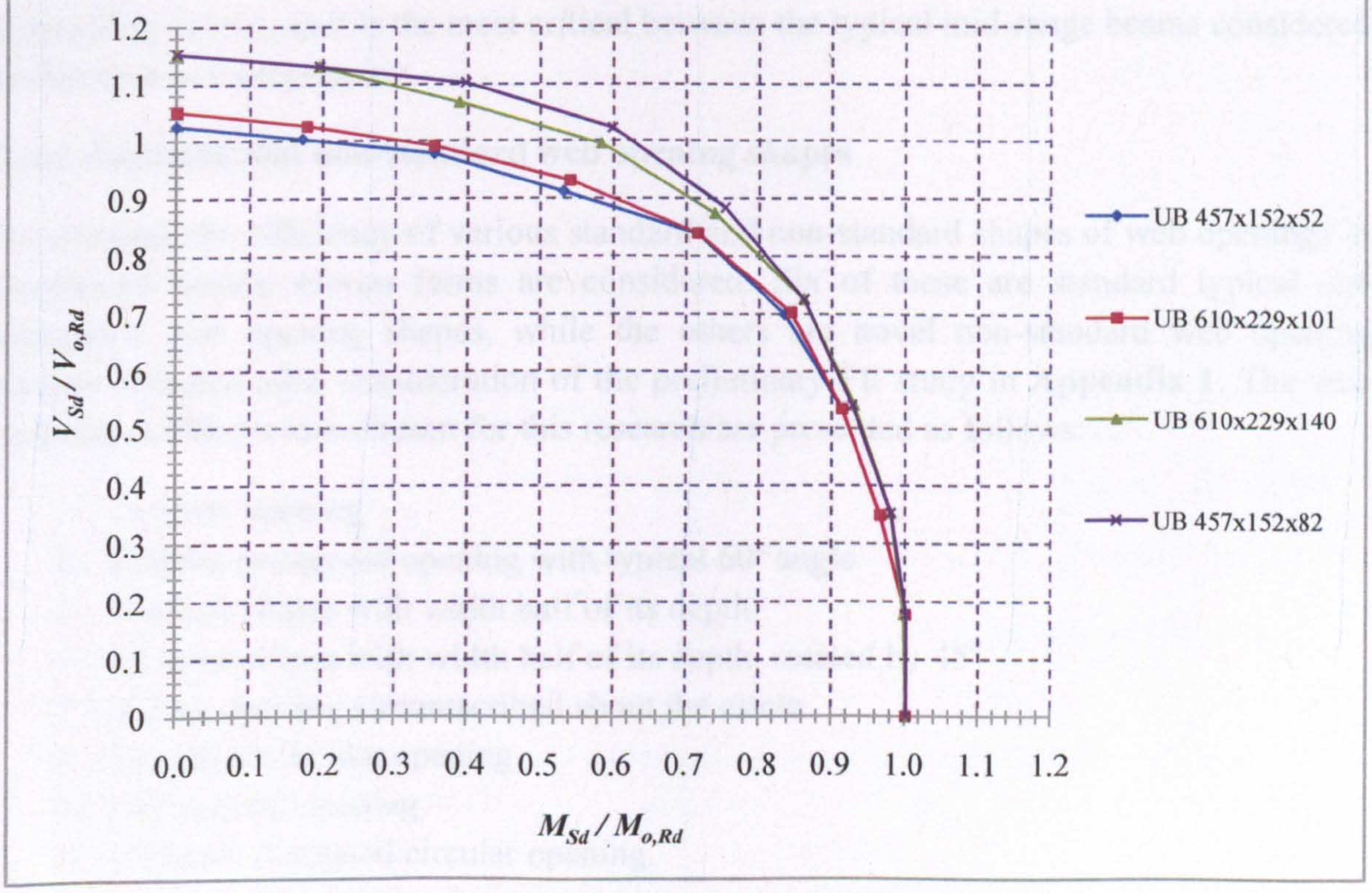

Figure 3.11: Shear-moment interaction FEM curves for web openings $d_o=0.75h$ (Chung et.al, 2000)

3.4 PARAMETRIC FE STUDY OF VARIOUS WEB OPENING SHAPES & SIZES

3.4.1 Introduction

Apart from the basic shear capacity of a perforated section which is determined in the literature review, it is essential to consider the effects of the local Vierendeel moments acting on the global shear capacity of a perforated section at the top and bottom tee-sections. Both global shear force and the local Vierendeel moment are 'coupled' as they act on the perforated sections simultaneously (**Figure 3.14**).

In order to demonstrate the structural performance of steel beams with various shapes and sizes of web openings, shear-moment interaction curves for perforated sections under global action will be generated for the low moment side (LMS) of the web openings. It should be noted that for the global bending moment there is always a global shear force which causes failure in the perforated sections.

Based on the results of the previous sub-chapter, it is decided that the *V/M* ratios of the perforated section with web opening diameter d_o equal to *0.8h* is going to sometimes represent all web openings of diameters d_o equal to *0.5h*, *0.65h* and *0.8h*. However, a detailed FE study is conducted on all sizes of web openings. The perforated section UB457x152x52 is used as reference for the establishment of the design shear-moment interaction curves, as it is the most critical between the typical mid-range beams considered in this research programme.

3.4.2 Standard and non-standard web opening shapes

To compare the efficiency of various standard and non-standard shapes of web openings in perforated beams, eleven forms are considered. Six of these are standard typical and elongated web opening shapes, while the others are novel non-standard web opening shapes designed after consideration of the preliminary FE study in **Appendix 1**. The web opening configurations chosen for this research are presented as follows:

1. Circular opening
2. Regular hexagonal opening with typical 60° angle
3. Vertical ellipse with width half of its depth
4. Inclined ellipse with width half of its depth, rotated by 45°
5. Square opening circumscribed about the circle
6. Elongated circular opening
7. Rectangular opening
8. Ultimate elongated circular opening.

From previous studies, it is known that the length of the uniform tee-section *'c'* above and below the web opening dramatically influences the load carrying capacity of perforated

sections as it has a major effect on the local applied moment on tee-sections. Therefore, a total of eleven web openings are considered (**Figure 3.12** and **3.13**) and the key dimensional parameter in all these web opening shapes is the opening length, *'c'*. Details of the aforementioned web opening shapes together with the associated values of *'c'* are listed as follows:

1. Circular opening with $c < 1.0d_o$ (A);
2. Regular hexagonal opening with $c = 0.423d_o$ (B);
3. Vertical ellipse with $c < 0.75d_o$ (C);
4. Inclined (rotated) ellipse with $c < 1.0d_o$ with do equal to the initial web opening depth. Rotating the vertical ellipse C, the final web opening vertical depth is shorter against the total section. Hence, the new depth is $0.883d_o$. Also, three beam configurations are studied with different web opening orientations presented as follows: i) & ii) web openings are mirrored to the mid-span of the beams while rotated by 45° (D & E respectively) and iii) the case that both web openings at the two sides rotated by 45 degrees at only one side (F). The three different options are presented in **Figure 3.13**. It is interesting to investigate the behaviour of perforated beams with such inclined web openings. This is because when rotated the opening length of the top and bottom tee-sections varies. Also, the web openings are not symmetrical to their centre-line anymore.
5. Inclined (rotated) ellipse with $c < 1.0d_o$ with d_o equal to the initial web opening depth (G);
6. Square opening with $c = 1.0d_o$ (H);
7. Elongated circular opening with $1.0d_o < c < 2.0d_o$ (I);
8. Rectangular opening with $c = 2.0d_o$ (J) and
9. Ultimate elongated circular opening with $2.0d_o < c < 3.0d_o$ (K).

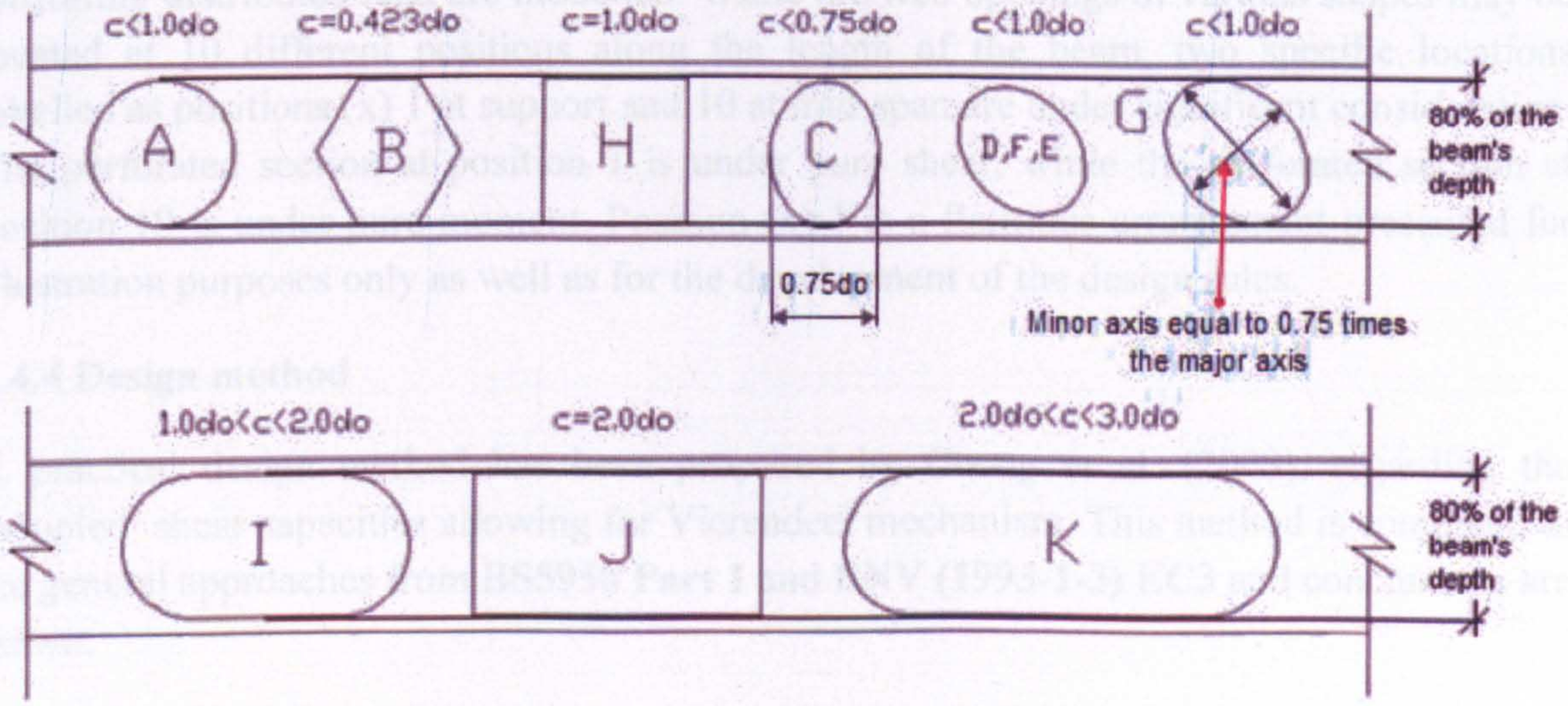

Figure 3.12: Geometric shapes of web openings

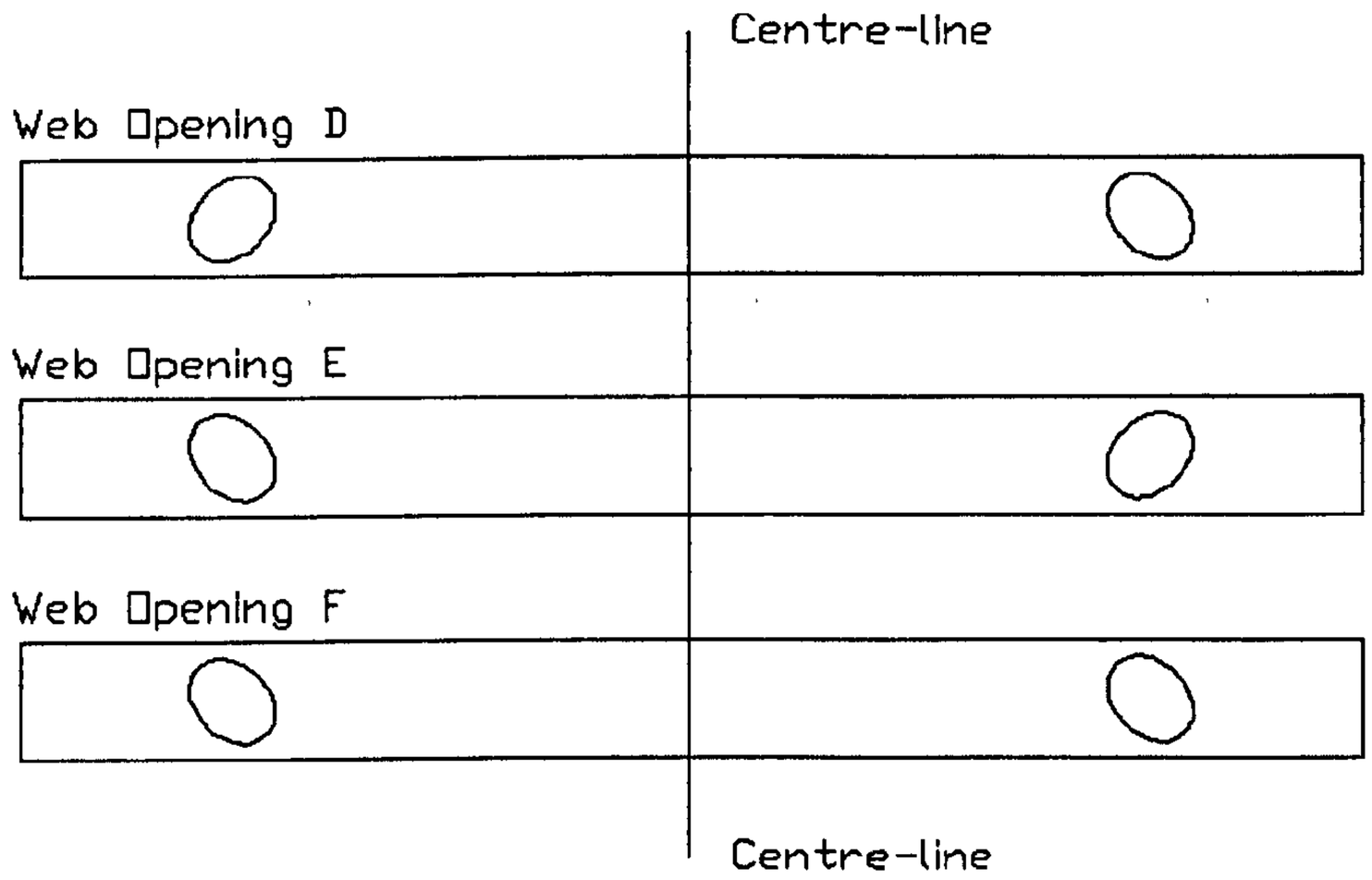

Figure 3.13: Possible combinations by using inclined ellipses

3.4.3 Introduction to the parametric FE study

1320 successful non-linear finite element runs are conducted in order to complete the parametric study. This is a result of four beam section sizes having web opening depths of 80%, 65% and 50% of the beams' depth. Establishing shear-moment interaction curves, ten different positions (x) of the web openings along the length of the beam, similar to **Table 3.2** are considered necessary. Finally, this procedure is repeated for perforated beams with eleven different web opening shapes.

Similar to the previous sub-chapter, simply supported beams with a span of 5m under a uniformly distributed load are modelled. While the web openings of various shapes may be located at 10 different positions along the length of the beam, two specific locations labelled as positions (x) 1 at support and 10 at mid-span are under significant consideration. The perforated section at position 1 is under pure shear, while the perforated section at position 10 is under pure moment. Position (x) 1 is a fictitious arrangement presented for illustration purposes only as well as for the development of the design rules.

3.4.4 Design method

A practical design method has been proposed by Chung et al. (2003), regarding the 'coupled' shear capacities allowing for Vierendeel mechanism. This method is compared to the general approaches from **BS5950 Part 1** and **ENV (1993-1-3) EC3** and conclusions are drawn.

As it is aforementioned, the behaviour of perforated sections is characterized by three actions: global bending action, global shear action and local 'Vierendeel' action. The global shear capacities of the perforated sections attain their maximum values in the absence of axial forces due to global moment. However, any increase in the global moment at the perforated sections will induce local axial forces in the tee-sections, and hence local yielding of the tee-sections. Both the global shear force and the local 'Vierendeel' moment are 'coupled' as they act on the perforated section simultaneously. This phenomenon is known as 'coupled' Vierendeel mechanism and it is represented in **Figure 3.14**. The effect of 'Vierendeel' mechanism is incorporated into the shear capacities of perforated sections resulting the 'coupled' shear capacities of perforated sections. Therefore, it is now reasonable to claim that perforated sections with large opening length subjected under large global moment, will have significantly reduced shear capacities. Moreover, it should be noted that the amount of coupling in perforated sections is very complicated, depending on the shapes and sizes of web openings and also on the applied global shear forces and moments at the perforated sections.

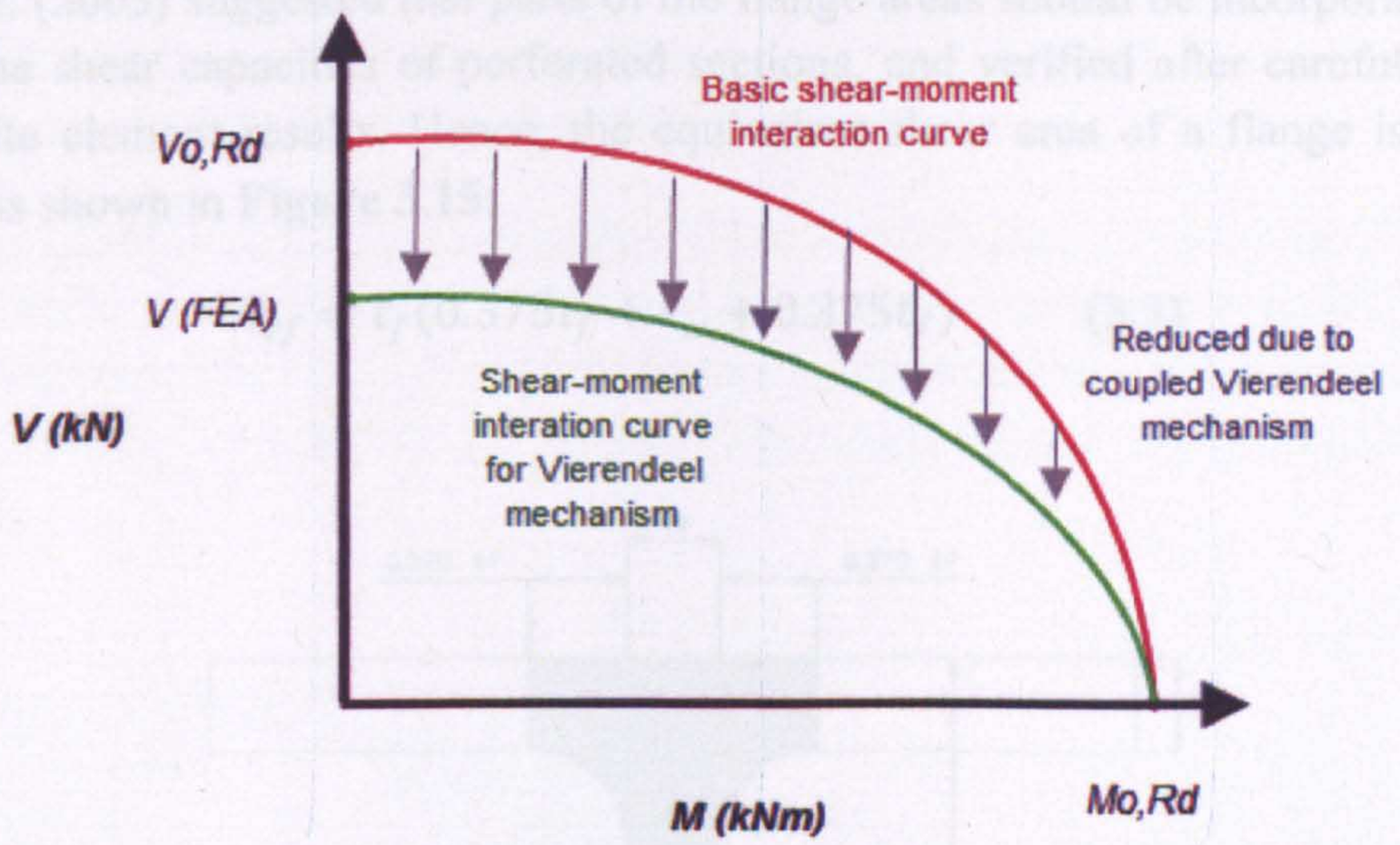

Figure 3.14: Reduction in *V/M* interaction curve due to 'coupled Vierendeel mechanism' (Chung et. al, 2003)

Following this re-arrangement, non-dimensional shear-moment interaction (FEM) curves lay below both curves LMS and HMS. Hence, a FEM curve is recommended to allow for the presence of co-existing global shear force and moment on perforated sections.

3.4.5 Basic moment capacity

The applied global moment and shear force at the centre-line of the web opening are $M_{o,Sd}$ and $V_{o,Sd}$, respectively. The moment capacity, $M_{o,Rd}$, of a perforated section is given by **Formula 2.1**.

3.4.6 Basic shear capacity

Modern steel codes such as British Standards define the shear area of an I-section as ht_w, based on the simple plastic section analysis, where h is the overall section depth. This approximation is widely considered, as the flanges are mainly resisting the bending moment while the web is resisting the shear force. However, in an I-section with a large web opening the shear area of the web is sensibly reduced. Therefore, the shear areas of the flanges are taken into consideration when assessing the shear capacity of the perforated section. Hence, the shear capacity of the perforated section is higher compared to the simplified prediction.

Chung et al. (2003) suggested that parts of the flange areas should be incorporated in order to assess the shear capacities of perforated sections, and verified after careful calibration against finite element results. Hence, the equivalent shear area of a flange is as follows below and is shown in **Figure 3.15**:

$$A_{vf} = t_f(0.375t_f + t_w + 0.375t_f) \qquad (3.3)$$

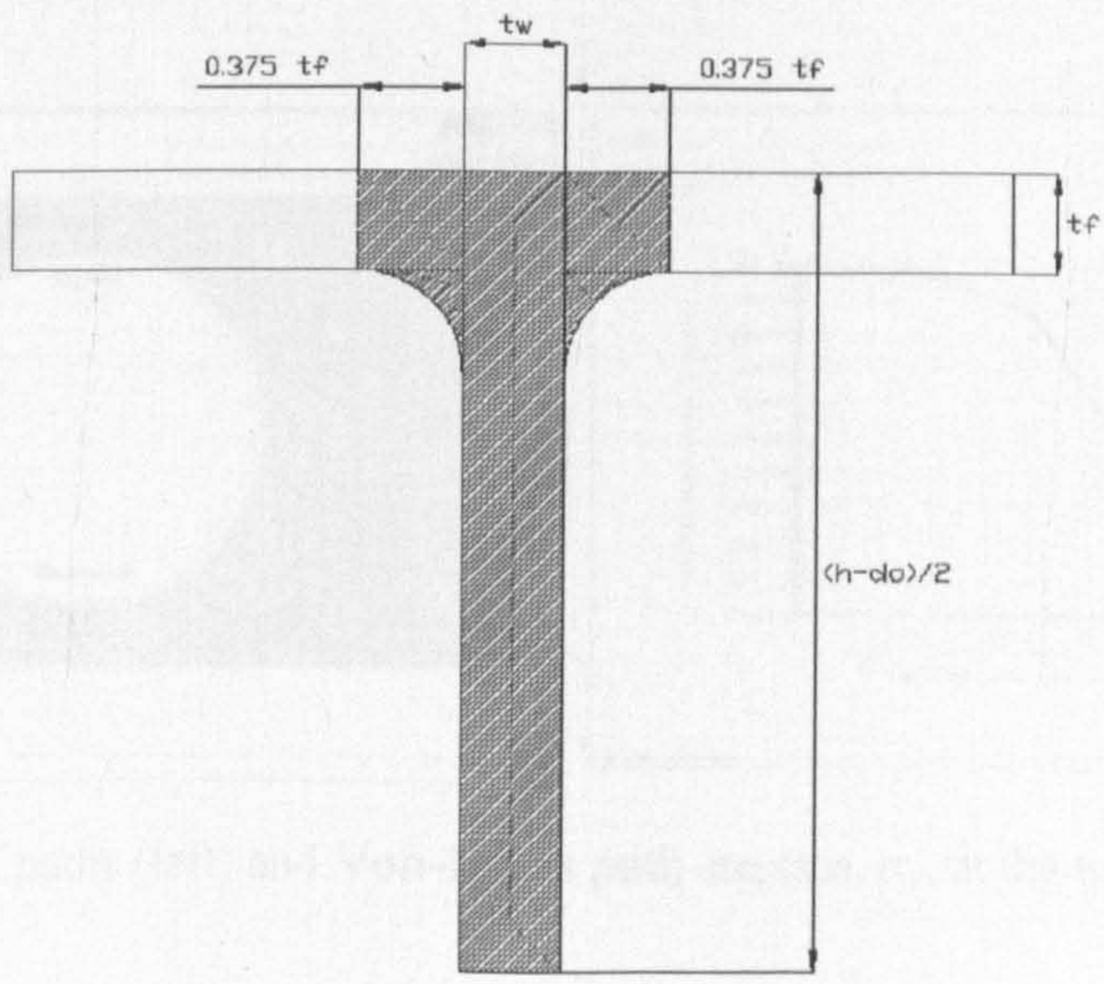

Figure 3.15: Equivalent shear area in tee-section (Chung et. al, 2003)

Consequently, the plastic shear resistance of the perforated section, $V_{o,Rd}$, which is given by **Formula 2.2**, becomes the following:

$$V_{o,Rd} = f_v A_{vo} \geq V_{o,Sd}$$

$$\rightarrow V_{o,Rd} = f_v (A_v - d_o t_w) \geq V_{o,Sd}$$

$$\rightarrow V_{o,Rd} = f_v \left[\left(h t_w + 2\left(0.75 t_f^2\right) \right) - d_o t_w \right] \geq V_{o,Sd}$$

$$\rightarrow V_{o,Rd} = \frac{0.577 f_y}{\gamma_{Mo}} \left[\left(h t_w + 2\left(0.75 t_f^2\right) \right) - d_o t_w \right] \geq V_{o,Sd} \qquad (3.4)$$

By using the above formula and the flange contribution to the shear capacity for a typical beam section such as an UB457x152x52 (S275), it is found that the larger the web opening the higher percentage of increase in the shear capacity is obtained. This percentage could be from 10% to 21% for perforated sections with web opening of d_o/h equal to 0.5 to 0.75, respectively. Moreover, beams with thick flanges have an increased shear capacity over 30%. The above percentages are specific for the particular section size and they can only be considered for mid-range UB sections with circular web openings. Further estimations of percentages are obtained later on in this research programme.

It should be mentioned that no root radius is modelled in the FE model as shell elements are used. This is something that would also increase the shear capacity of the analyzed perforated sections. The Von-Mises path stresses at the centre-line of the top tee-section are plotted to illustrate the effect of the flange on the shear capacity of the perforated section (**Figure 3.16**).

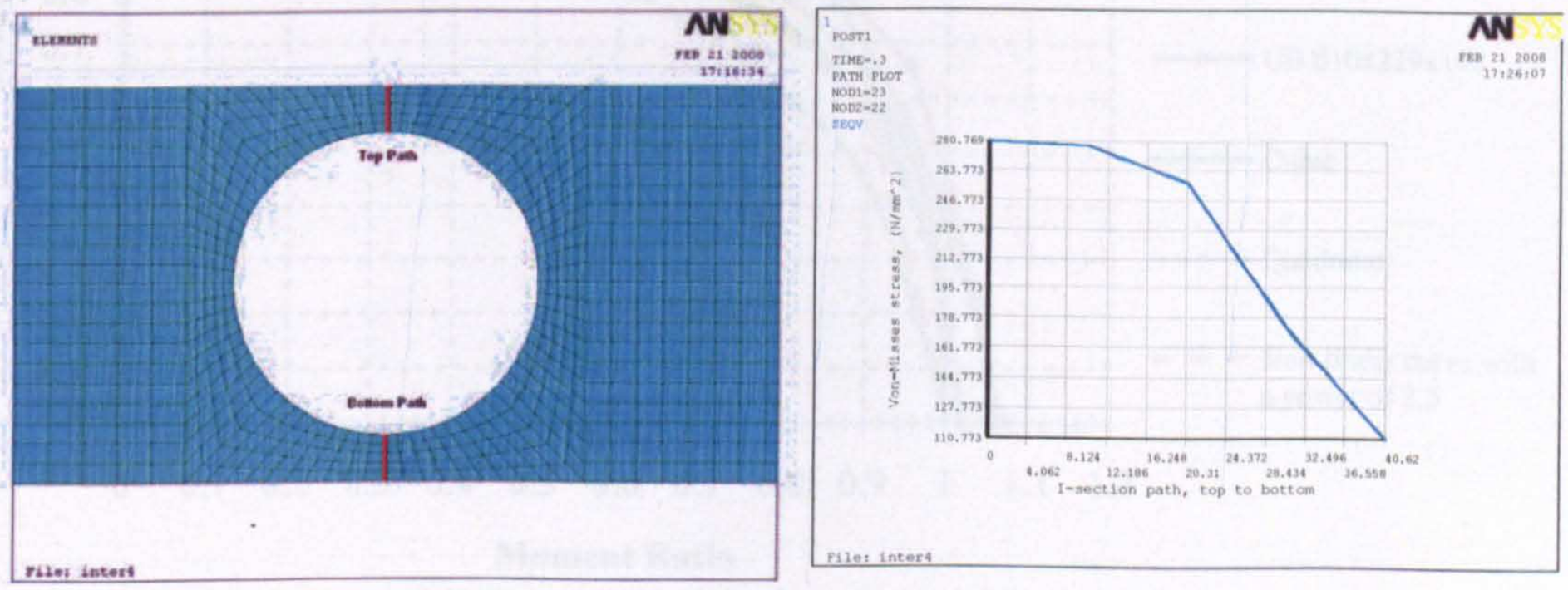

Figure 3.16: Plot of paths (left) and Von-Mises path stresses, σ_v, at the top tee-section (right)

3.4.7 Comparison of *V/M* ratios for various section sizes

Initially, a comparison study was established between the four mid-range sections sizes with selected web opening shapes of maximum size. This is done, in order to investigate

the difference on the coupled shear capacities by using the following three approaches for the cross section shear area:

- In the simple plastic section analysis, the shear area of an I-section is taken as ht_w (**BS5950 Part 1**) for practical reasons.
- The one as considered in **ENV (1993-1-3) EC 3** where the length of the fillet radius between the web and the flange is equal to the effective width of the flange (**Formula 3.5**).
- The proposed equivalent shear area of a tee-section based on FEA investigation as given earlier in **Formula 3.3**.

$$A_{VZ} = A - 2b_f t_f + (t_w + 2r)t_f \qquad (3.5)$$

Typical circular (A), vertical ellipse (C), and elongated (I) web openings are selected to be examined in this study in order to cover all three main categories. The shear-moment interaction curves are presented for ease of comparison (**Figure 3.17** and **3.25**) and the results are summarized in **Table 3.4**.

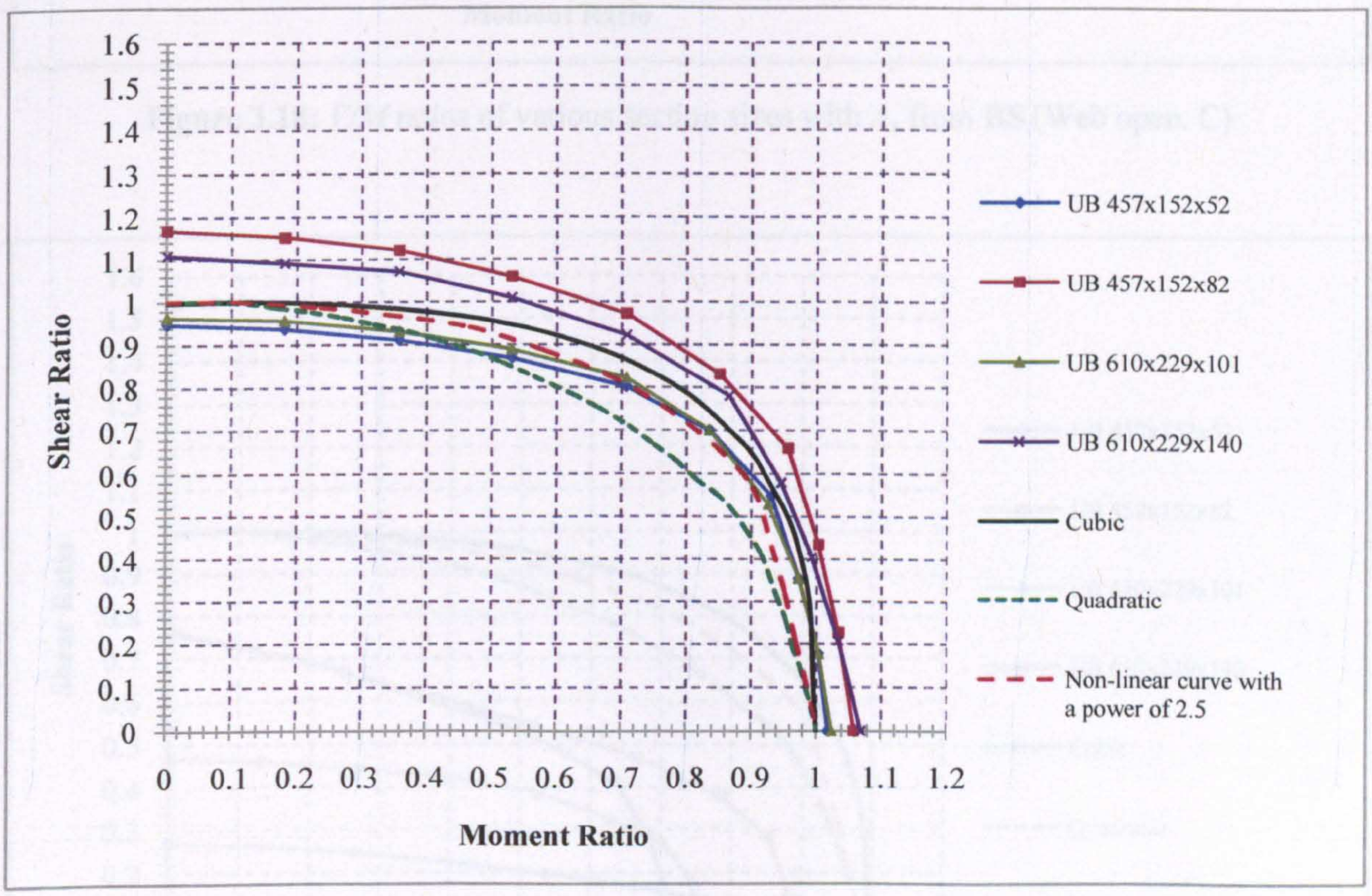

Figure 3.17: *V/M* ratios of various section sizes with A_v from **BS** (Web open. A)

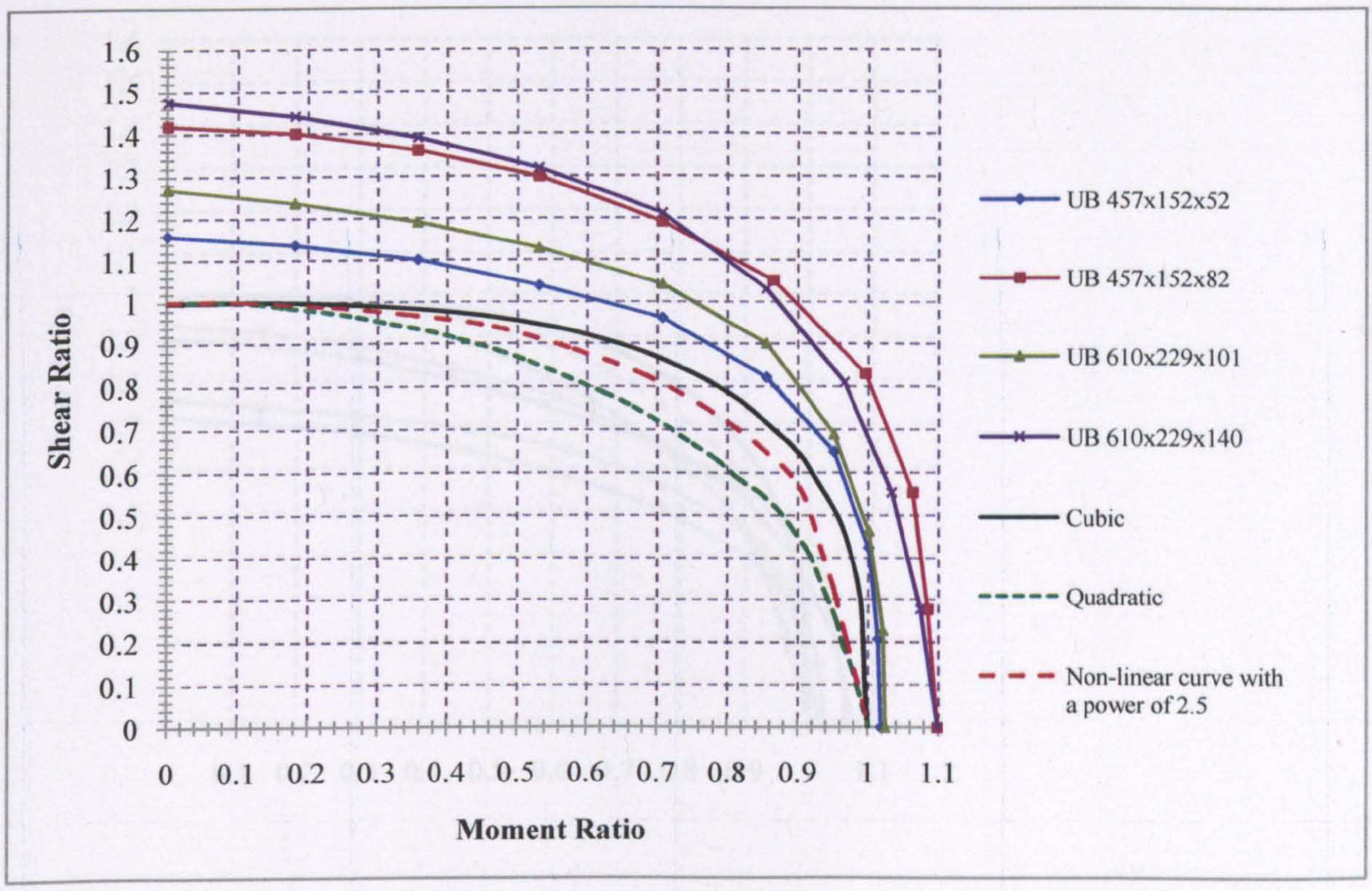

Figure 3.18: *V/M* ratios of various section sizes with A_v from **BS** (Web open. C)

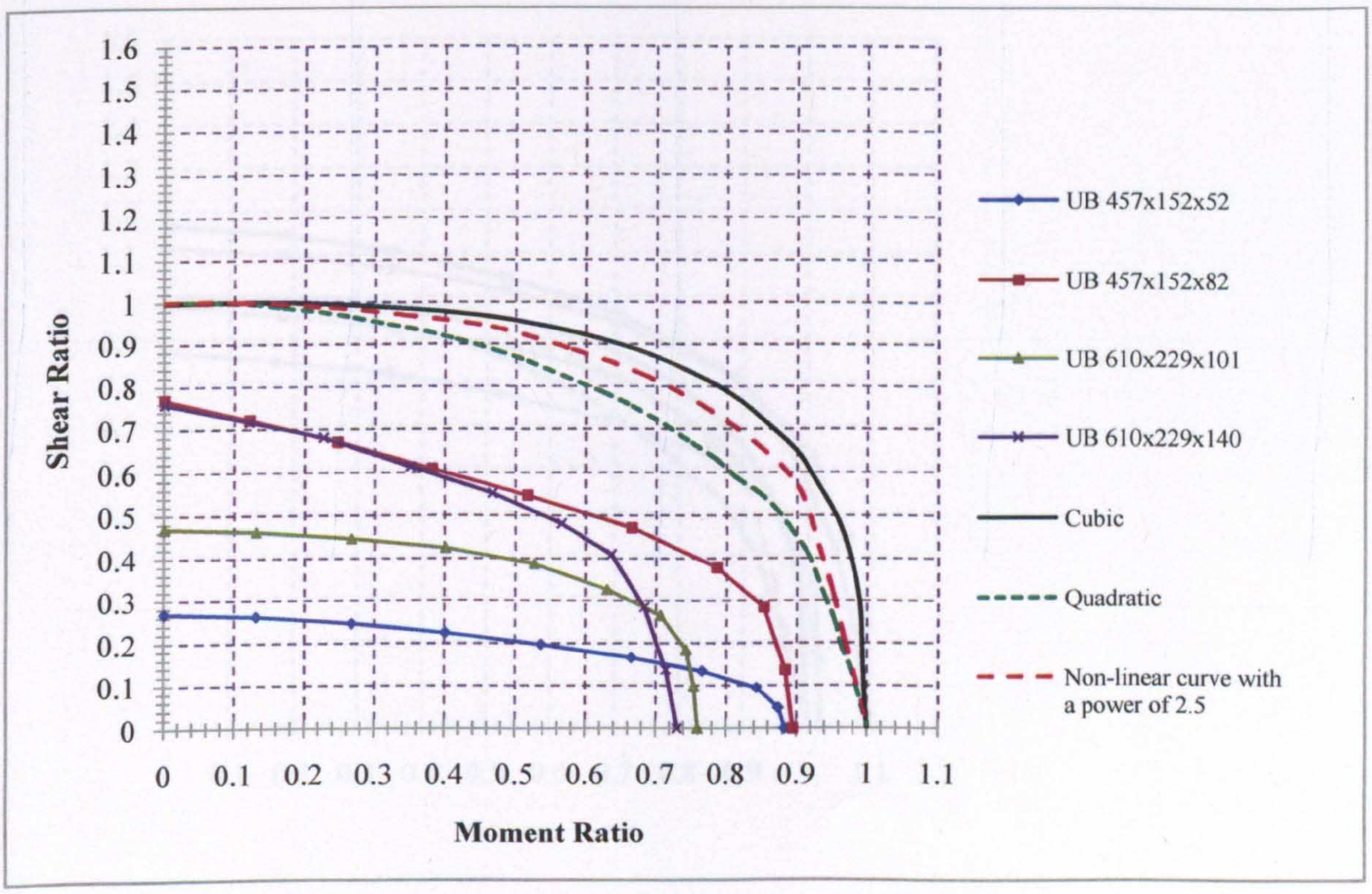

Figure 3.19: *V/M* ratios of various section sizes with A_v from **BS** (Web open. I)

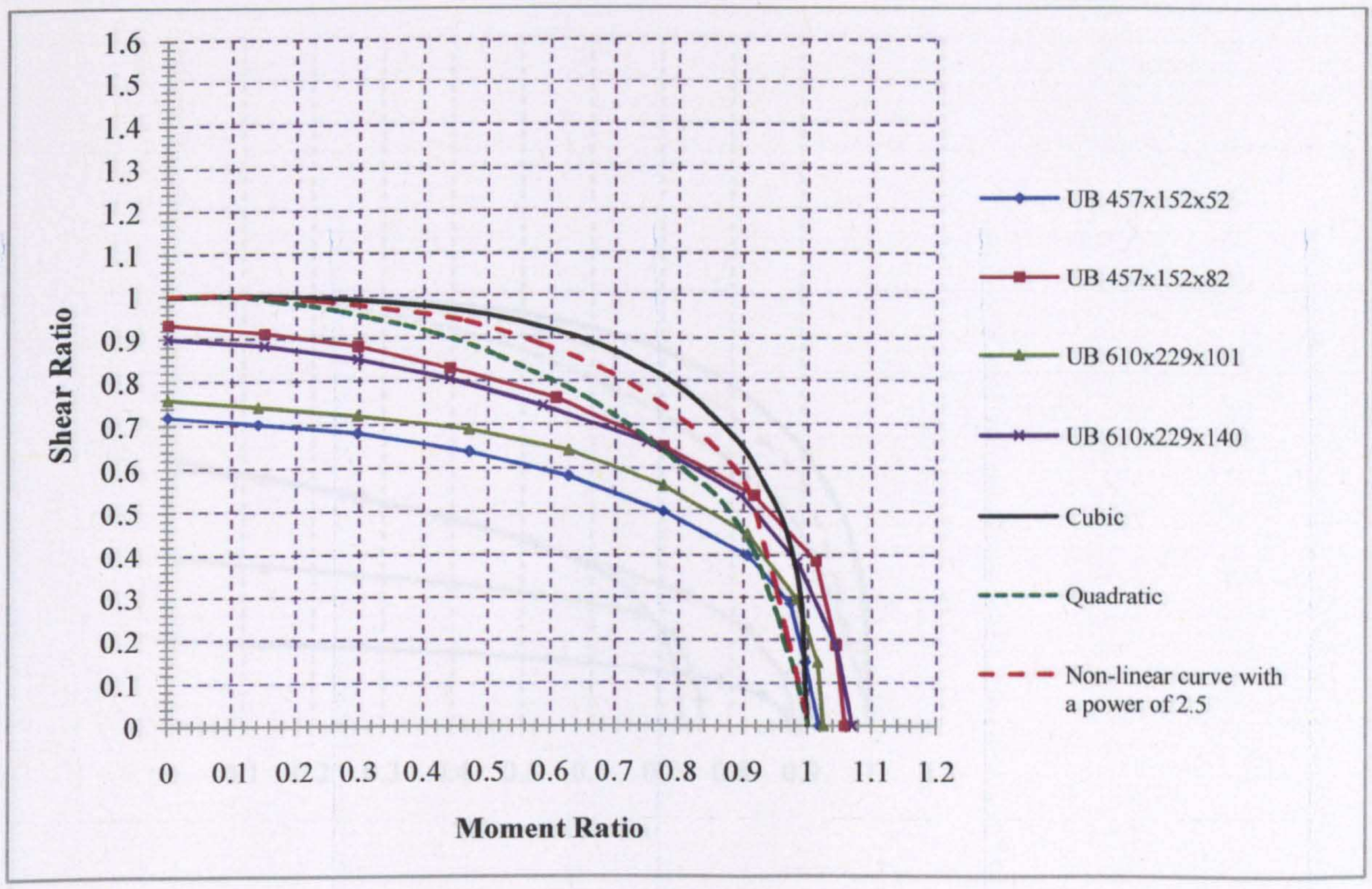

Figure 3.20: *V/M* ratios of various section sizes with A_v from **EC3** (Web open. A)

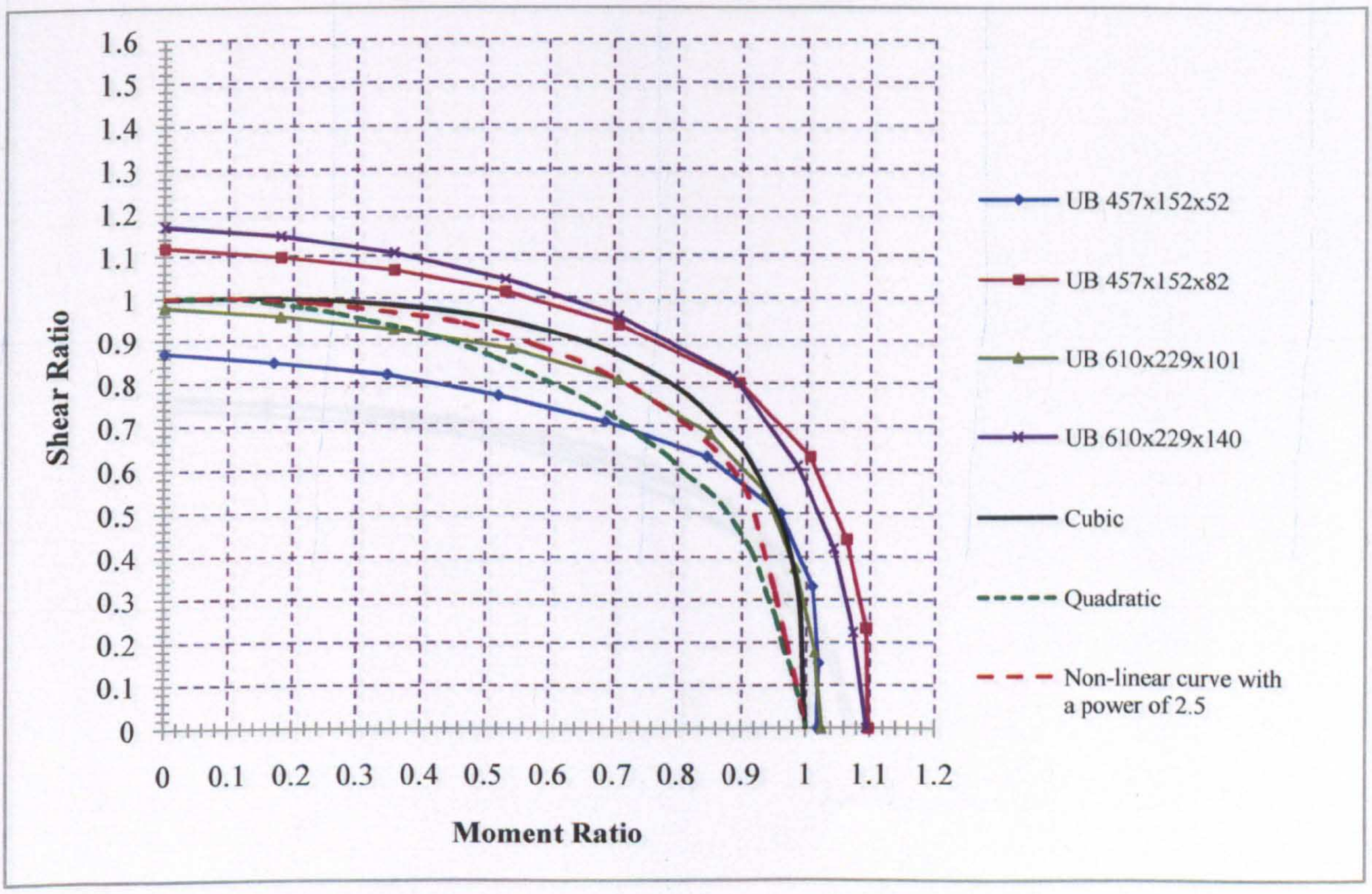

Figure 3.21: *V/M* ratios of various section sizes with A_v from **EC3** (Web open. C)

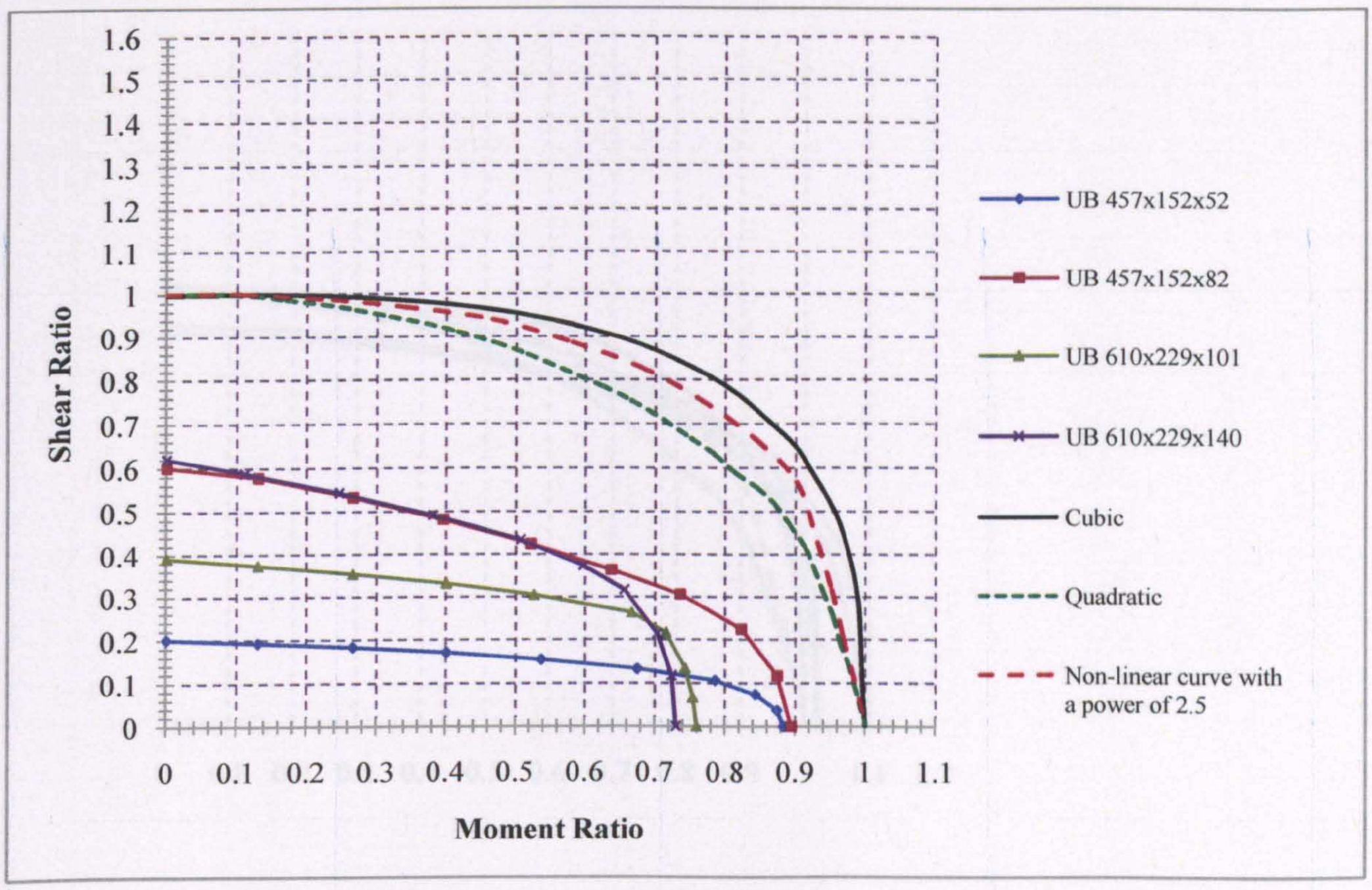

Figure 3.22: *V/M* ratios of various section sizes with A_v from **EC3** (Web open. I)

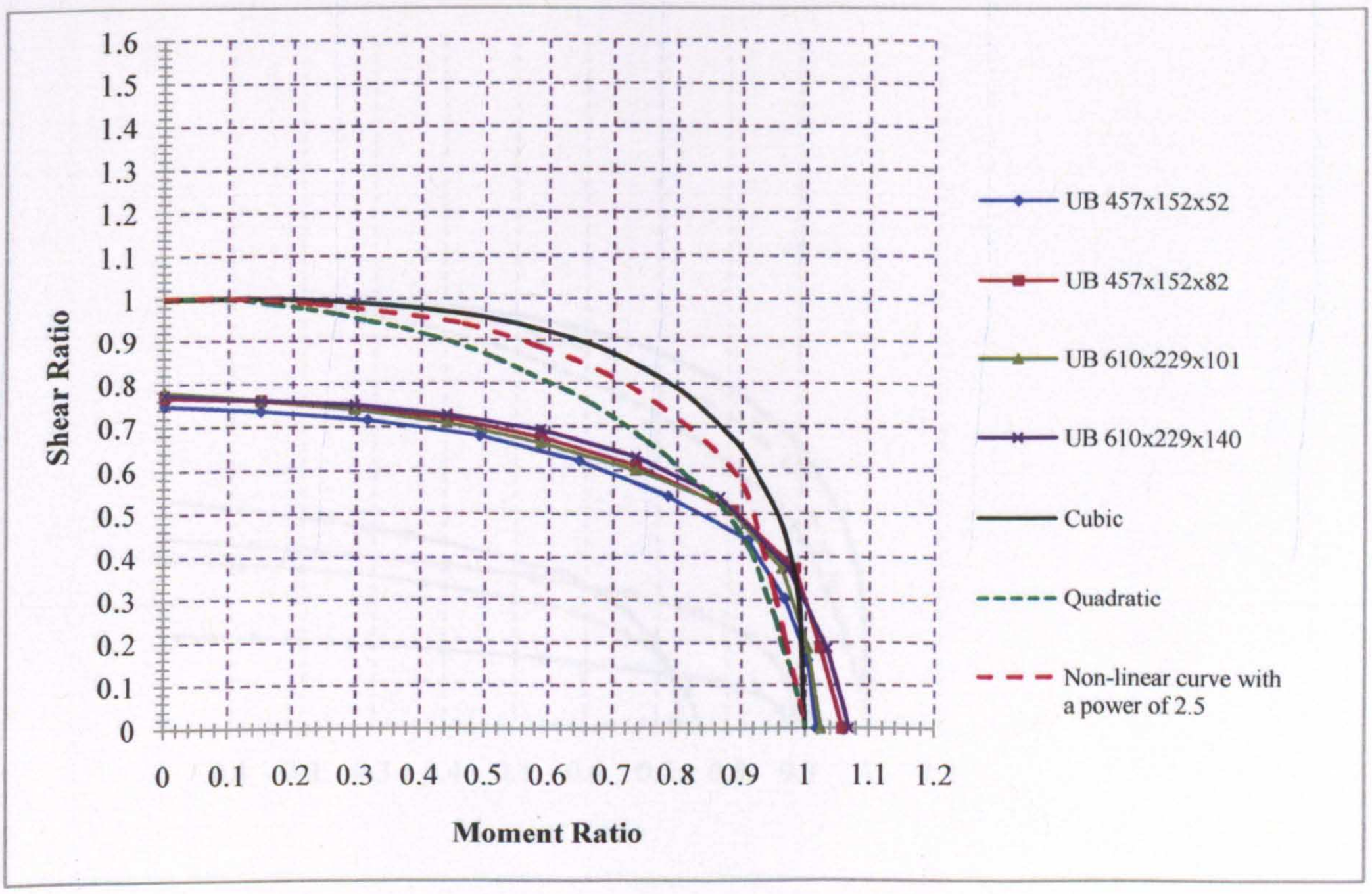

Figure 3.23: *V/M* ratios of various section sizes with A_v as proposed in **Formula 3.3** (Web open. A)

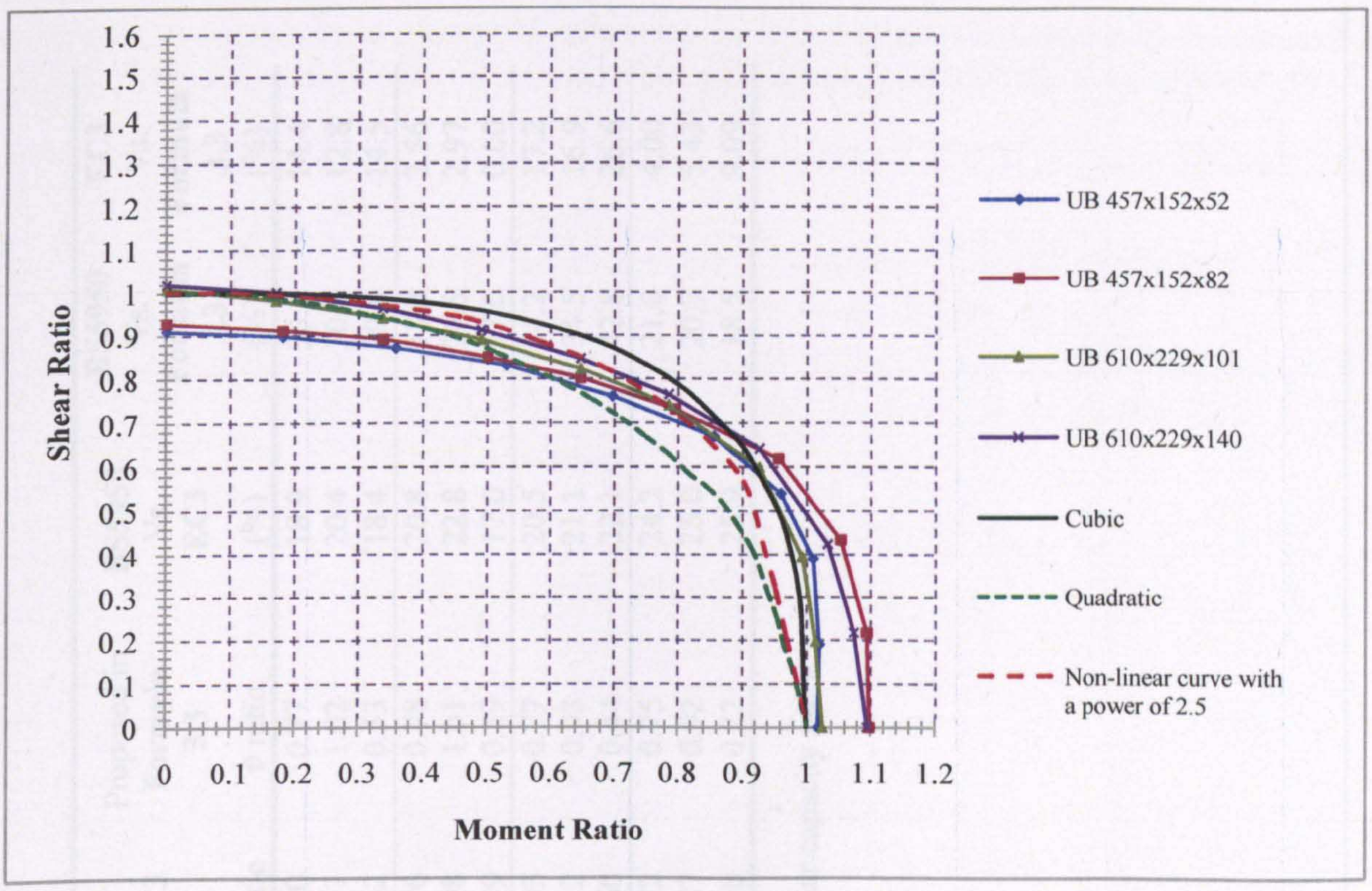

Figure 3.24: *V/M* ratios of various section sizes with A_v as proposed in **Formula 3.3** (Web open. C)

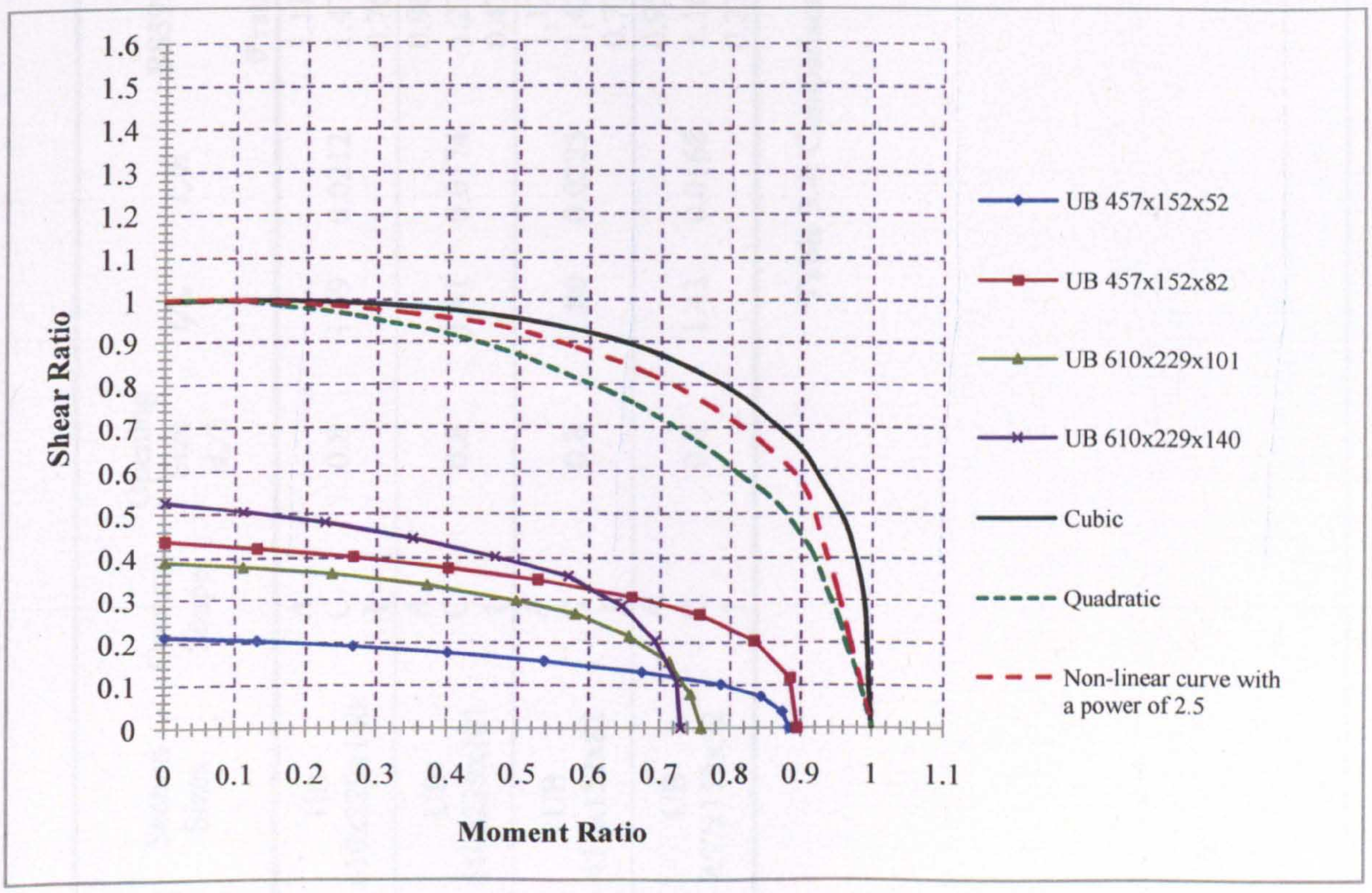

Figure 3.25: *V/M* ratios of various section sizes with A_v as proposed in **Formula 3.3** (Web open. I)

Section Sizes	Opening Shape	Opening Size d_o/h	t_f/t_w	t_w/h	BS5950 $\bar{v}$ ratio	EC3 $\bar{v}$ ratio	Proposed in **Formula 3.3** $\bar{v}$ ratio	**BS5950 Vs. EC3** (%)	**BS5950 Vs. Formula 3.3** (%)	**EC3 Vs. Formula 3.3** (%)
UB 610x229x140	A	0.8	1.69	0.0212	1.11	0.90	0.77	18.9	30.6	14.4
	C				1.47	1.17	1.02	20.4	30.6	12.8
	I				0.76	0.62	0.53	18.4	30.3	14.5
UB 610x229x101	A	0.8	1.41	0.0174	0.96	0.76	0.78	20.8	18.8	2.56
	C				1.27	0.98	1.01	22.8	20.5	2.97
	I				0.47	0.39	0.39	17.0	17.0	0.00
UB 457x152x82	A	0.8	1.80	0.0225	1.17	0.93	0.77	20.5	34.2	17.2
	C				1.42	1.12	0.93	21.1	34.5	16.9
	I				0.77	0.60	0.44	22.1	42.8	26.6
UB 457x152x52	A	0.8	1.43	0.0168	0.95	0.72	0.75	24.2	21.0	4.00
	C				1.16	0.87	0.92	25.0	20.7	5.43
	I				0.27	0.20	0.22	25.9	18.5	9.09

Table 3.4: Comparison of the shear capacity ratios

Studying all the above data, several conclusions are drawn concerning the three approaches for the evaluation of the shear cross sectional area, A_v, and they are given as follows:

- It is observed that beams with the same serial size have a similar moment ratio and only the shear ratio is altered.
- Among beams with the same serial size but with different weights per unit length, the lighter is always the one having a lower coupled shear capacity ratio, $\bar{v}$.
- Among beams of different serial sizes but with the same web thickness the ones with the thicker flanges have always higher $\bar{v}$ ratios. In most cases, as the ratio t_f/t_w is increased the $\bar{v}$ ratio is also increased.

The above statement is justified regarding the UB457x152x82 which has the highest t_f/t_w ratio among the particular beam sections. By using the shear area (**Formula 3.3**), this beam has the maximum decrease of the $\bar{v}$ ratio compared to the other beams. The percentage of difference is decreased when perforated sections with smaller web opening sizes are considered.

Observing **Table 3.4** it is noticed that the maximum deviation of the shear capacity ratios is found between the conservative shear area assumption taken from **BS5950 Part 1** and the shear area assumption taken from **Formula 3.3**. On the other hand, shear capacities estimated by using the assumptions from **EC3** and **Formula 3.3**, especially for beams sections UB457x152x52 and UB610x229x101, yielded very close results. This is due to the small flange thickness which little contributes to the shear capacity.

3.4.8 Comparison of *V/M* ratios for various web opening shapes and sizes

The non-dimensional shear-moment interaction (FEM) curves for the perforated section UB457x152x52 with various standard and non-standard web opening shapes and sizes are presented in **Figure 3.26**. FEM curves are arranged in a rational manner for easy comparison and reference. The global shear force, V_{Sd}, and the global moment, M_{Sd}, at the centre-line of the perforated sections at failure as taken from FEA are non-dimensionalised with respect to the global section capacities of the perforated sections, $V_{o,Rd}$ and $M_{o,Rd}$. The 'coupled' utilization ratios are represented as $\bar{v}$ (y-axis) and $\bar{m}$ (x-axis), respectively in **Figure 3.26**. As it is shown, all interaction curves are generally similar in pattern and consequently this enhances the feasibility of the application of a generalized shear-moment interaction curve for the practical design of perforated sections with web openings of various shapes.

To analyze the structural performance of perforated sections and the effects of both shapes and sizes of web openings, it is necessary to relate the opening depth, d_o, with the opening length, c. Therefore, for web openings with the same values of d_o but with different values of c, the load capacities of the perforated sections should be inversely proportional to the values of c. Regarding all elliptical web openings it is found that as the web opening size

becomes bigger the shear ratio increases, inversely to the typical beams. The explanation for this is given below, relating the load capacity with the assumption of the shear cross sectional area assumption in the global section capacity formula.

As anticipated, the reduction in the shear capacity is more pronounced when compared to the reduction in the moment capacity as the presence of the web opening reduces the shear area of the section significantly but the reduction of the plastic section modulus is small. At times it is noticed that the 'coupled' moment utilization ratio is slightly higher than 1.0. However, significant reduction of the moment capacity is obtained for perforated beams with elongated web openings.

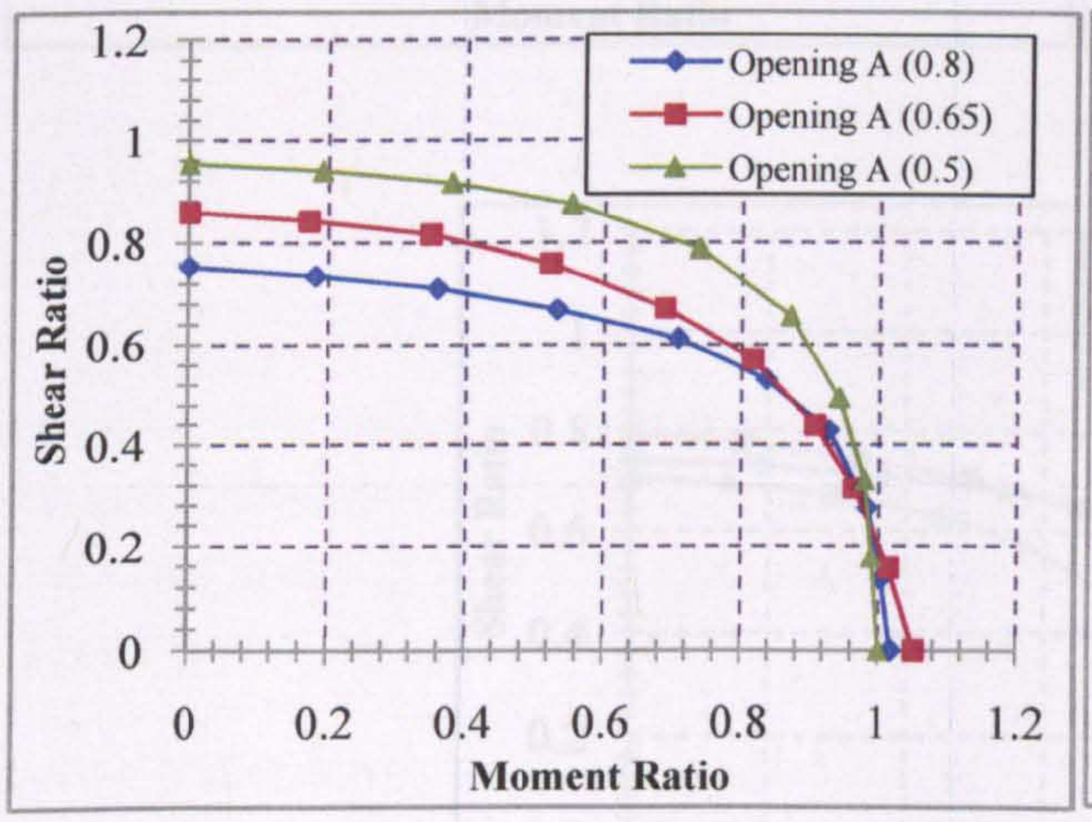

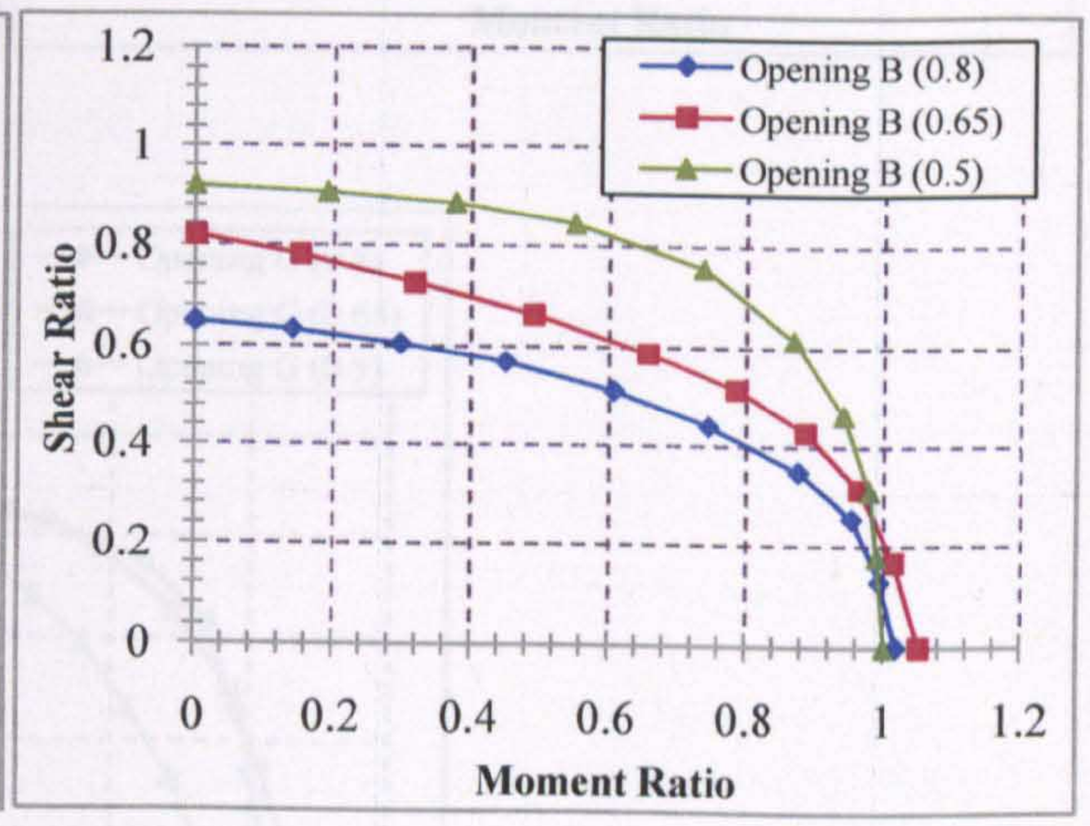

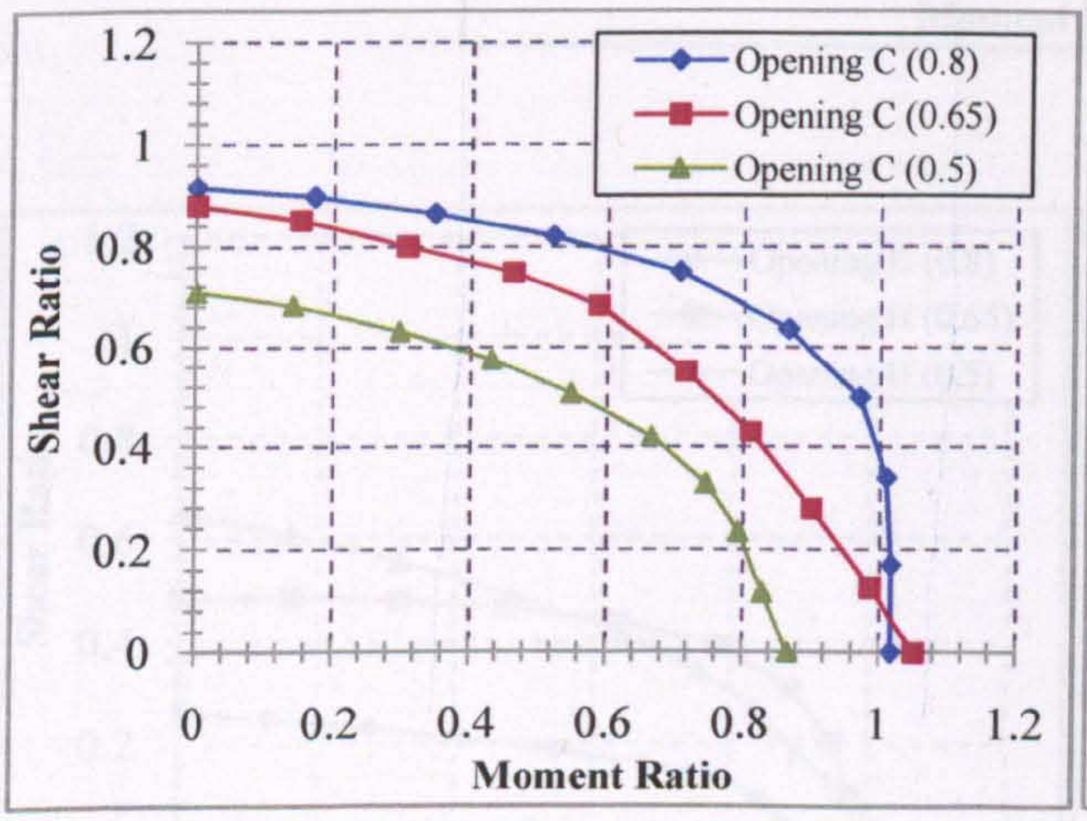

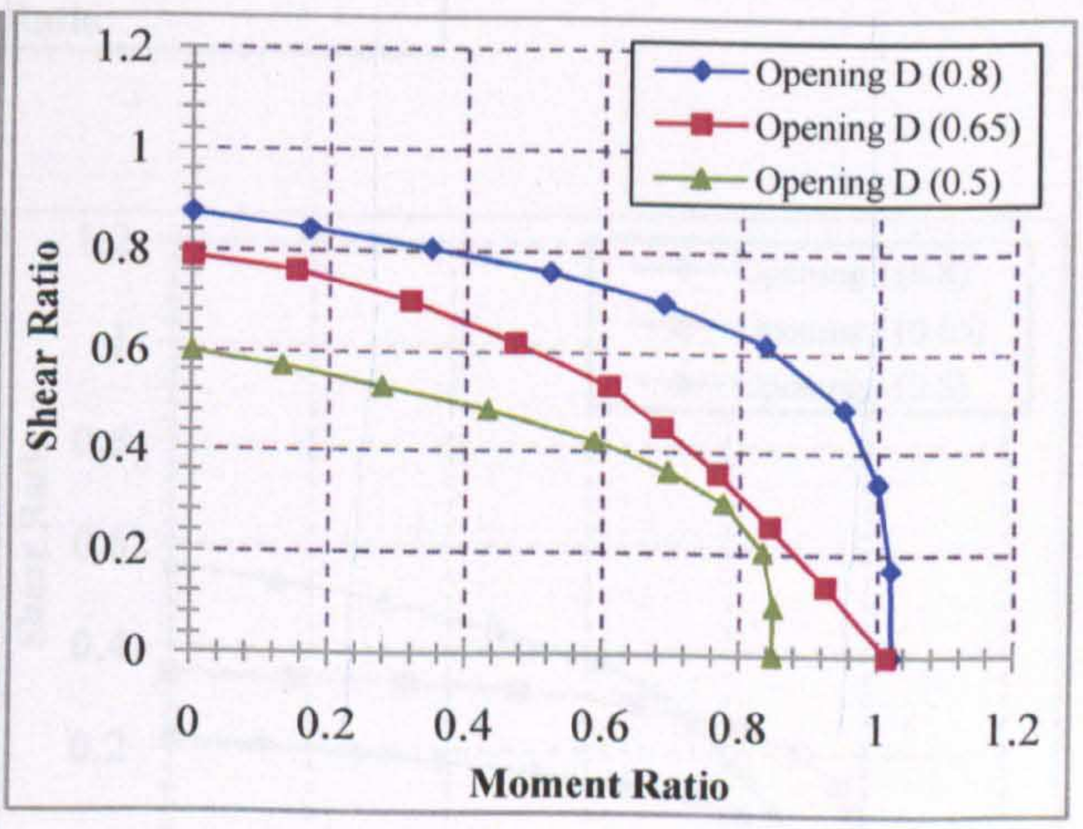

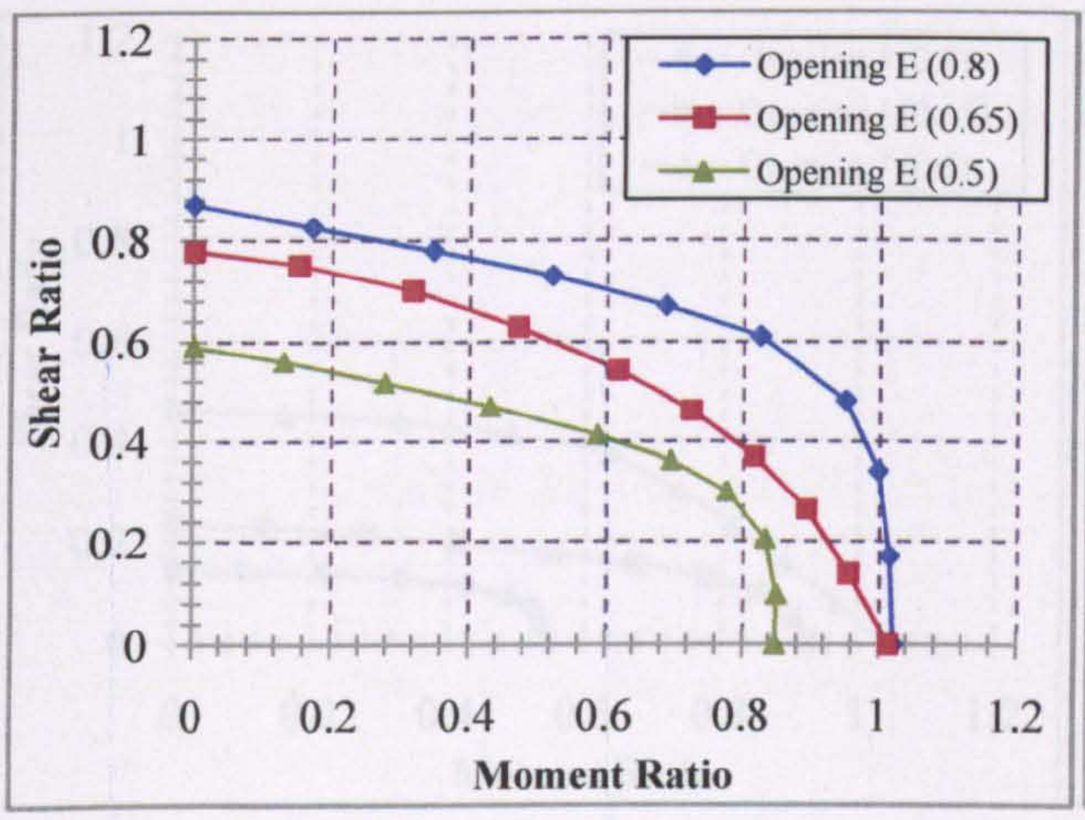
Opening E (0.8)
Opening E (0.65)
Opening E (0.5)
Shear Ratio
Moment Ratio
0
0.2
0.4
0.6
0.8
1
1.2

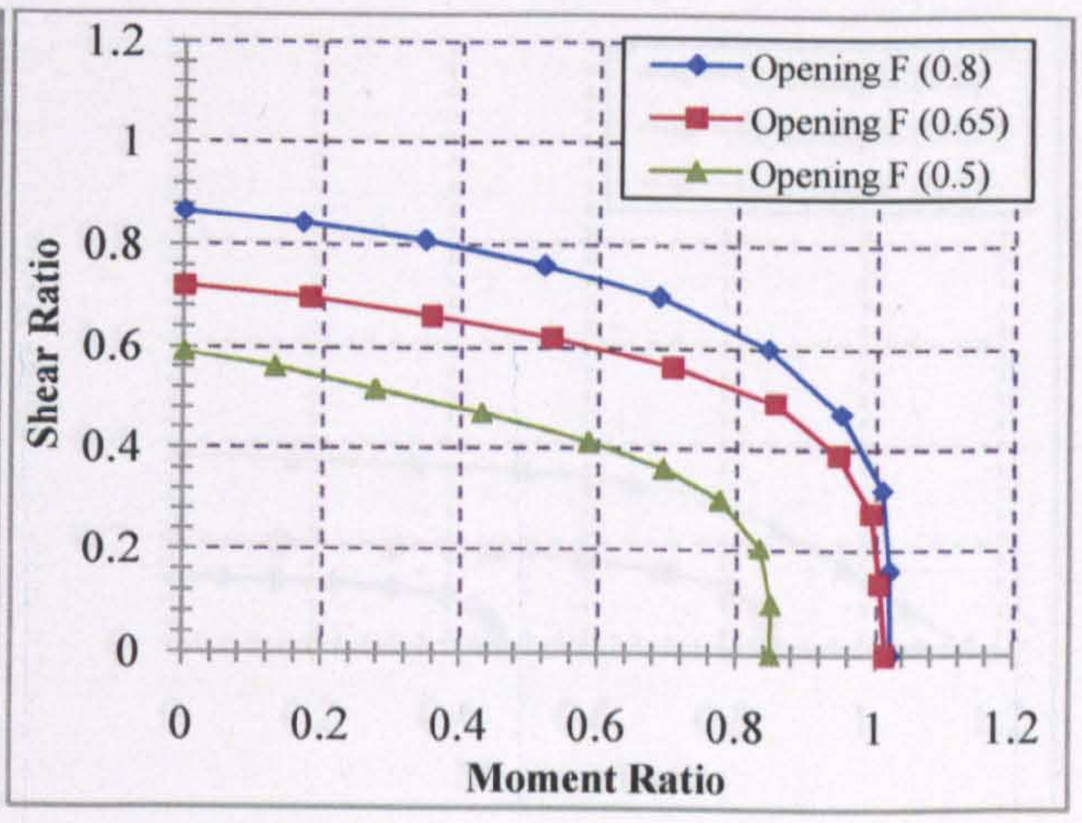
Opening F (0.8)
Opening F (0.65)
Opening F (0.5)
Shear Ratio
Moment Ratio
0
0.2
0.4
0.6
0.8
1
1.2

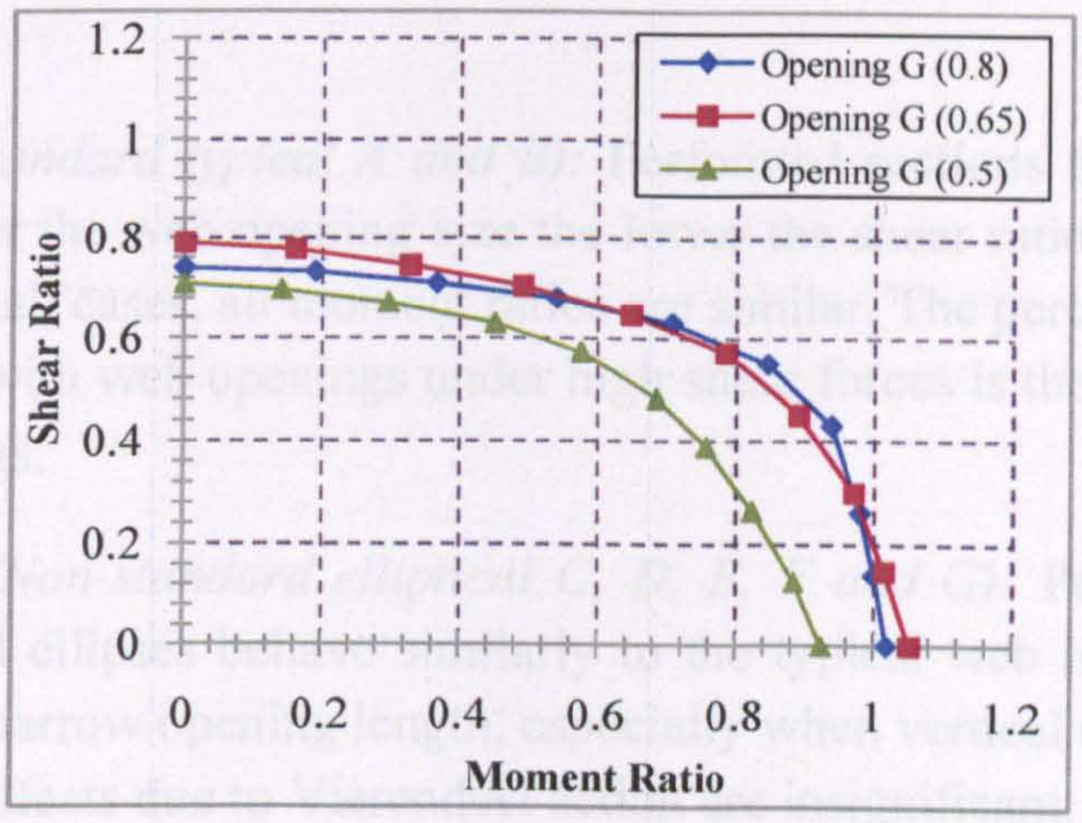
Opening G (0.8)
Opening G (0.65)
Opening G (0.5)
Shear Ratio
Moment Ratio
0
0.2
0.4
0.6
0.8
1
1.2

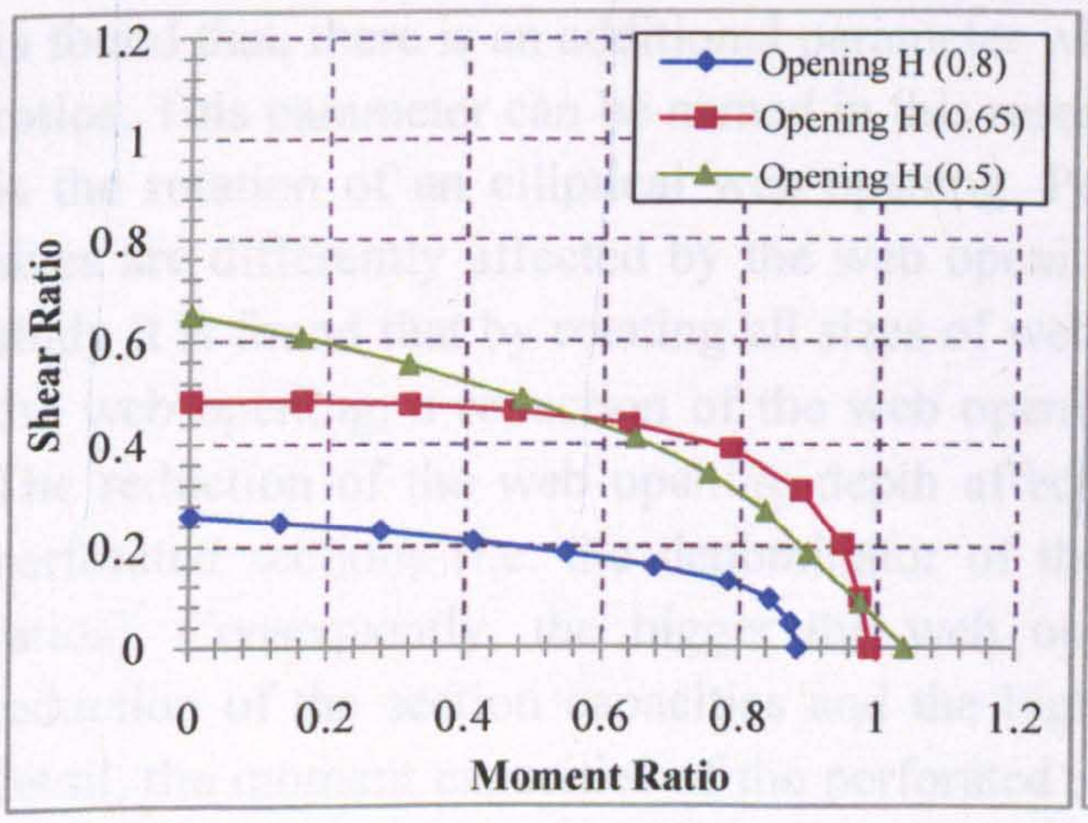
Opening H (0.8)
Opening H (0.65)
Opening H (0.5)
Shear Ratio
Moment Ratio
0
0.2
0.4
0.6
0.8
1
1.2

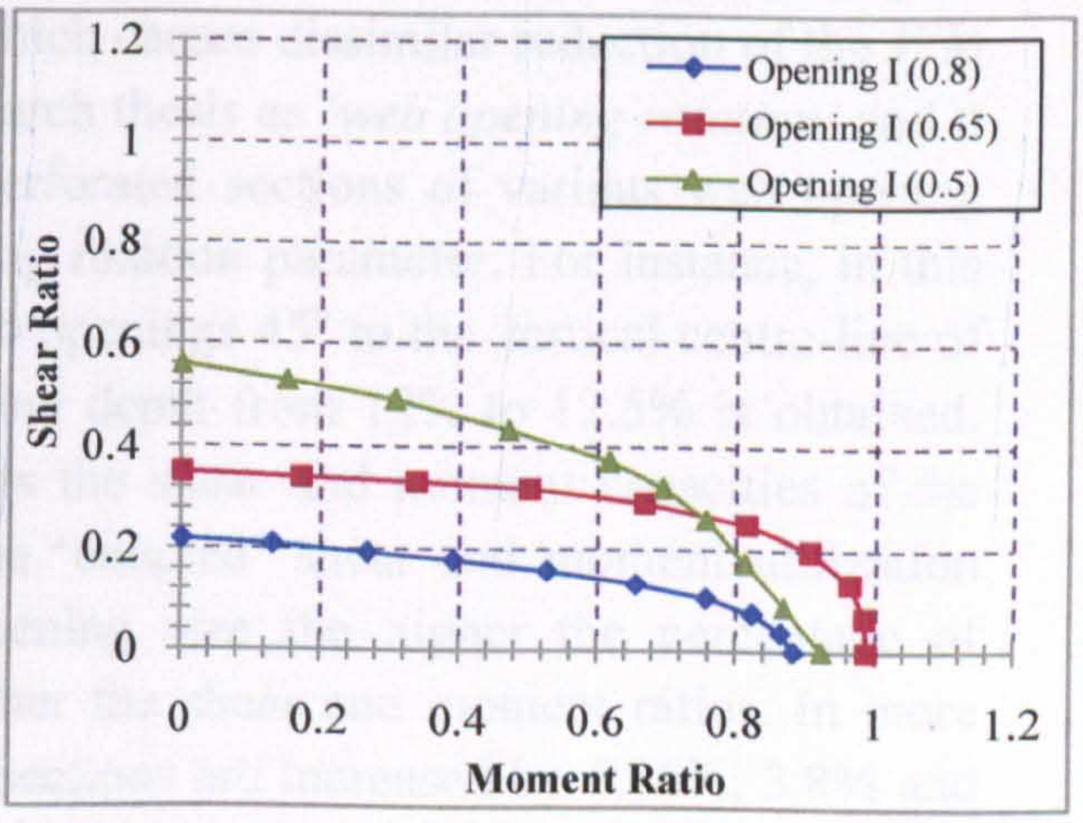
Opening I (0.8)
Opening I (0.65)
Opening I (0.5)
Shear Ratio
Moment Ratio
0
0.2
0.4
0.6
0.8
1
1.2

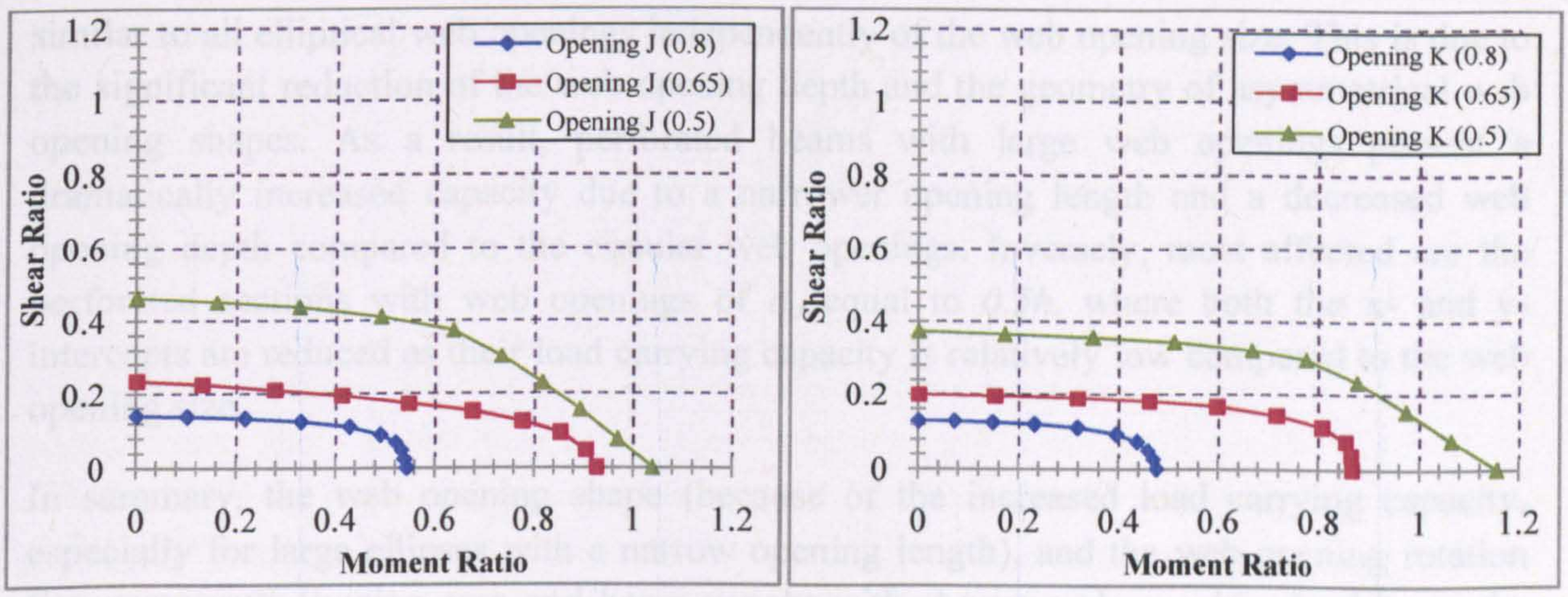

Figure 3.26: Non-dimensional *V/M* interaction curves for various web opening shapes and sizes

First category – (Standard typical A and B): Perforated sections in this category behave normally. The bigger the web opening size the lower the shear ratio is. Independent of the web opening size in all cases, all moment ratios are similar. The percentage of reduction for perforated sections with web openings under high shear forces is the same among the three sizes of web openings.

Second category - (Non-standard elliptical C, D, E, F and G): Perforated sections with vertical and inclined ellipses behave similarly to the typical web opening configurations. As the latter have a narrow opening length, especially when vertical elliptical web openings are considered, the effects due to Vierendeel action are insignificant.

When comparing the FEM curves between circular and inclined elliptical web openings it is found that, there is an additional parameter which causes dissimilar reduction of the *V/M* ratios. This parameter can be named in this research thesis as *'web opening rotation'* and it is the rotation of an elliptical web opening. Perforated sections of various web opening sizes are differently affected by the web opening rotation parameter. For instance, in this study it is found that by rotating all sizes of web openings 45° to the vertical centre-line of the web opening, a reduction of the web opening depth from 12% to 12.5% is obtained. The reduction of the web opening depth affects the shear and moment capacities of the perforated sections (i.e. the denominator of the 'coupled' shear and moment utilization ratios). Consequently, the bigger the web opening size the higher the percentage of reduction of the section capacities and the higher the shear and moment ratios. In more detail, the moment capacities of the perforated sections are increased by 6.36%, 3.8% and 2.1% for a perforated section UB457x152x52 with web openings of d_o equal to *0.8h*, *0.65h* and *0.5h*, respectively. The corresponding percentages for shear capacities of the perforated sections are 37%, 18.8% and 10.5%. The latter behaviour results in a significant re-arrangement of the M/V ratios. In addition, it is found that the load carrying capacities are

similar to all elliptical web openings independently of the web opening size. This is due to the significant reduction of the web opening depth and the geometry of asymmetrical web opening shapes. As a result, perforated beams with large web openings present a dramatically increased capacity due to a narrower opening length and a decreased web opening depth compared to the circular web openings. Inversely, most affected are the perforated sections with web openings of d_o equal to *0.5h*, where both the x- and y-intercepts are reduced as their load carrying capacity is relatively low compared to the web opening size.

In summary, the web opening shape (because of the increased load carrying capacity, especially for large ellipses with a narrow opening length), and the web opening rotation (i.e. same web opening area and beam weight with shorter web opening depth), are the main factors which cause dissimilar reduction of the 'coupled' shear and moment utilization ratios when elliptical web openings are considered.

Observing the *V/M* ratios it is also found that perforated sections with web opening sizes d_o equal to *0.65h* and *0.8h*, while they have different y-intercepts, the x-intercepts are similar and very close to unity. On the other hand, all perforated sections of this category with a web opening size d_o equal to *0.5h*, have reduced moment ratios. Another cause of this result is the uneven stress distribution in the vicinity of elliptical web openings.

Inclined elliptical web openings (G) with d_o equal to *0.8h*, *0.65h* and *0.5h*, present similar *V/M* ratios, while the overall behaviour is like the other perforated sections with elliptical web openings. The y-intercepts are closer here as there is no reduction of the opening depth, d_o, for this web opening shape. It should be noted that, the area of the maximum web opening is only 3.7% smaller than the area of the typical circular web openings, whereas the d_o are the same. Moreover, when comparing the performance of these two perforated sections it can be easily concluded that apart from the opening length, *c*, the web opening shape also controls the performance due to the movement of the stress concentration points.

Third category – (Non-standard elongated H, I, J and K): In these perforated sections the size of the opening length dramatically affects their structural behaviour. Perforated sections with relatively large web openings H and I have FEM curves of similar pattern and relatively close moment ratios. Moreover, perforated sections with dramatically elongated web openings J and K have FEM curves of similar patterns, while the moment ratios also significantly changed dependent on the web opening size. It is observed that perforated sections with the elongated web opening shapes and d_o equal to *0.8h* present considerably reduced moment ratios when the web openings are located at a high moment region. The important reduction of the moment ratios dominated in this category is justified by the existence of high bending moments applied on perforated sections with large web openings located close to mid-span.

3.4.9 Comparison of yield patterns for various web opening shapes and sizes

The yield patterns for perforated beams with all eleven web opening shapes of the three diameters (d_o equal to *0.8h*, *0.65h* and *0.5h*) located at four different positions (position x is equal to 2, 4, 8 and 10) are extensively presented in **Appendix 6**. Von-Mises stresses in the vicinity of the web openings at failure points (i.e. at the FE convergence solution points) represent the plastic hinges which are always formed at both ends of the tee-sections, under different *V/M* ratios. The global shear force and bending moment acting on the perforated sections are related to the local co-existing forces and moments acting on the tee-sections above and below the web openings. In **Figure 3.27** to **3.30**, the Von-Mises stresses in the vicinity of selected perforated beams with web openings with diameter, d_o, equal to *0.8h* are only plotted for direct comparison, while they are under high shear forces. Moreover, an idea of addition local deflections can be obtained by the above figures.

An overview of the results by a comprehensive study of **Appendix 6** and general comparisons are given as follows. Also, in perforated sections with a smaller diameter of web openings, the overall structural behaviour remains the same. When the perforated sections are under high global shear and low global bending moment, the plastic hinges at the LMS and HMS of the perforated sections are shown to be fully developed (e.g. **Figure 3.27**). On the other hand, when the perforated sections are under low global shear force and high global bending moment, plastic hinges at both ends of the tee-sections above and below the web openings are mobilized by the action of large local axial forces (e.g. **Figure 3.28**). Hence, only the plastic hinges of the LMS of the perforated sections are shown to be fully developed. At the same time highly stressed compression flanges are found on the HMS. It is also observed, that for most of the perforated sections with narrow opening length, *c*, such as perforated sections with web openings A, C, D, E, F and G, the yield zones at both the LMS and HMS of the perforated sections are significantly overlapped (e.g. **Figure 3.29**). Finally, when the perforated sections are under pure bending moment, axial forces due to the global bending moment action exist in the tee-sections, and highly stressed top tee-sections are observed.

Furthermore, it should be noted that an additional deflection (i.e. Vierendeel deflection) is observed in perforated sections with square, elongated elliptical and rectangular web openings (e.g. **Figure 3.30**). These perforated sections suddenly failed at low loading levels by exceeded element deformation/distortion. This was a result of high shear forces and Vierendeel bending moments applied on the long opening length, *c*, of the top tee-section.

Knowing the position of the plastic hinges when the web openings are located at high shear regions, the actual critical opening length, *c*, of each web opening is given and is considered for further investigation.

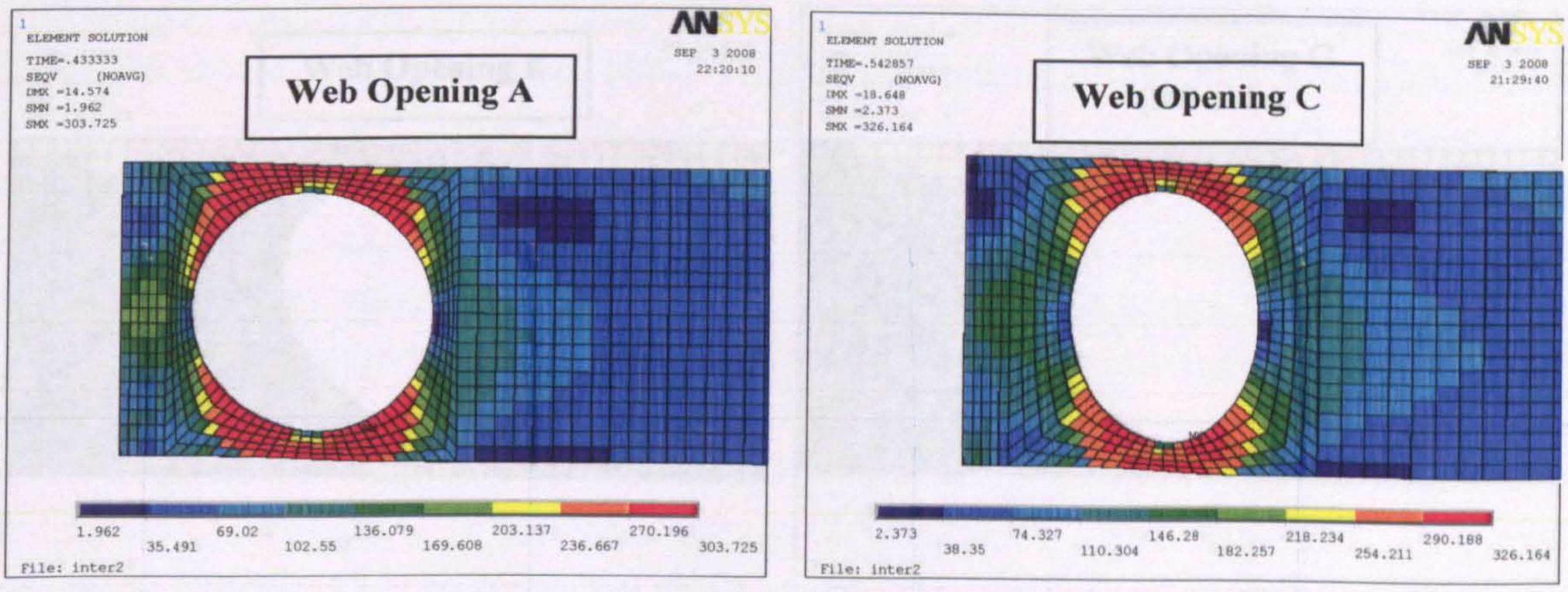

Figure 3.27: Failure stresses with web opening at high shear region ($d_o/h=0.8$)

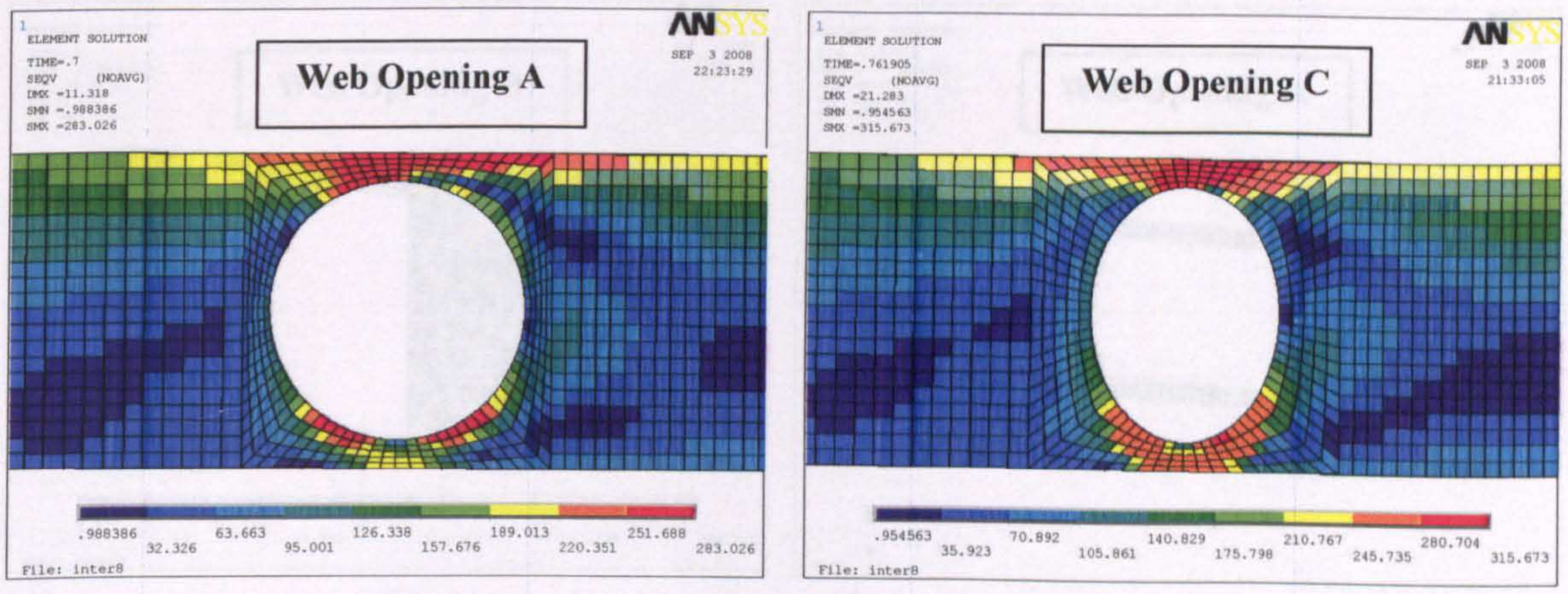

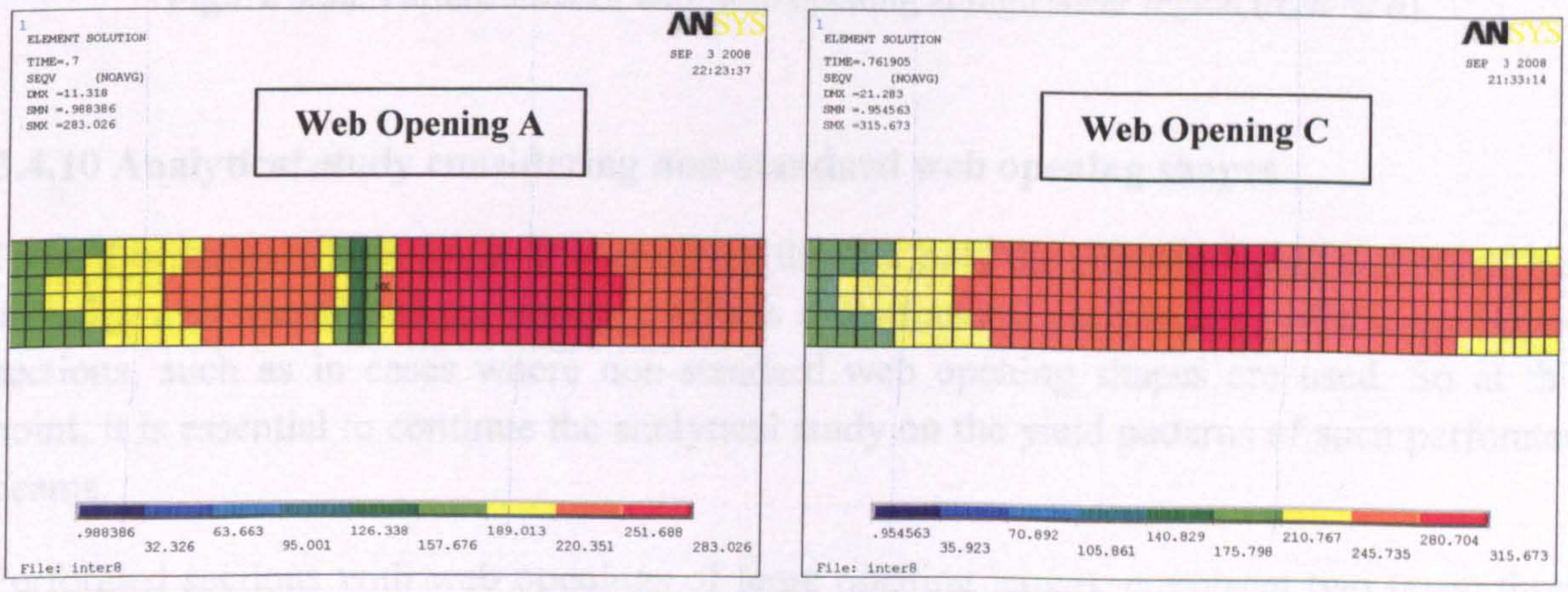

Figure 3.28: Failure stresses with web opening at high moment and low shear region ($d_o/h=0.8$)

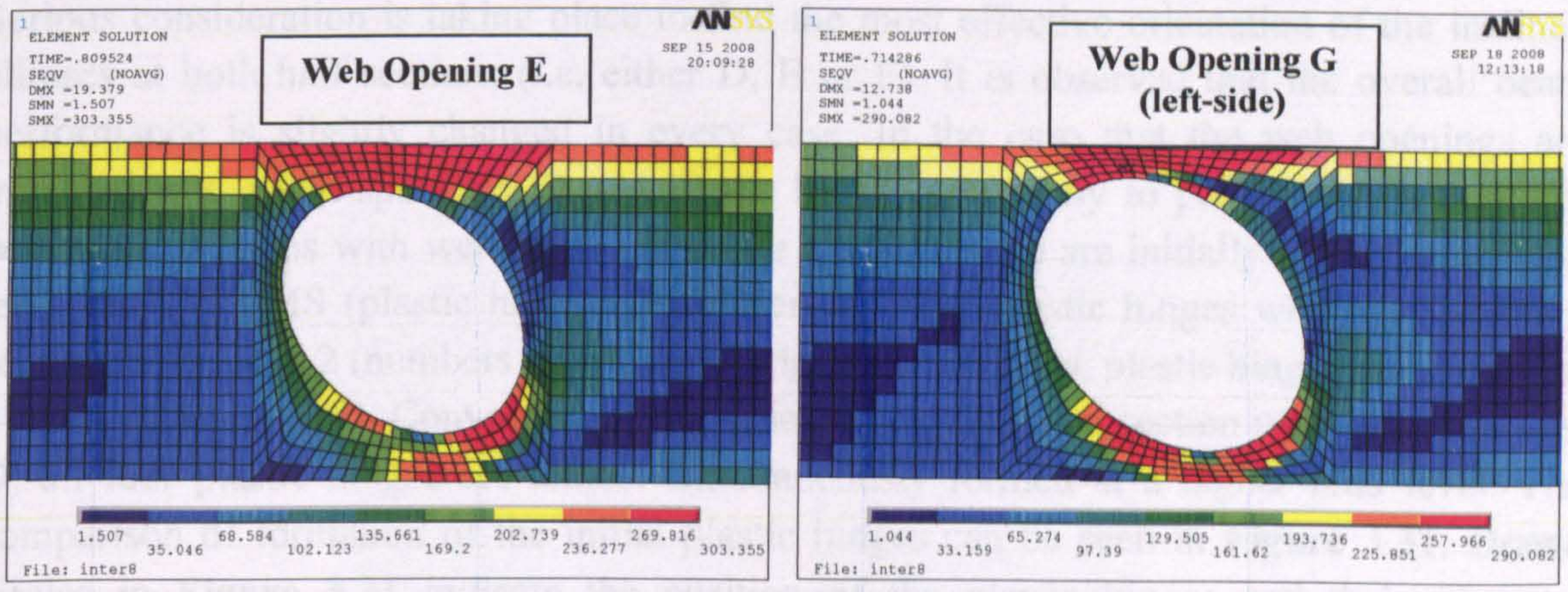

Figure 3.29: Failure stresses with web opening at high moment and low shear region ($d_o/h=0.8$)

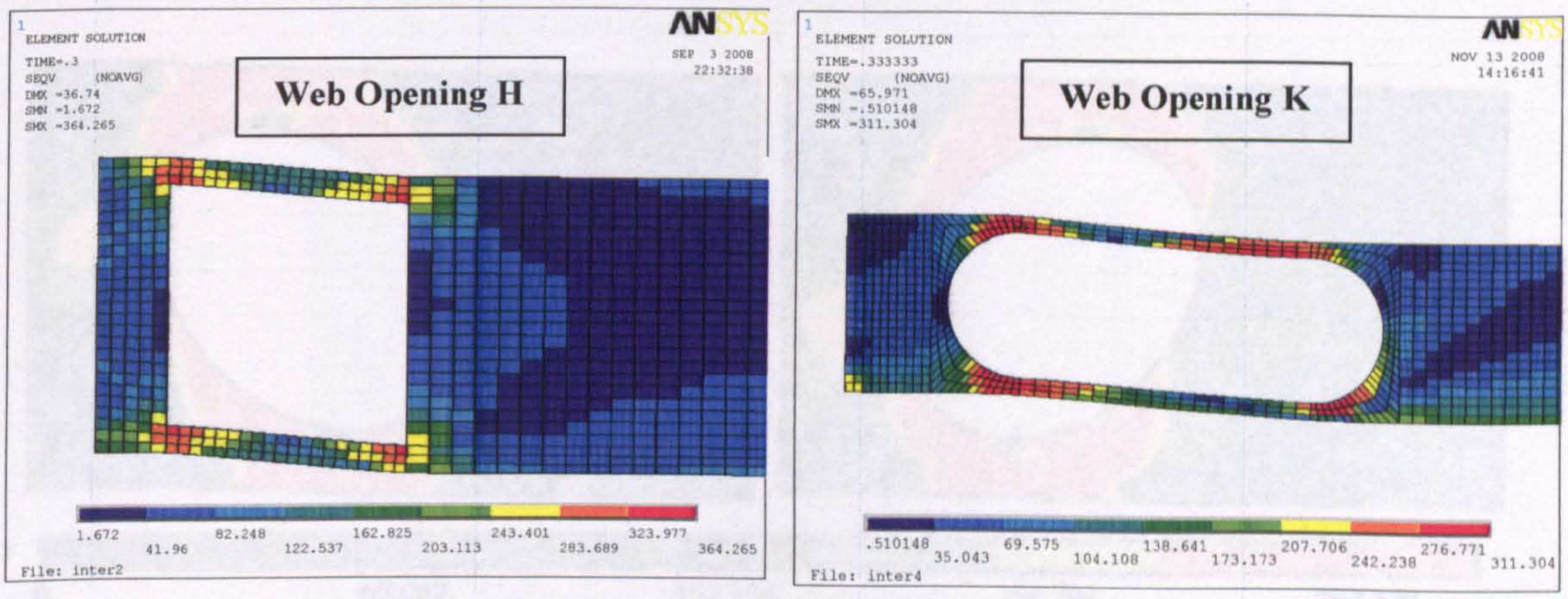

Figure 3.30: Failure stresses with web opening at high shear region ($d_o/h=0.8$)

3.4.10 Analytical study considering non-standard web opening shapes

From this parametric FE study it is observed that not only the opening length and depth, but also the web opening shape strongly affects the structural performance of the perforated sections, such as in cases where non-standard web opening shapes are used. So at this point, it is essential to continue the analytical study on the yield patterns of such perforated beams.

Perforated sections with web openings of large opening length, c, present two (even three sometimes; i.e. see K) plastic hinges on the top tee-section. This is mainly observed when the web opening is under high bending moments. On the other hand, when perforated sections with small critical opening length such as A, B, C, D, E, F and G are considered, one highly stressed point is found while the yield zones at both the LMS and HMS of the perforated sections overlapped significantly.

Serious consideration is taking place to find the most effective orientation of the inclined ellipses at both half sections (i.e. either D, E or F). It is observed that the overall beam performance is slightly changed in every case. In the case that the web openings are mirrored to the mid-span (i.e. D and E) the behaviour is easy to predict. Particularly, in perforated sections with web openings E, the plastic hinges are initially formed at the top tee-section at LMS (plastic hinge 1) and then all other plastic hinges with the following sequence: 4, 3 and 2 (numbers according to **Figure 2.13**). Also, plastic hinges are formed at a low load level point. Conversely, in the case of the perforated section with web openings D, all four plastic hinges are almost simultaneously formed at a higher load level. The comparison of formation of the initial plastic hinges can be seen in **Figure 3.31**. Drawn circles in **Figure 3.31** indicate the position of the plastic hinges and their diameter demonstrates the stress concentration magnitude at these points.

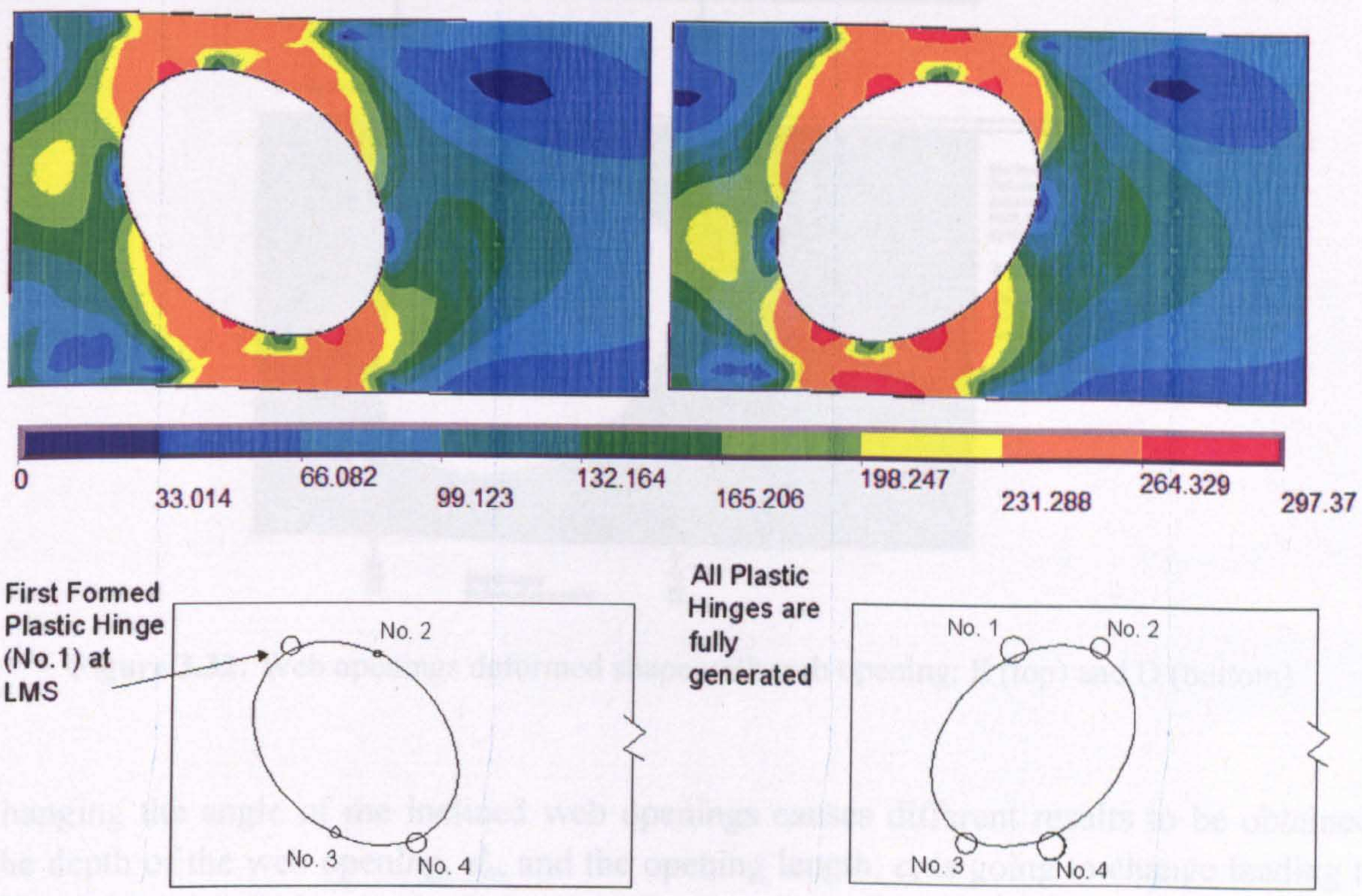

Figure 3.31: Plastic hinges at perforated section with web opening; E (left) and D (right)

In more detail, the FEA shows that in cases of perforated sections with web openings E; the ellipse is significantly elongated while its minor axis is shortening by stretching the shape due to the additional deflection. Hence, the total displacement of the beam is large and easily seen. Inversely, in cases of perforated sections with web openings D the elliptical shape tends to transform to an approximate 'circular' shape. Therefore, the additional

displacement of the perforated section is smaller and the deformation of the web opening is not easily seen. The deformation effects of the web opening edges can be seen in **Figure 3.32**.

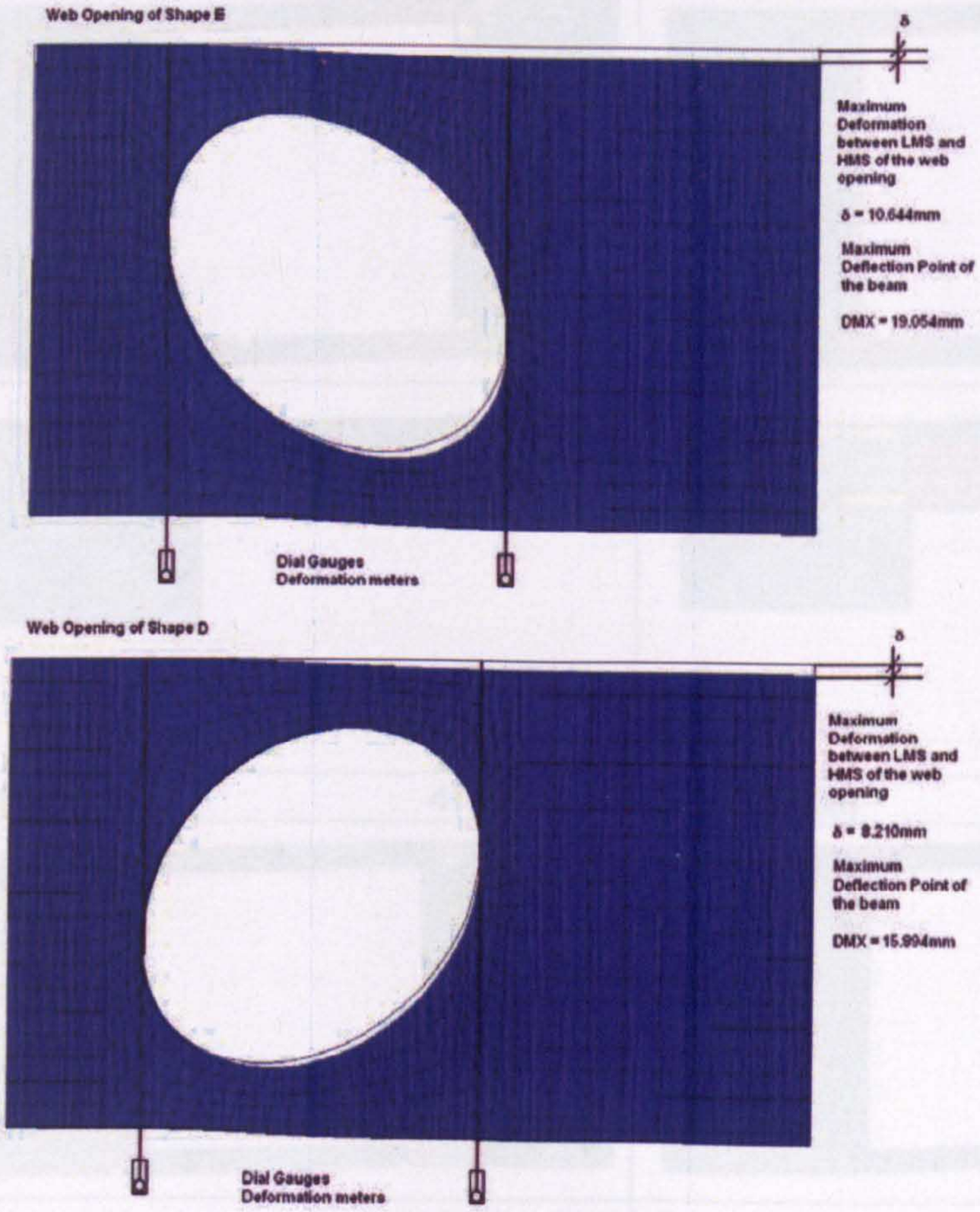

Figure 3.32: Web openings deformed shape with web opening; E (top) and D (bottom)

Changing the angle of the inclined web openings causes different results to be obtained. The depth of the web opening, d_o, and the opening length, c, is going to change leading to different results. The angle is limited in this study to 45° and it generates same angles to both quadrants. However, further investigation in **Chapter 4** illustrates which are the most effective 'rotation angles' for web opening shapes based on the novel inclined elliptical geometry.

3.4.11 UB section sizes

It is important to clarify that this parametric FE study concerns only typical universal beams. Insignificant differences in terms of shear-moment interaction curves, failure modes, yield patterns and deformation characteristics are observed when studying the four different typical mid-range universal beams, as noted at the beginning of this study.

3.4.12 Mesh refinement study

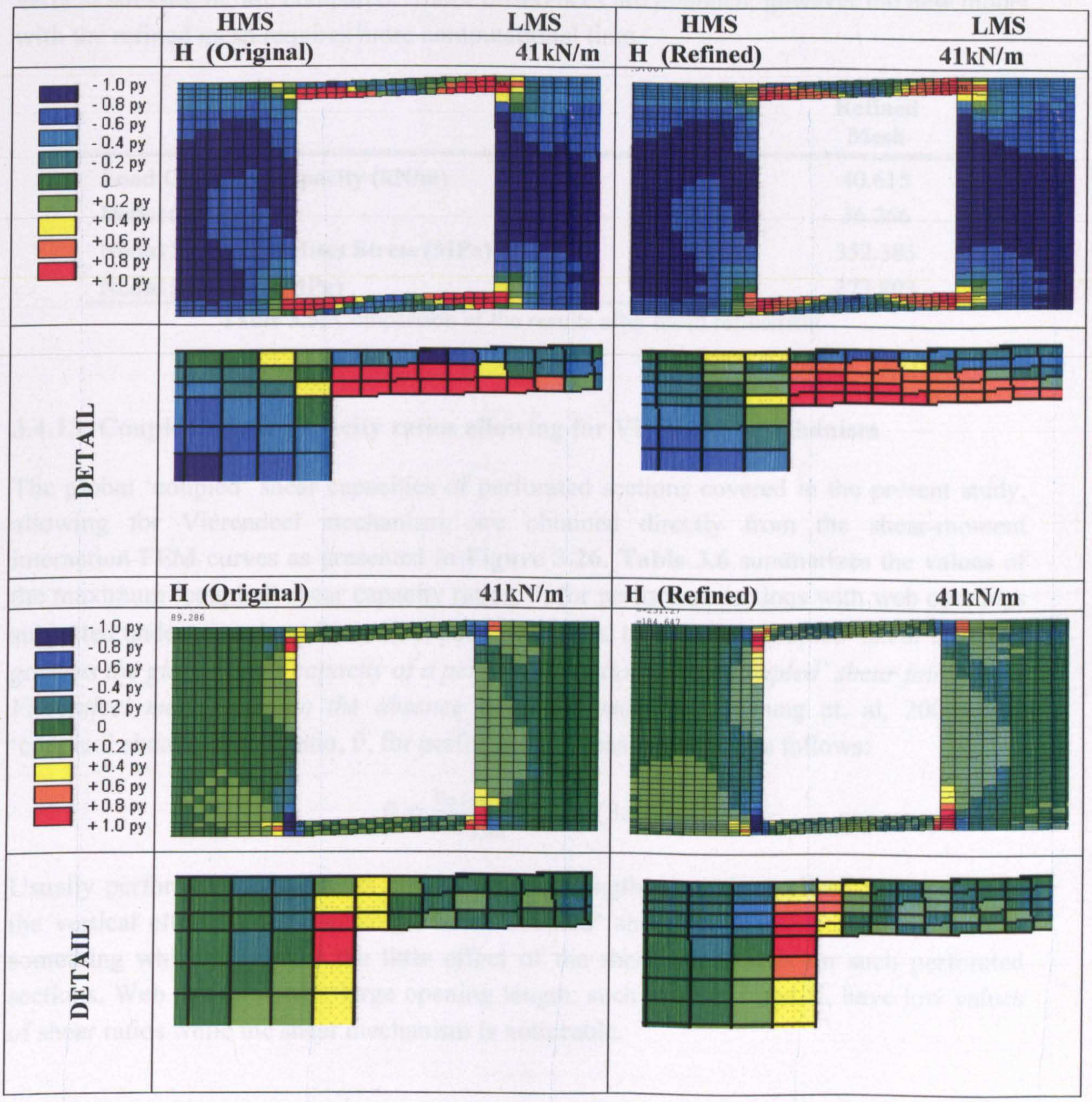

Figure 3.33: Failure stresses at position x equal to 8 for perforated section with web opening H

A mesh refinement study is carried out again to examine the need for smaller elements and in order to validate the FE results. The yield patterns of the perforated beams with square web openings (H) under high bending moments and low shear forces (position x=8), are examined with coarser (original) as well as refined mesh, as it is shown in **Figure 3.33**. The results of both the LMS and HMS of the perforated sections with the original and the refined mesh are similar to each other, after the mesh refinement. More analytical, in **Table**

3.5 the magnitudes of the load carrying capacities, deflections, Von-Mises and nodal vertical stresses, σ_y, are compared. Minor differences are obtained, however the new model with the refined mesh requires more computational time.

	Original Mesh	**Refined Mesh**
Load Carrying Capacity (kN/m)	40.615	40.615
Deflection (mm)	35.334	36.266
Nodal Max. Von-Mises Stress (MPa)	344.713	352.385
Nodal Stress, σ_y (MPa)	277.585	277.893

Table 3.5: Comparison of the results after mesh refinement

3.4.13 'Coupled' shear capacity ratios allowing for Vierendeel mechanism

The global 'coupled' shear capacities of perforated sections covered in the present study, allowing for Vierendeel mechanism, are obtained directly from the shear-moment interaction FEM curves as presented in **Figure 3.26**. **Table 3.6** summarizes the values of the maximum 'coupled' shear capacity ratios, $\bar{v}$, for perforated sections with web openings subjected under pure shear forces (i.e. position x equal to 1). *"The 'coupled' shear capacity governs the global shear capacity of a perforated section under 'coupled' shear failure and Vierendeel mechanism, in the absence of global moment."* (Chung et. al, 2003) The 'coupled' shear capacity ratio, $\bar{v}$, for perforated sections is defined as follows:

$$\bar{v} = \frac{V_{o,Sd(FEA)}}{V_{o,Rd}} \qquad (3.6)$$

Usually perforated sections with narrow opening length, c, as the inclined and especially the vertical elliptical web openings, have 'coupled' shear ratios closer to unity. This is something which illustrates the little effect of the shear mechanism on such perforated sections. Web openings with large opening length; such as H, I, J and K, have low values of shear ratios while the shear mechanism is noticeable.

Opening Types	Opening Shapes	Opening Length, *c*	Maximum 'Coupled' Shear Ratios, $\bar{v}$ ($M_{Sd}/M_{o,Rd}=0$)					
			0.44h	*0.5h*	*0.57h*	*0.65h*	*0.7h*	*0.8h*
Standard Typical	**A**	0.23	-----	0.95	-----	0.86	-----	0.75
	B	0.43	-----	0.92	-----	0.82	-----	0.65
Non-Standard Elliptical	**C**	0.14	-----	0.71	-----	0.88	-----	0.92
	D	0.25	0.60	-----	0.79	-----	0.88	-----
	E	0.25	0.59	-----	0.78	-----	0.87	-----
	F	0.25	0.59	-----	0.72	-----	0.87	-----
	G	0.21	-----	0.71	-----	0.79	-----	0.74
Standard Elongated	**H**	1.00	-----	0.65	-----	0.48	-----	0.26
	I	1.16	-----	0.56	-----	0.35	-----	0.22
	J	2.00	-----	0.46	-----	0.23	-----	0.14
	K	2.23	-----	0.37	-----	0.20	-----	0.13

Table 3.6: Summary of 'coupled' shear capacity ratios, $\bar{v}$

It is worth noting that, in order to find the critical opening length, *c*, for each web opening configuration, the Von-Misses stress distribution at the top tee-section needs to be considered when the web opening of the perforated section is under high shear forces (i.e. $M_{o,Sd}=0$).

3.4.14 Generalized non-dimensional *V/M* interaction design curves

A generalized non-dimensional shear-moment interaction curve is presented herein, based on the general design theoretical model found from Chung et al. (2003). This is an interaction curve with an elliptical expression which can be used to allow for an interaction between the shear force and the moment in solid rectangular plates; following the same concept with codes of practices and it is shown below:

$$v^2 + m^2 = 1 \qquad (3.7) \quad \text{or} \quad v = \sqrt{1 - m^2} \qquad (3.8)$$

Where: v is the shear utilization ratio $= \frac{V_{Sd}}{V_{o,Rd}}$

m is the moment utilization ratio $= \frac{M_{Sd}}{M_{o,Rd}}$

For perforated sections, this interaction curve is modified to allow for the presence of Vierendeel mechanism. The above expressions are modified to cover the new FEM curves which are obtained for non-standard and elongated web openings. Proposed design curves are drawn for each particular case. For practical reasons it is decided to follow the same categorization of the beams as before.

The reviewed generalized proposed method is presented herein:

For $\bar{v} \geq 0.72 \rightarrow \quad \bar{\bar{v}} = \bar{v}(1 - m^z)^k \qquad (3.9)$

For $\bar{v} < 0.72 \rightarrow \quad \bar{\bar{v}} = \bar{v} - q + q(1 - m^z)^{\,k}$ (3.10)

The z, k and q factors, can be adopted in two different ways; from either **Table 3.7** or from **Table 3.8** for $\bar{v} \geq 0.72$ and **Table 3.9** for $\bar{v} < 0.72$. The combination of the factors is not unique, however well agreement between the design curve and the FEM values is achieved. In **Table 3.8** and **3.9**, for practical convenience the web opening types are categorized to minimize the number of factors. The 'coupled' shear capacity ratio, $\bar{v}$, should always be higher than the design 'coupled' shear capacity ratio, $\bar{\bar{v}}$. Also, when the 'coupled' shear capacity ratio, $\bar{v}$, has a negative value, it is assumed as zero.

Web Opening Depth, d_o		***0.5h***			***0.65h***			***0.8h***		
Factors		***q***	***z***	***k***	***q***	***z***	***k***	***q***	***z***	***k***
Web Openings Shapes	**A**	-----	2.50	0.30	-----	1.30	0.30	-----	1.80	0.30
	B	-----	2.00	0.30	-----	1.00	0.30	0.70	1.50	0.40
	C	1.40	2.00	0.50	-----	2.00	0.70	-----	1.20	0.20
	D	1.40	2.00	0.45	-----	1.70	0.80	-----	1.00	0.20
	E	1.40	2.00	0.45	-----	1.60	0.60	-----	0.80	0.20
	F	1.40	2.00	0.45	-----	1.00	0.20	-----	1.10	0.20
	G	1.20	2.00	0.40	-----	1.60	0.30	-----	1.70	0.20
	H	0.70	1.50	0.60	0.50	3.50	0.40	0.50	1.60	0.40
	I	0.70	1.50	0.60	0.40	2.00	0.30	0.50	1.60	0.35
	J	0.50	2.50	0.70	0.50	2.00	0.30	0.80	3.00	1.10
	K	0.50	2.00	0.20	0.50	3.50	0.55	0.80	3.00	1.50

Table 3.7: Summary of the factors for all perforated sections

Web Opening Depth, d_o		***0.5h***		***0.65h***		***0.8h***	
Factors		***z***	***k***	***z***	***k***	***z***	***k***
Typical		2.50	0.40	1.30	0.40	2.00	0.40
Elliptical	**Mirrored**	-----	-----	2.00	0.80	1.00	0.30
	Non-mirrored	-----	-----	1.50	0.30	1.50	0.30

Table 3.8: Summary of the factors for perforated sections with $\bar{v} \geq 0.72$

Web Opening Depth, d_o		***0.5h***			***0.65h***			***0.8h***		
Factors		***q***	***z***	***k***	***q***	***z***	***k***	***q***	***z***	***k***
Typical		-----	-----	-----	-----	-----	-----	0.70	1.50	0.40
Elliptical	**Mirrored**	1.30	2.00	0.50	-----	-----	-----	-----	-----	-----
	Non-mirrored				-----	-----	-----	-----	-----	-----
Elongated	$\boldsymbol{c = 1.0d_o}$	0.70	1.50	0.60	0.50	2.50	0.40	0.40	1.50	0.60
	$\boldsymbol{1.0d_o \leq c < 2.0d_o}$				0.40					0.45
	$\boldsymbol{c = 2.0d_o}$	0.50	2.00	0.60	0.50	2.00	0.30	0.80	2.00	0.55
	$\boldsymbol{2.0d_o \leq c < 3.0d_o}$			0.20			0.40			0.70

Table 3.9: Summary of the factors for perforated sections with $\bar{v} < 0.72$

The trend of the curves is changed from case to case in order to avoid significant underestimation of the results. A conservative design domains for the non-standard elliptical web openings and particularly for the perforated sections with extreme web opening depths d_o equal to *0.8h* and *0.5h*, as the current knowledge is limited and the design should be done cautiously. Also, conservatism is well established at the elongated web openings and particularly for the perforated sections with a web opening depth d_o equal to *0.8h*. This is because the trend of the FEM curves differs a lot and their large opening length makes the perforated sections vulnerable to high loads. In the latter category, the opening length varies a lot. Therefore, it is decided that the longer the opening length the higher the degree of conservatism should be applied.

An example is given in **Figure 3.34** and **3.35** where the proposed design shear-moment interaction curves for web openings with various sizes are plotted for direct comparison with the FEM curves. Generally, the design curves for 'coupled' shear capacity ratios are larger or equal to 0.72 and have the same trend as the LMS curves. However, the design curves for 'coupled' shear capacity ratios are less than 0.72, are presented as a parabola. The distinction between these two cases can be easily notified in the following figures. It should be noted again that, these design curves are limited to universal steel beams with typical mid-range section sizes. Little effort was used to develop these design curves, as more accurate results can be directly exported from the non-dimensional shear-moment interaction (FEM) curves in **Figure 3.26**.

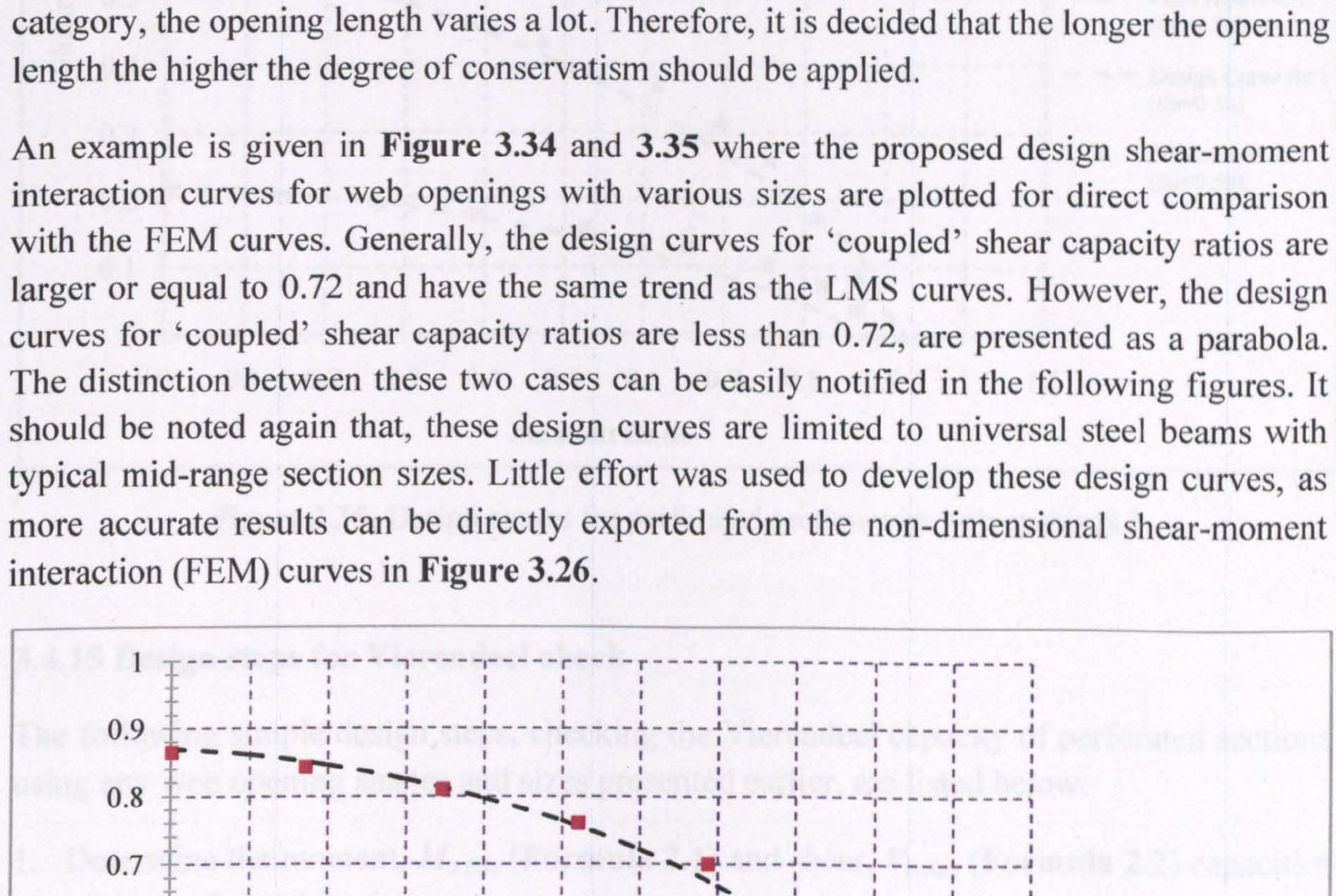

Figure 3.34: Design curves for perforated section with web openings F

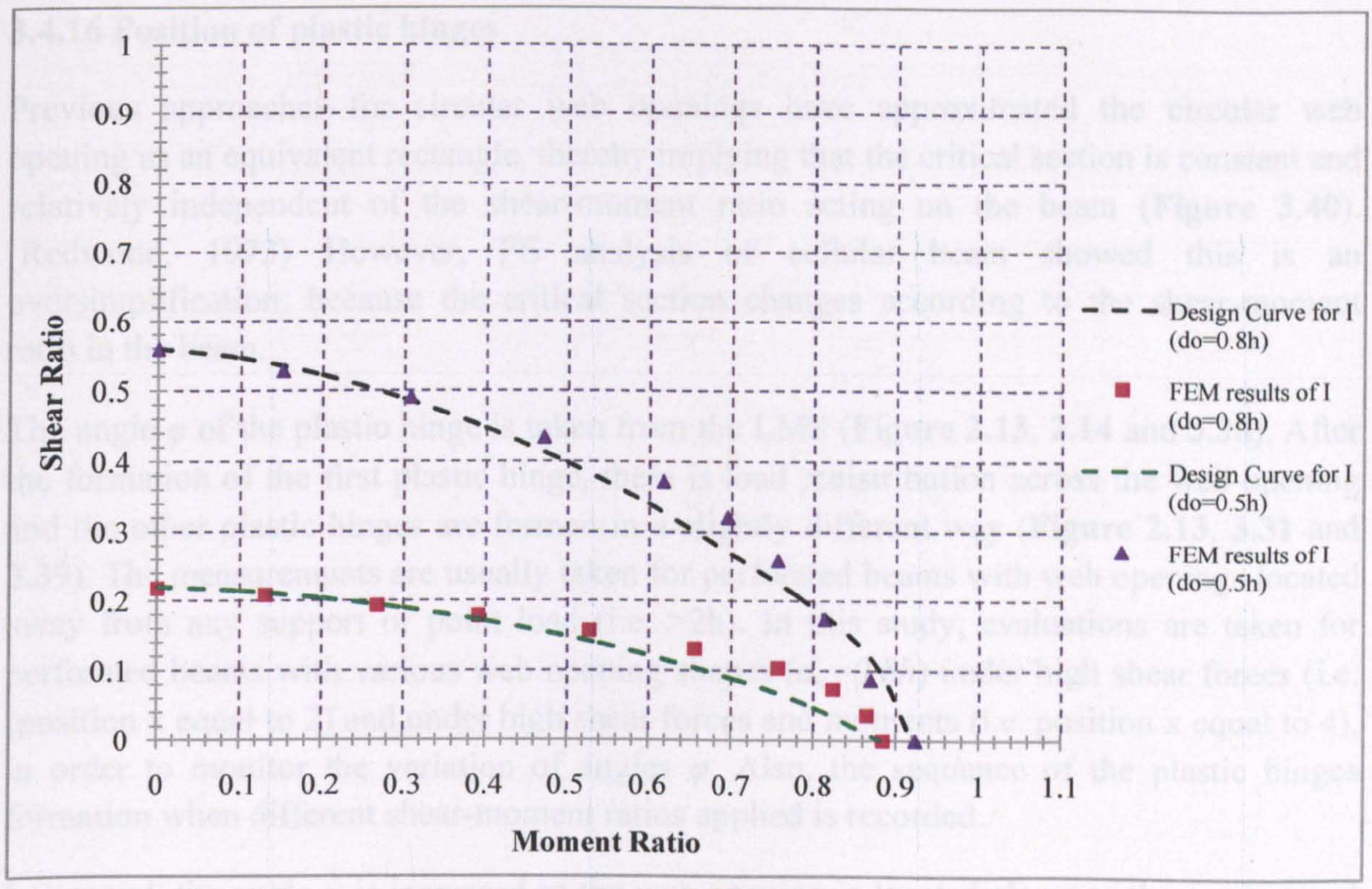

Figure 3.35: Design curves for perforated section with web openings I

3.4.15 Design steps for Vierendeel check

The following simple design steps, checking the Vierendeel capacity of perforated sections using any web opening shapes and sizes presented earlier, are listed below:

1. Determine the moment, $M_{o,Rd}$, (**Formula 2.1**) and shear, $V_{o,Rd}$, (**Formula 2.2**) capacities of the perforated sections.
2. Determine the applied moment, M_{Sd}, (**Formula 3.1**) and applied shear force, V_{Sd}, (**Formula 3.2**) at the centre-line of the web openings.
3. Find in **Table 3.6** the appropriate 'coupled' shear capacity ratio, $\bar{v}$.
4. From **Formula 3.9** or **3.10** and by using the suitable combination of factors from either **Table 3.7** or **Table 3.8** & **3.9**, determine the design 'coupled' shear capacity ratios, $\bar{\bar{v}}$, at any moment utilization ratio, m (in case $\bar{\bar{v}} \leq 0$ then it is assumed that $\bar{\bar{v}} = 0$ and a lower m ratio should be examined).
5. Then multiply the 'coupled' shear capacity ratio, $\bar{\bar{v}}$, with the shear capacity of the perforated section, $V_{o,Rd}$, and
6. Compare the result with the applied shear force, V_{Sd}, at the centre-line of the web opening and the particular loading (i.e. $\bar{\bar{v}} * V_{o,Rd} \geq V_{Sd}$).

3.4.16 Position of plastic hinges

Previous approaches for circular web openings have approximated the circular web opening as an equivalent rectangle, thereby implying that the critical section is constant and relatively independent of the shear-moment ratio acting on the beam (**Figure 3.40**). (Redwood, 1973) However, FE analysis of cellular beam showed this is an oversimplification, because the critical section changes according to the shear-moment ratio in the beam.

The angle φ of the plastic hinge is taken from the LMS (**Figure 2.13, 2.14** and **3.38**). After the formation of the first plastic hinge, there is load redistribution across the web opening and the other plastic hinges are formed in a slightly different way (**Figure 2.13, 3.31** and **3.39**). The measurements are usually taken for perforated beams with web openings located away from any support or point load (i.e. >2h). In this study, evaluations are taken for perforated beams with various web opening shapes (d_o=*0.8h*) under high shear forces (i.e. (position x equal to 2) and under high shear forces and moments (i.e. position x equal to 4), in order to monitor the variation of angles φ. Also, the sequence of the plastic hinges formation when different shear-moment ratios applied is recorded.

In general, the angle φ is increased as the web opening is located closer to the support and the stress is transformed from elastic to plastic under the increased local bending moment, M_φ. Stresses at the top tee-section are more compressive compared to stresses in the flange (**Figure 2.14**). The corresponding φ evaluations for perforated sections with circular web openings, as they were formulated in the literature are: 0° under pure moment conditions and 28° under pure shear conditions. Typically, φ_p equal to 25° was conservatively established for perforated sections with circular web openings. The approximate plastic hinge positions at the LMS of the top tee-section are synopsized in **Table 3.10**, and the critical opening length, *c*, can be determined. It is worth mentioning that, in cases with asymmetrical web openings on perforated beams both values are given.

Opening Shapes	Unger high shear (pos. x equal to 2)	Unger high shear and moment (pos. x equal to 4)
	φ (degrees)	φ (degrees)
A	23 / both open.	19 / both open.
B	22 / both open.	22 / both open.
C	17 / both open.	14 / both open.
D	16 / both open.	8 / both open.
E	33 / both open.	31 / both open.
F	34 / left open. 14 / right open.	32 / left open. 9 / right open.
G	32 / left open. 11 / right open.	29 / left open. 7 / right open.
H	41 / both open.	41 / both open.
I	49 / both open.	49 / both open.
J	60 / both open.	59 / both open.
K	64 / both open.	64 / both open.

Table 3.10: Approximate (±1°) angle, φ, of the first plastic hinge at top tee-section and LMS

It is verified that the angle φ is increased at perforated beams with web openings close to the supports (**Figure 3.36** and **3.37**). Typically, the larger the opening length, *c*, the higher the φ value is. However, as is shown in **Figure 3.37** the shape of the web opening (i.e. symmetrical or not) also significantly affects the position of the plastic hinges which is then affects the value φ. This is the explanation as to why despite the fact that perforated beams with web openings D, E and F, which they all have a critical length equal to 0.25, in the perforated beam with web opening D the angle φ of the plastic hinge is much smaller than the one with web openings E and F. The schematic drawing in **Figure 3.38** demonstrates this difference. Furthermore, from figures below it can be concluded that in perforated beams with elongated web openings as well as hexagonal web openings (generally regular polygons) the φ of the first plastic hinge slightly varies independently of the web opening positions along the length of the beam. This is clearly shown in **Figure 3.36** and **3.37** (i.e. identical points). The reason for this is that the stress is more likely to be concentrated at the sharp corners.

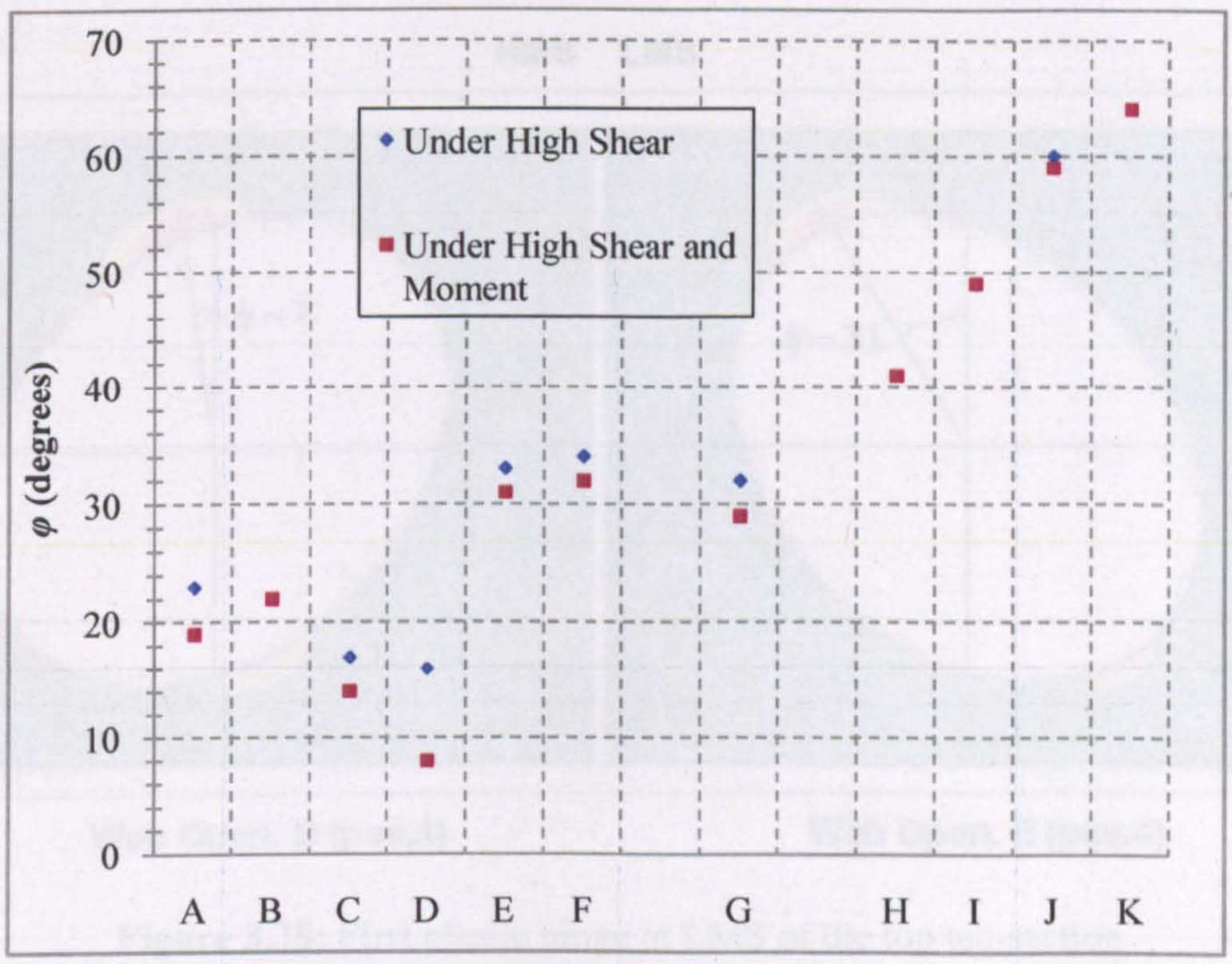

Figure 3.36: φ value of first plastic hinge categorized according to web opening shapes

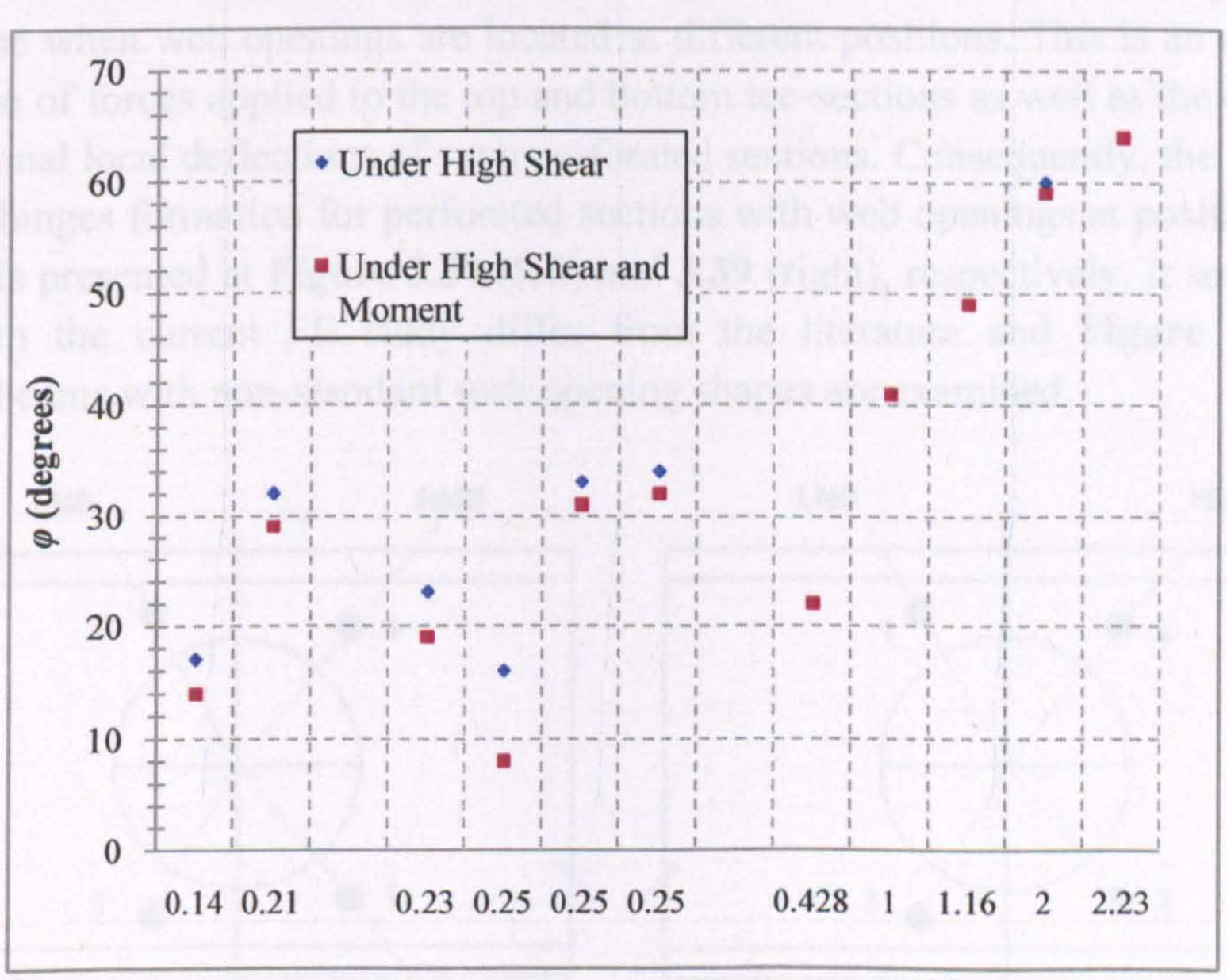

Figure 3.37 φ value of first plastic hinge in respect to critical opening length, c

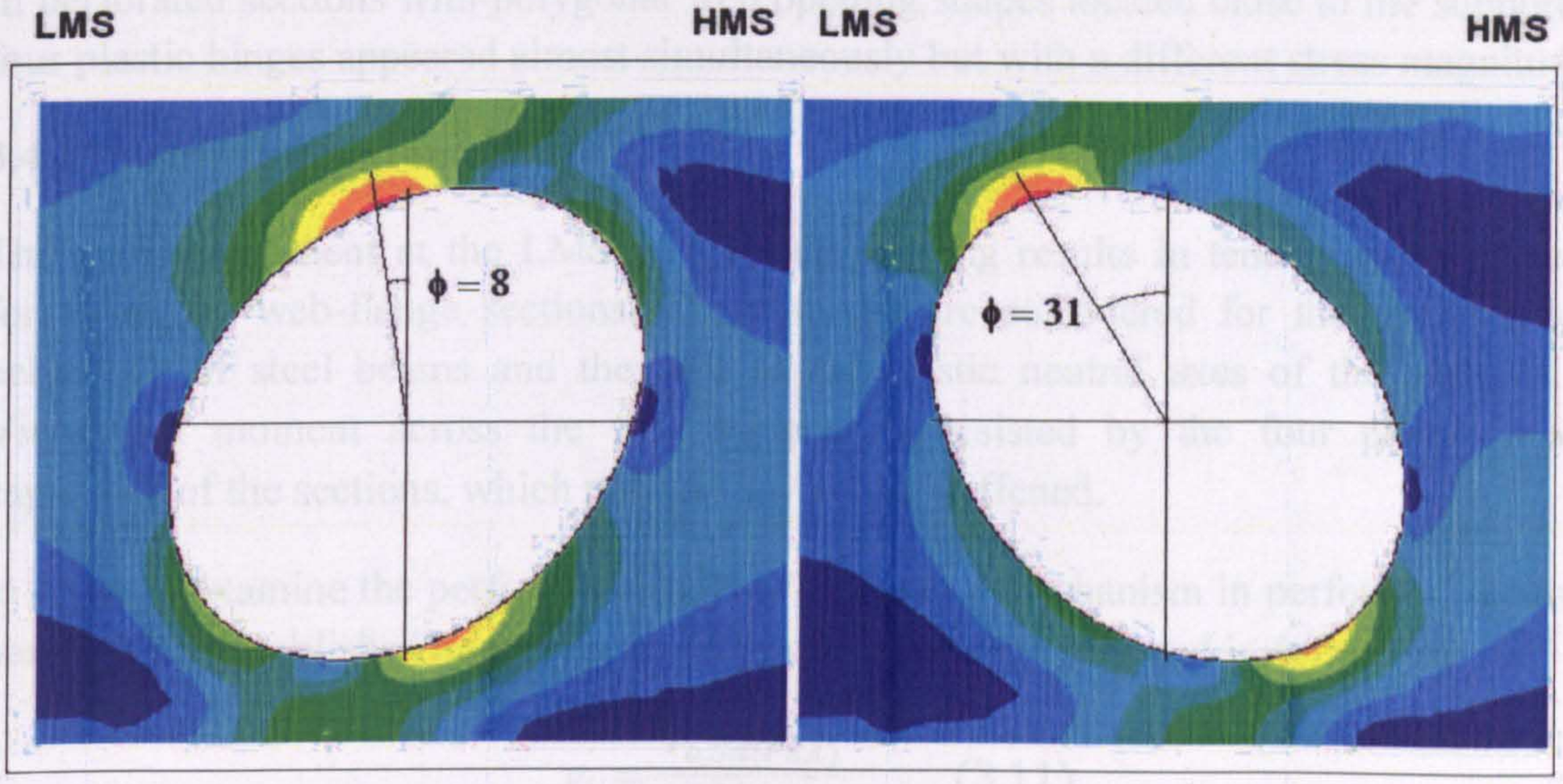

Figure 3.38: First plastic hinge at LMS of the top tee-section

As it is aforementioned, the sequence of the formation of the plastic hinges is not a standard one when web openings are located at different positions. This is an effect of the combination of forces applied to the top and bottom tee-sections as well as the effect of the high additional local deflections of such perforated sections. Consequently, the sequence of the plastic hinges formation for perforated sections with web openings at positions x equal to 2 and 4 is presented at **Figure 3.39** (left) and **3.39** (right), respectively. It seems that the results from the current FE study differ from the literature and **Figure 2.13**, when perforated beams with non-standard web opening shapes are examined.

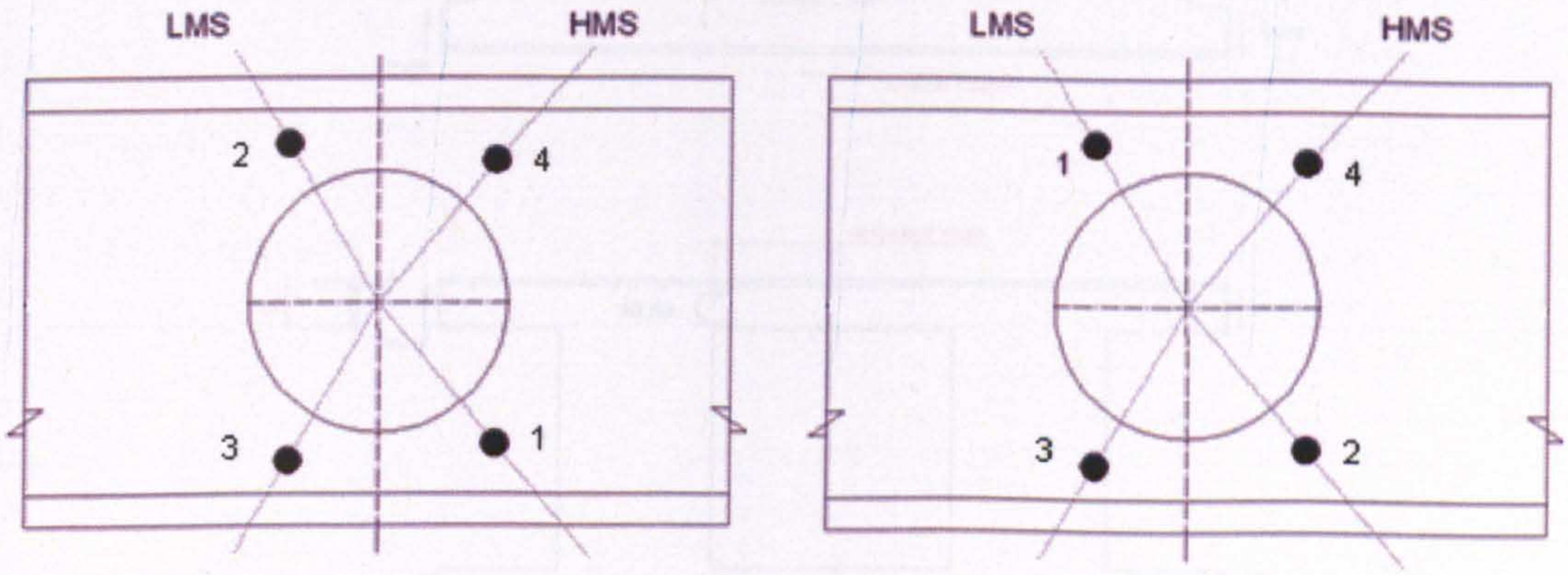

Figure 3.39: Sequence of plastic hinges formation at; under high shear (left) and under high shear and moments (right)

In perforated sections with polygonal web opening shapes located close to the supports, all four plastic hinges appeared almost simultaneously but with a different stress magnitude.

3.4.17 Vierendeel parameter

The applied moment at the LMS of the web opening results in tensile and compressive forces in the web-flange sections. These forces are considered for the analysis of the behaviour of steel beams and they act at the elastic neutral axes of the sections. The Vierendeel moment across the web opening is resisted by the four plastic moment capacities of the sections, which may or may not be stiffened.

In order to examine the performance of the Vierendeel mechanism in perforated sections, a parameter is established known as the Vierendeel parameter, v_i, and is defined as:

$$v_i = \frac{V_{o,Sd(FEA)}}{\frac{4M_{T,Rd}}{c}} \qquad (3.11)$$

Where $M_{T,Rd}$ is the basic shear capacity of the tee-sections under zero axial and shear forces and $V_{o,Sd(FEA)}$ is the global 'coupled' shear capacity of perforated sections as obtained from FEA. The Vierendeel resistance of a web opening is given by the sum of the four bending resistances at the corners (**Figure 3.40**). The shear and axial forces decrease the plastic moment capacities of the sections.

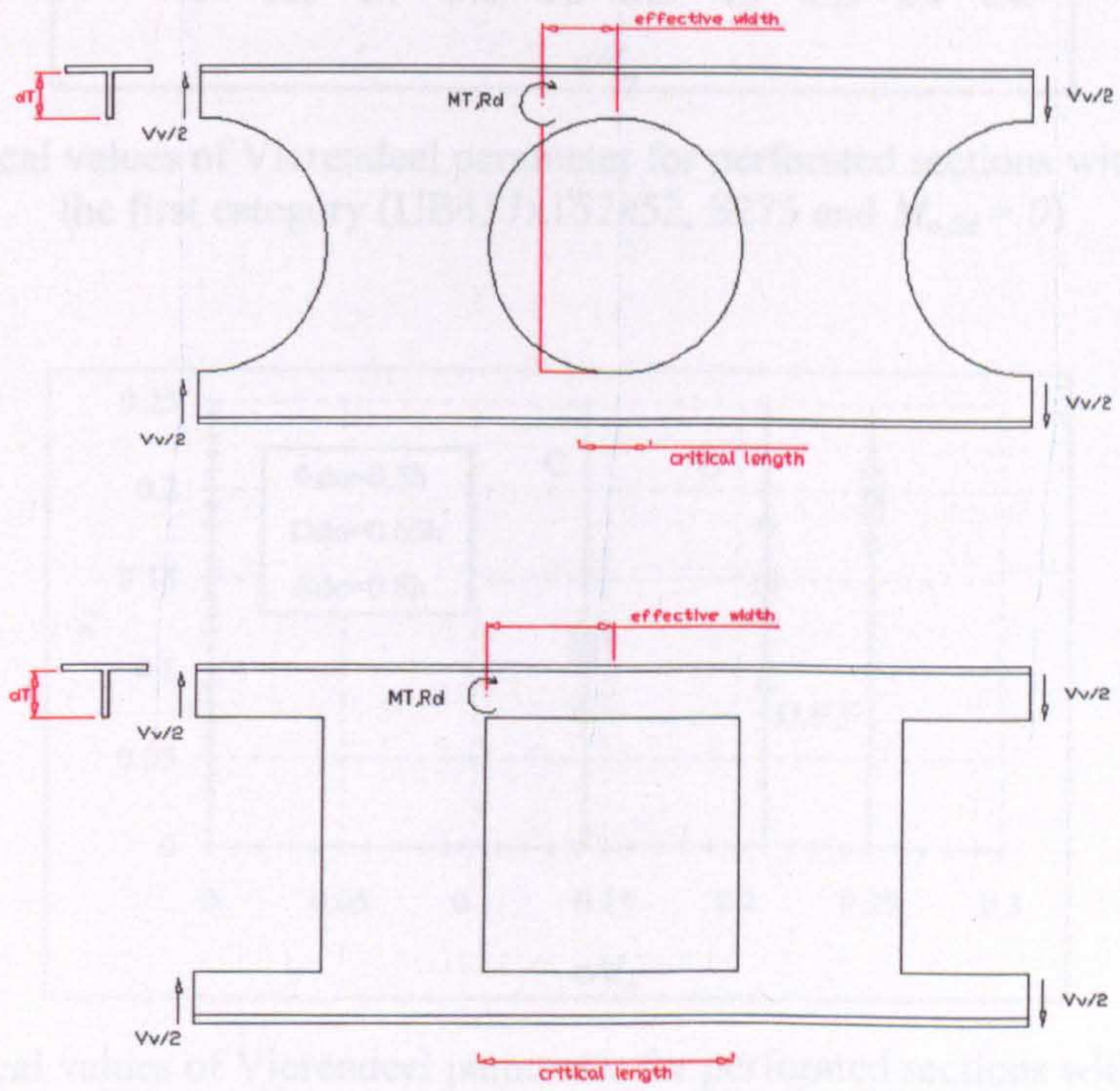

Figure 3.40: Effective width – Critical length of typical circular and square web openings

An illustration of the importance of the Vierendeel mechanism in perforated sections with standard and non-standard web openings of various shapes and sizes is presented; as a plot of the Vierendeel parameter, v_i, against the critical opening length ratio, c/d_o, for perforated sections under zero global moment. This is shown in **Figure 3.41**, **3.42** and **3.43**.

As the critical opening length increases the Vierendeel parameter also increases (close to unity). However, this trend is not absolutely applied to all perforated beams, especially when the diameters of the web openings d_o are equal to *0.5h* and *0.65h*. From the figures, it is also shown that the Vierendeel mechanism is strongly taken into consideration for perforated sections with elongated web openings, whereas the Vierendeel action is almost ignored when perforated sections with elliptical web openings are considered, i.e. $v_i < 0.1$. Perforated sections with standard typical web openings are categorized as mid-range among the FE analyses in terms of Vierendeel parameter.

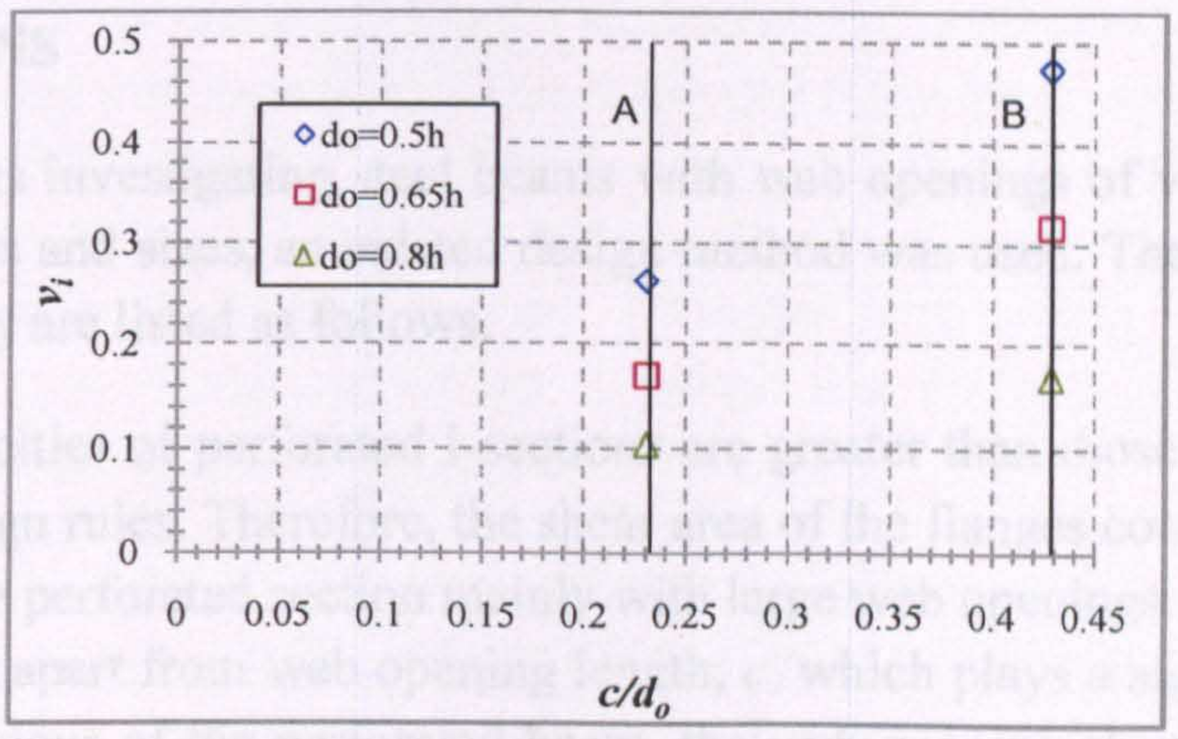

Figure 3.41: Typical values of Vierendeel parameter for perforated sections with web openings of the first category (UB457x152x52, S275 and $M_{o,Sd} = 0$)

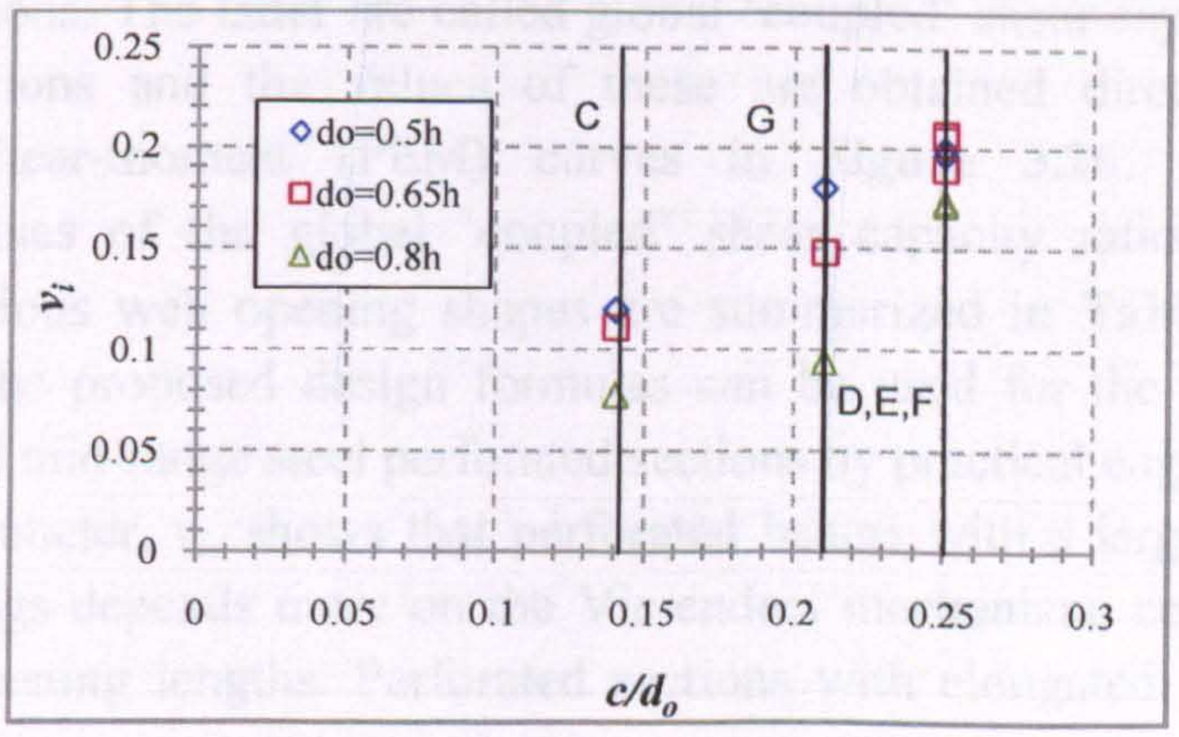

Figure 3.42: Typical values of Vierendeel parameter for perforated sections with web openings of the second category (UB457x152x52, S275 and $M_{o,Sd} = 0$)

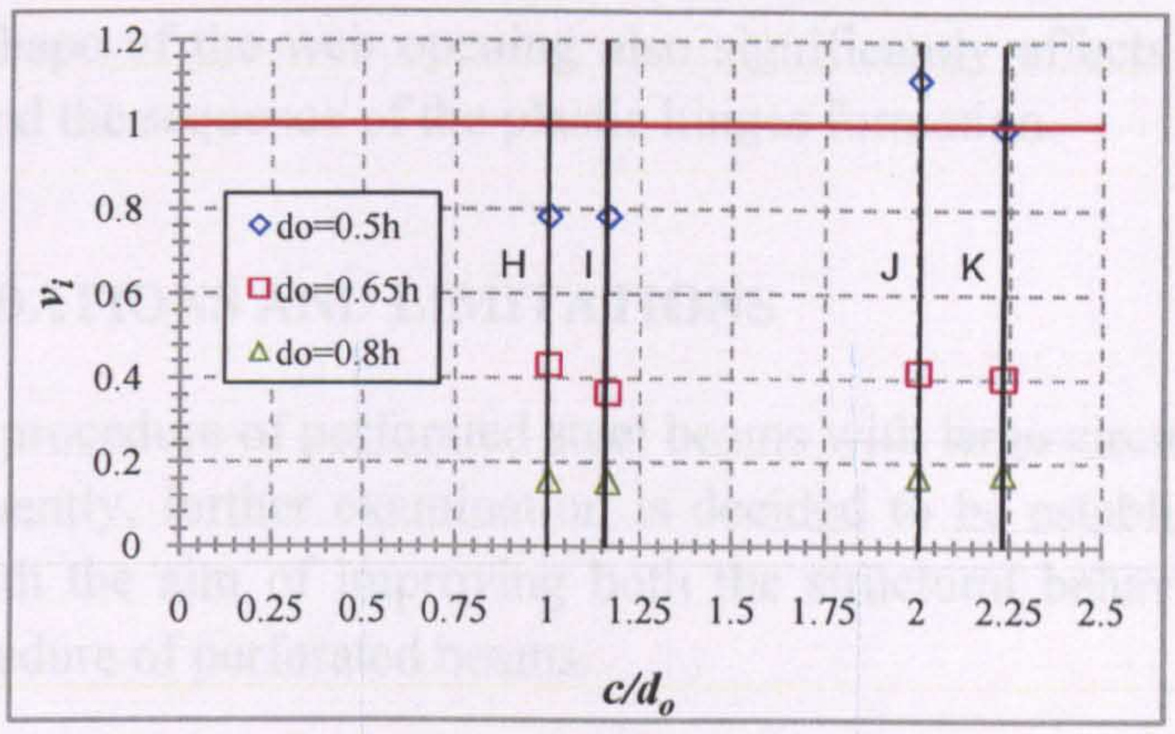

Figure 3.43: Typical values of Vierendeel parameter for perforated sections with web openings of the third category (UB457x152x52, S275 and $M_{o,Sd} = 0$)

3.5 CONCLUSIONS

Based on FE results investigating steel beams with web openings of various standard and non-standard shapes and sizes, an existed design method was used. The main results of the parametric FE study are listed as follows:

1. The shear capacities of perforated I-sections are greater than those evaluated by using the current design rules. Therefore, the shear area of the flanges contributes to the shear capacities of the perforated section mainly with large web openings.
2. It is shown that apart from web opening length, c, which plays a significant role on the structural behaviour of the perforated beam, the web opening shape (e.g. orientation), size, and the position of the web opening can cause significantly different results.
3. The effect of the local Vierendeel moments acting onto the tee-sections above and below the web openings, results in a reduction of the global shear capacities of perforated sections. The latter are called global 'coupled' shear capacities, $V_{o,Sd(FEA)}$, of perforated sections and the values of these are obtained directly from the non-dimensional shear-moment (FEM) curves in **Figure 3.26**. The corresponding normalized values of the global 'coupled' shear capacity ratios, , for perforated sections of various web opening shapes are summarized in **Table 3.6**. These ratios together with the proposed design formulas can be used for the structural adequacy check of typical mid-range steel perforated sections by practical engineers.
4. Vierendeel parameter, v_i, shows that perforated beams with a large opening length at the web openings depends more on the Vierendeel mechanism, compared to the ones with narrow opening lengths. Perforated sections with elongated web openings have high Vierendeel parameters.
5. It is now verified that angle φ increases at perforated sections with web openings close to the supports. Typically, the larger the opening length, c, the higher the φ value is.

However, the shape of the web opening also significantly affects the position of the plastic hinges and the sequence of the plastic hinges formation.

3.6 RECOMMENDATIONS AND LIMITATIONS

The manufacturing procedure of perforated steel beams with large circular web openings is expensive. Consequently, further examination is decided to be established on novel web opening shapes, with the aim of improving both the structural behaviour as well as the manufacturing procedure of perforated beams.

Generally, by introducing these new non-standard web opening shapes it is interesting to note that apparently other geometrical parameters of the web openings, such as the web opening shape and its orientation, also affect the structural behaviour of the perforated beams. This FE study is limited to typical mid-range UB perforated sections. Finally, it should be clearly noted that instead of the web opening diameter d_o equal to $0.75h$, d_o equal to $0.8h$ is used in this research programme aiming at lighter steel beams or a more conservative design. As it was questioned from the literature review (for instance web openings with $d_o=0.8h$ the deflections are 2.5 times higher than web openings with $d_o=0.7h$), the examination was carried out to ensure that the structural behaviour is not changed and the deflections are not dramatically increased.

Following an overall check of all eleven web opening shapes, it is strongly believed that perforated sections with vertical and inclined elliptical web openings behave more effectively compared to circular and hexagonal web openings mainly in terms of stress distribution. This was anticipated especially for vertical elliptical web openings as the web opening length, c, is very narrow and the web opening depth remains the same. Also, elliptical web openings provide smooth opening edges that avert the formation of plastic hinges at a low load level. Therefore, instead of circular and hexagonal web openings, elliptical web openings can be used in construction. Economy in terms of steel is also a positive factor. Although the results obtained from **Figure 3.26** and **Table 3.6** are non-dimensionalised, an overall estimation indicates that perforated sections with vertical elliptical web opening shapes have a percentage of improvement compared to the perforated beams with standard typical circular (A) and hexagonal (B) web opening shapes. These are approximately 18.5% and 29% respectively, for the biggest web opening sizes. The above percentages are lower when inclined elliptical web opening shapes are compared to the circular and hexagonal web opening shapes as they have a more critical opening length, c. Similarly, the above percentages are decreased when perforated beams with smaller web opening sizes are considered.

However, the complex geometry of defining an ellipse and its high asymmetry make this shape difficult to manufacture and control. Therefore, the next phase of this research

programme will introduce novel elliptical web opening shapes that overcome the above problems combining the overall form of elliptical shapes but also facilitate their manufacturing procedure.

CHAPTER 4

VIERENDEEL STUDY OF NON-COMPOSITE BEAMS WITH NOVEL WEB OPENING SHAPES

4.1 INTRODUCTION

Based on the results of the previous parametric FE study of perforated beams with various web opening shapes and sizes (**Chapter 3**), a new parametric study of the optimization of the circular and elliptical web openings is carried out in order to develop novel effective web opening shapes. The FE model used for the optimization study is initially validated with an experimental work conducted in this research programme. The web opening diameter, d_o, equal to $0.8h$ is used again, in the parametric study. The beam configuration is designed so that high shear forces are applied at the centre-line of the web openings, and so the shear mechanism is critical. This chapter consists of the following three parts:

1. *Experimental work:*

An experimental investigation is conducted on a short span deep perforated universal beam. The purpose of this test is to visualize the stresses, local buckling and deflections of a perforated beam with large web openings subjected under high shear forces and moments.

2. *Validation of the FE model with the experimental work:*

A brief comparison between the experimental test and the new FE model is made, to validate the FE model and to securely conduct further parametric FE study of the optimization of the novel web opening shapes. Loads, deflections, strains and yield patterns are mainly compared.

3. *Parametric FE study of the perforated beams with novel web opening shapes:*

After validation against the experimental work, a comprehensive FE investigation on stresses and deflections of the perforated beams with novel web opening shapes at certain load levels is considered. A detailed sensitivity study of the geometric parameters, which

construct these new web opening shapes, is considered and the results are discussed in order to determine the most effective configurations.

4.2 EXPERIMENTAL WORK

4.2.1 Test specimen

UB305x165x40 (S355) steel section is chosen and it is tested in such a way that the web openings are subjected to both high shear forces and bending moments, while formation of four plastic hinges is expected. The web opening diameter, d_o, is equal to $0.76h$, where h is the beam section depth. The end distance between the web openings and the support centre-line is equal to $1.3d_o$ (**Figure 4.1**). The beam is symmetrical to the mid-span. The shear capacity and the Vierendeel bending stresses will be examined as an effect of the shear transfer.

To ensure reasonable stress distribution in the beam, bearing plates at supports are utilised as well as a load spreader at the mid-span between the hydraulic jacks and the compression steel flange. The dimensions of the bearing plates at supports depend of the prevailing profile. The thickness of all bearing plates is constant and same as the flange thickness (10.2mm). Bearing plates are welded to both flanges and web. There is a gap at the fillet position between the plate and the fillet and its purpose is to allow fillets to distribute the load evenly from the flanges to the web. Load spreader is used to provide uniform distribution of the stresses caused by the two point loads applied (**Figure 4.1**). The thickness of this plate is 20mm.

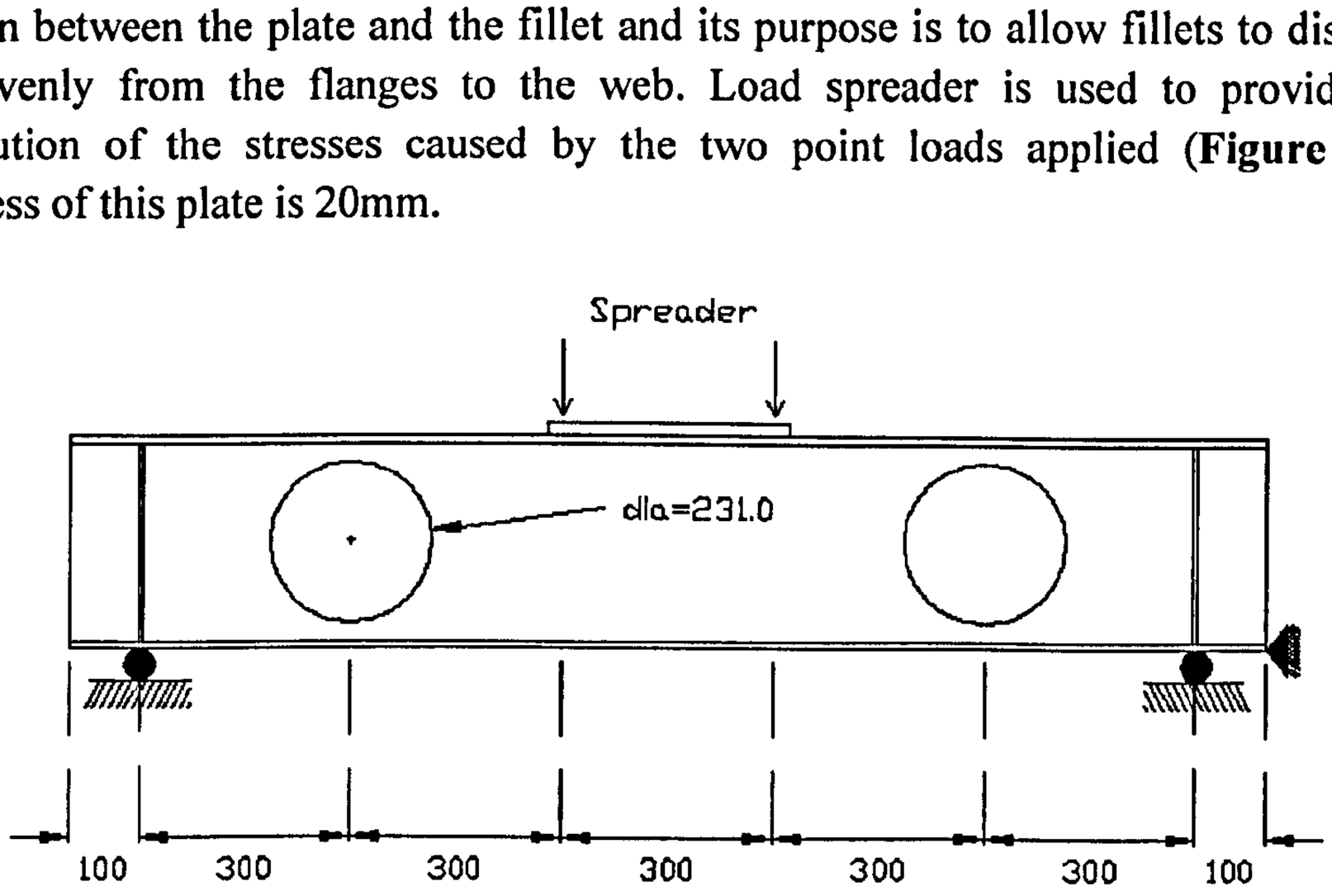

Figure 4.1: Experimental test beam configuration (all dimensions are in mm)

The beam design is approved by the Steel Construction Institute (SCI). By the use of the design software from ASD Westok ltd. (CELLBEAM) and **BS5950 Part 1:2000** is

estimated that the resistance load of the steel section (S355) is around 200kN. Also, it is found that the Vierendeel bending is the most critical failure mode for the particular beam configuration (**Appendix 7**).

4.2.2 Rig setup

The system is a single-span beam under bending; both ends are simply supported so that the system is statically determinate. The load is applied through the extension of the two hydraulic jacks on the load spreader and the supports consist of mild steel rods. The applied bending moment is obtained from the recorded displacements and the applied loading from the load cells connected to the jacks. The rig setup and test arrangement are shown in **Figure 4.2**. Each specimen is placed into test setup using the laboratory crane, in the same manner it would be raised into place in the field. During the test, data acquisition programs are used in order to control the test by varying the load increments for more precise results.

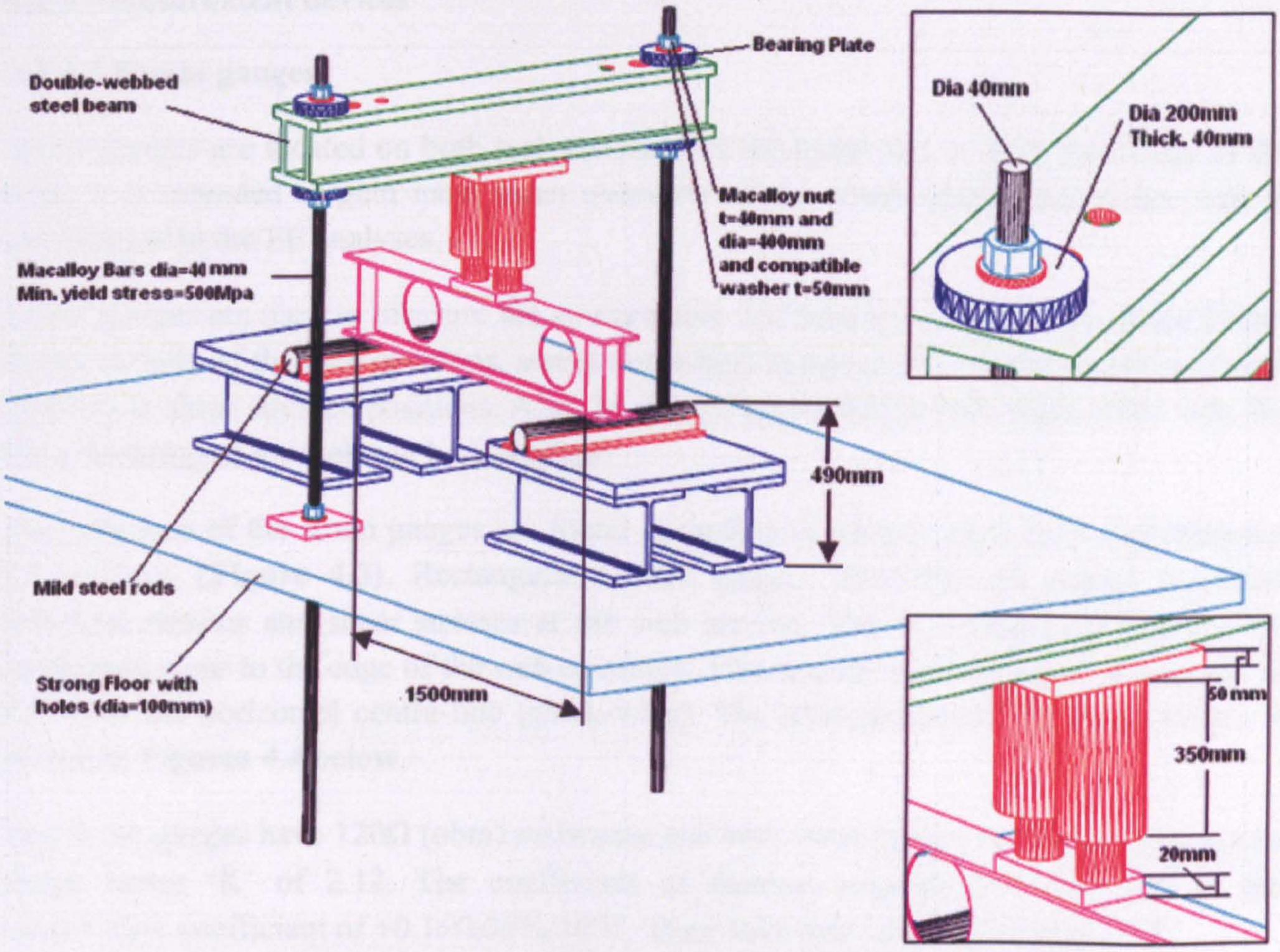

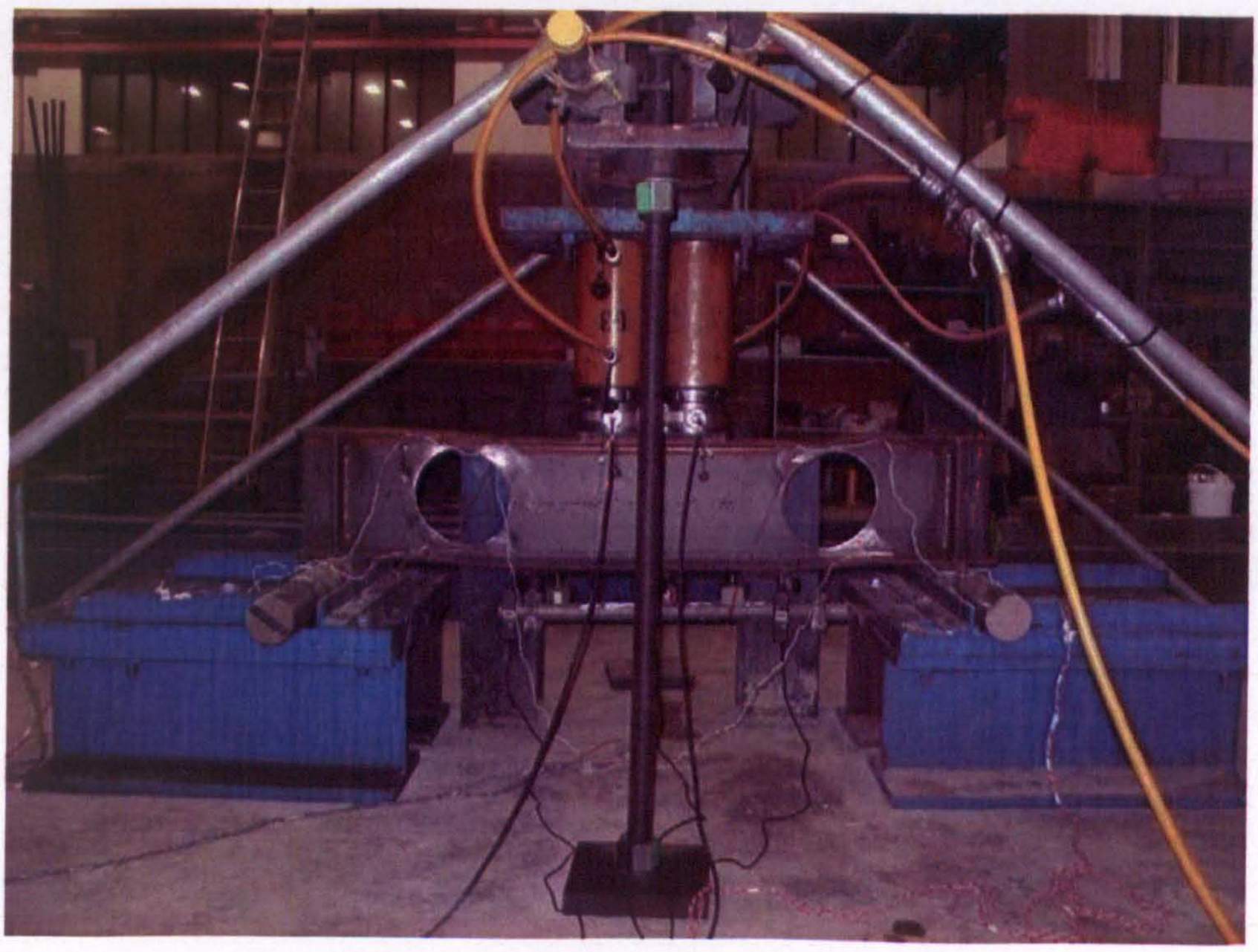

Figure 4.2: Rig setup and test arrangement

4.2.3 Measurement devices

4.2.3.1 Strain gauges

Strain gauges are located on both web openings of the beam and on both face sides of the web. It is intended to gain most exact overview of the strain distribution in the web as verification to the FE analyses.

Strain gauges are used to measure the compressive and tensile surface strains of the beams in the vicinity of the web openings, something which is useful in the determination of steel yielding at shear stressed positions. Also, by gauges positioned at both sides of the web, the local buckling of the web can be identified.

The locations of the strain gauges are found according to contour plots from a preliminary FE analysis (**Figure 4.3**). Rectangular rosette gauges (0-45-90) are placed to obtain principal stresses and shear stresses at the web section. The foil rectangular rosettes are positioned close to the edge of the web openings; 15mm away from the edge, at an angle of 55° from the horizontal centre-line (clock-wise). The arrangement of the strain gauges is shown in **Figures 4.4** below.

The strain gauges have 120Ω (ohm) resistance and both three gauges on each rosette have a gauge factor 'K' of 2.12. The coefficient of thermal expansion is 11.8×10^{-6}/°C and temperature coefficient of +0.1±0.05%/10°C. Their tolerance is ±0.85 [(μm/m)/°C].

A quarter Wheatstone bridge circuit is used and it is non-linear under certain conditions; generally where there are non-symmetrical resistance changes within the bridge and when large resistance changes are involved. For most measurements on metals within the elastic range where the changes in resistance are small, this non-linearity is negligible. As a rule-of-thumb, the non-linearity equal to the percentage strain, i.e. 0.1% strain (1000με) would give 0.1% non-linearity. This assumes a constant voltage supply and the effect can be reduced with a constant current supply (Window and Holister, 1982).

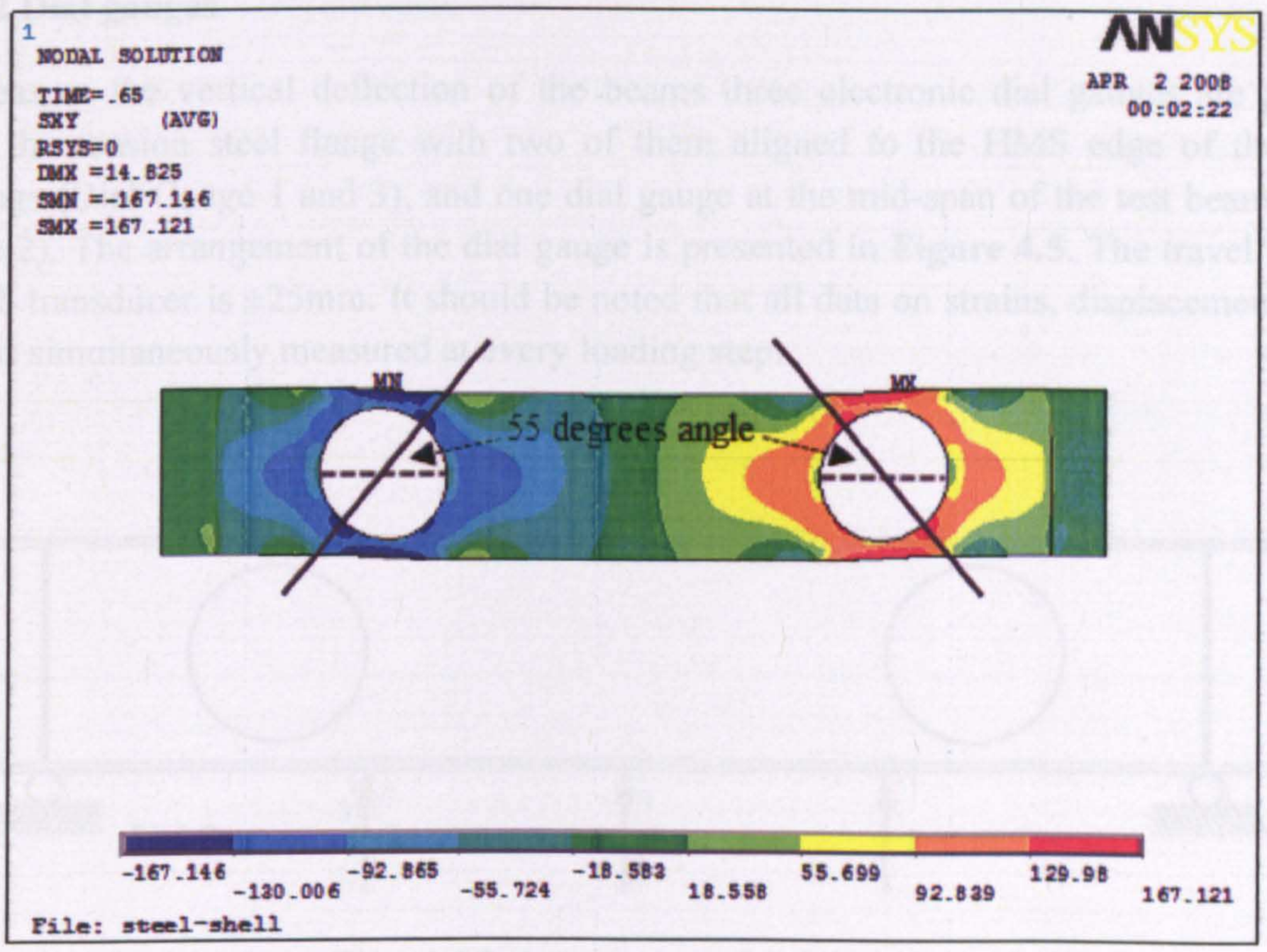

Figure 4.3: Shear stress distribution, τ_{xy}

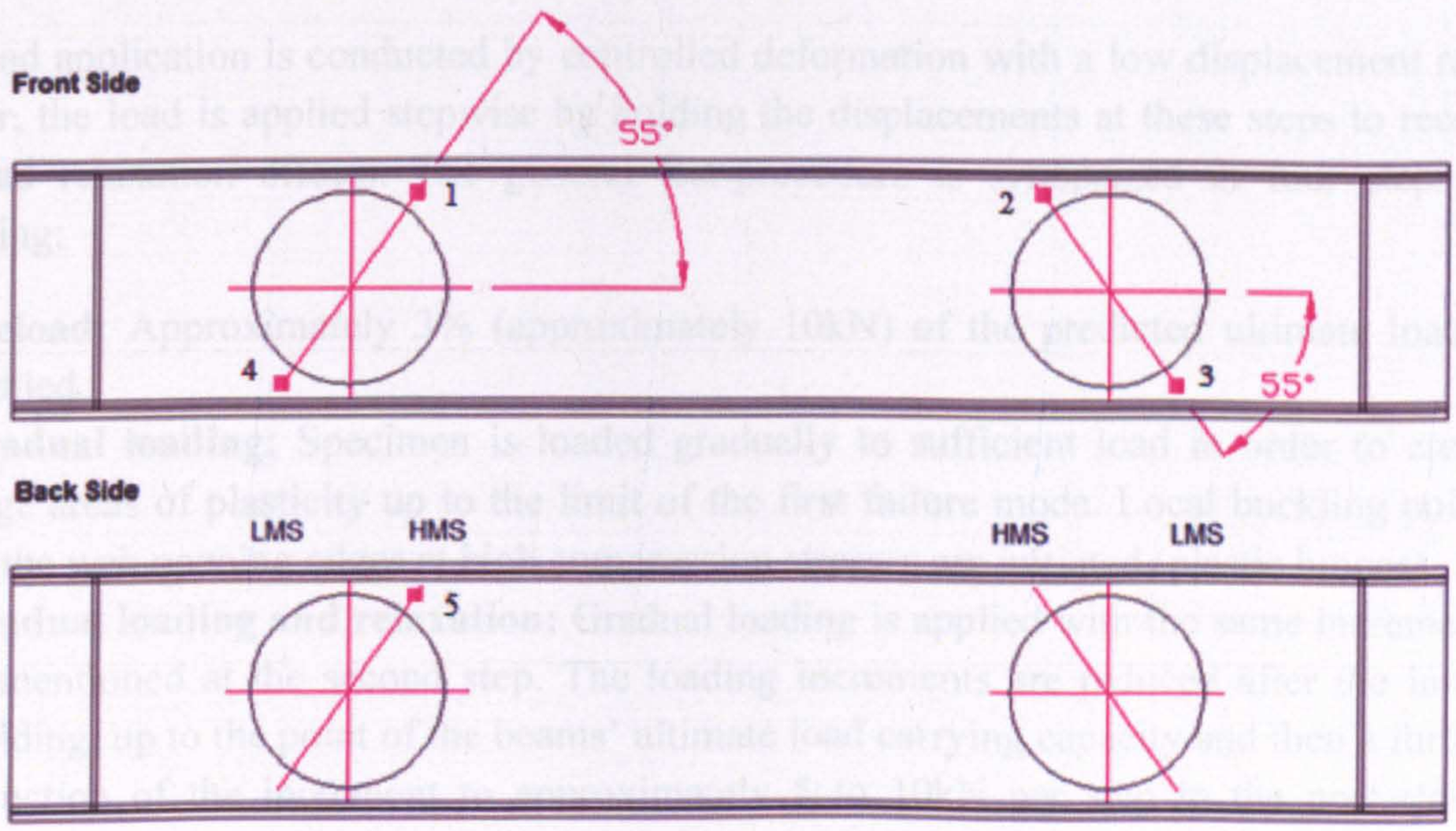

Figure 4.4: Arrangement of strain gauges

4.2.3.2 Dial gauges

To measure the vertical deflection of the beams three electronic dial gauges are placed under the tension steel flange with two of them aligned to the HMS edge of the web openings (Dial Gauge 1 and 3), and one dial gauge at the mid-span of the test beam (Dial Gauge 2). The arrangement of the dial gauge is presented in **Figure 4.5**. The travel length of each transducer is ±25mm. It should be noted that all data on strains, displacements and loads is simultaneously measured at every loading step.

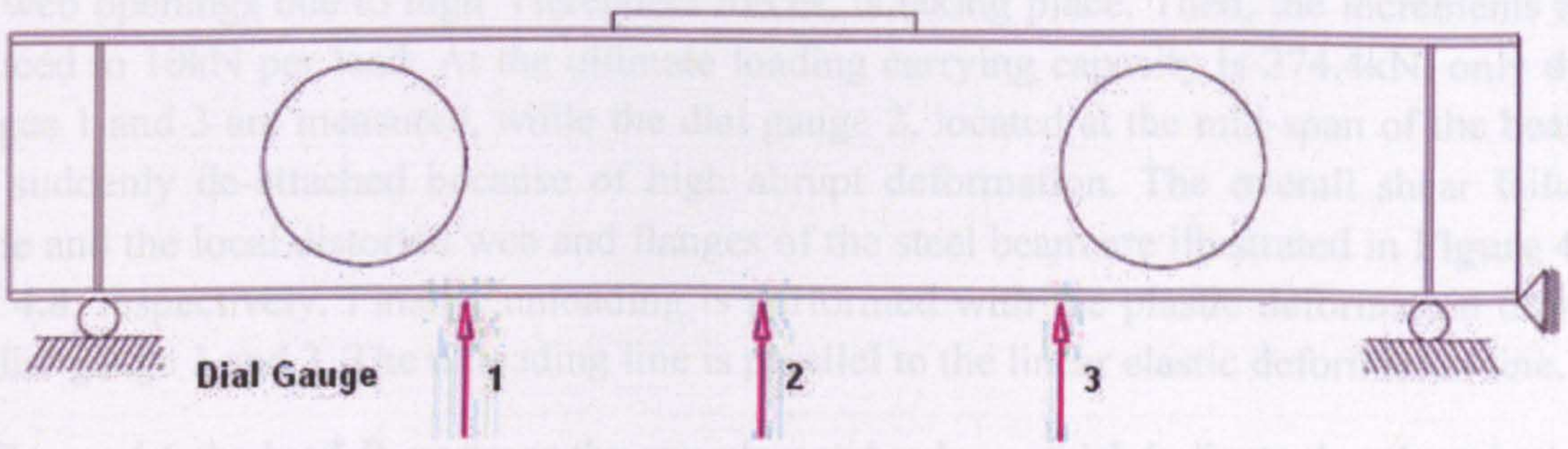

Figure 4.5: Arrangement of dial gauges

4.2.4 Test procedure

The load application is conducted by controlled deformation with a low displacement rate. Further, the load is applied stepwise by holding the displacements at these steps to record the load relaxation effects. The general test-procedure is synopsized in four steps as following:

1. **Preload:** Approximately 3% (approximately 10kN) of the predicted ultimate load is applied.
2. **Gradual loading:** Specimen is loaded gradually to sufficient load in order to create large areas of plasticity up to the limit of the first failure mode. Local buckling points on the web opening edges at high compression stresses are initiated (plastic hinges).
3. **Gradual loading and relaxation:** Gradual loading is applied with the same increments as mentioned at the second step. The loading increments are reduced after the initial yielding, up to the point of the beams' ultimate load carrying capacity and then a further reduction of the increment to approximately 5 to 10kN per step in the post-elastic region.
4. **Unloading:** Full unloading is conducted. The measurements of the plastic-permanent deformation of the beams are recorded.

4.2.5 Load-deflection relationships

The load against deflection curves for all three dial gauges, applied on the steel perforated beam with circular web openings, is shown in **Figure 4.6**. Surface loading approximately 10kN is initially applied when the dial gauges are zeroed. Then the load is released and subsequently the gradual loading starts with 15 to 20kN increments. Up to the level of 176.2kN, linear behaviour is obtained, which is the 64.2% of the ultimate load carrying capacity of the beam. At this stage high deformation is not observed yet. At the load of 256kN, high local buckling points which are due to compression in the vicinity of the web openings are observed. Moreover, well formed yielding of the compression flange above the web openings due to high Vierendeel forces, is taking place. Then, the increments are reduced to 10kN per load. At the ultimate loading carrying capacity is 274.4kN, only dial gauges 1 and 3 are measured, while the dial gauge 2, located at the mid-span of the beam, has suddenly de-attached because of high abrupt deformation. The overall shear failure mode and the local distorted web and flanges of the steel beam are illustrated in **Figure 4.7** and **4.8**, respectively. Finally, unloading is performed with the plastic deformation drawn by dial gauge 1 and 3. The unloading line is parallel to the linear elastic deformation line.

In **Figure 4.6** the load P_y portrays the experimental values which indicate that the edges of the circular web openings have initially yielded. The buckling load $P_{cr.}$ of the web and the flanges is determined by using the beam deflections at the HMS of each web opening, where high relaxation of the beam is obtained (Dial Gauge 1 and 3). The yield load P_y is smaller than $P_{cr.}$ and $P_{ult.}$, because the edges of the circular web openings in addition to the normal bending moment and shearing force, carry both additional moments by Vierendeel action and the longitudinal shear forces (fully plastic hinges formation). Therefore, it seems that this local yielding of the edges is directly related to the ultimate strength of the beam.

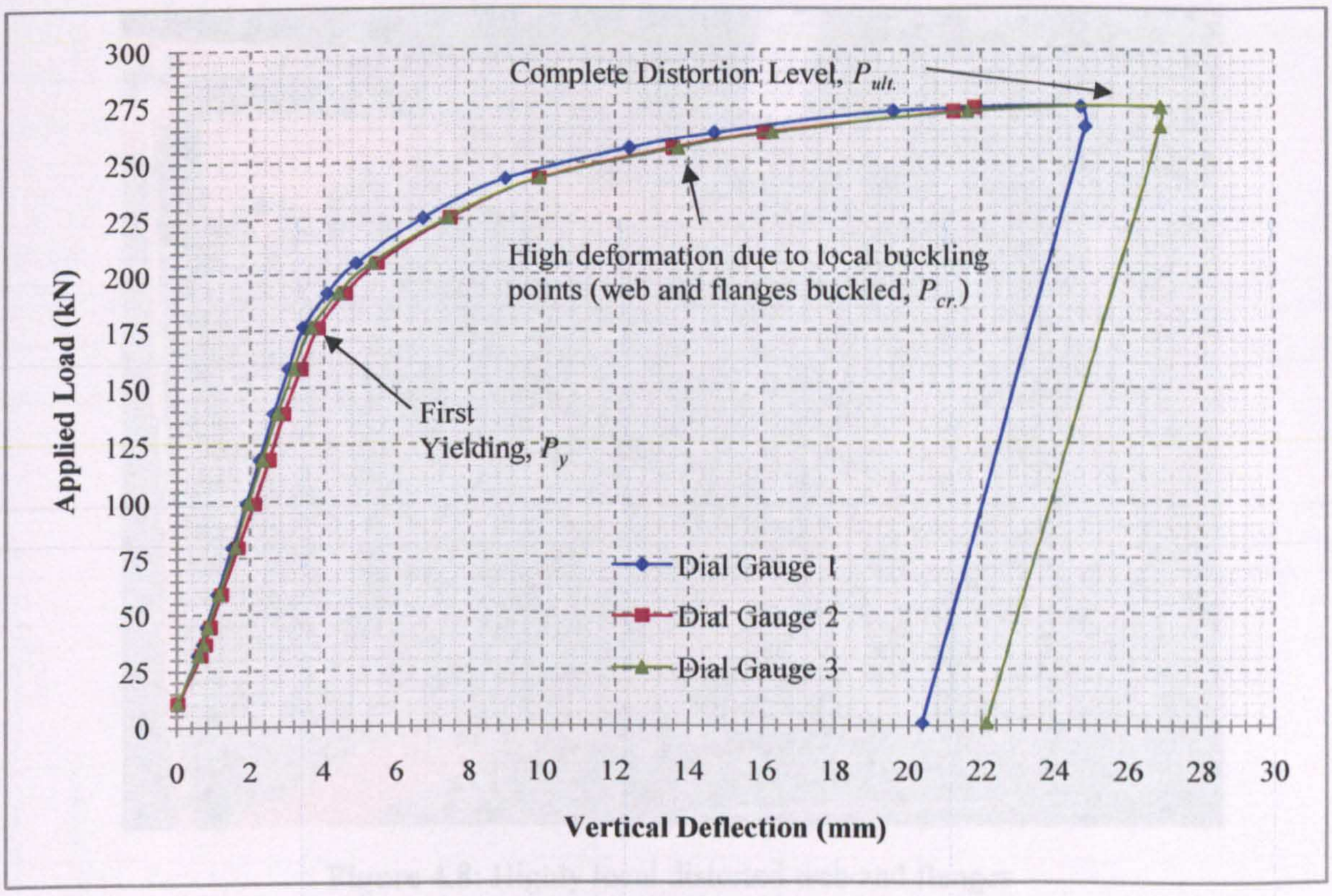

Figure 4.6: Load-deflection curves for experimentally tested steel perforated beam

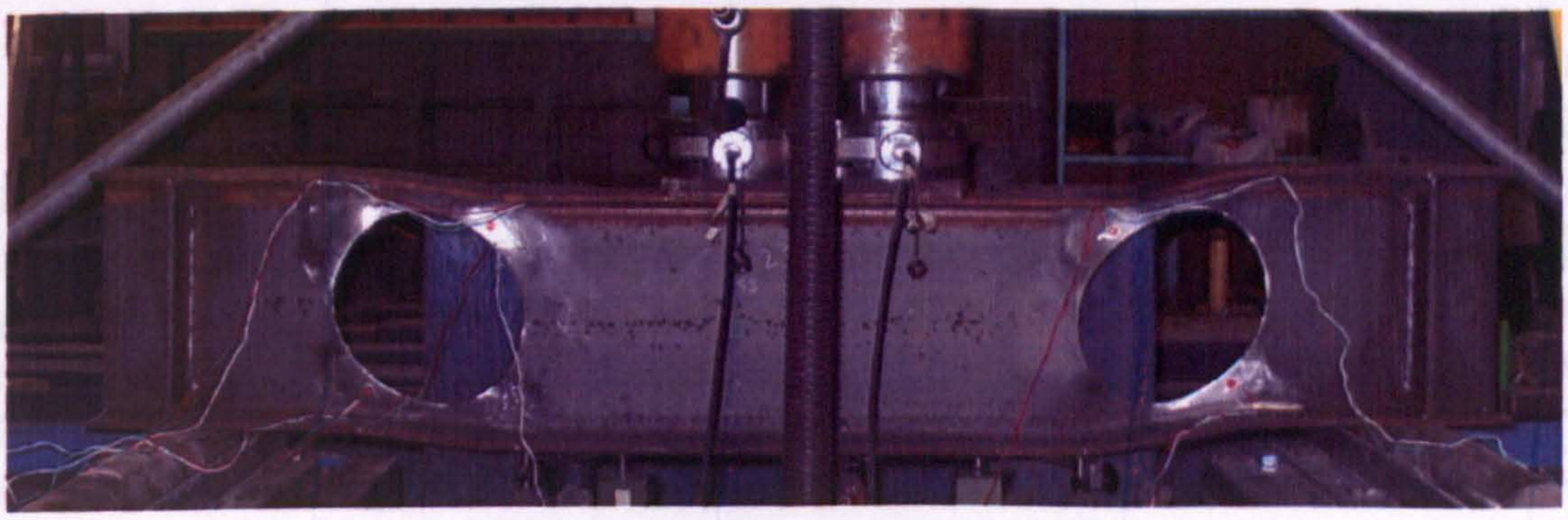

Figure 4.7: Overall shear failure mode

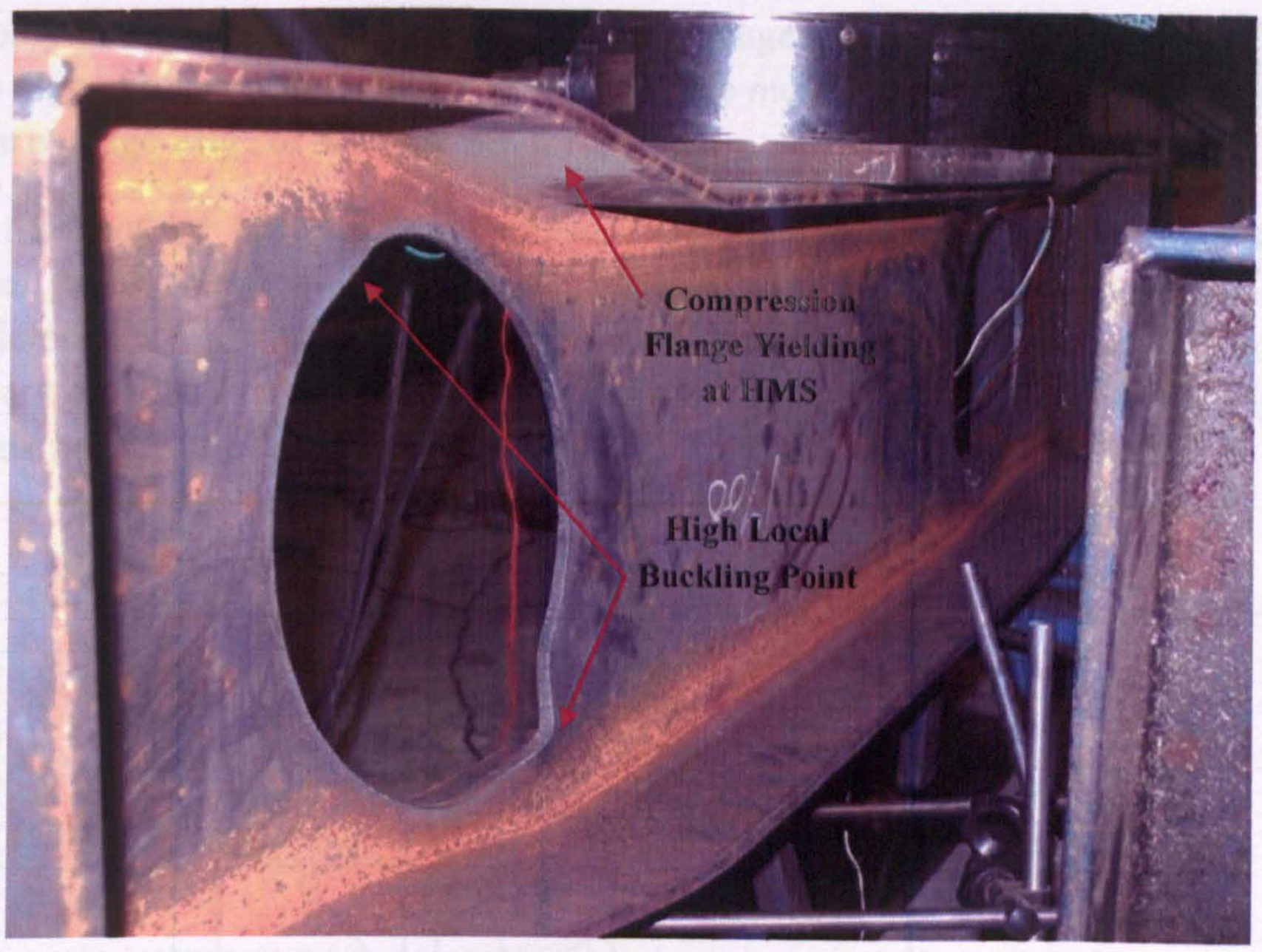

Figure 4.8: Highly local distorted web and flanges

4.2.6 Strain evaluations

2D horizontal, ε_x, vertical, ε_y, and shear, ε_{xy}, web strains in the vicinity of the web openings are recorded and plotted together with the load level as shown in **Figure 4.9** to **4.13**. The negative values of strains indicate compression. Because of high ductility in the plastic region large magnitude of strains are recorded. In some cases at the few last load steps, large constant strains are observed as the strain gauges were over-strained due to high distortion of the steel. It is worth noted that both Rosette 1 and 5 (**Figure 4.9** and **4.13**), which are attached at the same position on the web, show similar tensile vertical strains, but different horizontal and shear strains because of local flexural stresses (i.e. membrane strains) resulting from buckling. General interpretation of the strain graphs behaviour can be as follows:

Phase 1: Linear elastic behaviour according to theory, no normal strains occur.
Phase 2: Change to plasticity and in-plane membrane effects lead to the development of normal strains.
Phase 3: Overlaying of instability effects such as local buckling and change of sign of the strains can finally occur. Also, very large strain evaluations are obtained after steel totally yielded.

Since only 3mm gauge length is used for strain gauges, it makes the gauges very sensitive only to high stress concentration points. It must be mentioned that the strain gauges record only the average value of strain across their length.

Up to the level of 176.2kN, where linear behaviour is obtained by the load-deflection graph, all fifteen strain evaluations are varying in similar low range; approximately 0 to 3500microstrain. Moving to the plastic region, gradually higher compression and tension strains are recorded. After the point of high deformation (i.e. 256kN) a sudden significant increase or decrease of strains is recorded.

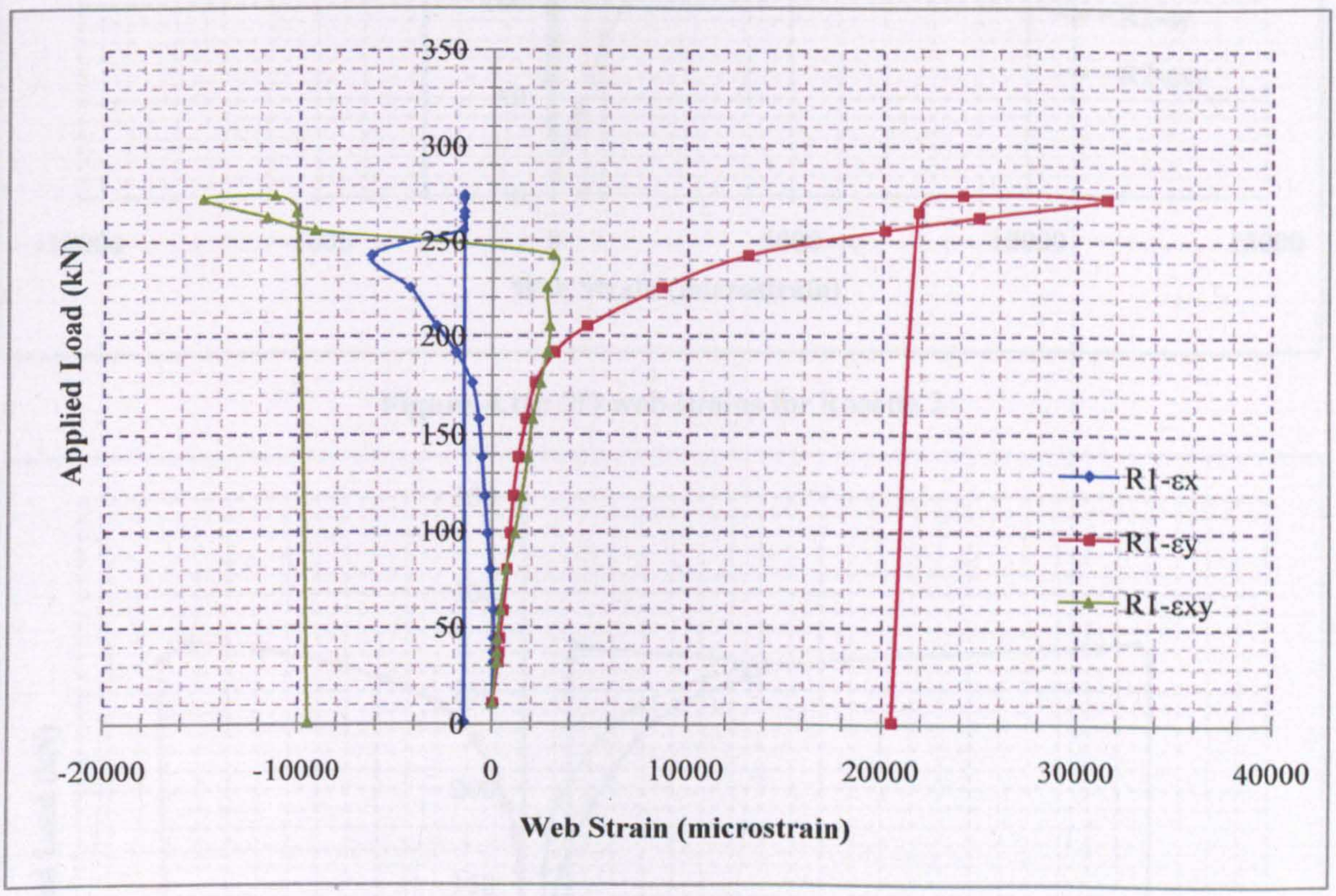

Figure 4.9: 2D web strains for Rosette 1

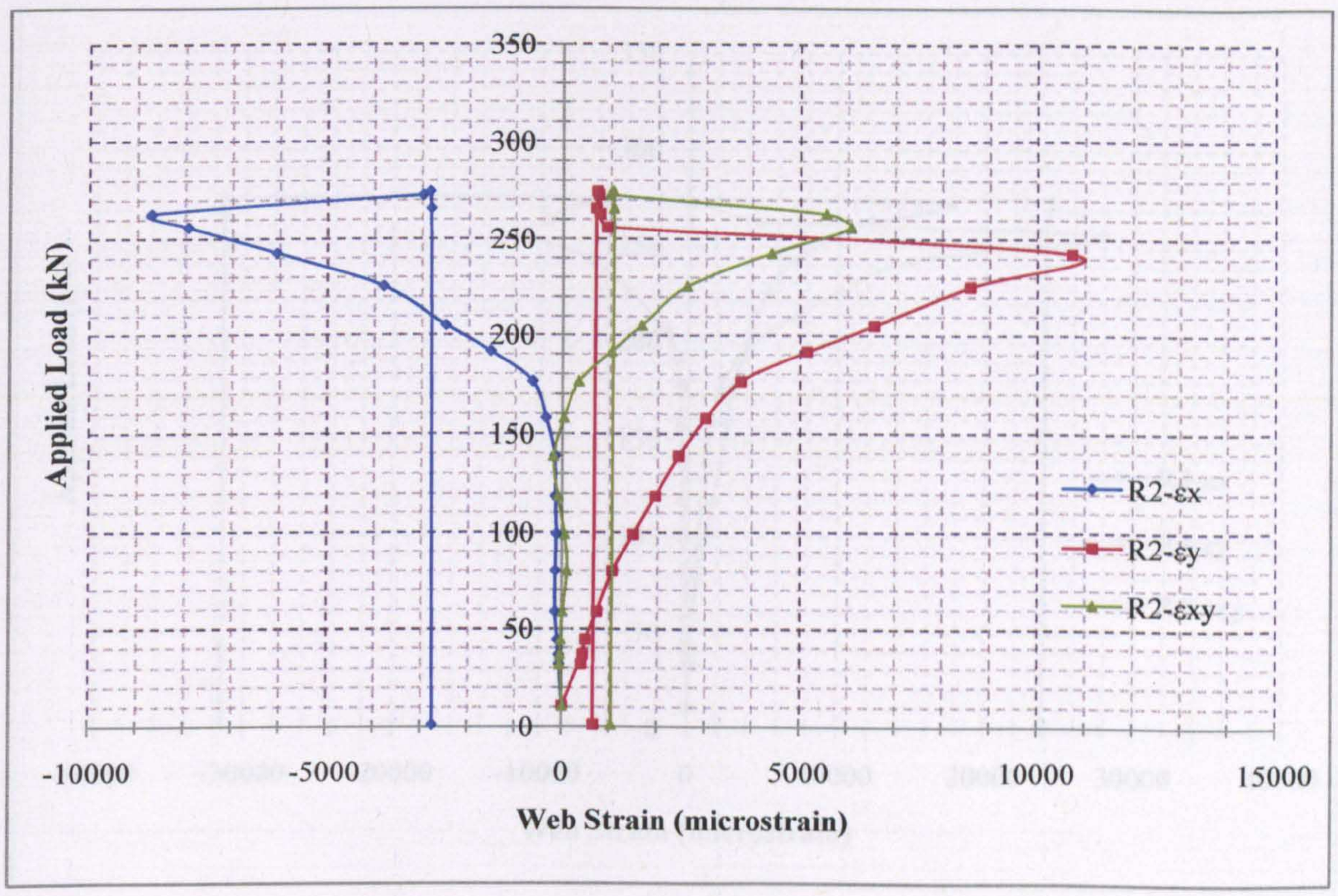

Figure 4.10: 2D web strains for Rosette 2

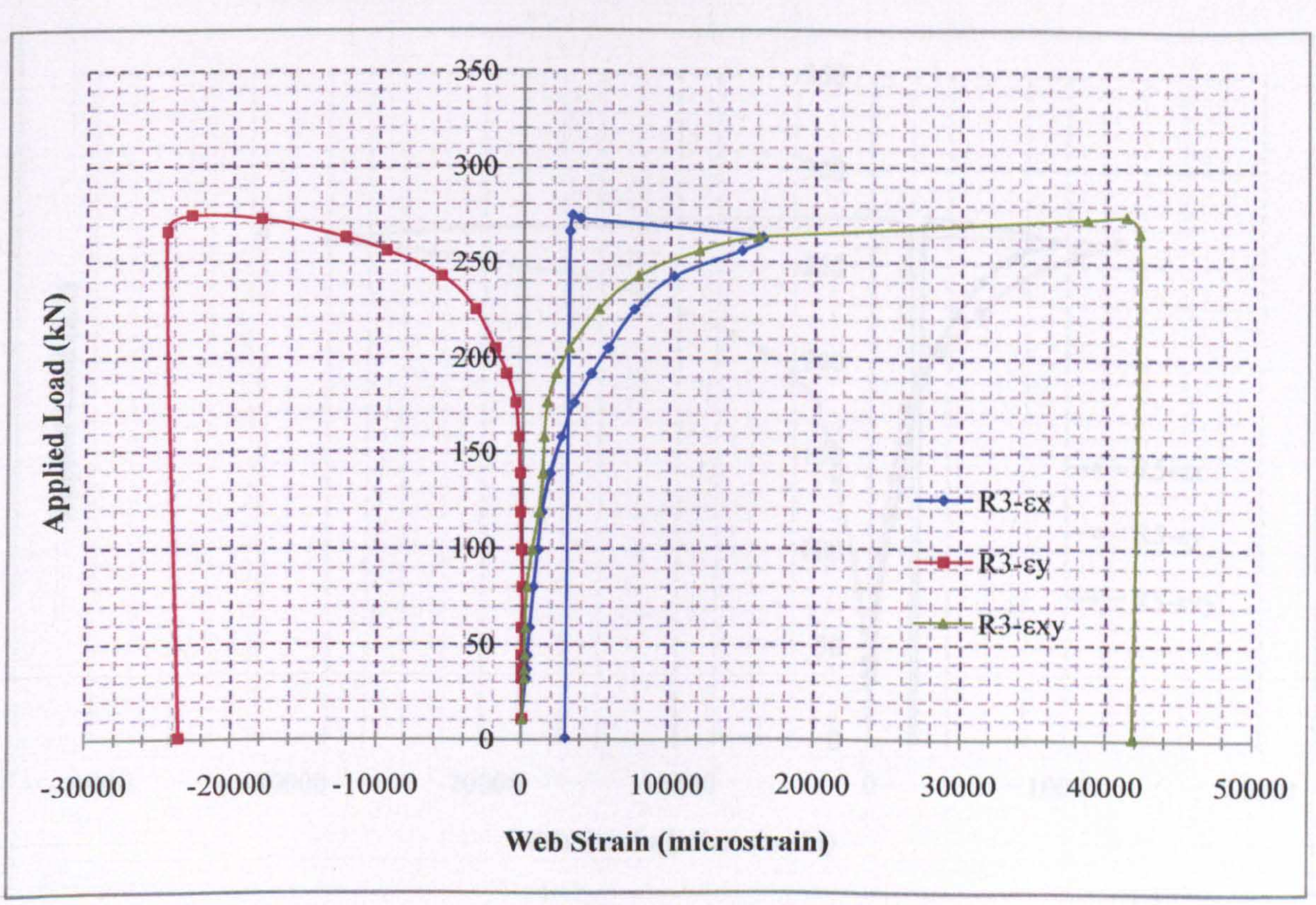

Figure 4.11: 2D web strains for Rosette 3

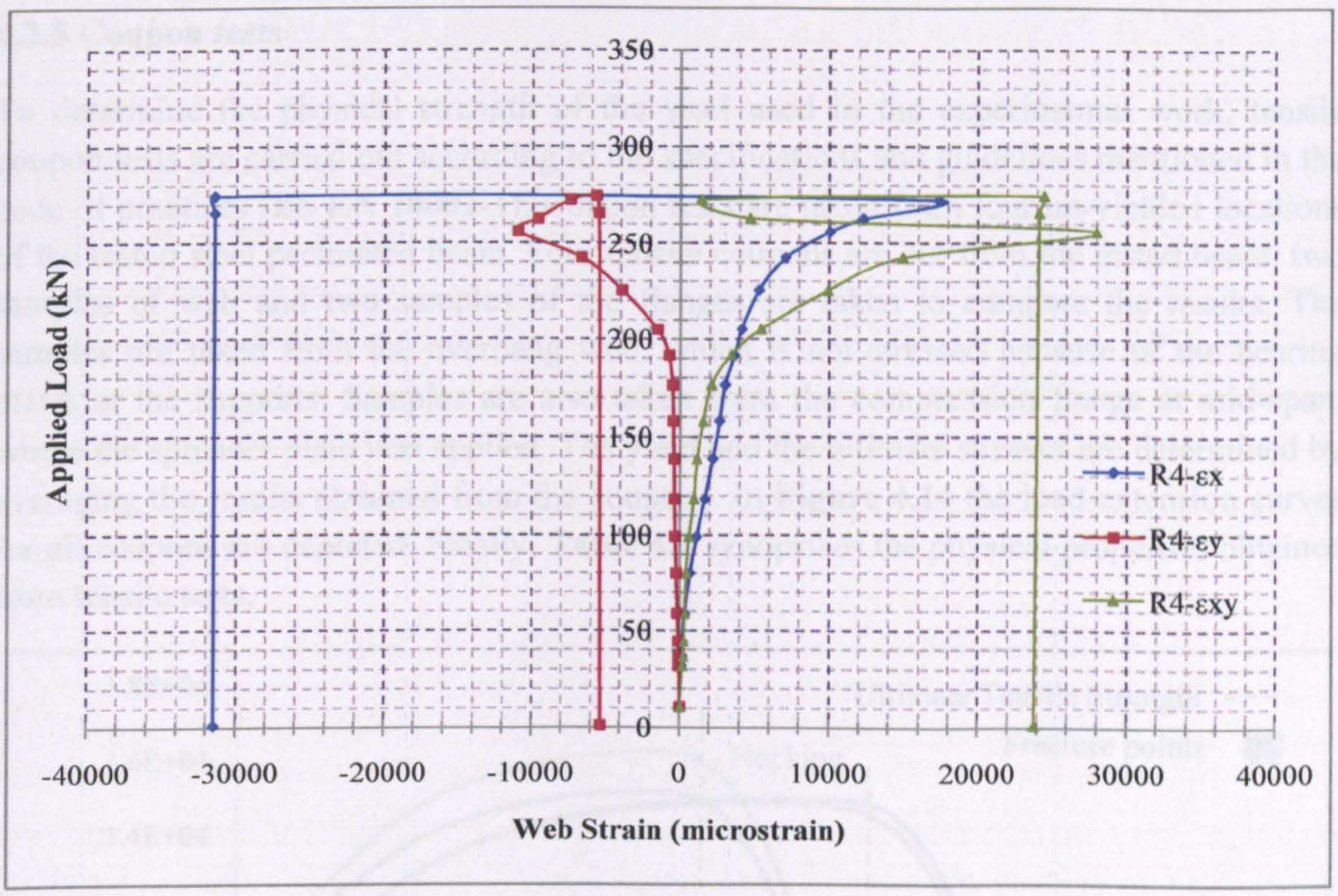

Figure 4.12: 2D web strains for Rosette 4

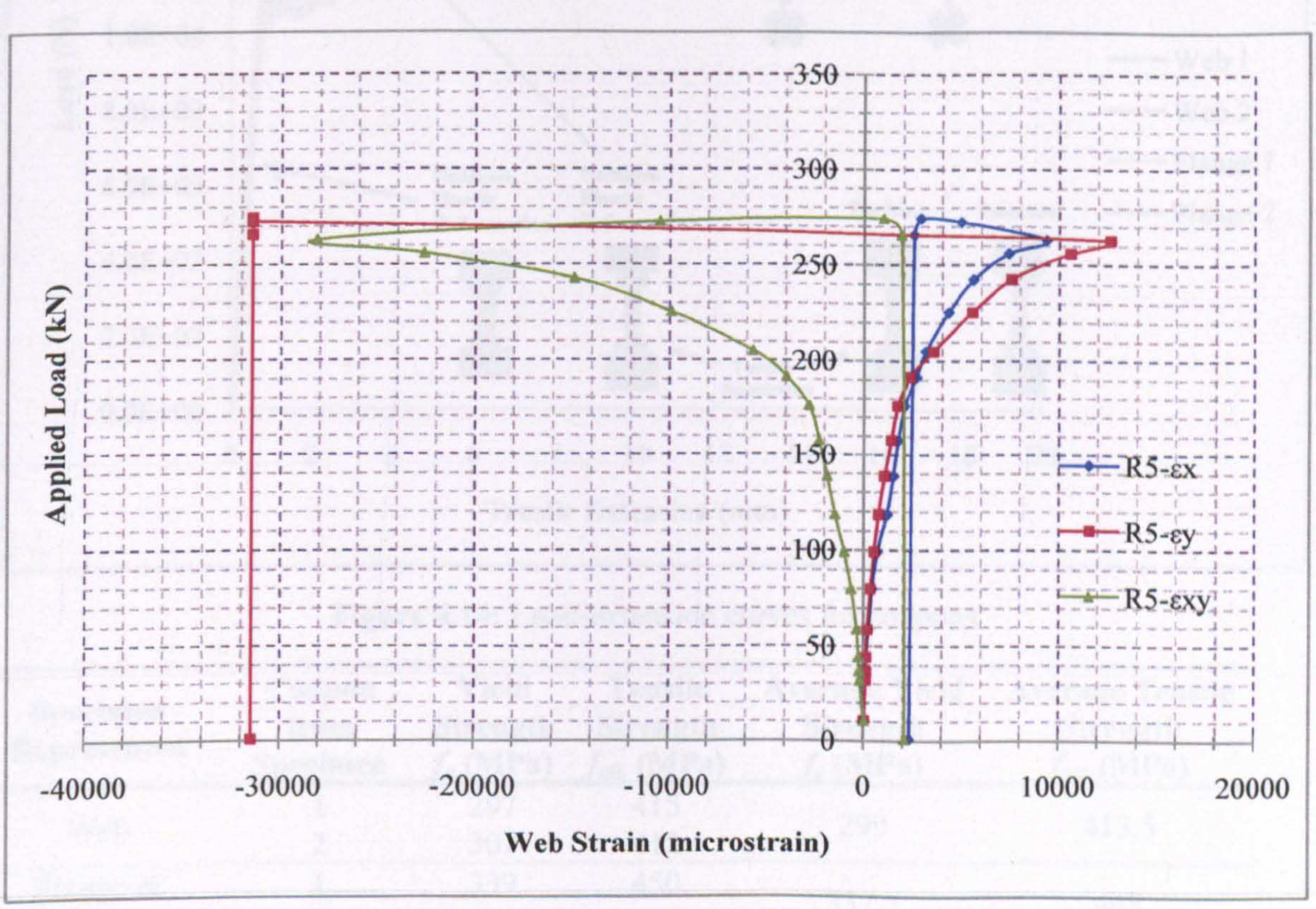

Figure 4.13: 2D web strains for Rosette 5

4.2.8 Coupon tests

To determine the physical strength of the steel used in the experimental work, tensile coupon tests are carried out according to the specifications and guidelines mentioned in the code of practices (**BS EN 10002-1**). Coupon tests are taken from four un-yielded locations of the tested steel perforated beam. Four tensile coupons are cut from the tested beam, two samples of web and two samples of the flanges are taken to compare the results. The samples are taken from the overhang web, which is not stressed because of the bearing plates at the supports. Samples are also taken from the compression flange at mid-span; where the spreader plate was applied. The yield and the ultimate stresses are determined by averaging the results obtained from the coupons. In **Figure 4.14** the load-extension curves for all coupons are depicted. Finally, **Table 4.1** synopsizes the physical properties obtained from tensile tests.

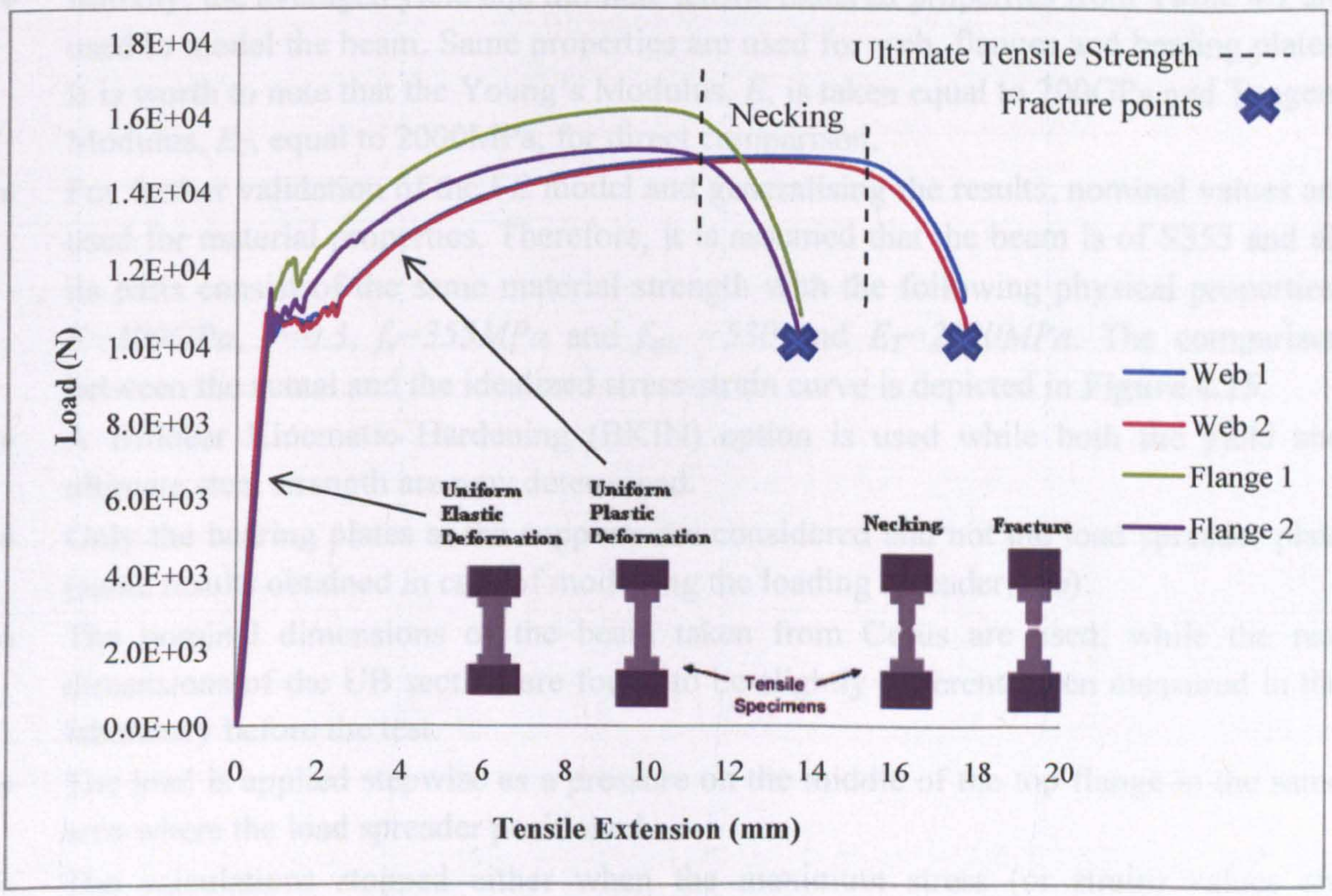

Figure 4.14: Load-extension curves for coupons

Specimen Represented	Coupon from Specimen	Yield Strength f_y (MPa)	Tensile Strength $f_{ult.}$ (MPa)	Average Yield Strength f_y (MPa)	Average Tensile Strength $f_{ult.}$ (MPa)
Web	**1**	297	415	299	413.5
	2	301	412		
Flange & Bearing Plate	**1**	339	450	337.5	448
	2	336	446		

Table 4.1: Measured material physical properties

4.3 VALIDATION OF THE FE MODEL WITH THE EXPERIMENTAL WORK

4.3.1 FE model

A non-linear (material and geometric) elasto-plastic analysis is conducted herein in order to compare and validate the FE model of the steel beam with the experimental test conducted above. Load-deflection curves are mainly compared, and the results will be used as a reference for the following parametric study of the optimization of the web opening shapes. Failure mechanism and stresses are also examined to better understand the behaviour of such perforated steel beam.

The non-linear analysis is carried out similarly to that in **Chapter 3**. Any differences are synopsized as follows:

- Initially, the averaged yield and ultimate tensile material properties from **Table 4.1** are used to model the beam. Same properties are used for web, flanges and bearing plates. It is worth to note that the Young's Modulus, E, is taken equal to 200GPa and Tangent Modulus, E_T, equal to 2000MPa, for direct comparison.
- For further validation of the FE model and generalising the results, nominal values are used for material properties. Therefore, it is assumed that the beam is of S355 and all its parts consist of the same material strength with the following physical properties: $E=200GPa$, $v=0.3$, $f_y=355MPa$ and $f_{ult.}=530$ and $E_T=2000MPa$. The comparison between the actual and the idealized stress-strain curve is depicted in **Figure 4.15**.
- A Bilinear Kinematic Hardening (BKIN) option is used while both the yield and ultimate steel strength are now determined.
- Only the bearing plates at the supports are considered and not the load spreader plate (same results obtained in case of modelling the loading spreader, too).
- The nominal dimensions of the beam taken from Corus are used; while the real dimensions of the UB section are found to be slightly different when measured in the laboratory before the test.
- The load is applied stepwise as a pressure on the middle of the top flange in the same area where the load spreader positioned.
- The calculations stopped either when the maximum stress (or strain) values are reached, when the node's displacement exceeded the default values (default by ANSYS), or displacement started to increase very rapidly without sufficient load changing.

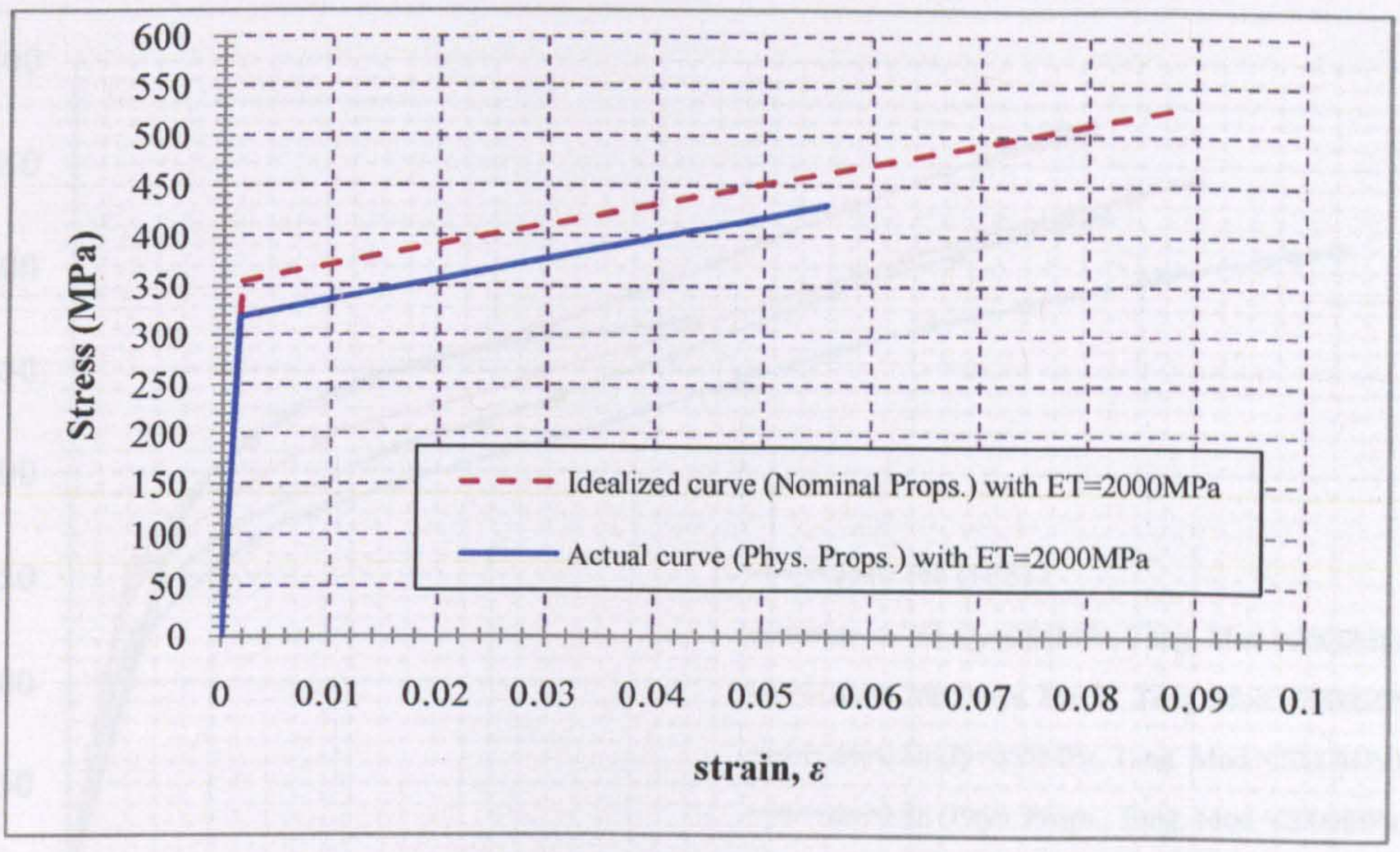

Figure 4.15: Idealized bi-linear stress-strain curve of the steel material used in ANSYS

4.3.2 Load-deflection relationships

The load-deflection curves obtained from FE modelling and experimental test are plotted in **Figure 4.16** for direct comparison. Comparing the experimental load-deflection curve at the mid-span with the FE curve obtained by using the nominal material properties, it is observed that the FE model provides significant stiffness in the elastic region. This is also an overestimation of the FE model due to the limited number of the nodes on each element (i.e. only four nodes), as well as the 'reduced integration points' function, which is used to avoid numerical problems, such as shear locking on shell elements. However, the yielding and plasticity of the FE model adequately compares with the experimental test. Finally, as the yield and ultimate tensile material strengths are used to model the steel, the FE analyses only converge (i.e. stop) when the ultimate tensile stress is reached. Therefore, an increased strain hardening is observed before the models converge.

From tensile coupon tests it is also found that the stiffness of the steel is very low and it is not representing the theoretical Young's Modulus. Hence, the nominal Young's Modulus ($E=200GPa$) is used in FEM. Such nominal material strength properties are used for the next parametric FE study.

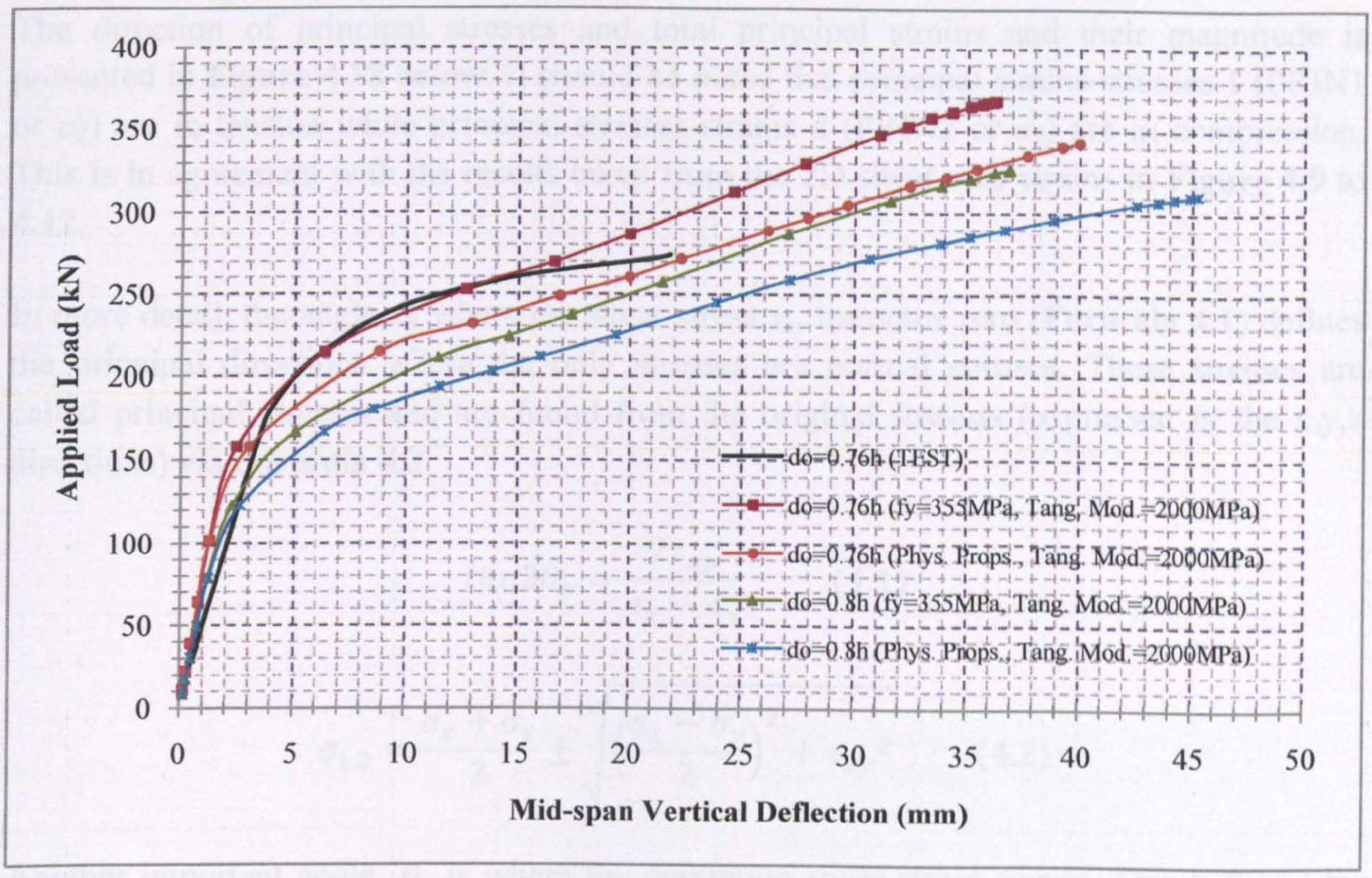

Figure 4.16: Load against deflection curves at mid-span for steel perforated beam

4.3.3 Stress distribution

It is interesting to examine the stress distribution in the vicinity of the web openings of the perforated beam at both the yield and failure (i.e. divergence of the FE solution) point; to better understand the formation of the stresses and the plastic hinges (**Appendix 8**). The Von-Mises stress distribution and the deformed shapes for both load levels are presented in **Figure 4.17**. The maximum Von-Mises stresses are observed at the same positions as in the experimental beams (**Figure 4.17**).

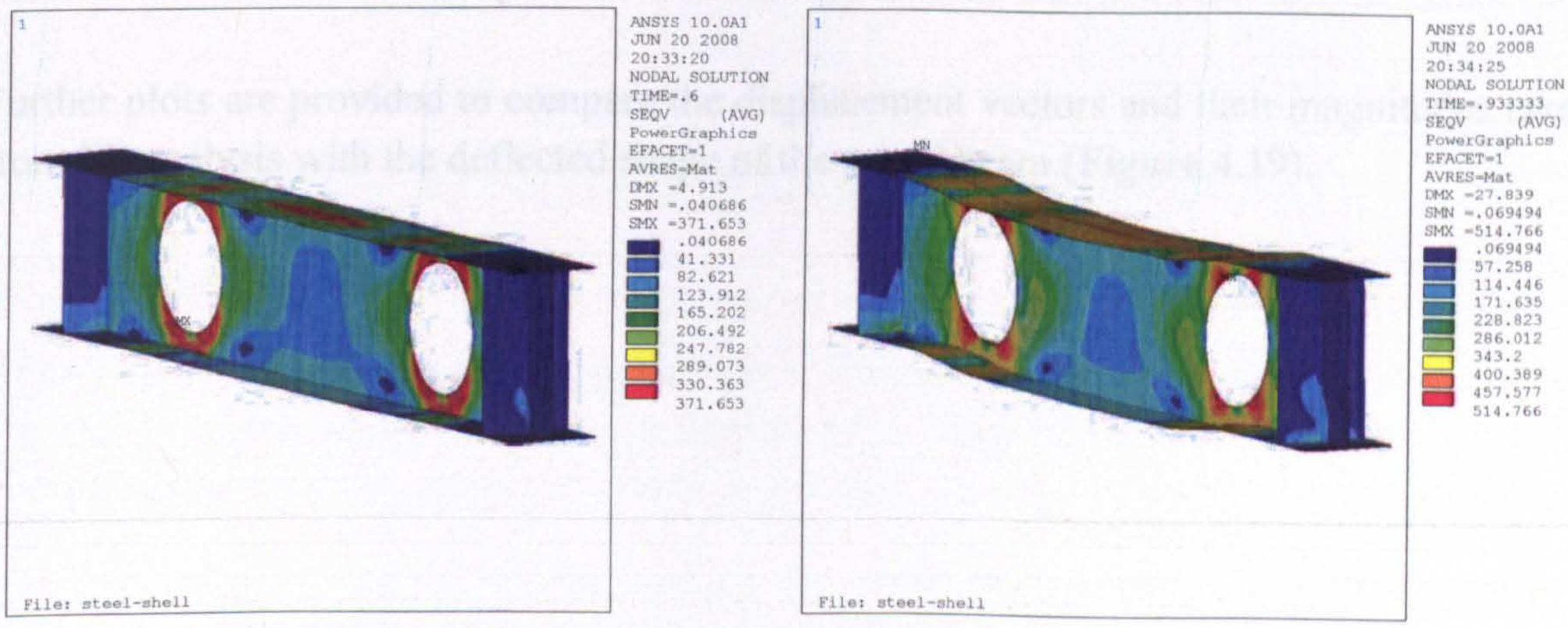

Figure 4.17: Von-Mises stresses at yield point (left) and failure point (right)

The direction of principal stresses and total principal strains and their magnitude is presented in **Figure 4.18** below. It should be noted that principal strains-stresses 1 (PRIN1 or σ_1) are in tension while principal stresses-strains 2 (PRIN2 or σ_2) are in compression. This is in agreement with the results taken from the 2D shear web strains in **Figure 4.9** to **4.12**.

In more detail, the angle θ_p where the shear stress τ_{xy} becomes zero (**Formula 4.1**) defines the principal directions where the only stresses are normal stresses. These stresses are called principal stresses and are found from the original stresses (expressed in the x,y,z directions) via **Formula 4.2**.

$$tan2\theta_p = \frac{2\tau_{xy}}{\sigma_x - \sigma_y} \qquad (4.1)$$

$$\sigma_{1,2} = \frac{\sigma_x + \sigma_y}{2} \pm \sqrt{\left(\frac{\sigma_x - \sigma_y}{2}\right)^2 + {\tau_{xy}}^2} \qquad (4.2)$$

Another important angle, θ_s, is where the maximum shear stress occurs. This is found by finding the maximum of the shear stress transformation equation, and solving for θ. The result is:

$$tan2\theta_s = -\frac{\sigma_x - \sigma_y}{2\tau_{xy}} \qquad (4.3) \quad \rightarrow \quad \theta_s = \theta_p \pm 45^o \qquad (4.4)$$

The maximum shear stress is equal to one-half the difference between the two principal stresses:

$$\tau_{max} = \sqrt{\left(\frac{\sigma_x - \sigma_y}{2}\right)^2 + {\tau_{xy}}^2} = \frac{\sigma_1 - \sigma_2}{2} \qquad (4.5)$$

Further plots are provided to compare the displacement vectors and their magnitudes taken from FE analysis with the deflected shape of the tested beam (**Figure 4.19**).

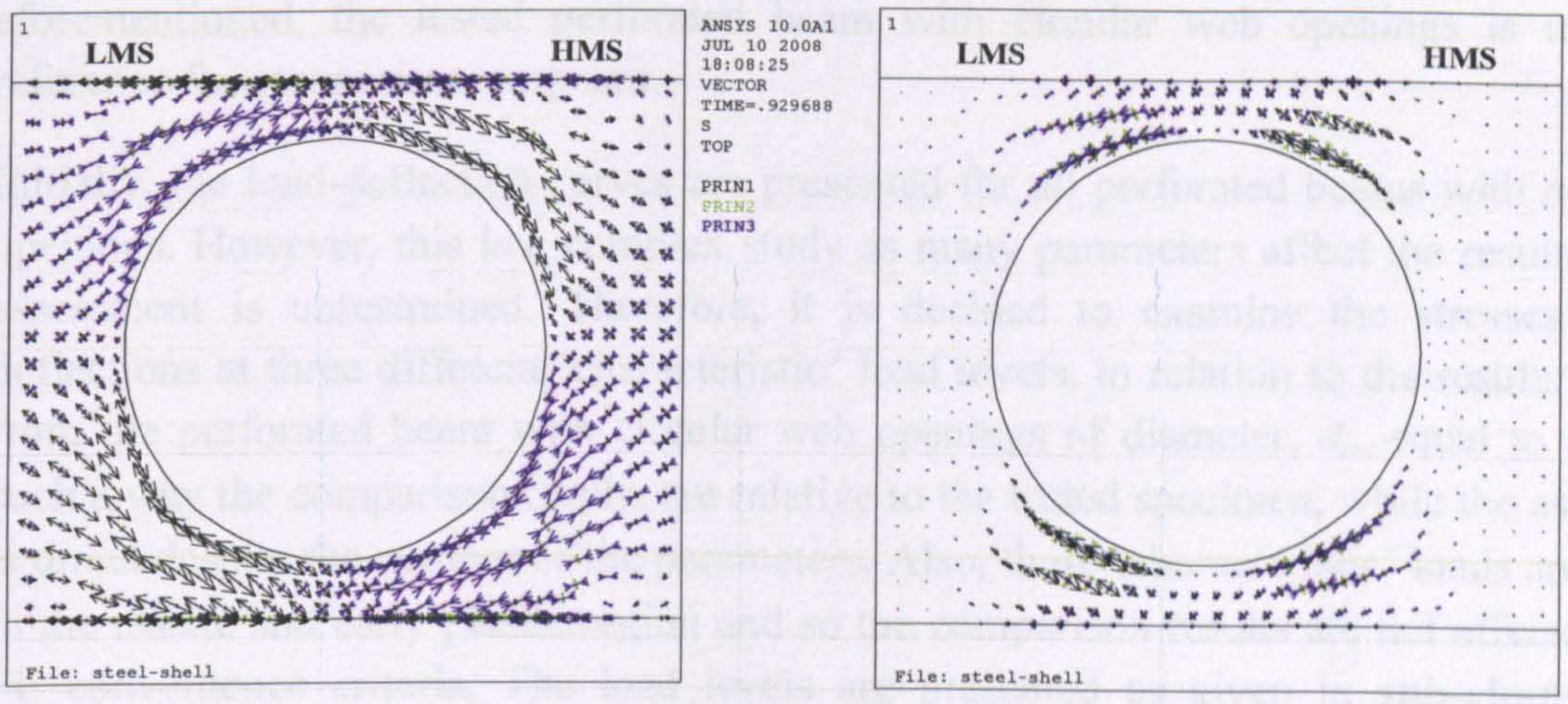

Figure 4.18: Principal stress vectors (left) and total principal strain (right)

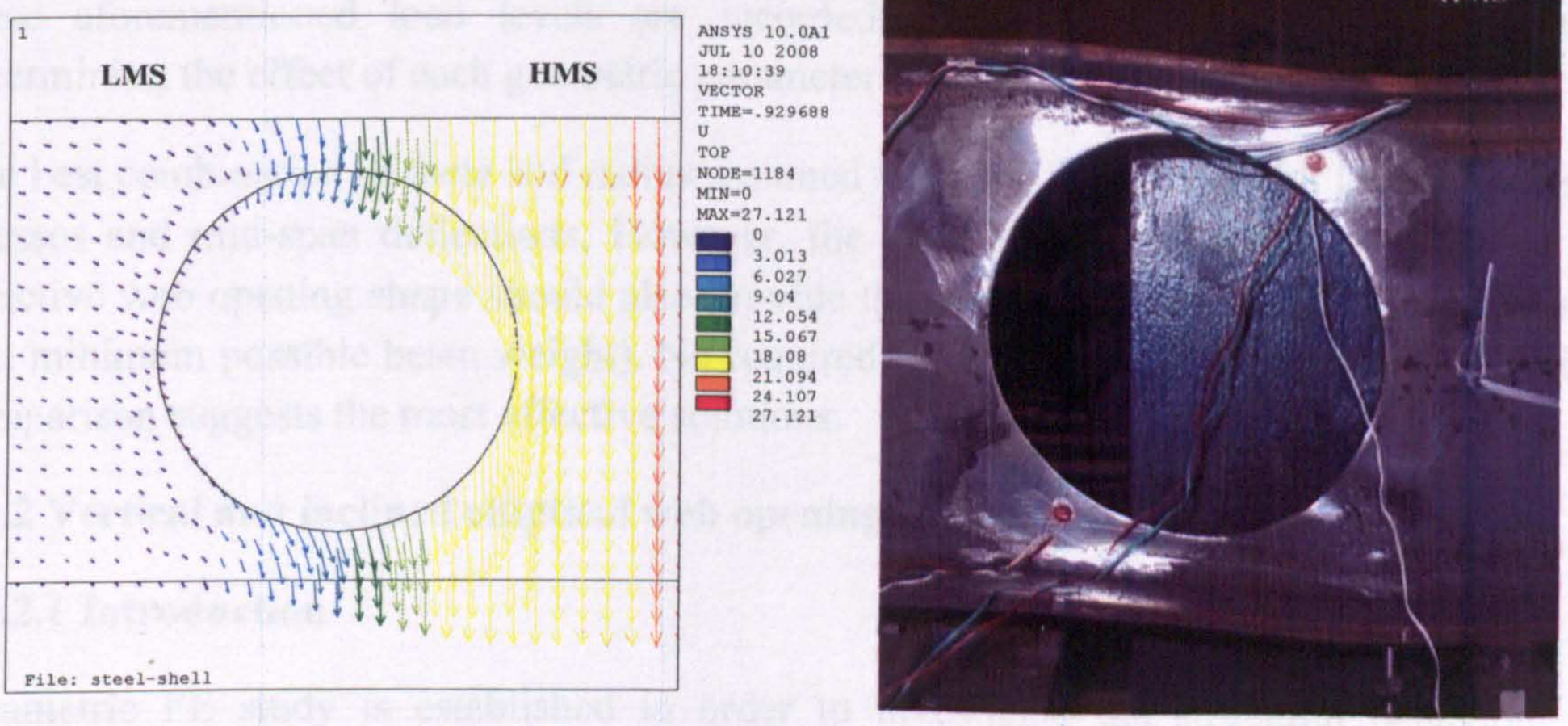

Figure 4.19: Displacement vectors (left) and deflected shape (right) of the perforated beam

4.4 PARAMETRIC FE STUDY OF NOVEL WEB OPENING SHAPES

4.4.1 Method of study

As it is difficult to find the best combination of the parameters, and complicated to achieve this due to mathematical difficulty in dealing with many unknowns and formulas, finite element analysis enables us to avoid such problems.

The validation of the FE model against the experimental work (d_o=*0.76h*) and the agreement of the results, provides credibility to the novel beam models. As it is

aforementioned, the tested perforated beam with circular web openings is used as a reference for comparison purposes.

Initially, the load-deflection curves are presented for all perforated beams with novel web openings. However, this is a complex study as many parameters affect the results and the assessment is unrestrained. Therefore, it is decided to examine the stresses and the deflections at three different 'characteristic' load levels, in relation to the results obtained from the perforated beam with circular web openings of diameter, d_o, equal to *0.76h*. In such a way the comparison results are relative to the tested specimen, while the assessment is direct despite the number of the parameters. Also, these 'characteristic' loads are varying in the elastic and early plastic region and so the comparison results are not affected by the FE convergence criteria. The load levels are presented as given in **sub-chapter 4.2.5** (P_y=*176.2kN*, $P_{cr.}$=*256kN* and $P_{ult.}$=*274.4kN*). The results from the perforated beams with circular web openings of diameter, d_o, equal to *0.8h* is also plotted. Then, the magnitude of differences between the perforated beams with circular web openings of both diameters and the novel web openings shapes are depicted. The Von-Mises stresses and the deflections at these aforementioned load levels are recorded and used for comparison purposes, determining the effect of each geometric parameter.

The best combination of theta and radius assumed to be for the beams with low Von-Mises stresses and mid-span deflections. However, the combination of theta and radius of an effective web opening shape should also provide the maximum possible web opening area (i.e. minimum possible beam weight). No required limits are defined; however the relative comparison suggests the most effective solutions.

4.4.2 Vertical and inclined elliptical web openings

4.4.2.1 Introduction

Parametric FE study is established in order to investigate the structural behaviour of perforated beams with novel web opening shapes. Regarding the results from **Appendix 1** and **2** as well as **Chapter 3**, an idea of a new web opening shape is developed from a combination of hexagonal and circular web openings. The general geometry of this web opening is elliptical and it is decided for it to be investigated in a vertical and in an inclined configuration, in the perforated beam which is previously presented in this chapter. A high shear-moment interaction is applied to the centre-line of the two isolated web-openings, in order to investigate their Vierendeel mechanism behaviour.

Web opening depth, d_o, equal to *0.8h* is considered, similarly to **Chapter 3**, while two are the main parameters considered, introducing various web opening configurations with different web opening areas. The angle (THETA) of the straight lines and the radius, R, of the semi-circles at the top and bottom tee-sections; are the two main parameters of this study. These are shown in **Figure 4.20**. Four angles (10°, 20°, 30° and 40°) as well as four

radii ($0.15d_o$, $0.2d_o$, $0.25d_o$ and $0.3d_o$) and their combinations are modelled. Hence, sixteen different web openings are modelled regarding the vertical elliptical configuration. The same concept is followed for the development of the inclined elliptical web openings, while the top and bottom tee-sections (i.e. semi-circles with radius, R) are slightly moved to the opposite directions and form an inclined elliptical shape (**Figure 4.20**). Another sixteen different perforated beams are modelled regarding the inclined elliptical configuration. Moreover, the perforated beam with circular web openings and diameter, d_o, equal to *0.8h*, is modelled for direct comparison. In total thirty-three (16+16+1) non-linear FE simulations are conducted to cover the needs of this part of the study to optimise the shape of the novel elliptical web openings, under a critical shear mechanism. It is considered necessary to analyze all 33 FE models, as it is found that some perforated beams present significant high stress concentration at specific points indicated with black arrows in **Figure 4.20** and **4.29**, due to the combination of R and THETA.

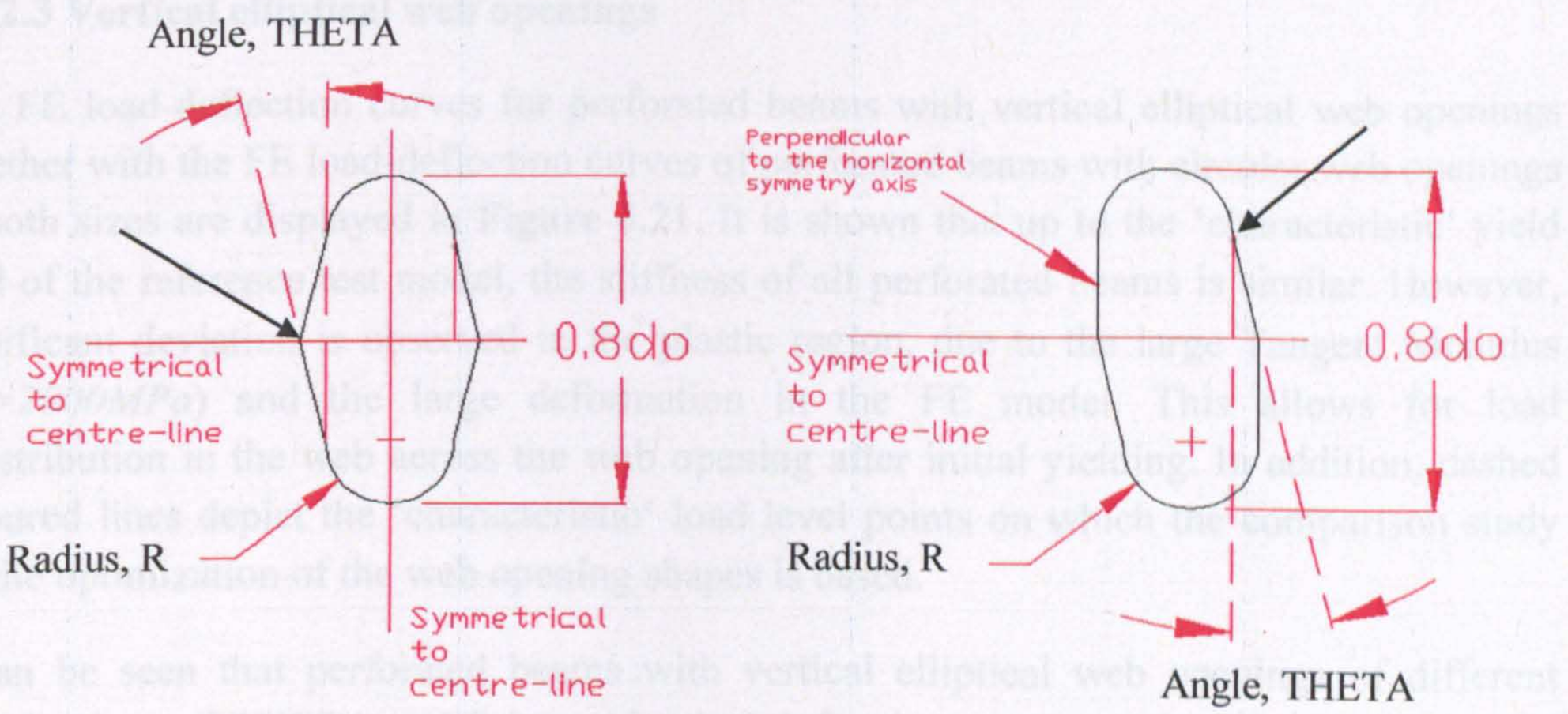

Figure 4.20: Geometric parameters (Angle, THETA and radius, R)

4.4.2.2 FE results

Table 4.2 synopsizes the necessary reference values of nodal stresses and mid-span vertical deflections to establish the following comparison between the perforated beams with circular web openings of either test or FE model and the perforated beams with novel web opening shapes.

	at P_y=176kN		at $P_{cr.}$=256kN		at $P_{ult.}$=274.4kN		FEA Solution Diverged		
	δ (mm)	Von-Mises (MPa)	δ (mm)	Von-Mises (MPa)	δ (mm)	Von-Mises (MPa)	Load, P (kN)	δ (mm)	Von-Mises (MPa)
TEST MODEL CIRCULAR $d_o=0.76h$	3.82	-----	13.56	-----	21.8	-----	-----	-----	-----
FEM CIRCULAR $d_o=0.76h$	3.6	372.784	13.56	453.745	21.8	510.296	293	32.43	529.04
FEM CIRCULAR $d_o=0.8h$	6	398.597	21	522.464	24.7	526.597	339.4	41.1	529.71

Table 4.2: Initial evaluations for perforated beams with circular web openings

4.4.2.3 Vertical elliptical web openings

The FE load-deflection curves for perforated beams with vertical elliptical web openings together with the FE load-deflection curves of perforated beams with circular web openings of both sizes are displayed in **Figure 4.21**. It is shown that up to the 'characteristic' yield load of the reference test model, the stiffness of all perforated beams is similar. However, significant deviation is observed in the plastic region, due to the large Tangent Modulus (E_T=*2000MPa*) and the large deformation in the FE model. This allows for load redistribution in the web across the web opening after initial yielding. In addition, dashed coloured lines depict the 'characteristic' load level points on which the comparison study for the optimization of the web opening shapes is based.

It can be seen that perforated beams with vertical elliptical web openings of different combinations of THETA and R have identical deflections at certain load levels. It is noted that a few of them have similar stress magnitudes too, whilst the web opening areas are different.

Figure 4.22 to **4.24** present the FE results of Von-Mises nodal stresses and mid-span vertical deflections in relation to the angle THETA of the straight lines and the radius of the semi-circles, R. The results are given in sequence; starting (i.e. Name 1) with the web opening shape, which provides the smaller web opening area. The name of each web opening shape and its web opening area are summarized in **Table 4.3,** below.

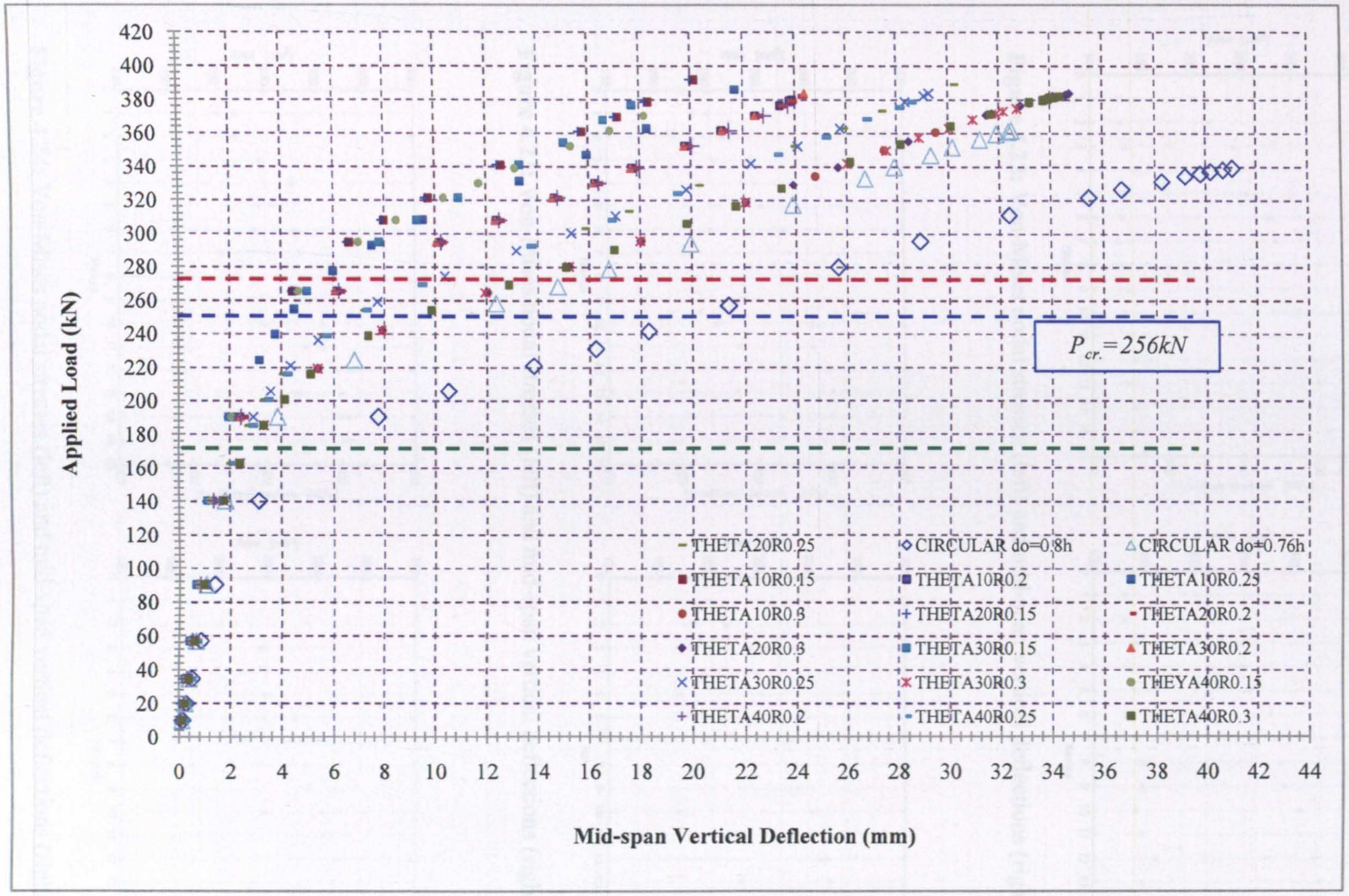

Figure 4.21: Load against deflection FE curves for perforated beams with vertical elliptical web openings

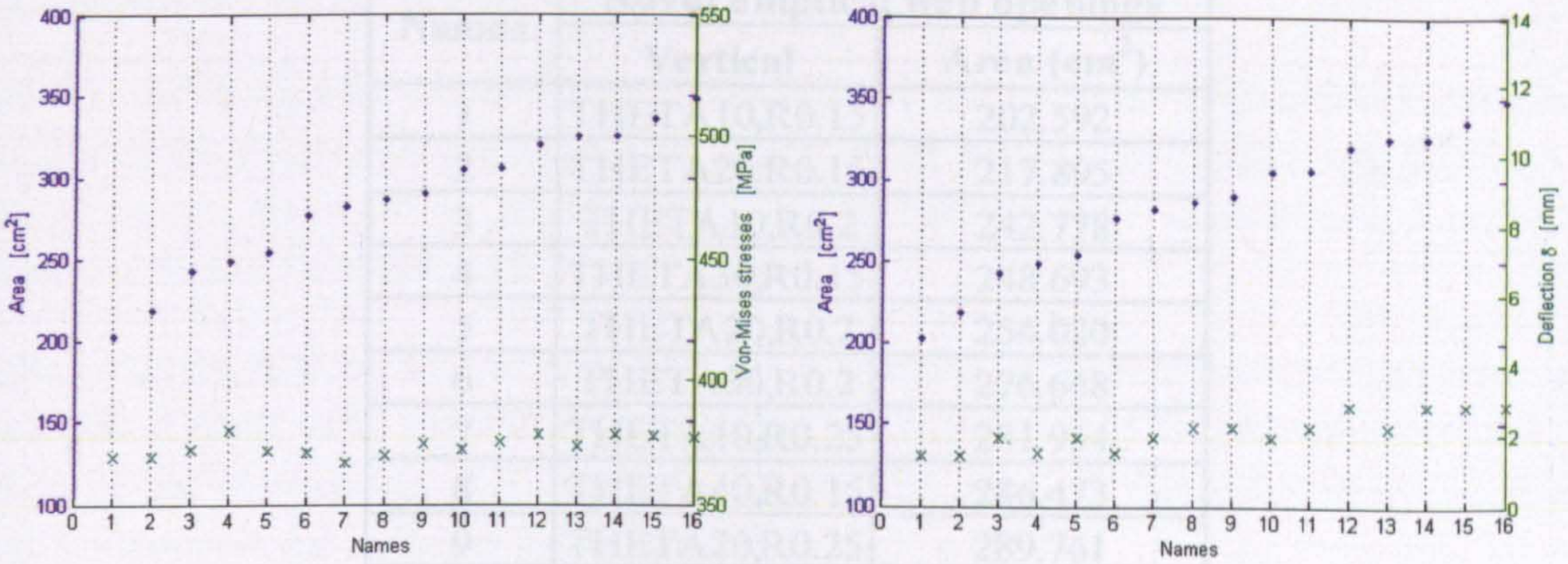

Figure 4.22: Von-Mises nodal stresses (left) and mid-span vertical deflections (right) at P_y

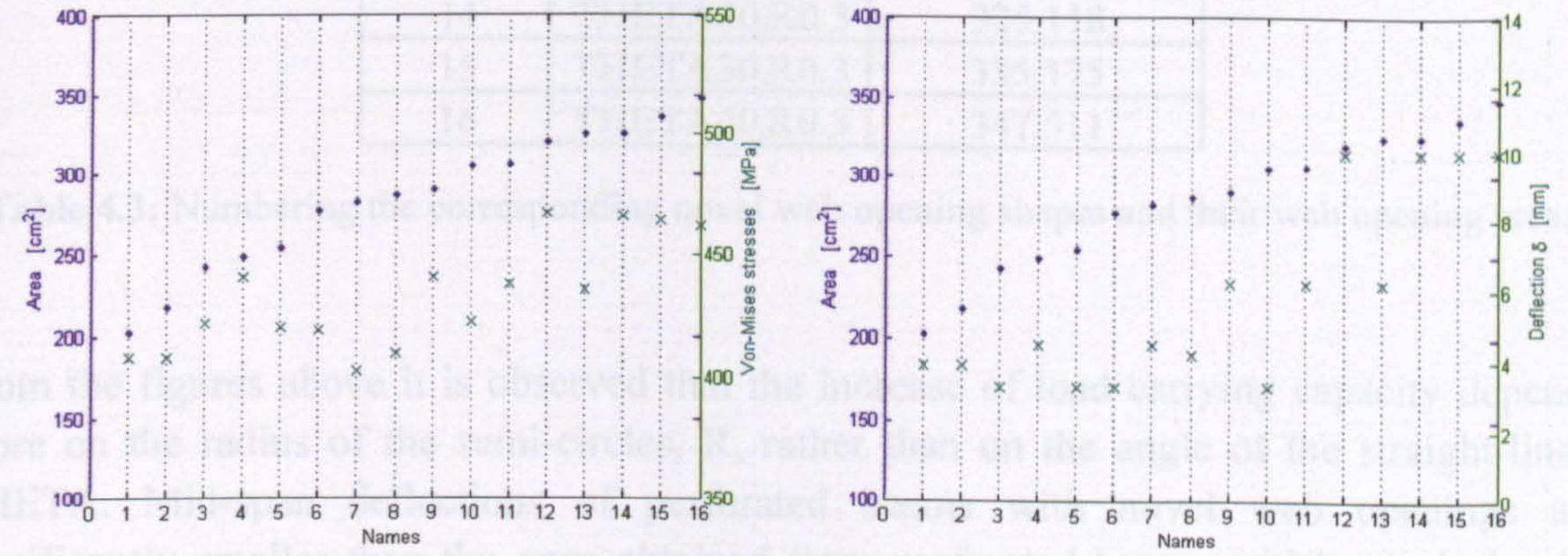

Figure 4.23: Von-Mises nodal stresses (left) and mid-span vertical deflections (right) at $P_{cr.}$

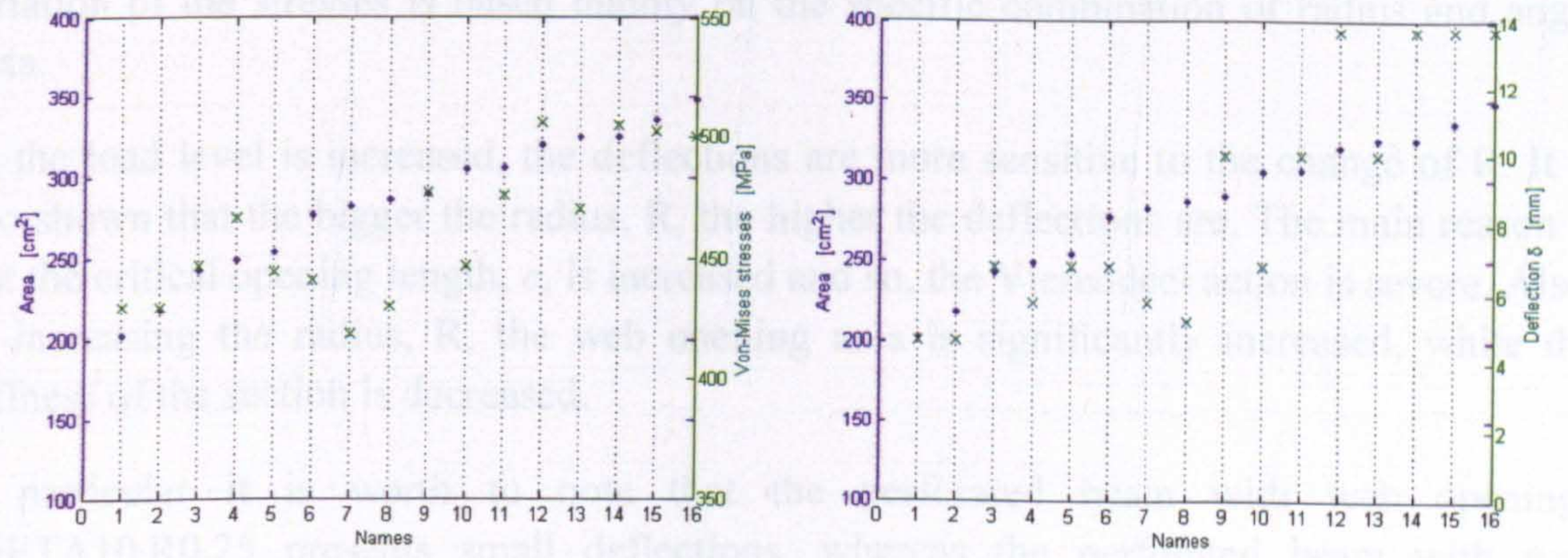

Figure 4.24: Von-Mises nodal stresses (left) and mid-span vertical deflections (right) at $P_{ult.}$

Names	Novel elliptical web openings	
	Vertical	Area (cm^2)
1	THETA10,R0.15	202.592
2	THETA20,R0.15	217.895
3	THETA10,R0.2	242.778
4	THETA30,R0.15	248.693
5	THETA20,R0.2	254.020
6	THETA30,R0.2	276.648
7	THETA10,R0.25	281.954
8	THETA40,R0.15	286.473
9	THETA20,R0.25	289.761
10	THETA40,R0.2	304.404
11	THETA30,R0.25	305.475
12	THETA10,R0.3	320.121
13	THETA40,R0.25	324.750
14	THETA20,R0.3	325.118
15	THETA30,R0.3	335.175
16	THETA40,R0.3	347.511

Table 4.3: Numbering the corresponding novel web opening shapes and their web opening areas

From the figures above it is observed that the increase of load carrying capacity depends more on the radius of the semi-circles, R, rather than on the angle of the straight-lines, THETA. Mid-span deflections of perforated beams with novel web openings are significantly smaller than the ones obtained from perforated beams with typical circular web openings of both diameter sizes. In contrast, perforated beams with circular web openings provide a smooth transition of the stresses at the edge of the web openings, and in some cases, the novel perforated beams behave worse in terms of stresses. Hence, the variation of the stresses is based mainly on the specific combination of radius and angle theta.

As the load level is increased, the deflections are more sensitive to the change of R. It is also shown that the bigger the radius, R, the higher the deflections are. The main reason is that the critical opening length, *c*, is increased and so, the Vierendeel action is severe. Also, by increasing the radius, R, the web opening area is significantly increased, while the stiffness of the section is decreased.

In particular it is worth to note that the perforated beam with web openings THETA10,R0.25 presents small deflections, whereas the perforated beam with web openings THETA30,R0.15 presents significantly increased stresses. The reason behind the observed changes is the high stress concentration at the sharp corners on the web opening edge, created by the combination of the specific THETA and R.

4.4.2.4 Inclined elliptical web openings

The FE load-deflection curves for perforated beams with inclined elliptical web openings, along with the FE load-deflection curves of perforated beams with circular web openings of both sizes are displayed in **Figure 4.25**. Similar load carrying capacities and mid-span vertical defections are observed.

Again, **Figure 4.26** to **4.28** demonstrate the FE results of Von-Mises nodal stresses and mid-span vertical deflections in relation to the angle THETA of the straight lines and the radius of the semi-circles, R. The name of each web opening shape and its web opening area are summarized in **Table 4.4**, below.

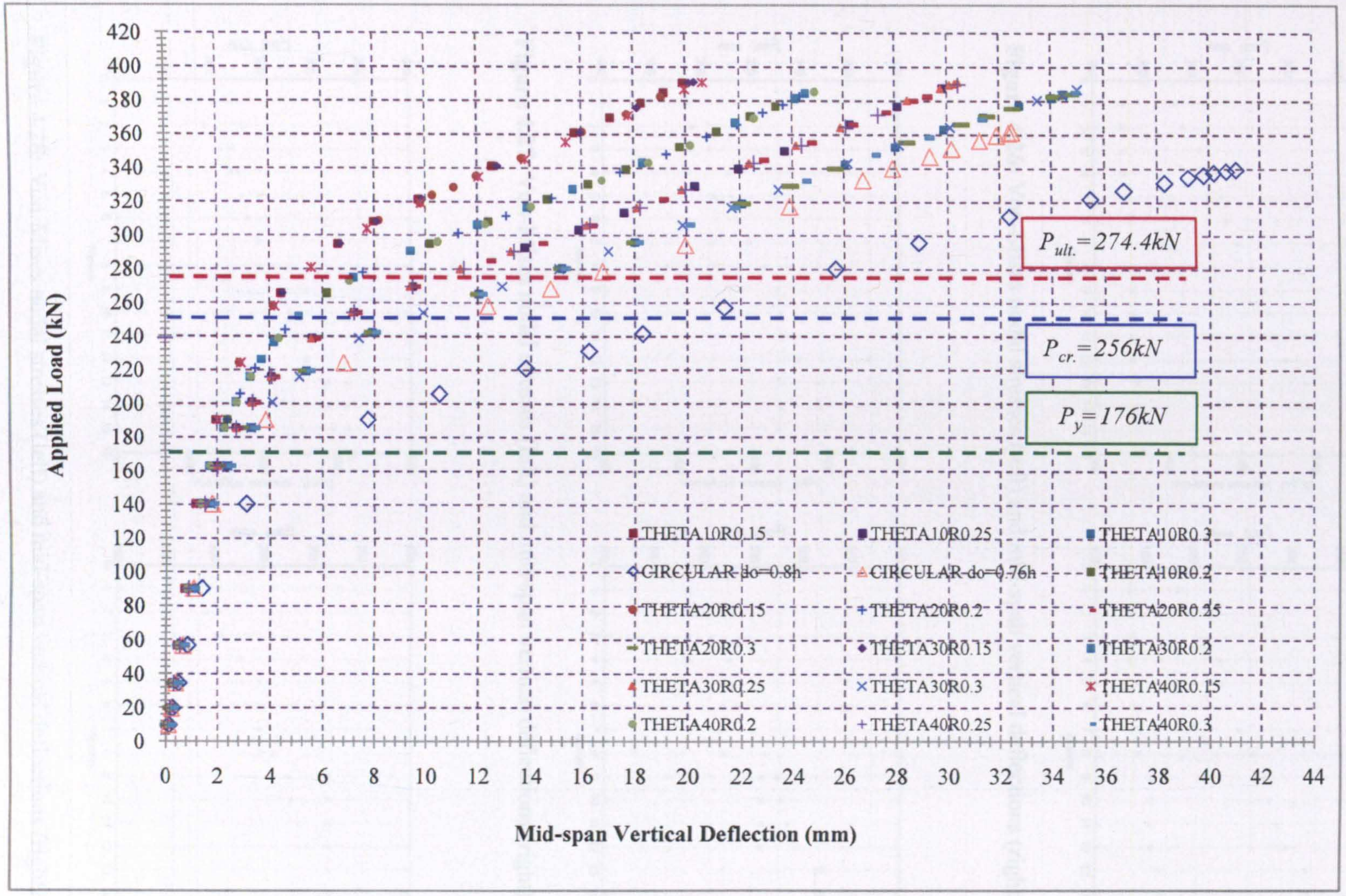

Figure 4.25: Load against deflection FE curves for perforated beams with inclined elliptical web openings

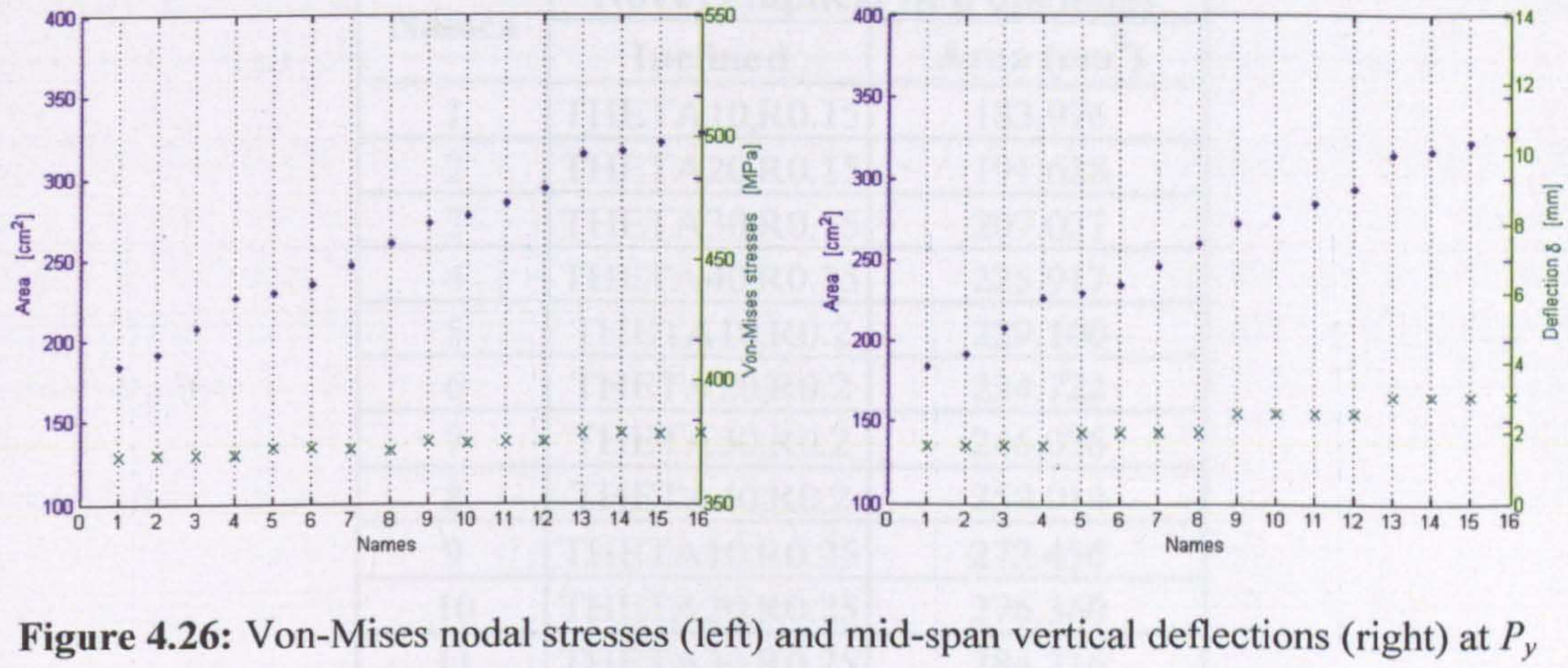

Figure 4.26: Von-Mises nodal stresses (left) and mid-span vertical deflections (right) at P_y

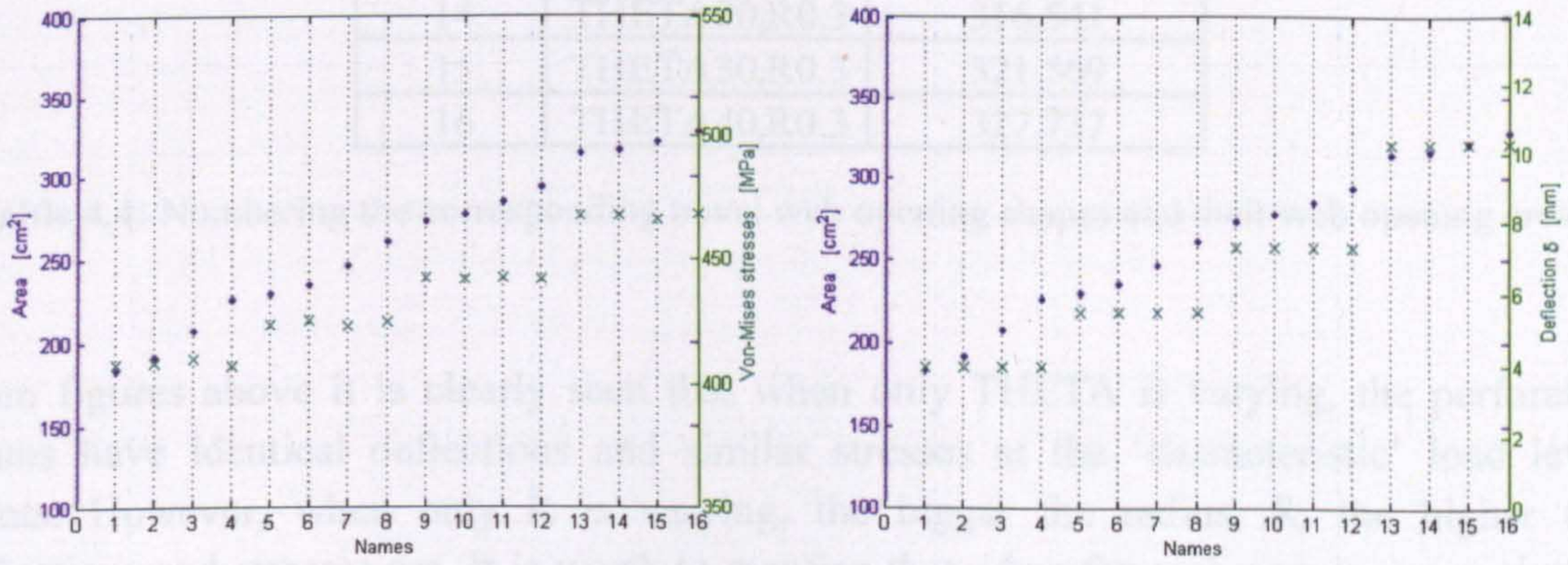

Figure 4.27: Von-Mises nodal stresses (left) and mid-span vertical deflections (right) at $P_{cr.}$

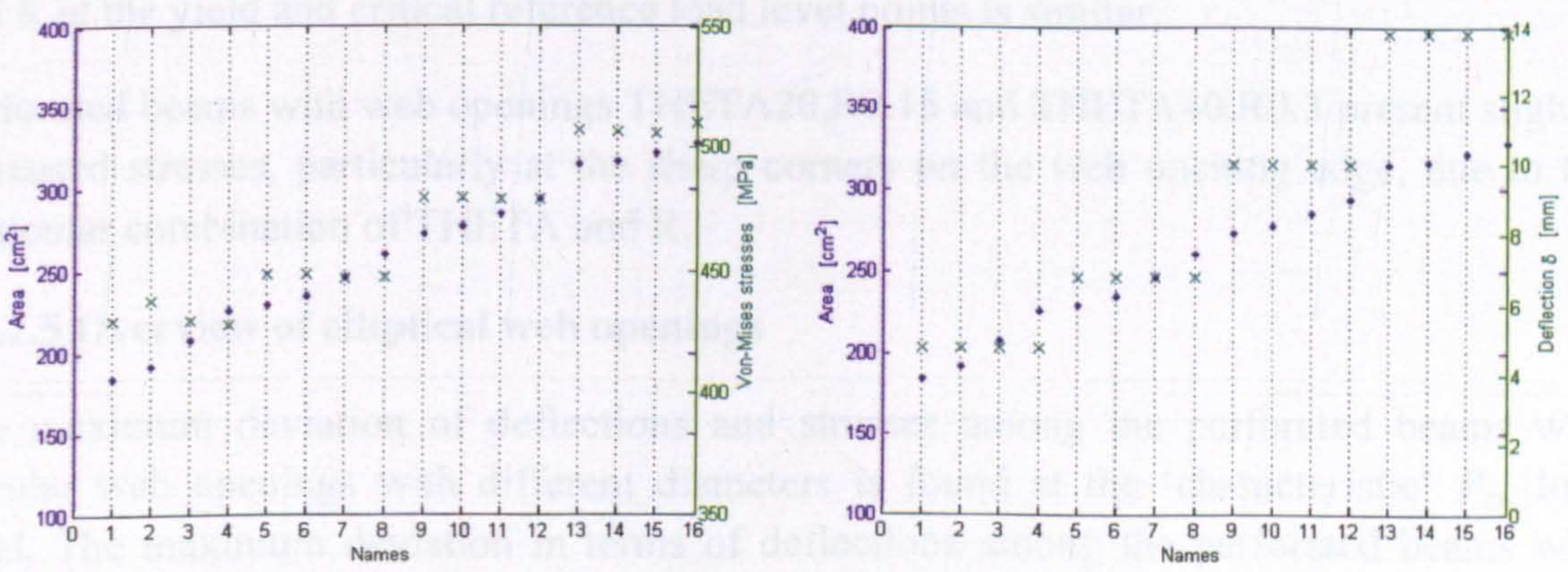

Figure 4.28: Von-Mises nodal stresses (left) and mid-span vertical deflections (right) at $P_{ult.}$

Names	Novel elliptical web openings	
	Inclined	Area (cm^2)
1	THETA10,R0.15	183.976
2	THETA20,R0.15	191.628
3	THETA30,R0.15	207.027
4	THETA40,R0.15	225.917
5	THETA10,R0.2	229.100
6	THETA20,R0.2	234.722
7	THETA30,R0.2	246.036
8	THETA40,R0.2	259.914
9	THETA10,R0.25	272.456
10	THETA20,R0.25	276.360
11	THETA30,R0.25	284.216
12	THETA40,R0.25	293.854
13	THETA10,R0.3	314.042
14	THETA20,R0.3	316.541
15	THETA30,R0.3	321.569
16	THETA40,R0.3	327.737

Table 4.4: Numbering the corresponding novel web opening shapes and their web opening areas

From figures above it is clearly seen that when only THETA is varying, the perforated beams have identical deflections and similar stresses at the 'characteristic' load level points. However, when only R is varying, the bigger the radius, R, the higher the deflections and stresses are. It is worth to mention that when the web openings are plotted with sequence in terms of the web opening area, a rational order is found. By plotting the results in this way, it is now easier to indentify the influence of any of the parameters on the structural performance of the perforated beams. Also, the sensitivity for both THETA and R at the yield and critical reference load level points is similar.

Perforated beams with web openings THETA20,R0.15 and THETA40,R0.3 present slightly increased stresses, particularly at the sharp corners on the web opening edge, due to the particular combination of THETA and R.

4.4.2.5 Overview of elliptical web openings

The maximum deviation of deflections and stresses among the perforated beams with circular web openings with different diameters is found at the 'characteristic' $P_{cr.}$ load level. The maximum deviation in terms of deflections among the perforated beams with any circular and novel elliptical web openings is obtained at the 'characteristic' $P_{ult.}$ load level. Similarly, the maximum deviation in terms of stresses is obtained at the 'characteristic' $P_{cr.}$ load level. In addition to that, higher fluctuation of deflections and stresses among the perforated beams with the novel web opening shapes is found as the

load level is increased. Therefore, the main differences are taking place in the plastic region, where the stiffness of the models is dependent on the Tangent Modulus, E_T.

All perforated beams with novel web opening shapes are stiffer compared to the perforated beams with circular web openings with diameter equal to *0.76h* and *0.8h*. Smaller mid-span vertical deflections are always observed, however increased stresses are found at the 'characteristic' load level points P_y and $P_{cr.}$ in the perforated beams, with the following web opening shapes:

- *Vertical Elliptical Web Openings*
  P_y: THETA30,R0.15 / THETA20-40,R0.25 / THETA10-40,R0.3
- *Vertical and Inclined Elliptical Web Openings*
  P_{cr}: THETA10-40,R0.3

Both vertical and inclined elliptical web openings, THETA40,R0.25 (No.13 and No.12; for vertical and inclined web openings, respectively), have a relatively big web opening area, while they behave well to be characterized as effective solutions. Furthermore, the web openings THETA10,R02.5 and THETA40,R0.15 (No.7 and No.8 respectively) for vertical elliptical web openings and THETA40,R0.15 (No.4) for inclined elliptical web openings, show the maximum difference between the biggest possible web opening area and the relatively small deflection and low stresses.

Yield patterns and deflected shapes of perforated beams, with various selected novel web opening shapes at the three 'characteristic' load level points, are presented in **Appendix 9.** In addition to that, yield patterns and deflected shapes of perforated beams with circular web openings of diameter, d_o, equal to *0.8h* are presented for direct comparison.

4.4.3 Circular web openings with filleted edges at the mid-depth

4.4.3.1 Introduction

Four circular web openings with fillet radius of 15, 25, 35 and 45mm of fillet radius, *r*, are examined (**Figure 4.29**). There is no reason to investigate bigger radii of fillets since the circular shape is then dramatically changed and thus, the concept and benefits of using the circular web opening shape are totally jeopardized. Another four non-linear FE simulations are conducted herein.

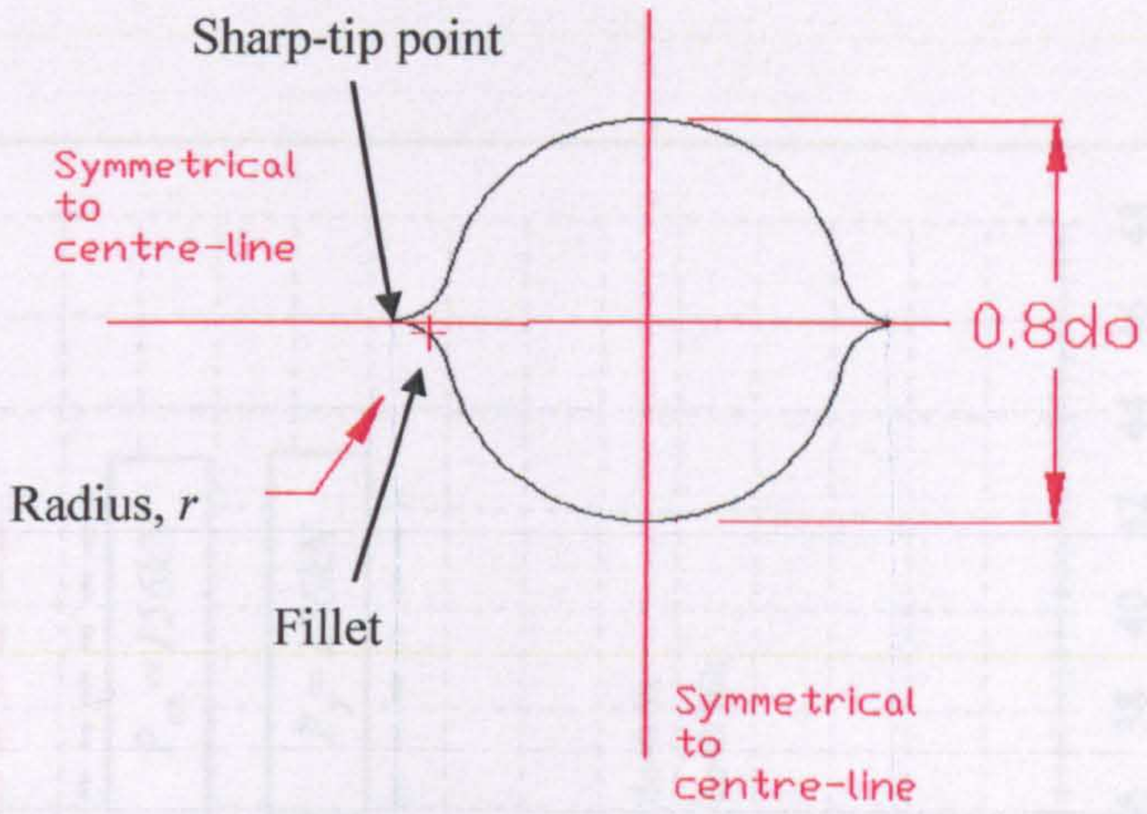

Figure 4.29: Geometric parameters (Radius of fillet, r, in mm)

4.4.3.2 FE results

The FE load-deflection curves for perforated beams with filleted circular web openings together with the FE load-deflection curves of perforated beams with circular web openings of both sizes are displayed in **Figure 4.30**. It is observed that all the perforated beams with novel web openings of diameter, d_o, equal to *0.8h*, have the same stiffness and identical load-deflection curves with the perforated beam with circular web opening of the same size. Slight differences are only shown at Von-Mises stress evaluations, while higher fluctuation is observed at the 'characteristic' critical load level point, $P_{cr.}$.

Figure 4.31 to **4.33** present the FE results of Von-Mises nodal stresses and mid-span vertical deflections in relation to the radius of fillet, r. The name of each web opening shape and its web opening area are summarized in **Table 4.5**, below.

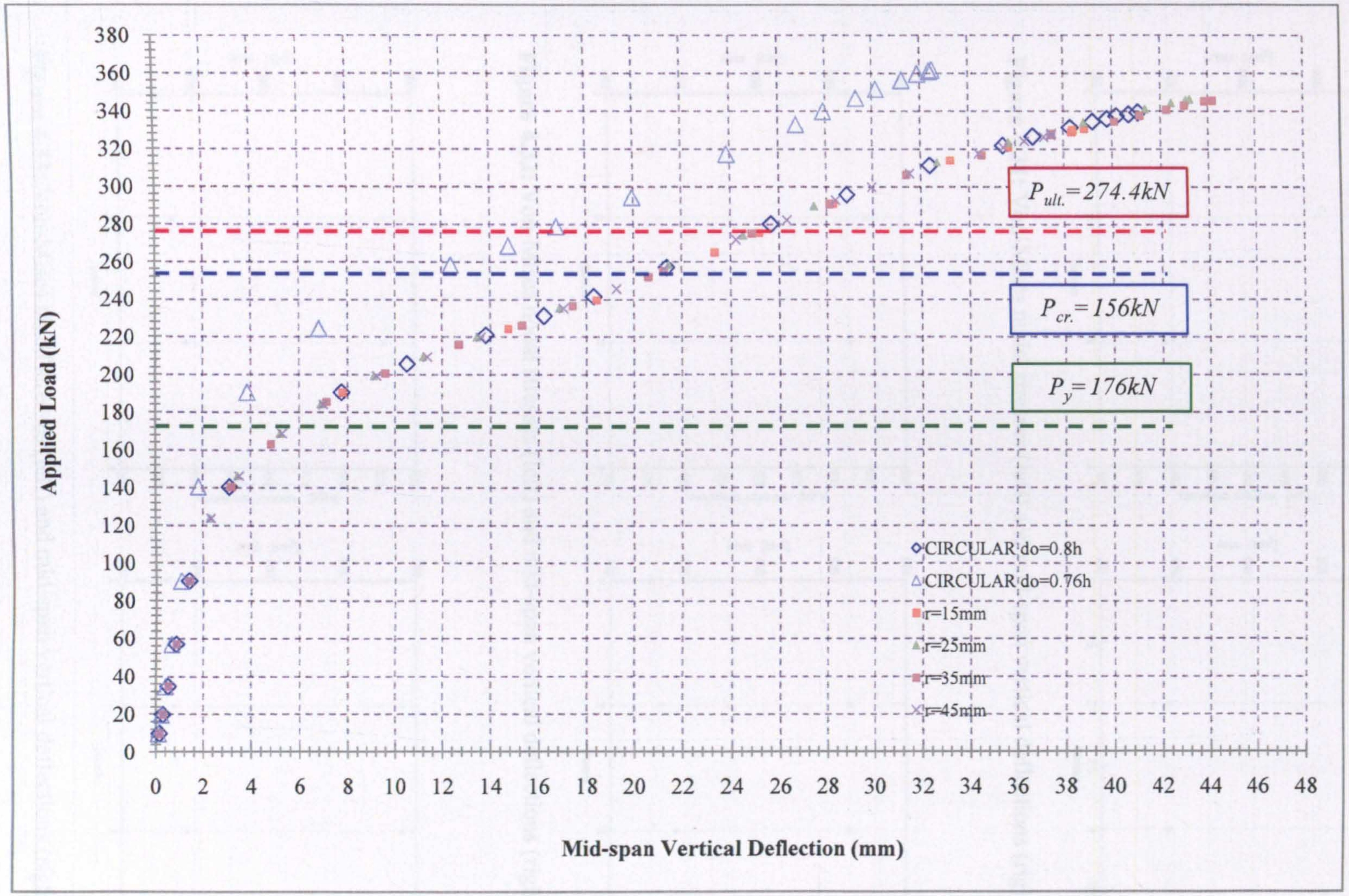

Figure 4.30: Load against deflection FE curves for perforated beams with filleted circular web openings

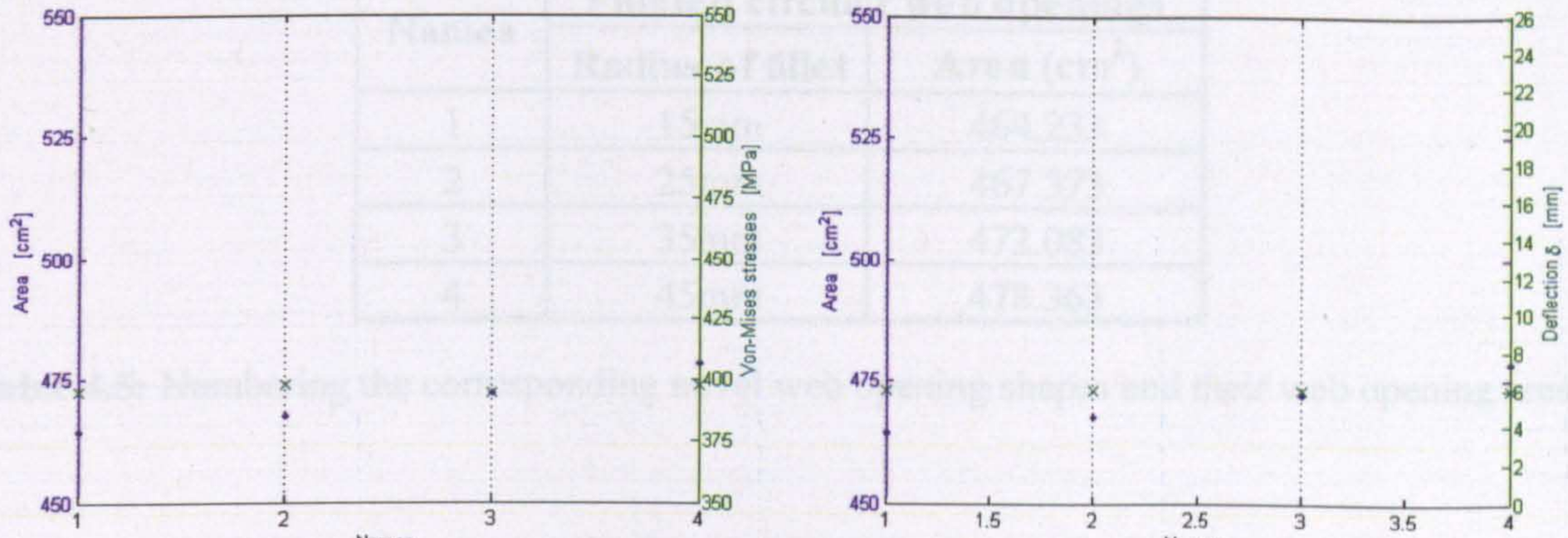

Figure 4.31: Von-Mises nodal stresses (left) and mid-span vertical deflections (right) at P_y

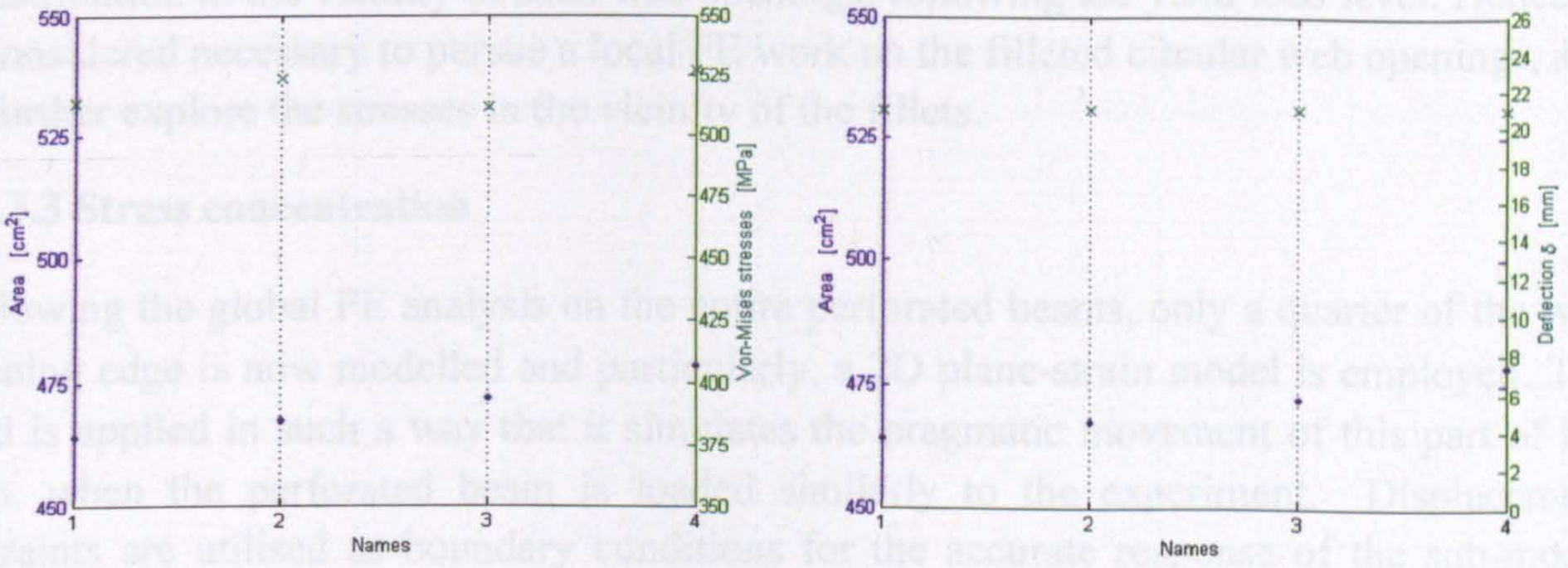

Figure 4.32: Von-Mises nodal stresses (left) and mid-span vertical deflections (right) at $P_{cr.}$

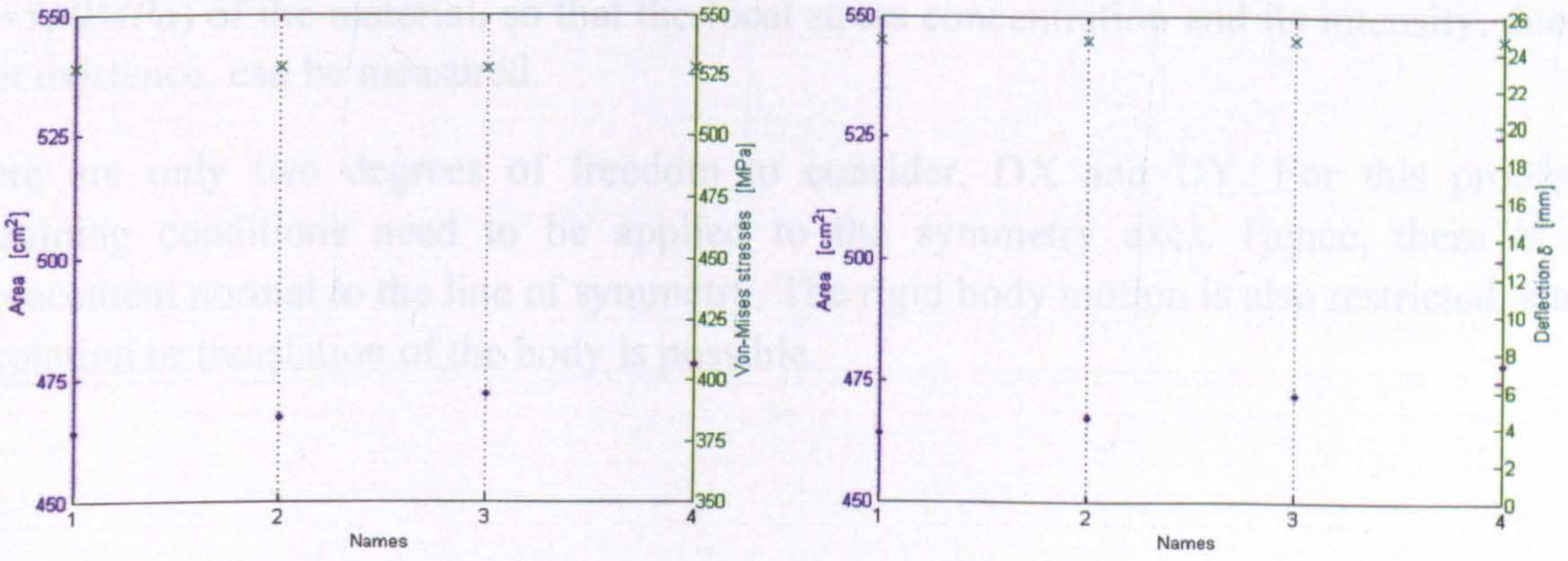

Figure 4.33: Von-Mises nodal stresses (left) and mid-span vertical deflections (right) at $P_{ult.}$

Names	Filleted circular web openings	
	Radius of fillet	Area (cm^2)
1	15mm	464.233
2	25mm	467.373
3	35mm	472.083
4	45mm	478.363

Table 4.5: Numbering the corresponding novel web opening shapes and their web opening areas

High stresses are concentrated at the sharp-tip points; the connection between the top and bottom fillet at the mid-depth of the web openings. The overall results have not changed, as these web openings are located away from each other and the stresses are not increased. However, stress variation is observed at the 'characteristic' $P_{cr.}$, due to the difficult redistribution in the vicinity of such web openings, following the yield load level. Hence, it is considered necessary to pursue a local FE work on the filleted circular web openings, and to further explore the stresses in the vicinity of the fillets.

4.4.3.3 Stress concentration

Following the global FE analysis on the entire perforated beams, only a quarter of the web opening edge is now modelled and particularly, a 2D plane-strain model is employed. The load is applied in such a way that it simulates the pragmatic movement of this part of the web, when the perforated beam is loaded similarly to the experiment. Displacement restraints are utilised as boundary conditions for the accurate response of the sub-model **(Figure 4.34)**.

It should be clearly mentioned that, in local analysis the load does not represent the load carrying capacity. The modelled plate is tested up to the ultimate stress level (i.e. $f_{ult.}=530MPa$) of the material, so that the local stress concentration and its intensity, due to fillet existence, can be measured.

There are only two degrees of freedom to consider, DX and DY. For this problem, restraining conditions need to be applied to the symmetry axes. Hence, there is no displacement normal to the line of symmetry. The rigid body motion is also restricted, since no rotation or translation of the body is possible.

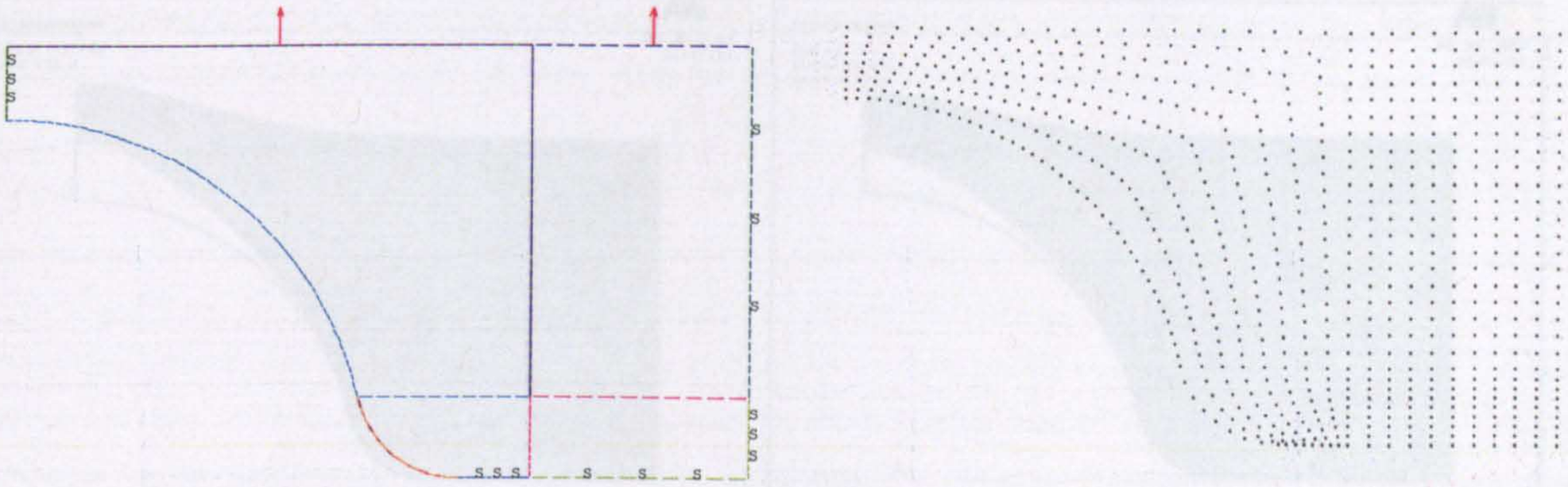

Figure 4.34: Boundary conditions (left) and reactions (right)

4.4.3.4 Hot spot stress

Structural hot spot stresses; also called geometric stresses, include nominal stresses and stresses from structural discontinuities. The latter are not the stresses because of the presence of welds.

The hot spot stresses may be determined using stress concentration factors, obtained from parametric formulas within their domains of validity, a finite element analysis, or an experimental model. *"The hot spot stresses or strains arrived at in this manner are divided by the nominal stress or strain to arrive at the stress concentration factor (SCF) or strain concentration factor (SNCF)"* (Von Wingerde, Packer and Wardenier, 1995).

It should be noted that the FE modelling might influence the calculated stress at the hot spot region. The parameters affecting this are the following:

- Type of elements used.
- Size of elements at the hot spot region.
- The way the stresses derive from the analysis (Gaussian stress, nodal stress, etc.).

4.4.3.5 Stress concentration by FEA

A convergence study is initially established with mesh refinement at three different stages. **Figure 4.35** and **Figure 4.36** present the mesh refinement and the convergence of the results as relatively increasing the number of elements. Fine mesh is finally used for this research study. The Von-Mises nodal stress obtained from FEA is divided by the nominal yield material stress (f_y=*355MPa*), denoted as SCF. In **Figure 4.37**, the SCF is plotted against the distance from the sharp-tip point, where the top and bottom fillets are connected. The FE analysis is conducted for four plates with different radii of fillets and one without fillets.

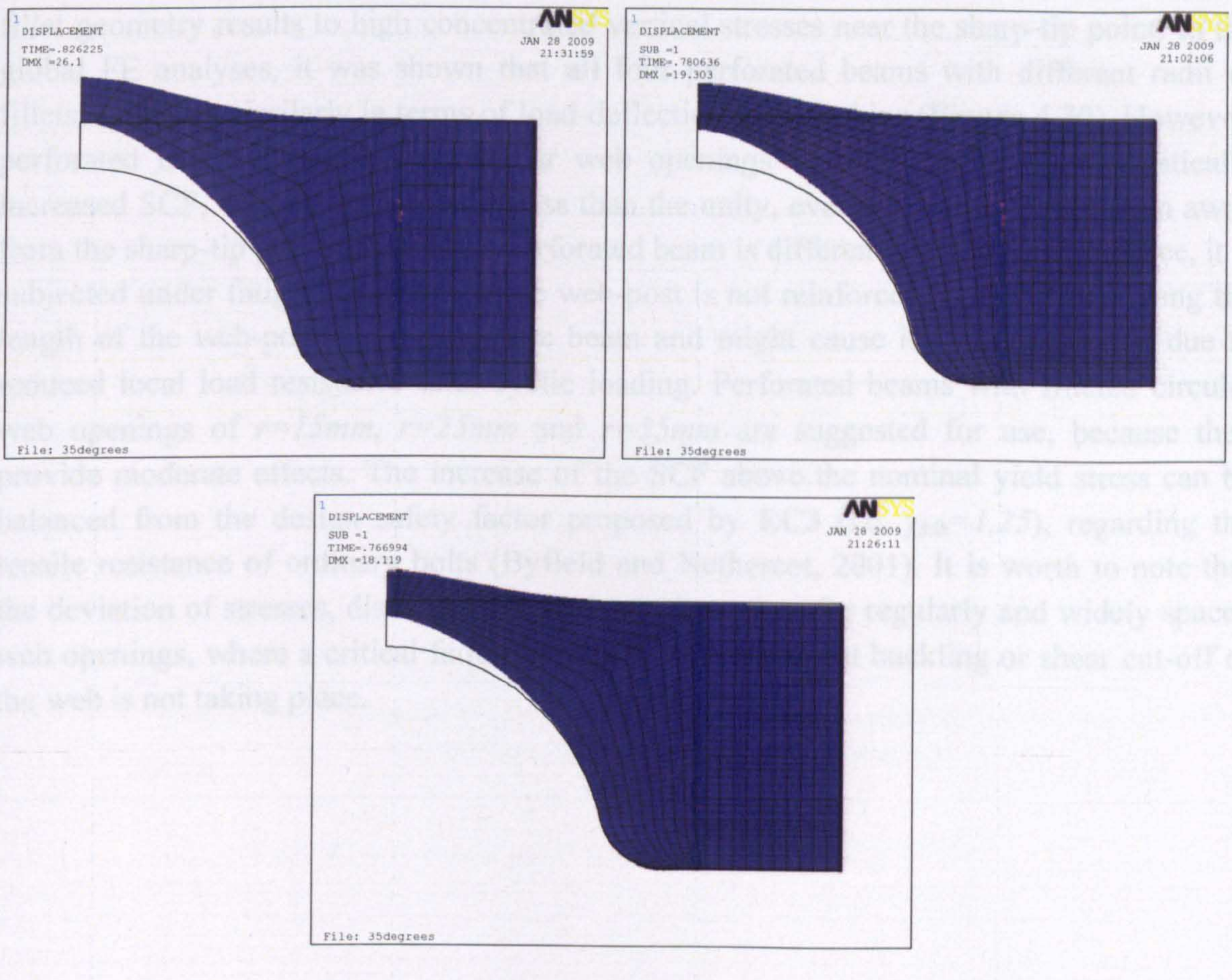

Figure 4.35: The three stages of the mesh refinement – Deformed model with un-deformed edge

In **Figure 4.37**, there is a critical distance of nearly 15mm where the SCF is above the unity and so local buckling or shear cut-off might occur, causing local failure of the perforated beam. Instead, when there are no fillets and the beam is highly loaded; the SCF is equal to unity at this critical distance. The safe distance from the sharp-tip point is presented by the steep decrease of the SCF. The bigger the fillet radius is, the higher the SCF is, while the rate of SCF's reduction is lower.

It is worth to clarify that this study is on the maximum possible web opening diameter, $d_o=0.8h$, whereas the web thickness is limited to 6mm plate; as taken from the particular beam tested previously in this chapter.

Figure 4.38 presents the contour plots of the stressed areas for all five FE models. Von-Mises and vertical stresses, σ_y, are plotted for comparison in order to draw the highly stressed points and the areas under tension and compression.

The position and the magnitude of the four plastic typical hinges are affected by the existence of the fillet, but not affected from the radius of the fillet. The introduction of the

fillet geometry results to high concentrated vertical stresses near the sharp-tip point. In the global FE analyses, it was shown that all four perforated beams with different radii of fillets, *r*, behave similarly in terms of load-deflection relationships (**Figure 4.30**). However, perforated beams with filleted circular web openings of *r=45mm* have a dramatically increased SCF, which is not reduced less than the unity, even at a distance of 90mm away from the sharp-tip point. In case this perforated beam is differently loaded, for instance, it is subjected under fatigue loading and the web-post is not reinforced, high stresses along the length of the web-post can damage the beam and might cause its failure. This is due to reduced local load resistance after cyclic loading. Perforated beams with filleted circular web openings of *r=15mm*, *r=25mm* and *r=35mm* are suggested for use, because they provide moderate effects. The increase of the SCF above the nominal yield stress can be balanced from the design safety factor proposed by **EC3** (i.e. $\gamma_{Mb}=1.25$), regarding the tensile resistance of ordinary bolts (Byfield and Nethercot, 2001). It is worth to note that the deviation of stresses, discussed above, is not important for regularly and widely spaced web openings, where a critical failure mode, such as web-post buckling or shear cut-off of the web is not taking place.

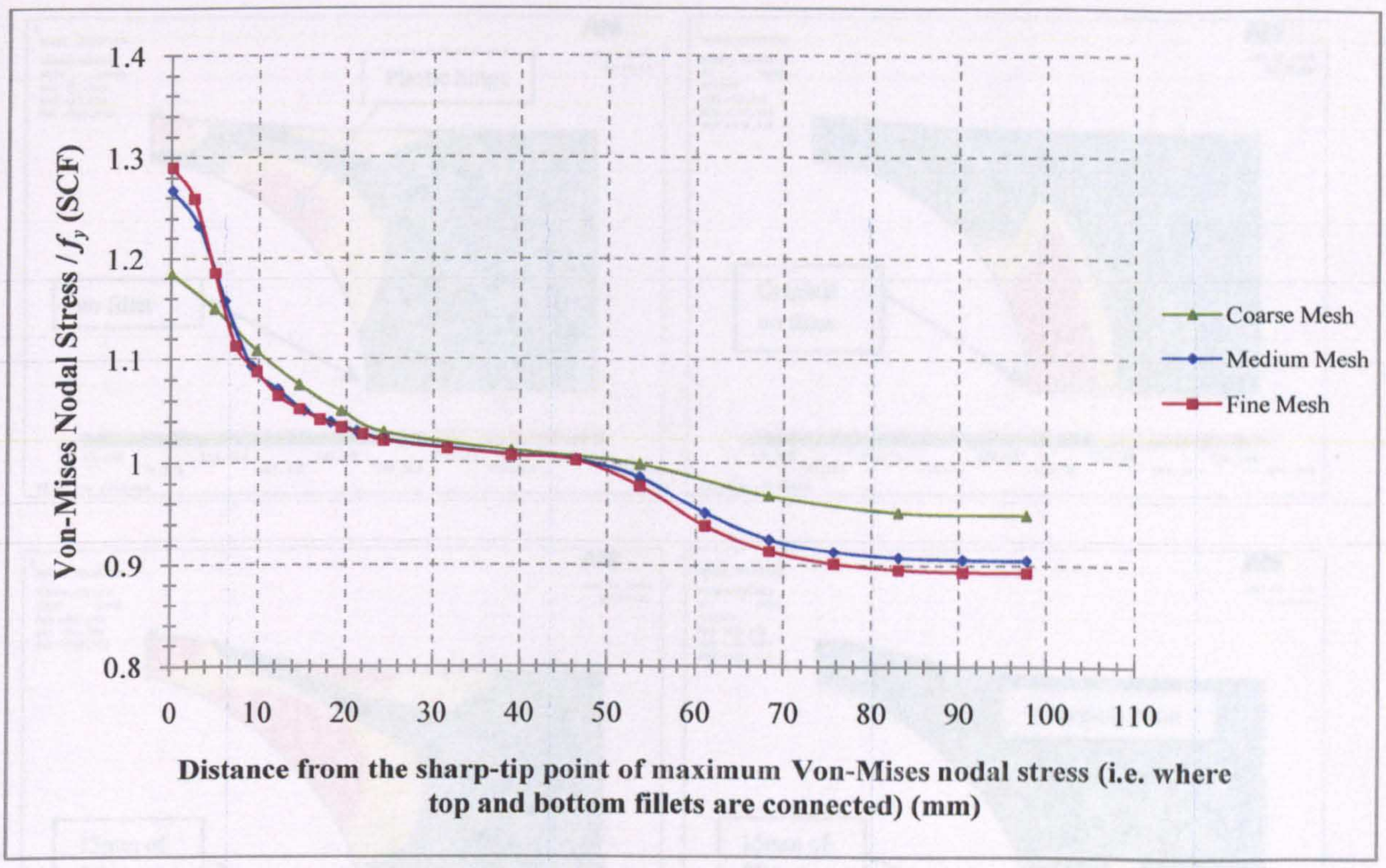

Figure 4.36: Mesh refinement for plate with 35mm of fillet

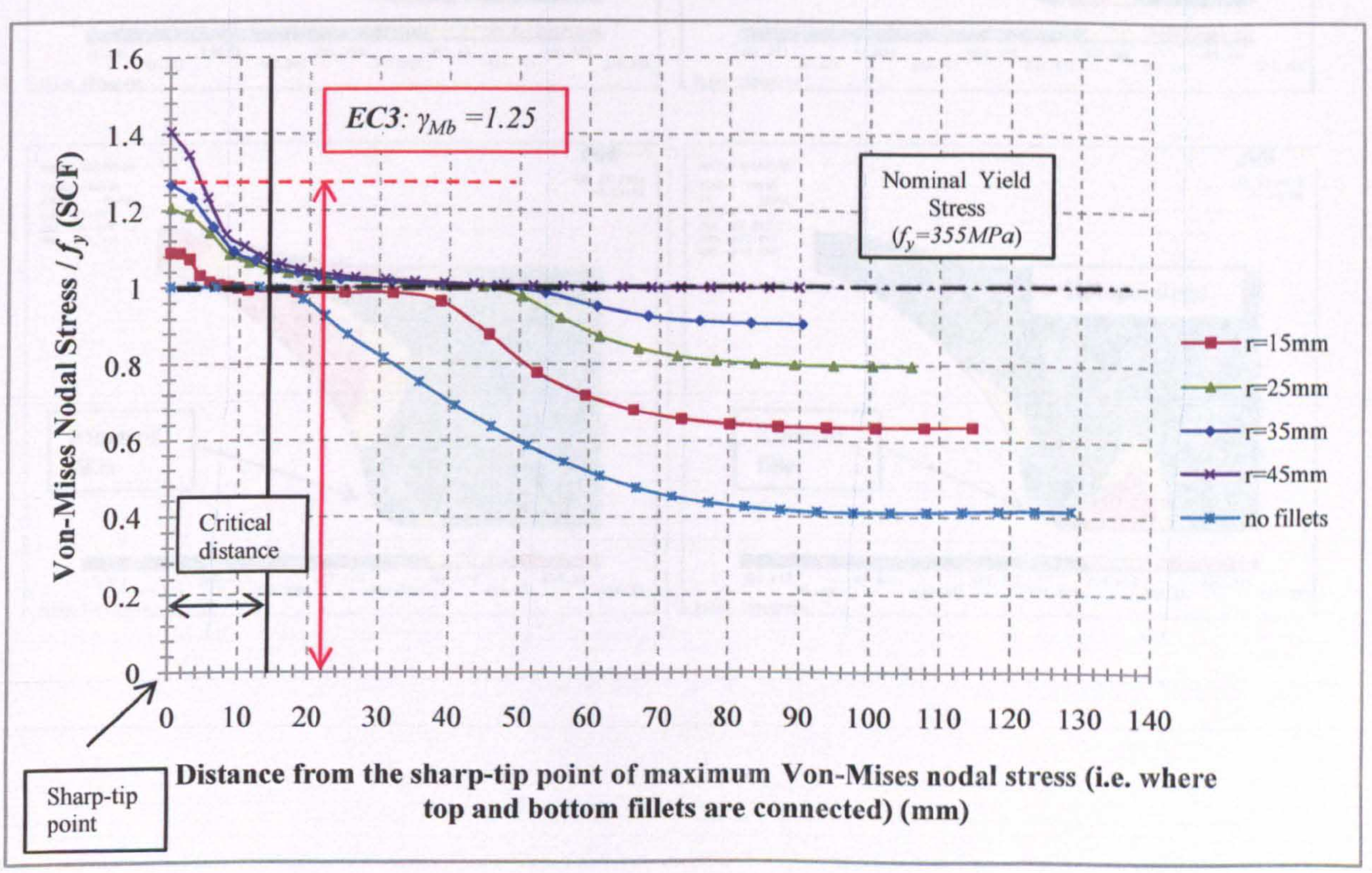

Figure 4.37: The variation of the maximum Von-Mises nodal stresses against the distance from the point of maximum stress

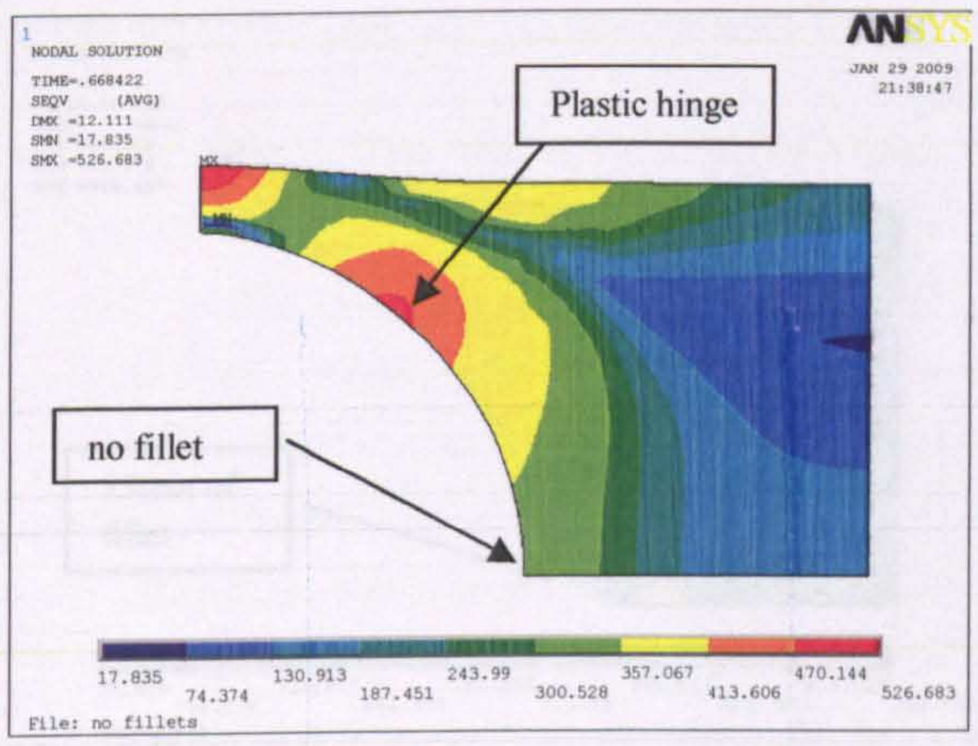
NODAL SOLUTION
TIME=.668422
SEQV (AVG)
DMX =12.111
SMN =17.835
SMX =526.683
JAN 29 2009
21:38:47
Plastic hinge
no fillet
17.835
74.374
130.913
187.451
243.99
300.528
357.067
413.606
470.144
526.683
File: no fillets

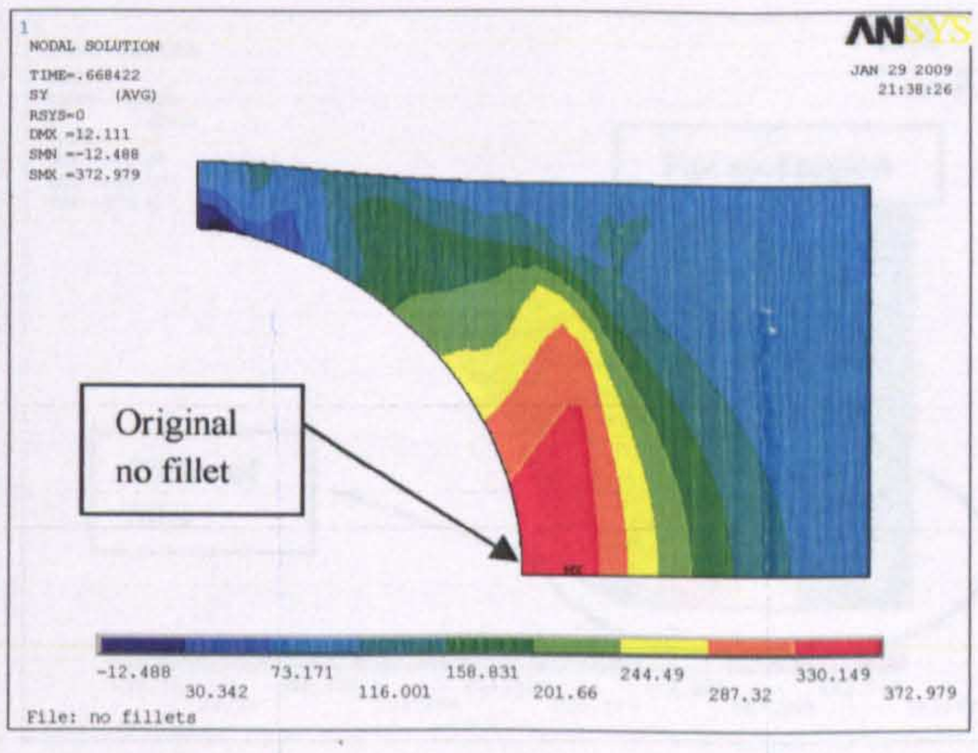
NODAL SOLUTION
TIME=.668422
SY (AVG)
RSYS=0
DMX =12.111
SMN =-12.488
SMX =372.979
JAN 29 2009
21:38:26
Original
no fillet
-12.488
30.342
73.171
116.001
158.831
201.66
244.49
287.32
330.149
372.979
File: no fillets

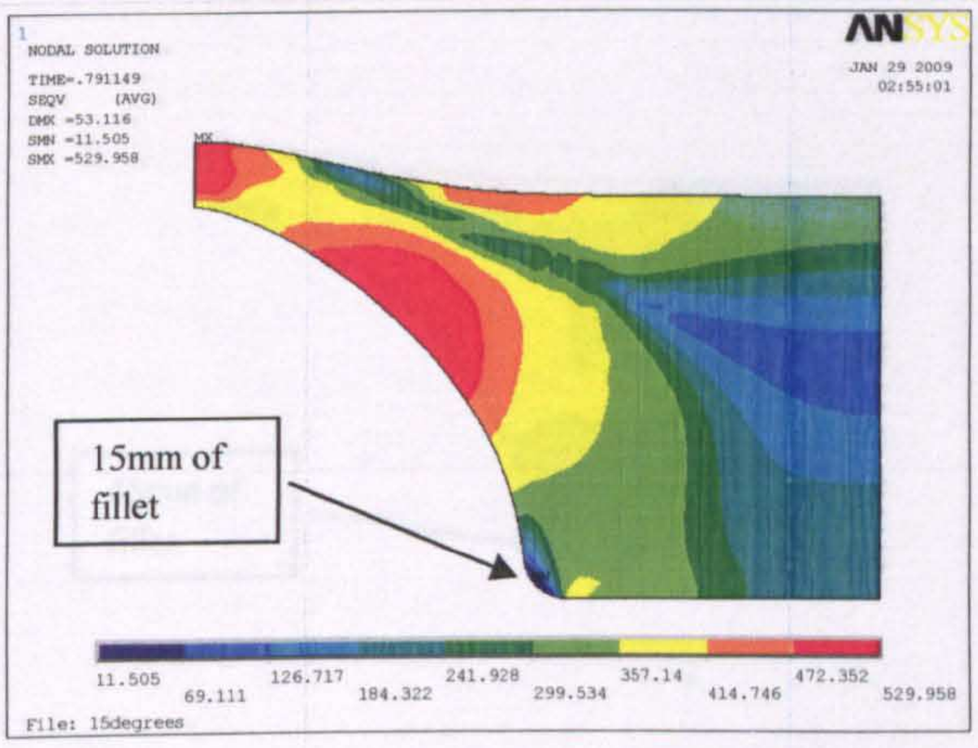
NODAL SOLUTION
TIME=.791149
SEQV (AVG)
DMX =53.116
SMN =11.505
SMX =529.958
JAN 29 2009
02:55:01
15mm of
fillet
11.505
69.111
126.717
184.322
241.928
299.534
357.14
414.746
472.352
529.958
File: 15degrees

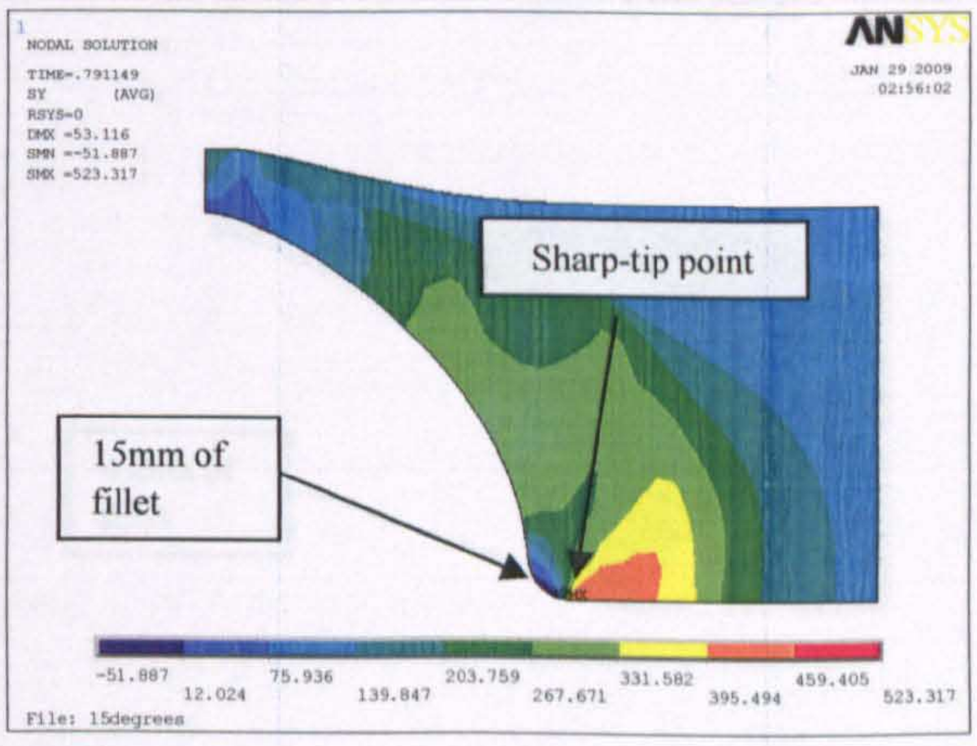
NODAL SOLUTION
TIME=.791149
SY (AVG)
RSYS=0
DMX =53.116
SMN =-51.887
SMX =523.317
JAN 29 2009
02:56:02
Sharp-tip point
15mm of
fillet
-51.887
12.024
75.936
139.847
203.759
267.671
331.582
395.494
459.405
523.317
File: 15degrees

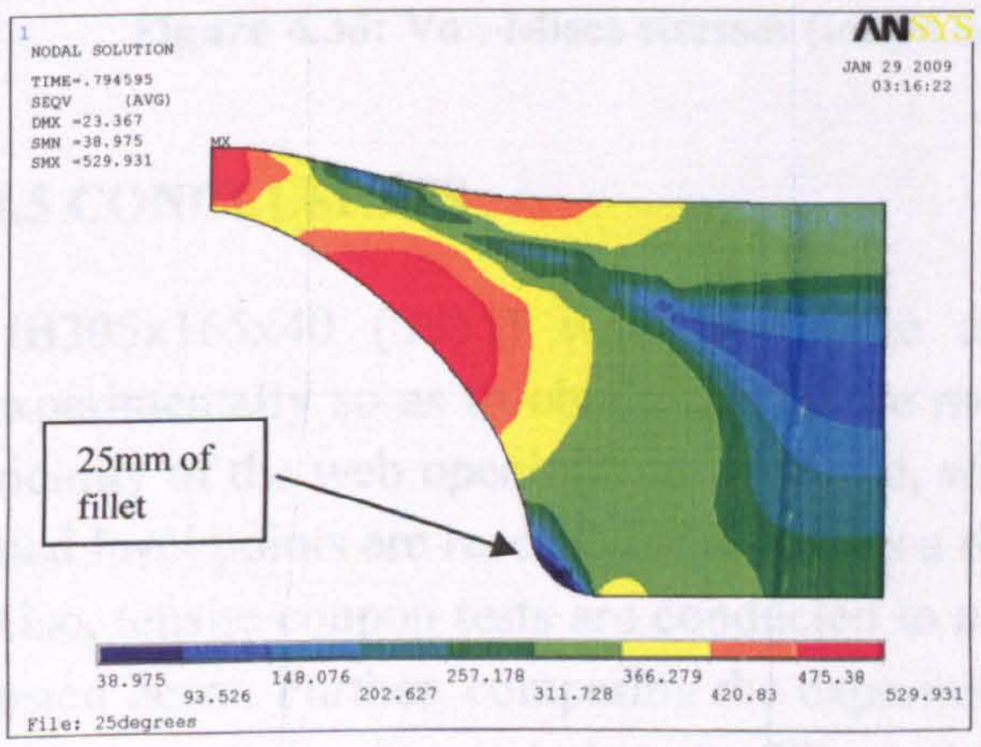
NODAL SOLUTION
TIME=.794595
SEQV (AVG)
DMX =23.367
SMN =38.975
SMX =529.931
JAN 29 2009
03:16:22
25mm of
fillet
38.975
93.526
148.076
202.627
257.178
311.728
366.279
420.83
475.38
529.931
File: 25degrees

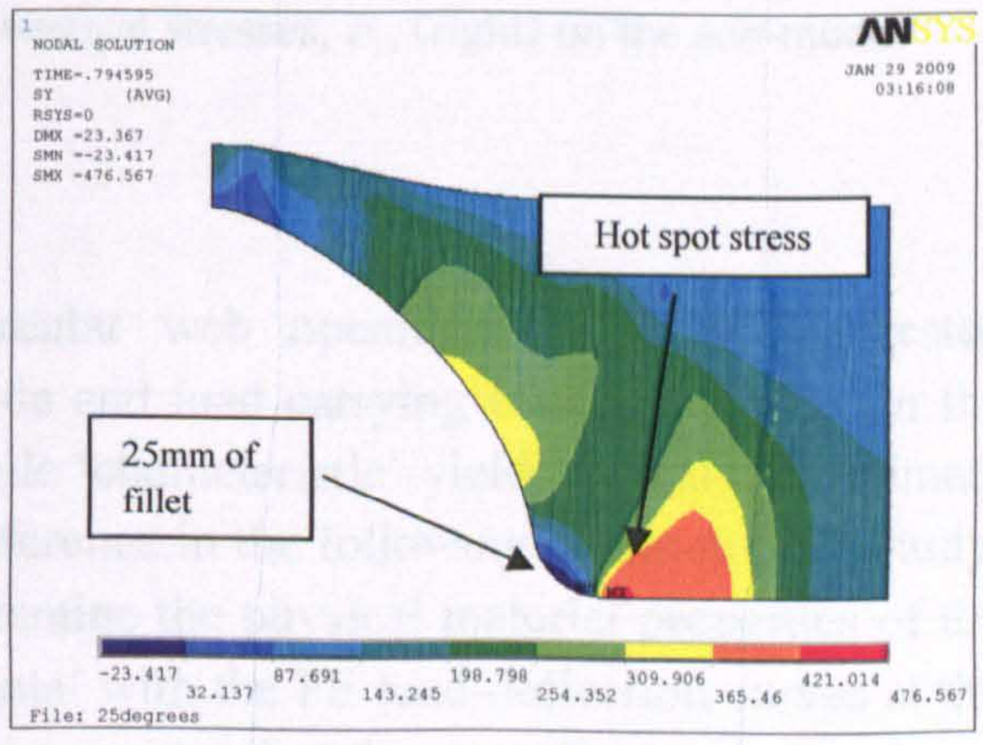
NODAL SOLUTION
TIME=.794595
SY (AVG)
RSYS=0
DMX =23.367
SMN =-23.417
SMX =476.567
JAN 29 2009
03:16:08
Hot spot stress
25mm of
fillet
-23.417
32.137
87.691
143.245
198.798
254.352
309.906
365.46
421.014
476.567
File: 25degrees

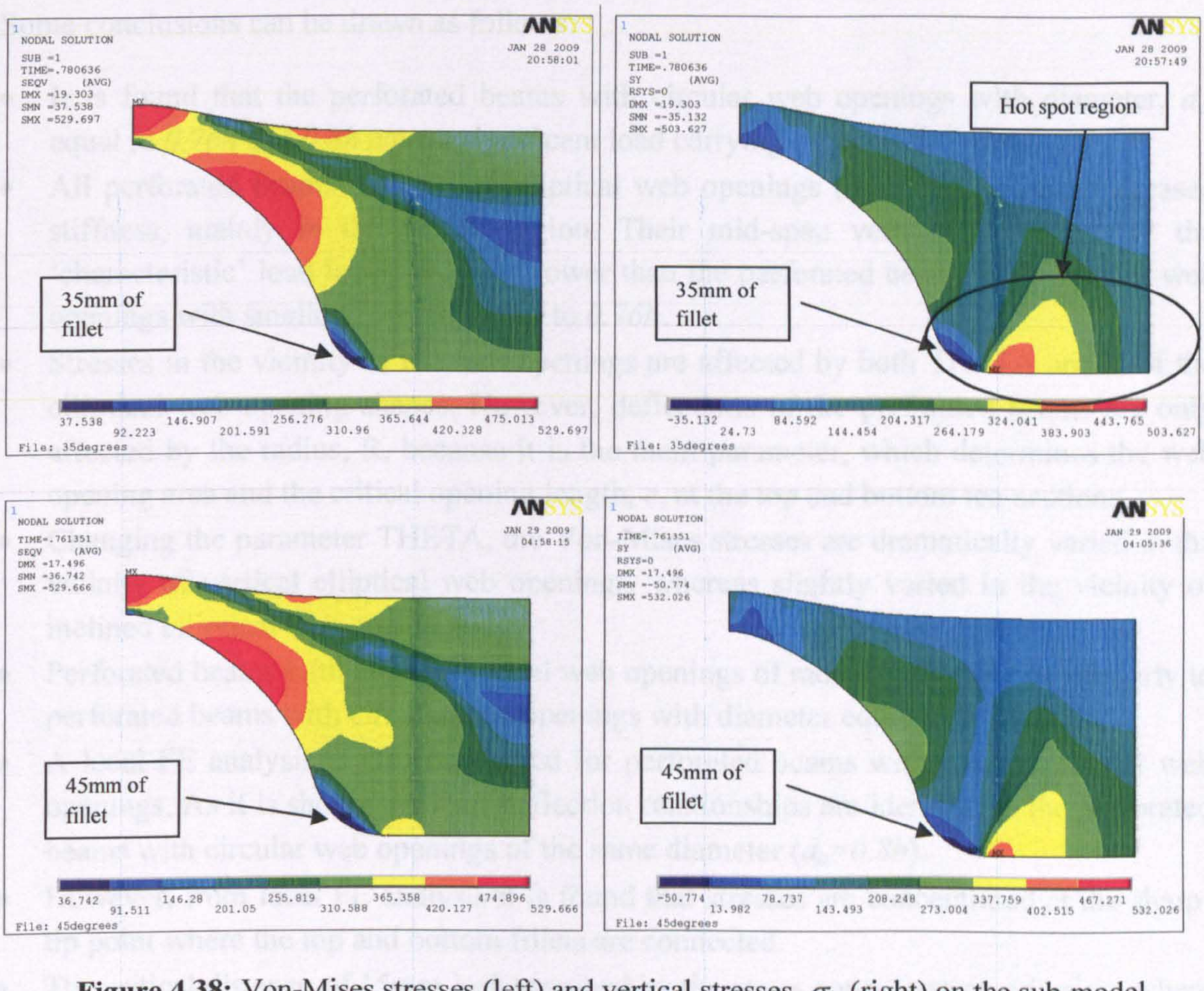

Figure 4.38: Von-Mises stresses (left) and vertical stresses, σ_y, (right) on the sub-model

4.5 CONCLUSIONS

UB305x165x40 (S355) with two large circular web openings (d_o=*0.76h*) is tested experimentally so as to obtain the failure mode and load carrying capacity. Strains in the vicinity of the web openings are acquired, while 'characteristic' yield, critical and ultimate load level points are recorded and used as a reference in the following parametric FE study. Also, tensile coupon tests are conducted to examine the physical material properties of the tested beam. Further, comparing the experimental with the FE load-deflection curves at the mid-span, it is observed that the FE models provide significant stiffness in the elastic region. However, the yielding and plasticity of the FE model with the nominal strength material properties adequately compare with the experimental test.

Comprehensive FE investigation on perforated beams with circular and novel web opening shapes is carried out, while the typical FE model is validated against the experimental results presented in this chapter as well. The beam model examined in this optimization study is a mid-range thin and deep web steel beam with isolated large web openings, subjected under high shear forces and moments.

Some conclusions can be drawn as follows:

- It is found that the perforated beams with circular web openings with diameter, d_o, equal to *0.76h* and *0.8h* have a significant load carrying capacity difference.
- All perforated beams with novel elliptical web openings (d_o=*0.8h*), present increased stiffness, mainly in the plastic region. Their mid-span vertical deflections at the 'characteristic' load levels are even lower than the perforated beams with circular web openings with smaller diameter equal to *0.76h*.
- Stresses in the vicinity of the web openings are affected by both THETA and R of the elliptical web opening shapes. However, deflections of the perforated beams are only affected by the radius, R, because it is the main parameter, which determines the web opening area and the critical opening length, *c*, at the top and bottom tee-sections.
- Changing the parameter THETA, the Von-Mises stresses are dramatically varied in the vicinity of vertical elliptical web openings, whereas slightly varied in the vicinity of inclined elliptical web openings.
- Perforated beams with novel elliptical web openings of radius R0.3, behave similarly to perforated beams with circular web openings with diameter equal to *0.76h*.
- A local FE analysis is also conducted for perforated beams with filleted circular web openings. As it is shown the load-deflection relationships are identical to the perforated beams with circular web openings of the same diameter (d_o=*0.8h*).
- However, from local FE analysis it is found that stresses are concentrated at the sharp-tip point where the top and bottom fillets are connected.
- The critical distance of 15mm is determined by the stress concentration criterion, where the stresses at the sharp-tip points are dramatically decreased.
- Among perforated beams with filleted circular web openings, the ones with radius of fillet, *r*, 15 to 35mm should only be utilised in common applications as they do not provide critical stresses at the sharp-tip points and their further examination is not necessary.

4.6 RECOMMENDATIONS AND LIMITATIONS

The study of crack propagation is of particular importance for the fatigue design of perforated beams manufactured by profile cutting and then welding the top and bottom tee-sections. Large heavy structures such as highway or railway bridges and marine structures (e.g. tankers) are subjected to repeated loading conditions and the effect of fatigue on them should be seriously considered.

Further investigation is needed for larger-range of I-sections with various sizes of web openings subjected to different loading cases. In **Chapter 5**, the experimental and FE web-post buckling study of perforated beams with selected novel web openings is established.

CHAPTER 5

WEB-POST STUDY OF NON-COMPOSITE PERFORATED BEAMS

5.1 INTRODUCTION

Perforated beams are widely used and with the popularity of architectural emphasis on exposed structures, typical circular, hexagonal and elongated web openings are common practice. Often, perforated beams have webs penetrated by large closely spaced web openings over almost the full span. Although such beams are usually utilised for long spans that have to carry a light uniform load, some heavy-mass structures such as bridges are constructed using perforated beams at full span.

The standard European sections of the 1960s and 1970s had web slenderness of lesser magnitudes. For this reason, it was common practice to fill in the panels in high shear regions in order to avoid the principal concern with web-post buckling between web openings. Generally web-post buckling results from the horizontal shear generated in the web-post, under global bending action. In the case where the advantage of automation is to be fully exploited, such special details (i.e. fill) must be minimized. It is therefore considered necessary to review existing information on web-post buckling and to examine this mode of behaviour in light perforated beams, with closely spaced web openings of various novel shapes.

Based on the results of the previous parametric FE study of perforated beams with optimum novel web opening shapes (**Chapter 4**), a further programme of experimental and FE work is conducted to investigate the web-post behaviour of perforated beams with closely spaced novel web openings. The FE model used for the web-post buckling study is initially validated with experimental work conducted in this research programme. This chapter consists of the following three parts:

1. *Experimental work:*

Experimental work is conducted on seven short span deep perforated universal beams. The purpose of this test is to visualize the stresses, web-post buckling modes and vertical as well as out-of-plane deflections of perforated beams with large web openings subjected to constant shear forces and moments.

2. *Validation of the FE model with the experimental work:*

An analytical comparison between the experimental test and the new FE models is made, to validate the FE model for this complex failure mode. A further local parametric FE study of the web-post buckling model, with novel web opening shapes, is conducted. Loads, vertical and out-of-plane deflections and yield patterns are mainly compared.

3. *Parametric local FE study of sub-models with novel web opening shapes:*

A general approach of the FE model with nominal material properties is used to conduct the local parametric FE study. An extensive investigation on stresses of the sub-models with novel web opening shapes is considered. Study of the geometric parameters is conducted on five certain selected novel web opening shapes from **Chapter 4**. A proposed simple design method is then developed for practical design of steel perforated beams with the above new web opening shapes.

5.2 EXPERIMENTAL WORK ON WEB-POST BUCKLING

5.2.1 Test specimens

For simplicity, it is decided to examine only one web-post (i.e. two adjacent web openings) symmetrically located to the mid-span. Web post-buckling is usually taking place at deep perforated beams with large web openings located adjacent to each other. Preliminary FE study was taking place in order to avoid failure of the perforated section due to Vierendeel mechanism (shear mechanism), but to be able to record the web-post buckling effects and the double web curvature and out-of-plane displacements follow the plastic hinges formation. Therefore, a preferably large web opening depth is adopted (d_o=*0.7h*) with the web openings located relatively close (*S*, equal to $1.2d_o$ and $1.3d_o$). The above beam configurations are considered designing the experimental test specimens. However, in the FE study the spacing of the web openings is varying and it is under investigation, as the structural performance of the web-posts when various web openings shapes are utilised, is thoroughly examined.

UB457x152x52 (S355) is chosen for the ease of comparison to the other chapters of this research thesis. Seven beams with spans of 1.7m have been experimentally tested. Two different sets of tests have been investigated and categorized as follows:

- The first category consists of three specimens. One perforated beam with circular web openings and two beams with filleted circular web openings of 25mm and 45mm of fillet radius (**Figure 5.1**). The web opening spacing is kept constant ($S=1.3d_o$). Hence the critical web-post width is decreased as the fillet radius, r, is increased. It is aforementioned that, in case the advantage of profile cutting is used, the bigger the fillet radius, the greater the depth of the final section and consequently the moment of inertia.
- In the second category four specimens with different web opening shapes are examined. One perforated beam with circular web openings, two beams with novel vertical elliptical web openings and one beam with novel inclined elliptical web openings (**Figure 5.2**). The critical web-post width is kept constant ($S=1.2d_o$), while the comparison of the horizontal shear capacity at the web-posts is made possible.

For all seven beams the position of the web-post is constant in relation to the load application point and the supports. The beams are symmetrical to the mid-span. Hence, constant vertical shear forces are generated at the web-posts. **Appendix 10** provides the technical engineering drawings for all seven specimens, including dimensioning details.

FIRST CATEGORY

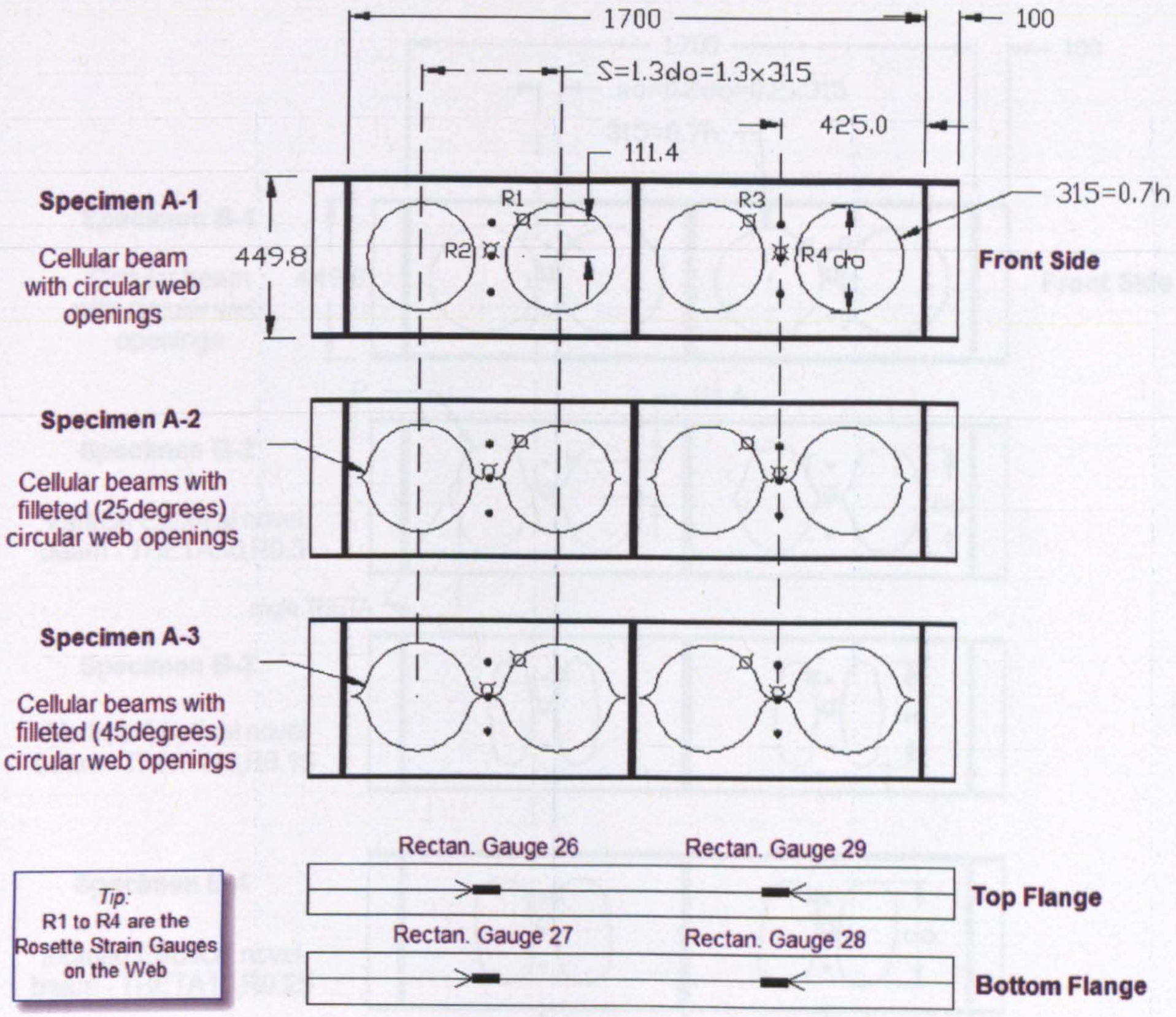

Figure 5.1: Experimental test beams in the first category

SECOND CATEGORY

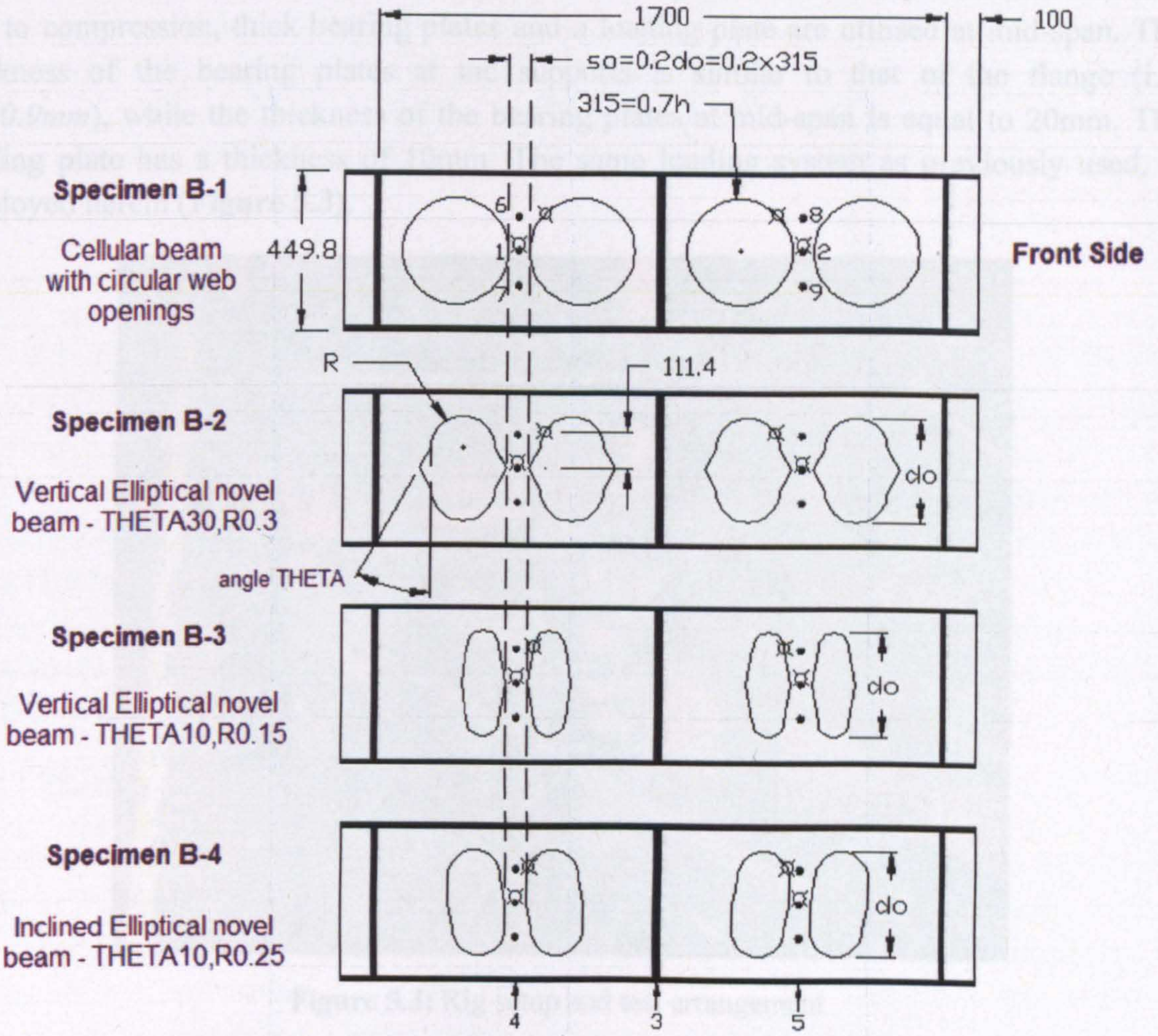

Tip:
Bullet points re-presenting the Dial Gauges transverse to the Web
and
Arrows re-presenting the Dial Gauges transverse to the Flanges
(look from front side of the beam)

Rosette Strain Gauges on the Web (0-45-90)

Rectangular Strain Gauges on the Flanges

Dial Gauges Transverse to the Web

Dial Gauges Transverse to the Flanges

Figure 5.2: Experimental test beams in the second category

5.2.2 Test setup

To ensure load distribution across the beams and to prevent failure by LTB and buckling due to compression, thick bearing plates and a loading plate are utilised at mid-span. The thickness of the bearing plates at the supports is similar to that of the flange (i.e. t_f=*10.9mm*), while the thickness of the bearing plates at mid-span is equal to 20mm. The loading plate has a thickness of 10mm. The same loading system as previously used, is employed herein (**Figure 5.3**).

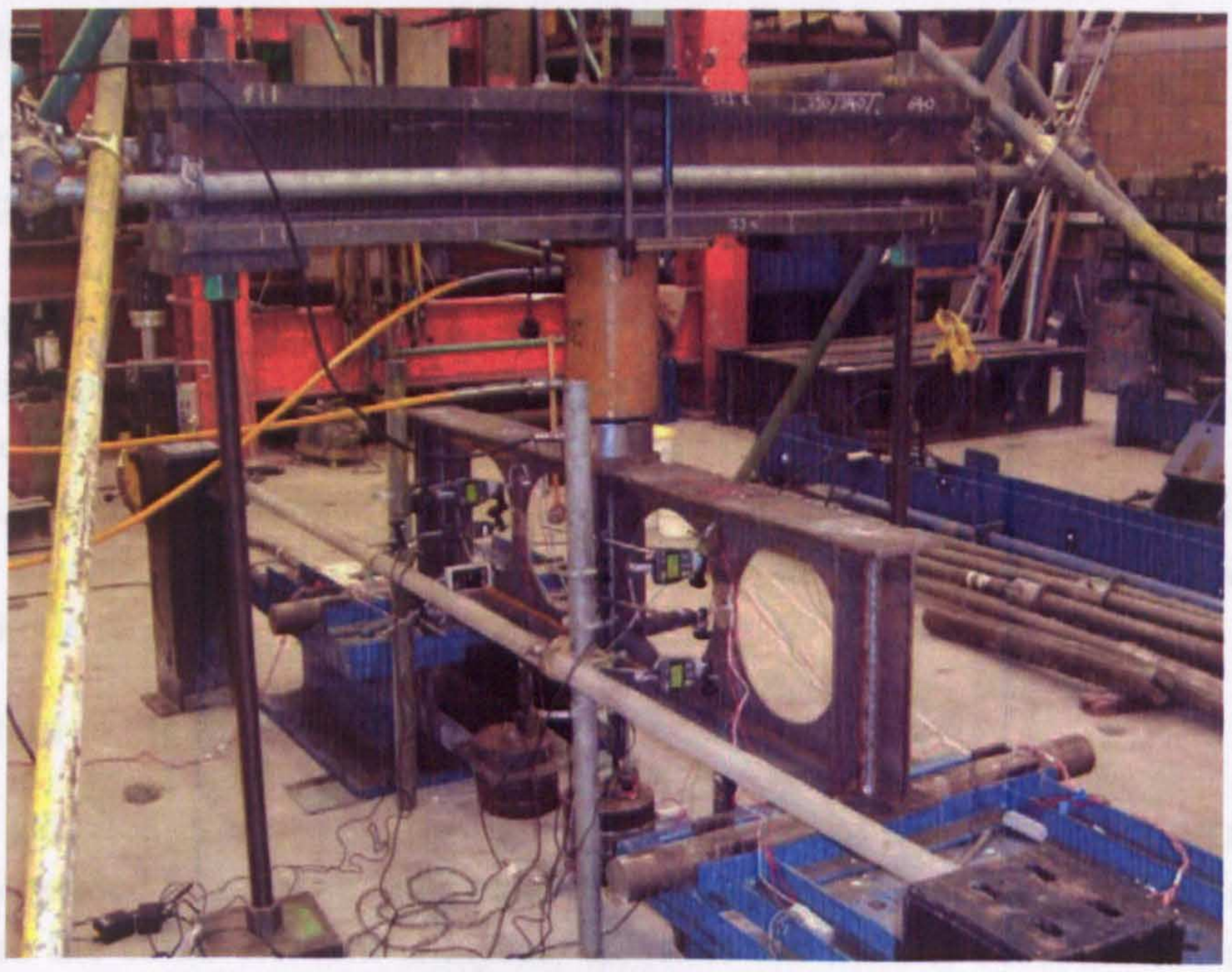

Figure 5.3: Rig setup and test arrangement

5.2.3 Test procedure

The beam is designed as simply supported and the load is applied at mid-span through a hydraulic jack. The load application is applied using a low displacement rate and the load is applied stepwise. By holding the displacements at every step, it is possible to record the load relaxation and buckling (i.e. deformation) effects. The tests are performed until a sufficient branch of the descending load deformation (i.e. post-elastic) curve is recorded, following the maximum load carrying capacity. At the end of the tests, full unloading is performed to obtain the plastic effect and permanent deformation of the beams. The extensive description of each test is separately presented in **sub-chapter 5.2.5**.

5.2.4 Measurement devices

In an attempt to identify a primary mode of failure that is either a web-post buckling; formation of a yield mechanism with plastic hinges, or a flange local buckling, heavily instrumentation is used. These measures included the asymptotes of maximum web strains, web strain differences, flange strains, vertical beam deflections and out-of-plane web displacements. It should be noted that all data are acquired simultaneously at every load step.

Instrumentation shown in **Figure 5.1** and **5.2** consists of:

- Strain measurements (Rosettes) placed on the compressed inclined edge of the web openings adjacent to the load point and on the mid-distance of the critical web-post width.
- Strain measurements (Rectangular gauges) placed on the top of the compression steel flange and the bottom of the tension steel flange are also used. These are also aligned on the centre-line of the web-posts similarly to the dial gauges.
- Vertical beam deflections (Dial gauges) and out-of-plane web displacements (Dial gauges) placed on the centre-line of the web posts are also applied to visualise the failure mode shape.

5.2.4.1 Position of strain gauges

Rosettes are attached in the same position on both sides of the web to evaluate membrane strains. It is intended to gain the most exact overview of the strain distribution in the web as verification to the finite element analyses. Rosettes are used to measure the compressive and tensile surface strains of the beams in the vicinity of the web openings, which is necessary to determine the yielding, web buckling and highly stressed positions of the steel beams. Rectangular strain gauges are applied along the length of the compression and tension flanges, so as to obtain primarily bending stresses.

The rosettes are placed in the same position on all specimens in both categories. For the first category which consists of three perforated beams with circular web openings, the rosettes are positioned on the compressed inclined edge of the web opening adjacent to the point load at an angle of 45° to the centre-line of the web opening. Hence, they are located at a distance of 111.4mm from the mid-depth of the beam. The rosettes are not rotated around the gauge axis and positioned as close as possible to the edge of the web openings. In the second category which consists of four perforated beams with novel elliptical web openings the rosettes are located at a standard distance of 111.4mm from the mid-depth of the beam. Since, the web opening shapes are different; the rosettes are not neccssarily at an angle of 45°. Finally, the rectangular strain gauges placed at the compression and tension steel flanges, as well as rosettes placed at the mid-distance of the critical web-post at the

mid-depth of the beams and they are adjacent to the centre-line of each web-post. In **Figure 5.1** and **5.2,** the rosettes are indicated as circles with three lines (0°-45°-90°) and the rectangular strain gauges as solid rectangles. The numbering of the strain gauges at the front side is provided for identification in the following graphs. Strains found at the back side (**Figure 5.1**) compared well with the ones found at the front side and it is considered unnecessary to present them in the thesis (**Appendix 11**).

5.2.4.2 Position of dial gauges

To measure the vertical deflection of the beams, three dial gauges are placed under the tension steel flange. One is placed at mid-span, while the other two are placed adjacent to the centre-line of the web-posts. A further six dial gauges are positioned transverse to the web at the front side only, to record the out-of-plane displacements. The gauges placed at the top and bottom tee-sections are located at a distance of 111.4mm from the mid-depth of the beam, similar to the rosettes (**Figure 5.1** and **5.2**). The dial gauges are indicated as vertical arrows (vertical dial gauges) and black solid dots (transverse to the web dial gauges). The numbering of all dial gauges is provided (**Figure 5.2**) for identification in the following graphs.

5.2.5 Experimental results

The key features of each specimen are discussed separately. The results from vertical deflections (dial gauge 3, 4 and 5) and transverse to the web displacements (dial gauges 1, 2, 6, 7, 8 and 9) are presented. Web strains only from rosettes positioned at the front side of the beams are presented as the results from the back side are similar. Results from both sides could be used in order to investigate the drift at each position and the local buckling of the web due to membrane strains. The latter test data is tabulated and provided in **Appendix 11**. Similarly to **Chapter 4 (Figure 4.9** to **4.13)**, the effects of local flexural stresses resulting from buckling show, in some cases, considerable lack of symmetry (e.g. **Table 5.1** and **5.2**). In addition to this, in some specimens it is observed that the left and right web-posts are buckled differently and especially at different load levels. This is mainly a result of either the test setup, imperfections of the specimens or due to the resultant force applied on the rotated compression flange while the applied load is always vertical. However, the general buckling form is the same and as it is seen later on in this thesis, it is well compared to the FE analyses. Flange strains are also presented, to demonstrate the steel yielding point and the load at which high deflections are induced. In the analysis of the test results critical load, $P_{cr.}$, defined as the load point at which the first visible web-post buckling or rupture is occurred, and it should be higher than yield load, P_y. Ultimate load carrying capacity, $P_{ult.}$, is the ultimate load point recorded in the test; usually a sudden drop of load is following. At the end of this sub-chapter, a summary of the results shows these overall comparisons.

Specimen A-1

Specimen A-1 is similar to Specimen B-1, where the only difference is their web opening spacing. In Specimen A-1, very small out-of-plane web movement is observed up to the yield load, as the tee-sections are symmetrically moved to opposite sides (i.e. double curvature). The first visible web movement is located at the left half span of the beam, at a load of approximately 257kN (i.e. $P_{cr.}$). At the left half span side, as the web-post is buckled and the specimen is loaded the steel begins to distort greatly while at the right half span, no web-post buckling is observed at this point. Dial gauges show that both sides experience high yielding and web-post buckling at the end of the experiment (**Figure 5.4**). By observing the load-deflection curves and the flange strains, they confirm that both sides have similar stiffness. The ultimate load carrying capacity, $P_{ult.}$, is around 289kN, where the beam starts to behave plastically with strain hardening up to a deflection at almost of 65mm. **Figure 5.5** shows the yielding of the compression area; the yielding of top portion of the flange and the yielding of the web extending into the flange. This represents the secondary effects of shear.

Vertical deflections recorded from dial gauges, flange strains obtained from the rectangular strain gauges and transverse displacements of out-of-plane movement are presented in **Figure 5.6** and **5.7**. Also, horizontal, diagonal and vertical strains obtained from the rosettes are presented in **Figure 5.8** and **5.9**. Indicated maximum strains observed at the critical load, $P_{cr.}$, and ultimate load, $P_{ult.}$, at the flanges and the front side of the beam are presented in **Table 5.1**.

	Characteristic Loading Level Points							
	@ $P_{cr.}$	**@ $P_{ult.}$**	**@ $P_{cr.}$**	**@ $P_{ult.}$**	**@ $P_{cr.}$**	**@ $P_{ult.}$**	**@ $P_{cr.}$**	**@ $P_{ult.}$**
Rectangular	**26 (με)**		**27 (με)**		**28 (με)**		**29 (με)**	
Stain Gauges	-355	-665	256	155	225	221	-329	-434
2D Strain	**R1 (με)**		**R2 (με)**		**R3 (με)**		**R4 (με)**	
ε_x	-1122	-6364	1825	3288	-1002	-1135	1758	4080
ε_y	-769	11010	-1287	-2627	-364	-109	-1065	-1950
Shear, ε_{xy}	1866	-5156	7716	13851	1289	1183	3813	15169

Table 5.1: Indicated strains at $P_{cr.}$ and $P_{ult.}$

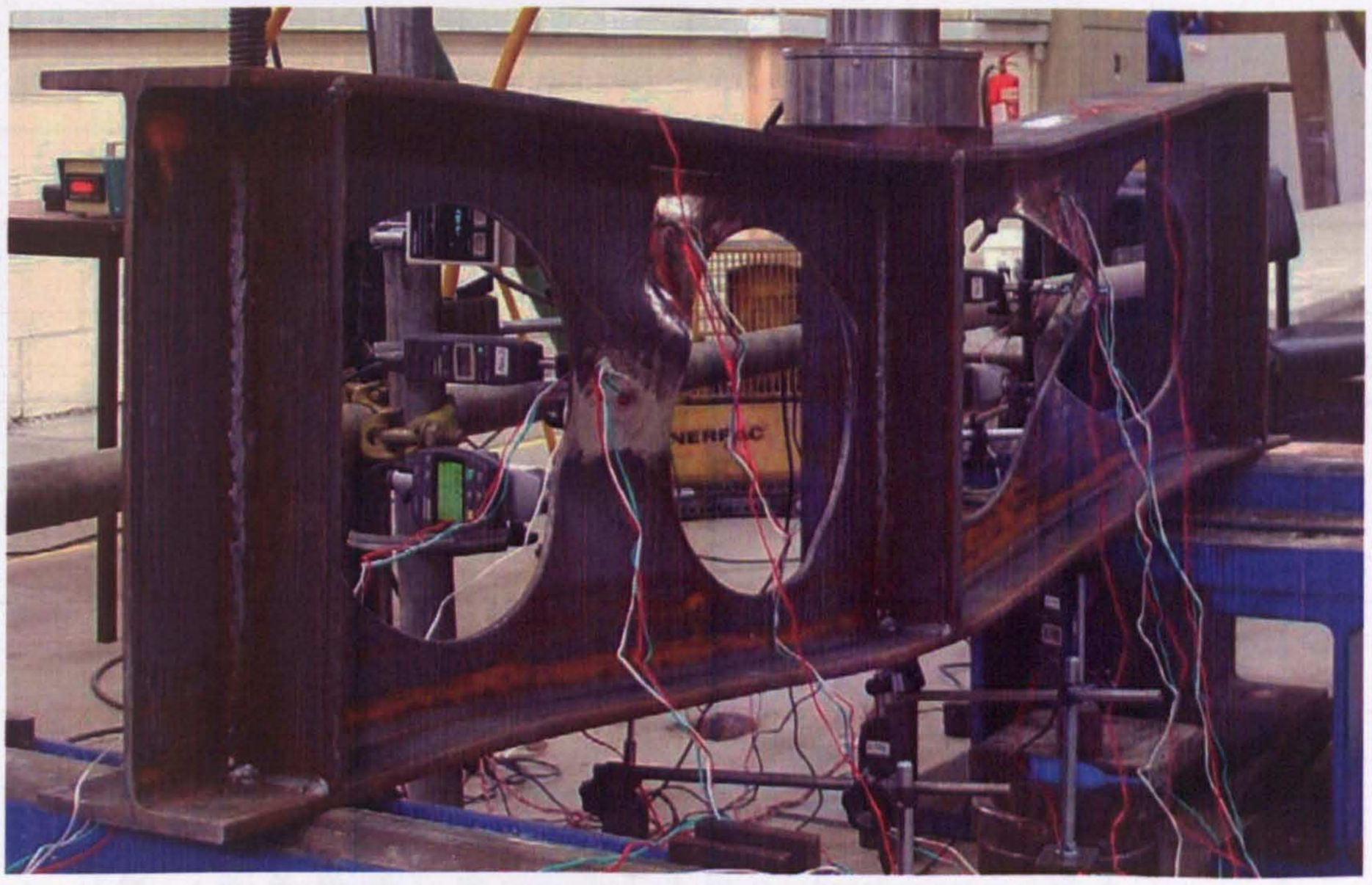

Figure 5.4: High yielding and web-post buckling at both sides (Specimen A-1)

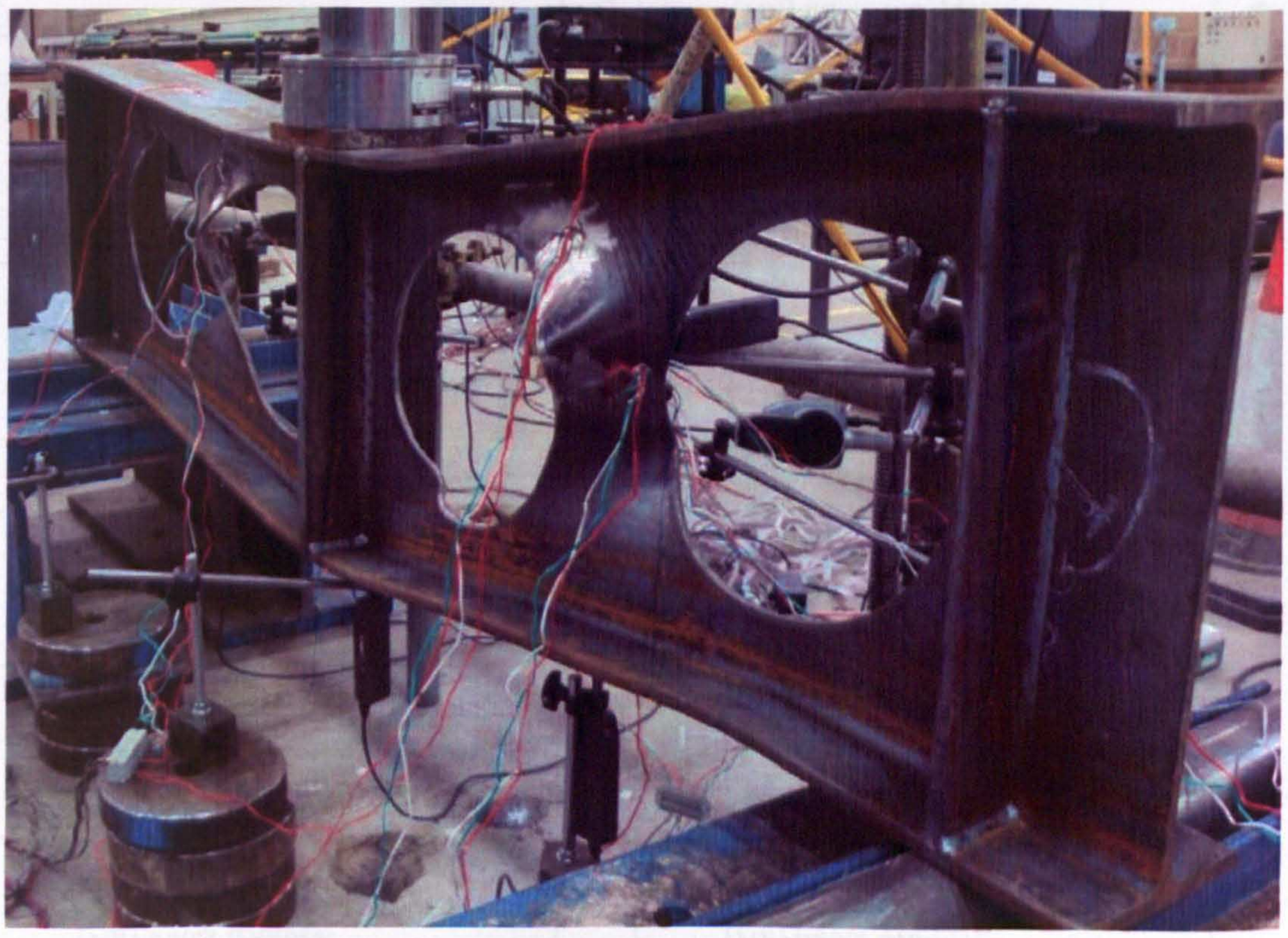

Figure 5.5: Yielding of compression area (Specimen A-1)

Specimen A-1

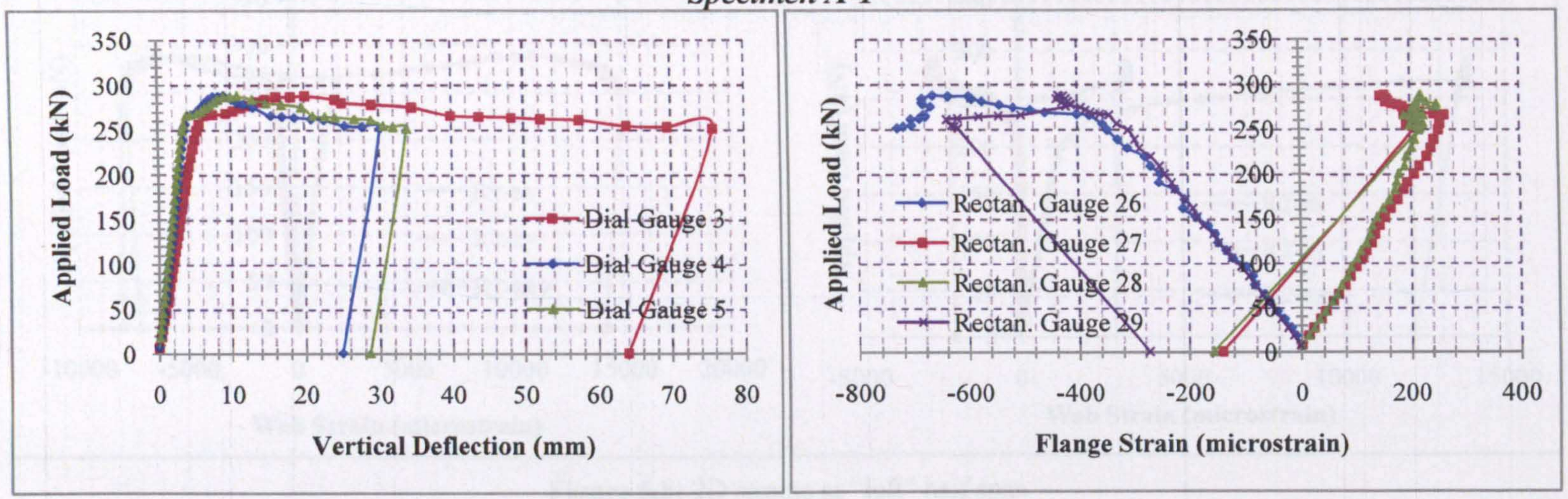

Figure 5.6: Vertical deflections along the bottom flange and flange strains at both half spans

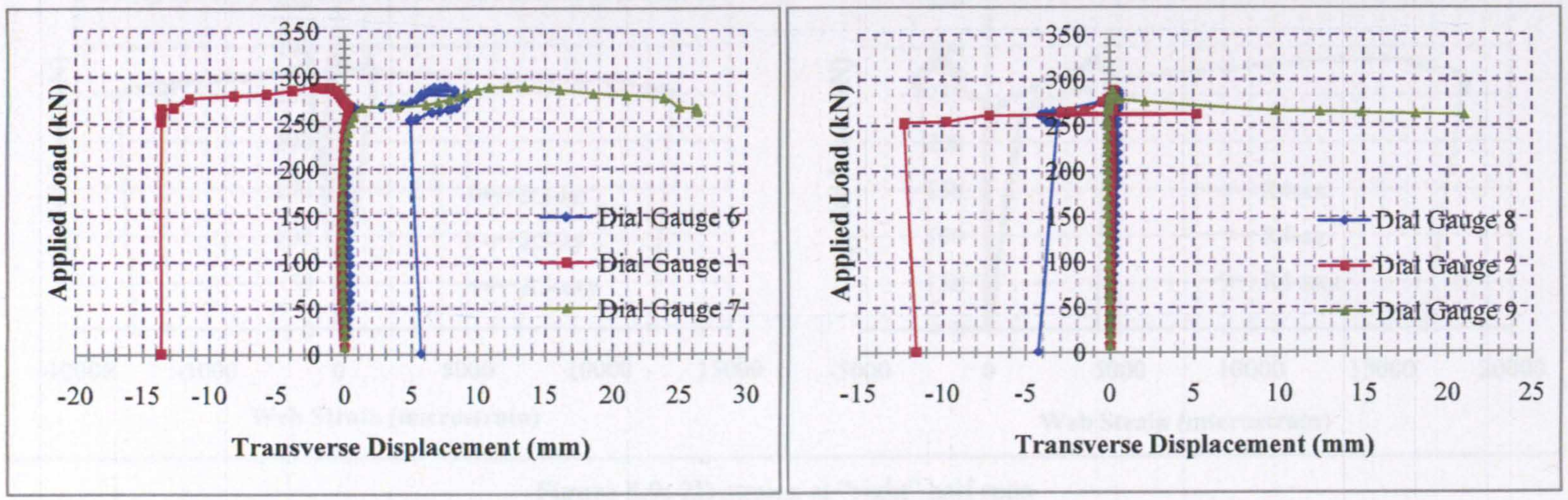

Figure 5.7: Web transverse displacements at "left" and "right" half spans

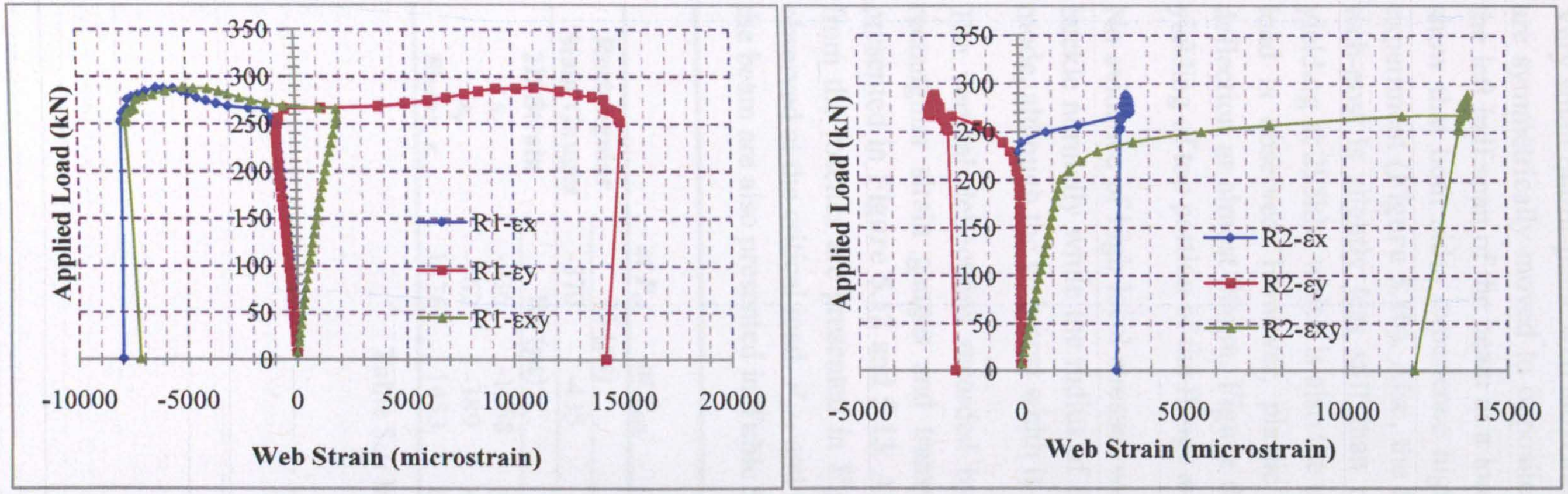

Figure 5.8: 2D strains at "left" half span

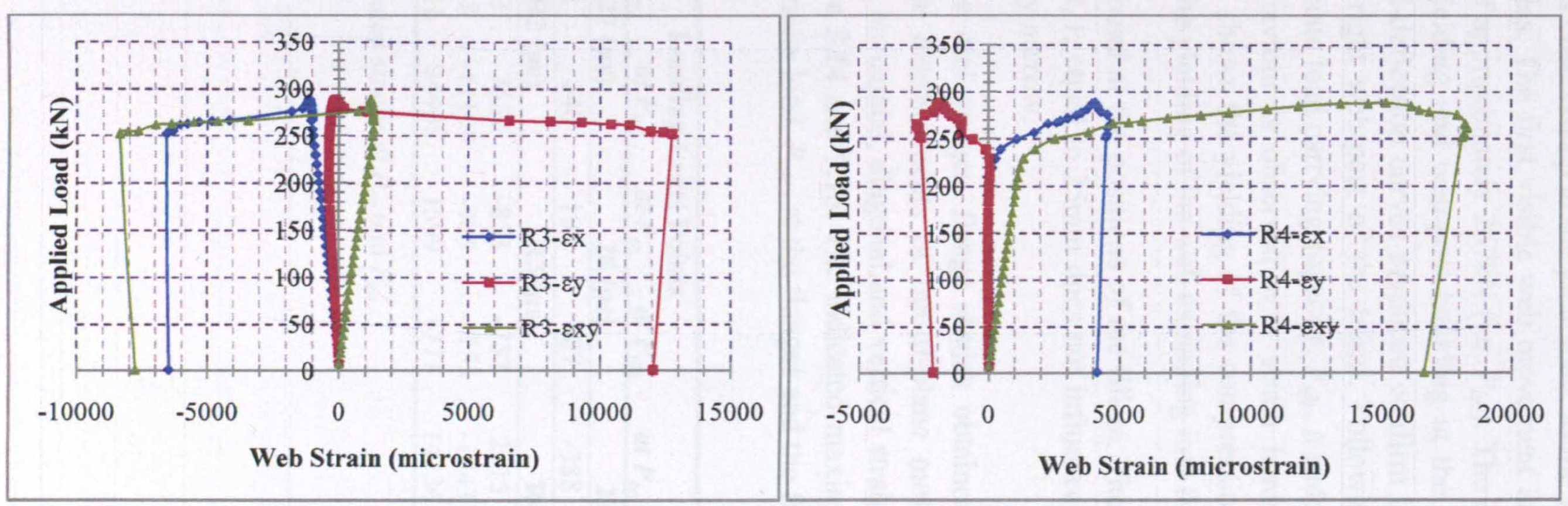

Figure 5.9: 2D strains at "right" half span

Specimen A-2

Very small out-of-plane web movement is observed up to the yield load, as the tee-sections are symmetrically moved to opposite sides. The first visible web movement is located at the left half span of the beam at a load of approximately 267kN (i.e. $P_{cr.}$). The dial gauges show that both sides experience high yielding and web-post buckling at the end of the experiment (**Figure 5.10**). Also, the load-deflection curves produced confirm that the left web-post is slightly less stiff than the right web-post of the beam. Following the full yielding at 295kN, which is also the ultimate load carrying capacity, $P_{ult.}$, a sudden drop of load is observed. However, plastic behaviour is observed with strain hardening to a deflection at almost 50mm. **Figure 5.11** shows the yielding of the compression area; the yielding of top portion of the flange and the yielding of the web extending into the flange.

No evidence of high local stresses was found at the positions of the fillets. The web-posts buckle normally while the radius of fillet, *r*, equal to 25mm does not influence the failure mode, although the web-post width is very narrow.

The vertical deflections recorded by the dial gauges, flange strains obtained from the rectangular strain gauges and transverse displacements of out-of-plane movement are presented in **Figure 5.12** and **5.13**. Also, horizontal, diagonal and vertical strains obtained from the rosettes are presented in **Figure 5.14** and **5.15**. The indicated maximum strains observed at the critical load, $P_{cr.}$, and ultimate load, $P_{ult.}$, at the flanges and the front side of the beam are also presented in **Table 5.2**.

	Loading Level Points							
	at $P_{cr.}$	***at $P_{ult.}$***	***at $P_{cr.}$***	***at $P_{ult.}$***	***at $P_{cr.}$***	***at $P_{ult.}$***	***at $P_{cr.}$***	***at $P_{ult.}$***
Rectangular	**26 (με)**		**27 (με)**		**28 (με)**		**29 (με)**	
Stain Gauges	-370	-435	218	240	198	207	-388	-443
2D Strain	**R1 (με)**		**R2 (με)**		**R3 (με)**		**R4 (με)**	
ε_x	-936	-1068	4853	7652	-853	-757	2515	2719
ε_y	-562	-389	-7518	-11109	-905	-1153	-1543	-533
Shear, ε_{xy}	1476	1453	15881	24468	1599	1777	14136	20906

Table 5.2: Indicated strains at $P_{cr.}$ and $P_{ult.}$

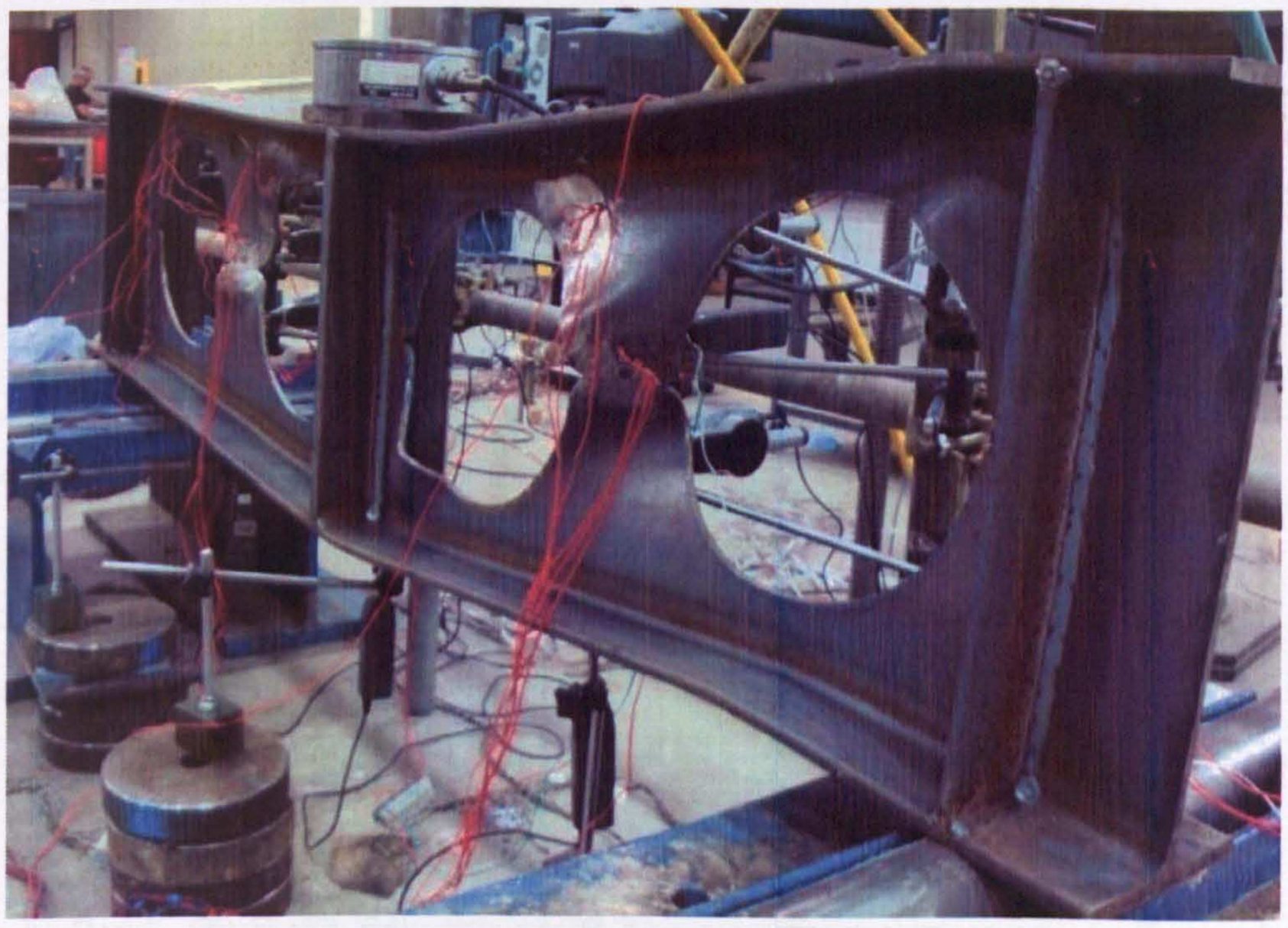

Figure 5.10: High yielding and web-post buckling at both sides (Specimen A-2)

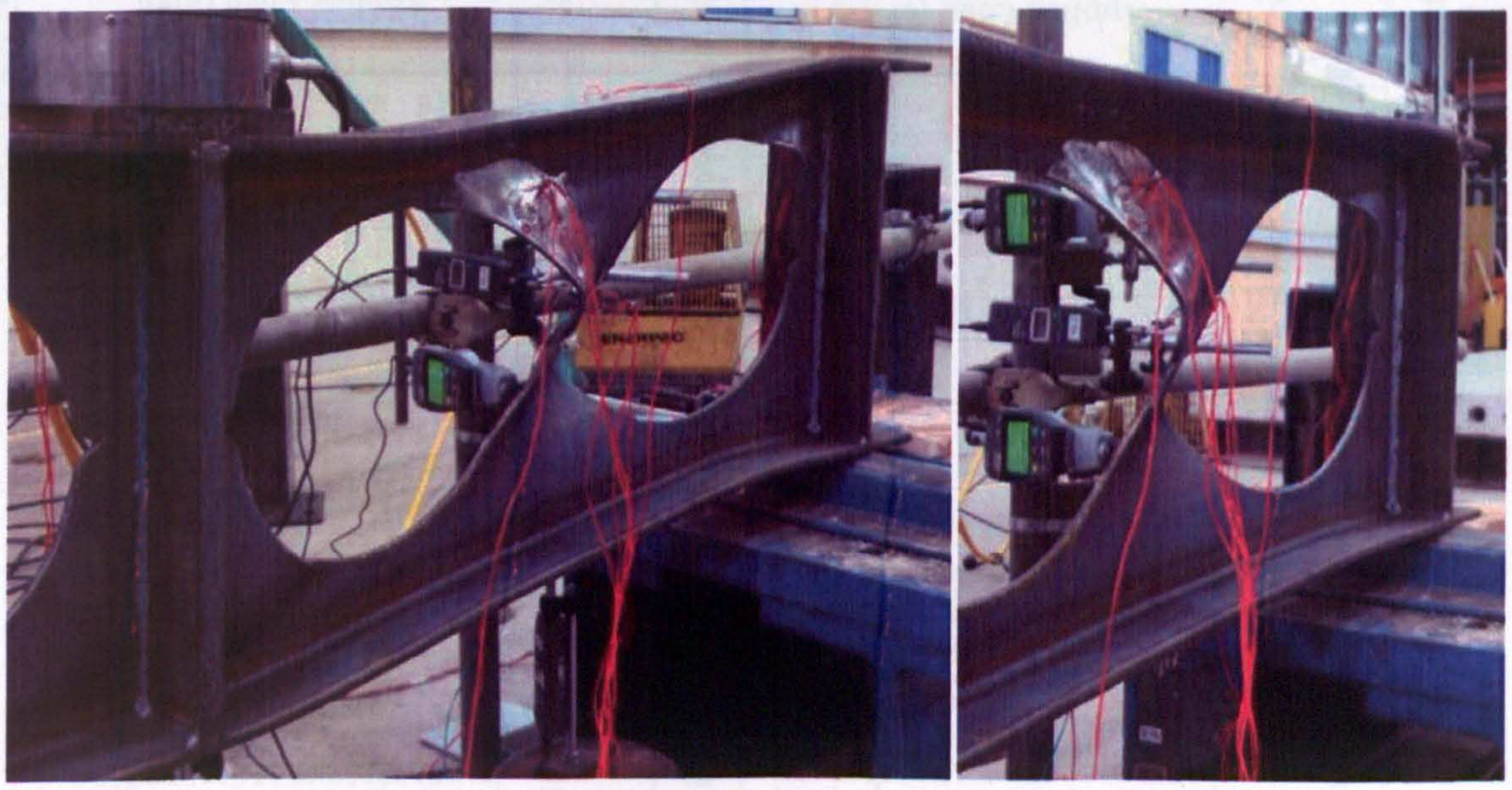

Figure 5.11: High yielding of compression area (Specimen A-2)

Specimen A-2

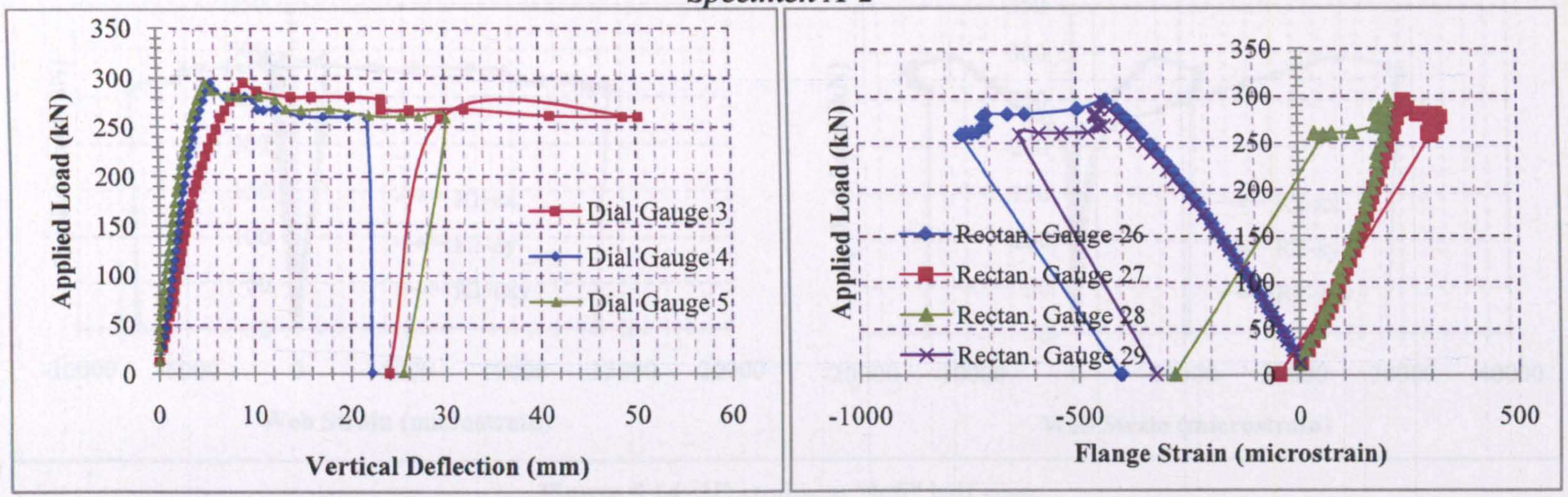

Figure 5.12: Vertical deflections along the bottom flange and flange strains at both half spans

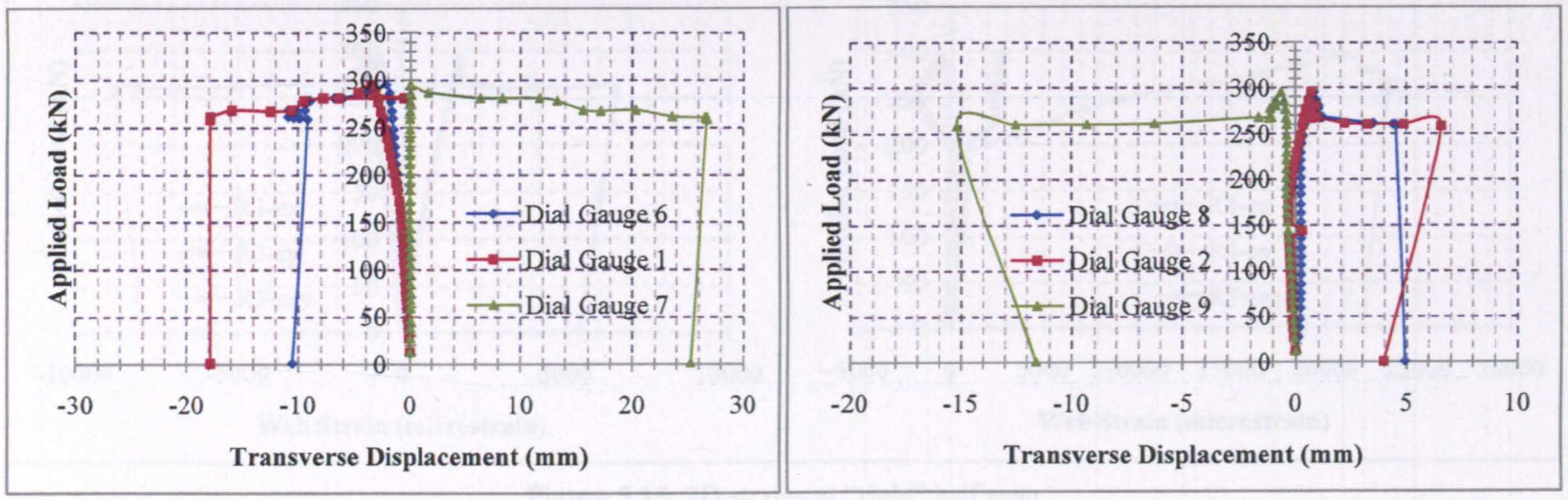

Figure 5.13: Web transverse displacements at "left" and "right" half spans

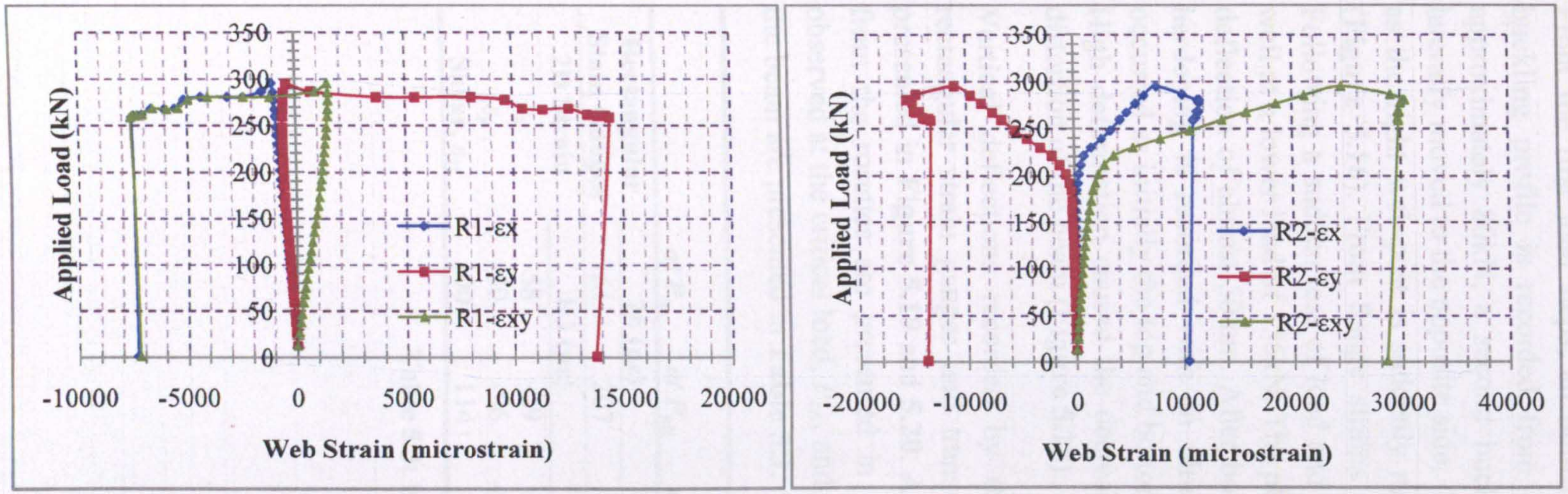

Figure 5.14: 2D strains at "left" half span

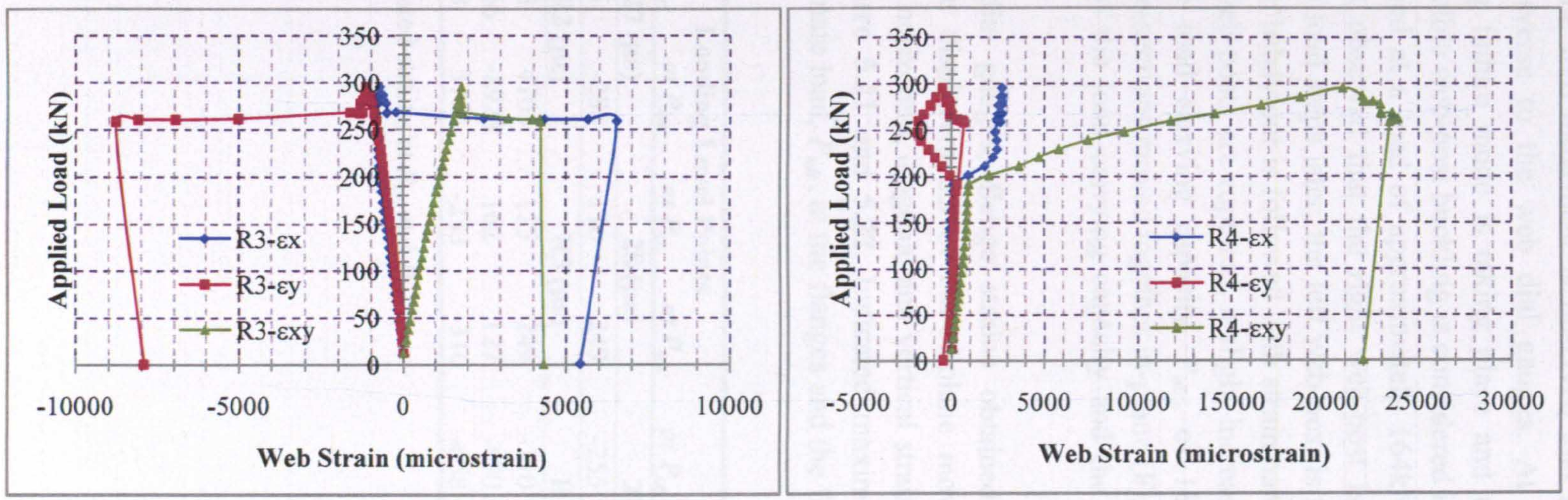

Figure 5.15: 2D strains at "right" half span

Specimen A-3

From the first load steps, an out-of-plane web movement is observed and a web-post buckling profile is recorded from transverse to the web dial gauges. At a load of approximately 80kN, a second buckling failure mode is taking place and the web is laterally moved to the opposite side. Invisible web-post buckling is considered in this case, as the right web-post is suddenly ruptured at a load of approximately 164kN (i.e. $P_{cr.}$) **(Figure 5.16)**. From flange strains it is observed that the right web-post is less stiff. Following a sudden loss of load and two load steps later, the left web-post is ruptured as well at a lower load of 156kN. The plastic behaviour is followed with strain hardening to a deflection of almost 50mm. After both web-posts are ruptured, a slight increase of strain hardening is recorded with an ultimate load carrying capacity, $P_{ult.}$, of 186kN. This occurred as initially the top and bottom tee-sections moved together in-plane (**Figure 5.17**). High deformation caused the decrease of the load carrying capacity and the permanent distortion of the beam (**Figure 5.18**).

Vertical deflections recorded by the dial gauges, flange strains obtained from the rectangular strain gauges and transverse displacements of out-of-plane movement are presented in **Figure 5.19** and **5.20**. Also, horizontal, diagonal and vertical strains obtained from the rosettes are presented in **Figure 5.21** and **5.22**. Indicated maximum strains observed at the critical load, $P_{cr.}$, and ultimate load, $P_{ult.}$, at the flanges and the front side of the beam are presented in **Table 5.3**.

	Loading Level Points							
	at $P_{cr.}$	***at $P_{ult.}$***	***at $P_{cr.}$***	***at $P_{ult.}$***	***at $P_{cr.}$***	***at $P_{ult.}$***	***at $P_{cr.}$***	***at $P_{ult.}$***
Rectangular	**26 (με)**		**27 (με)**		**28 (με)**		**29 (με)**	
Stain Gauges	161	207	-275	-288	176	249	-255	-279
2D Strain	**R1 (με)**		**R2 (με)**		**R3 (με)**		**R4 (με)**	
ε_x	-58	-29	5193	4705	115	249	-110	-204
ε_y	-50	-96	-10966	-8928	162	127	-690	-695
Shear, ε_{xy}	100	114	3388	3704	-233	-310	-658	-735

Table 5.3: Indicated strains at $P_{cr.}$ and $P_{ult.}$

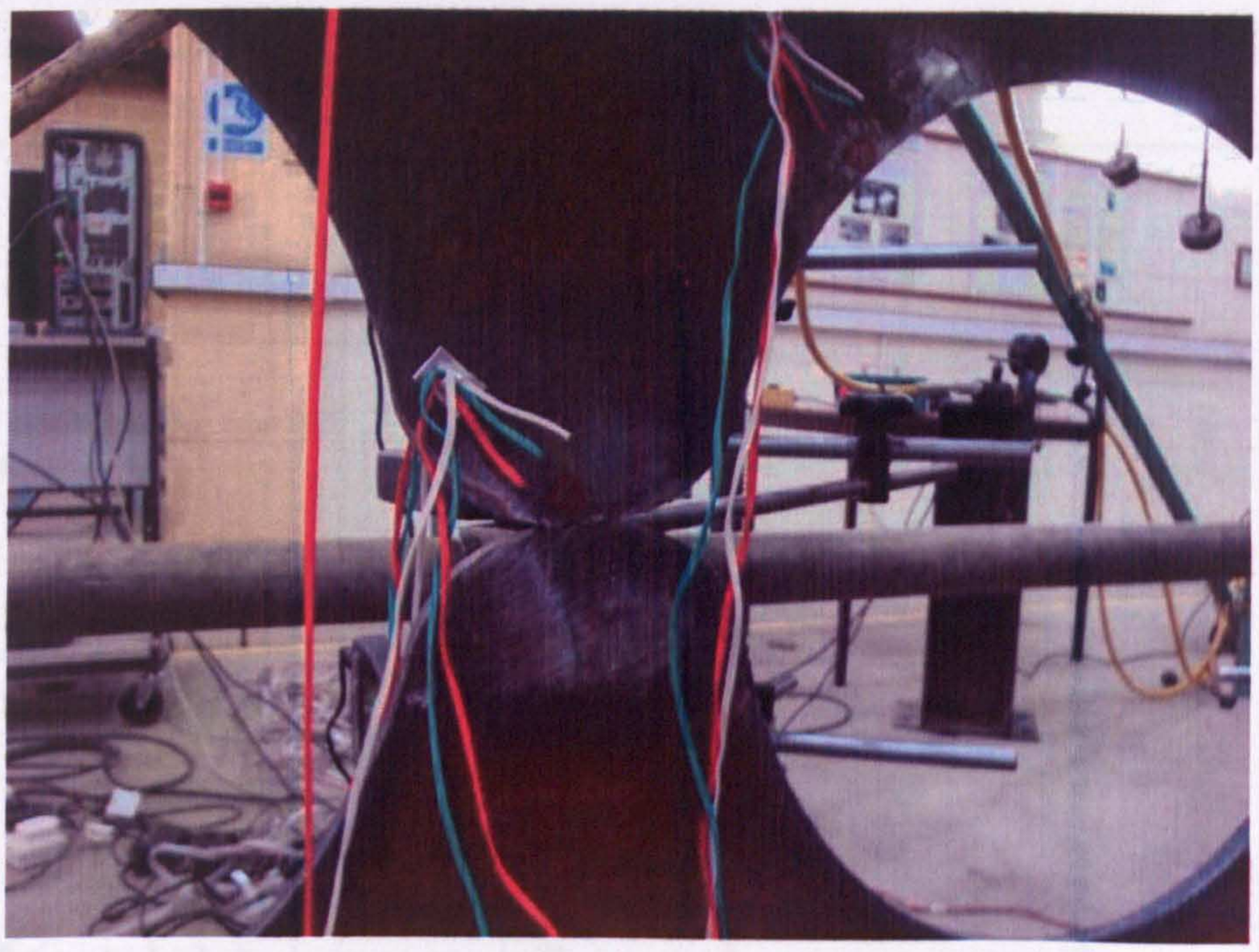

Figure 5.16: Rupture of the "right" web-post (Specimen A-3)

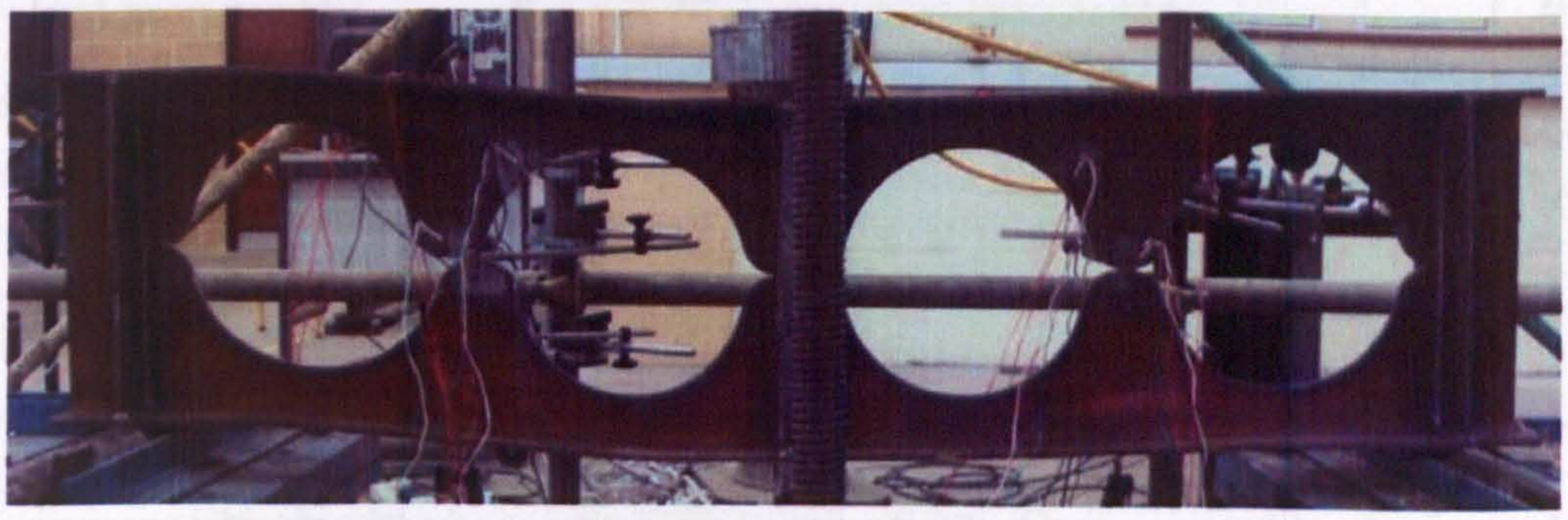

Figure 5.17: Tee-sections moved together in-plane (Specimen A-3)

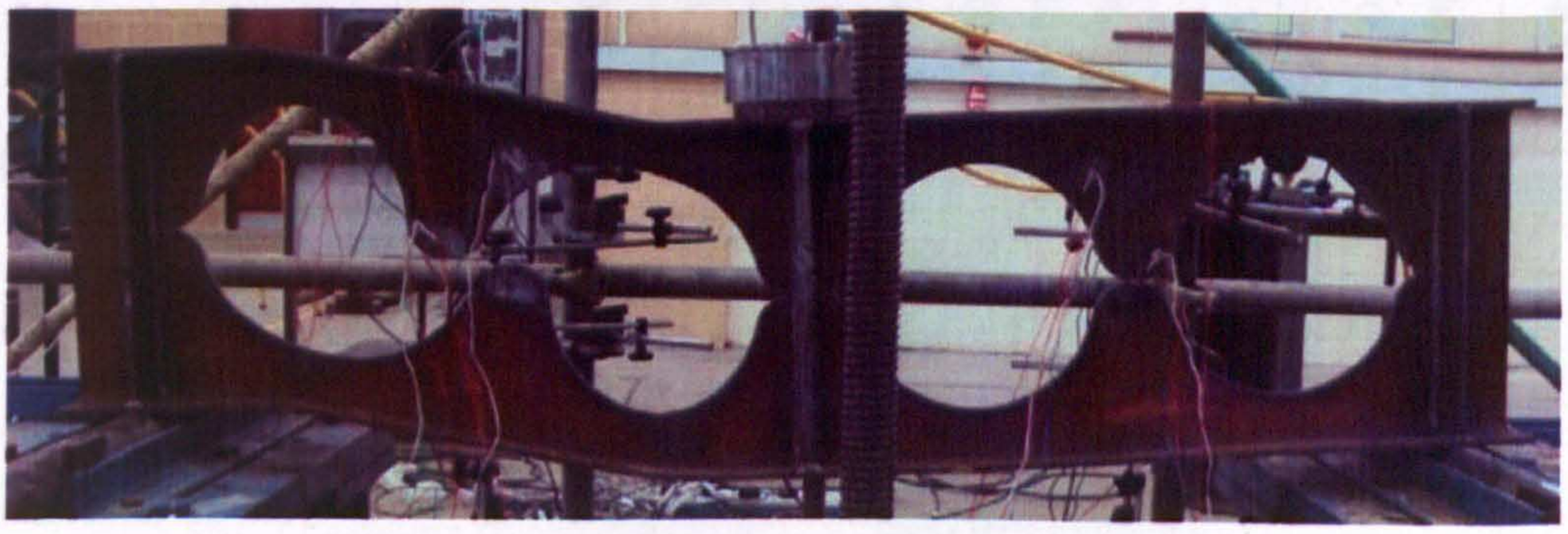

Figure 5.18: High deflection at failure load (Specimen A-3)

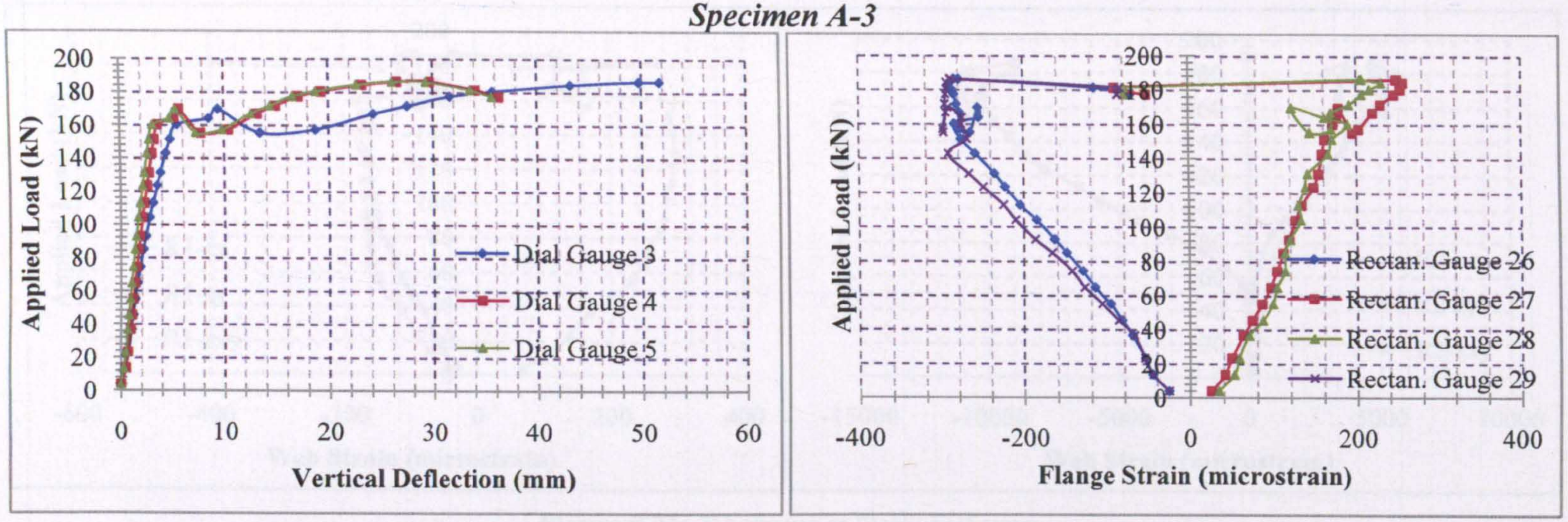

Figure 5.19: Vertical deflections along the bottom flange and flange strains at both half spans

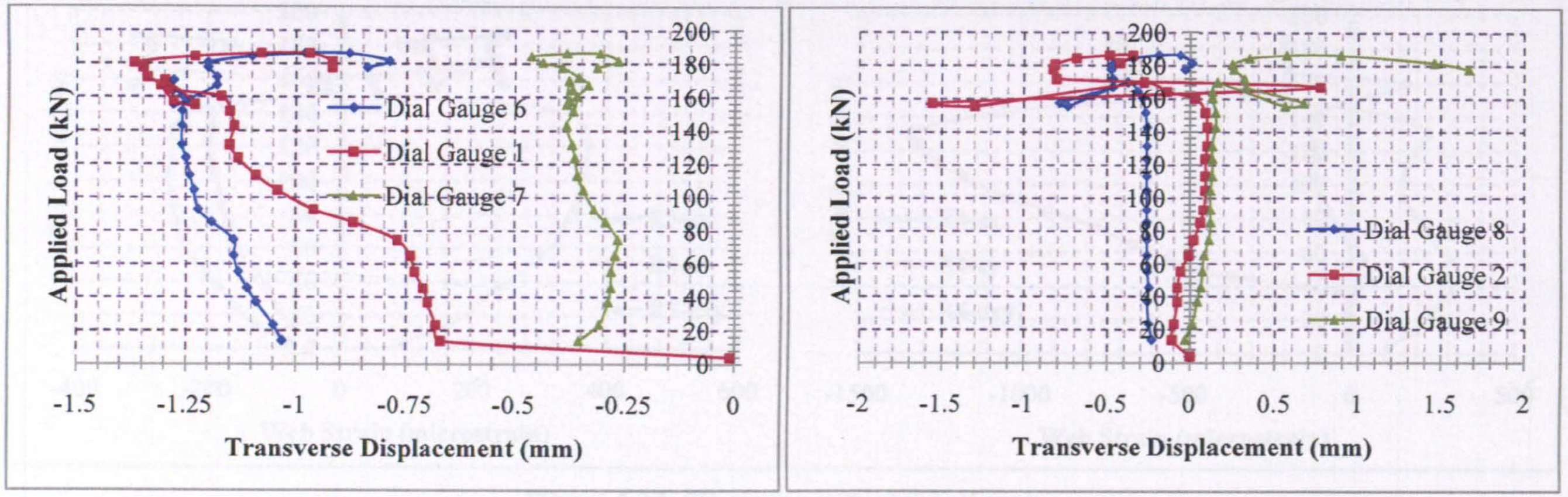

Figure 5.20: Web transverse displacements at "left" and "right" half spans

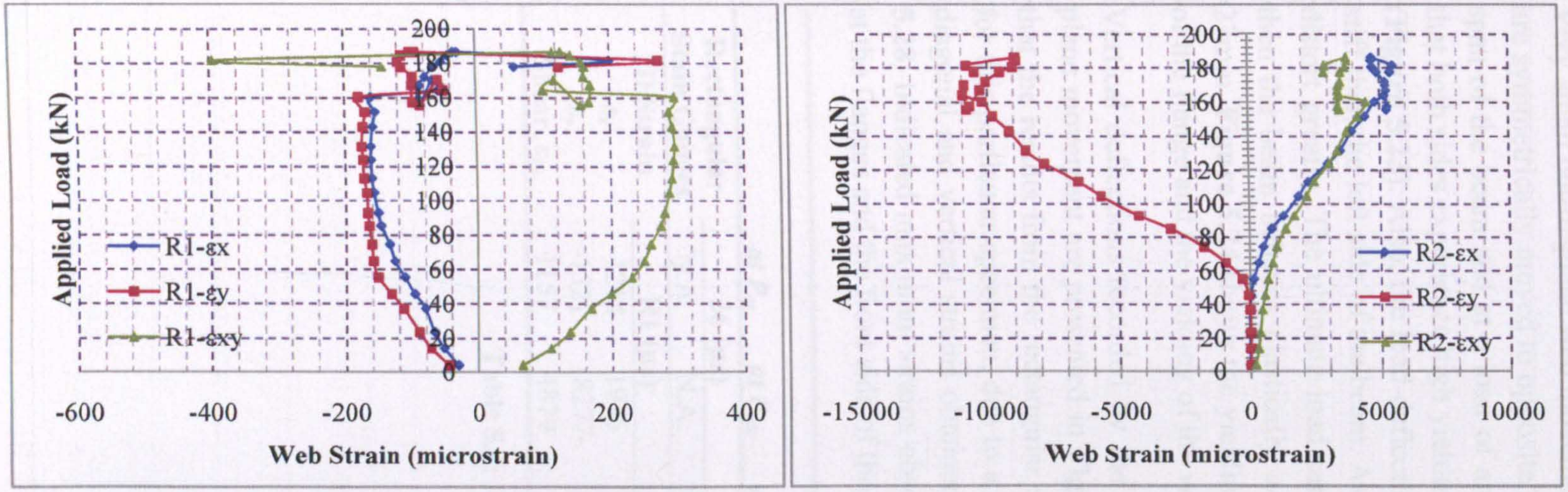

Figure 5.21: 2D strains at "left" half span

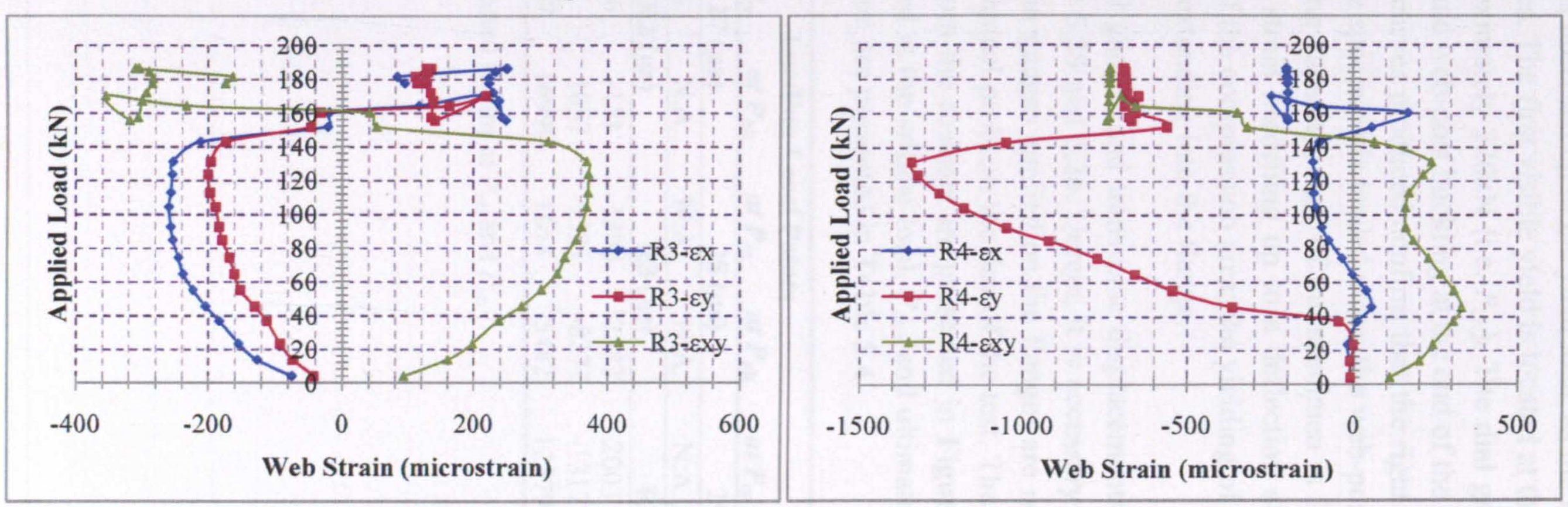

Figure 5.22: 2D strains at "right" half span

Specimen B-1

Very small out-of-plane web movement is observed up to the yield load, as the tee-sections are symmetrically moved to opposite sides. The first visible yield is located at the right half span of the beam and at a load of approximately 220kN (i.e. $P_{cr.}$). The dial gauges show that both sides experience high yielding and web-post buckling at the end of the experiment **(Figure 5.23)**. Also, the load-deflection curves produced confirm that the right side is less stiff than the left side of the beam. As the specimen is loaded more, the web-post begins to distort greatly. The ultimate load carrying capacity, $P_{ult.}$, of the specimen is 256kN, and then the beam behaves plastically with strain hardening up to a deflection at almost of 27mm. **Figure 5.24** shows the yielding of the compression area; the yielding of top portion of the flange and the yielding of the web extending into the flange.

Vertical deflections recorded by the dial gauges and transverse displacements of out-of-plane movement are presented in **Figure 5.25** and **5.26**. Herein, it is necessary to mention that the results from the rectangular strain gauges applied on the flanges are not recorded for this particular specimen, due to a technical problem the day of the test. The horizontal, diagonal and vertical strains obtained from the rosettes are presented in **Figure 5.27** and **5.28**. Indicated maximum strains observed at the critical load, $P_{cr.}$, and ultimate load, $P_{ult.}$, at the flanges and the front side of the beam are presented in **Table 5.4**.

	Loading Level Points							
	at $P_{cr.}$	***at $P_{ult.}$***	***at $P_{cr.}$***	***at $P_{ult.}$***	***at $P_{cr.}$***	***at $P_{ult.}$***	***at $P_{cr.}$***	***at $P_{ult.}$***
Rectangular	**26 (με)**		**27 (με)**		**28 (με)**		**29 (με)**	
Stain Gauges	N.A.	N.A.	N.A.	N.A.	N.A.	N.A.	N.A.	N.A.
2D Strain	**R1 (με)**		**R2 (με)**		**R3 (με)**		**R4 (με)**	
ε_x	-1214	1976	-796	-151	-1398	2382	2003	1589
ε_y	-1521	-8277	85	1057	-1521	-8277	-1317	686
Shear, ε_{xy}	1157	4879	2867	16999	1658	5442	12879	15868

Table 5.4: Indicated strains at $P_{cr.}$ and $P_{ult.}$

Figure 5.23: Web-post buckling at both sides (Specimen B-1)

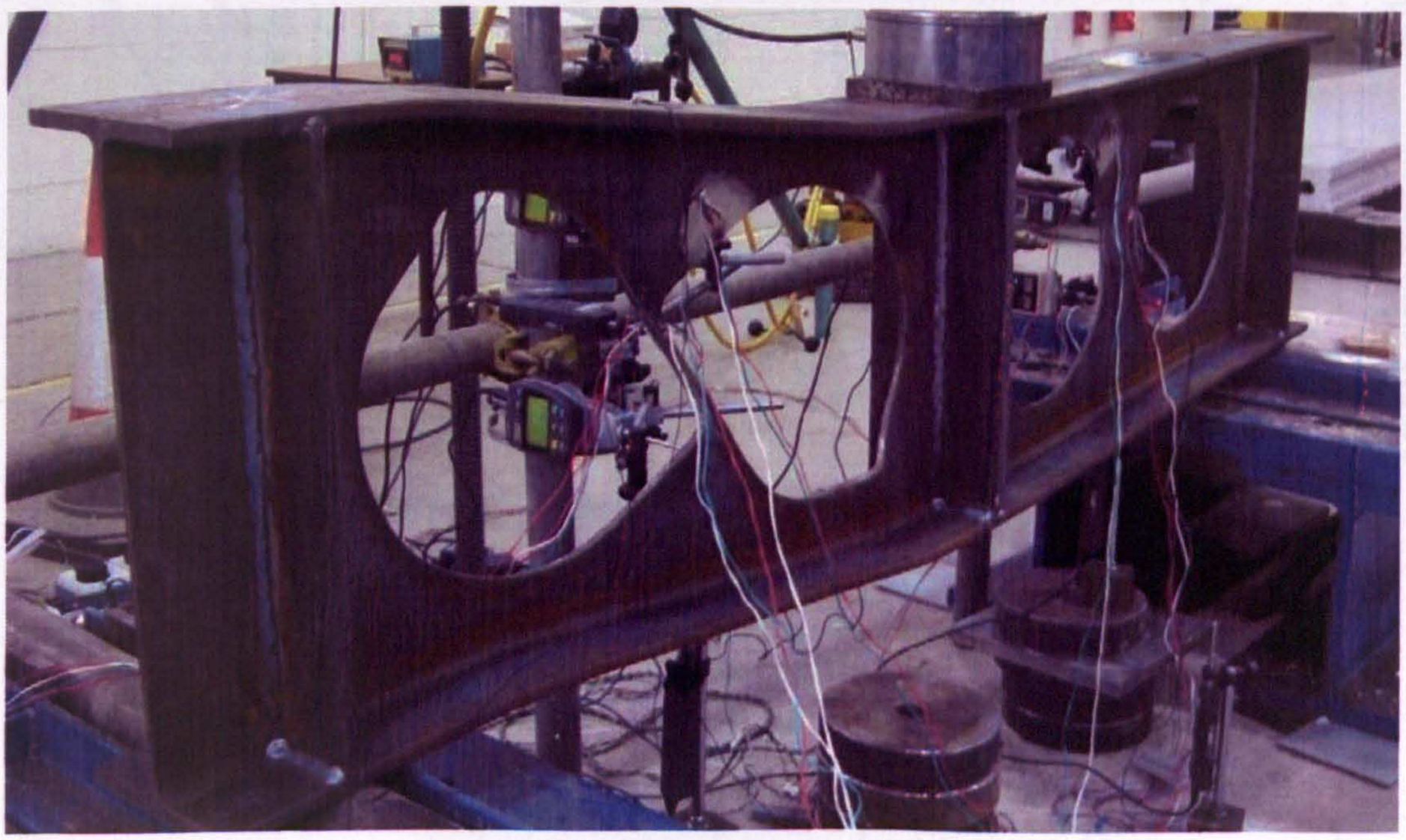

Figure 5.24: Yielding of compression area (Specimen B-1)

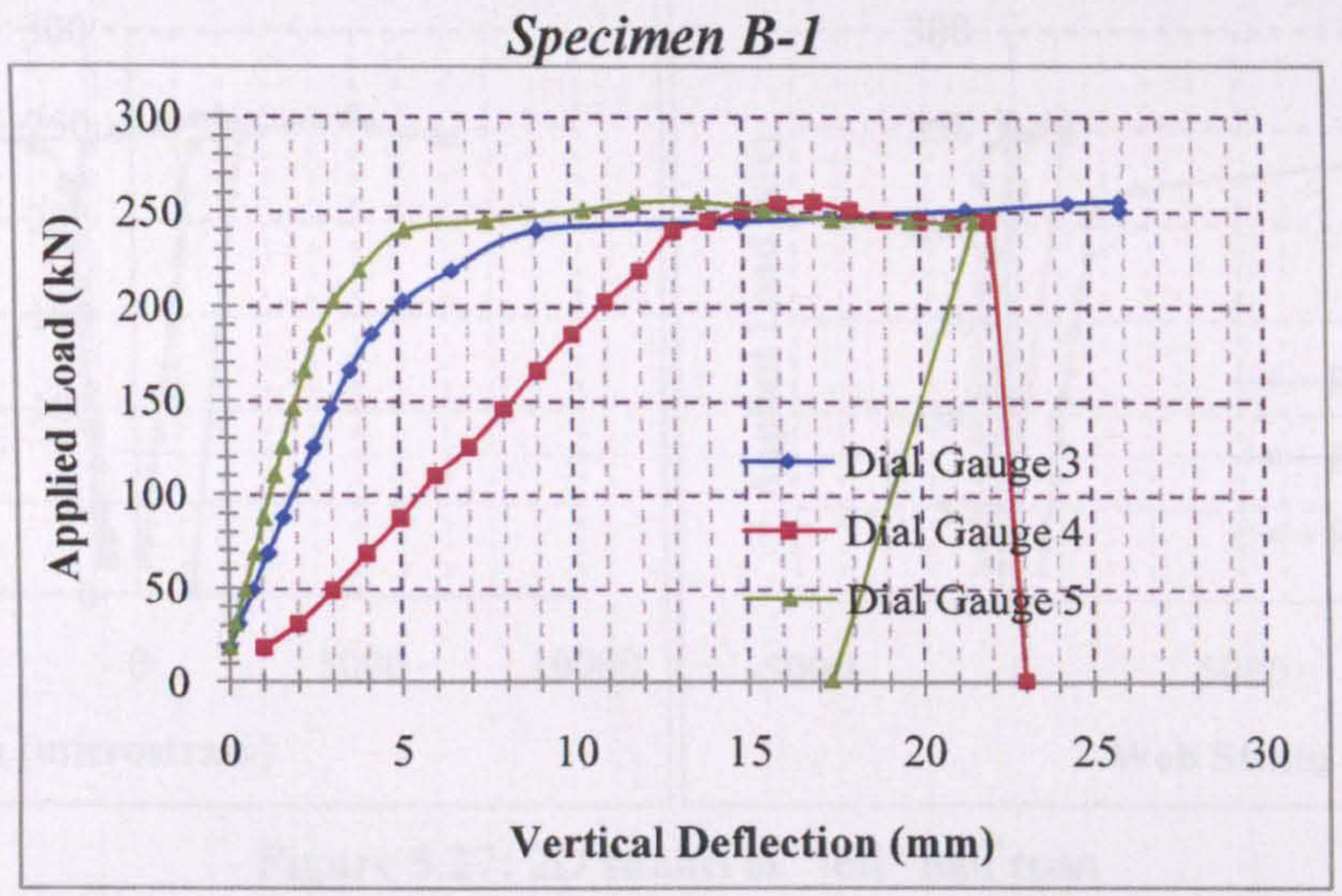

Figure 5.25: Vertical deflections along the bottom flange

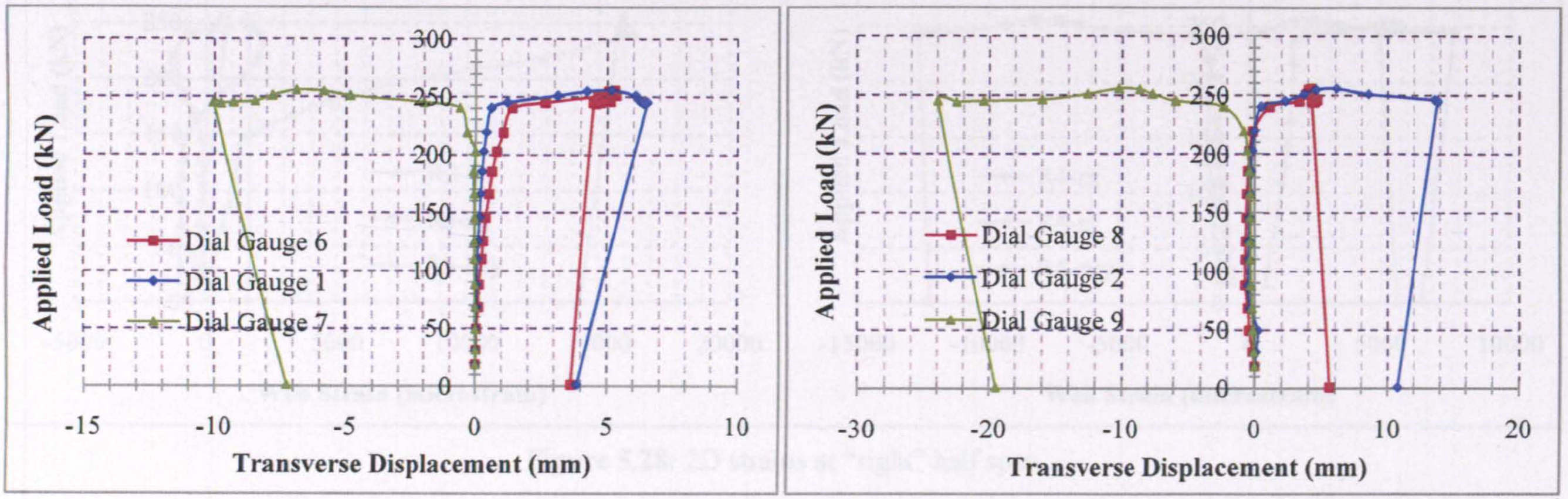

Figure 5.26: Web transverse displacements at "left" and "right" half span

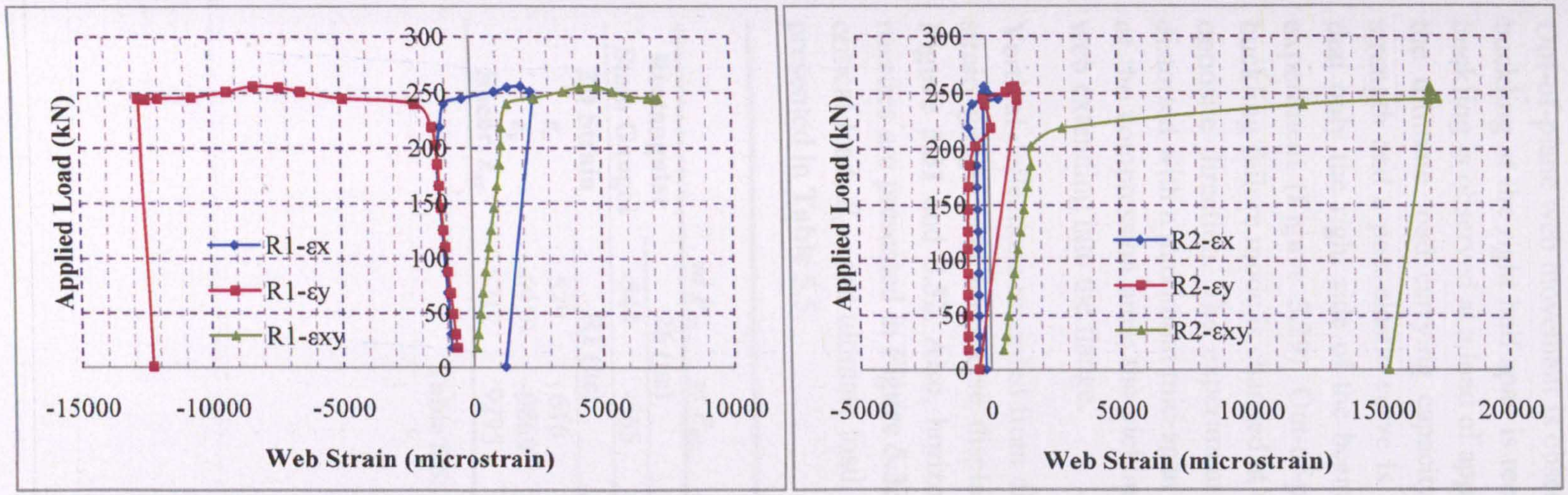

Figure 5.27: 2D strains at "left" half span

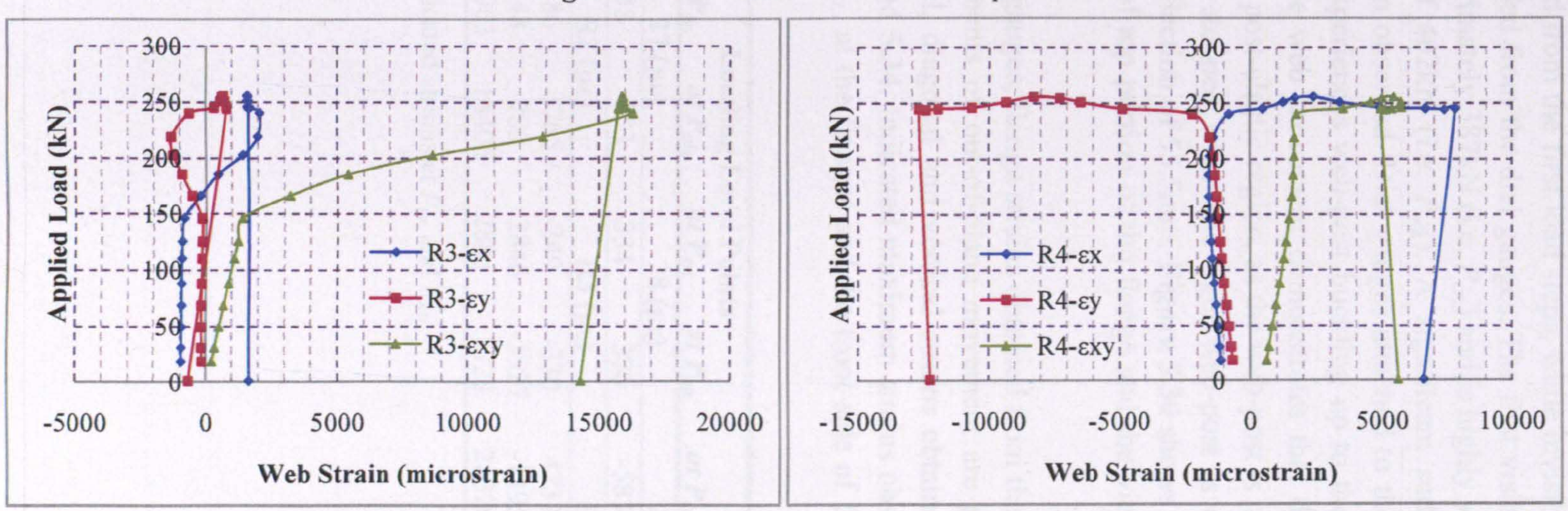

Figure 5.28: 2D strains at "right" half span

Specimen B-2

Out-of-plane web movement is observed from the first load steps, while invisible web-post buckling at the right half span is recorded from the dial gauges. The first visible web-post buckling is observed at a load of approximately 387kN (i.e. $P_{cr.}$) and is highly yielded up to the ultimate load carrying capacity of 402kN (i.e. $P_{ult.}$). A significant sudden loss of strength and a post-elastic curve is then observed. Dial gauges attached to the web show that only the right side of the beam experiences web-post buckling up to the end of the experiment (**Figure 5.29**). Out-of-plane web movement demonstrates that the web-post buckling failure mode is changed at the post-elastic region, as the web-post is moved in the opposite direction. The experiment is stopped when the right web-post is dramatically distorted with a maximum mid-span deflection of 55.5mm. **Figure 5.30** shows the yielding of the compression area; the yielding of top portion of the flange and the yielding of the web extending into the flange.

Vertical deflections recorded from dial gauges, flange strains obtained from the rectangular strain gauges and transverse displacements of out-of-plane movement are presented in **Figure 5.31** and **5.32**. Also, horizontal, diagonal and vertical strains obtained from the rosettes are presented in **Figure 5.33** and **5.34**. Indicated maximum strains observed at the critical load, $P_{cr.}$, and ultimate load, $P_{ult.}$, at the flanges and the front side of the beam are presented in **Table 5.5**.

	Loading Level Points							
	at $P_{cr.}$	***at $P_{ult.}$***	***at $P_{cr.}$***	***at $P_{ult.}$***	***at $P_{cr.}$***	***at $P_{ult.}$***	***at $P_{cr.}$***	***at $P_{ult.}$***
Rectangular	**26 (με)**		**27 (με)**		**28 (με)**		**29 (με)**	
Stain Gauges	-544	-565	348	353	334	370	-583	-616
2D Strain	**R1 (με)**		**R2 (με)**		**R3 (με)**		**R4 (με)**	
ε_x	579	616	1386	3765	-349	-330	4733	2675
ε_y	-6950	-9869	1548	785	-2846	-3527	-1195	744
Shear, ε_{xy}	5712	9295	24963	18406	2885	3723	26320	8703

Table 5.5: Indicated strains at $P_{cr.}$ and $P_{ult.}$

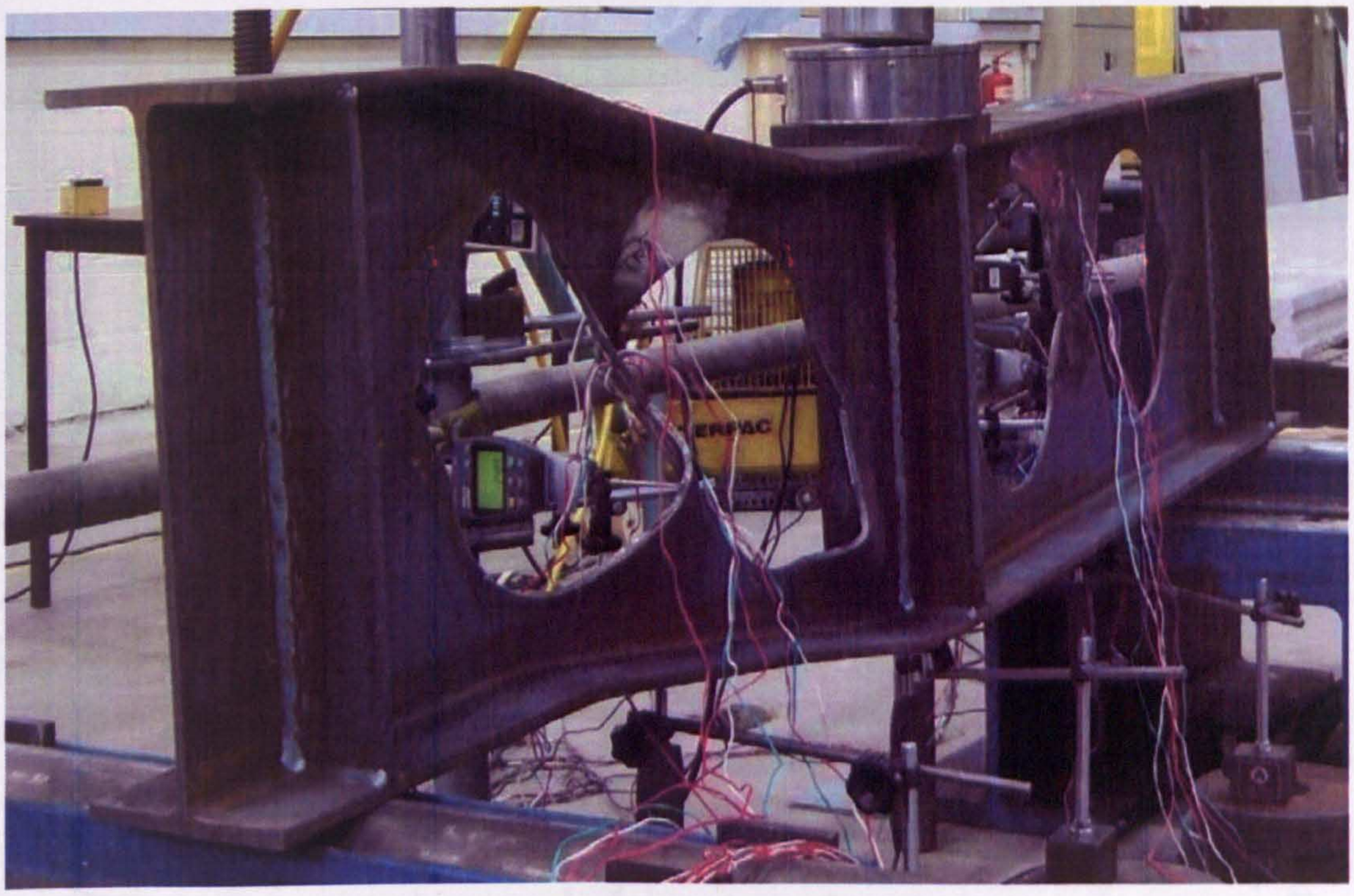

Figure 5.29: High yielding and web-post buckling at the "right" side (Specimen B-2)

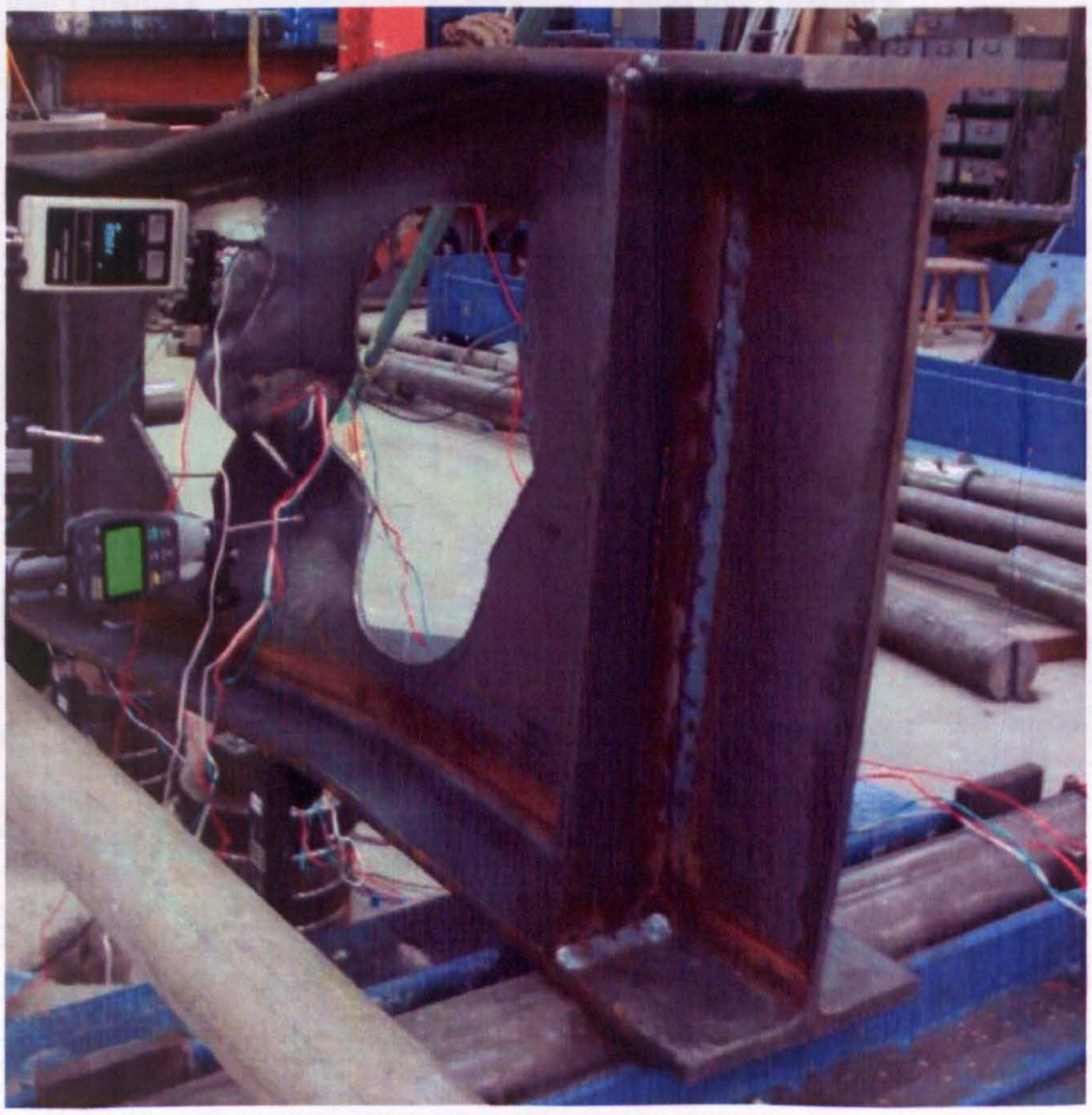

Figure 5.30: Yielding of compression area (Specimen B-2)

Specimen B-2

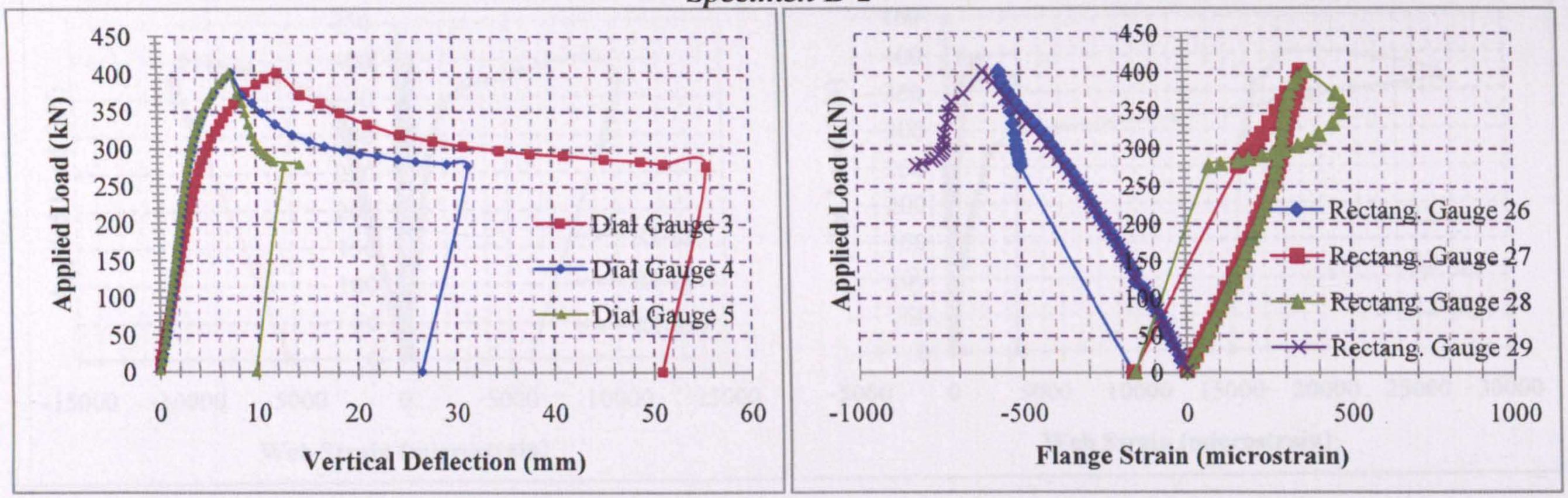

Figure 5.31: Vertical deflections along the bottom flange and flange strains at both half spans

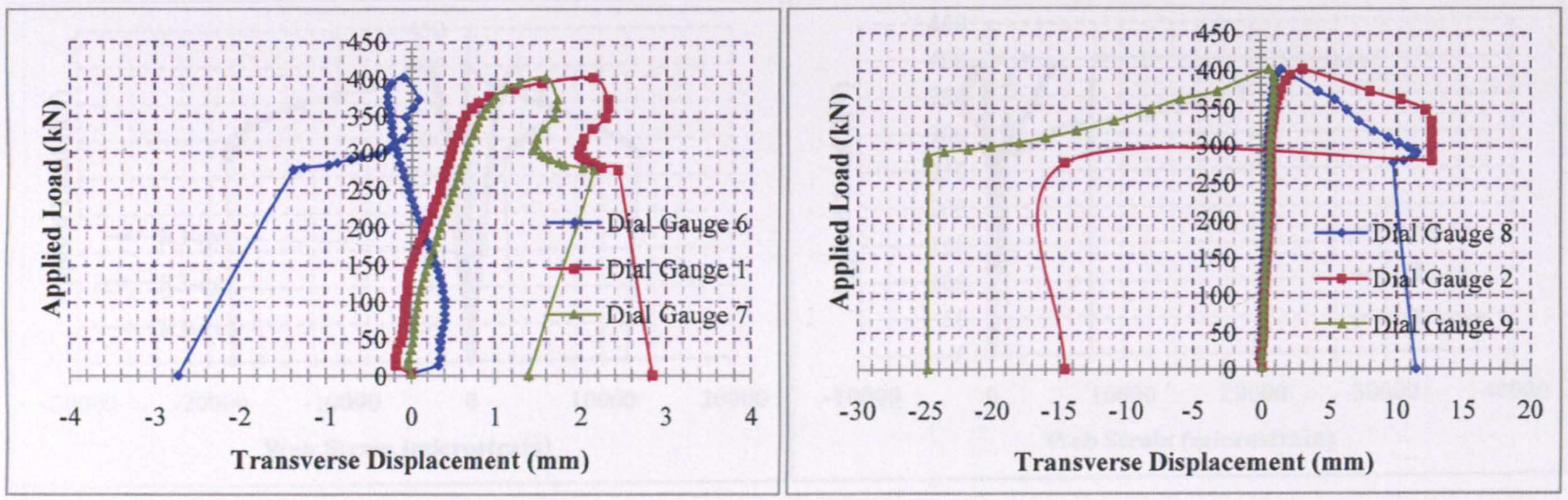

Figure 5.32: Web transverse displacements at "left" and "right" half spans

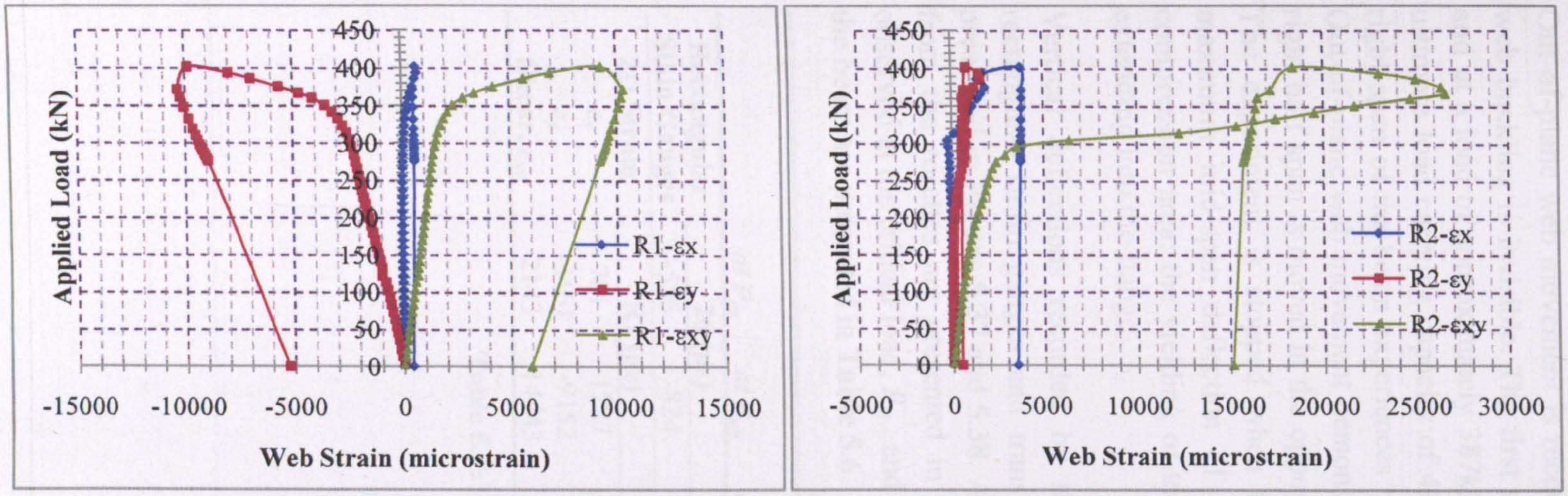

Figure 5.33: 2D strains at "left" half span

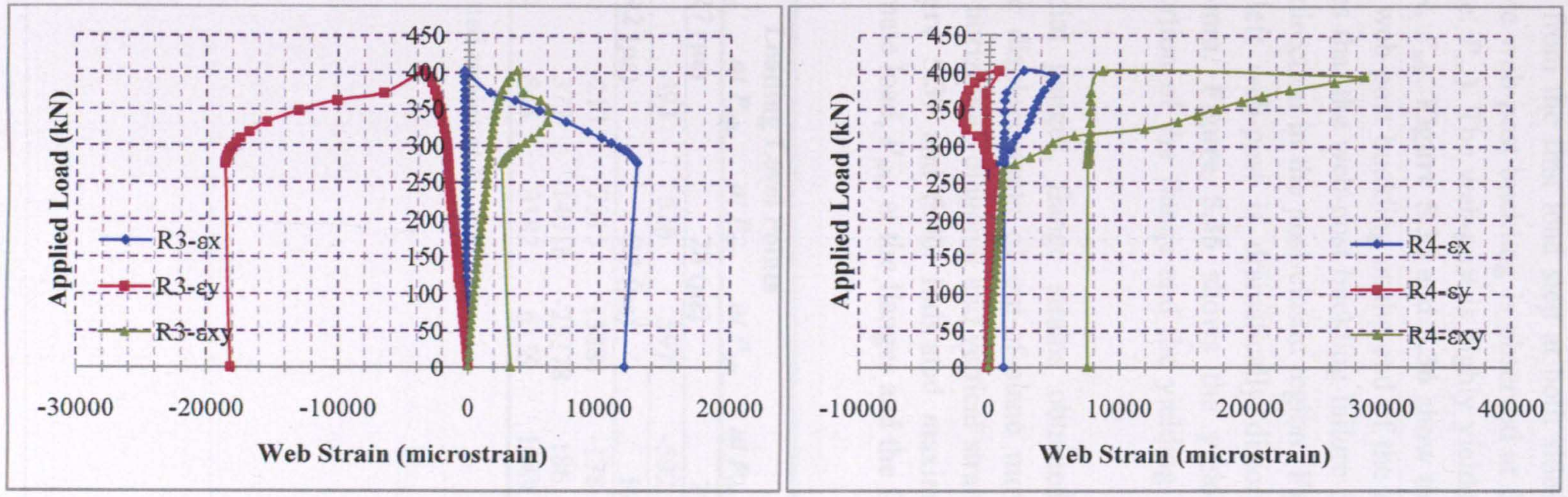

Figure 5.34: 2D strains at "right" half span

Specimen B-3

Out-of-plane web movement is recorded from the first load step at both sides, while the web buckling is invisible. The first visible web-post buckling is observed at the left side and at a load of approximately 387kN (i.e. $P_{cr.}$). The web-post is highly yielded up to the ultimate load carrying capacity of 416kN, $P_{ult.}$. **Figure 5.35** and **5.36** show that only the right span of the beam experiences high web-post buckling at the end of the experiment. Out-of-plane web movement demonstrates that the web-post buckling failure mode at the right half span is moved in the opposite direction in the post-elastic region (**Figure 5.38**). The experiment is stopped when the left web-post is dramatically distorted with a maximum mid-span deflection of 36.5mm. **Figure 5.36** shows the yielding of the compression area; the yielding of top portion of the flange and the yielding of the web extending into the flange.

Vertical deflections recorded by the dial gauges, flange strains obtained from the rectangular strain gauges and transverse displacements of out-of-plane movement are presented in **Figure 5.37** and **5.38**. Also, horizontal, diagonal and vertical strains obtained from the rosettes are presented in **Figure 5.39** and **5.40**. Indicated maximum strains observed at the critical load, $P_{cr.}$, and ultimate load, $P_{ult.}$, at the flanges and the front side of the beam are presented in **Table 5.6**.

	Loading Level Points							
	at $P_{cr.}$	***at $P_{ult.}$***	***at $P_{cr.}$***	***at $P_{ult.}$***	***at $P_{cr.}$***	***at $P_{ult.}$***	***at $P_{cr.}$***	***at $P_{ult.}$***
Rectangular	**26 (με)**		**27 (με)**		**28 (με)**		**29 (με)**	
Stain Gauges	-556	-824	549	493	526	597	-592	-639
2D Strain	**R1 (με)**		**R2 (με)**		**R3 (με)**		**R4 (με)**	
ε_x	701	1227	-104	-213	7315	13881	-178	-223
ε_y	-3461	-9152	60	372	-14018	-25278	186	264
Shear, ε_{xy}	2143	14443	1059	845	3182	6159	1049	1094

Table 5.6: Indicated strains at $P_{cr.}$ and $P_{ult.}$

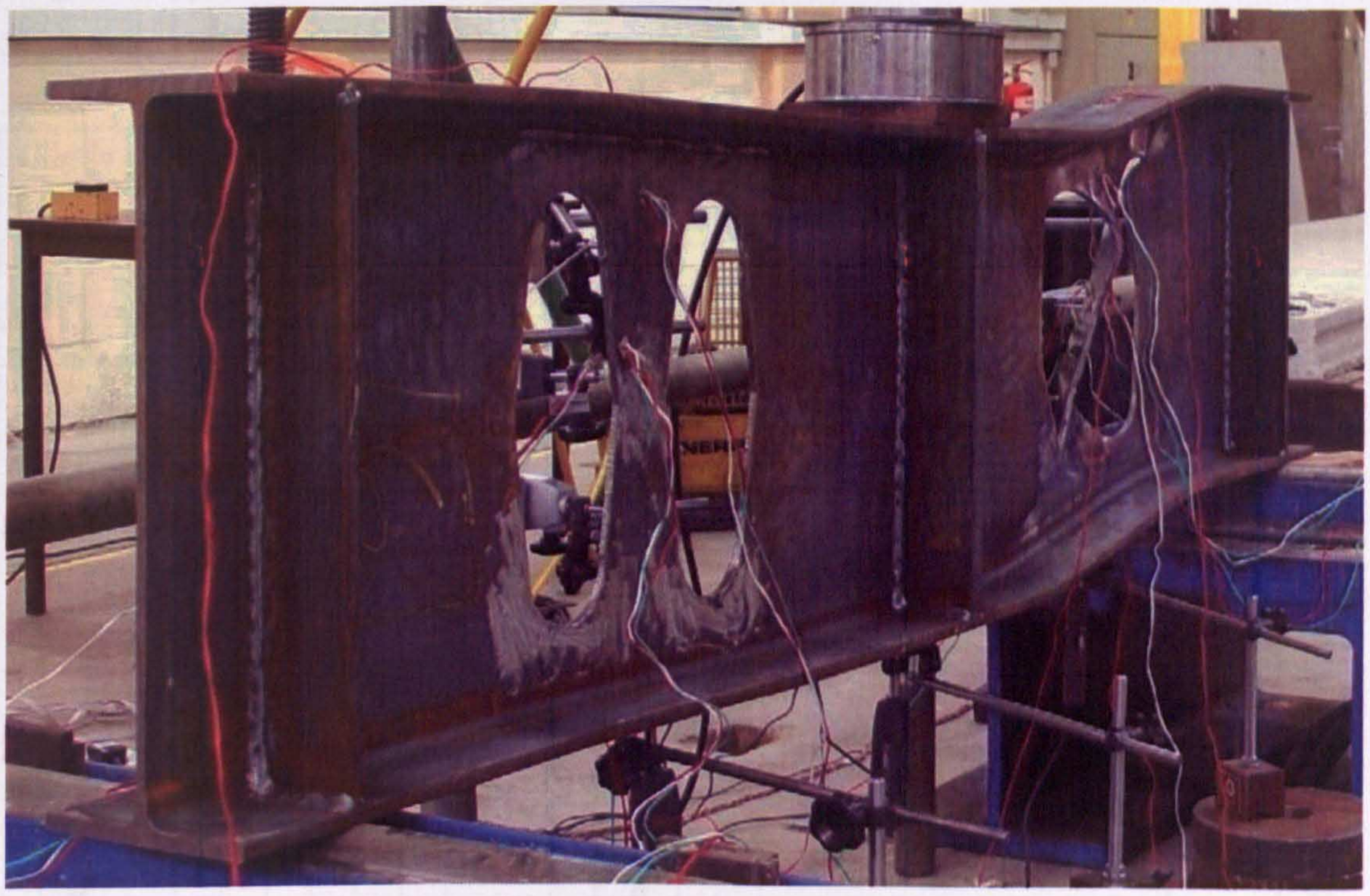

Figure 5.35: High yielding and web-post buckling at the "left" side (Specimen B-3)

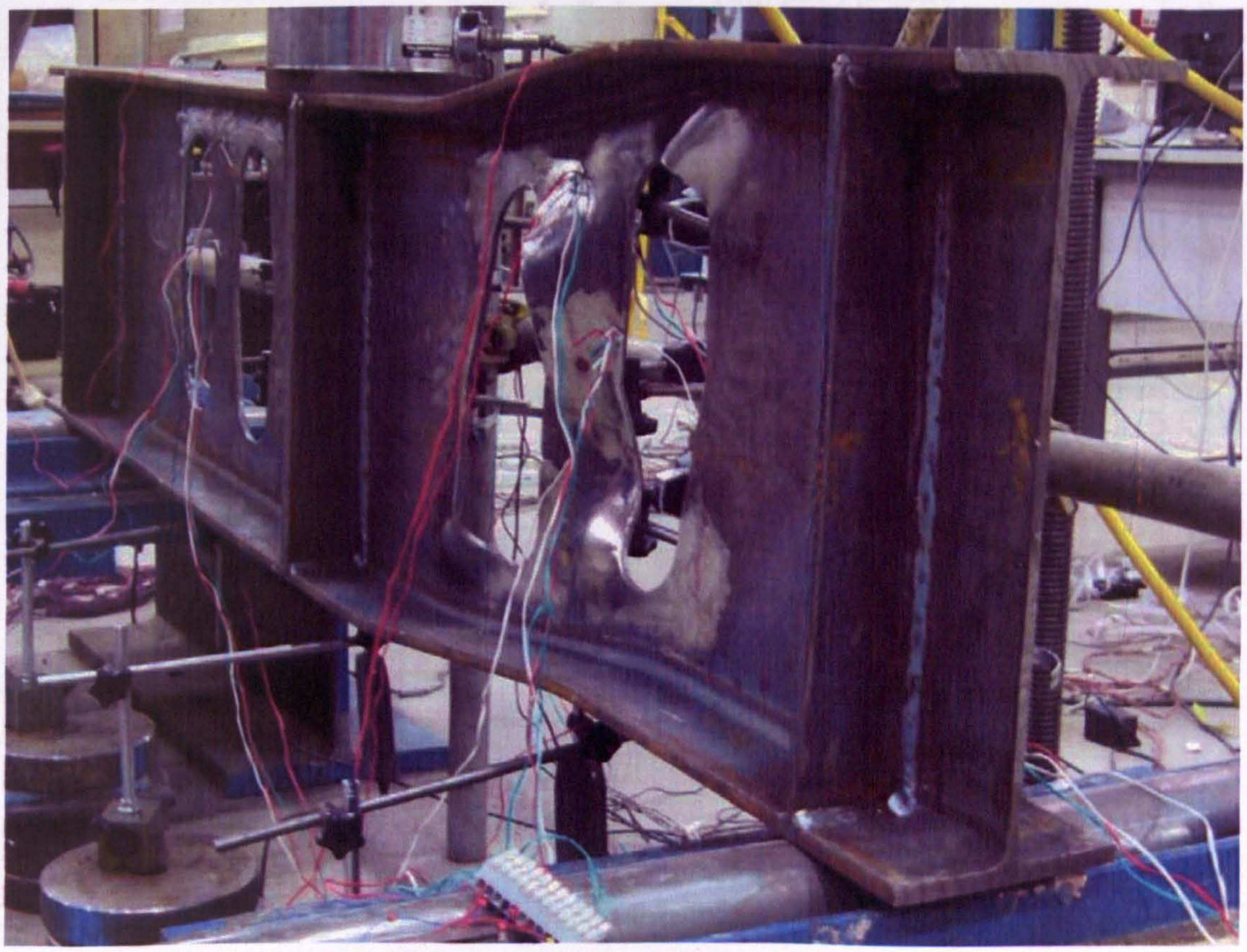

Figure 5.36: High yielding of compression area (Specimen B-3)

Specimen B-3

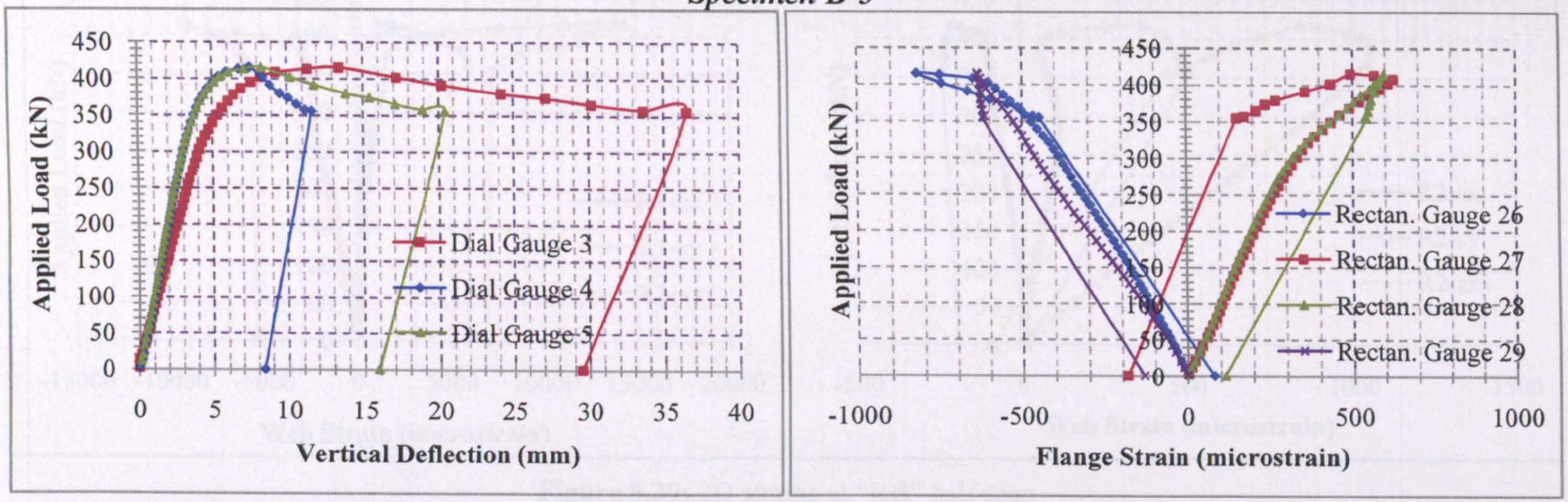

Figure 5.37: Vertical deflections along the bottom flange and flange strains at both half spans

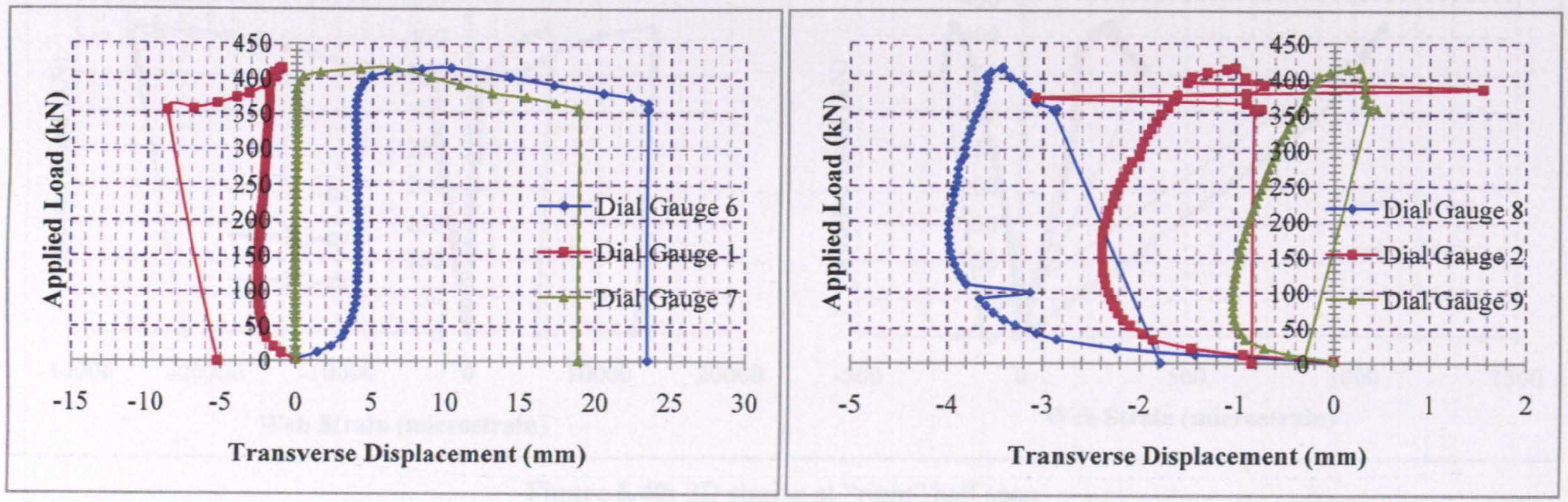

Figure 5.38: Web transverse displacements at "left" and "right" half span

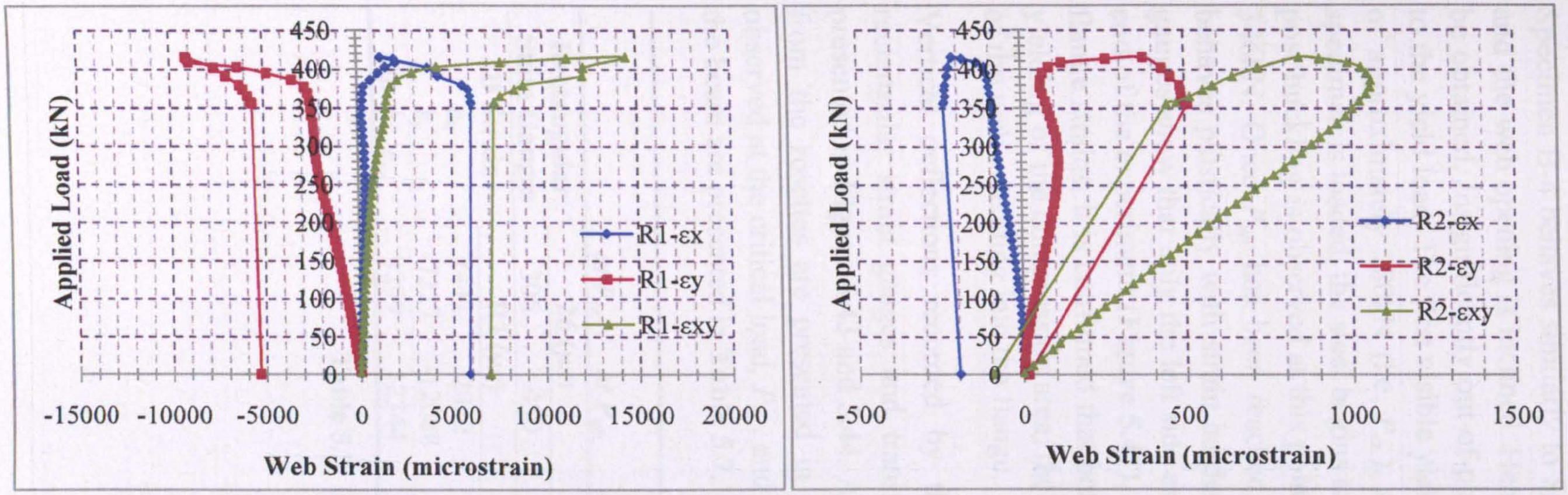

Figure 5.39: 2D strains at "left" half span

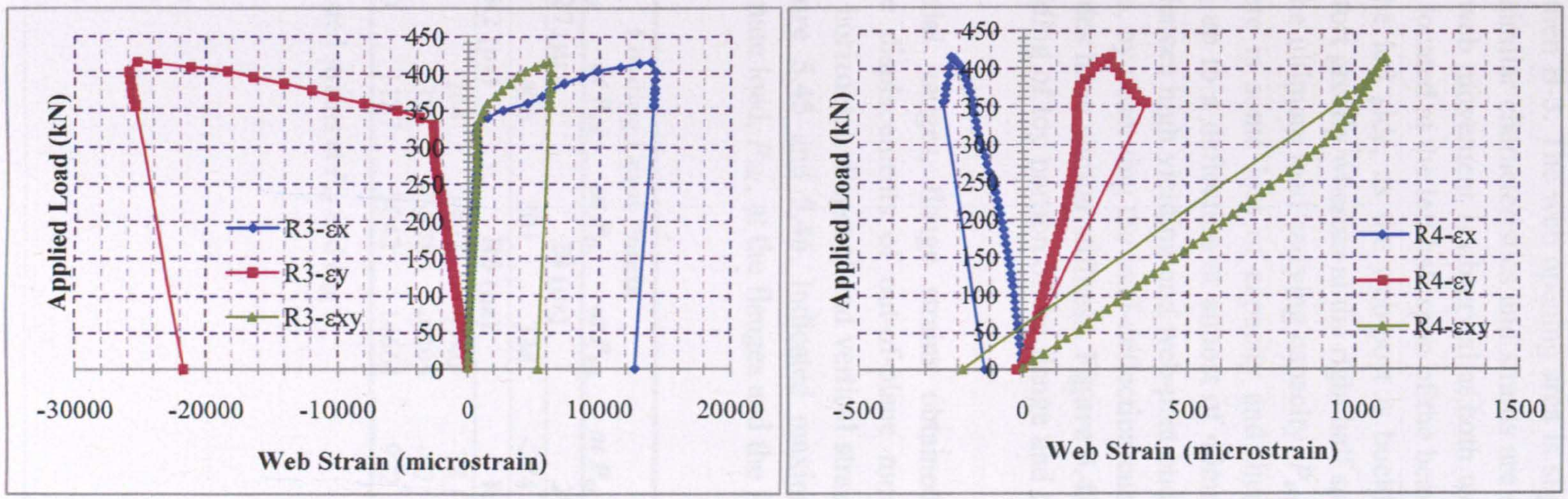

Figure 5.40: 2D strains at "right" half span

Specimen B-4

Specimen B-4 behaves similarly to Specimen B-3. The web opening area is slightly larger and the web opening is inclined. Hence, similar characteristics and strains are expected to be obtained. Insignificantly out-of-plane web movement is observed at both web-posts up to the yield load. The first visible yield is located at the left half span of the beam, at a load of approximately 280kN (i.e. $P_{cr.}$). At the left side, as the web-post is buckled and the specimen is loaded, the steel begins to distort greatly whereas at the right half span no web-post buckling is observed at this point. The ultimate load carrying capacity, $P_{ult.}$, is around 346kN. Once $P_{ult.}$ has been reached, there is some loss of capacity and then the beam behaves plastically with strain hardening up to a deflection at almost of 40mm. The dial gauges show that only the left side experiences high yielding and web-post buckling at the end of the experiment (**Figure 5.41**). Also, by observing the load-deflection curves and the flange strains, it is confirmed that both sides have similar stiffness. **Figure 5.42** shows the yielding of the compression area; the yielding of top portion of the flange and the yielding of the web extending into the flange.

Vertical deflections recorded by the dial gauges, flange strains obtained from the rectangular strain gauges and transverse displacements of out-of-plane movement are presented in **Figure 5.43** and **5.44**. Also, horizontal, diagonal and vertical strains obtained from the rosettes are presented in **Figure 5.45** and **5.46**. Indicated maximum strains observed at the critical load, $P_{cr.}$, and ultimate load, $P_{ult.}$, at the flanges and the front side of the beam are presented in **Table 5.7**.

	Loading Level Points							
	at $P_{cr.}$	***at $P_{ult.}$***	***at $P_{cr.}$***	***at $P_{ult.}$***	***at $P_{cr.}$***	***at $P_{ult.}$***	***at $P_{cr.}$***	***at $P_{ult.}$***
Rectangular	**26 (με)**		**27 (με)**		**28 (με)**		**29 (με)**	
Stain Gauges	-306	-450	322	406	301	334	-274	-413
2D Strain	**R1 (με)**		**R2 (με)**		**R3 (με)**		**R4 (με)**	
ε_x	2441	2022	92	264	1403	-140	78	172
ε_y	-7227	-12088	-25	-323	-5878	-8895	-87	-199
Shear, ε_{xy}	3299	12344	1099	1127	3042	14661	922	894

Table 5.7: Indicated strains at $P_{cr.}$ and $P_{ult.}$

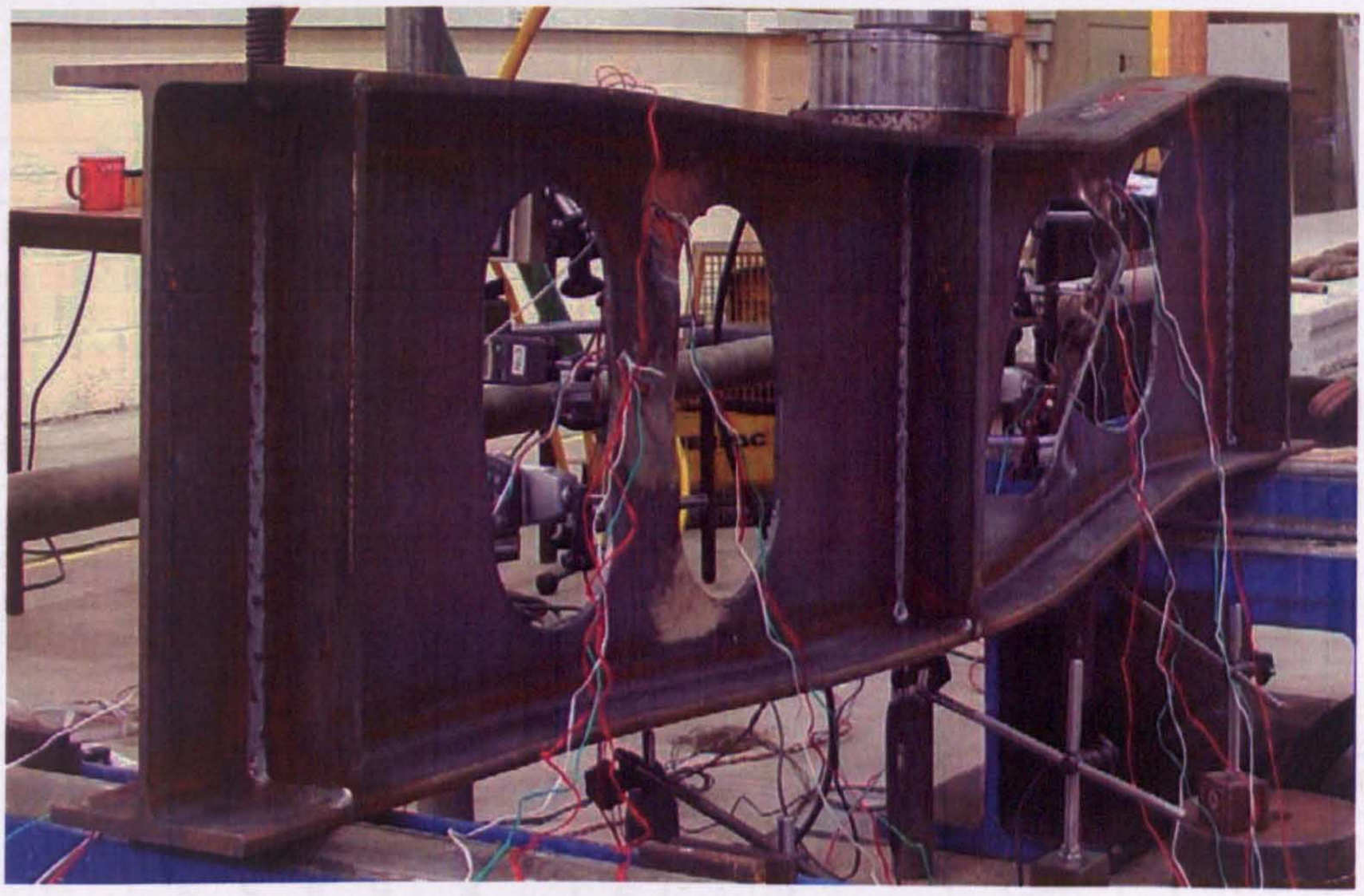

Figure 5.41: High yielding and web-post buckling at the "left" side (Specimen B-4)

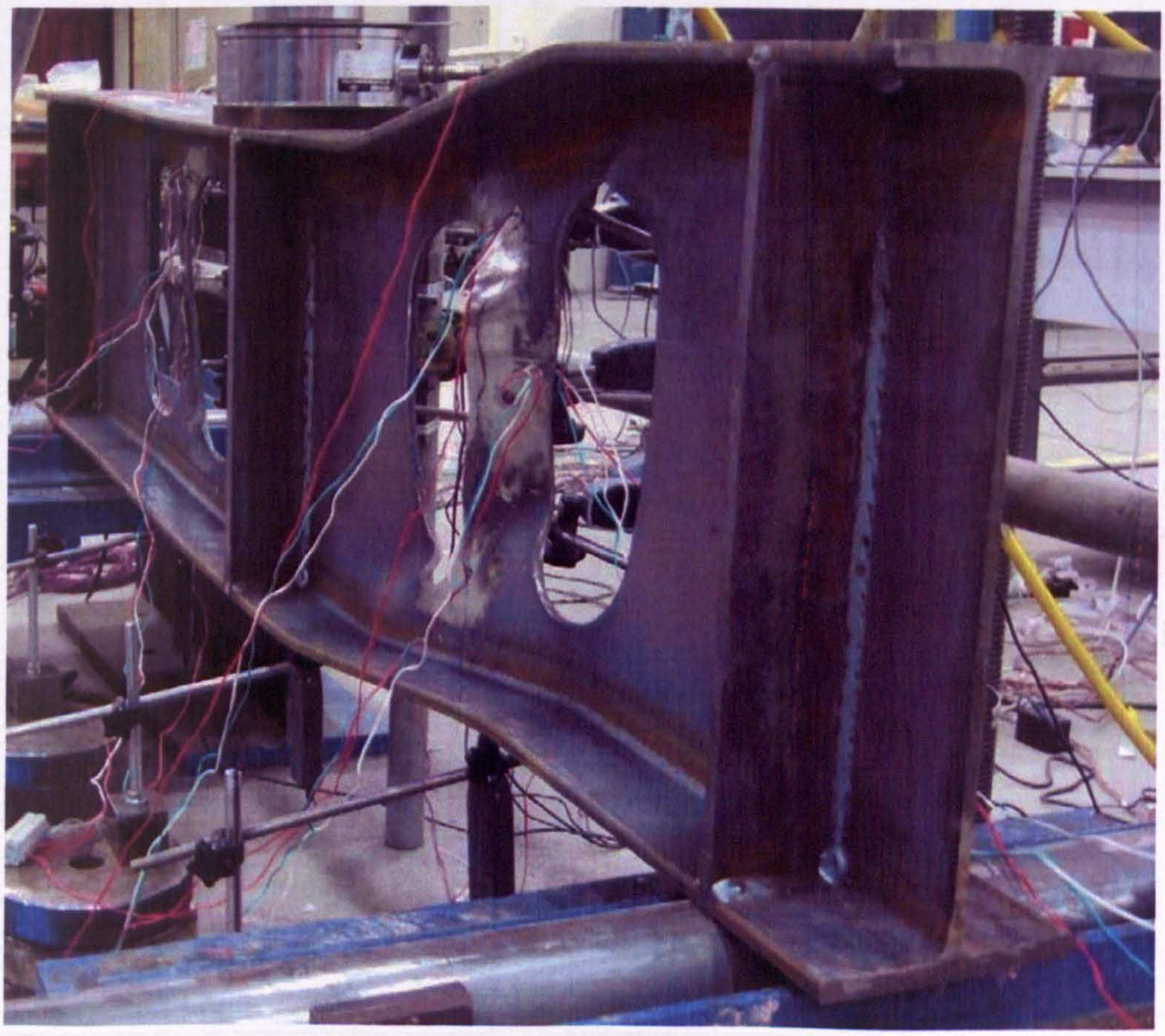

Figure 5.42: High yielding of compression area (Specimen B-4)

Specimen B-4

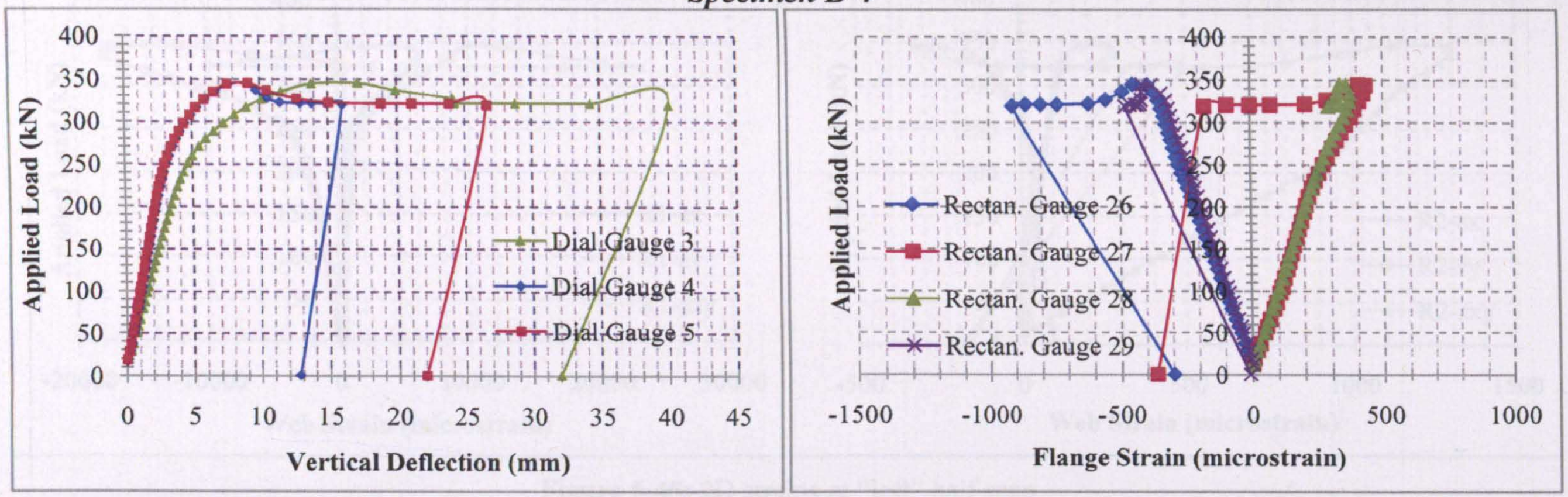

Figure 5.43: Vertical deflections along the bottom flange and flange strains at both half spans

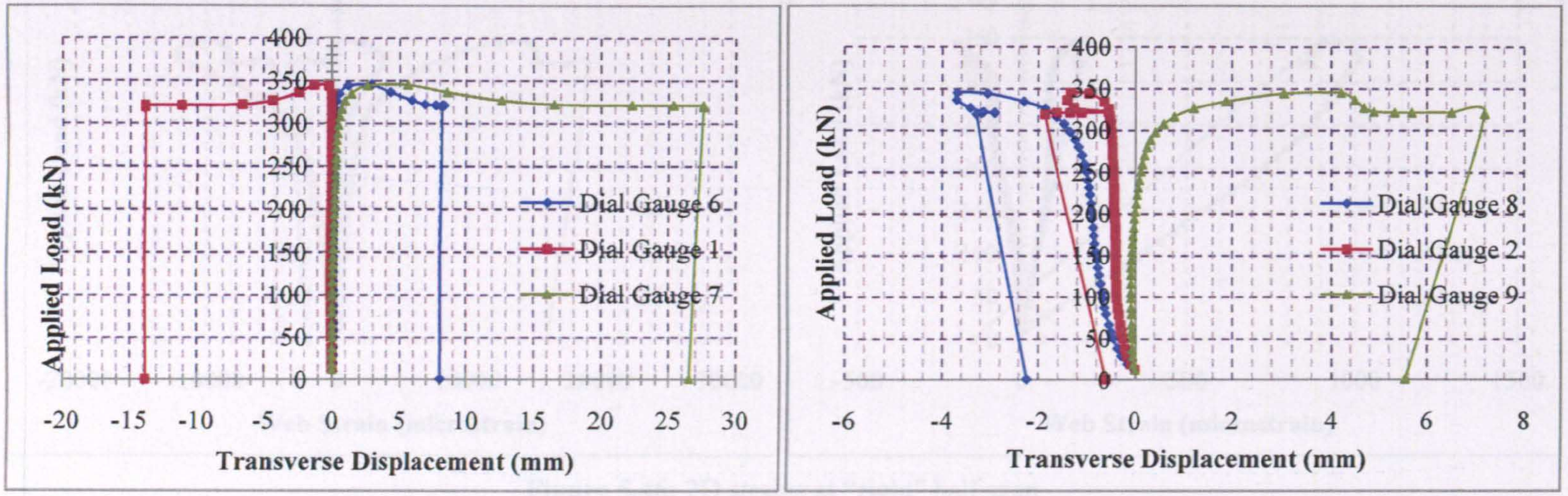

Figure 5.44: Web transverse displacements at "left" and "right" half spans

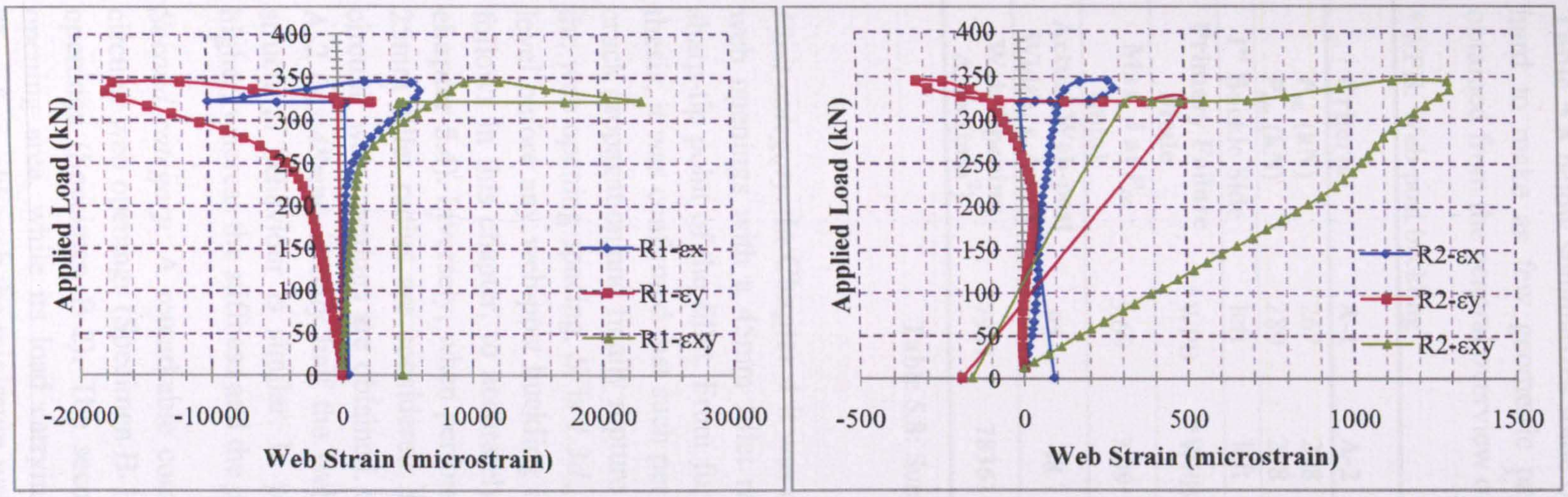

Figure 5.45: 2D strains at "left" half span

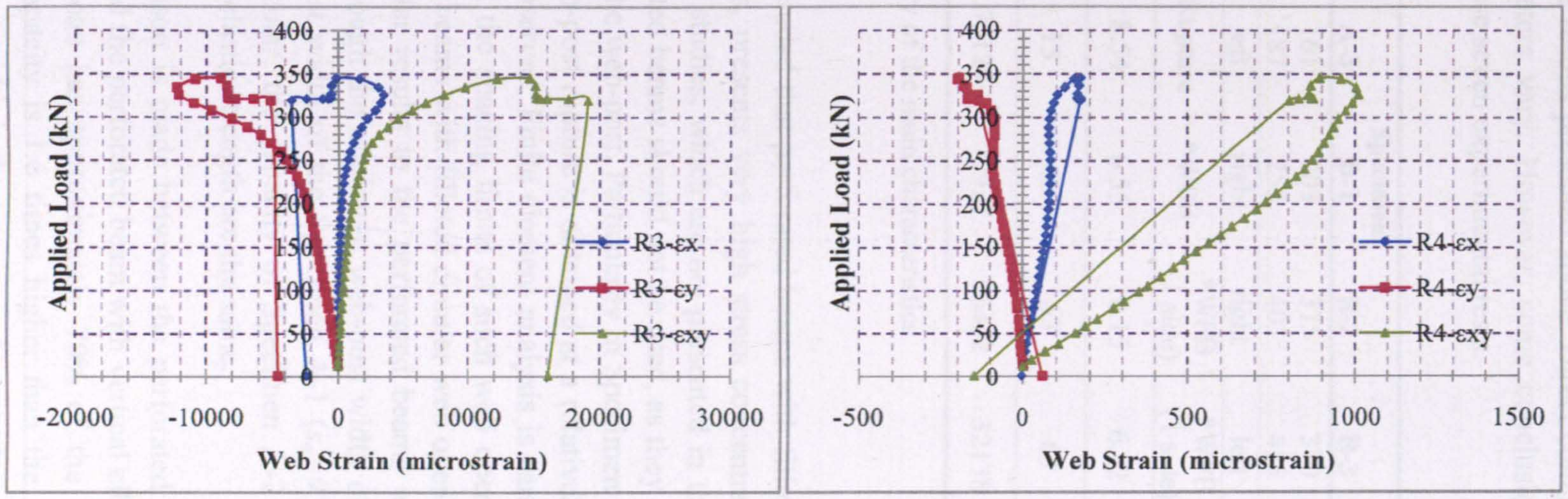

Figure 5.46: 2D strains at "right" half span

5.2.6 Summary of test results

Table 5.8 below summarizes some of the results presented above. Direct comparisons are hard to make as few geometric parameters vary. However, some conclusions can be obtained from the general overview of these seven experimental tests.

*WPB: Web-post buckling

	Specimen						
Criteria	**A-1**	**A-2**	**A-3**	**B-1**	**B-2**	**B-3**	**B-4**
$P_{cr.}$ (kN)	267	298	161	203	375	370	290
$P_{ult.}$ (kN)	289	298	187	255	403	415	351
1st Buckle Side	left	left	left	right	right	left	left
Primary Failure Mode	*WPB	*WPB	Rupture	*WPB	*WPB (1 side)	*WPB (1 side)	*WPB (1 side)
Max. δ at $P_{cr.}$ (mm)	5.69	7.09	8.54	6.55	10.15	6.92	5.99
Actual Web-post Width, s_o (mm)	95	48	15	63	63	63	63
Web Opening Area (mm^2)	77931	78361	79129	77931	56452	32138	45383

Table 5.8: Summary of the main characteristics

First category: In **Chapter 4** it was concluded that perforated beams with filleted circular web openings with a 45mm fillet radius, presents very high stress concentration at the sharp-tip point of the fillet. From further studies, which are not presented in this research thesis, it was confirmed that such perforated beams should not be used, as they can initiate crack propagation and finally rupture of the web-post. Particularly in Specimen A-3, where the web opening spacing, S, is $1.3d_o$, web-post rupture is obtained at a relatively low load level before any web-post buckling is observed. Finite element analysis is carried out, as follows in this chapter, to accurately set the spacing limits of such web openings (**sub-chapter 5.4**). Inversely, when perforated beams with filleted circular web openings with a 25mm fillet radius are considered, similar results to the perforated beams with typical circular web openings are obtained. Although the minimum web-post width of Specimen A-2 (s_o=*48mm*) is only half the web-post width of the Specimen A-1 (s_o=*95mm*), their structural behaviour is similar. In particular, the capacity of Specimen A-2 is slightly higher, whereas the stiffness and the post-elastic strength are the same.

Second category: A remarkable comparison is made between the perforated beam with circular web openings (Specimen B-1) and the perforated beam with vertical elliptical web openings (Specimen B-2). The second one has approximately 70% of the first's web opening area, while its load carrying capacity is 1.6 times higher than the first's one. Therefore, although the minimum web-post width is the same (s_o=*63mm*), the angle of the strut line (i.e. buckling line) is rotated towards the horizontal direction in the Specimen B-

2, because of the new shape of the web-post and thus it gains stiffness. Similarly in Specimen B-3 and B-4, the strut line is rotated dependent on the position of the sharp corners at the edge of the web openings (**Figure 5.48**). It should be remarked, that all perforated beams with the novel elliptical web openings behave asymmetrically to the mid-span, with only one side to be fully distorted by web-post buckling. The reason for this behaviour is the enhanced stiffness of the new web-posts between elliptical web openings, as buckling is now taking place at high load level points. Hence, as the beam is loaded and deflected, the load is not applied perfectly transverse to the top flange, by the time of buckling occurs. Therefore, when one web-post loses its stiffness, it is more vulnerable and begins to distort dramatically, while the other side is not yet affected.

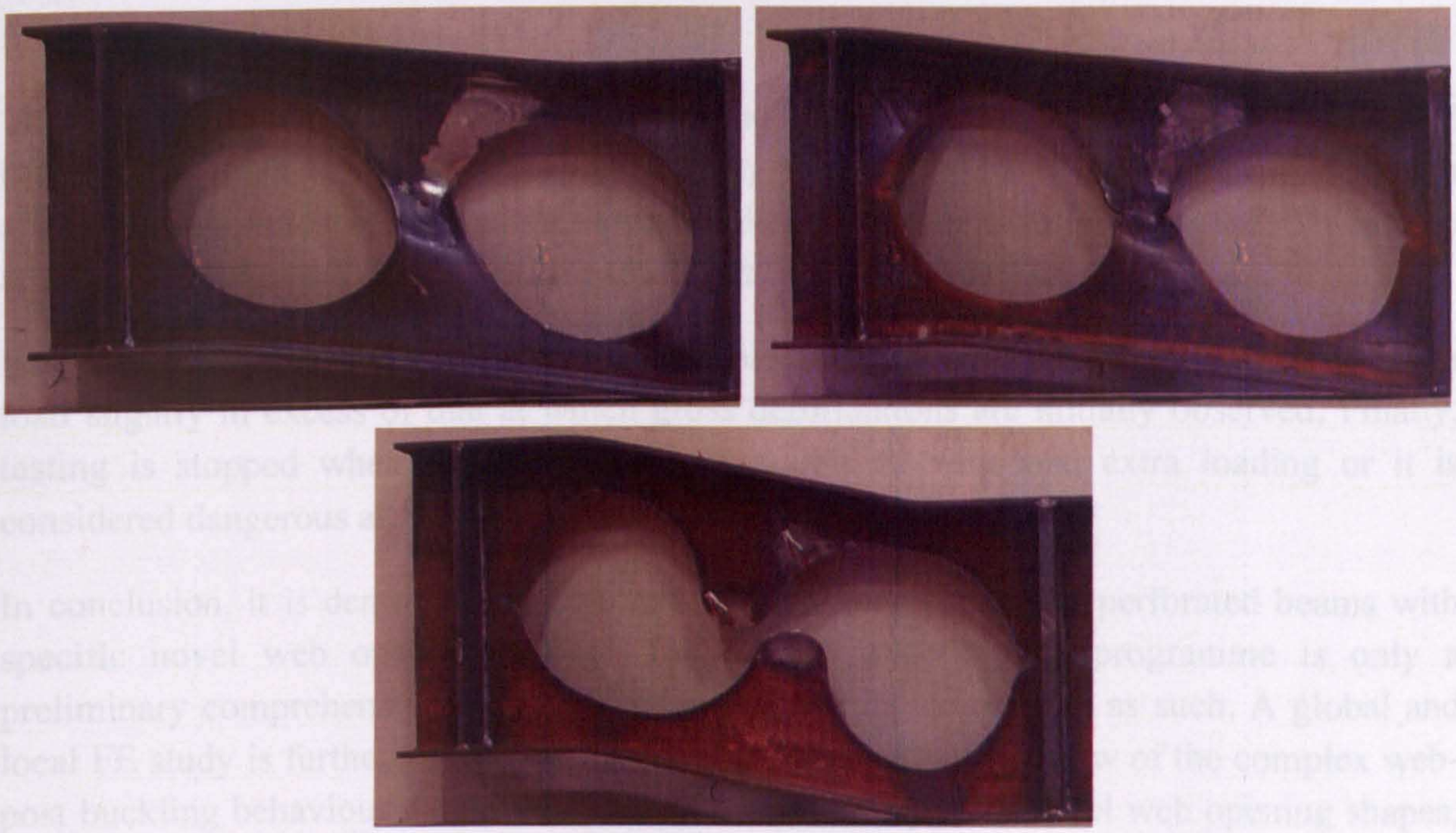

Figure 5.47: Strut buckling lines of the web-posts for perforated beams with novel filleted circular web openings

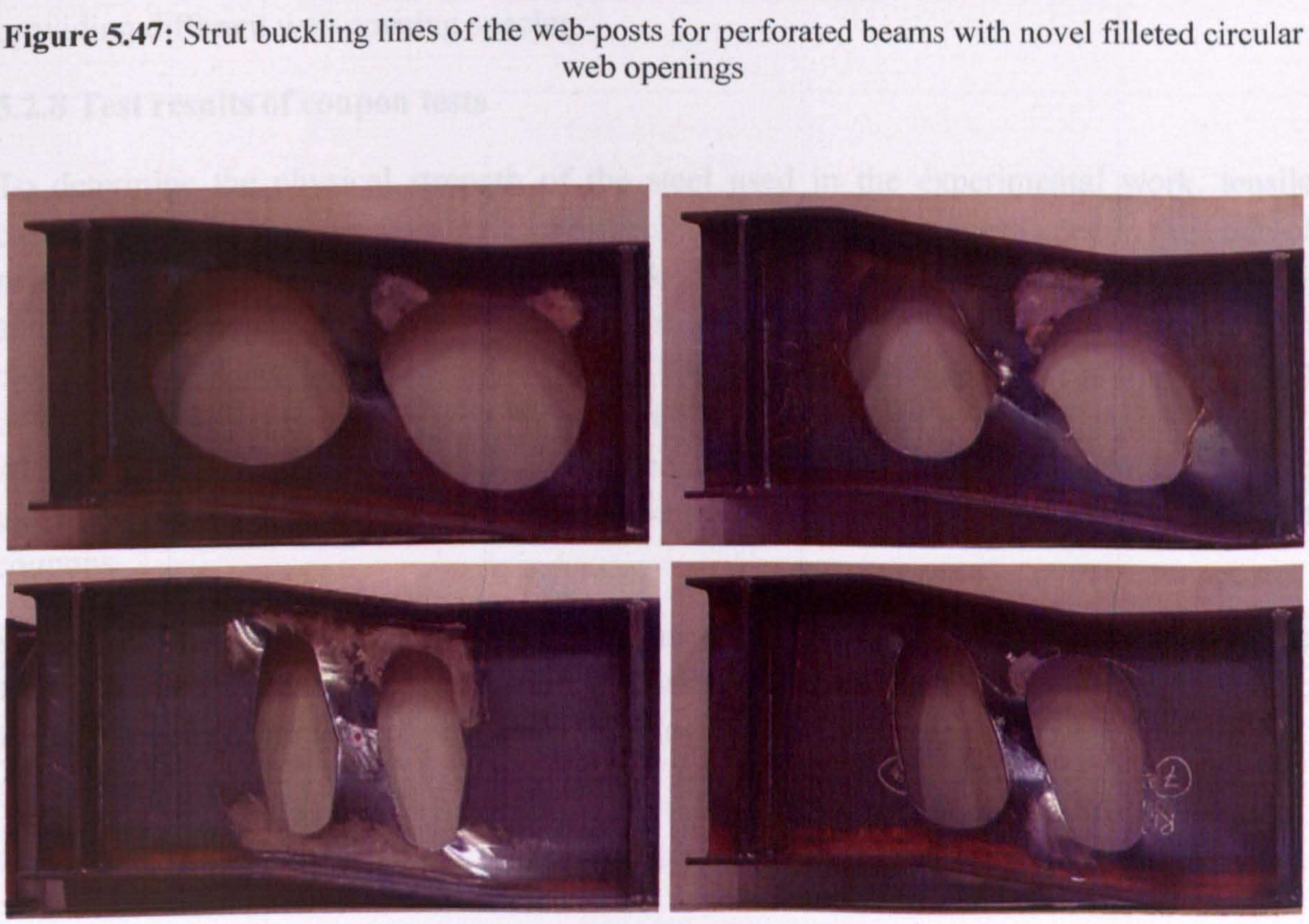

Figure 5.48: Strut buckling lines of the web-posts for perforated beams with novel elliptical web openings

5.2.7 Discussion of test results

The tests described, provide information on the elastic and plastic behaviour of perforated beams with various selected novel web opening shapes introduced in **Chapter 4**. Although a limited experimental programme is undertaken involving a single standard UB section and beam configuration, it is possible to draw a few preliminary conclusions.

Extensive yielding occurs at the web-post of all specimens. Web-post buckling occurs at a load slightly in excess of that at which gross deformations are initially observed. Finally, testing is stopped when the beam either is unable to withstand extra loading or it is considered dangerous as the beam is dramatically distorted.

In conclusion, it is demonstrated that similar behaviour occurs for perforated beams with specific novel web opening shapes. The present experimental programme is only a preliminary comprehensive investigation, and should be considered as such. A global and local FE study is further carried out, to acquire a more complete view of the complex web-post buckling behaviour for perforated beams with the specific novel web opening shapes, providing different web opening spacing.

5.2.8 Test results of coupon tests

To determine the physical strength of the steel used in the experimental work, tensile coupon tests are carried according to the specifications and guidelines stated in the code of practices (**BS EN 10002-1**). Coupons are taken from two un-yielded locations (one flange and one web) of four already tested steel beams. Eight tensile coupons are cut in total from the tested steel beams to compare the results. The samples are taken from the overhang part of the web, which is not stressed because of the bearing plate existence at the supports. Also, samples are taken from the un-yielded compression flange close to the mid-span. The yield and the ultimate stresses are determined by averaging the results obtained from the coupons.

Similar to **Chapter 4**, the shape and dimensions of coupons and the tensile testing machine are used. In **Figure 5.49** the load against extension curves for all the coupons are presented. and **Table 5.9** synopsizes the physical properties obtained from tension tests.

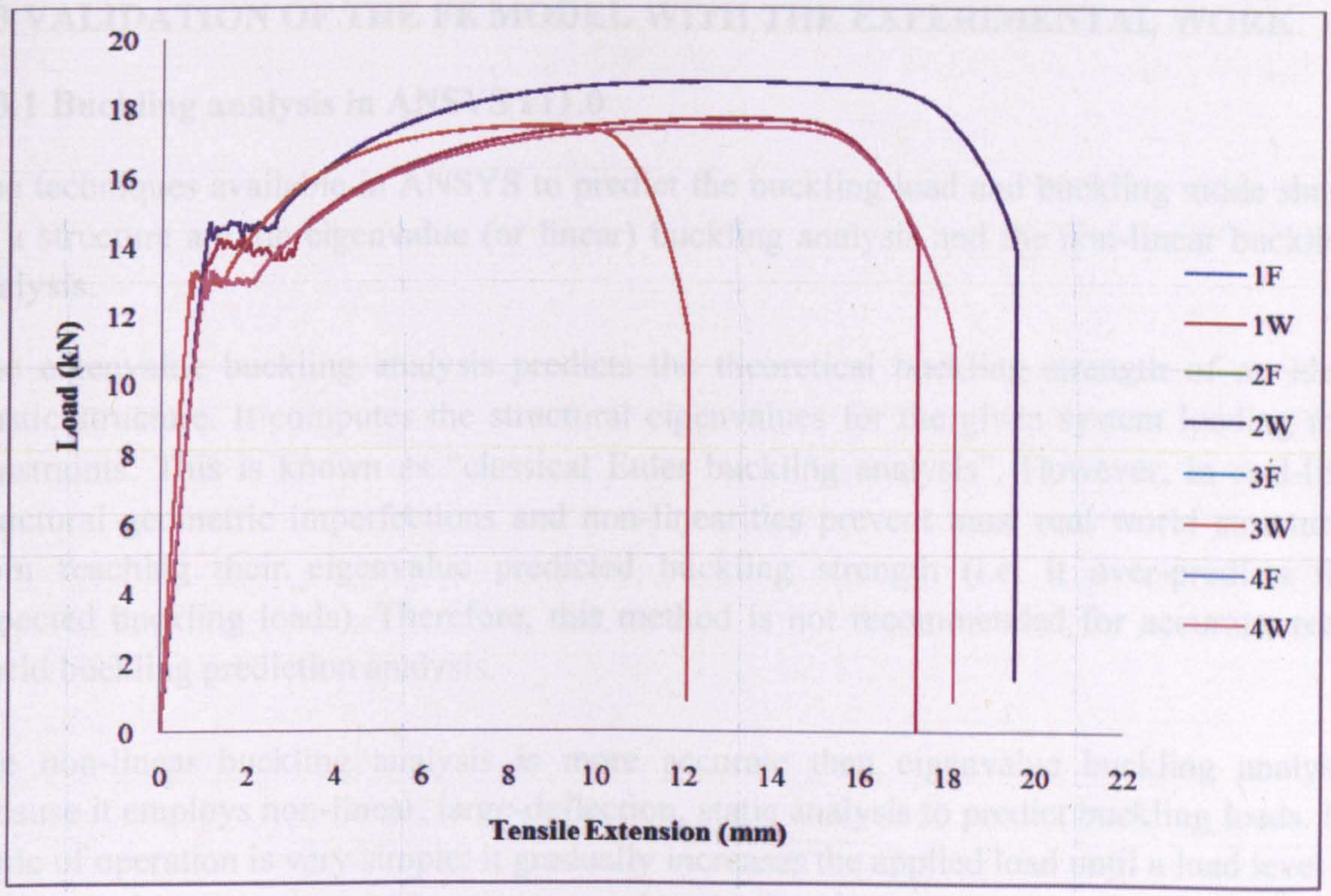

Figure 5.49: Load-extension curves for steel coupons

Tested Part of the Beam	Coupon from Specimen	Yield Strength f_y (MPa)	Tensile Strength $f_{ult.}$ (MPa)	Average Yield Strength f_y (MPa)	Average Tensile Strength $f_{ult.}$ (MPa)
Web	1	383.9	491.1	375.3	492.7
	2	395.9	516.3		
	3	361.2	480.1		
	4	360.0	483.4		
Flange and Bearing Plate	1	358.1	481.0	359.7	480.9
	2	361.8	481.8		
	3	355.8	477.8		
	4	363.0	483.1		

Table 5.9: Measured material physical properties

5.3 VALIDATION OF THE FE MODEL WITH THE EXPERIMENTAL WORK

5.3.1 Buckling analysis in ANSYS v11.0

The techniques available in ANSYS to predict the buckling load and buckling mode shape of a structure are the eigenvalue (or linear) buckling analysis and the non-linear buckling analysis.

The eigenvalue buckling analysis predicts the theoretical buckling strength of an ideal elastic structure. It computes the structural eigenvalues for the given system loading and constraints. This is known as "classical Euler buckling analysis". However, in real-life, structural geometric imperfections and non-linearities prevent most real world structures from reaching their eigenvalue predicted buckling strength (i.e. it over-predicts the expected buckling loads). Therefore, this method is not recommended for accurate, real-world buckling prediction analysis.

The non-linear buckling analysis is more accurate than eigenvalue buckling analysis because it employs non-linear, large-deflection, static analysis to predict buckling loads. Its mode of operation is very simple: it gradually increases the applied load until a load level is found whereby the structure becomes unstable (i.e. suddenly a very small increase in the load will cause very large deflections). The true non-linear nature of this analysis thus permits the modelling of geometric imperfections, load perturbations, material nonlinearities and gaps. For this type of analysis, note that small eccentric loads are necessary to initiate the desired buckling mode.

According to **Figure 5.50**, the buckling load calculated from an eigenvalue buckling analysis is higher than the actual buckling load (blue line in **Figure 5.50**). The simple non-linear buckling analysis provides a better estimation of the real behaviour of the beam, when the load is applied correctly (black line in **Figure 5.50**). For better understanding of this method of analysis a preliminary FE step-by-step buckling study simulating an experiment, is provided in **Appendix 12**.

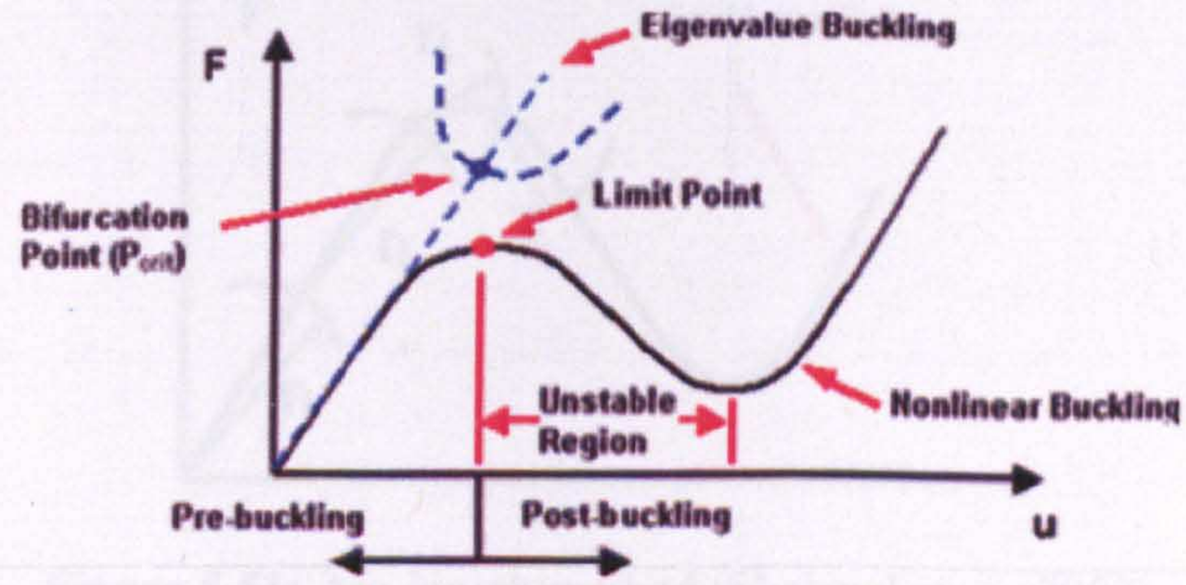

Figure 5.50: Eigenvalue against non-linear analysis (Beck and Depaillet, 2008)

In this research programme, perfect FE models are utilised, thus both the above FEA buckling methodologies needed to be carried out in order to obtain accurate, real-world results. The outcome of this research study is compared to the experimental work conducted before, and the measurements are used as a reference for future studies. The methodology simulating the real buckling behaviour of perforated beams is described as follows:

Initially, a static linear buckling analysis is performed, then an eigenvalue buckling analysis is conducted and finally a more reliable non-linear buckling analysis is implemented by using the scaled results from the previous eigenvalue buckling analysis. Eigenvalue buckling provides a "classical" solution to a buckling problem, but the critical load determined is un-conservative. However, an estimation of the critical load to induce buckling, as well as various buckling mode shapes can be obtained as they are of interest. In the eigenvalue buckling analysis settings, four buckling mode shapes are chosen to verify whether or not there is a possibility of multiple buckling mode shapes being triggered (e.g. **Figure 2** in **Appendix 12**). Thereafter, the lowest buckling mode shape is extrapolated to vector-loads, scaled (the same scale factor is always used), and applied on the highly stressed nodes (e.g. **Figure 3** in **Appendix 12**) to generate the initial out-of-plane web movement in the following non-linear buckling analysis. It should be noted that when the model is non-converged, near the point of geometric instability, ANSYS bisects the solution until the maximum number of sub-steps is reached and the solution is converged.

As the post-buckling behaviour is also of interest, one of the following different techniques should be used. If the loading is not displacement-controlled, calculating the response past the buckling point is typically not a problem. Hence, a quasi-static analysis by including inertial effects (i.e. transient analysis), an arc-length method (**Figure 5.51**) or the non-linear stabilization technique introduced in ANSYS v11.0 should be implemented. The arc-length method is found to be the most suitable and used for this web-post buckling study.

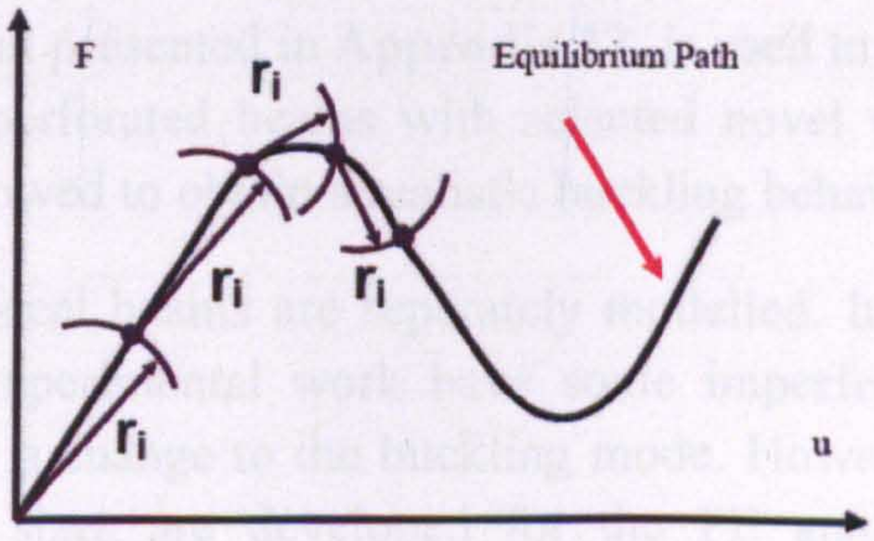

Figure 5.51: Arc-length method (Shahzad et al., 2007)

5.3.2 Theory of linear (eigenvalue) buckling analysis followed by ANSYS

A linear buckling analysis is an eigenvalue problem and is formulated as follows:

$$([K] + l_{cr}[K_g])\{d\} = \{0\}$$

Where:
- *[K]* is the stiffness matrix
- l_{cr} is the eigenvalue for buckling mode.
- $[K_g]$ is the stress stiffness matrix. This matrix includes the effects of the membrane loads on the stiffness of the structure. The stress stiffening matrix is assembled based on the results of a previous linear static analysis.
- *{d}* is the displacement vector corresponding to the buckling mode shape.

The eigenvalue solution uses an iterative algorithm that extracts firstly the eigenvalues (l_{cr}) and secondly the displacements that define the corresponding mode shape (*{d}*). One set of these is extracted for each of the buckling modes of the structure (up to the user specified limit). It should be noted that the displacements given by the solution are not real displacements in the normal sense. They are simply a set of scaled values used solely for display purposes. The eigenvalue represents the ratio between the applied loads and the buckling loads. This can be expressed as follows:

$$l_{cr} = Buckling\ Load/Applied\ Load$$

The ANSYS postprocessor gives the buckling load as buckling load factor. For convenience sake, pressure load with unit intensity is applied. The result would then indicate the buckling load multiplied by unity. (Naeem-ur-Rehman and Muhammad Tanweer Khan, 2008)

5.3.3 FE model

A FE model, similar to that presented in **Appendix 12,** is used to simulate the experimental work conducted on the perforated beams with selected novel web opening shapes. The same methodology is followed to obtain a realistic buckling behaviour.

The seven experimental steel beams are separately modelled. It should be noted that the specimens used in the experimental work have some imperfections in their geometry, which can possibly cause a change to the buckling mode. However, perfect models based on the nominal section sizes are developed for the FE analyses. SHELL181 plastic elements used with an average size of 20mm in the vicinity of the web openings. Particularly in Specimen A-2 and A-3, significantly smaller triangular elements are

incorporated in the vicinity of the fillets for the ease of meshing, providing better stress distribution.

In case only the Newton-Raphson method is used, the tangent stiffness matrix becomes singular (or non-unique), causing severe convergence problems. For such cases, the arc-length method is activated to help avoid bifurcation points and track unloading (**Figure 5.50** and **5.51**). The load is applied directly to the compression flange through seven point loads on nodes. It is ensured from the experimental work that the load is transferred only via the bearing plate at the web, as an eccentric load could cause local buckling at the edges of the web openings close to the point load.

'Block Lanczos' extraction method is selected with four extracted modes for the eigenvalue buckling analyses. The 'Block Lanczos' method is used for large symmetric eigenvalue problems and it uses the sparse matrix solver. This method tends to converge fast, however in more complex analyses the 'Block Lanczos' method may not be adequate and the 'Subspace' method would have to be used. Furthermore, updating the geometry by some percentage of strain after the eigenvalue buckling analysis, the initial vector-loads with maximum amplitude of $t_w/200= 7.6/200=0.038$ are taken into account.

5.3.4 Model correlation

A non-linear (material and geometric) elasto-plastic analysis is conducted to compare and validate the FE model of the steel beam with the experimental test conducted earlier. The FE models are constructed similarly to those in **Chapter 3** and **4**. The key-points are summarized as follows:

- Linear elastic properties of the steel are assumed as 200GPa and 0.3 for Young's Modulus and Poisson's Ratio, respectively.
- Modelling the plastic properties, the averaged values taken from coupon tests (**Table 5.9**) are used such as Multi-linear Isotropic Model (MISO) with two branches (i.e. f_y and $f_{ult.}$). In addition to that, the nominal material properties are used (i.e. $f_y=355MPa$) and comparison is made possible.
- When nominal (idealized curve) and physical (actual curve) properties are used, various Tangent Modulus values are also examined in order to obtain different possible behaviour at the post-elastic region and to cover a range of potential E_T values that could have been evaluated from each particular specimen. Tangent Modulus is taken either as 2, 580 or 2000MPa. The comparison between the actual and the idealized stress-strain curves is depicted in **Figure 5.52**.
- The nominal dimensions of the beam taken from Corus are used, while the real dimensions of the UB section are found to be slightly different when measured in the laboratory before the test.

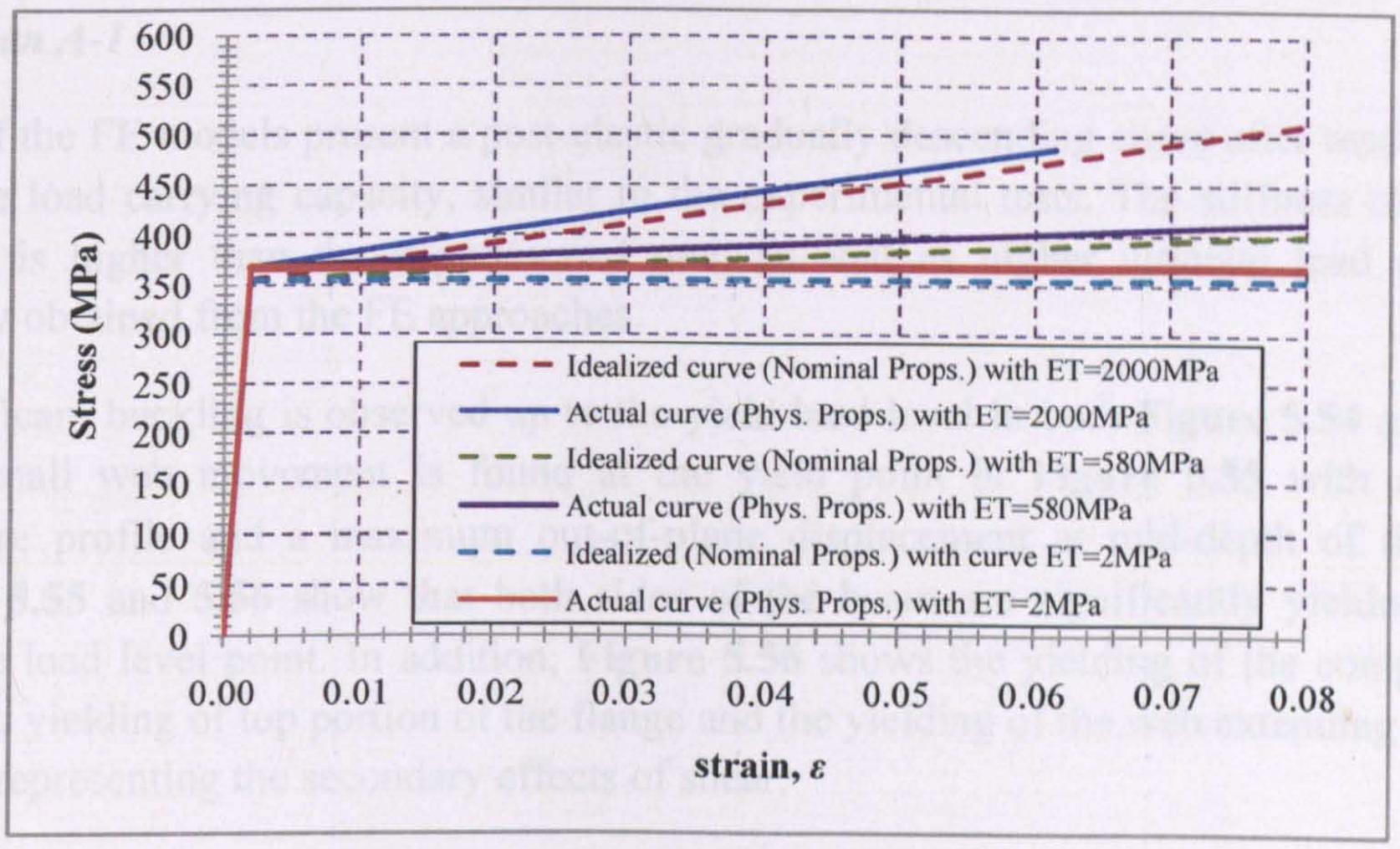

Figure 5.52: Idealized bi-linear stress-strain curves of the steel material used in ANSYS

5.3.5 FE results

The loads against the mid-span defections are separately presented for every perforated beam. Maximum out-of-plane web displacements at the positions of the dial gauges (i.e. maximum displacements between the left and right side), out-of-plane web displacement profiles for yield and ultimate load level points as well as Von-Mises stress distribution with the failure mode shapes are also presented in sequence. In order to minimize the amount of data presented and for the ease of comparison, the FE model with nominal properties and a Tangent Modulus, E_T, equal to 580Mpa, is used as a reference model as it seems that better simulates the real behaviour in overall, and its results are presented in detail.

Specimen A-1

Most of the FE models present a post-elastic gradually descending curve after reaching the ultimate load carrying capacity, similar to the experimental tests. The stiffness of the FE models is higher than the experimental one, as well as higher ultimate load carrying capacity obtained from the FE approaches.

Insignificant buckling is observed up to the yield load level in both **Figure 5.54** and **5.55**. Very small web movement is found at the yield point in **Figure 5.55** with a single curvature profile and a maximum out-of-plane displacement at mid-depth of the web. **Figure 5.55** and **5.56** show that both sides of the beam are significantly yielded at the ultimate load level point. In addition, **Figure 5.56** shows the yielding of the compression area; the yielding of top portion of the flange and the yielding of the web extending into the flange, representing the secondary effects of shear.

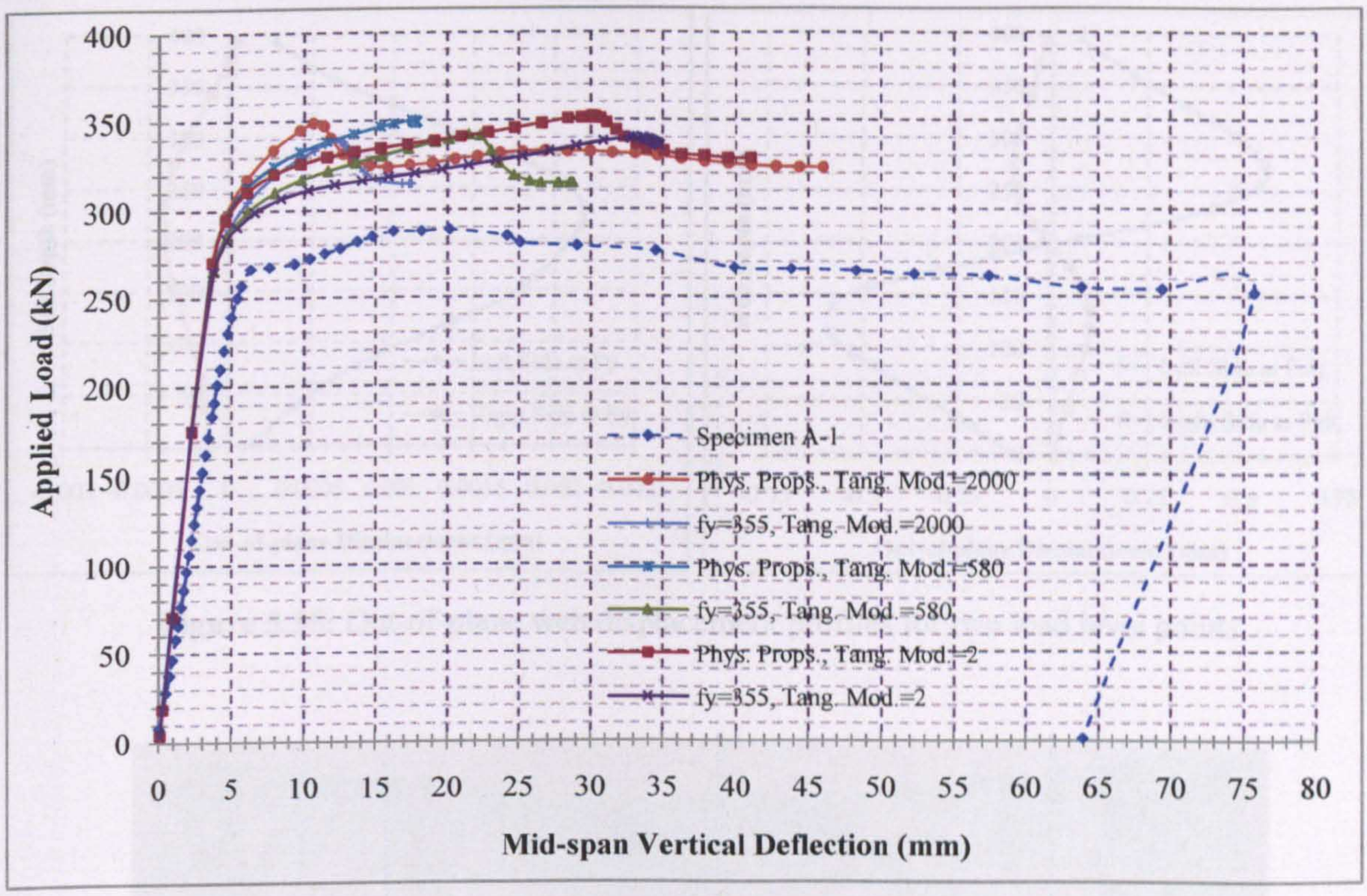

Figure 5.53: Experimental and FE load-deflection curves at mid-span

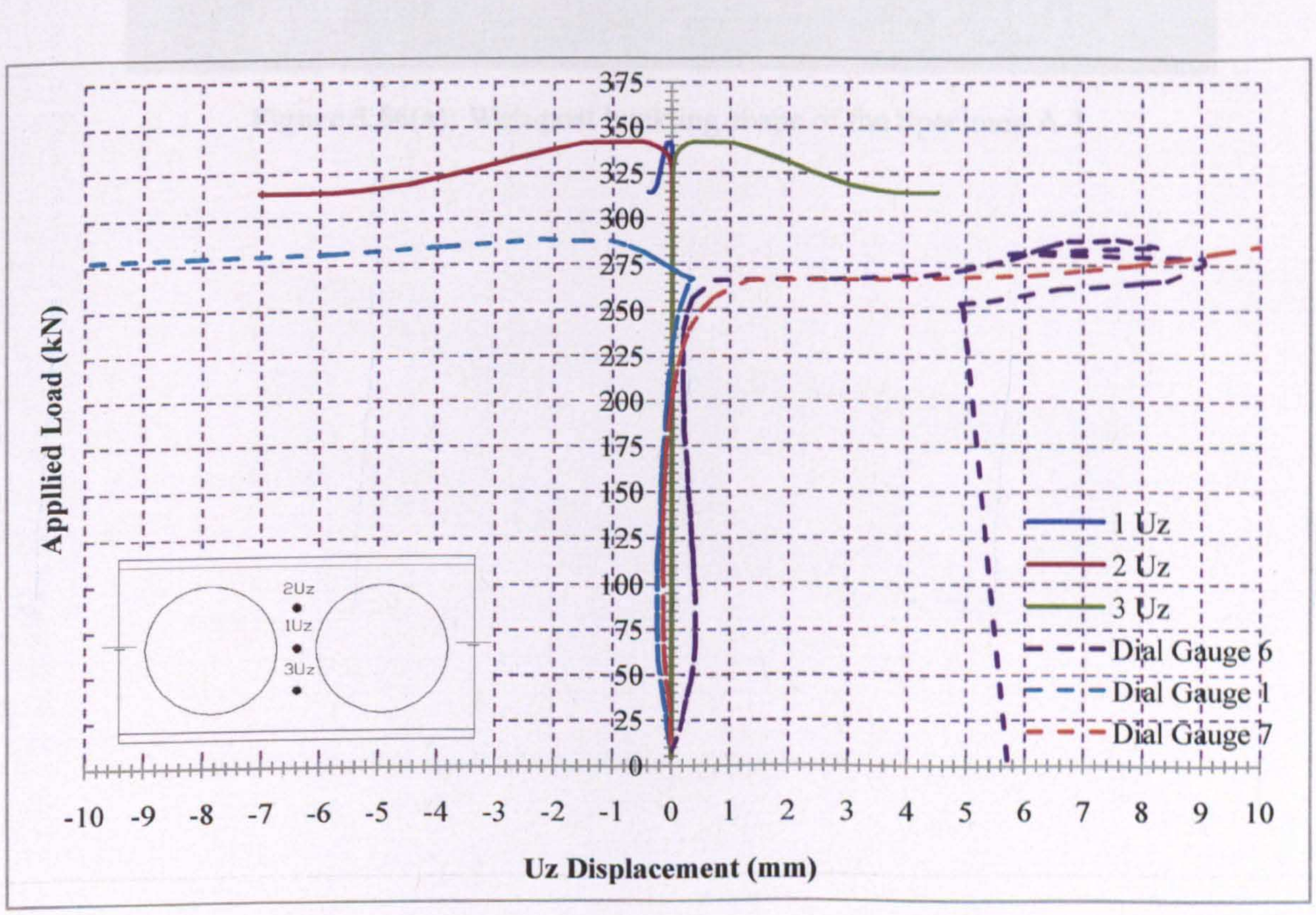

Figure 5.54: Maximum FE Uz web displacements at the positions of dial gauges

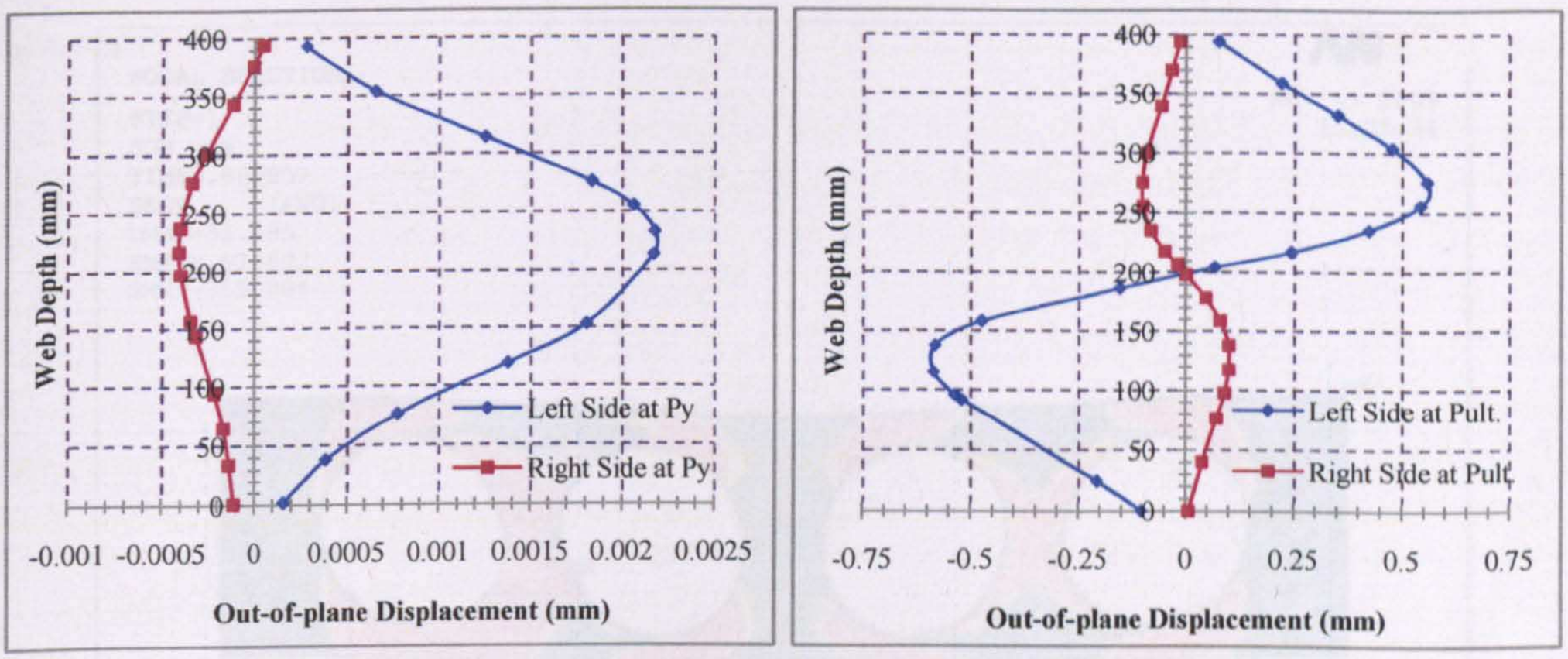

Figure 5.55: Out-of-plane web displacement profiles for two load level points

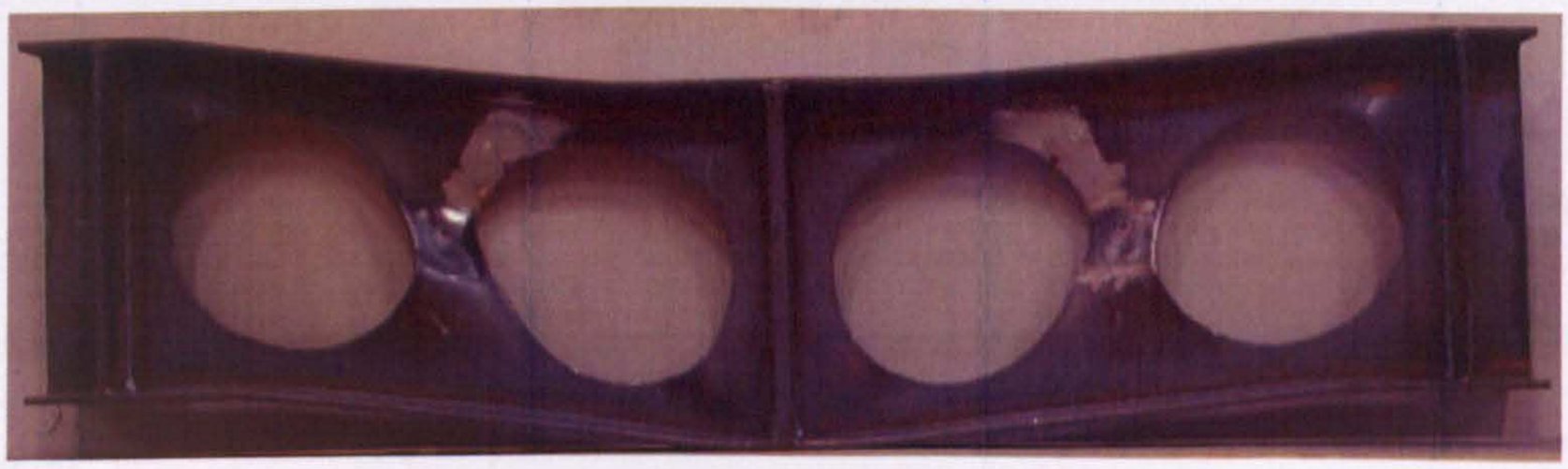

Figure 5.56(a): Web-post buckling shape of the Specimen A-1

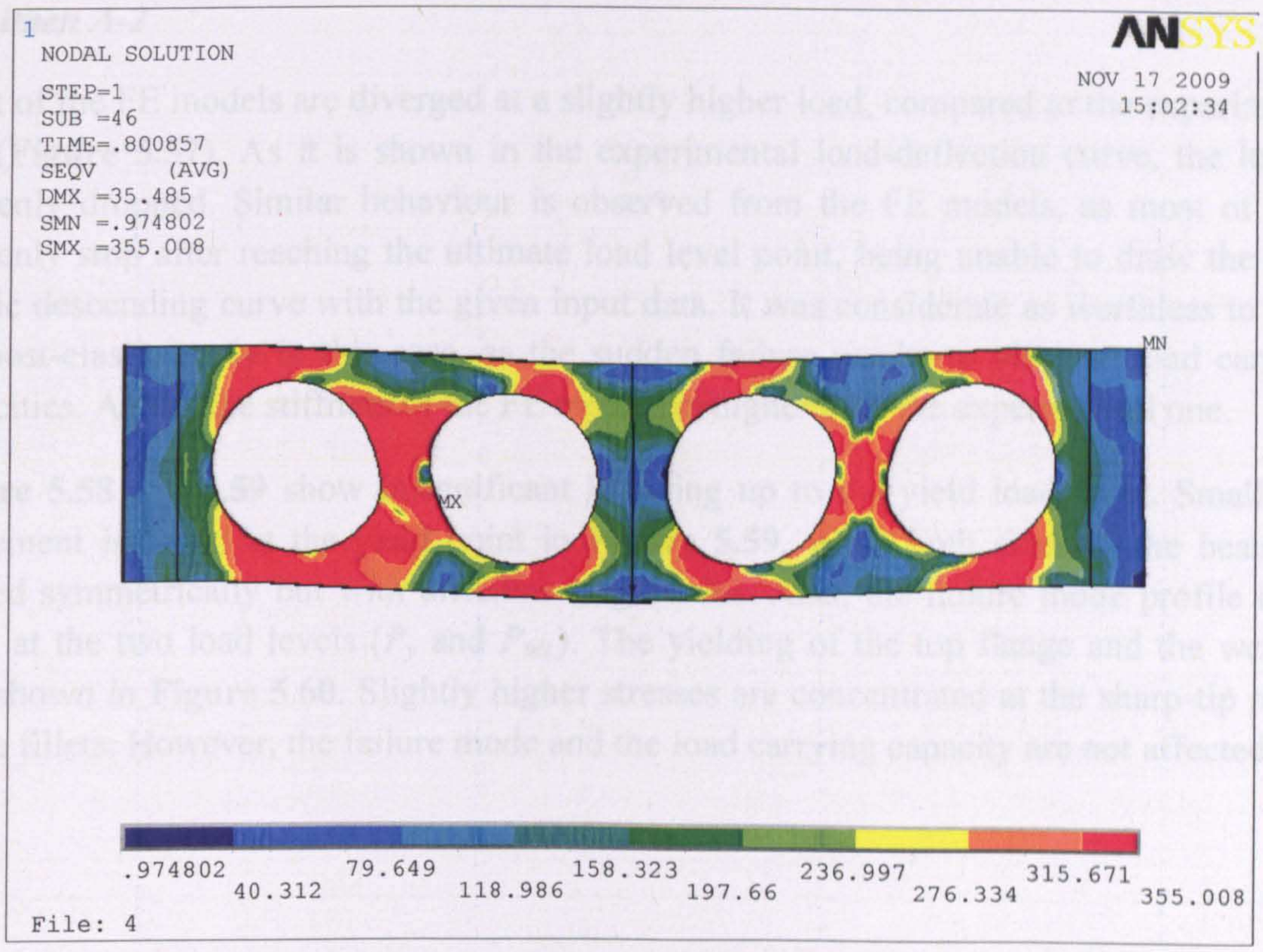

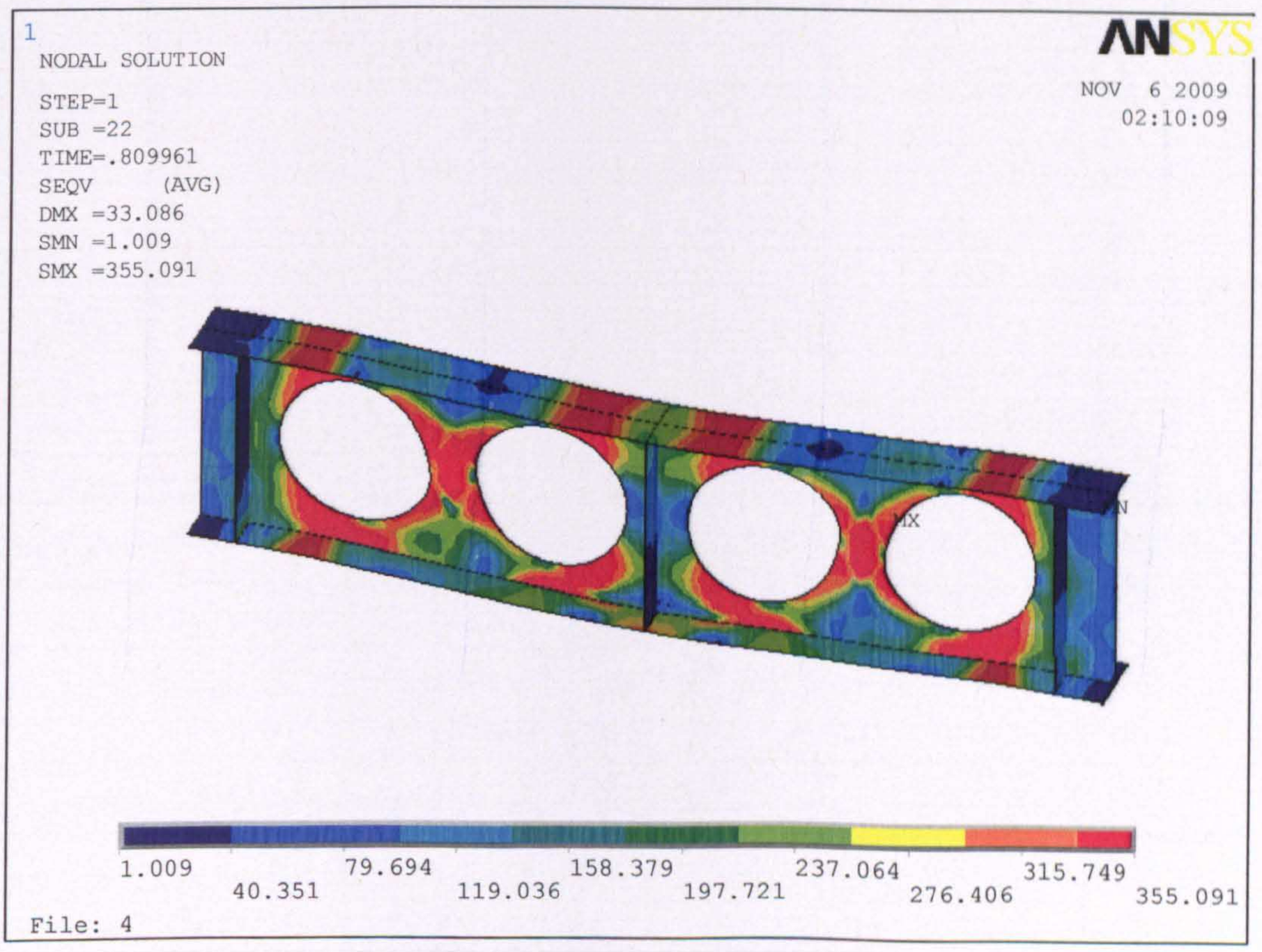

Figure 5.56(b): Von-Mises stresses in the Specimen A-1

Specimen A-2

Most of the FE models are diverged at a slightly higher load, compared to the experimental one (**Figure 5.57**). As it is shown in the experimental load-deflection curve, the load is suddenly dropped. Similar behaviour is observed from the FE models, as most of them suddenly stop after reaching the ultimate load level point, being unable to draw the post-elastic descending curve with the given input data. It was considerate as worthless to track the post-elastic curve in this case, as the sudden failure results to ultimate load carrying capacities. Again, the stiffness of the FE models is higher than the experimental one.

Figure 5.58 and **5.59** show insignificant buckling up to the yield load level. Small web movement is found at the yield point in **Figure 5.59**, while both sides of the beam are moved symmetrically but with different magnitudes. Also, the failure mode profile is the same at the two load levels (P_y and $P_{ult.}$). The yielding of the top flange and the web are also shown in **Figure 5.60**. Slightly higher stresses are concentrated at the sharp-tip points of the fillets. However, the failure mode and the load carrying capacity are not affected.

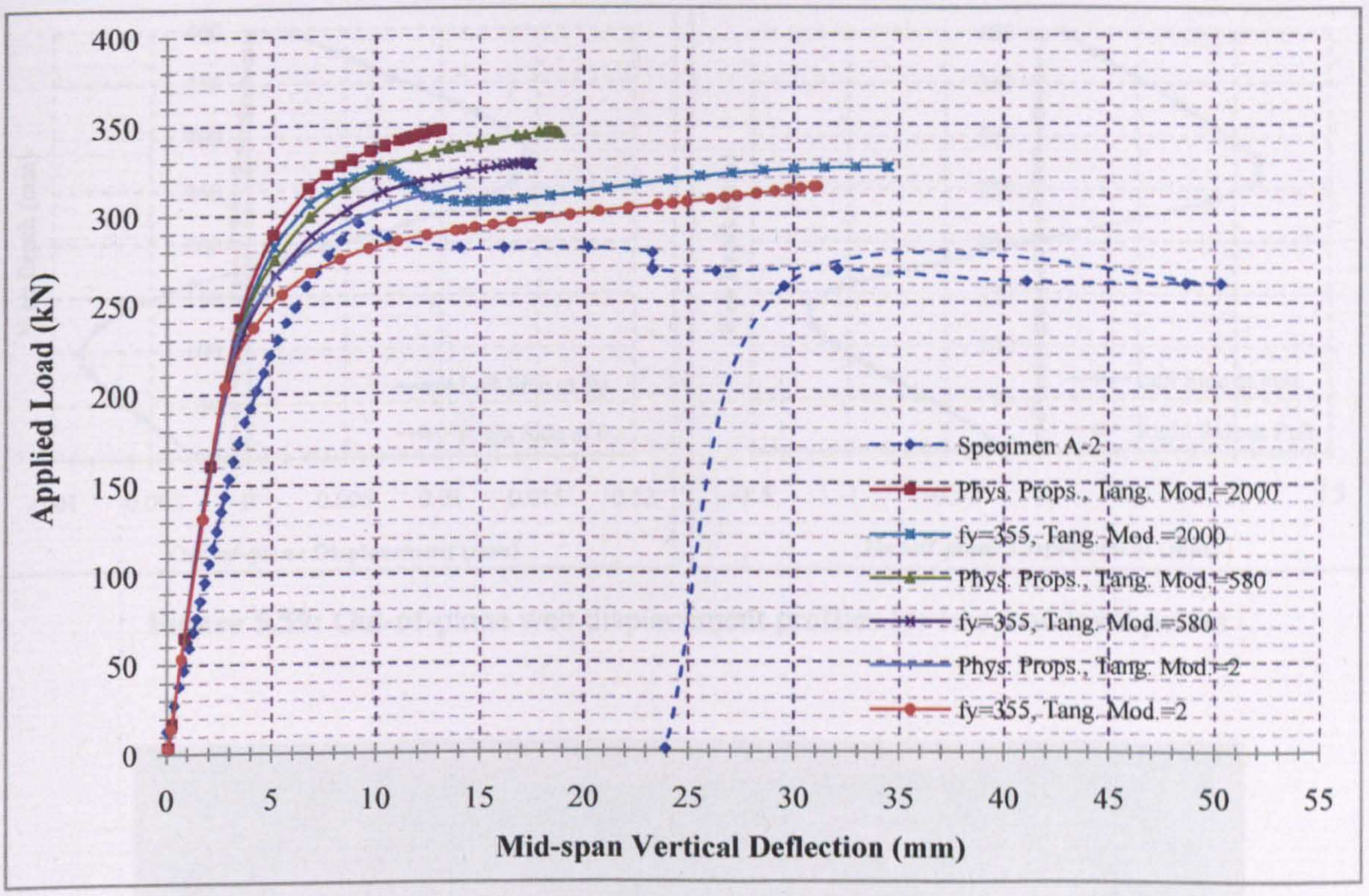

Figure 5.57: Experimental and FE load-deflection curves at mid-span

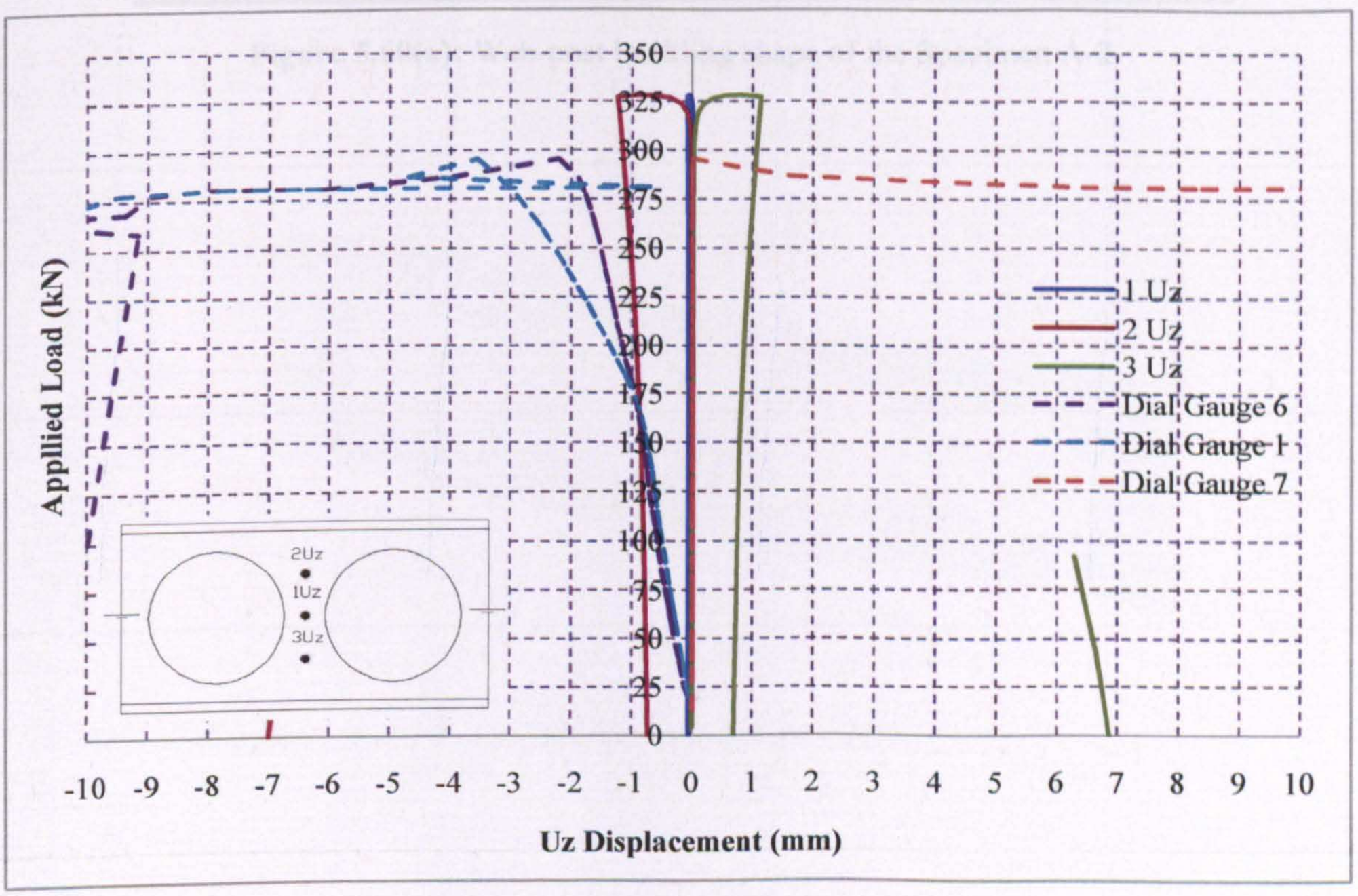

Figure 5.58: Maximum FE Uz web displacements at the positions of dial gauges

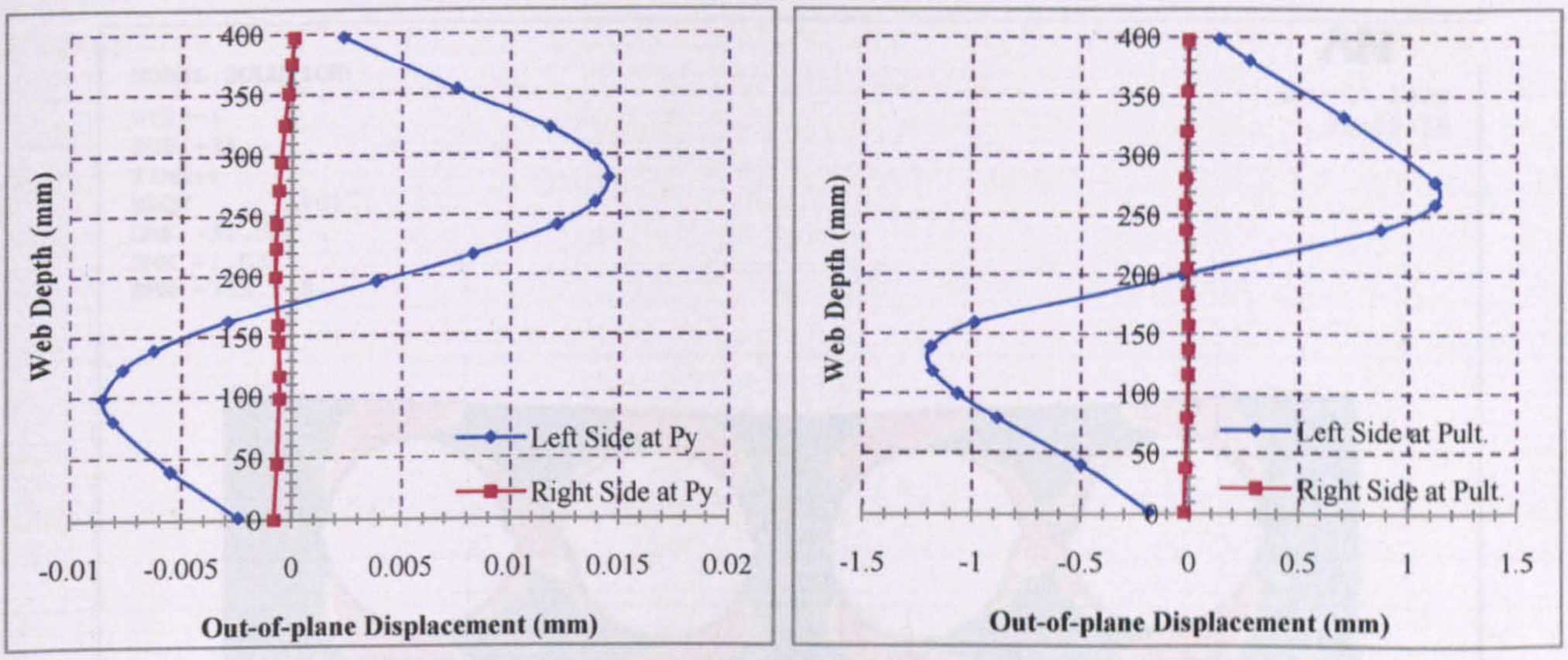

Figure 5.59: Out-of-plane web displacement profiles for two load level points

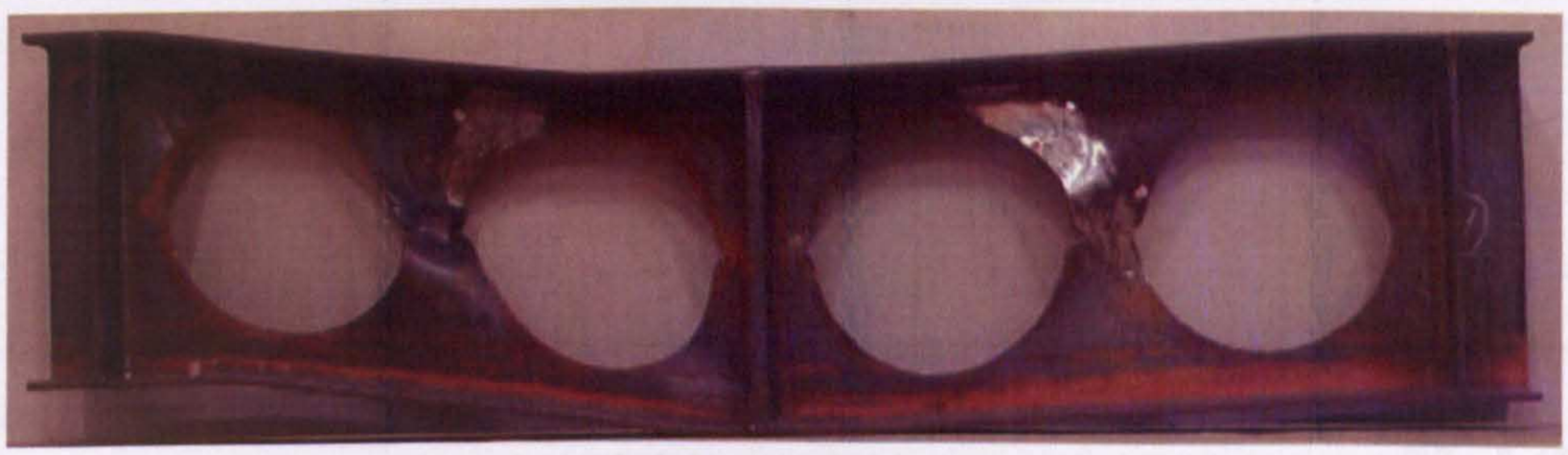

Figure 5.60(a): Web-post buckling shape of the Specimen A-2

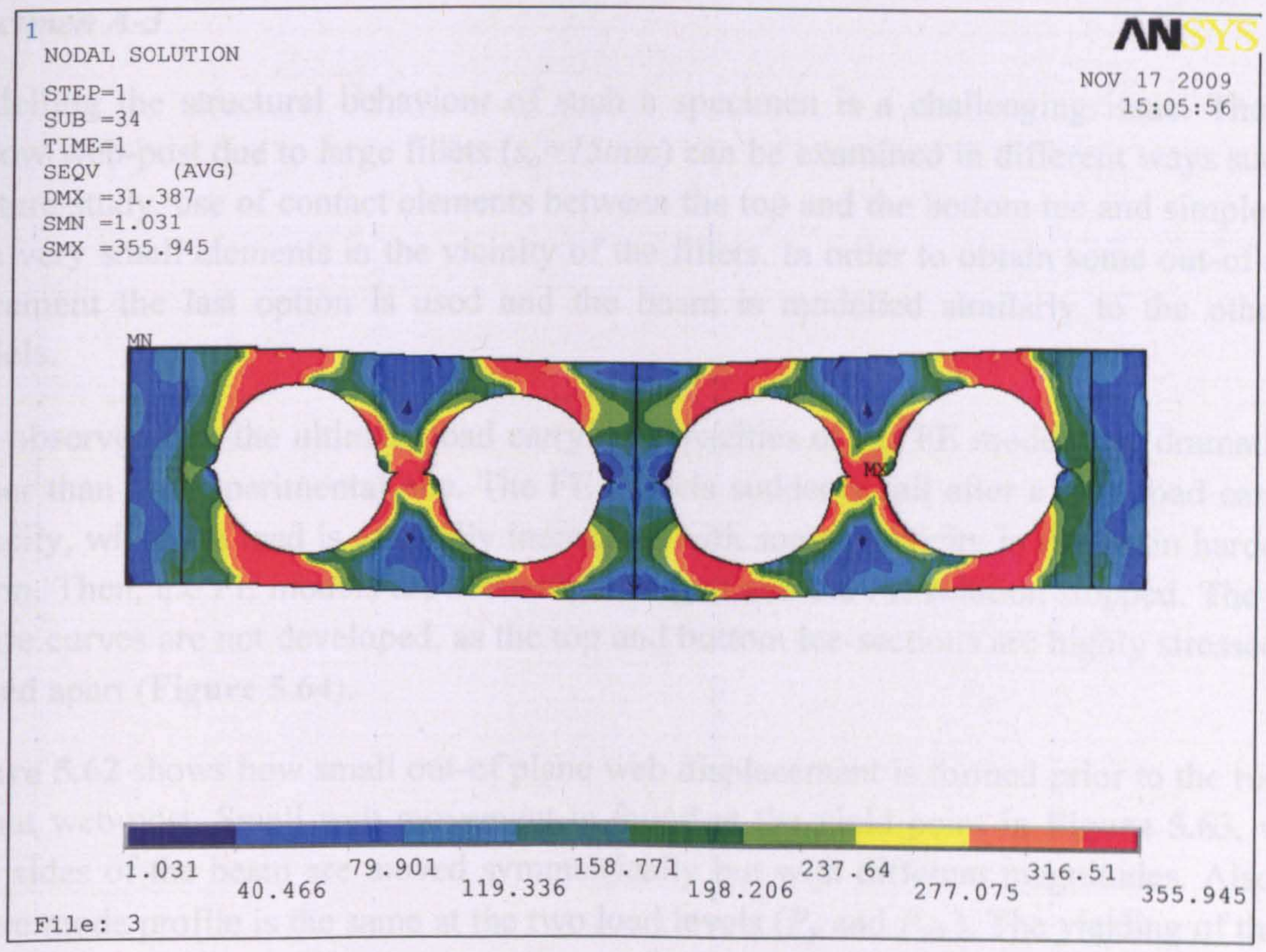

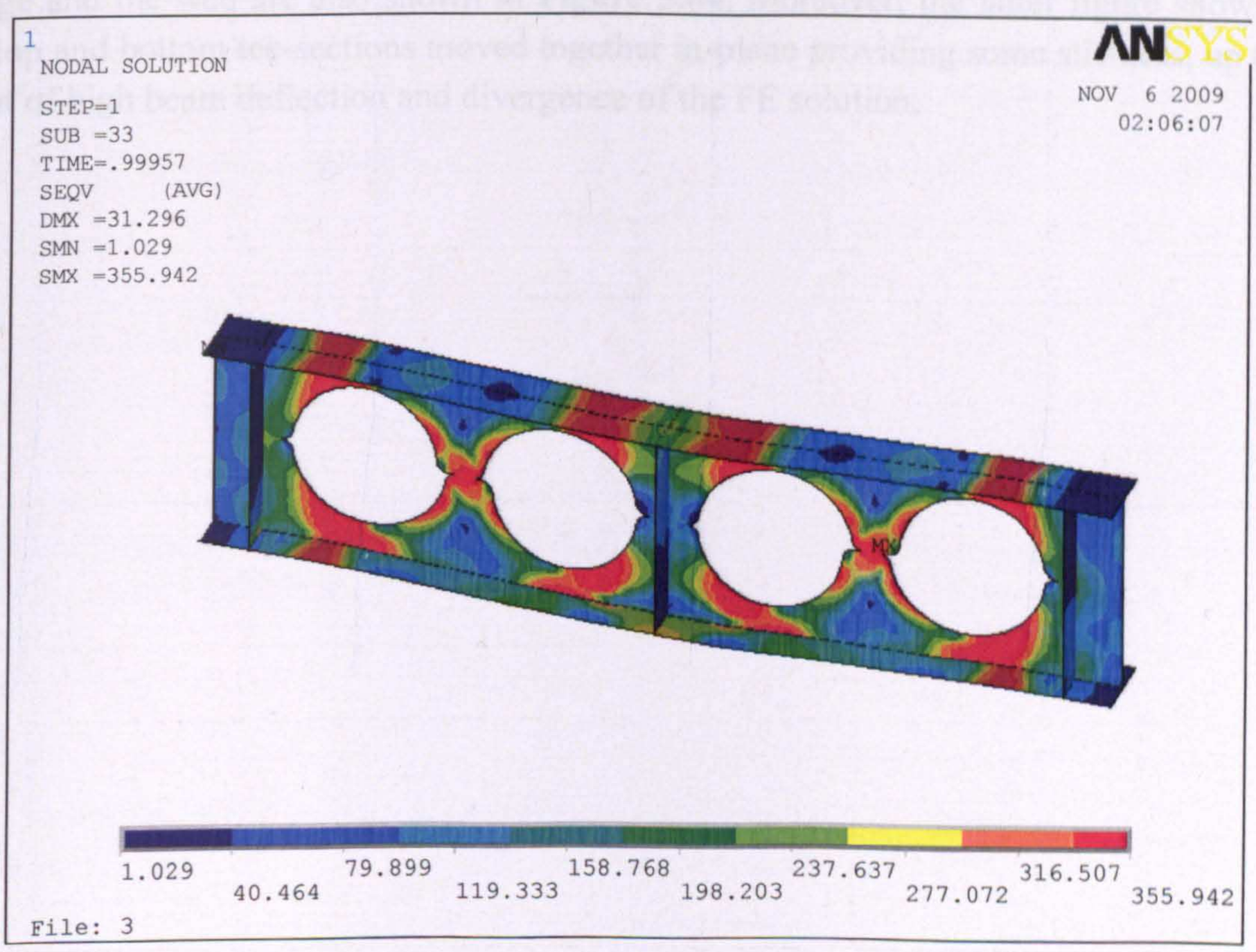

Figure 5.60(b): Von-Mises stresses in the Specimen A-2

Specimen A-3

Modelling the structural behaviour of such a specimen is a challenging issue. The very narrow web-post due to large fillets (s_o=*15mm*) can be examined in different ways such as: fracture study, use of contact elements between the top and the bottom tee and simple FEA with very small elements in the vicinity of the fillets. In order to obtain some out-of-plane movement the last option is used and the beam is modelled similarly to the other FE models.

It is observed that the ultimate load carrying capacities of the FE models are dramatically higher than the experimental one. The FE models suddenly fail after a high load carrying capacity, while the load is gradually increasing with some plasticity in the strain hardening region. Then, the FE models are suddenly diverged and the FE solution stopped. The post-failure curves are not developed, as the top and bottom tee-sections are highly stressed and moved apart (**Figure 5.64**).

Figure 5.62 shows how small out-of plane web displacement is formed prior to the rupture of that web-post. Small web movement is found at the yield point in **Figure 5.63**, while both sides of the beam are moved symmetrically but with different magnitudes. Also, the failure mode profile is the same at the two load levels (P_y and $P_{ult.}$). The yielding of the top flange and the web are also shown in **Figure 5.64**. Moreover, the latter figure shows that the top and bottom tee-sections moved together in-plane providing some stiffness, up to the point of high beam deflection and divergence of the FE solution.

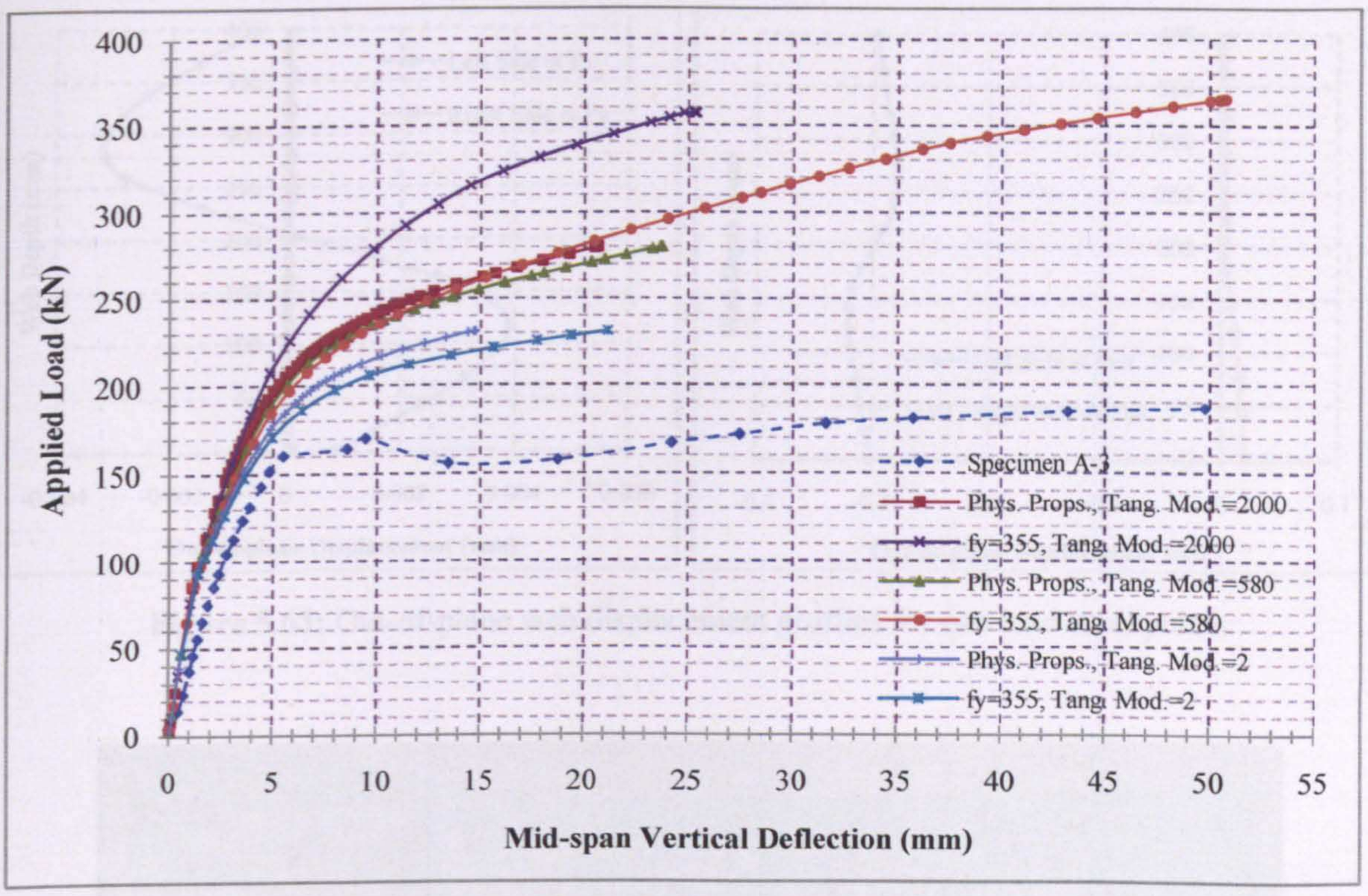

Figure 5.61: Experimental and FE load-deflection curves at mid-span

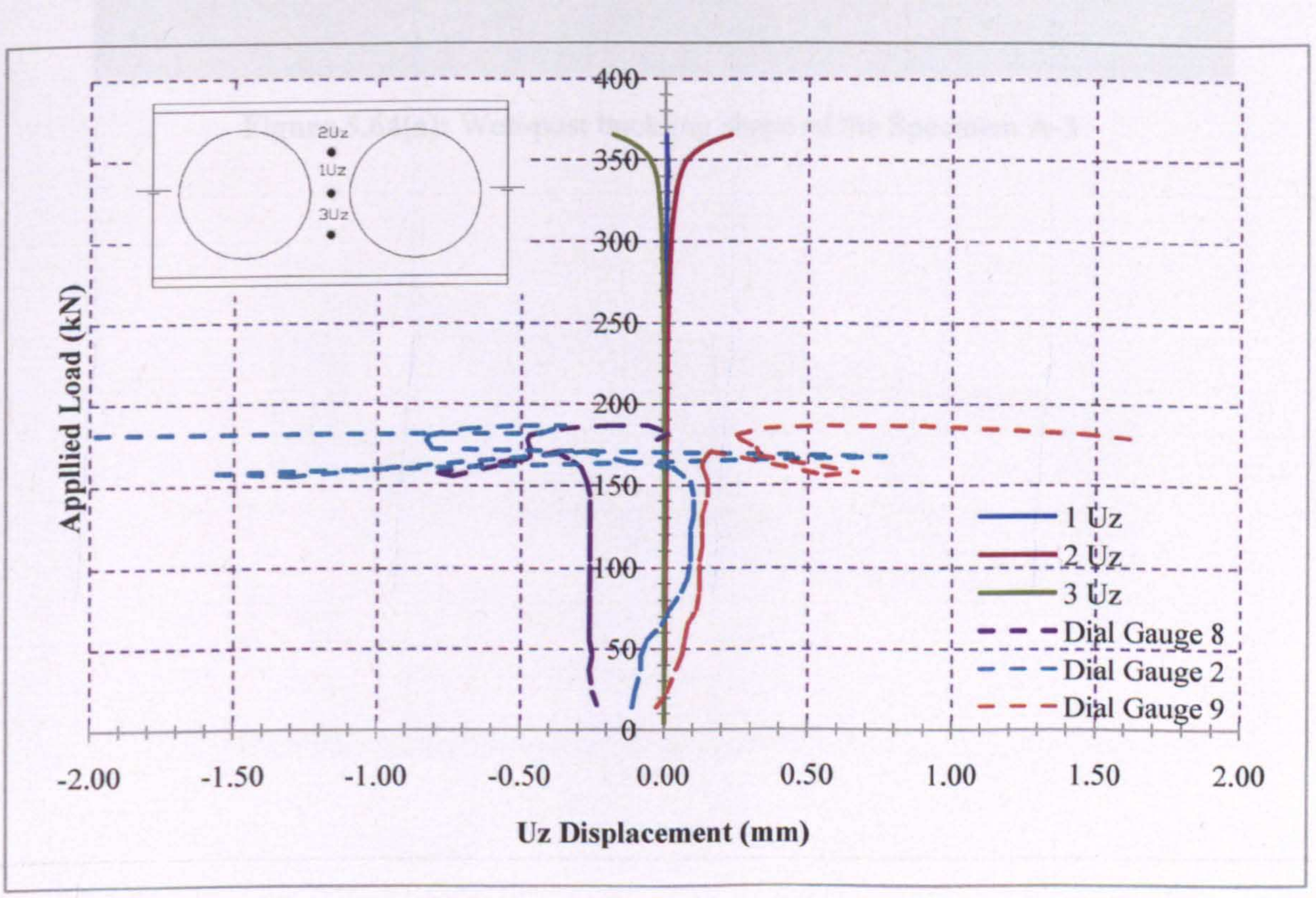

Figure 5.62: Maximum FE Uz web displacements at the positions of dial gauges

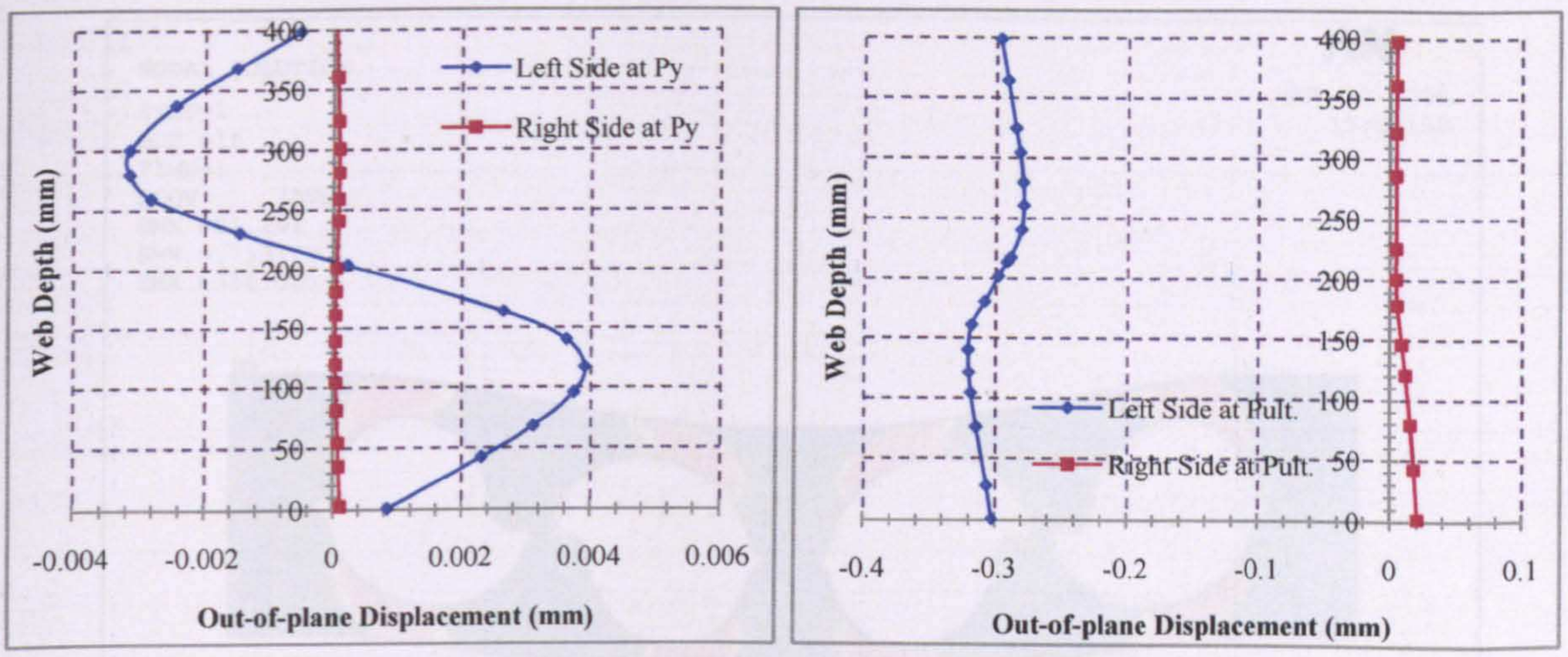

Figure 5.63: Out-of-plane web displacement profiles for two load level points

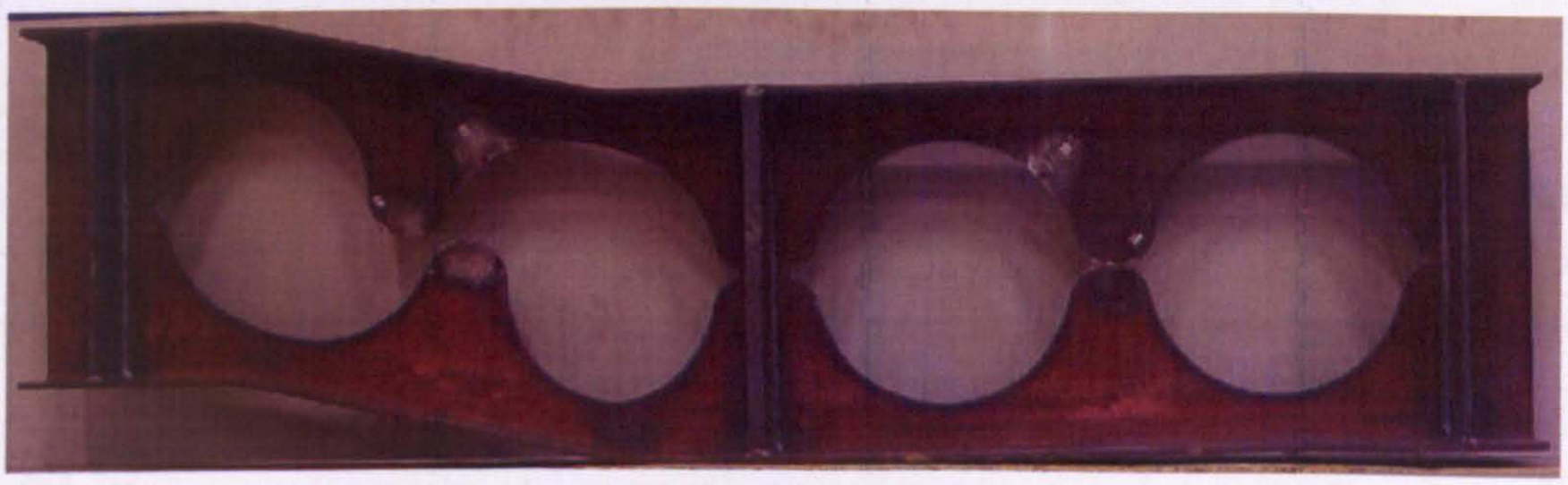

Figure 5.64(a): Web-post buckling shape of the Specimen A-3

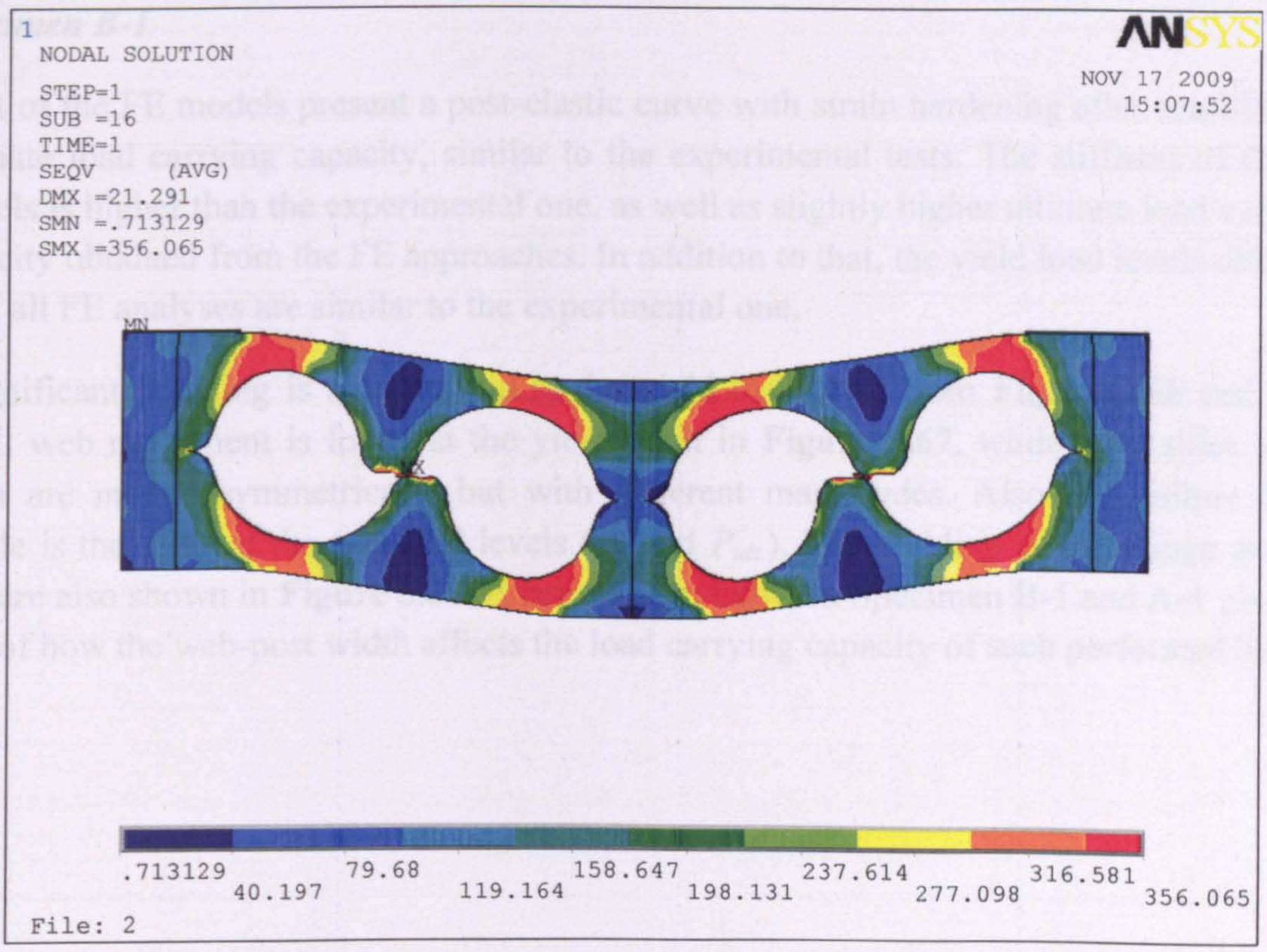

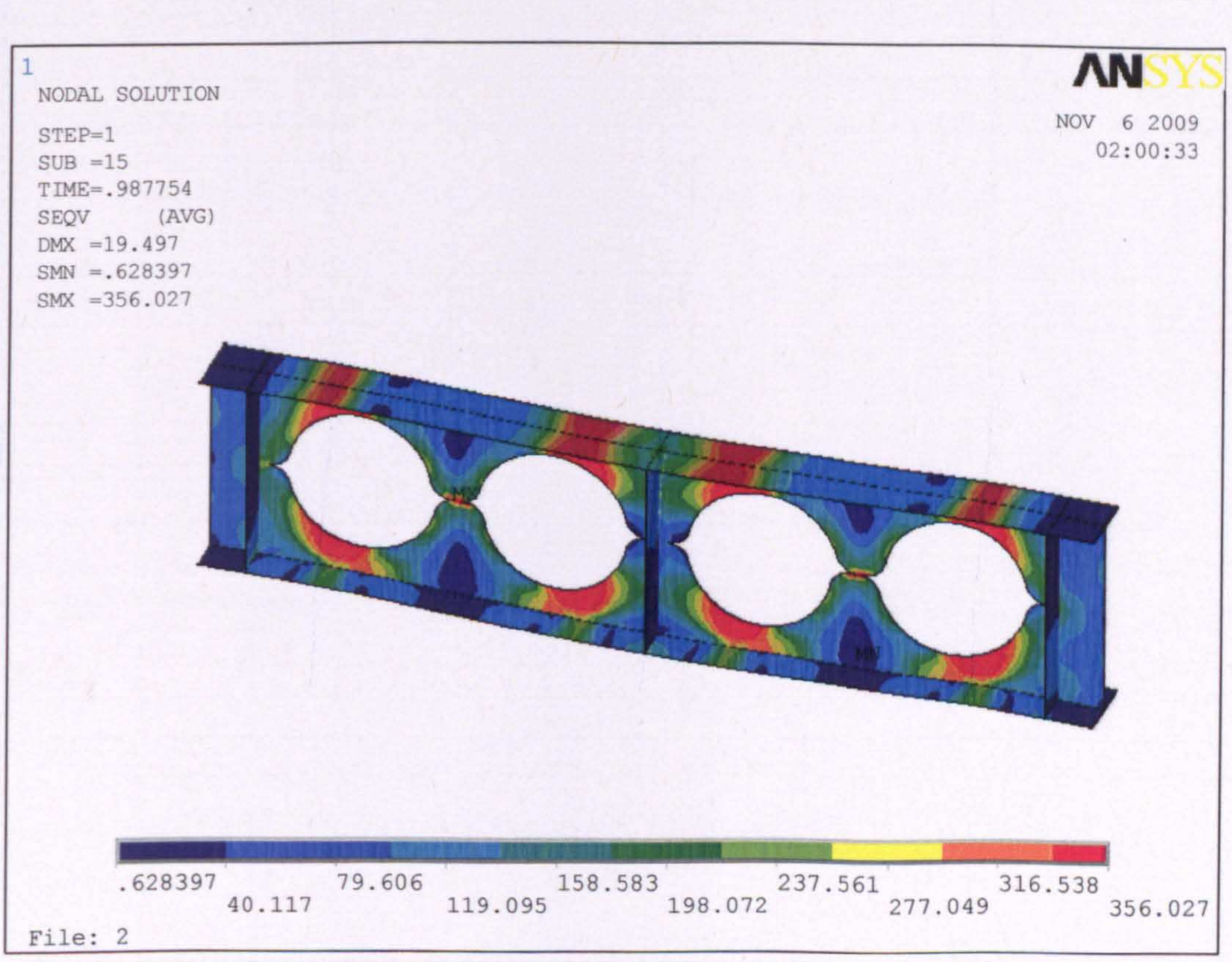

Figure 5.64(b): Von-Mises stresses in the Specimen A-3

Specimen B-1

Most of the FE models present a post-elastic curve with strain hardening after reaching the ultimate load carrying capacity, similar to the experimental tests. The stiffness of the FE models is higher than the experimental one, as well as slightly higher ultimate load carrying capacity obtained from the FE approaches. In addition to that, the yield load levels obtained from all FE analyses are similar to the experimental one.

Insignificant buckling is observed up to the yield load level from **Figure 5.66** and **5.67.** Small web movement is found at the yield point in **Figure 5.67**, while both sides of the beam are moved symmetrically but with different magnitudes. Also, the failure mode profile is the same at the two load levels (P_y and $P_{ult.}$). The yielding of top flange and the web are also shown in **Figure 5.67**. A comparison between Specimen B-1 and A-1 gives an idea of how the web-post width affects the load carrying capacity of such perforated beams.

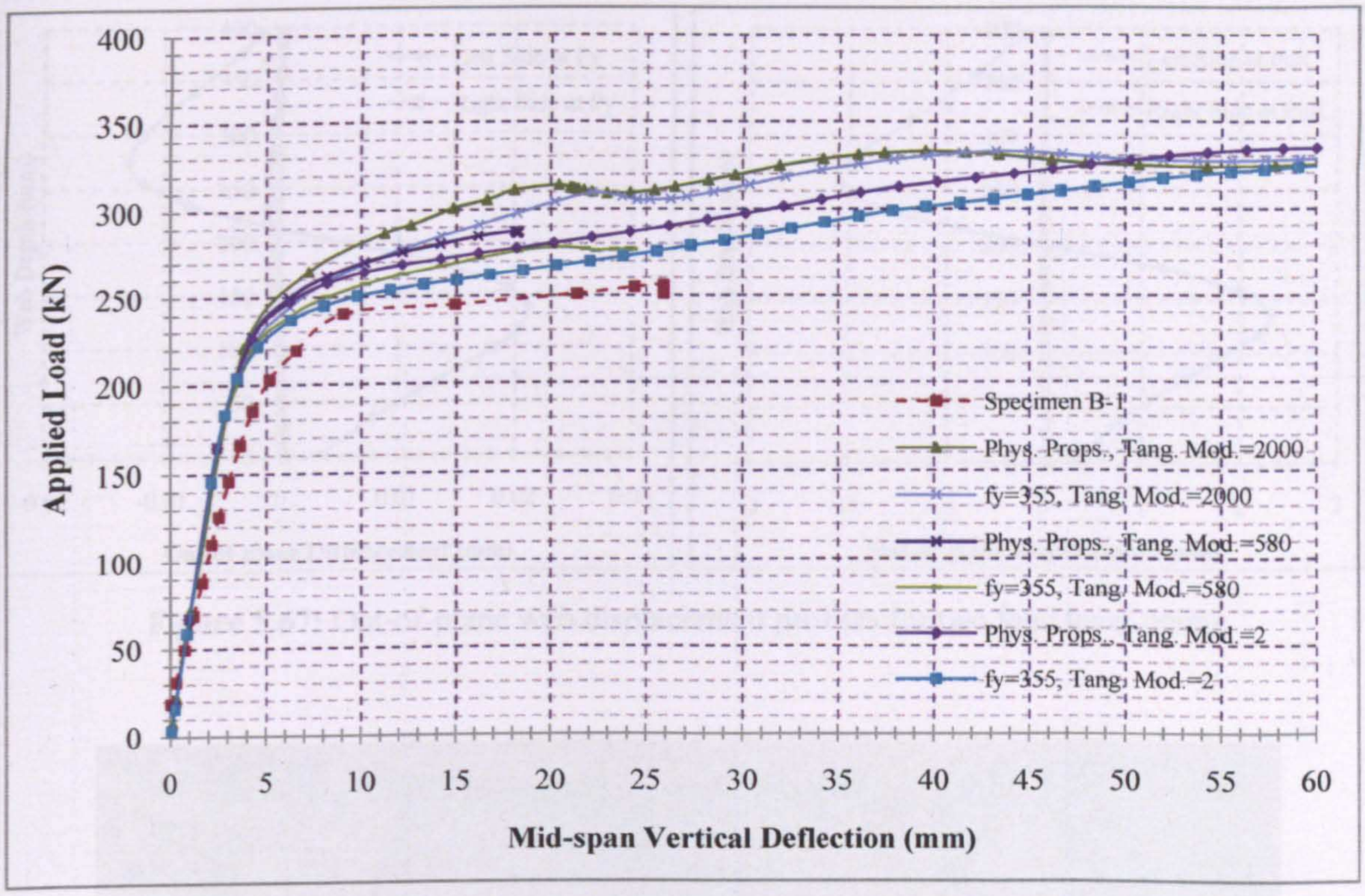

Figure 5.65: Experimental and FE load-deflection curves at mid-span

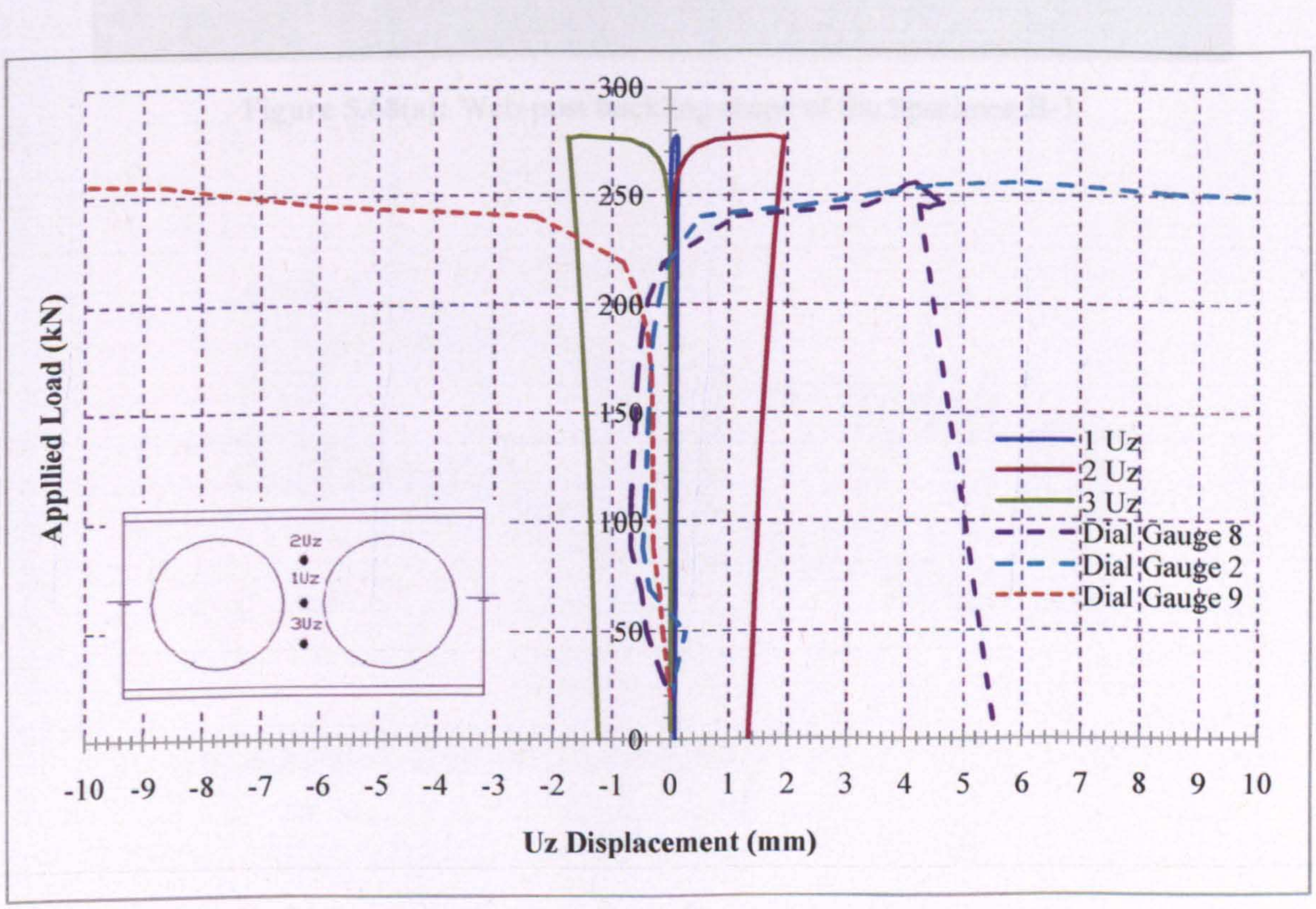

Figure 5.66: Maximum FE Uz web displacements at the positions of dial gauges

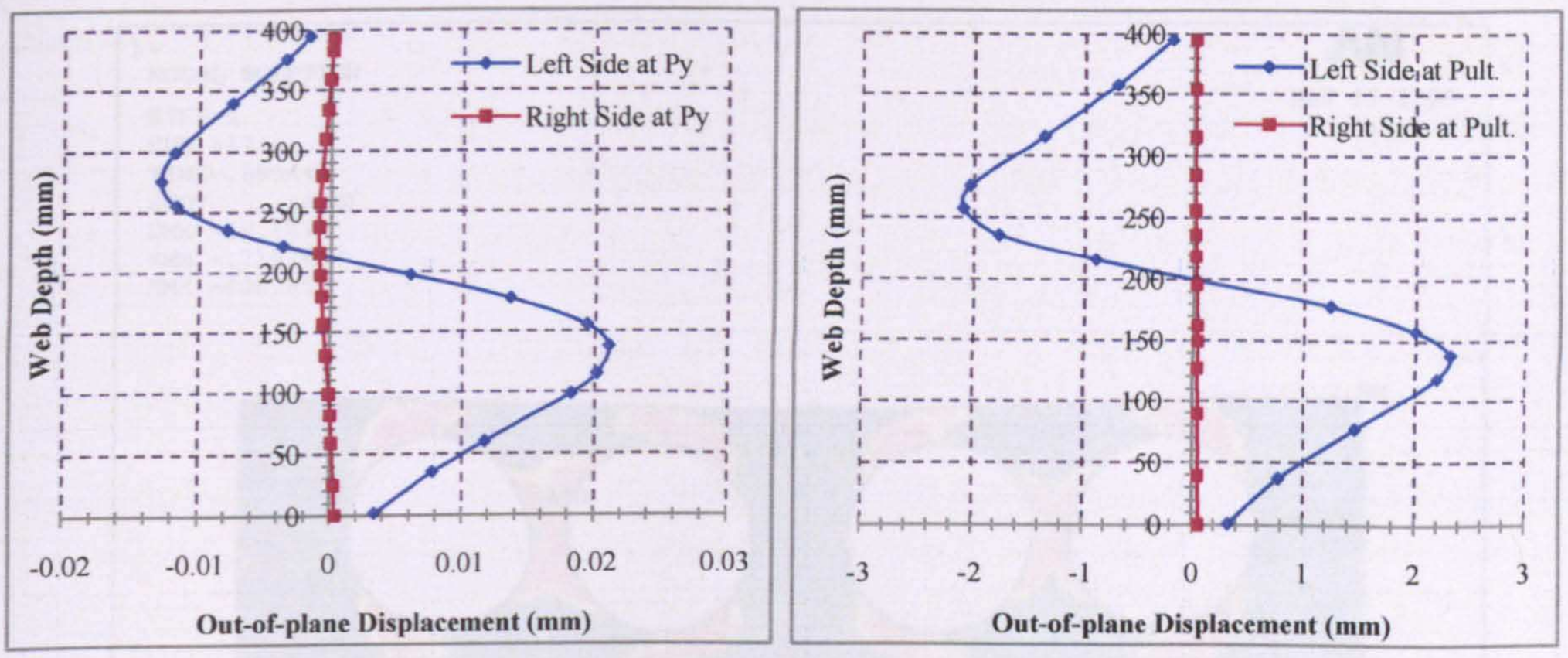

Figure 5.67: Out-of-plane web displacement profiles for two load level points

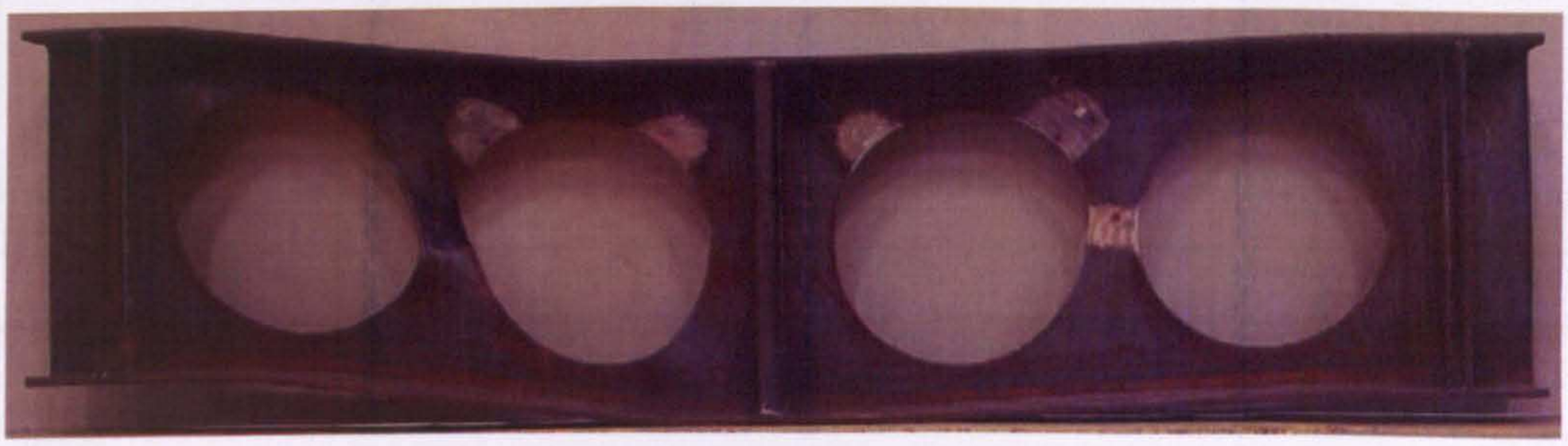

Figure 5.68(a): Web-post buckling shape of the Specimen B-1

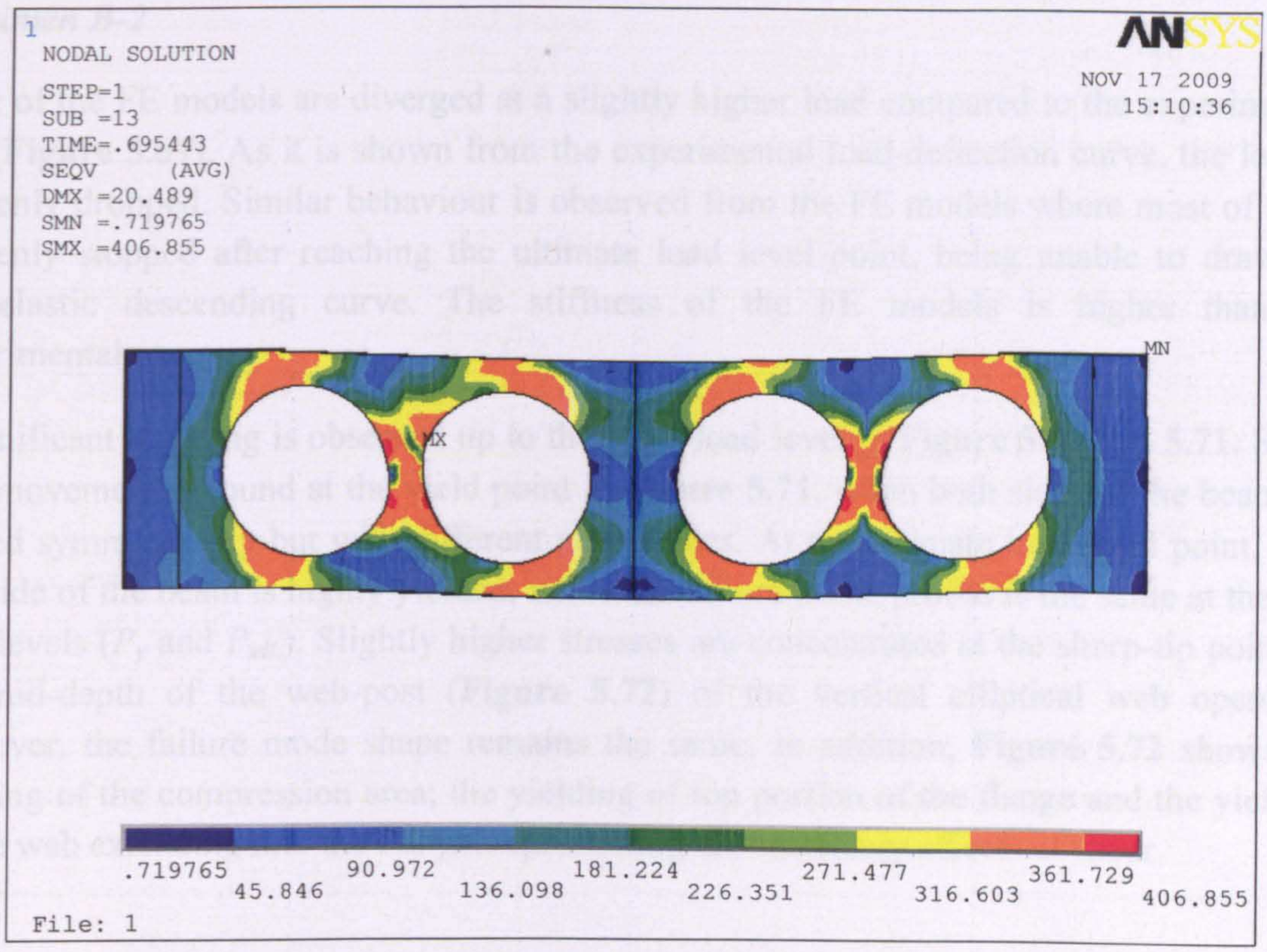

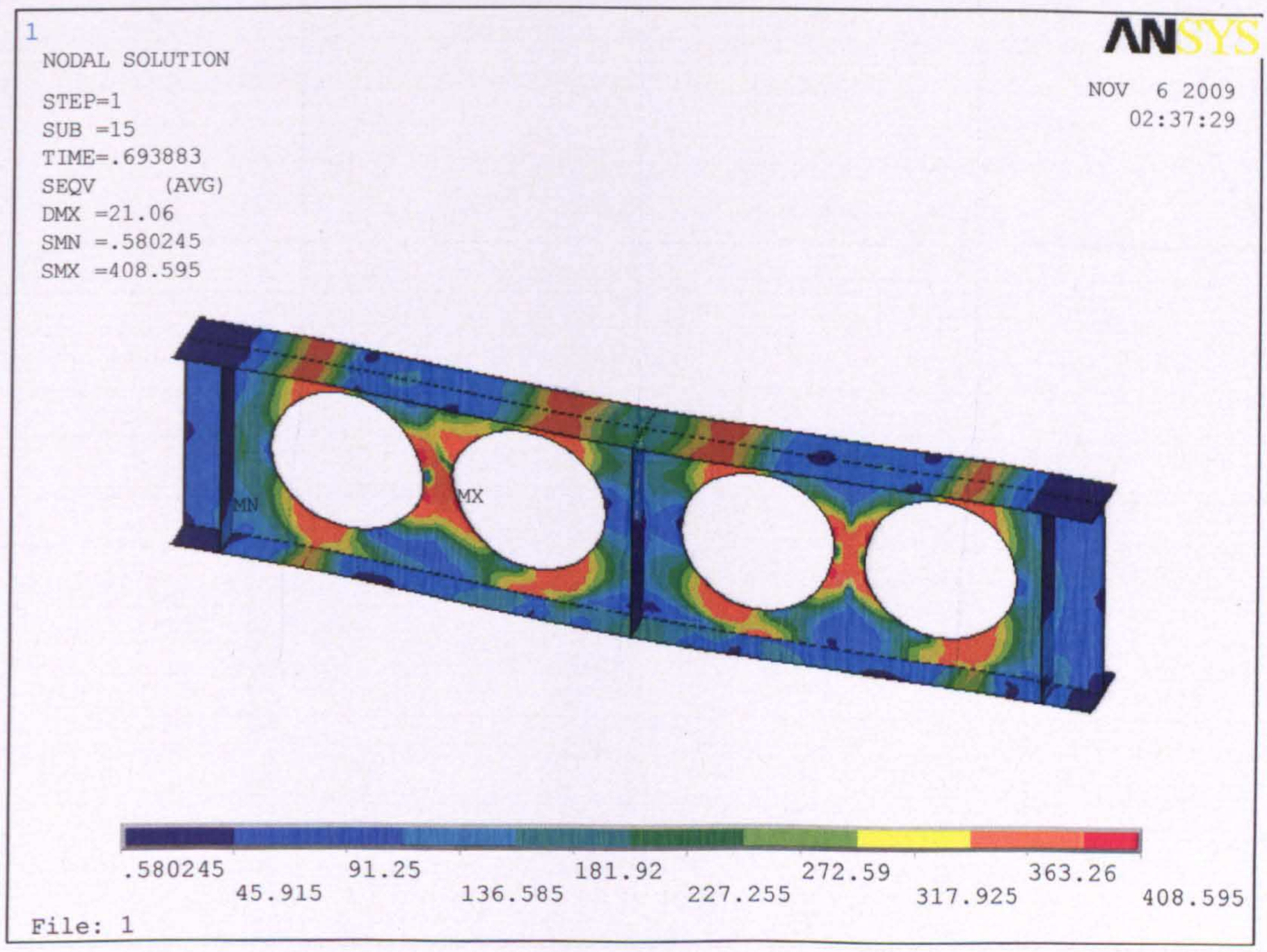

Figure 5.68(b): Von-Mises stresses in the Specimen B-1

Specimen B-2

Most of the FE models are diverged at a slightly higher load compared to the experimental one (**Figure 5.69**). As it is shown from the experimental load-deflection curve, the load is suddenly dropped. Similar behaviour is observed from the FE models where most of them suddenly stopped after reaching the ultimate load level point, being unable to draw the post-elastic descending curve. The stiffness of the FE models is higher than the experimental one.

Insignificant buckling is observed up to the yield load level in **Figure 5.70** and **5.71**. Small web movement is found at the yield point in **Figure 5.71**, when both sides of the beam are moved symmetrically but with different magnitudes. At the ultimate load level point, only one side of the beam is highly yielded, while the failure mode profile is the same at the two load levels (P_y and $P_{ult.}$). Slightly higher stresses are concentrated at the sharp-tip points at the mid-depth of the web-post (**Figure 5.72**) of the vertical elliptical web openings. However, the failure mode shape remains the same. In addition, **Figure 5.72** shows the yielding of the compression area; the yielding of top portion of the flange and the yielding of the web extending into the flange, representing the secondary effects of shear.

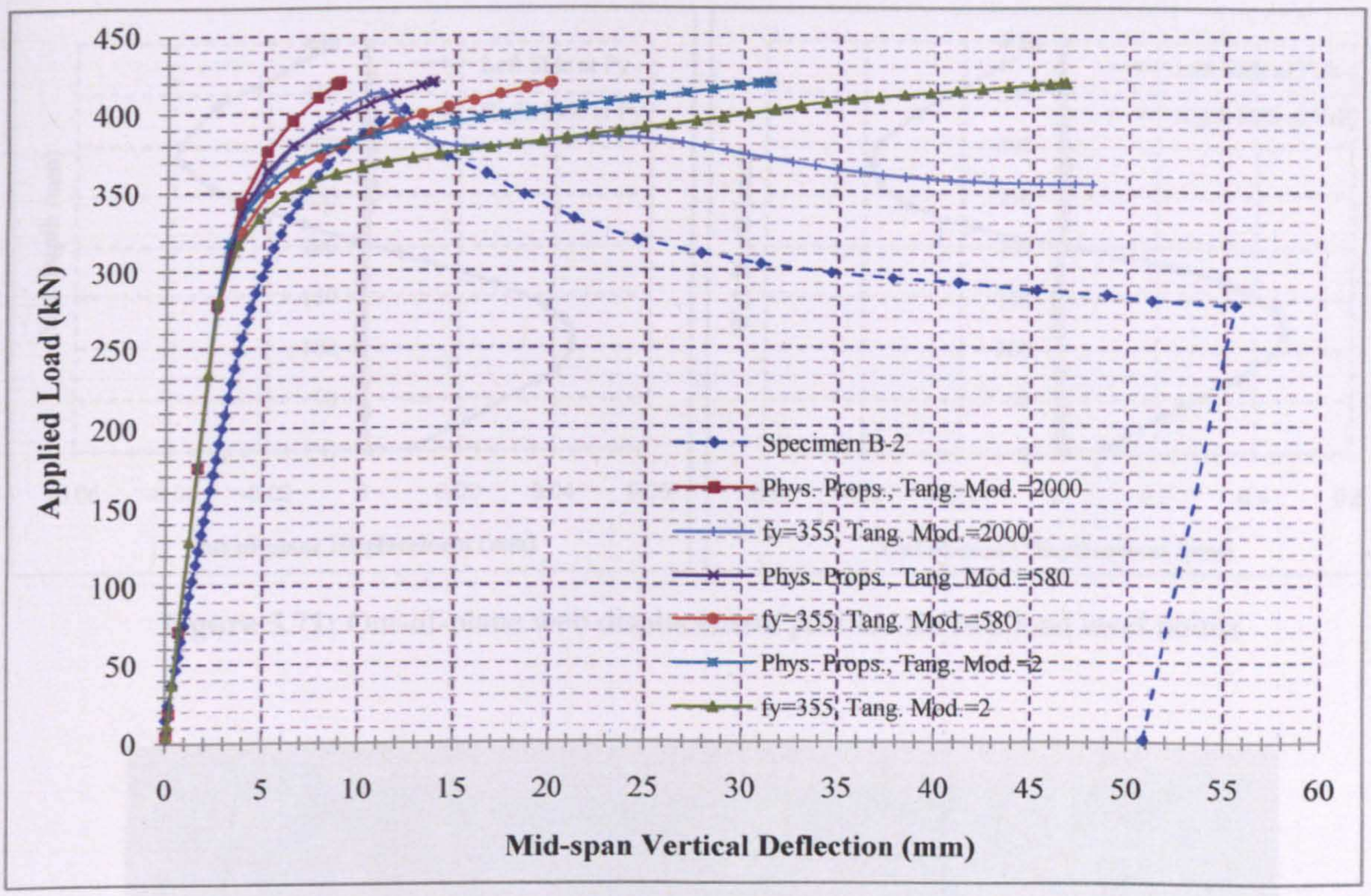

Figure 5.69: Experimental and FE load-deflection curves at mid-span

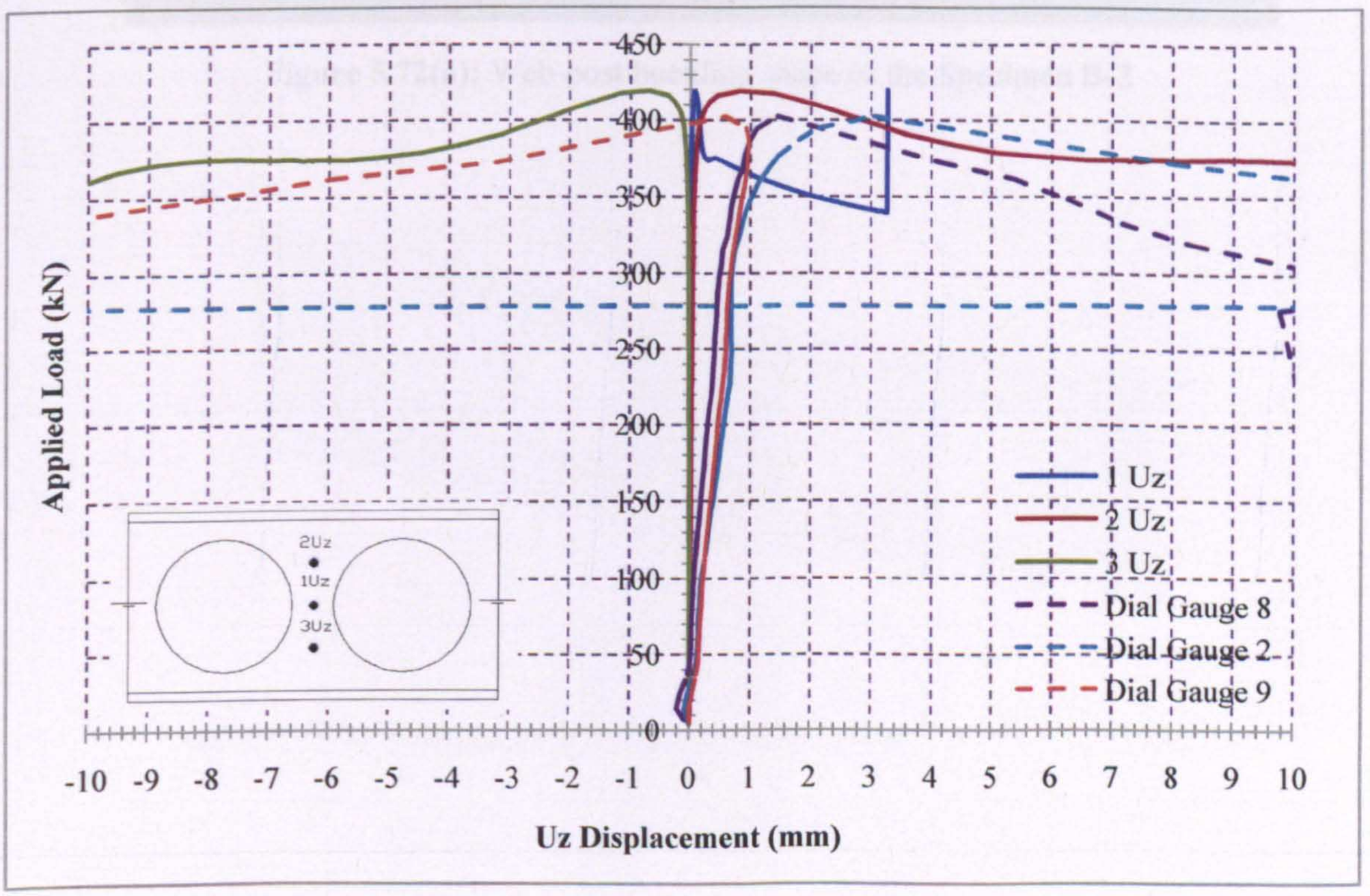

Figure 5.70: Maximum FE Uz web displacements at the positions of dial gauges

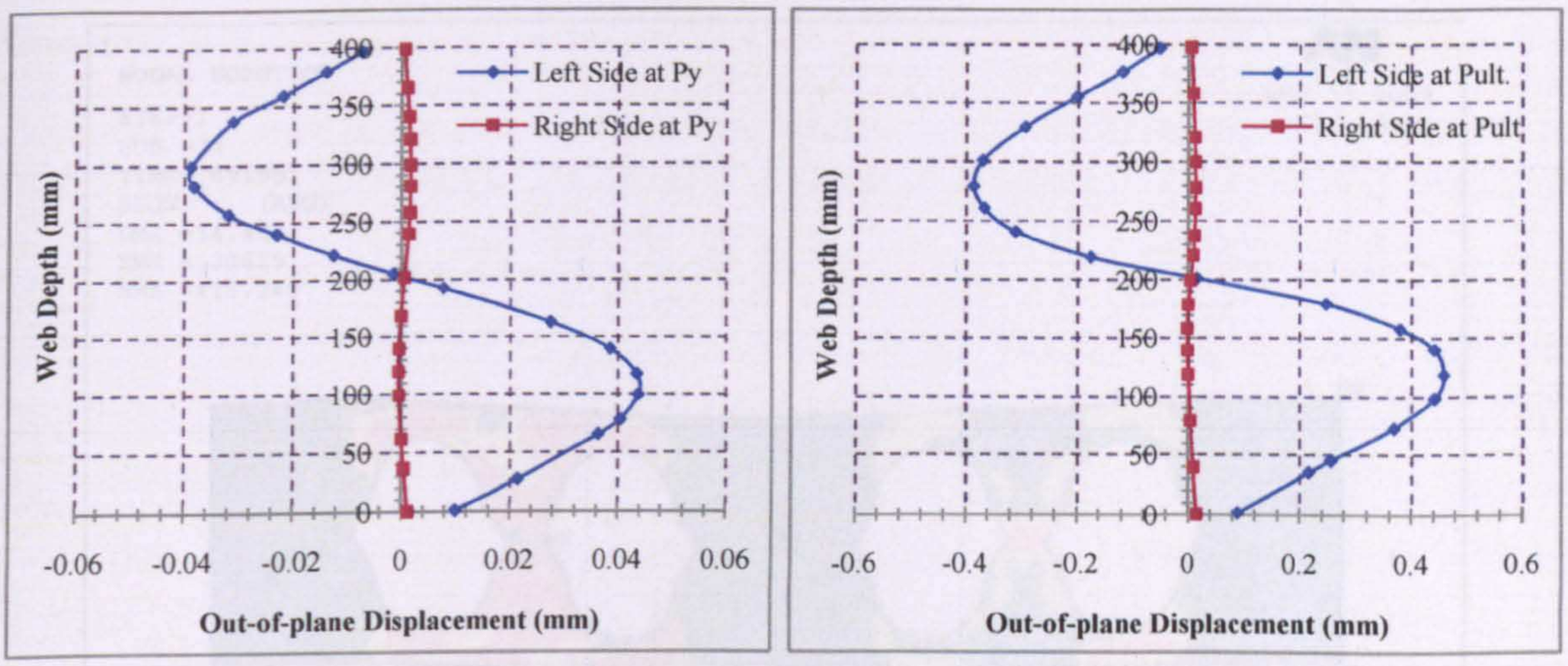

Figure 5.71: Out-of-plane web displacement profiles for two load level points

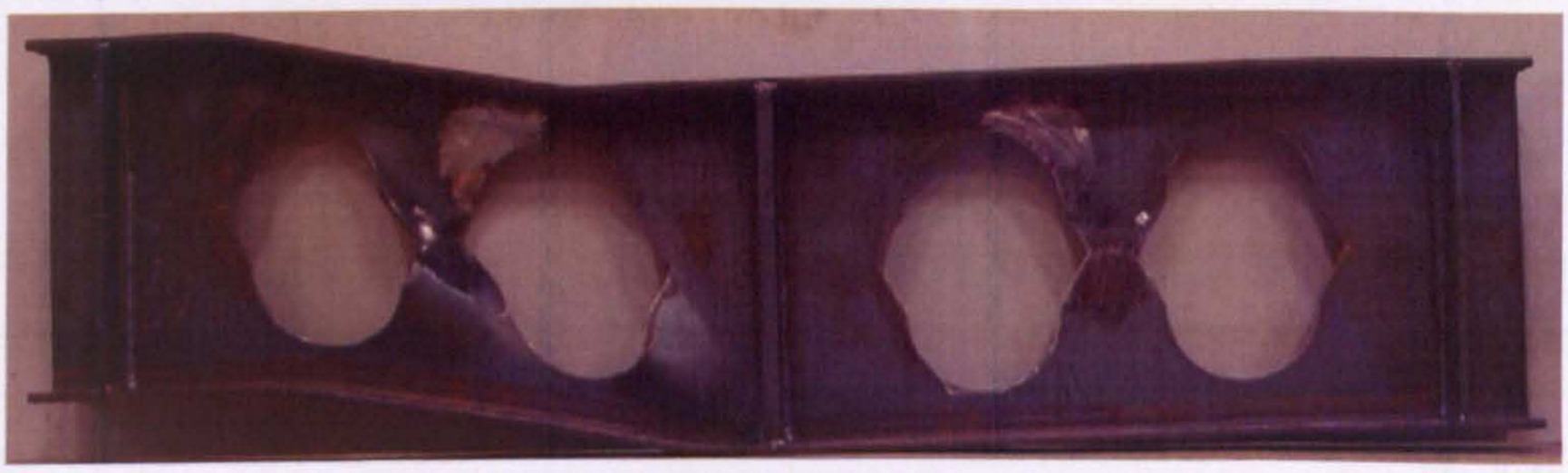

Figure 5.72(a): Web-post buckling shape of the Specimen B-2

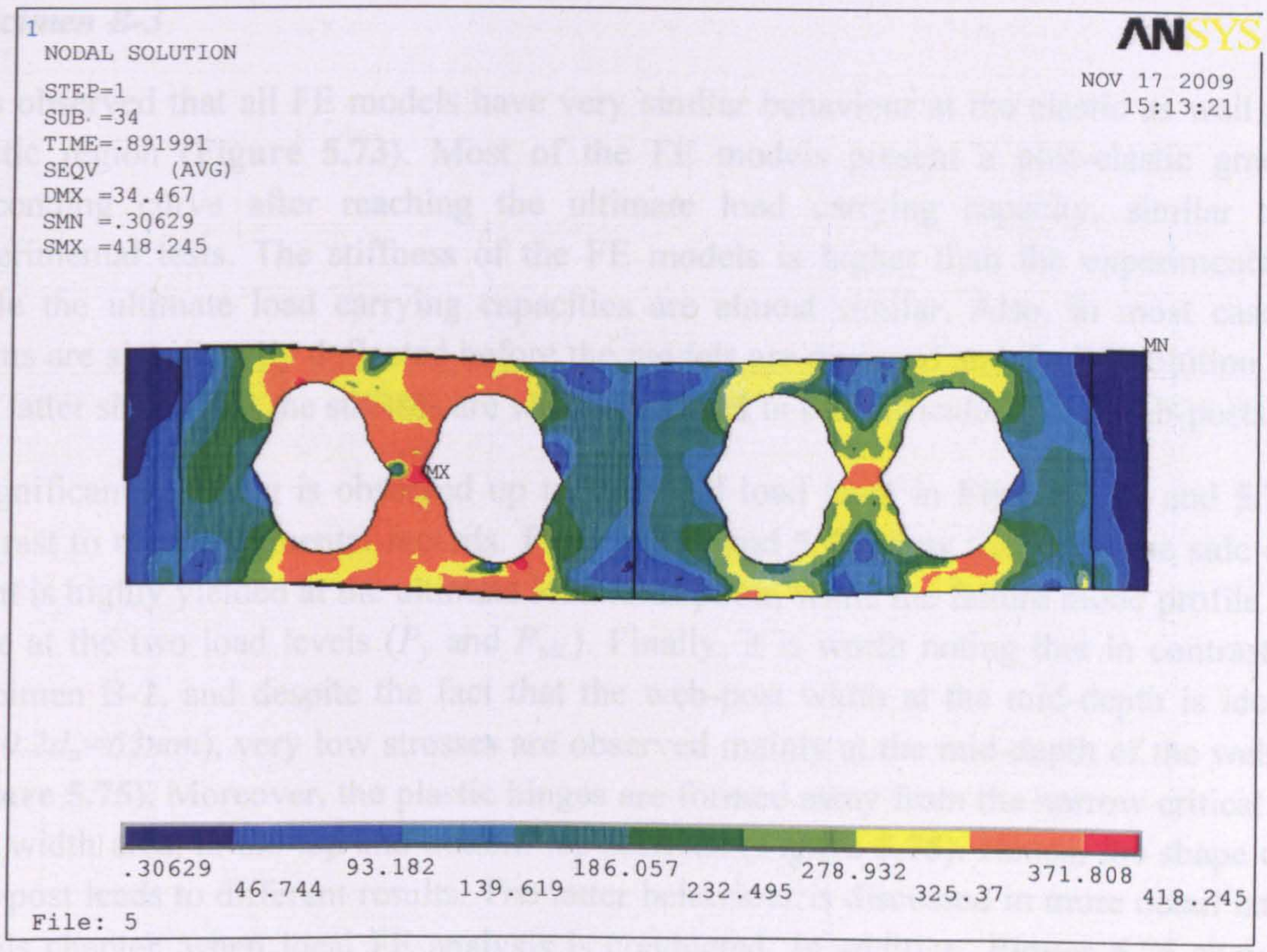

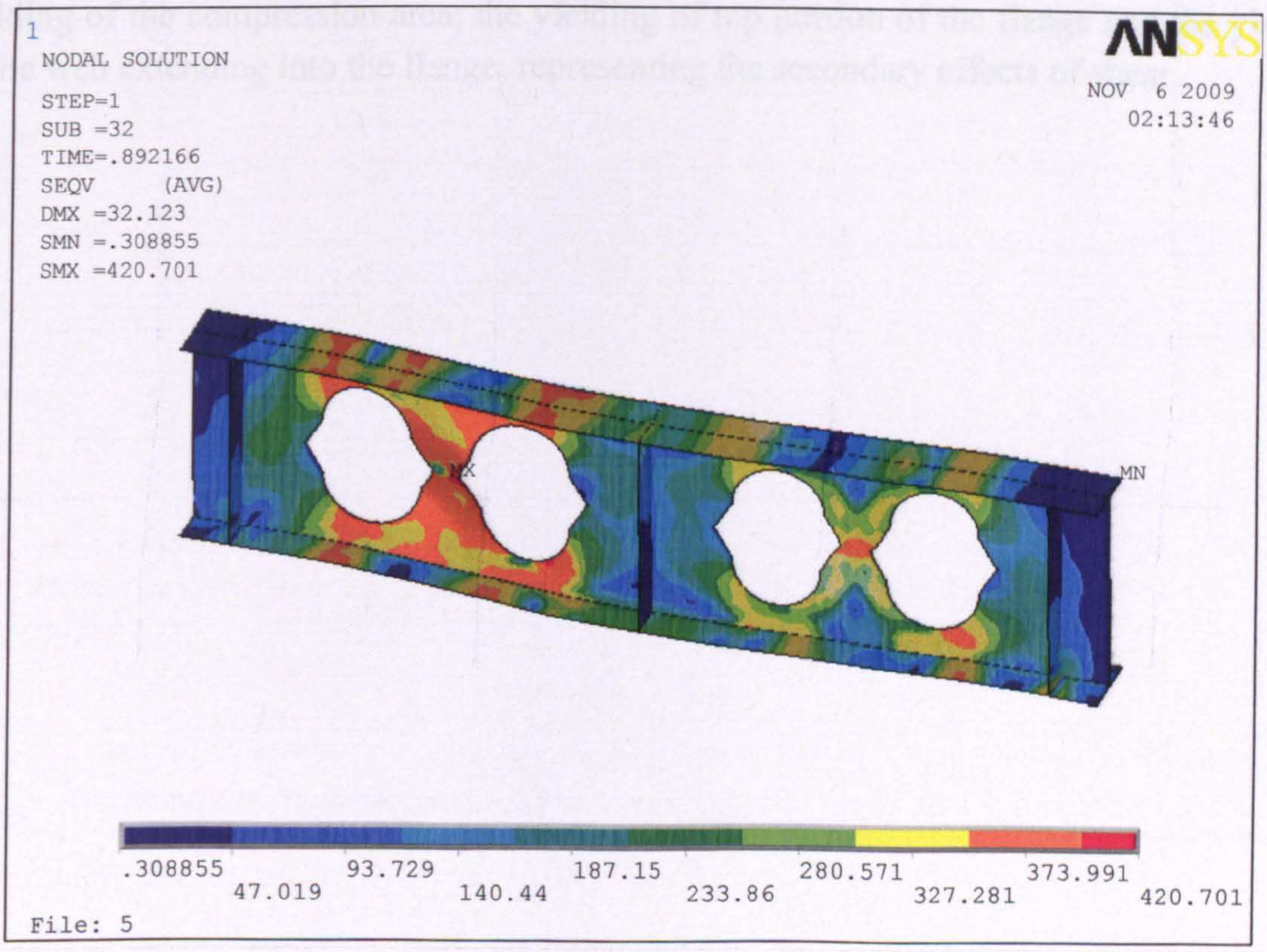

Figure 5.72(b): Von-Mises stresses in the Specimen B-2

Specimen B-3

It is observed that all FE models have very similar behaviour at the elastic as well as the plastic region (**Figure 5.73**). Most of the FE models present a post-elastic gradually descending curve after reaching the ultimate load carrying capacity, similar to the experimental tests. The stiffness of the FE models is higher than the experimental one while the ultimate load carrying capacities are almost similar. Also, in most cases the beams are significantly deflected before the models are diverged and the FE solution stops. The latter shows that the stresses are well distributed in the particular novel web-posts.

Insignificant buckling is observed up to the yield load level in **Figure 5.74** and **5.75**, in contrast to the experimental records. **Figure 5.75** and **5.76** show that only one side of the beam is highly yielded at the ultimate load level point, while the failure mode profile is the same at the two load levels (P_y and $P_{ult.}$). Finally, it is worth noting that in contrast with Specimen B-2, and despite the fact that the web-post width at the mid-depth is identical ($s_o=0.2d_o=63mm$), very low stresses are observed mainly at the mid-depth of the web-post (**Figure 5.75**). Moreover, the plastic hinges are formed away from the narrow critical web-post width area, at the top and bottom tee-sections (**Figure 5.75**). Hence, the shape of the web-post leads to different results. The latter behaviour is discussed in more detail later on in this chapter, when local FE analysis is conducted. In addition, **Figure 5.75** shows the yielding of the compression area; the yielding of top portion of the flange and the yielding of the web extending into the flange, representing the secondary effects of shear.

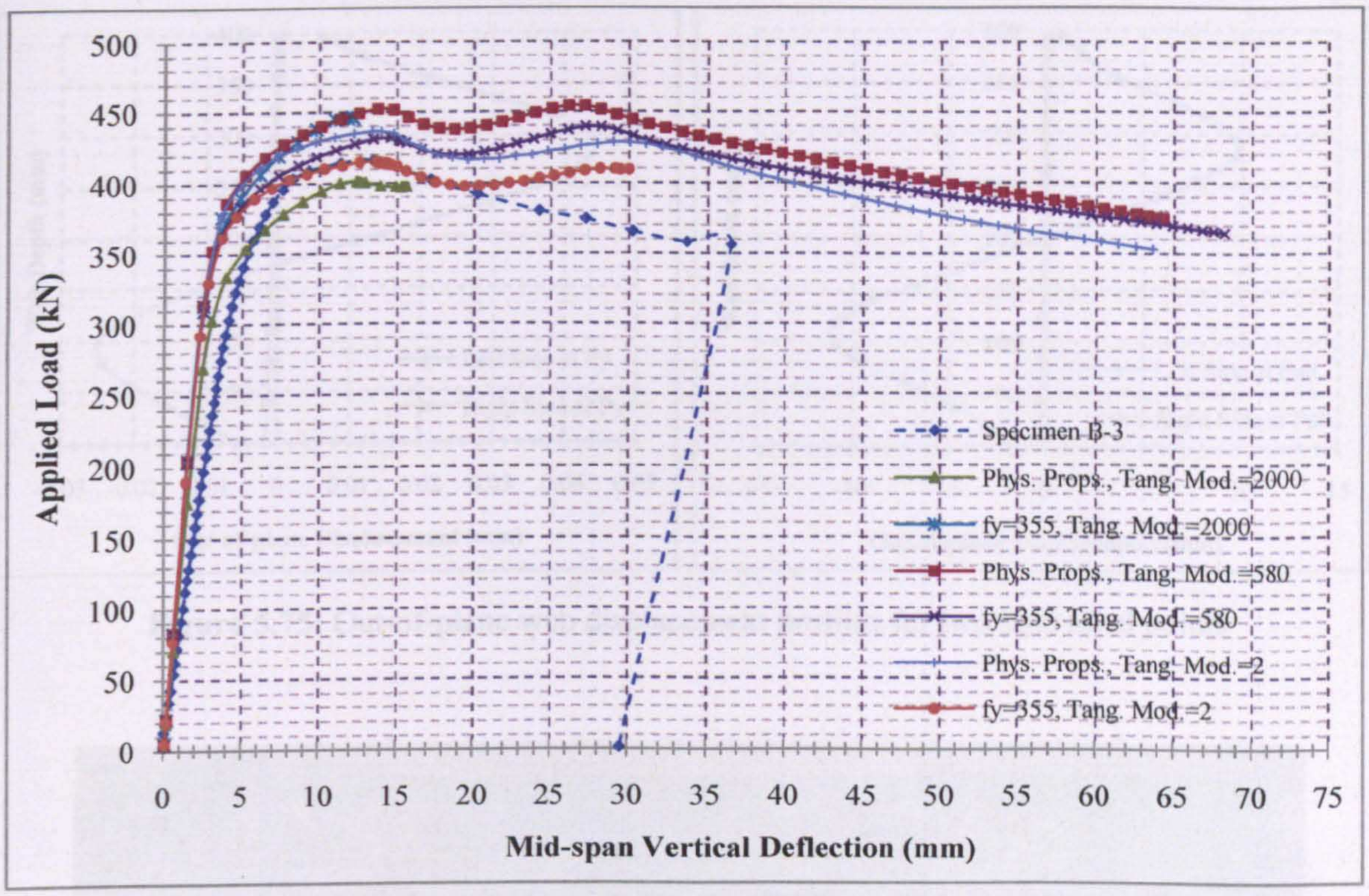

Figure 5.73: Experimental and FE load-deflection curves at mid-span

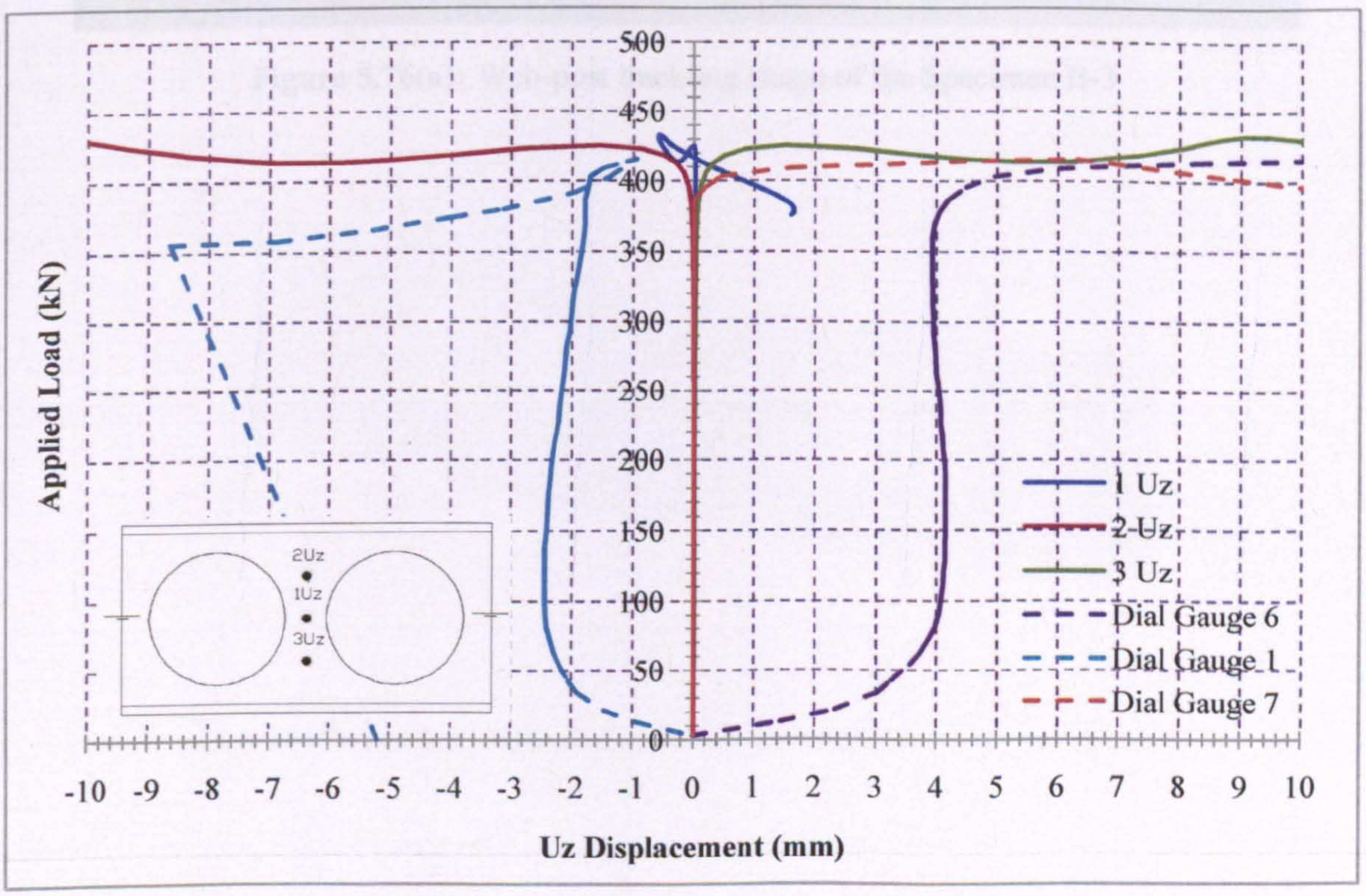

Figure 5.74: Maximum FE Uz web displacements at the positions of dial gauges

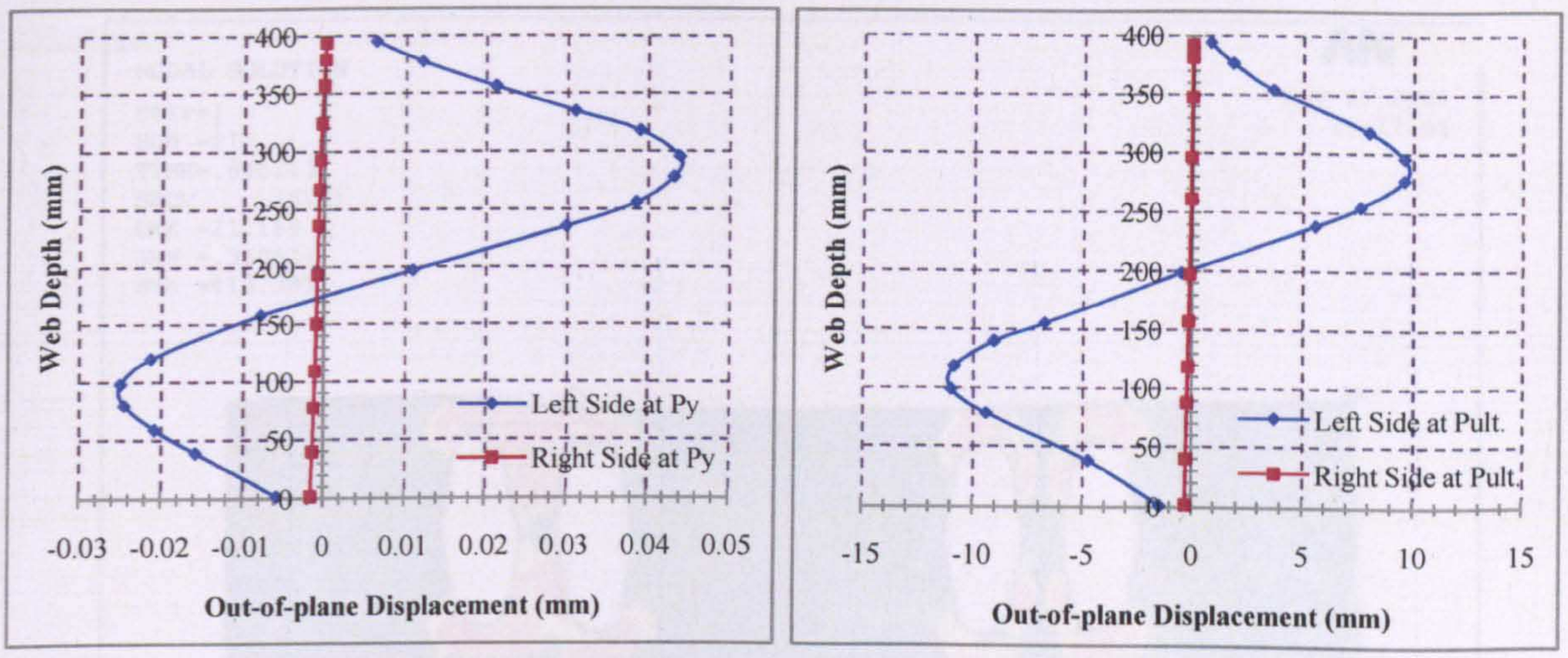

Figure 5.75: Out-of-plane web displacement profiles for two load level points

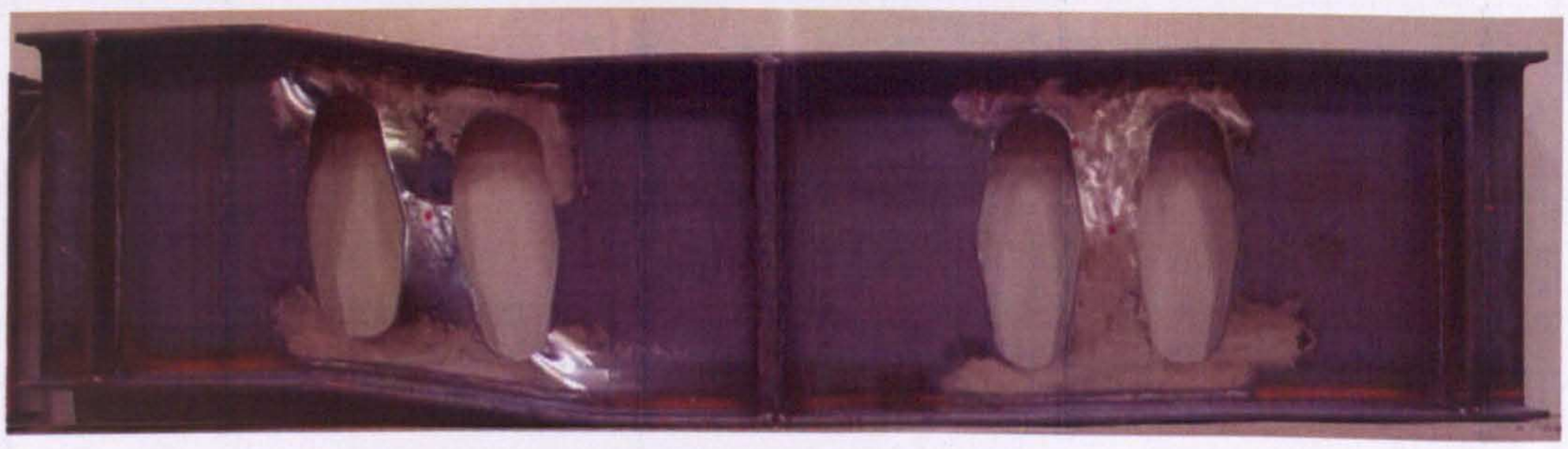

Figure 5.76(a): Web-post buckling shape of the Specimen B-3

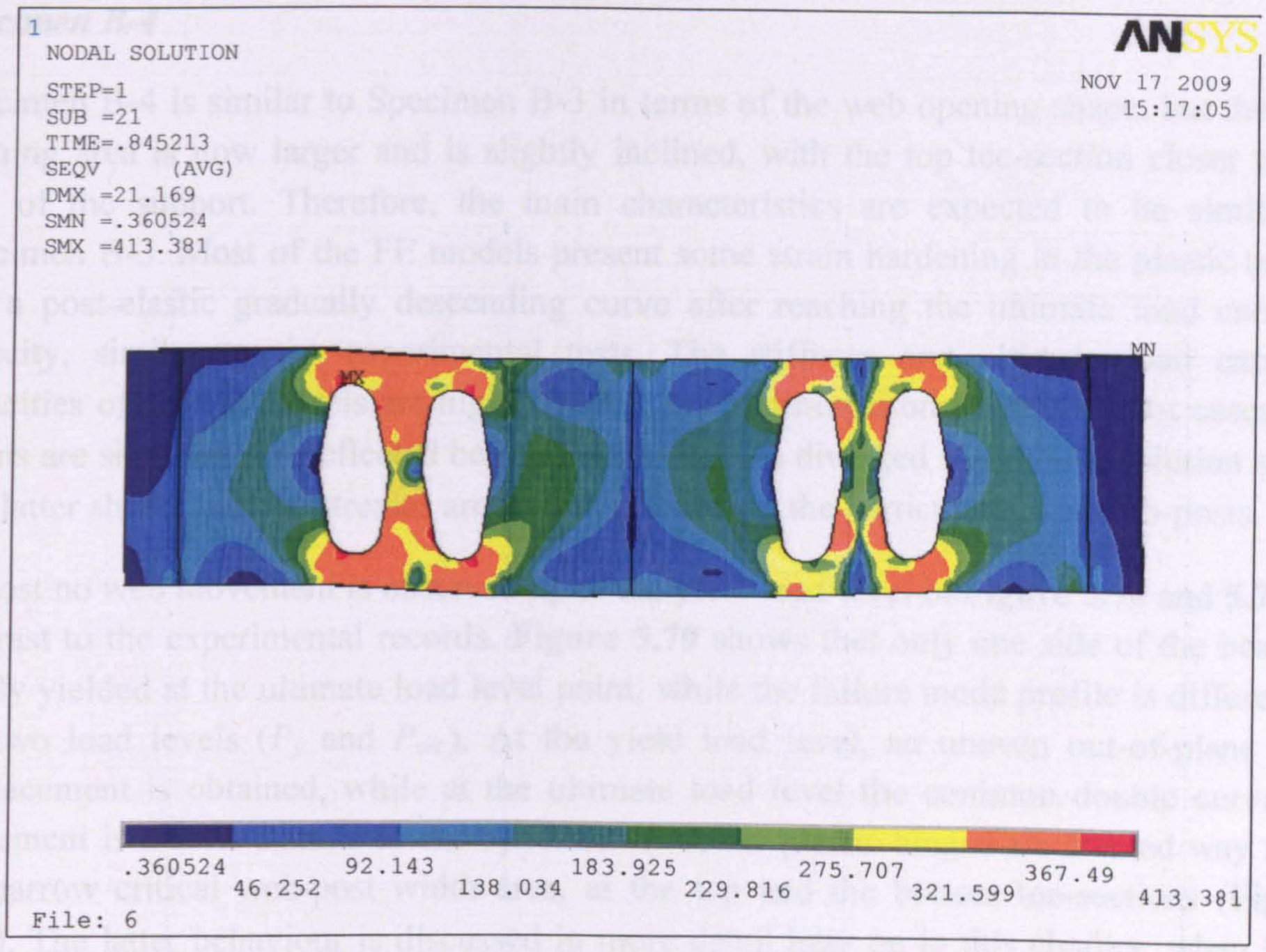

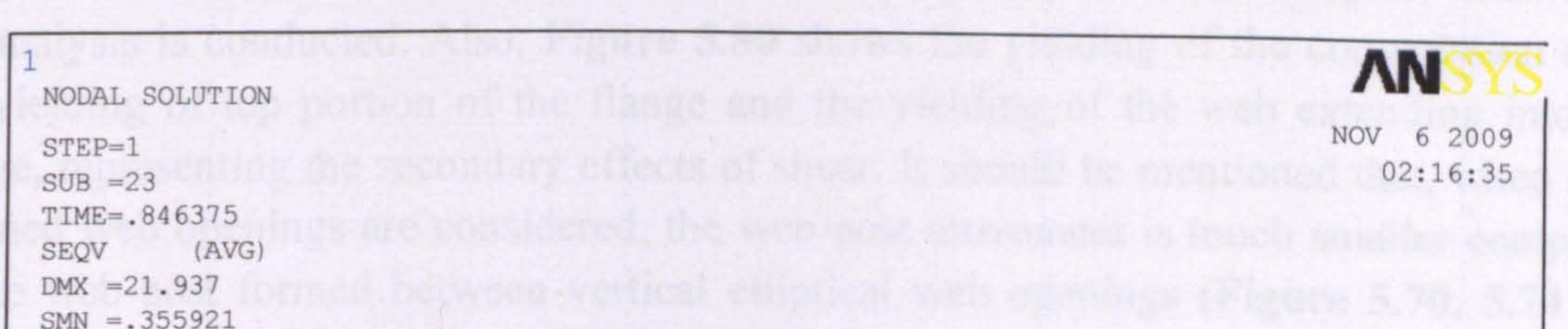

Figure 5.76(b): Von-Mises stresses in the Specimen B-3

Specimen B-4

Specimen B-4 is similar to Specimen B-3 in terms of the web opening shape, but the web opening area is now larger and is slightly inclined, with the top tee-section closer to the side of the support. Therefore, the main characteristics are expected to be similar to Specimen B-3. Most of the FE models present some strain hardening in the plastic region and a post-elastic gradually descending curve after reaching the ultimate load carrying capacity, similar to the experimental tests. The stiffness and ultimate load carrying capacities of the FE models are higher than the experimental one. Also in most cases, the beams are significantly deflected before the models are diverged and the FE solution stops. The latter shows that the stresses are well distributed in the particular novel web-posts.

Almost no web movement is observed up to the yield load level in **Figure 5.78** and **5.79**, in contrast to the experimental records. **Figure 5.79** shows that only one side of the beam is highly yielded at the ultimate load level point, while the failure mode profile is different at the two load levels (P_y and $P_{ult.}$). At the yield load level, an uneven out-of-plane web displacement is obtained, while at the ultimate load level the common double curvature movement is drawn. Similar to the Specimen B-3, the plastic hinges are formed way from the narrow critical web-post width area, at the top and the bottom tee-sections (**Figure 5.80**). The latter behaviour is discussed in more detail later on in this chapter, when local FE analysis is conducted. Also, **Figure 5.80** shows the yielding of the compression area; the yielding of top portion of the flange and the yielding of the web extending into the flange, representing the secondary effects of shear. It should be mentioned that, when such inclined web openings are considered, the web-post movement is much smaller compared to the web-post formed between vertical elliptical web openings (**Figure 5.70, 5.74** and **5.78**).

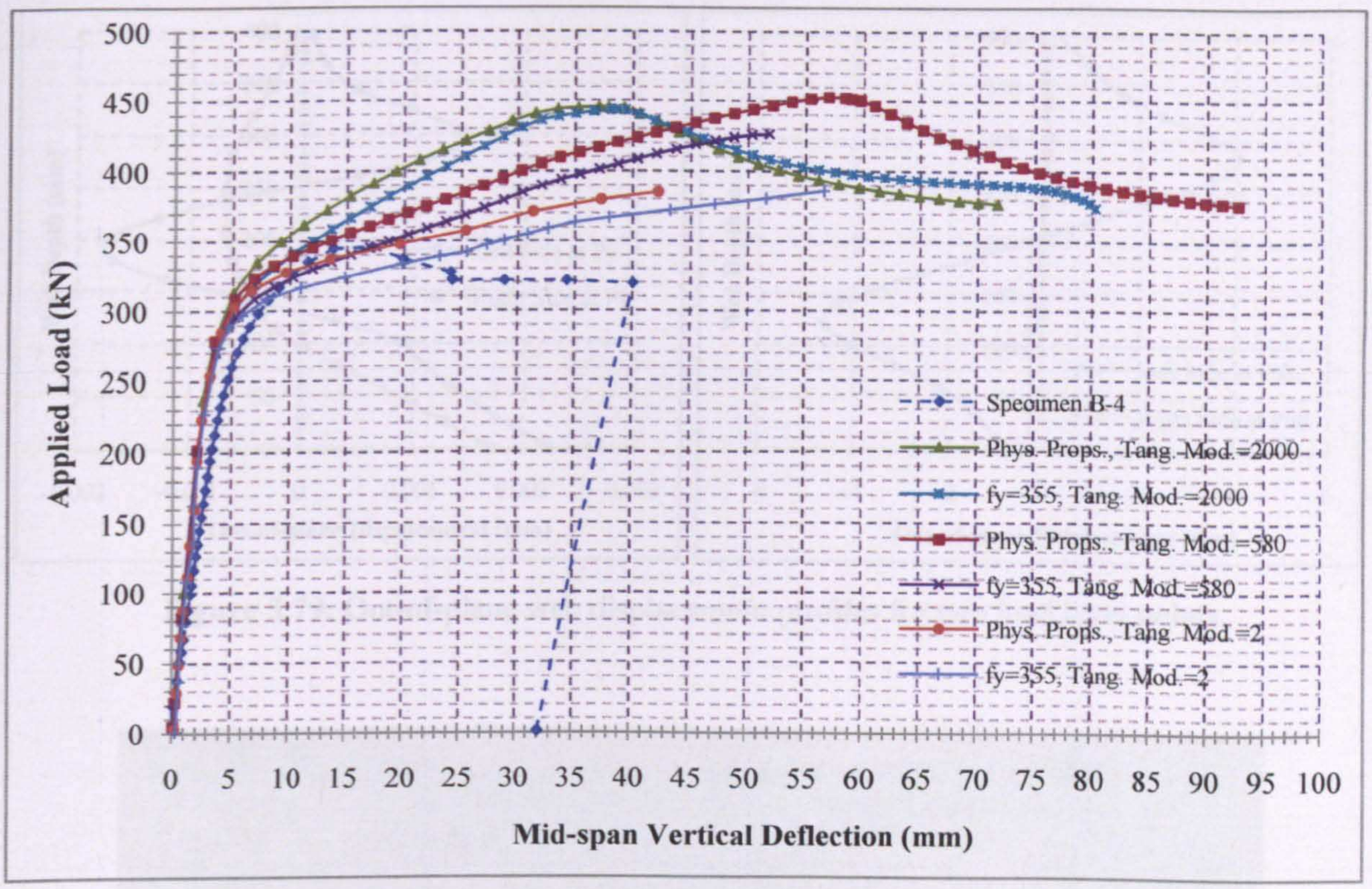

Figure 5.77: Experimental and FE load-deflection curves at mid-span

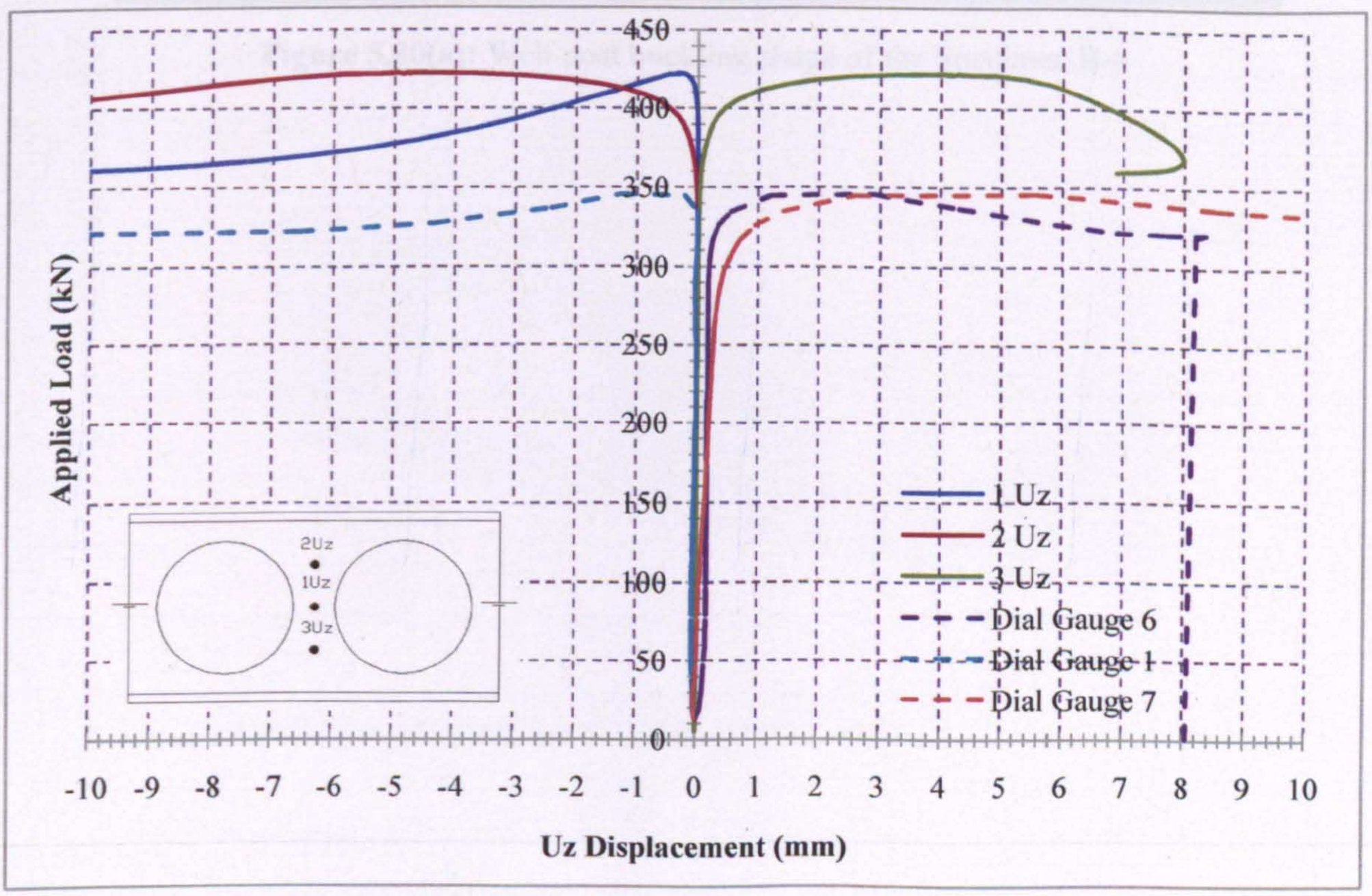

Figure 5.78: Maximum FE Uz web displacements at the positions of dial gauges

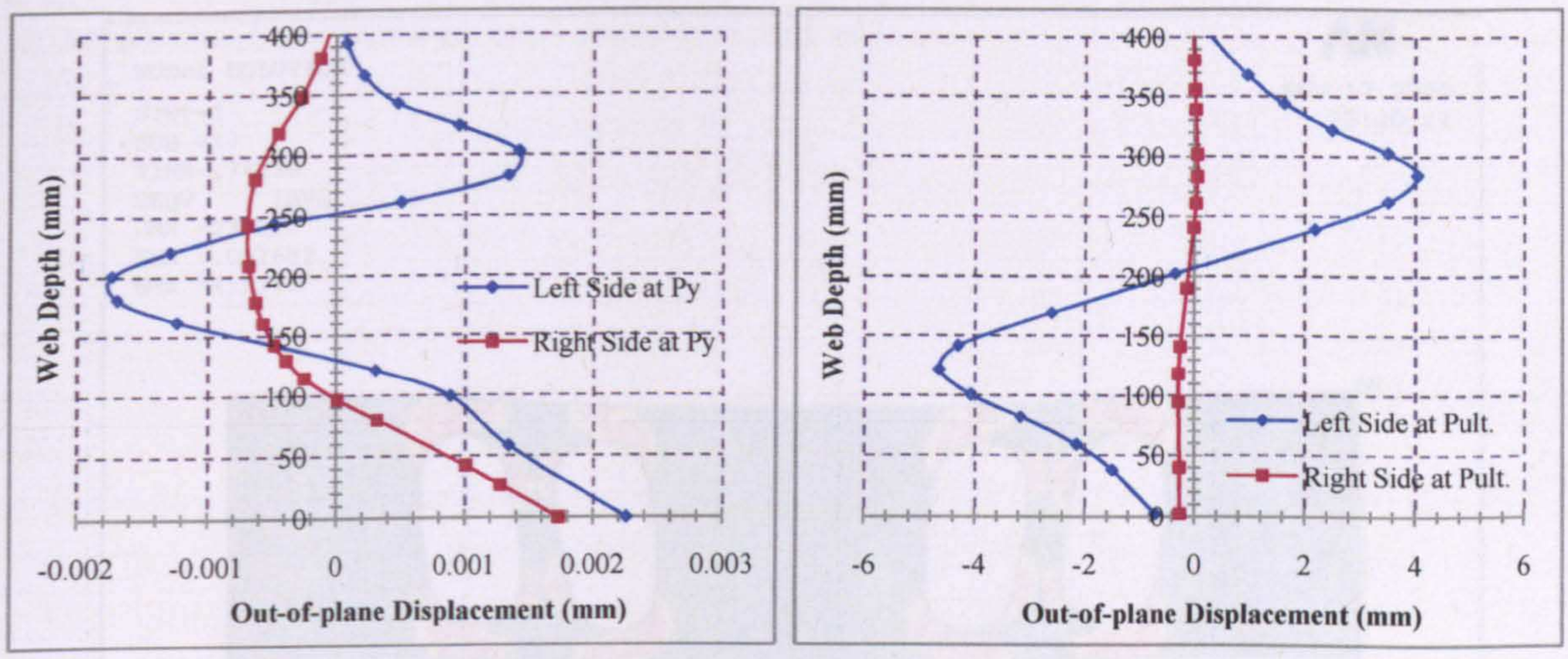

Figure 5.79: Out-of-plane web displacement profiles for two load level points

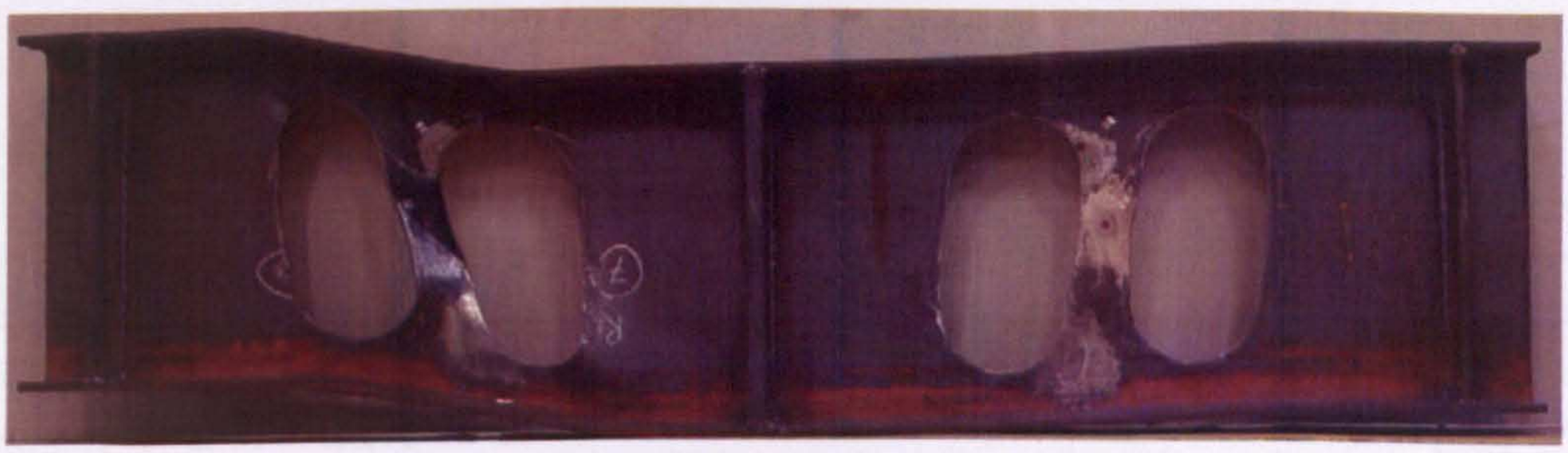

Figure 5.80(a): Web-post buckling shape of the Specimen B-4

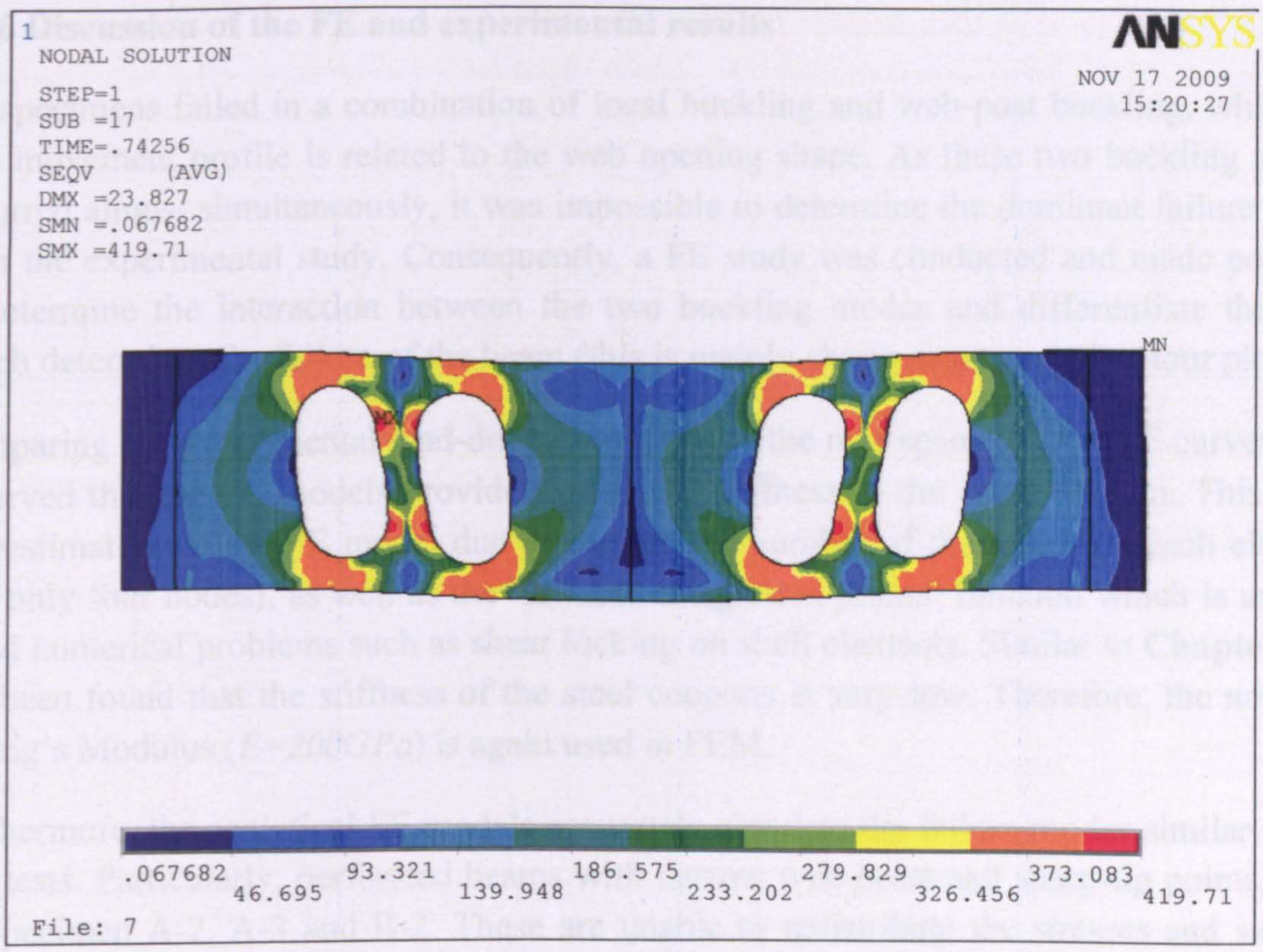

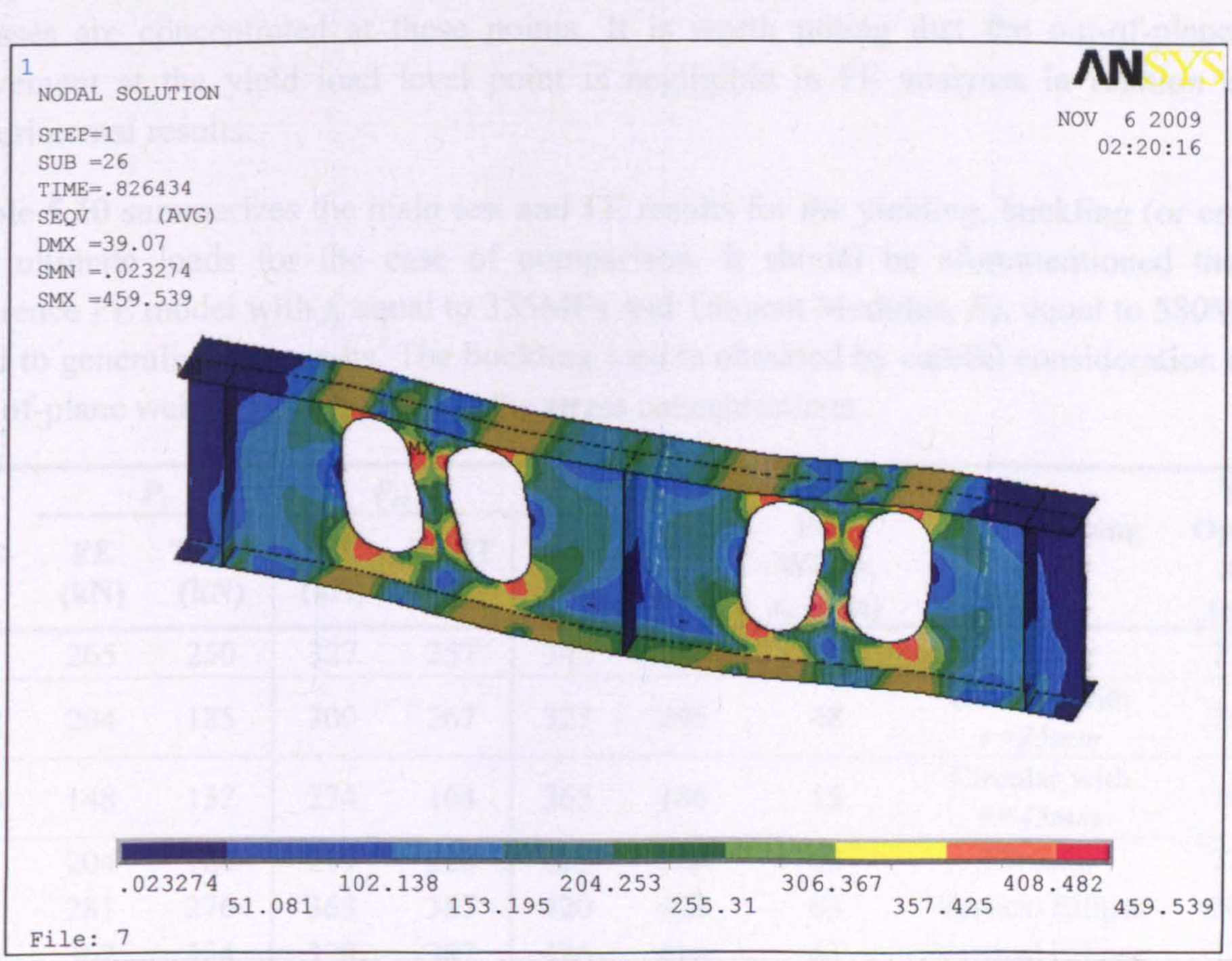

Figure 5.80(b): Von-Mises stresses in the Specimen B-4

5.3.6 Discussion of the FE and experimental results

All specimens failed in a combination of local buckling and web-post buckling, while the web movement profile is related to the web opening shape. As these two buckling modes occurred almost simultaneously, it was impossible to determine the dominant failure mode from the experimental study. Consequently, a FE study was conducted and made possible to determine the interaction between the two buckling modes and differentiate the area which determines the failure of the beam (this is mainly shown from stress contour plots).

Comparing the experimental load-deflection curve at the mid-span with the FE curves, it is observed that the FE models provide significant stiffness in the elastic region. This is an overestimation of the FE model due to the limited number of the nodes on each element (i.e. only four nodes), as well as the 'reduced integration points' function which is used to avoid numerical problems such as shear locking on shell elements. Similar to **Chapter 4**, it has been found that the stiffness of the steel coupons is very low. Therefore, the nominal Young's Modulus ($E=200GPa$) is again used in FEM.

Furthermore, the analytical FE models accurately simulate the failure modes similar to the real tests. Particularly, perforated beams with narrow web-posts and sharp-tip points, such as Specimen A-2, A-3 and B-2. These are unable to redistribute the stresses and so high stresses are concentrated at these points. It is worth noting that the out-of-plane web movement at the yield load level point is negligible in FE analyses in relation to the experimental results.

Table 5.10 summarizes the main test and FE results for the yielding, buckling (or critical) and ultimate loads for the ease of comparison. It should be aforementioned that the reference FE model with f_y equal to 355MPa and Tangent Modulus, E_T, equal to 580MPa is used to generalize the results. The buckling load is obtained by careful consideration of the out-of-plane web displacements and the stress concentrations.

Spec.	P_y		$P_{cr.}$		$P_{ult.}$		Web-Post Width, s_o (mm)	Web Opening Shape	Web Opening Area (mm^2)
	FE (kN)	TEST (kN)	FE (kN)	TEST (kN)	FE (kN)	TEST (kN)			
A-1	265	250	327	257	342	289	94.5	Circular	77931
A-2	204	185	300	267	325	295	48	Circular with *r=25mm*	78361
A-3	148	132	274	164	365	186	15	Circular with *r=45mm*	79129
B-1	204	186	219	220	275	256	63	Circular	77931
B-2	281	276	363	387	420	402	63	Vertical Ellipse	56452
B-3	362	354	378	387	426	416	63	Vertical Ellipse	32138
B-4	270	250	354	280	422	346	63	Inclined Ellipse	45383

Table 5.10: Summary of the test and the predicted (FE) loads

More analytically, **Figure 5.81** depicts the variations between the test to predict (FE) load ratios and the web opening areas as well as the web-post widths. For all seven examined perforated beams the mean value of the test to predicted yielding, buckling and ultimate load ratios are 0.934, 0.880 and 0.849, respectively. The corresponding coefficients of variation (COV) are 0.107, 0.114 and 0.118. These results confirm that a satisfactory prediction with low variability is provided by the particular FE approach, mainly at the yield load level. Especially P_y but also $P_{ult.}$ are satisfactorily predicted by FEM as shown in **Figure 5.81**. Perforated beams with small web opening areas and/or large web-post widths, mainly show good correlation between experimental and FE results. The test to predict buckling load ratio is independent of the web opening area and the web-post width. This is shown as there is a significant variation of some $P_{cr.}$ ratios while the web opening area or web-post width remains the same.

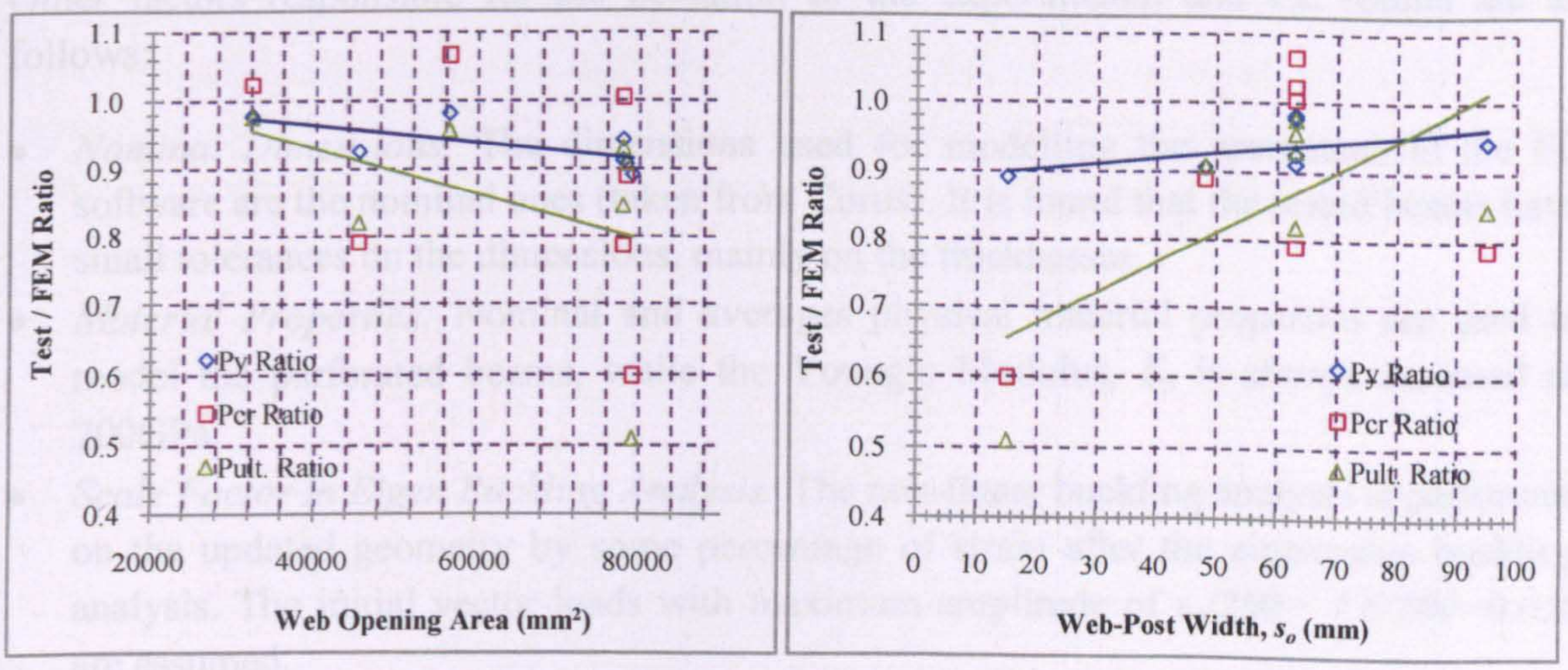

Figure 5.81: Variations of the test to predict (FE) loads

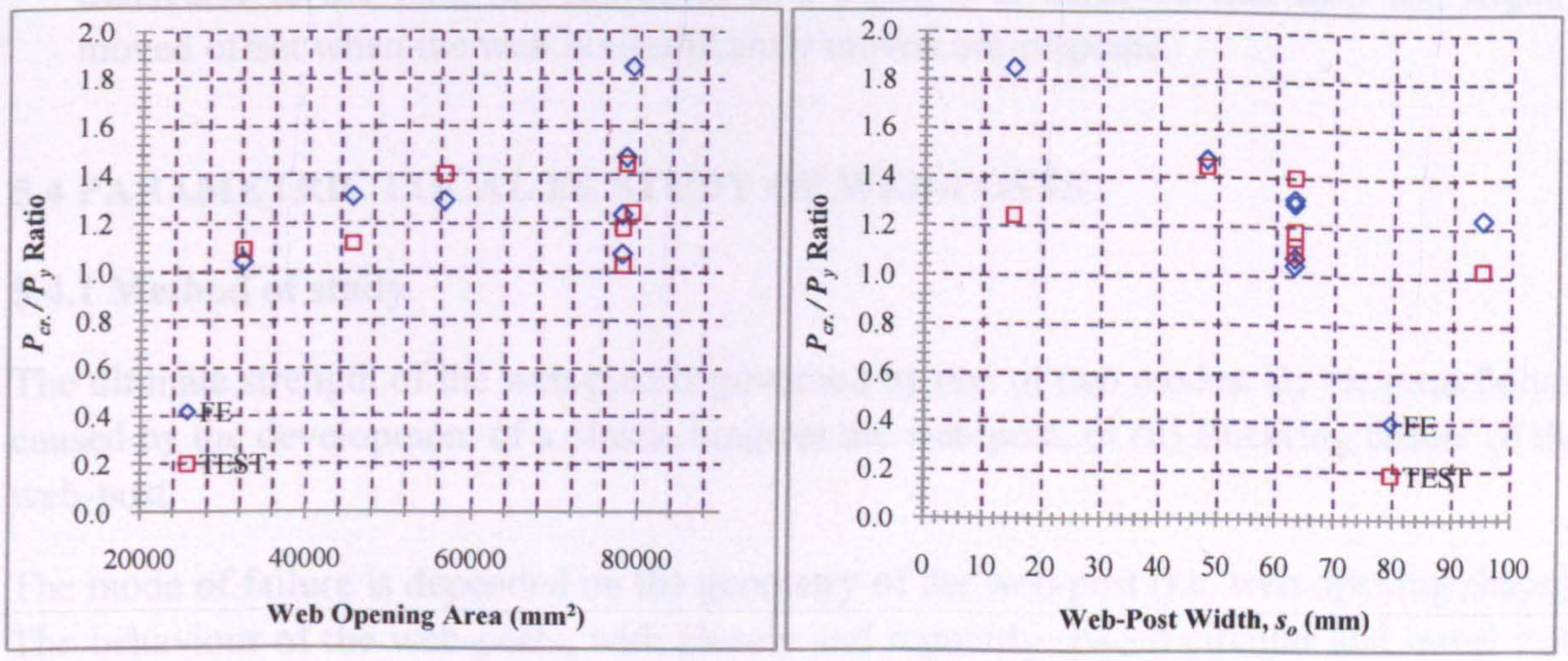

Figure 5.82: Variations of the predicted (FE) buckling to predict (FE) yielding loads

Figure 5.82 illustrates the variations of the buckling (critical) to yield load ratios for both tests and FE approaches. It is found that generally buckling to yield load ratio of both tests and FE models is independent of the web opening area and the web-post width. In both tests and FE approaches, the $P_{cr.}$ is higher than P_y.

5.3.7 Uncertainties

Geometric imperfections created by manufacturing procedures cause deviations of the critical buckling loads between the experimental and FE approaches. Regarding the particular specimens, a number of manufacturing geometric imperfections are found prior to the tests, especially in the perforated beams with the novel web opening shapes, due to lack of manufacturing capabilities at the present.

Other factors responsible for the deviation of the experimental and FE results are as follows:

- *Nominal Dimensions:* The dimensions used for modelling the specimens in the FE software are the nominal ones (taken from Corus). It is found that the tested beams have small tolerances on the dimensions, mainly on the thicknesses.
- *Material Properties:* Nominal and averages physical material properties are used to model the perforated beams, while the Young's Modulus, *E*, is always assumed as 200GPa.
- *Scale Factor in Eigen Buckling Analysis:* The non-linear buckling analysis is performed on the updated geometry by some percentage of strain after the eigenvalue buckling analysis. The initial vector-loads with maximum amplitude of $t_w/200 = 7.6/200 = 0.038$ are assumed.
- *Instrumental Errors:* The possibility of human and instrumental errors during the experimental work is also a dominant factor. Although the dial gauges, applied transverse to the web, are restrained at a point, it is observed that they are slightly moved offset when the web is significantly moved out-of-plane.

5.4 PARAMETRIC LOCAL FE STUDY OF WEB-POSTS

5.4.1 Method of study

The ultimate strength of the web-post is governed by one of two modes: (i) Flexural failure caused by the development of a plastic hinge in the web-post, or (ii) Buckling failure of the web-post.

The mode of failure is depended on the geometry of the web-post (i.e. web opening shape). The behaviour of the web-posts, with closely and regularly spaced circular and novel web

openings of fabricated steel beams, is investigated using a FE analysis. The FEA is carried out for a range of parameters, including the web slenderness.

The FEA included material non-linearity (i.e. plastic behaviour) and geometrical non-linearity (i.e. buckling). The model used in FEA is considered to be of a short section of beam between the centre-line of two adjacent web openings (**Figure 5.83**). The analyses are carried out for non-composite beams as this would give conservative results for composite beams. The main area of interest is the stability of the web-post under the combined effect of shear and compression, especially at the edge of the web openings, where the stabilizing effect of tension field action is less than at the centre of the web-post.

The main objective is to revise the design model of circular web openings for this complex web-post buckling failure mode, and establish new ones for the other five novel web openings. The design model developed is based on a strut analogy in which the stability of the web is checked using buckling curves from **BS 5950-1**. This strut analogy is presented in terms of the effective width, b_e, and effective length, l_e, of the strut, which are derived from the current FE study to give the best fit over the range of web opening parameters.

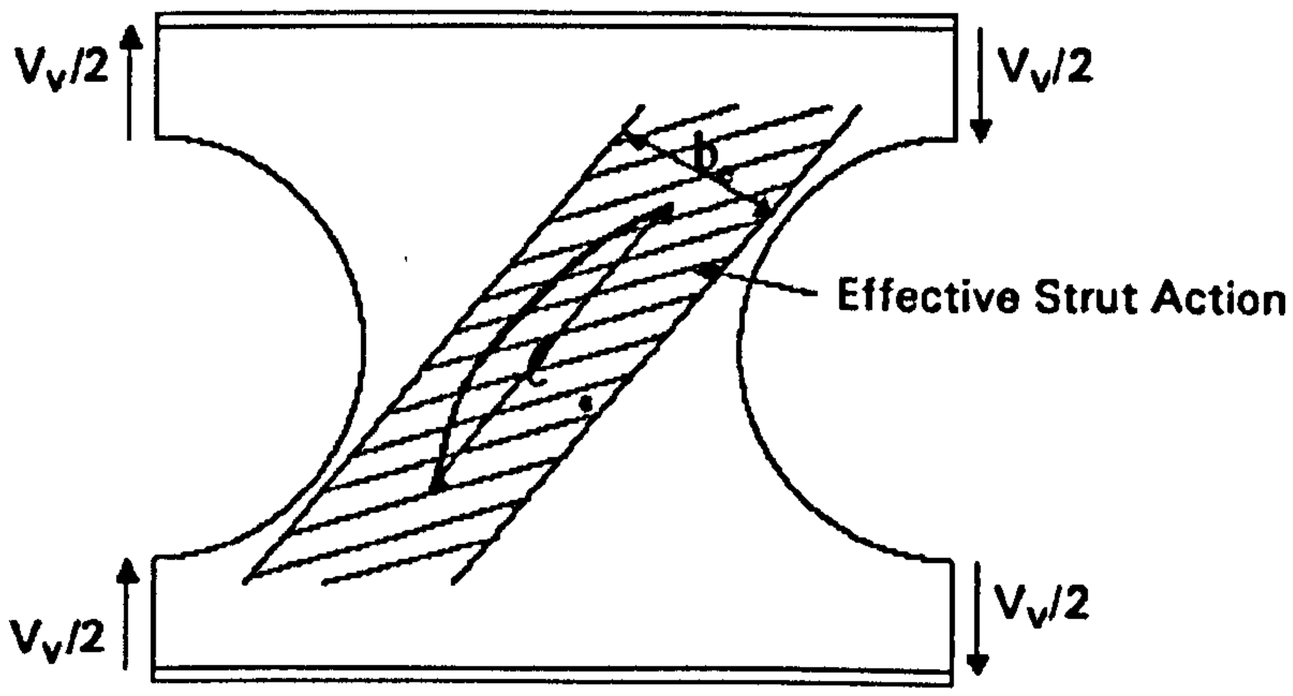

Figure 5.83: Strut model of web-post buckling (Fabsec Ltd.)

5.4.2 FE model

Basis of the model

The design model is based on buckling over an effective length, l_e, of web depending on the spacing of the web openings.

Two design cases may be investigated:

- Closely spaced web openings, where the proximity of the web openings causes an increase in stress acting on the web-post.
- Widely spaced web openings, where there is no interaction between the web openings.

The analysis for various web openings differs only in the effective length, l_e, of the web-post in compression. The transition from widely spaced to closely spaced openings is empirically taken to occur at an edge to edge spacing equal to the opening length (i.e. $s_o = d_o$ or l_o).

FE model parameters

Again the UB457x152x52 is used, for the ease of comparison and the conformity of the results. The web to flange fillet is not modelled, while the web thickness varies in order to accomplish the parametric study. Using the basic model, a model with 449.8mm depth and a web opening diameter, d_o, equal to $0.7h$, is considered and has a web opening diameter is of 315mm. The web thickness and the spacing of the web openings are only varied to assess the effect on web-post capacity. A parametric study is conducted to investigate the effect of S/d_o ratio on the resistance of the web-post (S is the centre to centre spacing of the web openings). Eight S/d_o ratios in the range 1.1 to 1.8 are studied with five web thicknesses of 3.9mm, 5.0mm, 6.0mm, 7.6mm (nominal thickness of this section) and 10.5mm (maximum possible thickness of this section), giving d_o/t_w ratios which vary from 30 to 80.8. As previously mentioned, the model is extended to examine all the novel web opening shapes of depth d_o, as investigated previously in this chapter, both experimentally and numerically.

It should be mentioned that the smallest web opening spacing, S, for Specimen A-2 and A-3 is $1.2d_o$ and $1.3d_o$, respectively. This is a result of the fillet existence at the mid-height of the web-post. From the combination of the above parameters, 225 FE models are developed, as presented in **Table 5.11** for the ease of identification.

Specimen A-1 & B-1								Specimen B-2						
S	Width (mm)	WEB THICKNESS, t_w (mm)						S	Width (mm)	WEB THICKNESS, t_w (mm)				
		3.9	5	6	7.6	10.5				3.9	5	6	7.6	10.5
$1.1d_o$	31.5	1	2	3	4	5		$0.931d_o$	31.5	106	107	108	109	110
$1.2d_o$	63	6	7	8	9	10		$1.031d_o$	63	111	112	113	114	115
$1.3d_o$	94.5	11	12	13	14	15		$1.131d_o$	94.5	116	117	118	119	120
$1.4d_o$	126	16	17	18	19	20		$1.231d_o$	126	121	122	123	124	125
$1.5d_o$	157.5	21	22	23	24	25		$1.331d_o$	157.5	126	127	128	129	130
$1.6d_o$	189	26	27	28	29	30		$1.431d_o$	189	131	132	133	134	135
$1.7d_o$	220.5	31	32	33	34	35		$1.531d_o$	220.5	136	137	138	139	140
$1.8d_o$	252	36	37	38	39	40		$1.631d_o$	252	141	142	143	144	145
Specimen A-2								Specimen B-3						
S	Width (mm)	WEB THICKNESS, t_w (mm)						S	Width (mm)	WEB THICKNESS, t_w (mm)				
		3.9	5	6	7.6	10.5				3.9	5	6	7.6	10.5
								$0.523d_o$	31.5	146	147	148	149	150
$1.2d_o$	63	71	72	73	74	75		$0.623d_o$	63	151	152	153	154	155
$1.3d_o$	94.5	76	77	78	79	80		$0.723d_o$	94.5	156	157	158	159	160
$1.4d_o$	126	81	82	83	84	85		$0.823d_o$	126	161	162	163	164	165
$1.5d_o$	157.5	86	87	88	89	90		$0.923d_o$	157.5	166	167	168	169	170
$1.6d_o$	189	91	92	93	94	95		$1.023d_o$	189	171	172	173	174	175
$1.7d_o$	220.5	96	97	98	99	100		$1.123d_o$	220.5	176	177	178	179	180
$1.8d_o$	252	101	102	103	104	105		$1.223d_o$	252	181	182	183	184	185
Specimen A-3								Specimen B-4						
S	Width (mm)	WEB THICKNESS, t_w (mm)						S	Width (mm)	WEB THICKNESS, t_w (mm)				
		3.9	5	6	7.6	10.5				3.9	5	6	7.6	10.5
								$0.65d_o$	31.5	186	187	188	189	190
								$0.75d_o$	63	191	192	193	194	195
$1.3d_o$	94.5	41	42	43	44	45		$0.85d_o$	94.5	196	197	198	199	200
$1.4d_o$	126	46	47	48	49	50		$0.95d_o$	126	201	202	203	204	205
$1.5d_o$	157.5	51	52	53	54	55		$1.05d_o$	157.5	206	207	208	209	210
$1.6d_o$	189	56	57	58	59	60		$1.15d_o$	189	211	212	213	214	215
$1.7d_o$	220.5	61	62	63	64	65		$1.25d_o$	220.5	216	217	218	219	220
$1.8d_o$	252	66	67	68	69	70		$1.35d_o$	252	221	222	223	224	225

Table 5.11: Number of every FE model with corresponding characteristics

Shell elements (SHELL181) with 6 degrees of freedom at each node are used to model the web-post. Depending on the S/d_o ratio and the web opening shape, refined FE meshes are implemented to model the web-posts. As the width of the web-post increases, the number of elements used to model its width also increases in order to maintain the element size. **Table 5.12** shows the range of S/d_o ratios for each mesh.

S/d_o	Number of Elements at Mid-depth of the Web-post					
	Spec. A-1 & B-1	Spec. A-2	Spec. A-3	Spec. B-2	Spec. B-3	Spec. B-4
1.1 to 1.2	10	10	-----	10	10	10
1.3	13	14	10	13	13	13
1.4	16	20	16	16	16	16
1.5	18	22	18	18	18	18
1.6	20	24	20	20	20	20
1.7	22	26	22	22	22	22
1.8	24	28	24	24	24	24

Table 5.12: Number of elements used to model web-posts depending on the S/d_o ratio

The FE model developed in **sub-chapter 5.2** is also used for this extensive parametric local study on web-posts. The three steps of linear, eigen buckling and non-linear analyses are conducted here as well, in order to initiate the out-of-plane movement of the web-post.

Linear elastic properties of the material are assumed as $E=200GPa$ and $v=0.3$. Plastic properties of the material are assumed as $f_y=355MPa$ and $E_T=580MPa$. The material model uses the Von-Mises criterion with bi-linear isotropic hardening plasticity, which is suitable for most metals, including steel. Arc-length method is not used herein, as it is found unnecessary. Vertical shear load is applied on the top and bottom web-flange tees at the right hand side of the FE model. The load is applied in 100 sub-steps, while its size is automatically controlled in order to achieve convergence as the solution approaching the failure load.

The boundary conditions used in the model are shown in **Figure 5.84** and **Table 5.13**. The web-flange connection is assumed to be pinned as a safe lower bound. In practice, some degree of fixity would exist, which increases the web buckling resistance.

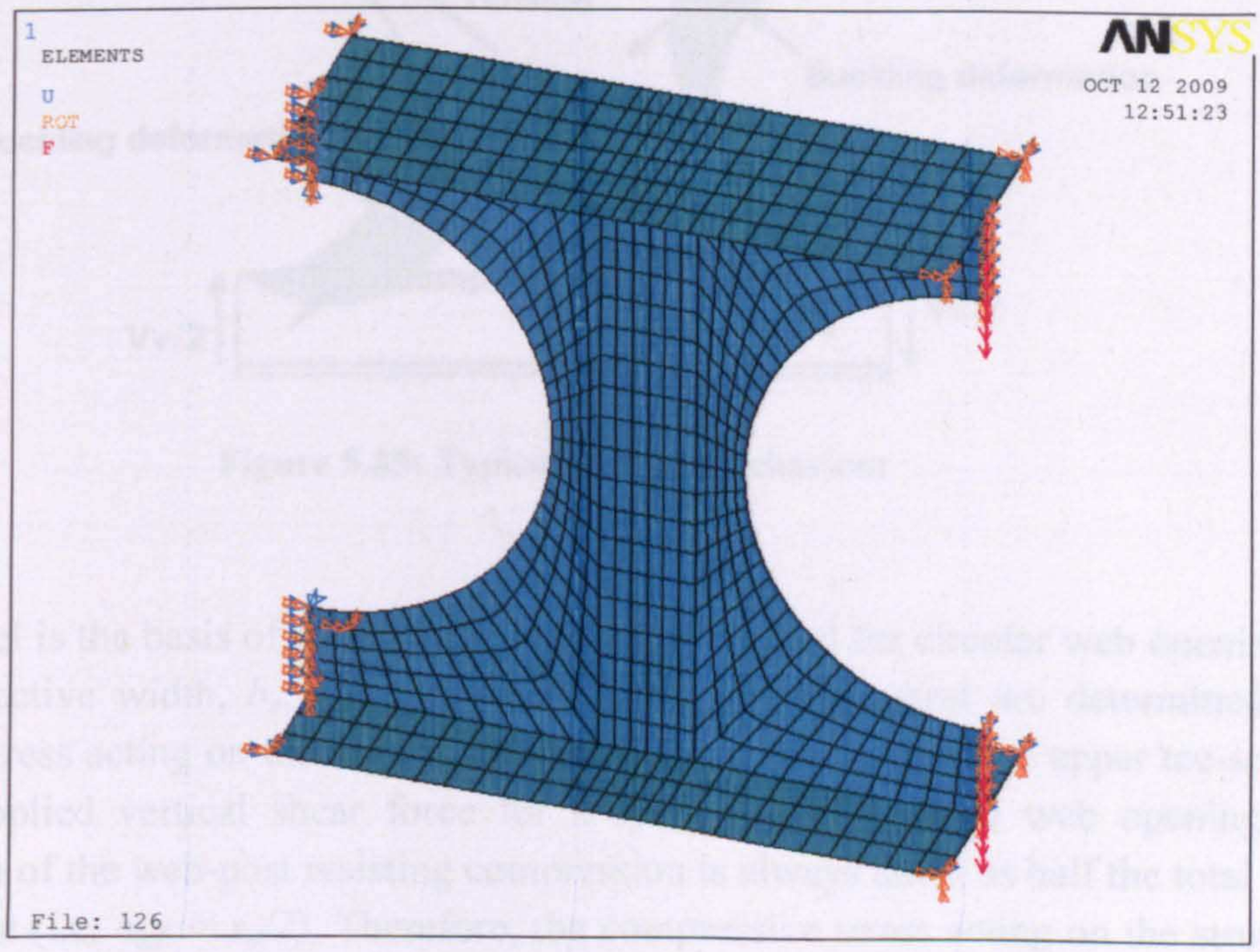

Figure 5.84: Applied loads and boundary conditions on a typical FE model

Location	UX	UY	UZ	ROT X	ROT Y	ROT Z
Flange (LHS)	FIXED	FREE	FIXED	FIXED	FREE	FIXED
Web (LHS)	FIXED	FIXED	FIXED	FIXED	FIXED	FREE
Flange (RHS)	FREE	FREE	FIXED	FIXED	FIXED	FIXED
Web (RHS)	FREE	LOAD	FIXED	FREE	FIXED	FIXED

Table 5.13: Applied boundary conditions used in the FE Model

5.4.3 FE results

The results of this parametric local FE study are thoroughly presented for Specimen A-1 and B-1. All data are graphically presented and tabulated with the same sequence for the rest of the specimens.

Compressive and tensile forces act across the web-post on opposite diagonals, as illustrated in **Figure 5.85**. Failure occurred when a local web buckle formed adjacent to the web opening as shown by the shaded areas in **Figure 5.85**.

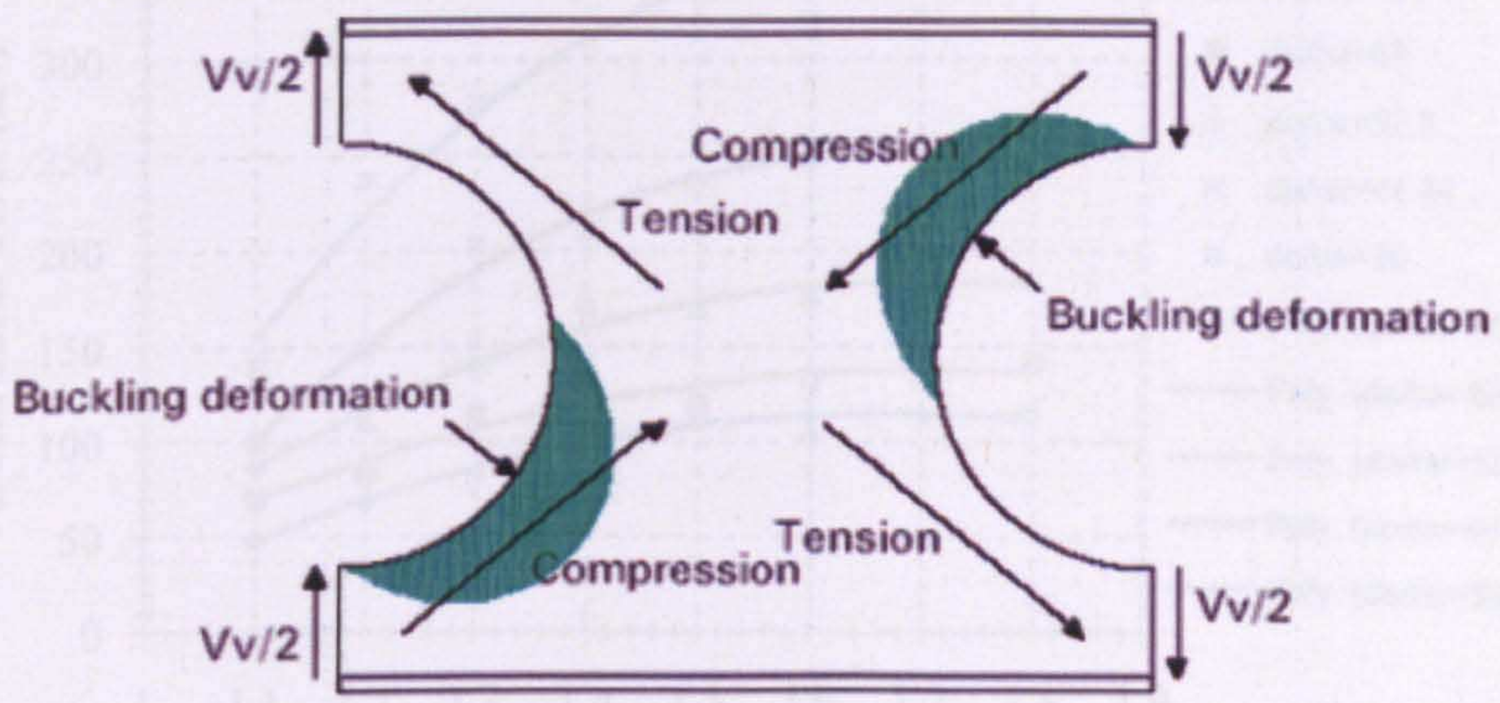

Figure 5.85: Typical web-post behaviour

The strut model is the basis of the already established method for circular web openings, in which the effective width, b_e, and effective length, l_e, of the strut are determined. The compressive stress acting on the strut is calculated using the force in the upper tee-section, or half the applied vertical shear force for a symmetrically placed web opening. The effective width of the web-post resisting compression is always taken as half the total width of the web-post (i.e. $b_{eff.} = s_o/2$). Therefore, the compressive stress acting on the strut is as follows:

$$\sigma = \frac{V_v}{2(^{s_o}/_2)t_w} = \frac{V_v}{s_o t_w} \qquad (5.1)$$

Specimen A-1 & B-1

The applied vertical shear forces at failure obtained from the FE analyses of the web-posts are graphically represented in **Figure 5.86**. Improved design formulas are developed which cover the range of $1.1 \leq S/d_o \leq 1.8$ as shown in **Table 5.14**.

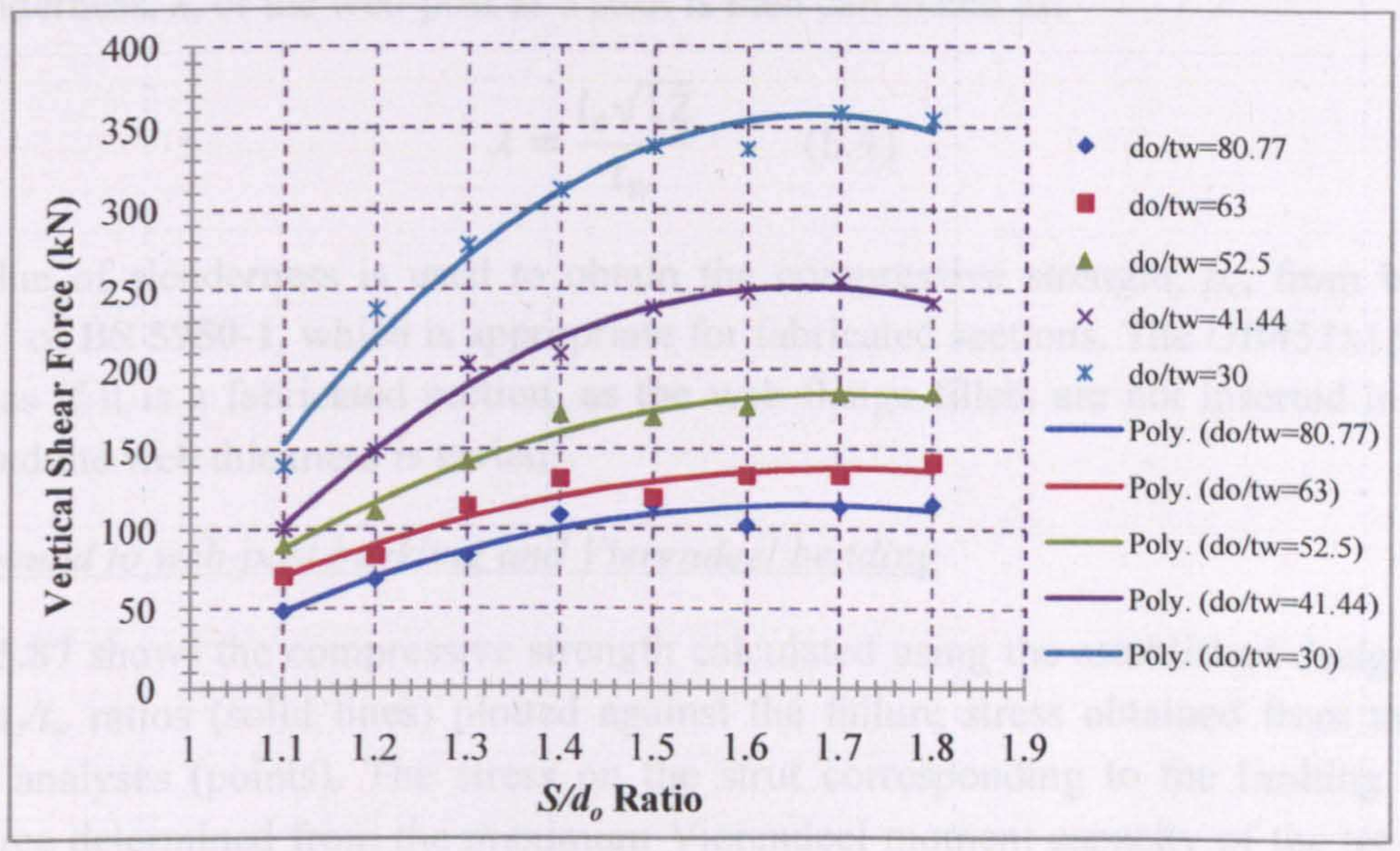

Figure 5.86: Applied vertical applied shear force (kN) at failure according to FE Model

t_w (mm)	d_o/t_w	*Formula*
3.9	**80.77**	$V_v = -\ 207.3\ (S/d_o)^2 + 692.4\ (S/d_o) - 462$
5.0	**63**	$V_v = -\ 180.8\ (S/d_o)^2 + 619.7\ (S/d_o) - 392.6$
6.0	**52.5**	$V_v = -\ 262.8\ (S/d_o)^2 + 896.5\ (S/d_o) - 580$
7.6	**41.44**	$V_v = -\ 471.7\ (S/d_o)^2 + 1569\ (S/d_o) - 1053$
10.5	**30**	$V_v = -\ 617.5\ (S/d_o)^2 + 2066\ (S/d_o) - 1371$

Table 5.14: Design formulas for Specimen A-1 & B-1

Basic design model for web-post between regularly spaced web openings

The design model derived from the finite element analyses is based on a simple strut model. The strut is considered to act diagonally across the member as shown before in **Figure 5.83**. The effective width, b_e, of the strut is always taken as half the width of the web-post for use in determining the compressive stresses.

$$b_e = 0.5 s_o \qquad (5.2)$$

The effective length, l_e, of the strut is calculated as the diagonal distance across the web-post using an effective length factor of 0.5 as assumed in the literature (l_e=*0.7* is assumed for square web openings), as follows:

$$l_e = 0.5\sqrt{{s_o}^2 + {d_o}^2} \qquad (5.3)$$

The slenderness, λ, of the web-post as a strut is then calculated as:

$$\lambda = \frac{l_e\sqrt{12}}{t_w} \qquad (5.4)$$

This value of slenderness is used to obtain the compressive strength, p_c, from buckling curve 'c' of **BS 5950-1**, which is appropriate for fabricated sections. The UB457x152x52 is studied as if it is a fabricated section, as the web-flange fillets are not inserted in the FE model and the web thickness is varied.

Lower bound to web-post buckling and Vierendeel bending

Figure 5.87 shows the compressive strength calculated using the established design model for all d_o/t_w ratios (solid lines) plotted against the failure stress obtained from the finite element analyses (points). The stress on the strut corresponding to the limiting vertical shear force determined from the maximum Vierendeel moment capacity of the tee-section is also plotted (dotty lines).

The limiting vertical shear force resulting from Vierendeel bending of the top tee-section is calculated by converting the circular web opening into an equivalent rectangular web opening with a width of $0.5d_o$ (equal to $1.0d_o$ for square web opening) and depth d_o, as shown in **Figure 3.40**. This conversion is based on the position of the plastic hinges when the web opening is subjected to high shear forces. The limiting vertical shear force in the top tee-section is given as follows:

$$\frac{V_v}{2} = \frac{M_{pt}}{0.25d_o} \qquad (5.5)$$

Where M_{pt} is the plastic moment capacity of the top tee-section and calculated as follows:

$$M_{pt\,(plastic)} = {A_{tee}}/{2}\left(\frac{\bar{x}_1}{2} + \bar{x}_2\right)p_y$$

and

$$A_{tee} = \left(bt_f\right) + \left(d_T t_w\right)$$

The centroids for equal areas are estimated from:

$$\bar{x}_1 = \frac{A_{tee}}{2b}$$

and

$$\bar{x}_2 = \frac{b\,(T-\bar{x}_1)^2/_2 + d_T t_w \left[(T-\bar{x}_1) + {}^{d_T}/_2\right]}{{}^{A_{tee}}/_2}$$

Where: $T = t_f - \bar{x}_1$

However, when d_T/t_w for the web of the tee-section exceeds the limit 9ε for a compact section (**BS 5950-1**), the moment capacity, M_{pt}, is calculated using elastic properties of the section, where d_T is the depth of the stem of the tee-section and $\varepsilon = \sqrt{275/p_y}$.

The FE analyses show that yielding rather than buckling occurs for stockier webs. This means that web-post buckling does not occur and the Vierendeel bending capacity is the governed design check rather than web-post buckling. **Figure 5.87** shows that the Vierendeel moment check is critical for d_o/t_w equal to 41.44 and 30 for S/d_o larger than 1.3 and 1.2, respectively.

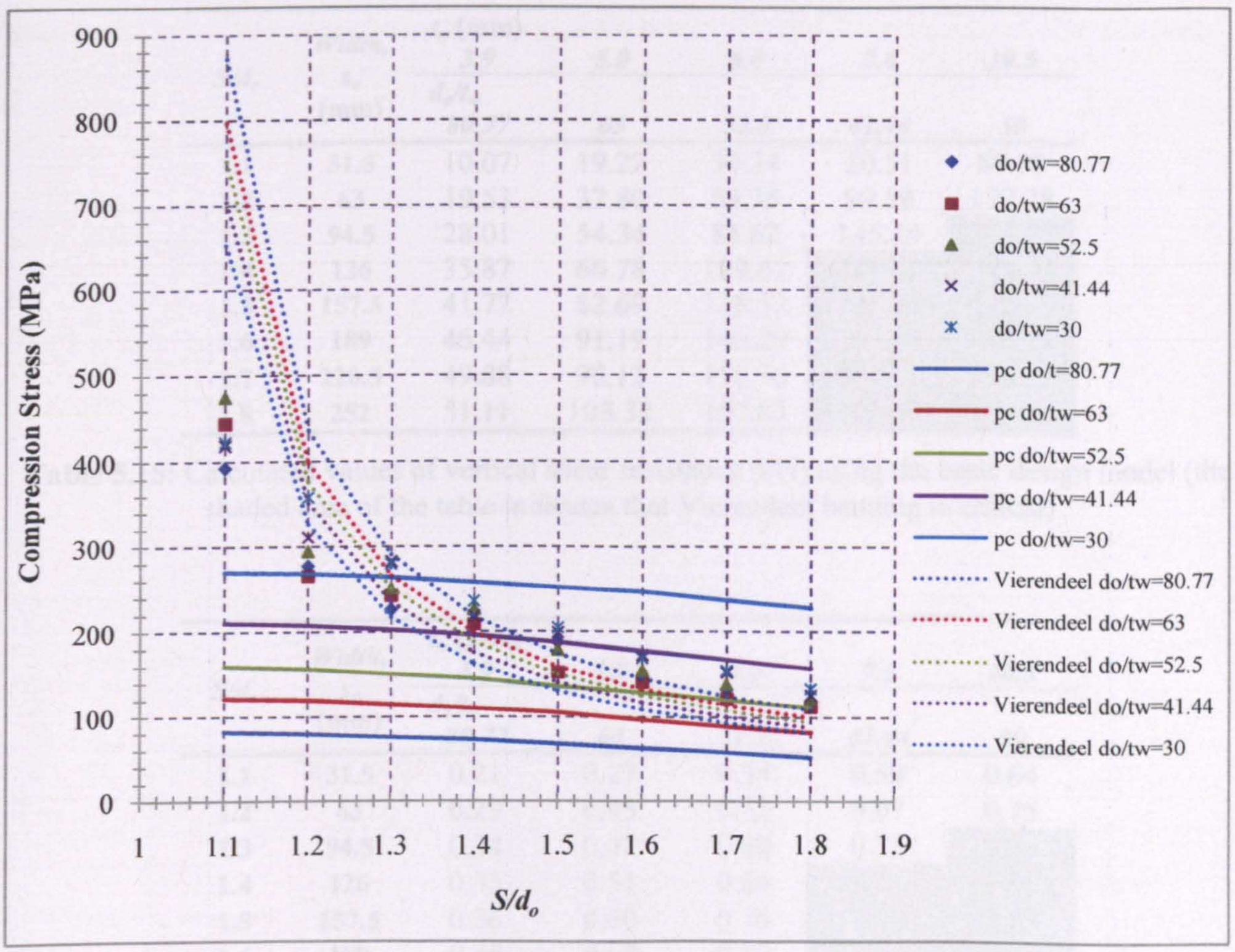

Figure 5.87: Compressive strength of the strut predicted by the design model and compared to FE failure stress and Vierendeel stress

Comparison with FEA

The vertical shear resistance, V_v, due to web-post buckling is calculated as follows:

$$V_v = 2b_e p_c t_w = p_c s_o t_w$$

Table 5.15 shows the vertical shear resistances calculated by using p_c derived from the effective slenderness of the web. **Table 5.16** represents the comparison of the vertical shear forces evaluated by the basic design model found in the literature (i.e. assuming l_e=*0.5*) and the FE model. There is conservatism up to approximately 80% for narrow and thin web-posts, but the level of conservatism is reduced for wider web-posts with greater web thicknesses. The shaded area indicates where the Vierendeel bending rather than the web-post buckling controls according to **Figure 5.87**. The un-conservative stresses resulting from the basic design model are not leading to unsafe design for this web slenderness, as the Vierendeel bending resistance is checked separately.

S/d_o	*Width,* s_o (mm)	t_w (mm) *3.9*	*5.0*	*6.0*	*7.6*	*10.5*
		d_o/t_w *80.77*	*63*	*52.5*	*41.44*	*30*
1.1	**31.5**	10.07	19.22	30.24	50.51	89.30
1.2	**63**	19.53	37.80	59.35	99.59	177.28
1.3	**94.5**	28.01	54.34	85.62	145.44	261.95
1.4	**126**	35.87	66.78	109.62	187.69	341.33
1.5	**157.5**	41.77	82.69	128.52	225.04	416.75
1.6	**189**	46.44	91.19	146.29	255.68	490.17
1.7	**220.5**	49.88	98.12	158.76	281.53	548.71
1.8	**252**	51.11	103.32	167.83	302.60	603.29

Table 5.15: Calculated values of vertical shear resistance (kN) using the basic design model (the shaded area of the table indicates that Vierendeel bending is critical)

S/d_o	*Width,* s_o (mm)	t_w (mm) *3.9*	*5.0*	*6.0*	*7.6*	*10.5*
		d_o/t_w *80.77*	*63*	*52.5*	*41.44*	*30*
1.1	**31.5**	0.21	0.27	0.34	0.50	0.64
1.2	**63**	0.29	0.45	0.53	0.67	0.75
1.3	**94.5**	0.34	0.47	0.60	0.72	0.94
1.4	**126**	0.33	0.51	0.64	0.90	1.10
1.5	**157.5**	0.36	0.69	0.76	0.95	1.23
1.6	**189**	0.45	0.68	0.83	1.03	1.46
1.7	**220.5**	0.44	0.73	0.86	1.10	1.53
1.8	**252**	0.44	0.73	0.91	1.25	1.70

Table 5.16: Ratio of vertical shear forces from the basic design model in literature and FE analyses (the shaded area of the table indicates that Vierendeel bending is critical)

Figure 5.88 demonstrates the minimum compressive strength as it is found for a web-post of any web thickness and a specific web opening spacing. This is an empirical method, evaluating the compressive stress at a web-post considering both the FE results and the theoretical evaluations based on plastic moment capacity of the top tee-section. A design formula is developed and shown below which covers the range of $1.1<S/d_o<1.8$.

$$Compression\ Stress = 659.4\left(\frac{S}{d_o}\right)^2 - 2276\left(\frac{S}{d_o}\right) + 2043 \qquad (5.6)$$

It is inevitable that by using this method some overestimation is considered for certain models. Moreover the new proposed effective length factors, producing the above compression stresses, are also presented in **Table 5.17** to illustrate the stiffening effect of the web above and below the web opening. Conservative but also economic results for web-posts under buckling and shear provisions are achieved. It is recommended that the

above models, those that are critical in Vierendeel, should be also separately checked for Vierendeel bending capacity.

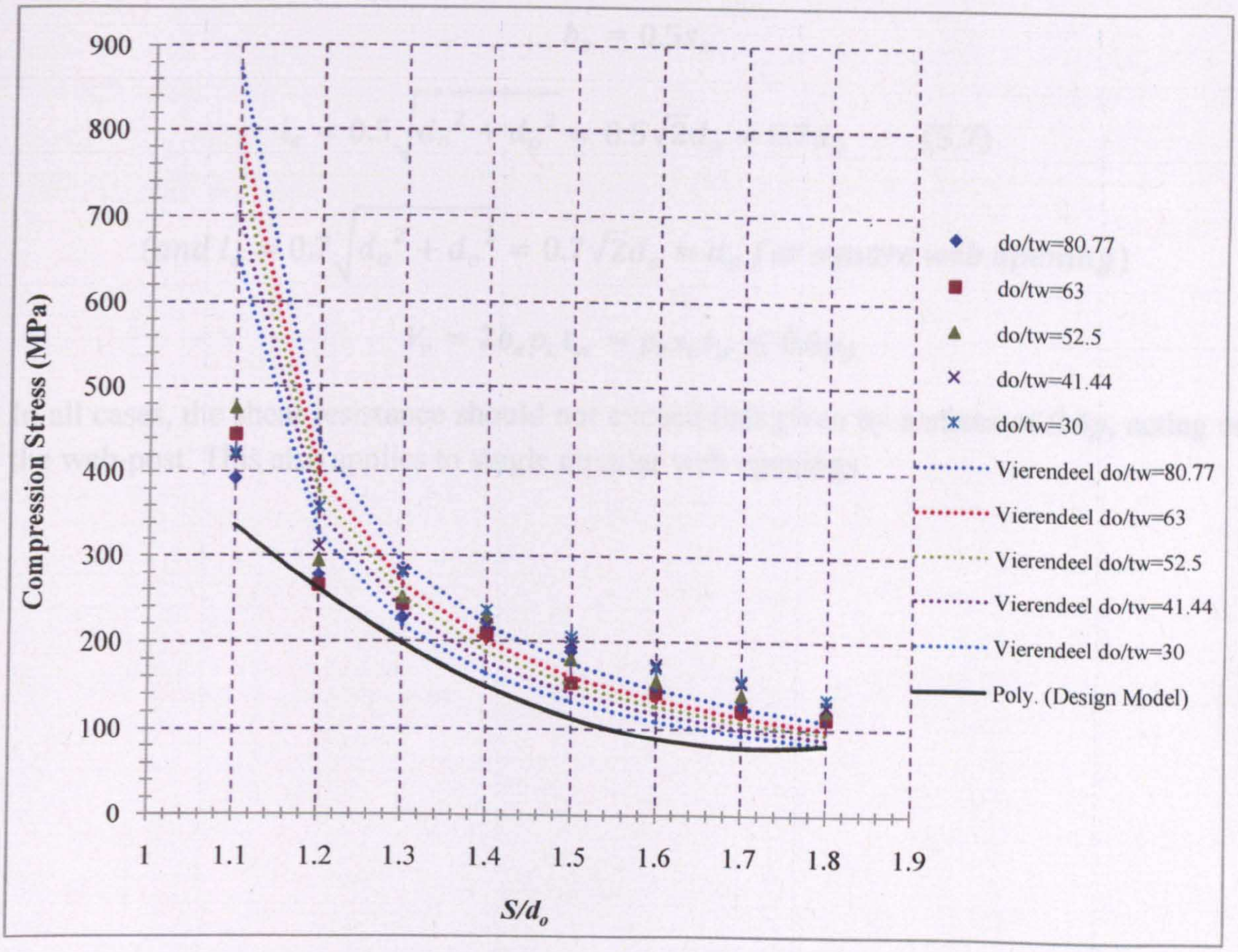

Figure 5.88: Empirical design model for compressive strength of the strut compared to FE failure stress and Vierendeel stress

S/d_o	*Width,* s_o (mm)	t_w (mm) *3.9*	*5.0*	*6.0*	*7.6*	*10.5*
		d_o/t_w *80.77*	*63*	*52.5*	*41.44*	*30*
1.1	**31.5**	0.05	0.07	0.08	0.10	0.14
1.2	**63**	0.22	0.28	0.34	0.43	0.59
1.3	**94.5**	0.26	0.34	0.41	0.51	0.71
1.4	**126**	0.32	0.41	0.49	0.62	0.86
1.5	**157.5**	0.36	0.46	0.55	0.70	0.96
1.6	**189**	0.39	0.50	0.59	0.75	1.04
1.7	**220.5**	0.40	0.52	0.62	0.78	1.08
1.8	**252**	0.42	0.54	0.64	0.82	1.13

Table 5.17: Proposed effective length factors

Basic design model for web-post between widely spaced web openings

For widely spaced web openings of any shape, the shear resistance obtained using $S/d_o=2.0$, is used as a cut-off in this analysis. In this limiting case:

$$b_e = 0.5s_o$$

$$l_e = 0.5\sqrt{{d_o}^2 + {d_o}^2} = 0.5\sqrt{2}d_o \approx 0.7d_o \qquad (5.7)$$

$$(and\ l_e = 0.7\sqrt{{d_o}^2 + {d_o}^2} = 0.7\sqrt{2}d_o \approx d_o\ for\ square\ web\ opening)$$

$$V_v = 2b_e p_c t_w = p_c s_o t_w \leq 0.6p_y$$

In all cases, the shear resistance should not exceed that given by a stress of $0.6p_y$ acting on the web-post. This also applies to single circular web openings.

Specimen A-2

The applied vertical shear forces at failure obtained from the FE analyses of the web-posts are graphically represented in **Figure 5.89**. Improved design formulas are developed, which cover the range of $1.1 \leq S/d_o \leq 1.8$ as shown in **Table 5.18**. The effective width, b_e, of the strut is taken as half the width of the web-post for use in determining the compressive stresses, similar to the web-post width of the circular web openings (**Formula 5.2**). This assumption provides some conservatism and simplifies the calculations. In such a way, there is no need to estimate the exact web-post width including the fillets.

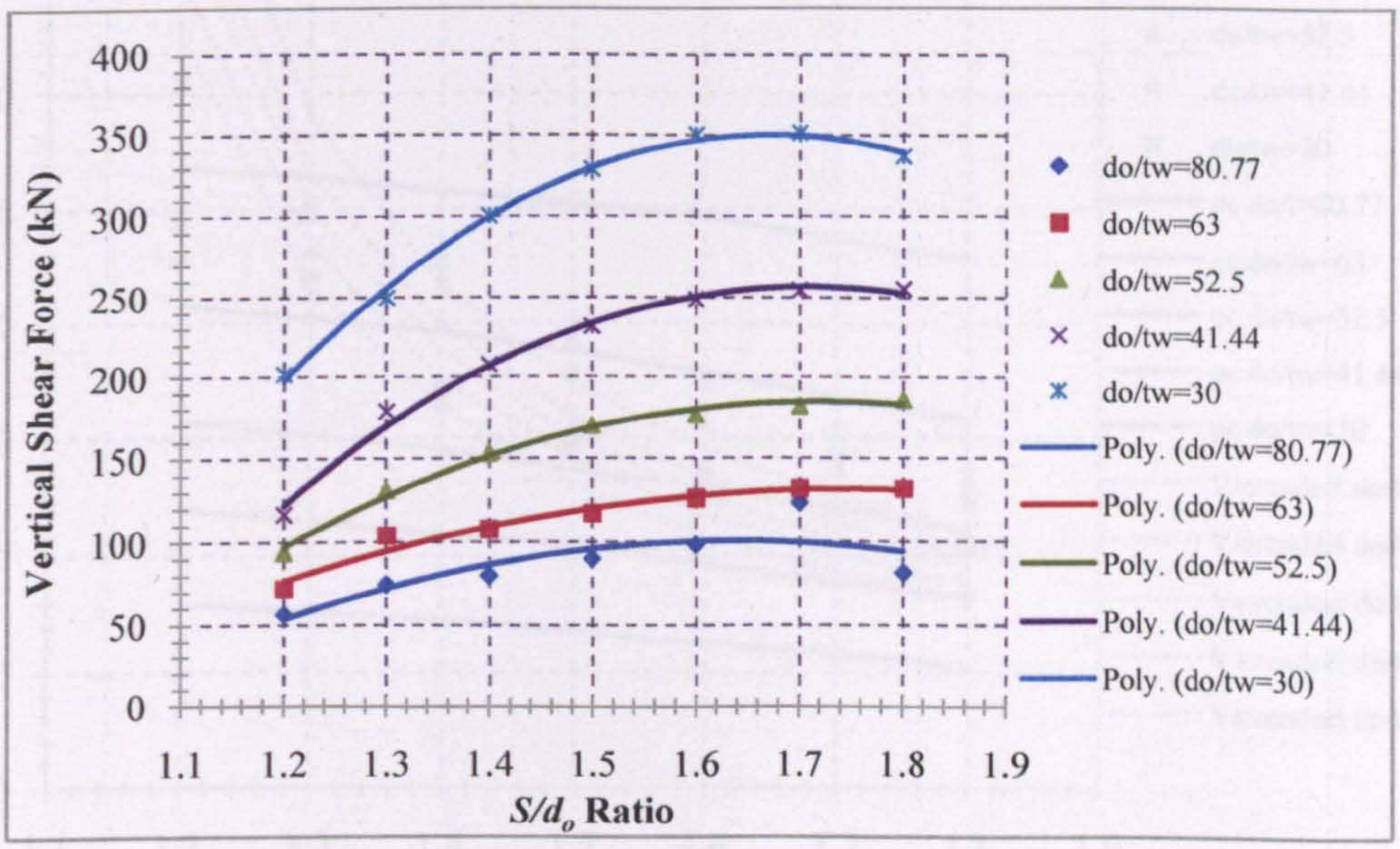

Figure 5.89: Applied vertical applied shear force (kN) at failure according to FE Model

t_w (mm)	d_o/t_w	*Formula*
3.9	**80.77**	$V_v = -181.1 (S/d_o)^2 + 633.4 (S/d_o) - 422.4$
5.0	**63**	$V_v = -245 (S/d_o)^2 + 802.8 (S/d_o) - 556.2$
6.0	**52.5**	$V_v = -320.3 (S/d_o)^2 + 1104 (S/d_o) - 766.8$
7.6	**41.44**	$V_v = -517 (S/d_o)^2 + 1768 (S/d_o) - 1255$
10.5	**30**	$V_v = -683.3 (S/d_o)^2 + 2285 (S/d_o) - 1560$

Table 5.18: Design formulas for Specimen A-2

Lower Bound to Web-Post Buckling and Vierendeel bending

Figure 5.90 shows that the Vierendeel moment check is critical for d_o/t_w equal to 52.5, 41.44 and 30 for S/d_o larger than 1.6, 1.3 and 1.2, respectively.

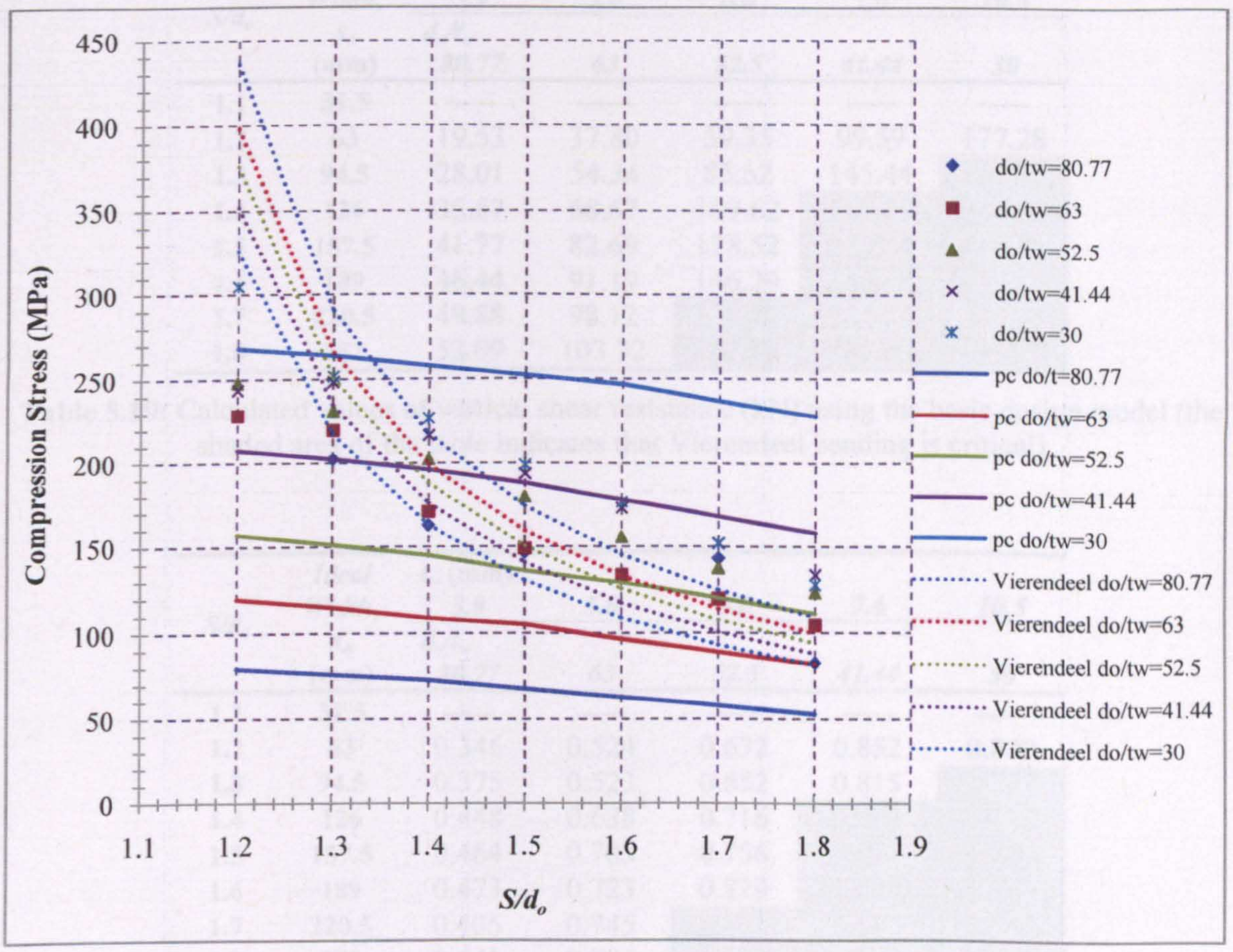

Figure 5.90: Compressive strength of the strut predicted by the design model and compared to FE failure stress and Vierendeel stress

Comparison with FEA

There is conservatism by up to approximately 65% for narrow and thin web-posts.

S/d_o	*Ideal Width,* s_o (mm)	t_w (mm) *3.9*	*5.0*	*6.0*	*7.6*	*10.5*
		d_o/t_w *80.77*	*63*	*52.5*	*41.44*	*30*
1.1	**31.5**	-----	-----	-----	-----	-----
1.2	**63**	19.53	37.80	59.35	99.59	177.28
1.3	**94.5**	28.01	54.34	85.62	145.44	261.95
1.4	**126**	35.87	68.67	109.62	187.69	341.33
1.5	**157.5**	41.77	82.69	128.52	225.04	416.75
1.6	**189**	46.44	91.19	146.29	255.68	490.17
1.7	**220.5**	49.88	98.12	158.76	281.53	548.71
1.8	**252**	52.09	103.32	167.83	302.60	603.29

Table 5.19: Calculated values of vertical shear resistance (kN) using the basic design model (the shaded area of the table indicates that Vierendeel bending is critical)

S/d_o	*Ideal Width,* s_o (mm)	t_w (mm) *3.9*	*5.0*	*6.0*	*7.6*	*10.5*
		d_o/t_w *80.77*	*63*	*52.5*	*41.44*	*30*
1.1	**31.5**	-----	-----	-----	-----	-----
1.2	**63**	0.346	0.524	0.632	0.852	0.879
1.3	**94.5**	0.375	0.523	0.652	0.815	1.049
1.4	**126**	0.448	0.638	0.716	0.904	1.136
1.5	**157.5**	0.464	0.705	0.756	0.971	1.267
1.6	**189**	0.473	0.723	0.829	1.029	1.399
1.7	**220.5**	0.405	0.745	0.873	1.106	1.562
1.8	**252**	0.641	0.785	0.902	1.185	1.790

Table 5.20: Ratio of vertical shear forces from the basic design model in literature and FE analyses (the shaded area of the table indicates that Vierendeel bending is critical)

A design formula is developed and shown below which covers the range of $1.2<S/d_o<1.8$.

$$Compression\ Stress = 230.2\left(\frac{S}{d_o}\right)^2 - 920.5\left(\frac{S}{d_o}\right) + 983.3 \qquad (5.8)$$

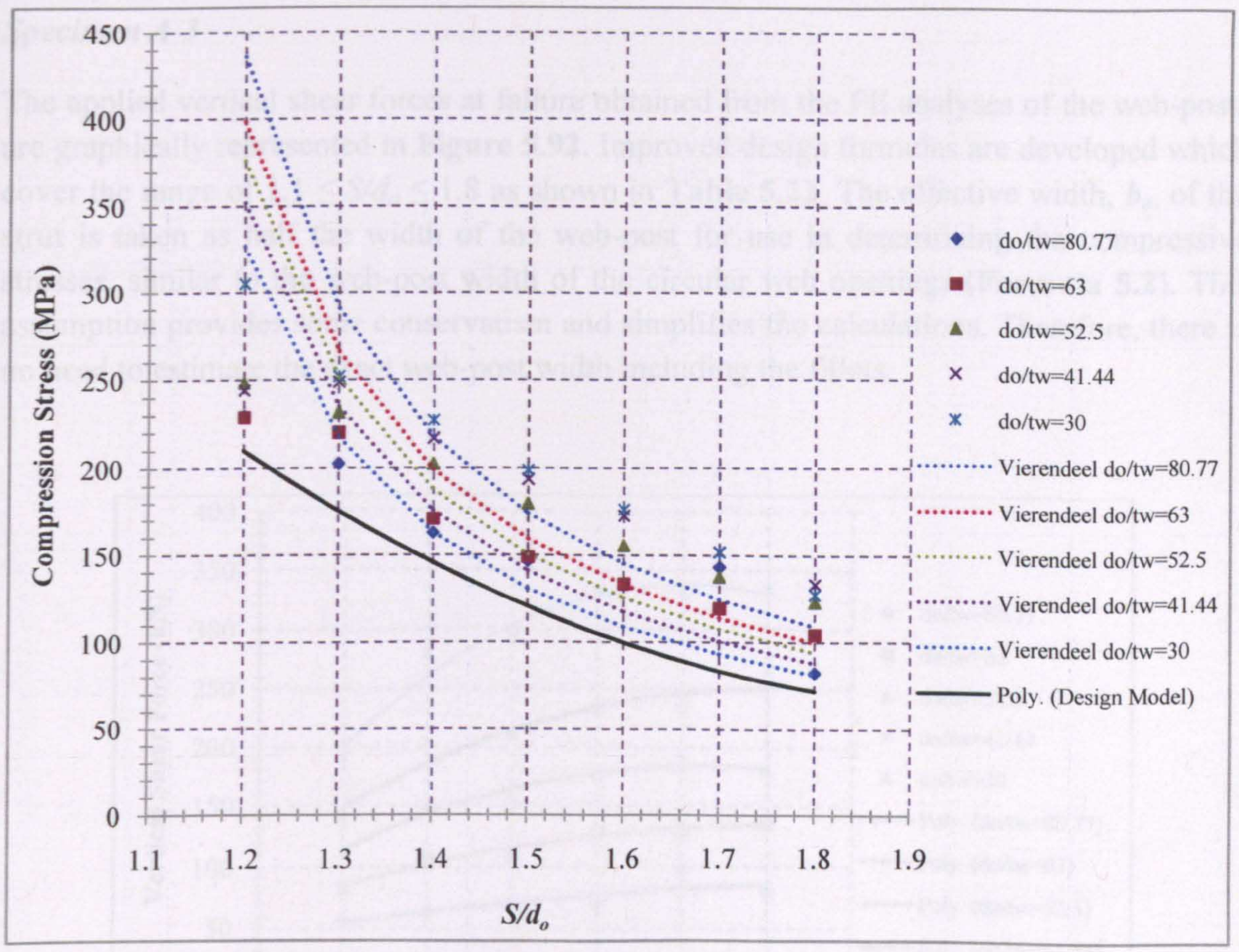

Figure 5.91: Empirical design model for compressive strength of the strut compared to FE failure stress and Vierendeel stress

S/d_o	*Ideal Width, s_o (mm)*	t_w (mm) *3.9*	*5.0*	*6.0*	*7.6*	*10.5*
		d_o/t_w *80.77*	*63*	*52.5*	*41.44*	*30*
1.1	**31.5**	-----	-----	-----	-----	-----
1.2	**63**	0.26	0.33	0.40	0.50	0.69
1.3	**94.5**	0.28	0.36	0.43	0.55	0.76
1.4	**126**	0.32	0.41	0.50	0.63	0.87
1.5	**157.5**	0.36	0.46	0.55	0.70	0.96
1.6	**189**	0.39	0.50	0.59	0.75	1.04
1.7	**220.5**	0.40	0.52	0.62	0.79	1.09
1.8	**252**	0.42	0.54	0.64	0.82	1.13

Table 5.21: Proposed effective length factors

Specimen A-3

The applied vertical shear forces at failure obtained from the FE analyses of the web-posts are graphically represented in **Figure 5.92**. Improved design formulas are developed which cover the range of $1.1 \leq S/d_o \leq 1.8$ as shown in **Table 5.22**. The effective width, b_e, of the strut is taken as half the width of the web-post for use in determining the compressive stresses, similar to the web-post width of the circular web openings (**Formula 5.2**). This assumption provides some conservatism and simplifies the calculations. Therefore, there is no need to estimate the exact web-post width including the fillets.

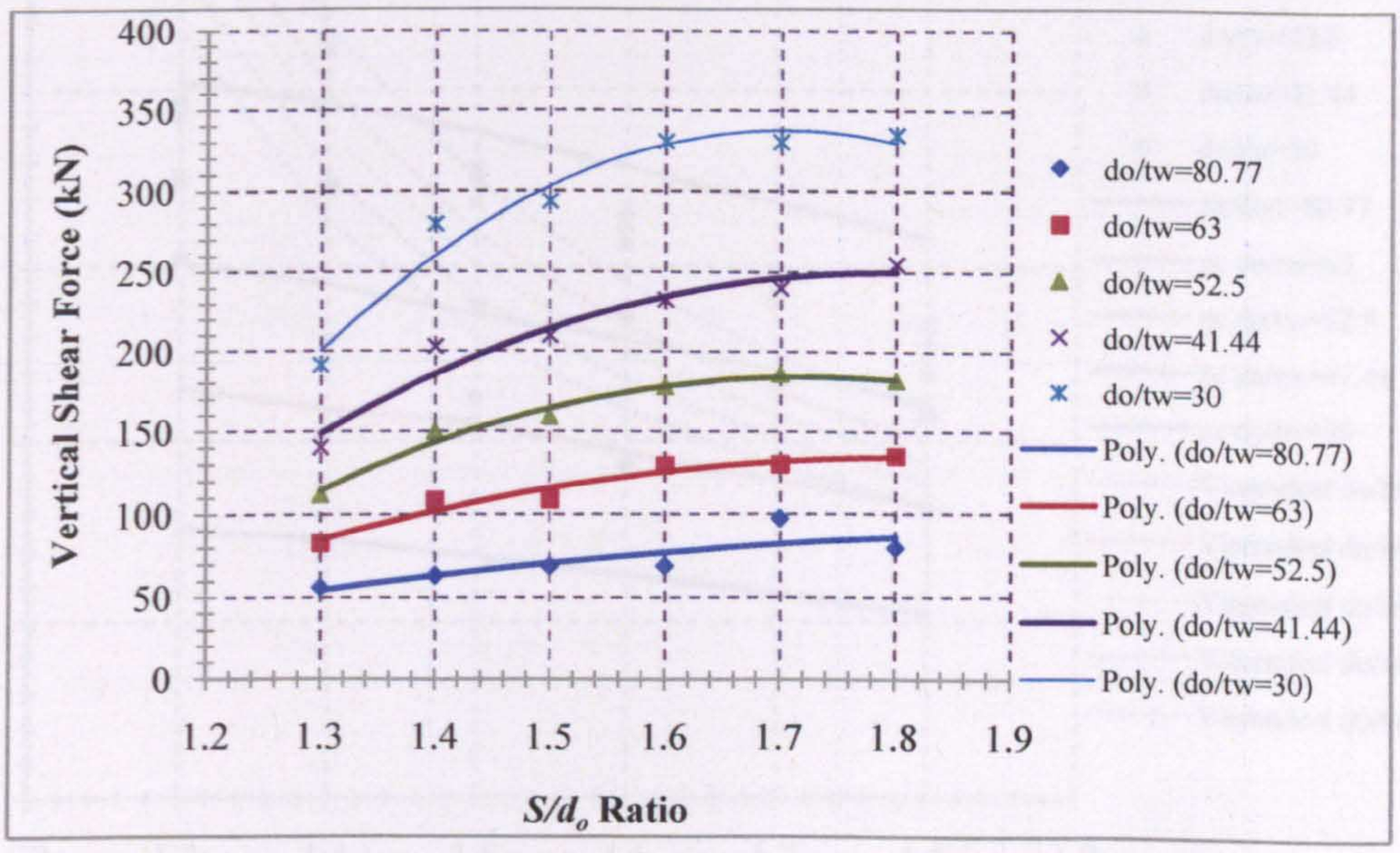

Figure 5.92: Applied vertical applied shear force (kN) at failure according to FE Model

t_w (mm)	d_o/t_w	*Formula*
3.9	**80.77**	$V_v = -57.25\,(S/d_o)^2 + 240\,(S/d_o) - 160.4$
5.0	**63**	$V_v = -180.3\,(S/d_o)^2 + 657.9\,(S/d_o) - 465.5$
6.0	**52.5**	$V_v = -379.4\,(S/d_o)^2 + 1312\,(S/d_o) - 950.5$
7.6	**41.44**	$V_v = -420.4\,(S/d_o)^2 + 1505\,(S/d_o) - 1097$
10.5	**30**	$V_v = -847.3\,(S/d_o)^2 + 2885\,(S/d_o) - 2118$

Table 5.22: Design formulas for Specimen A-3

Lower Bound to Web-Post Buckling and Vierendeel bending

Figure 5.93 shows that the Vierendeel moment check is critical for d_o/t_w equal to 52.5, 41.44 and 30 for S/d_o larger than 1.6, 1.3 and 1.2, respectively.

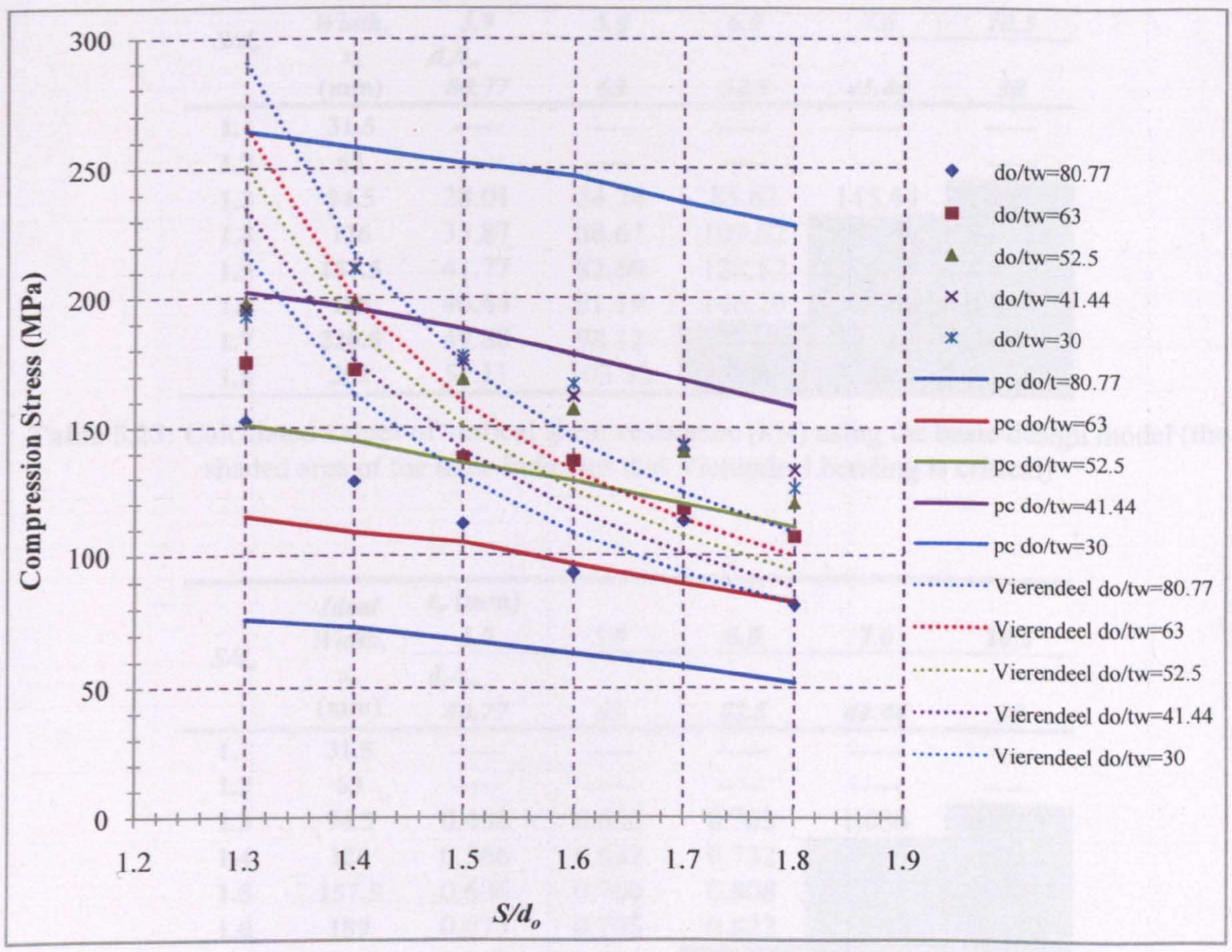

Figure 5.93: Compressive strength of the strut predicted by the design model and compared to FE failure stress and Vierendeel stress

Comparison with FEA

There is conservatism by up to approximately 50% for narrow and thin web-posts.

S/d_o	*Ideal Width, s_o* (mm)	t_w (mm) *3.9* d_o/t_w *80.77*	*5.0* *63*	*6.0* *52.5*	*7.6* *41.44*	*10.5* *30*
1.1	**31.5**	-----	-----	-----	-----	-----
1.2	**63**	-----	-----	-----	-----	-----
1.3	**94.5**	28.01	54.34	85.62	145.44	261.95
1.4	**126**	35.87	68.67	109.62	187.69	341.33
1.5	**157.5**	41.77	82.69	128.52	225.04	416.75
1.6	**189**	46.44	91.19	146.29	255.68	490.17
1.7	**220.5**	49.88	98.12	158.76	281.53	548.71
1.8	**252**	51.11	103.32	167.83	302.60	603.29

Table 5.23: Calculated values of vertical shear resistance (kN) using the basic design model (the shaded area of the table indicates that Vierendeel bending is critical)

S/d_o	*Ideal Width, s_o* (mm)	t_w (mm) *3.9* d_o/t_w *80.77*	*5.0* *63*	*6.0* *52.5*	*7.6* *41.44*	*10.5* *30*
1.1	**31.5**	-----	-----	-----	-----	-----
1.2	**63**	-----	-----	-----	-----	-----
1.3	**94.5**	0.498	0.656	0.763	1.036	1.367
1.4	**126**	0.566	0.632	0.732	0.925	1.221
1.5	**157.5**	0.606	0.760	0.808	1.072	1.421
1.6	**189**	0.675	0.705	0.822	1.099	1.482
1.7	**220.5**	0.512	0.755	0.854	1.173	1.661
1.8	**252**	0.642	0.764	0.921	1.186	1.803

Table 5.24: Ratio of vertical shear forces from the basic design model in literature and FE analyses (the shaded area of the table indicates that Vierendeel bending is critical)

A design formula is developed and shown below which covers the range of $1.3<S/d_o<1.8$.

$$Compression\ Stress = 204.4\left(\frac{S}{d_o}\right)^2 - 757.6\left(\frac{S}{d_o}\right) + 776.3 \qquad (5.9)$$

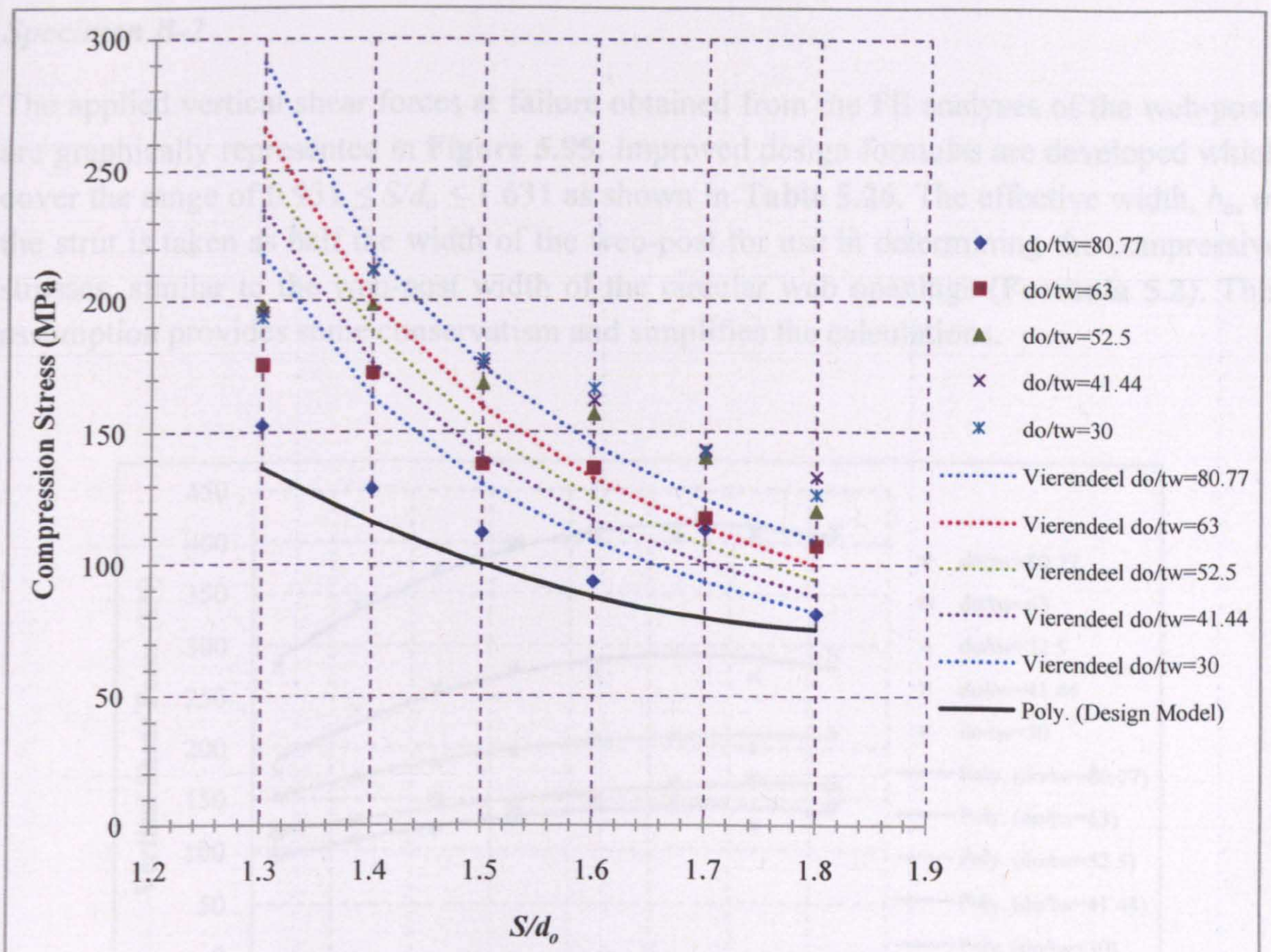

Figure 5.94: Empirical design model for compressive strength of the strut compared to FE failure stress and Vierendeel stress

S/d_o	*Ideal Width, s_o (mm)*	t_w (mm) *3.9*	*5.0*	*6.0*	*7.6*	*10.5*
		d_o/t_w *80.77*	*63*	*52.5*	*41.44*	*30*
1.1	**31.5**	-----	-----	-----	-----	-----
1.2	**63**	-----	-----	-----	-----	-----
1.3	**94.5**	0.35	0.44	0.53	0.67	0.93
1.4	**126**	0.38	0.48	0.58	0.73	1.01
1.5	**157.5**	0.39	0.51	0.61	0.77	1.06
1.6	**189**	0.42	0.54	0.65	0.83	1.14
1.7	**220.5**	0.41	0.52	0.63	0.79	1.10
1.8	**252**	0.42	0.53	0.64	0.81	1.12

Table 5.25: Proposed effective length factors

Specimen B-2

The applied vertical shear forces at failure obtained from the FE analyses of the web-posts are graphically represented in **Figure 5.95**. Improved design formulas are developed which cover the range of $0.931 \leq S/d_o \leq 1.631$ as shown in **Table 5.26**. The effective width, b_e, of the strut is taken as half the width of the web-post for use in determining the compressive stresses, similar to the web-post width of the circular web openings (**Formula 5.2**). This assumption provides some conservatism and simplifies the calculations.

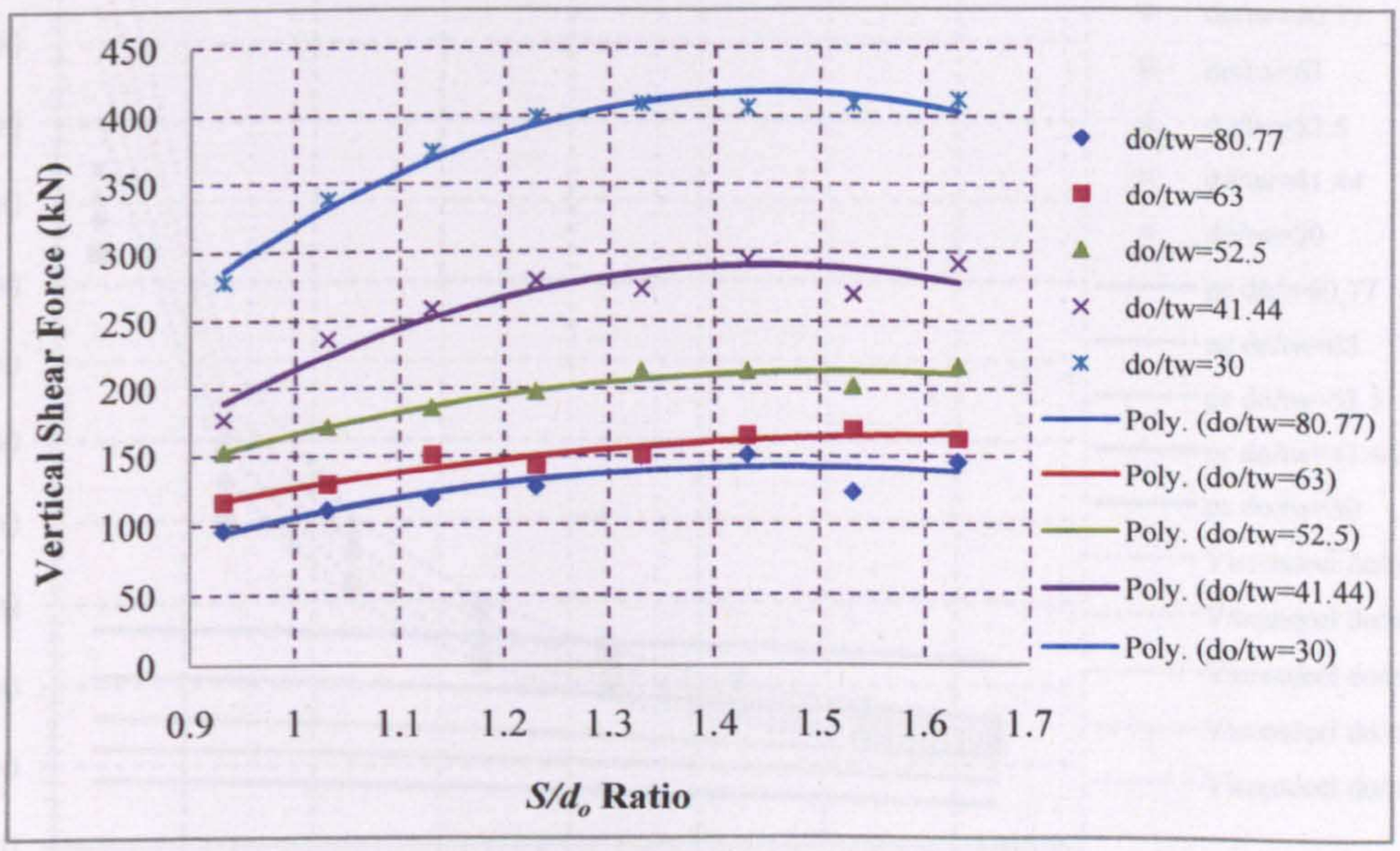

Figure 5.95: Applied vertical applied shear force (kN) at failure according to FE Model

t_w (mm)	d_o/t_w	*Formula*
3.9	**80.77**	$V_v = -160.2\,(S/d_o)^2 + 474\,(S/d_o) - 208.2$
5.0	**63**	$V_v = -96.46\,(S/d_o)^2 + 316.8\,(S/d_o) - 94.19$
6.0	**52.5**	$V_v = -172.4\,(S/d_o)^2 + 525\,(S/d_o) - 186.6$
7.6	**41.44**	$V_v = -379.6\,(S/d_o)^2 + 1099\,(S/d_o) - 505.6$
10.5	**30**	$V_v = -477.8\,(S/d_o)^2 + 1390\,(S/d_o) - 594$

Table 5.26: Design formulas for Specimen B-2

Lower Bound to Web-Post Buckling and Vierendeel bending

Figure 5.96 shows that the Vierendeel moment check is critical for d_o/t_w equal to 41.44 and 30 for S/d_o larger than 1.231 and 1.131, respectively.

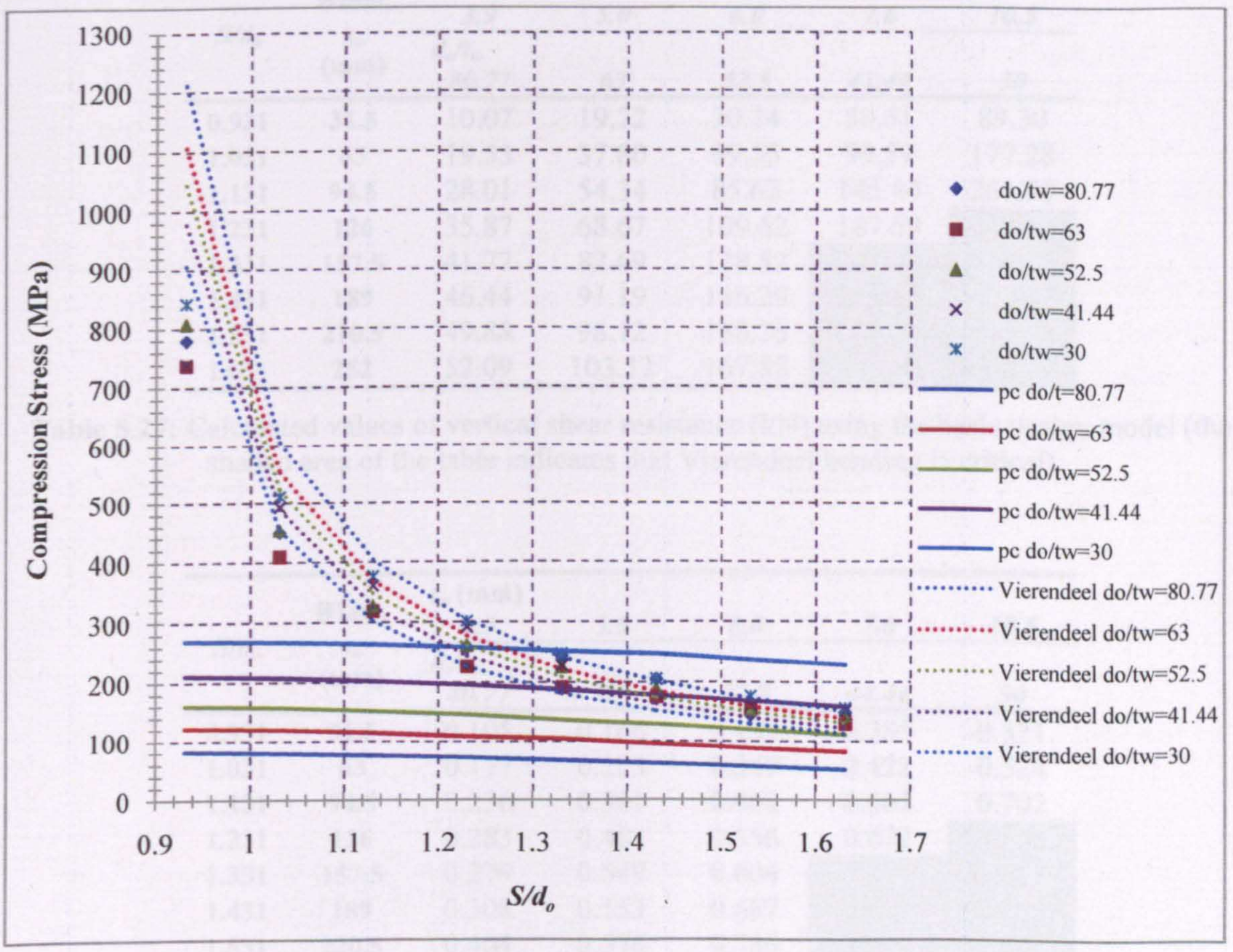

Figure 5.96: Compressive strength of the strut predicted by the design model and compared to FE failure stress and Vierendeel stress

Comparison with FEA

There is conservatism by up to approximately 90% for narrow and thin web-posts.

S/d_o	*Width,* s_o (mm)	t_w (mm) *3.9*	*5.0*	*6.0*	*7.6*	*10.5*
		d_o/t_w *80.77*	*63*	*52.5*	*41.44*	*30*
0.931	**31.5**	10.07	19.22	30.24	50.51	89.30
1.031	**63**	19.53	37.80	59.35	99.59	177.28
1.131	**94.5**	28.01	54.34	85.62	145.44	261.95
1.231	**126**	35.87	68.67	109.62	187.69	341.33
1.331	**157.5**	41.77	82.69	128.52	225.04	416.75
1.431	**189**	46.44	91.19	146.29	255.68	490.17
1.531	**220.5**	49.88	98.12	158.76	281.53	548.71
1.631	**252**	52.09	103.32	167.83	302.60	603.29

Table 5.27: Calculated values of vertical shear resistance (kN) using the basic design model (the shaded area of the table indicates that Vierendeel bending is critical)

S/d_o	*Width,* s_o (mm)	t_w (mm) *3.9*	*5.0*	*6.0*	*7.6*	*10.5*
		d_o/t_w *80.77*	*63*	*52.5*	*41.44*	*30*
0.931	**31.5**	0.105	0.166	0.198	0.285	0.321
1.031	**63**	0.177	0.293	0.347	0.422	0.524
1.131	**94.5**	0.236	0.361	0.461	0.562	0.702
1.231	**126**	0.283	0.482	0.556	0.672	0.855
1.331	**157.5**	0.279	0.549	0.604	0.824	1.018
1.431	**189**	0.308	0.553	0.687	0.870	1.205
1.531	**220.5**	0.404	0.576	0.786	1.044	1.341
1.631	**252**	0.358	0.635	0.776	1.040	1.464

Table 5.28: Ratio of vertical shear forces from the basic design model in literature and FE analyses (the shaded area of the table indicates that Vierendeel bending is critical)

A design formula is developed and shown below which covers the range of $0.931<S/d_o<1.631$.

$$Compression\ Stress = 1664\left(\frac{S}{d_o}\right)^2 - 4938\left(\frac{S}{d_o}\right) + 3759 \qquad (5.10)$$

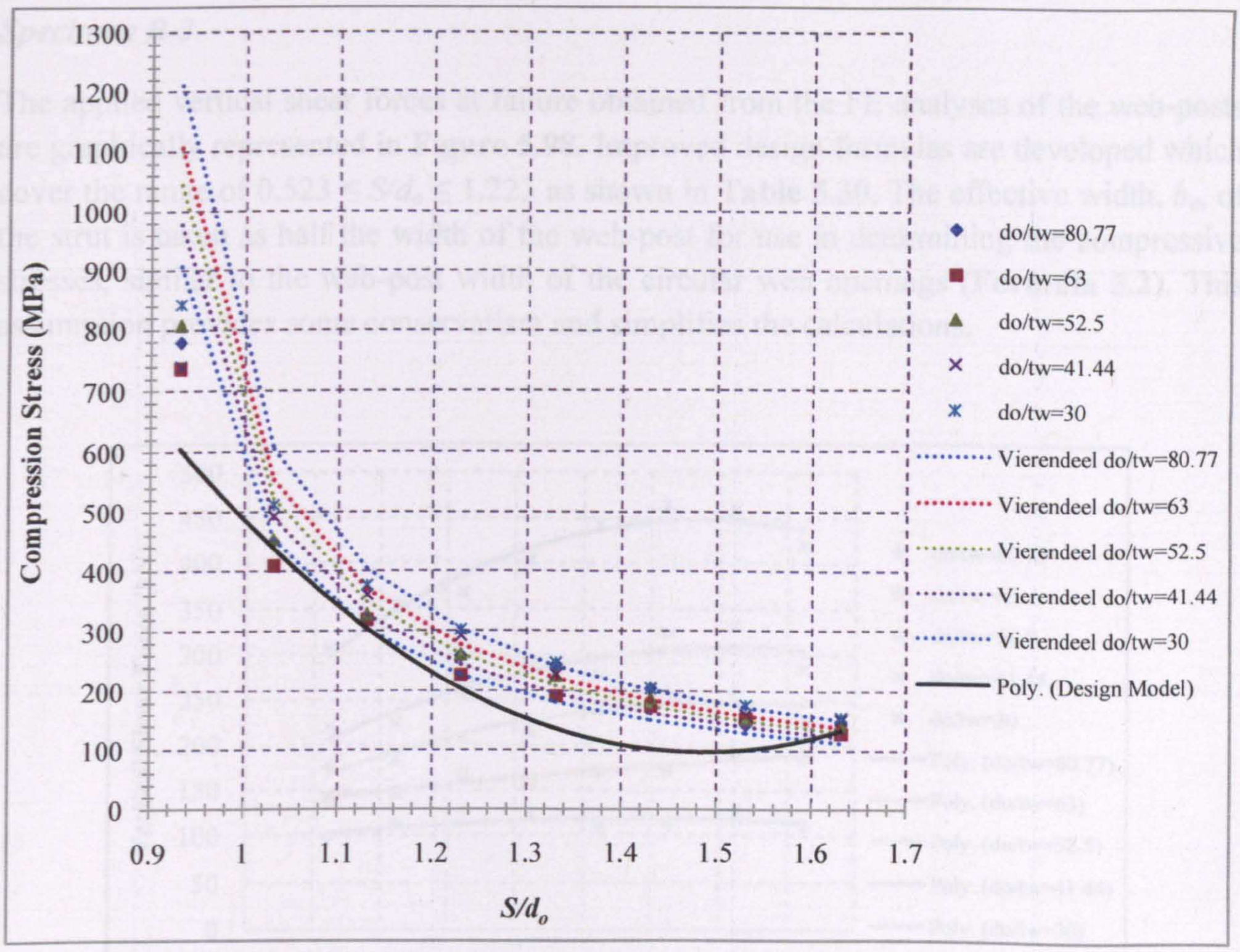

Figure 5.97: Empirical design model for compressive strength of the strut compared to FE failure stress and Vierendeel stress

S/d_o	*Width,* s_o (mm)	t_w (mm) *3.9*	*5.0*	*6.0*	*7.6*	*10.5*
		d_o/t_w *80.77*	*63*	*52.5*	*41.44*	*30*
0.931	**31.5**	0.05	0.07	0.08	0.10	0.14
1.031	**63**	0.05	0.07	0.08	0.10	0.14
1.131	**94.5**	0.17	0.22	0.27	0.34	0.47
1.231	**126**	0.25	0.31	0.38	0.48	0.66
1.331	**157.5**	0.29	0.37	0.44	0.56	0.77
1.431	**189**	0.31	0.40	0.48	0.61	0.84
1.531	**220.5**	0.33	0.42	0.51	0.64	0.89
1.631	**252**	0.34	0.44	0.53	0.67	0.92

Table 5.29: Proposed effective length factors

Specimen B-3

The applied vertical shear forces at failure obtained from the FE analyses of the web-posts are graphically represented in **Figure 5.98**. Improved design formulas are developed which cover the range of $0.523 \leq S/d_o \leq 1.223$ as shown in **Table 5.30**. The effective width, b_e, of the strut is taken as half the width of the web-post for use in determining the compressive stresses, similar to the web-post width of the circular web openings (**Formula 5.2**). This assumption provides some conservatism and simplifies the calculations.

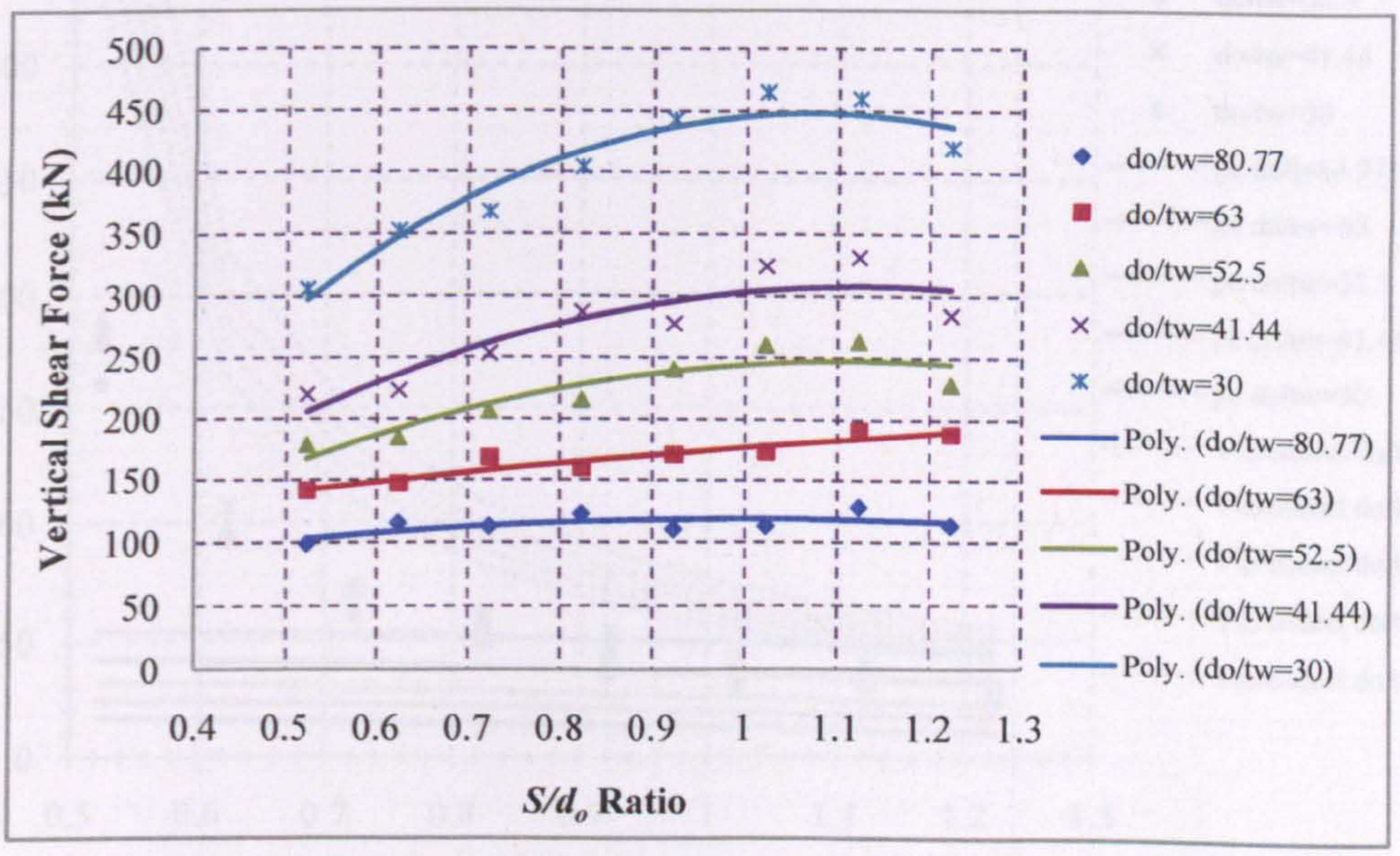

Figure 5.98: Applied vertical applied shear force (kN) at failure according to FE Model

t_w (mm)	d_o/t_w	*Formula*
3.9	**80.77**	$V_v = -\ 63.8\ (S/d_o)^2 + 129.8\ (S/d_o) - 52.63$
5.0	**63**	$V_v = -\ 17.66\ (S/d_o)^2 + 99.06\ (S/d_o) - 95.2$
6.0	**52.5**	$V_v = -\ 227.9\ (S/d_o)^2 + 509.2\ (S/d_o) - 36.82$
7.6	**41.44**	$V_v = -\ 279.5\ (S/d_o)^2 + 630.4\ (S/d_o) - 47.62$
10.5	**30**	$V_v = -\ 498.8\ (S/d_o)^2 + 1070\ (S/d_o) - 125.5$

Table 5.30: Design formulas for Specimen B-3

Lower Bound to Web-Post Buckling and Vierendeel bending

Figure 5.99 shows that the Vierendeel moment check is not critical for any d_o/t_w and S/d_o.

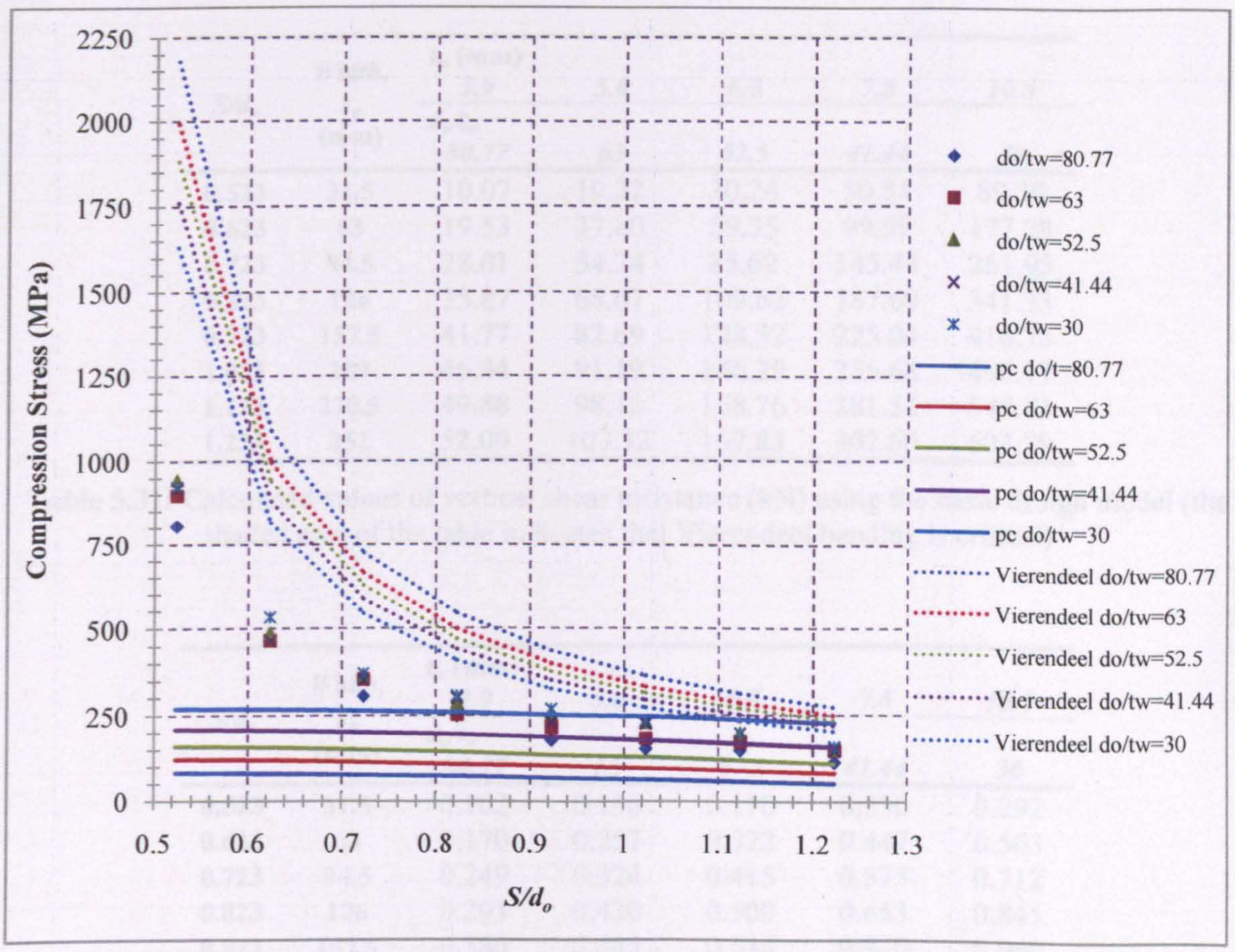

Figure 5.99: Compressive strength of the strut predicted by the design model and compared to FE failure stress and Vierendeel stress

Comparison with FEA

There is conservatism by up to approximately 90% for narrow and thin web-posts.

S/d_o	*Width,* s_o (mm)	t_w (mm) *3.9*	*5.0*	*6.0*	*7.6*	*10.5*
		d_o/t_w *80.77*	*63*	*52.5*	*41.44*	*30*
0.523	**31.5**	10.07	19.22	30.24	50.51	89.30
0.623	**63**	19.53	37.80	59.35	99.59	177.28
0.723	**94.5**	28.01	54.34	85.62	145.44	261.95
0.823	**126**	35.87	68.67	109.62	187.69	341.33
0.923	**157.5**	41.77	82.69	128.52	225.04	416.75
1.023	**189**	46.44	91.19	146.29	255.68	490.17
1.123	**220.5**	49.88	98.12	158.76	281.53	548.71
1.223	**252**	52.09	103.32	167.83	302.60	603.29

Table 5.31: Calculated values of vertical shear resistance (kN) using the basic design model (the shaded area of the table indicates that Vierendeel bending is critical)

S/d_o	*Width,* s_o (mm)	t_w (mm) *3.9*	*5.0*	*6.0*	*7.6*	*10.5*
		d_o/t_w *80.77*	*63*	*52.5*	*41.44*	*30*
0.523	**31.5**	0.102	0.136	0.170	0.230	0.292
0.623	**63**	0.170	0.257	0.322	0.447	0.503
0.723	**94.5**	0.249	0.324	0.415	0.575	0.712
0.823	**126**	0.293	0.430	0.509	0.653	0.845
0.923	**157.5**	0.380	0.485	0.534	0.810	0.940
1.023	**189**	0.412	0.527	0.562	0.790	1.053
1.123	**220.5**	0.390	0.514	0.603	0.851	1.192
1.223	**252**	0.459	0.550	0.735	1.063	1.435

Table 5.32: Ratio of vertical shear forces from the basic design model in literature and FE analyses (the shaded area of the table indicates that Vierendeel bending is critical)

A design formula is developed and shown below which covers the range of $0.523<S/d_o<1.223$.

$$Compression\ Stress = 1901\left(\frac{S}{d_o}\right)^2 - 4051\left(\frac{S}{d_o}\right) + 2263 \qquad (5.11)$$

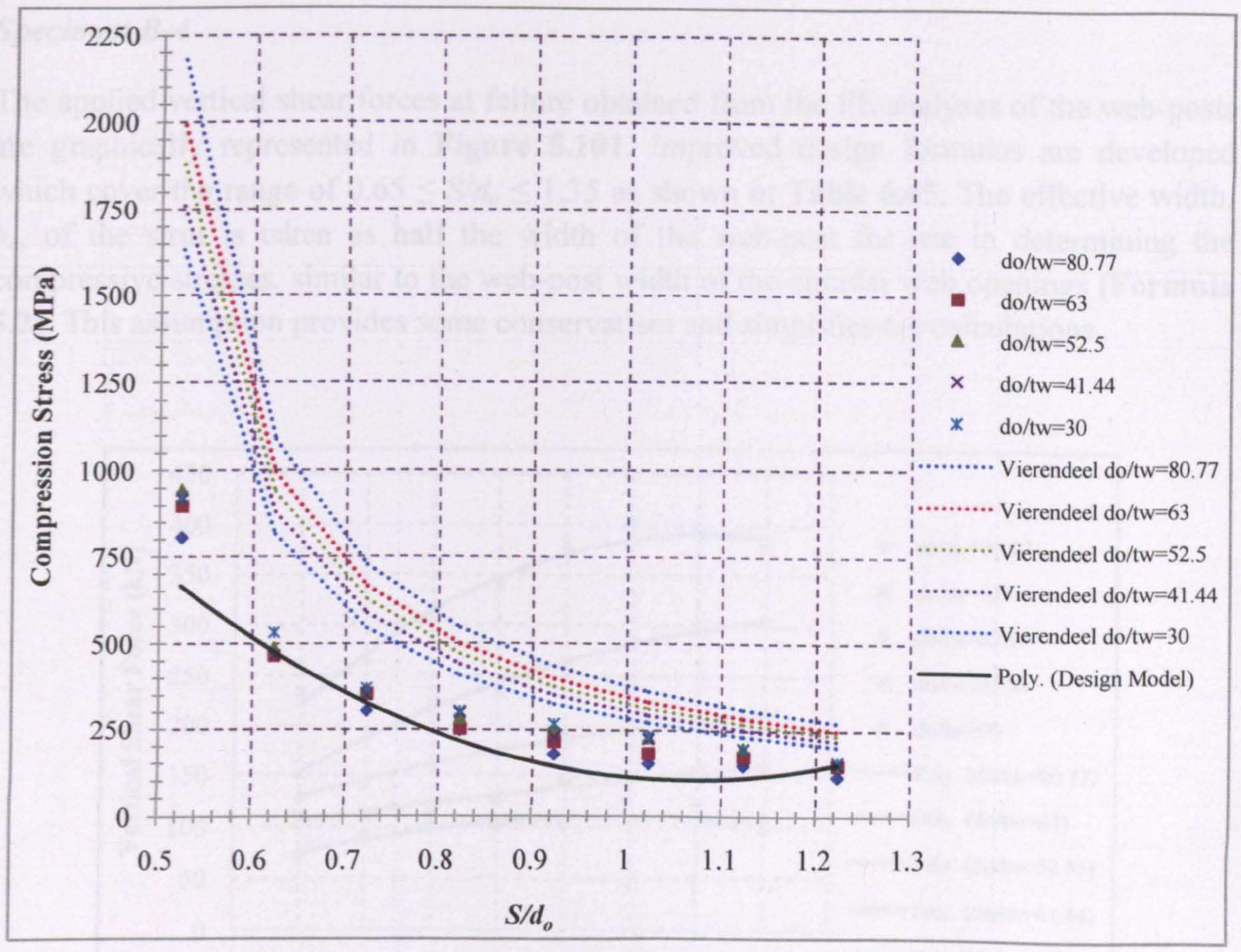

Figure 5.100: Empirical design model for compressive strength of the strut compared to FE failure stress and Vierendeel stress

S/d_o	*Width,* s_o (mm)	t_w (mm) *3.9*	*5.0*	*6.0*	*7.6*	*10.5*
		d_o/t_w *80.77*	*63*	*52.5*	*41.44*	*30*
0.523	**31.5**	0.05	0.07	0.08	0.10	0.14
0.623	**63**	0.05	0.07	0.08	0.10	0.14
0.723	**94.5**	0.17	0.22	0.26	0.33	0.46
0.823	**126**	0.22	0.28	0.34	0.43	0.59
0.923	**157.5**	0.29	0.37	0.45	0.57	0.78
1.023	**189**	0.31	0.40	0.48	0.60	0.83
1.123	**220.5**	0.27	0.35	0.42	0.53	0.73
1.223	**252**	0.34	0.43	0.52	0.66	0.91

Table 5.33: Proposed effective length factors

Specimen B-4

The applied vertical shear forces at failure obtained from the FE analyses of the web-posts are graphically represented in **Figure 5.101**. Improved design formulas are developed which cover the range of $0.65 \leq S/d_o \leq 1.35$ as shown in **Table 6.45**. The effective width, b_e, of the strut is taken as half the width of the web-post for use in determining the compressive stresses, similar to the web-post width of the circular web openings (**Formula 5.2**). This assumption provides some conservatism and simplifies the calculations.

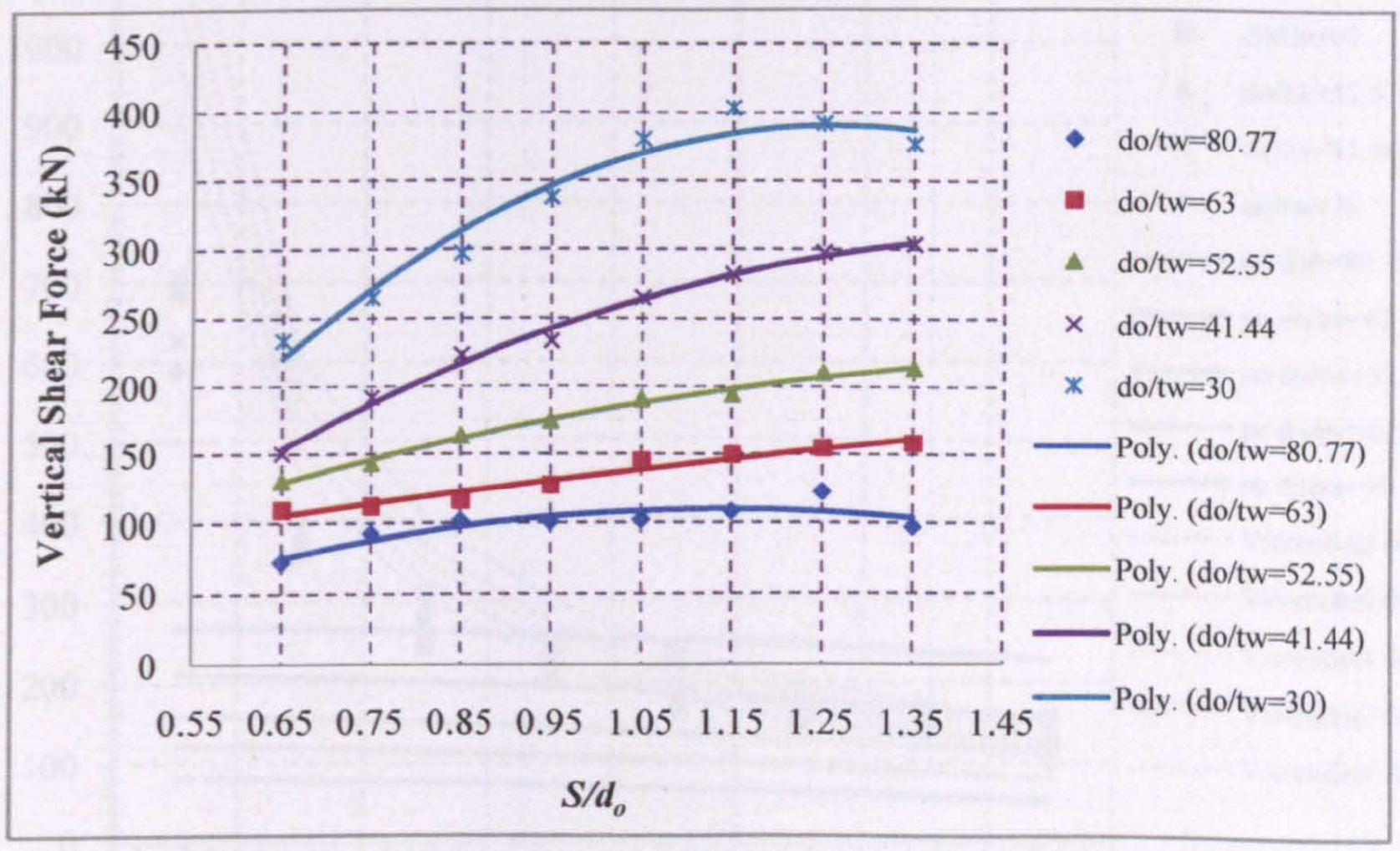

Figure 5.101: Applied vertical applied shear force (kN) at failure according to FE Model

t_w (mm)	d_o/t_w	*Formula*
3.9	**80.77**	$V_v = -\ 143.2\ (S/d_o)^2 + 327.2\ (S/d_o) - 77.12$
5.0	**63**	$V_v = -\ 9.958\ (S/d_o)^2 + 99.88\ (S/d_o) - 44.59$
6.0	**52.5**	$V_v = -\ 81.88\ (S/d_o)^2 + 285.8\ (S/d_o) - 22.31$
7.6	**41.44**	$V_v = -\ 202.2\ (S/d_o)^2 + 620.4\ (S/d_o) - 164.3$
10.5	**30**	$V_v = -\ 454.1\ (S/d_o)^2 + 1147\ (S/d_o) - 333.2$

Table 5.34: Design formulas for Specimen B-4

Lower Bound to Web-Post Buckling and Vierendeel bending

Figure 5.102 shows that the Vierendeel moment check is critical for d_o/t_w equal to 41.44 and 30 for S/d_o larger than 1.05 and 0.85, respectively.

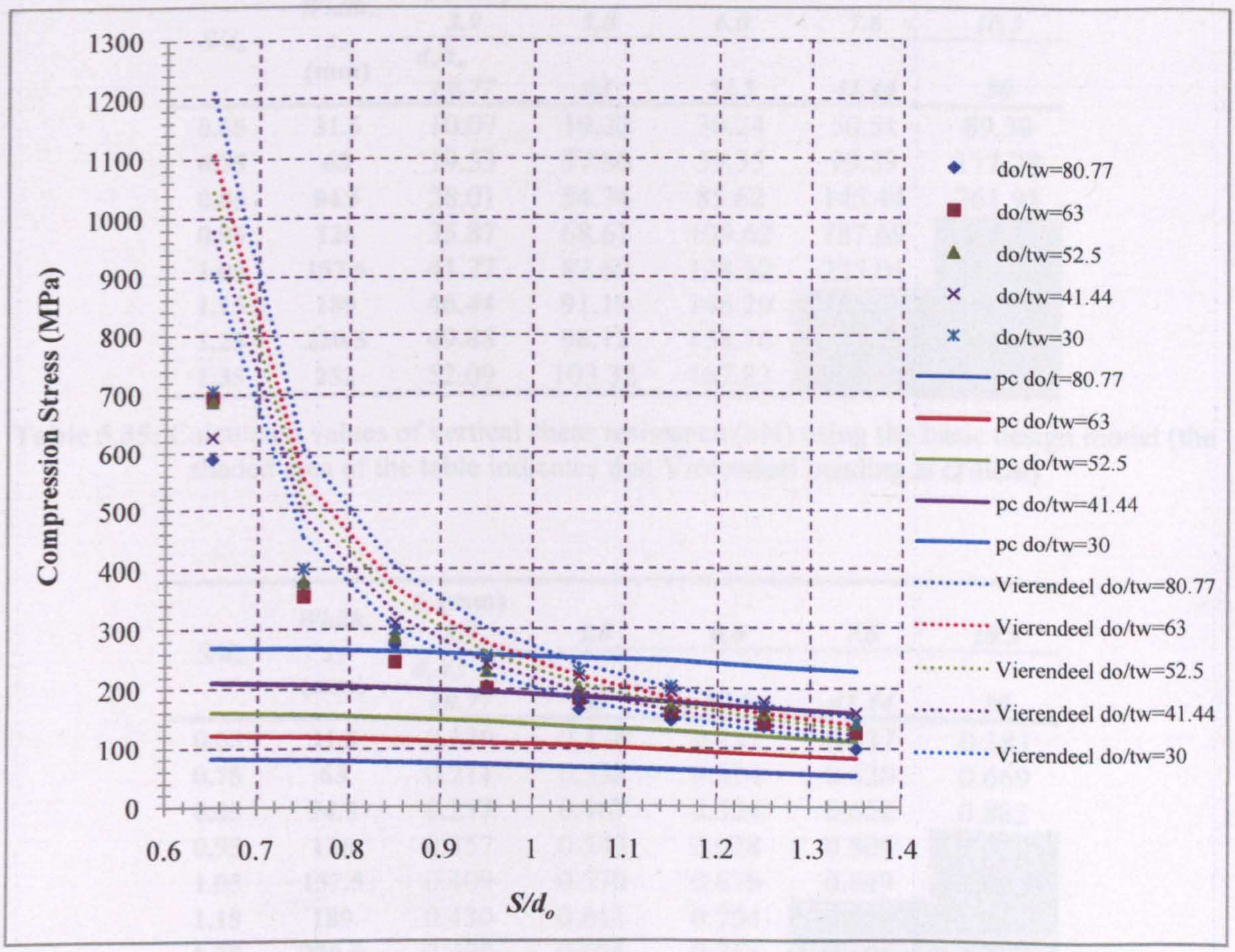

Figure 5.102: Compressive strength of the strut predicted by the design model and compared to FE failure stress and Vierendeel stress

Comparison with FEA

There is conservatism by up to approximately 85% for narrow and thin web-posts.

S/d_o	*Width,* s_o (mm)	t_w (mm) *3.9*	*5.0*	*6.0*	*7.6*	*10.5*
		d_o/t_w *80.77*	*63*	*52.5*	*41.44*	*30*
0.65	**31.5**	10.07	19.22	30.24	50.51	89.30
0.75	**63**	19.53	37.80	59.35	99.59	177.28
0.85	**94.5**	28.01	54.34	85.62	145.44	261.95
0.95	**126**	35.87	68.67	109.62	187.69	341.33
1.05	**157.5**	41.77	82.69	128.52	225.04	416.75
1.15	**189**	46.44	91.19	146.29	255.68	490.17
1.25	**220.5**	49.88	98.12	158.76	281.53	548.71
1.35	**252**	52.09	103.32	167.83	302.60	603.29

Table 5.35: Calculated values of vertical shear resistance (kN) using the basic design model (the shaded area of the table indicates that Vierendeel bending is critical)

S/d_o	*Width,* s_o (mm)	t_w (mm) *3.9*	*5.0*	*6.0*	*7.6*	*10.5*
		d_o/t_w *80.77*	*63*	*52.5*	*41.44*	*30*
0.65	**31.5**	0.139	0.176	0.233	0.337	0.383
0.75	**63**	0.211	0.338	0.414	0.520	0.669
0.85	**94.5**	0.277	0.467	0.524	0.652	0.882
0.95	**126**	0.357	0.540	0.628	0.806	1.010
1.05	**157.5**	0.409	0.570	0.676	0.849	1.095
1.15	**189**	0.430	0.611	0.754	0.907	1.214
1.25	**220.5**	0.408	0.635	0.755	0.946	1.398
1.35	**252**	0.537	0.653	0.786	0.997	1.599

Table 5.36: Ratio of vertical shear forces from the basic design model in literature and FE analyses (the shaded area of the table indicates that Vierendeel bending is critical)

A design formula is developed and shown below which covers the range of $0.65<S/d_o<1.35$.

$$Compression\ Stress = 1227\left(\frac{S}{d_o}\right)^2 - 2965\left(\frac{S}{d_o}\right) + 1894 \qquad (5.12)$$

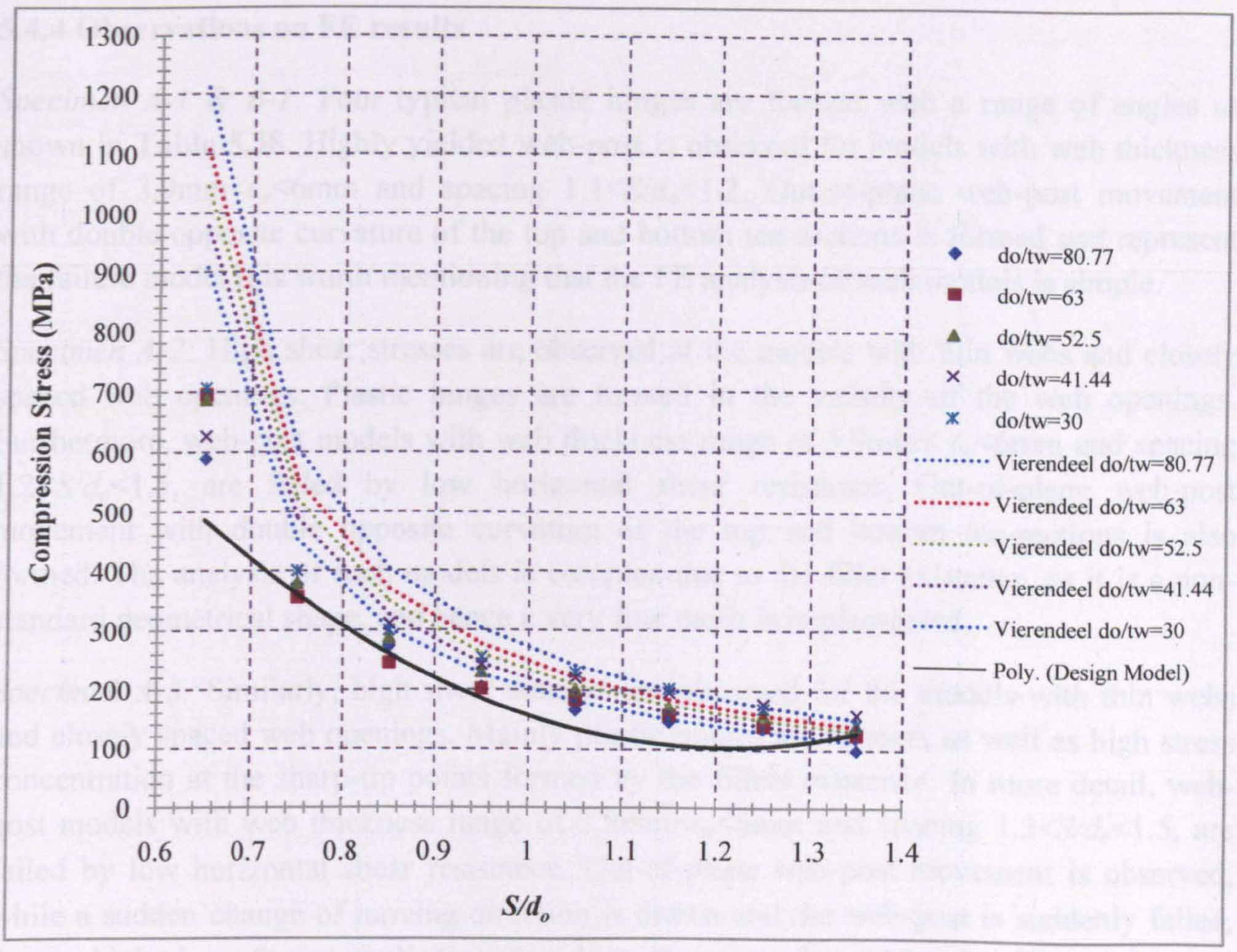

Figure 5.103: Empirical design model for compressive strength of the strut compared to FE failure stress and Vierendeel stress

S/d_o	*Width,* s_o (mm)	t_w (mm) *3.9*	*5.0*	*6.0*	*7.6*	*10.5*
		d_o/t_w *80.77*	*63*	*52.5*	*41.44*	*30*
0.65	**31.5**	0.05	0.07	0.08	0.10	0.14
0.75	**63**	0.11	0.14	0.17	0.22	0.30
0.85	**94.5**	0.23	0.30	0.36	0.46	0.63
0.95	**126**	0.27	0.35	0.42	0.53	0.74
1.05	**157.5**	0.29	0.37	0.44	0.56	0.77
1.15	**189**	0.31	0.40	0.48	0.61	0.84
1.25	**220.5**	0.33	0.42	0.51	0.64	0.89
1.35	**252**	0.34	0.44	0.53	0.67	0.92

Table 5.37: Proposed effective length factors

5.4.4 Observations on FE results

Specimen A-1 & B-1: Four typical plastic hinges are formed with a range of angles as shown in **Table 5.38**. Highly yielded web-post is observed for models with web thickness range of 3.9mm<t_w<6mm and spacing 1.1<S/d_o<1.2. Out-of-plane web-post movement with double opposite curvature of the top and bottom tee-sections is formed and represent the failure mode. It is worth mentioning that the FE analysis of such models is simple.

Specimen A-2: High shear stresses are observed at the models with thin webs and closely spaced web openings. Plastic hinges are formed in the vicinity of the web openings. Furthermore, web-post models with web thickness range of 3.9mm< t_w<6mm and spacing 1.2<S/d_o<1.5, are failed by low horizontal shear resistance. Out-of-plane web-post movement with double opposite curvature of the top and bottom tee-sections is also formed. The analysis of such models is complex due to the fillet existence, as it is a non-standard geometrical shape, and hence a very fine mesh is implemented.

Specimen A-3: Similarly, high shear stresses are observed for the models with thin webs and closely spaced web openings. Mainly plastic hinges are formed, as well as high stress concentration at the sharp-tip points formed by the fillets existence. In more detail, web-post models with web thickness range of 3.9mm<t_w<6mm and spacing 1.3<S/d_o<1.5, are failed by low horizontal shear resistance. Out-of-plane web-post movement is observed, while a sudden change of moving direction is drawn and the web-post is suddenly failed, due to high shear forces applied on the sharp-tip points formed by the fillets existence. Similar to Specimen A-2, the analysis of such models is very complex.

Specimen B-2: It is found that the sharp edges at the mid-depth of such web openings cause stress concentration. Mainly, plastic hinges are observed at the vertical centre-line of the web openings in the top and bottom tee-sections. Web-post models with closely spaced web openings, also present some stress concentration and at the sharp edge points of the top and bottom tees. In general, web-post models with any web thickness and web opening spacing 0.931<S/d_o<1.131 are highly stressed. Oppositely, web-posts with widely spaced web openings failed completely under Vierendeel bending moments. Out-of-plane web-post movement with double opposite curvature of the top and bottom tee-sections is formed representing the failure mode. Low to medium displacements are recorded, as the new web-posts are stiffer. Once the mesh of this novel web opening configuration is worked out, the analysis is relatively uncomplicated.

Specimen B-3: Such web-post models do not experience high shear stresses. It is observed that there is a smooth transition of the stresses in the web-posts along the strut line. Mainly, plastic hinges are observed at the vertical centre-line of the web openings in the top and bottom tee-sections. Also, four plastic hinges are formed in web-post models with any web thickness and web opening spacing 0.623<S/d_o<1.223, and are moving between the vertical

centre-line of the web opening and the sharp edge points at the top and bottom tees. Out-of-plane web-post movement with double opposite curvature of the top and bottom tee-sections is formed and represent the failure mode. Low displacements are recorded, as the new web-posts are much stiffer. Again, once the mesh of this novel web opening configuration is worked out, the analysis is relatively uncomplicated.

Specimen B-4: Similar to Specimen B-3, such web-post models do not experience high shear stresses. However, it is observed that there is an unequal transition of the stresses in the web-posts along the strut line, as the HMS and LMS of the web openings experience difference stresses, due to their asymmetry in relation to the centre-line of the web opening. Moreover, plastic hinges are observed at the vertical centre-line of the web openings in the top and bottom tee-sections. Furthermore, plastic hinges are formed in web-post models with web thickness range of $7.6\text{mm}<t_w<10.5\text{mm}$ and spacing $0.75<S/d_o<1.35$, and are moving between the vertical centre-line of the web opening and the sharp edge points at the top and bottom tees. Out-of-plane web-post movement with double opposite curvature of the top and bottom tee-sections is formed representing the failure mode. Low to medium displacements are recorded, as the new web-posts are stiffer. Once the mesh of this novel web opening configuration is worked out, the analysis is not too complex.

5.4.5 Position of plastic hinges and effective widths of the web openings

In **Table 3.10, Figure 3.36** and **Figure 3.37**, approximation of the plastic hinges positions at the top tee-sections and LMS for the non-standard web openings Λ to K was presented. At this stage, the position of the plastic hinges in the novel elliptical web openings are assumed similar to the ones found from the normal elliptical web openings in **Chapter 3**. The positions of the plastic hinges are not considered from the web-post buckling study, as the existence of two web openings closely spaced dramatically affects the results. The stress concentration points are shifted, as a combination of forces acting on the web-post simultaneously. It is noted that the plastic hinges positions, from the novel elliptical web openings given in **Table 5.38**, are unique and taken from the particular web opening shape with a certain angle, THETA, and radius, R.

Elliptical web openings have narrow top and bottom tee-sections, hence the opening length, c, is not critical. The angle, φ, defines the position of the plastic hinge at the top tee-section at LMS in relation to the centre-line of the web opening. The projection of this point, taken from the angle φ, to the horizontal centre-line of the web opening, defines the equivalent effective width of the web opening as shown in **Figure 5.104**. The latter one is the factor which determines the limiting vertical shear force, resulting from Vierendeel bending of the top tee-section at LMS, as defined by **Formula 5.5**. The smaller the effective width, the greater is the vertical shear force and so the load carrying capacity.

Analytically, the stress concentration points and the schematic representation of the strut model for all examined web opening shapes are shown in **Figure 5.104**. **Table 5.38** summarizes all the results, providing the evaluation of the effective width used in this chapter, in order to estimate the limiting vertical shear force resulting from Vierendeel bending in the top tee-section (i.e. it is used in the denominator of **Formula 5.5**).

*For closely spaced web openings
d_o: Web opening depth

Specimen	φ range due to mobilization (degrees)	Under Vierendeel Action		Under Web-Post Buckling Action		Max. used φ (degrees)
		φ (degrees)	Effective Opening Width	φ (degrees)	Effective Opening Width	
A-1/2/3 & B-1 (CIRCULAR)	20-29	28	$0.25d_o$	28	$0.25d_o$	**28**
B-2 (THETA30,R0.6)	13-22	22	$0.18d_o$	17	$0.14d_o$	**22**
B-3 (THETA10,R0.3)	12-22*	12	$0.1d_o$	12-14	0.1-$0.13d_o$	**12**
B-4 (THETA10,R0.5)	15-30	21	$0.18d_o$	17-45	0.15-$0.28d_o$	**21**

Table 5.38: Summarize of equivalent effective widths for novel web openings (schematic detail in **Figure 2.18** and **3.40**)

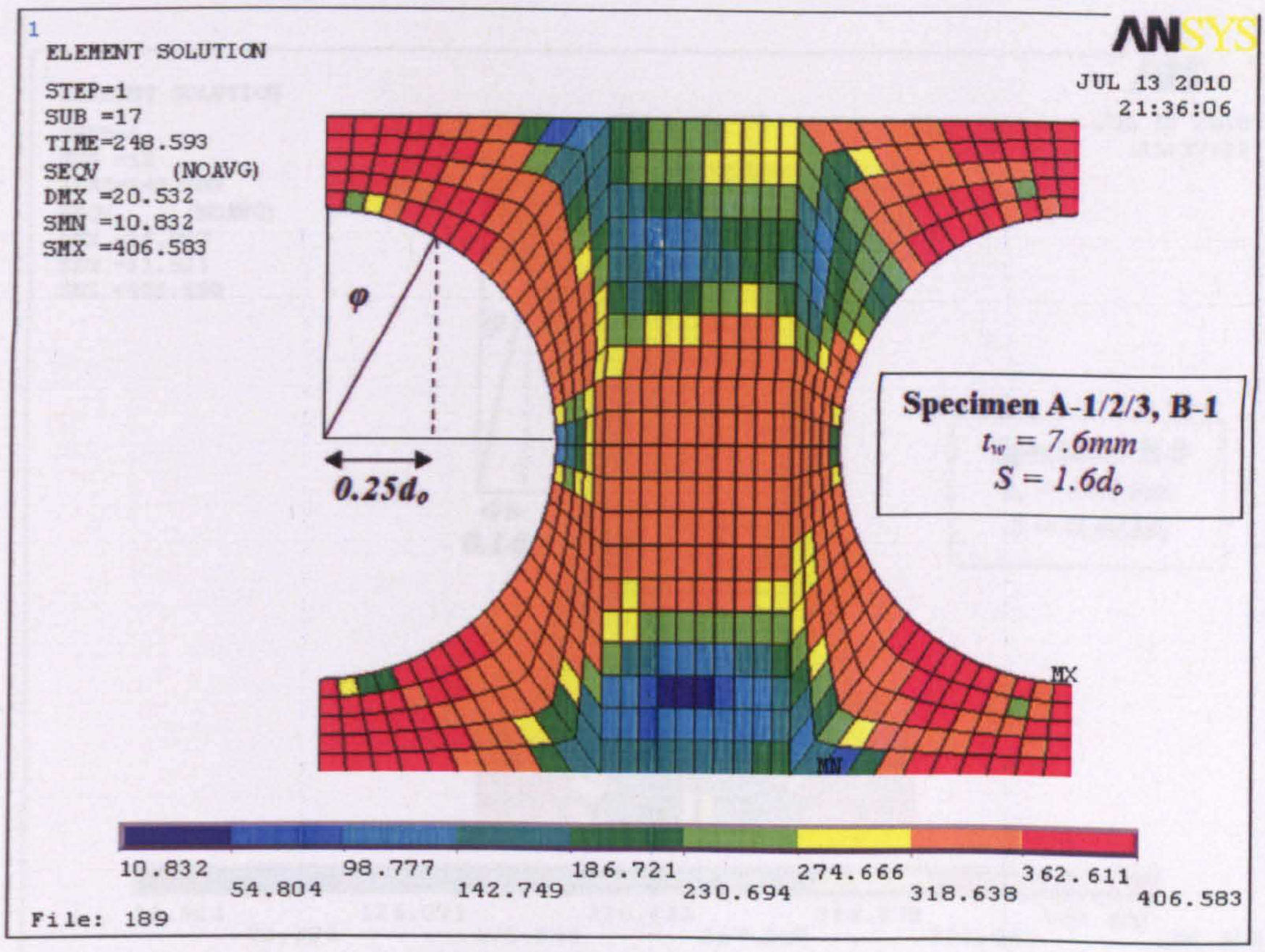

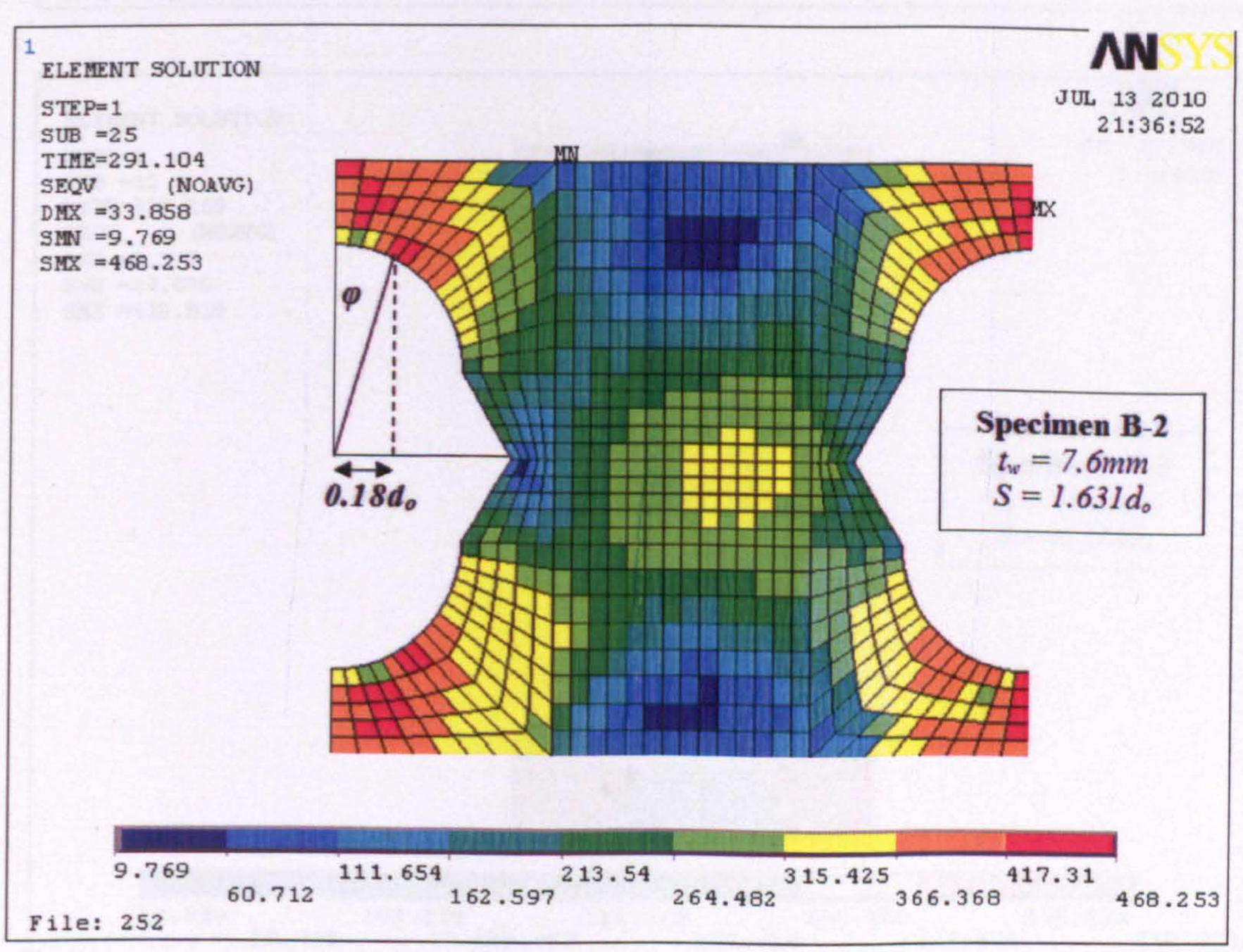

Figure 5.104(a): Stress concentration points and schematic representation of the strut model

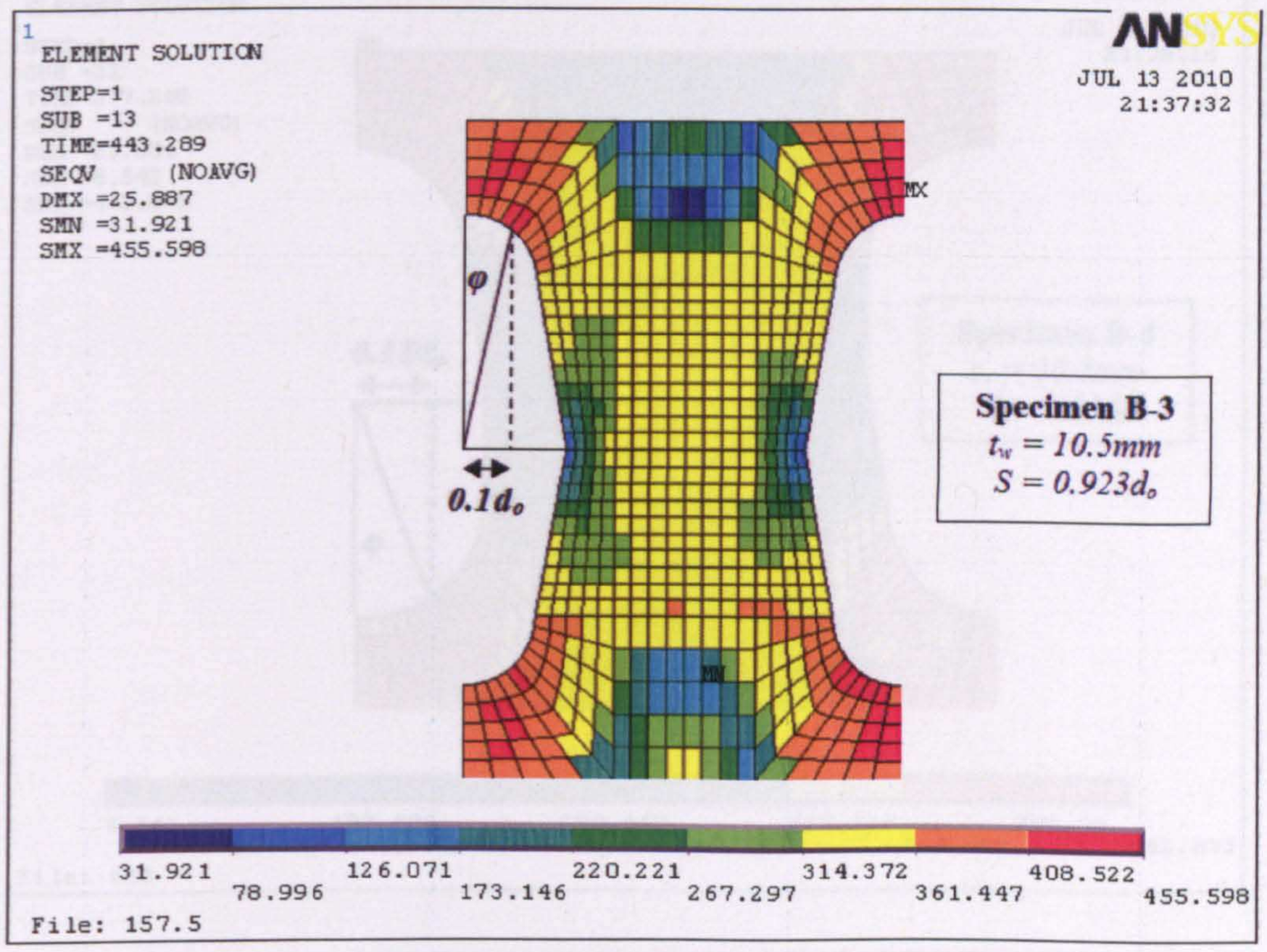

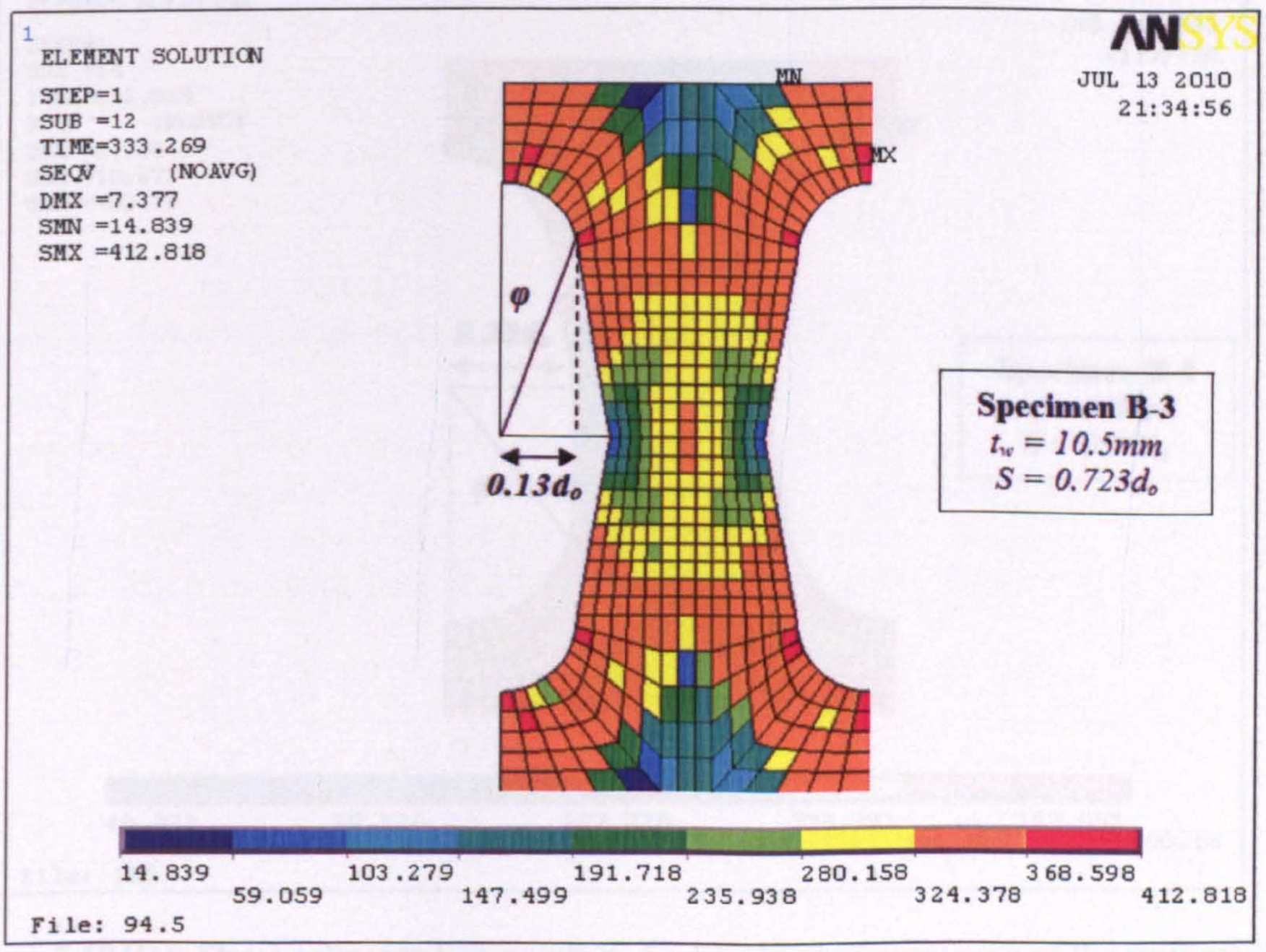

Figure 5.104(b): Stress concentration points and schematic representation of the strut model

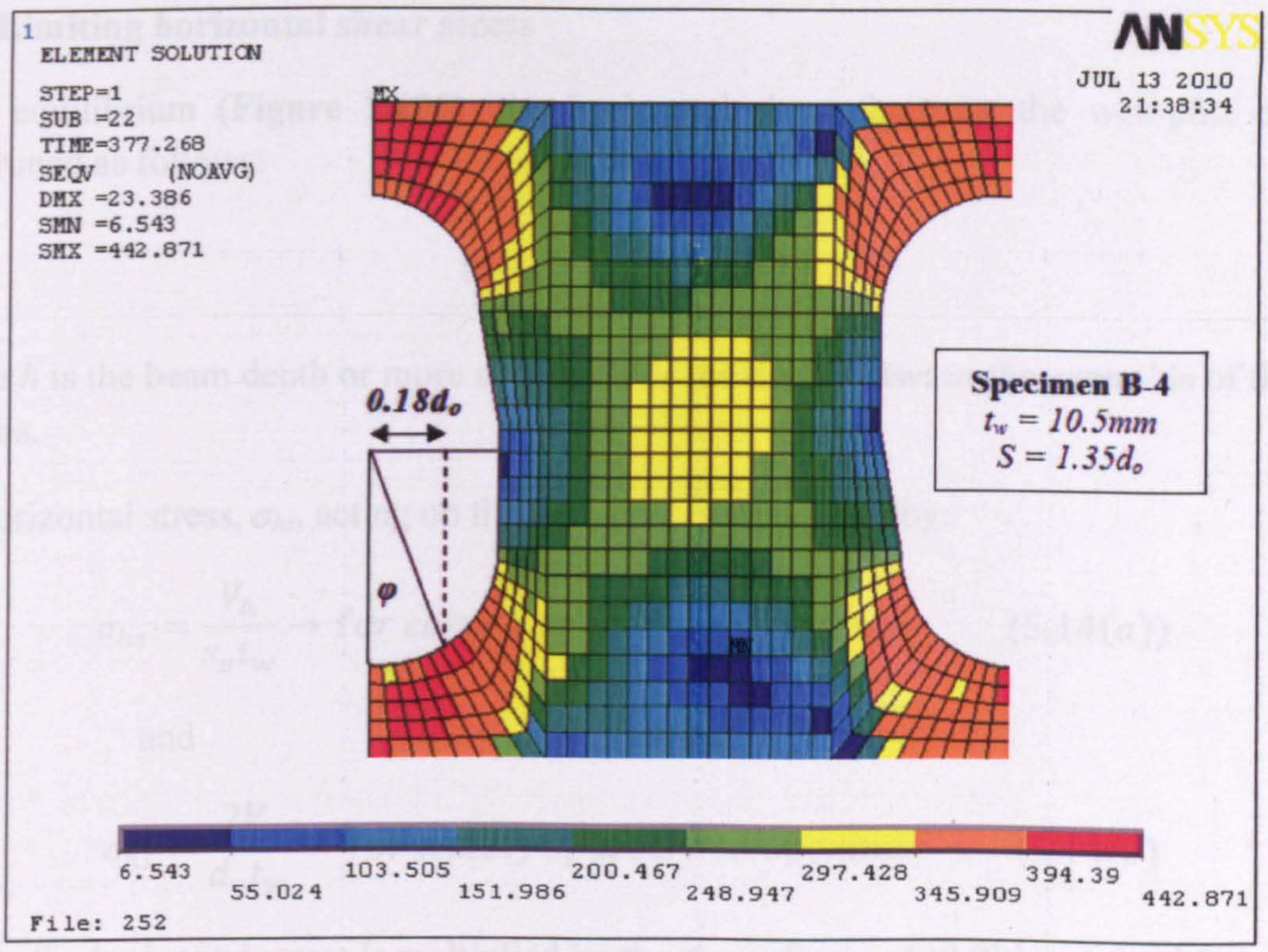

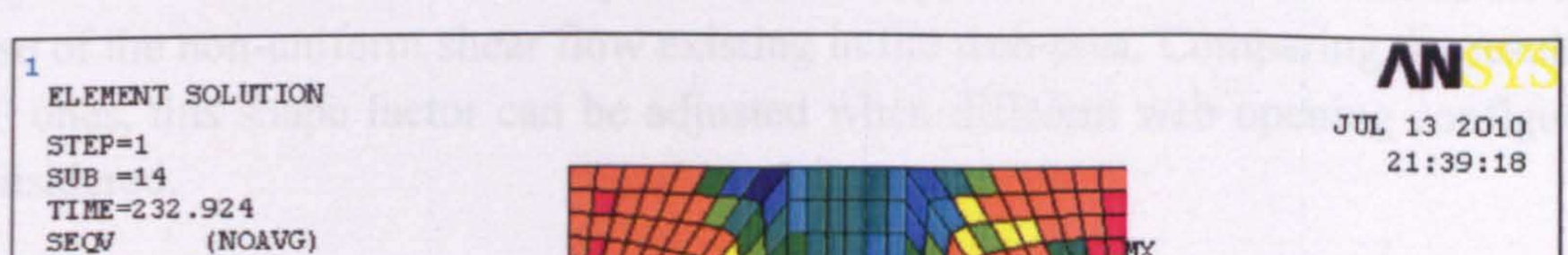

Figure 5.104(c): Stress concentration points and schematic representation of the strut model (the maximum angle φ is recorded)

5.4.6 Limiting horizontal shear stress

From equilibrium (**Figure 5.105**), the horizontal shear force on the web-post can be determined as follows:

$$V_h = \frac{S}{h} V_v \qquad (5.13)$$

Where h is the beam depth or more accurately is the depth between the centroids of the tee-sections.

The horizontal stress, σ_{hs}, acting on the web-post is then given by:

$$\sigma_{hs} = \frac{V_h}{s_o t_w} \rightarrow for\ closely\ spaced\ web\ openings \qquad (5.14(a))$$

and

$$\sigma_{hs} = \frac{2V_v}{d_o t_w} \rightarrow for\ widely\ spaced\ web\ openings \qquad (5.14(b))$$

Usually the horizontal stress is multiplied by the shape factor of '0.9' in retained for a plate, because of the non-uniform shear flow existing in the web-post. Comparing the results with the FE ones, this shape factor can be adjusted when different web opening configurations are considered.

The maximum shear stress is given by:

$$\sigma_{bs} = 0.6 f_y \qquad (5.15)$$

The horizontal shear resistance of the web-post is given by:

$$V_{h,Rd} = s_o t_w {}^{f_{yd}}\!/_{\sqrt{3}} \qquad (5.16)$$

Where: $f_{yd}/\sqrt{3}$ is the design shear strength of the web (p_w in **BS 5950 Part 1**)

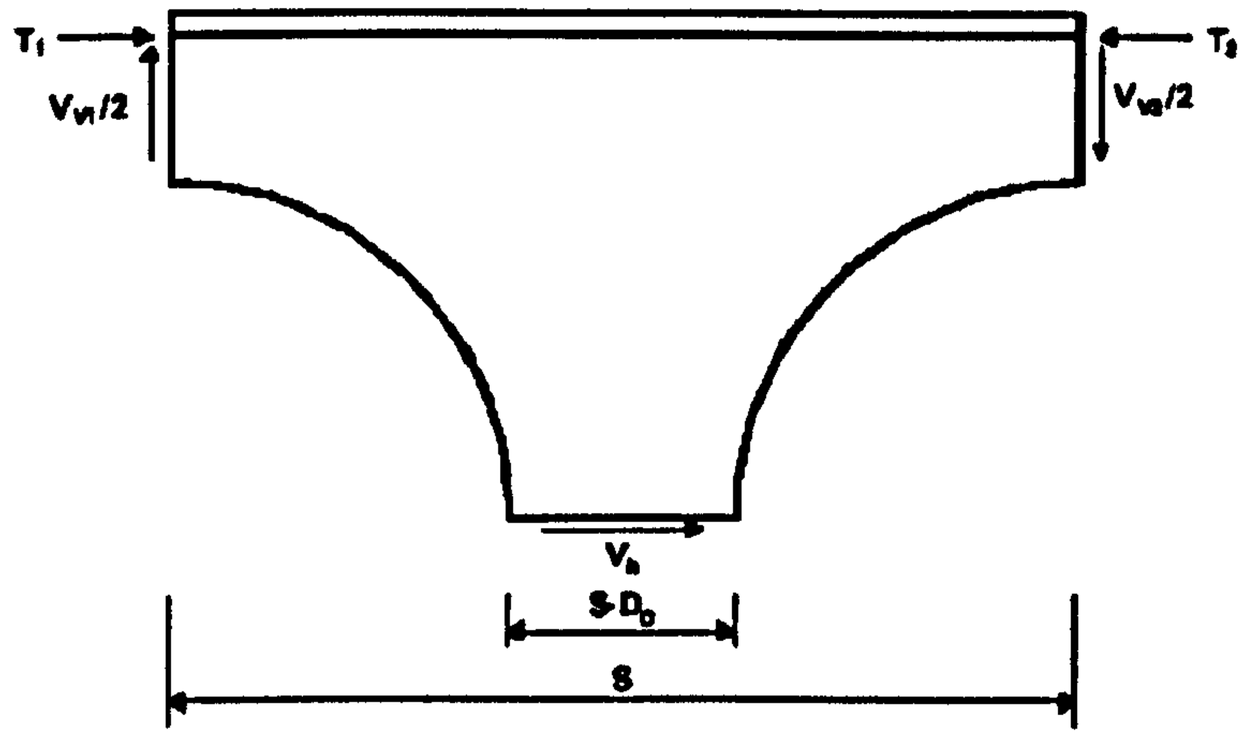

Figure 5.105: Forces acting on top tee-section of the web-post (Fabsec Ltd.)

Figure 5.106 below represents the stress variation estimated by using:

- The maximum nodal shear stresses at the mid-depth of the web-post as obtained from FEA.
- The vertical shear force obtained from FEA and inserted in **Formula 5.14**.
- The theoretical approach of the shear stress resistance as estimated by **Formula 5.16**.
- The vertical shear force obtained from the new design model (**Formula 5.8** to **5.12**) and inserted in **Formula 5.14**.

The following conclusions are drawn.

- Maximum nodal shear stresses adopted from FE models are relatively low due to better distribution, particularly for Specimen B-3 and B-4 with any web opening spacing, and Specimen B-2 with web opening spacing greater than $1.131d_o$. The above stresses are found to be lower than the theoretical horizontal shear stress resistance.
- It is shown again that Specimen A-2 and A-3 present high nodal shear stresses at the mid-depth of the web-post due to the fillet existence and especially for web-post models with spacing of $1.3d_o$ and $1.2d_o$, respectively. Also, Specimen B-1 presents relatively high nodal shear stresses at the mid-depth of the web-post. It is observed that when the spacing of the web openings is increased, the maximum nodal shear stresses are moved from the mid-depth of the web-post towards the centroids of the axial forces; closer to the flanges.
- The horizontal stresses, σ_{hsFEA}, (red triangles points [▲] in **Figure 5.106**) are evaluated by using the maximum vertical shear force, V_v, (i.e. shear capacity) from FEA. Therefore, high σ_{hsFEA} are observed in the novel elliptical web openings.
- The horizontal stresses, $\sigma_{hsDesign}$, (red dashed line in **Figure 5.106**) evaluated by using the vertical shear force, V_v, (i.e. design shear capacity) obtained by the new design

model, are also depicted. Significant underestimation of compression stresses is achieved, especially for web-posts with filleted circular web openings and web-posts with closely spaced elliptical web openings, for conservative design.

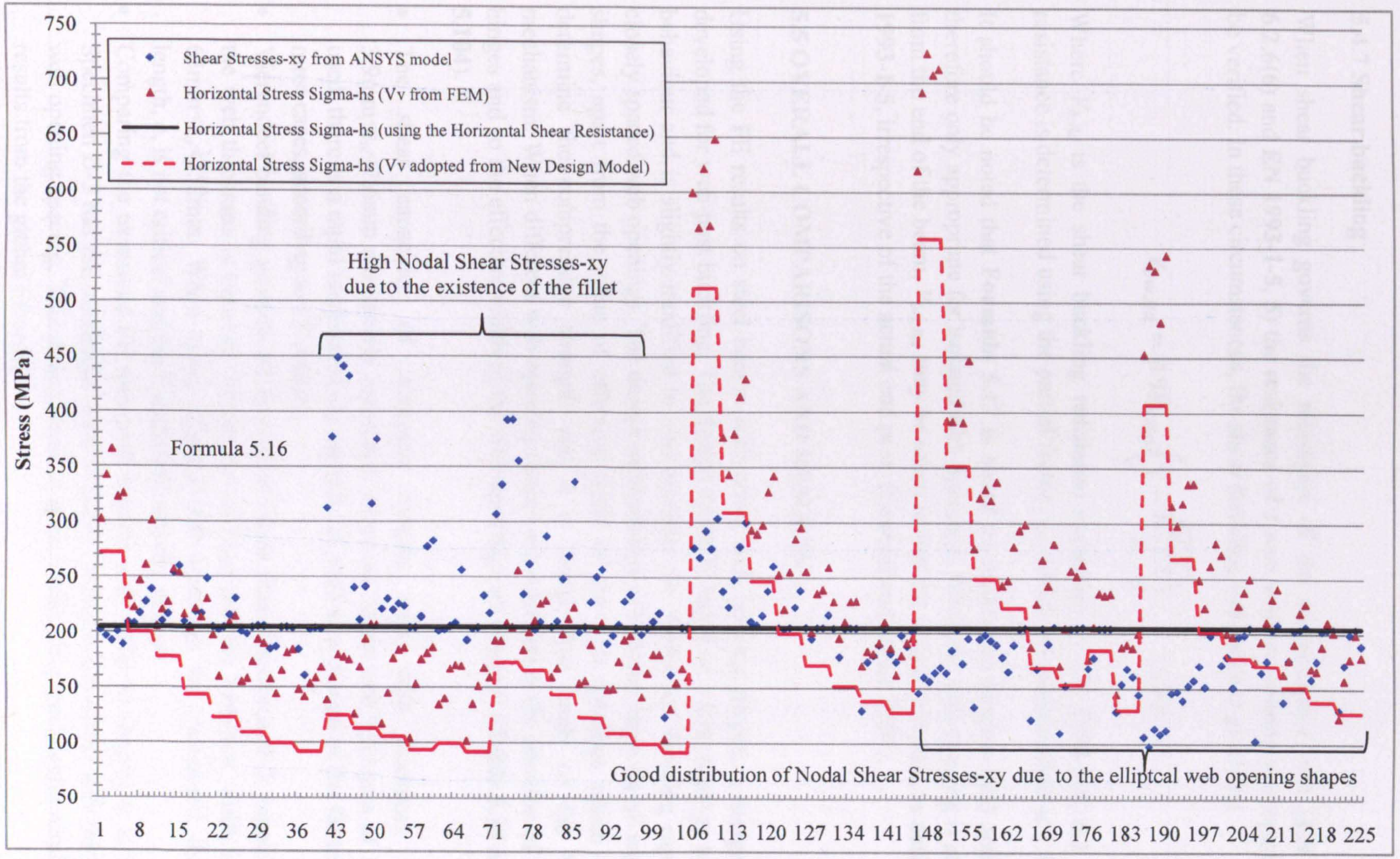

Figure 5.106: Comparison of stresses for all local FE models examined

5.4.7 Shear buckling

When shear buckling governs the resistance of the un-perforated web (**EN 1993-1-1, 6.2.6(6)** and **EN 1993-1-5, 5**) the resistance of a web with an isolated web opening should be verified. In these circumstances, the shear buckling resistance is given by:

$$V_{bw,Rd} = 0.9V_{b,Rd}\left(1 - \frac{\sqrt{d_o l_o}}{h}\right) \qquad (5.17)$$

Where $V_{b,Rd}$ is the shear buckling resistance according to **EN 1993-1-5, 5.2** (note this resistance is determined using the partial factor γ_{M1}, which is recommended as 1.1).

It should be noted that **Formula 5.17** is based on models on tension field action, and is therefore only appropriate for isolated web openings. When the web opening is at least *0.8h* from the end of the beam, $V_{bw,Rd}$ may be taken as that for a rigid end post, as defined in **EN 1993-1-5**, irrespective of the actual end post. (Lawson and Hicks, 2006)

5.5 OVERALL COMPARISONS AND RESULTS

Using the FE results on steel beams with novel web opening shapes, a design model is developed for web-post buckling. The design model is based on a strut analogy to web-post behaviour and is slightly modified to also consider the Vierendeel bending capacities for closely spaced web openings. The design methodology is kept the same for all web opening shapes, apart from the value of effective width of the web openings which is used to determine the compressive strength and it is found from study of the Vierendeel mechanism. When different web opening shapes are considered, the position of the plastic hinges and so the effective width of the web openings are changed (**Table 5.38** and **Figure 5.104**).

- The shear capacities of web-post models with web thickness range of 3.9mm<t_w<7.6mm are linearly increased. However, when web thickness of 10.5mm is used, there is a rapid increase of the capacity as well as a change of the failure mode in most cases, according to FE results.
- Vierendeel bending governs all specimens, apart from Specimen B-3, especially when the web thickness is between 7.6mm<t_w<10.5mm and the web-post width is between 63mm<s_o<252mm. When novel elliptical web openings are considered, the opening length, *c*, is not critical and the Vierendeel capacity is high.
- Comparing the examined FE web-post models with different shapes, it is found that Specimen B-3 has the maximum shear capacity, independent of the web thickness and web opening spacing. This arrangement is agreed with the experimental results and the results from the global FE study.

- Comparing the FE predictions with the theoretical evaluations for web-post buckling, using the typical effective length factor, l_e, equal to 0.5, a range of conservatism from 50% to 90% is found. Higher conservatism is obtained from FEA when perforated beams with closely spaced circular and elliptical web openings and thin webs are considered. Whereas lower conservatism is obtained when filleted circular web openings are considered. This is an effect of the fillets existence, and the decrease in the vertical shear forces due to difficulty in converging from the FE software.
- Specimen A-2 and A-3 behave similarly for regularly and widely spaced web openings, as a better stress distribution is achieved and the horizontal shear failure is avoided. Hence, the existence of fillets at the mid-depth of the web opening with different radiuses, does not really affect the vertical shear capacity of the web-posts, when do not jeopardize the shape of the circular web openings and so the web-post. The web opening spacing is the most critical parameter for such novel perforated beams.

5.6 RECOMMENDATIONS AND LIMITATIONS

Web-post buckling is a complex phenomenon and is dependent on the:

- Shape of the web opening.
- Slenderness of the web.
- Thickness of the tee-sections.
- Asymmetric shape of the web opening.
- Asymmetry of web opening positions (is not considered in the current research study).

The boundary conditions are very carefully applied on the local FE models, regarding the results from the global FE study. It is possible that the FE boundary conditions may have greater influence in the case of the slender web-posts, resulting in inflated buckling load predictions. The new design model provides some conservatism without further refinement. It is attempted to develop a consistent design model without numerous factors that will lead to complex usage.

There is only a finite amount of work that could be completed within the scope of this research thesis and the following limitations are applied:

1. This study is limited to a UB I-section. Extension of this study to other UB as well as to fabricated (plate welded) I-sections could be established.
2. In the present study the web opening depth size is not considered, as a constant depth, d_o, equal to $0.7h$ is used.

CHAPTER 6

STUDY OF VIERENDEEL MECHANISM OF PARTIALLY ENCASED PERFORATED BEAMS

6.1 INTRODUCTION

In modern building construction floor spans are becoming longer and one way of achieving this is to use composite beams. In order to minimize the structural depth of the composite (steel-concrete) beams, steel perforated beams are designed to act compositely with the floor slab. These new beams are known as Ultra Shallow Floor Beams (USFB). In the USFB, the concrete slab cast within the steel flanges and is connected through the web openings, providing enhanced longitudinal and vertical shear resistance. In real-life application the steel deck used in conventional composite beams sits on the bottom flange of an asymmetric perforated I-section and the slab is cast and it is allowed to pass through the web openings. Mechanical shear connectors such as: shear studs, reinforcement re-bars and ducting pass through the web openings to provide longitudinal shear strength tying up the concrete in both sides of the web. For service integration, some web openings (usually one every other) are not in-filled with concrete. Usually, the web openings follow the U-shaped steel deck form (**Figure 2.10**).

The aim of this study is to investigate the contribution of concrete in perforated steel beams in resisting the vertical shear when the concrete is cast between the flanges of the steel beam (**Figure 6.1**). It should be noted that this experimental programme is not simulating the real structural form of the USFB; however the percentage of the steel enhancement and its additional shear capacity is examined when the web openings are in-filled with pure concrete. It is expected that the concrete between the flanges will provide the load path to transfer the vertical shear force while the position of the concrete cracks as well as the load carrying capacity is under investigation. Consequently, following the Vierendeel study of the non-composite steel beam in **Chapter 4**, a similar study is established to investigate the composite behaviour of the USFB and the contact behaviour between the steel and the concrete. The structural and loading arrangement of the USFBs (**Figure 6.1**) are identical to **Chapter 4** (**Figure 4.1** and **4.4**). This chapter consists of the following two parts:

1. Experimental work:

Experiments are carried out on composite sections, under high static load. Four USFBs are tested in this research programme. These are directly compared with the experimental work conducted in **Chapter 4**. Similarly, the web opening diameter, d_o, is equal to *0.76h*. For small web opening diameters, for instance 30% of the beams depth, it is easy to claim that a load path of 45° between flanges transfer the load across the web opening. However, for larger web openings the load path is not so clear.

2. Sensitivity FE study of the USFBs with circular web openings:

For the computational approach to the problem, a three-dimensional FE model is developed, in which contact elements are implemented at the interface of the concrete and steel. Several material model parameters are varied, such as the steel and concrete strength, the constitutive relationships which model the materials, as well as the steel and concrete contact strength. Therefore, the parameters that possess the beams' capacity and their sensitivity to these changes are examined.

6.2 OBJECTIVES FOR STUDY OF COMPOSITE USFBs

The objective of this work is to investigate the enhanced vertical load shear capacity of composite perforated beams when compared to bare perforated steel beams. Also, the failure mechanism of USFBs is examined. When observing the load-deflection relationship as well as the steel stresses and concrete cracks, the main task is to validate the new approach.

Hence, the sub-objectives of this research study are listed as follows:

- To demonstrate significant shear enhancement because of the concrete infill.
- To provide a minimum concrete vertical shear contribution that can be applied in all cases of USFBs based on the concrete encasement and the contact behaviour between the steel and the concrete.
- To establish FE models, which are capable of predicting the structural behaviour of simply supported USFBs with large isolated circular web openings.
- To examine both the load carrying capacities and the failure modes of the USFBs. Also, to study the steel buckles, the concrete internal stresses (cracks), as well as the angles of the concrete cracks, by both experimental and FE means.
- To perform a sensitivity FE study based on both concrete and steel material properties and their constitutive relationships.

The further scope of this study is to update and validate some approximate formulas existing in the CELLBEAM-USFB v1.0 software package developed by ASD Westok Ltd. manufacturers.

6.3 EXPERIMENTAL WORK

6.3.1 Test specimen

The same test configuration described in **Chapter 4** is used in this study. The advantage of this selection is that high shear forces are going to be generated in the area of the web openings and so the existence of the concrete will dramatically affect the results. A UB305x165x40 with material physical properties shown in **Table 6.1** is used. The web openings' diameter, d_o, is equal to $0.76h$, the spacing between the web openings and the support is equal to $1.3d_o$ and the beam is symmetrical to the mid-span. Assuming that the partial steel encasement with the concrete in-fill has 100% increase in Vierendeel bending and shear capacity, a failure load of approximately 600kN was anticipated.

Previous experience from coupon tests has shown that beams of steel grade S275 behave approximately as beams of steel grade S355 (**Table 4.1**), whilst beams of steel grade S355 behave approximately as beams of steel grade S450. This phenomenon is based on the underestimation of the steel material properties mainly for conservative reasons. The results of this behaviour are clearly shown in **Table 6.3**. For precautionary reasons, it is decided to test all the beams at the 14th day of curing, aiming for 25 to 30MPa (to be no greater that 35MPa) concrete strength at the day of the test.

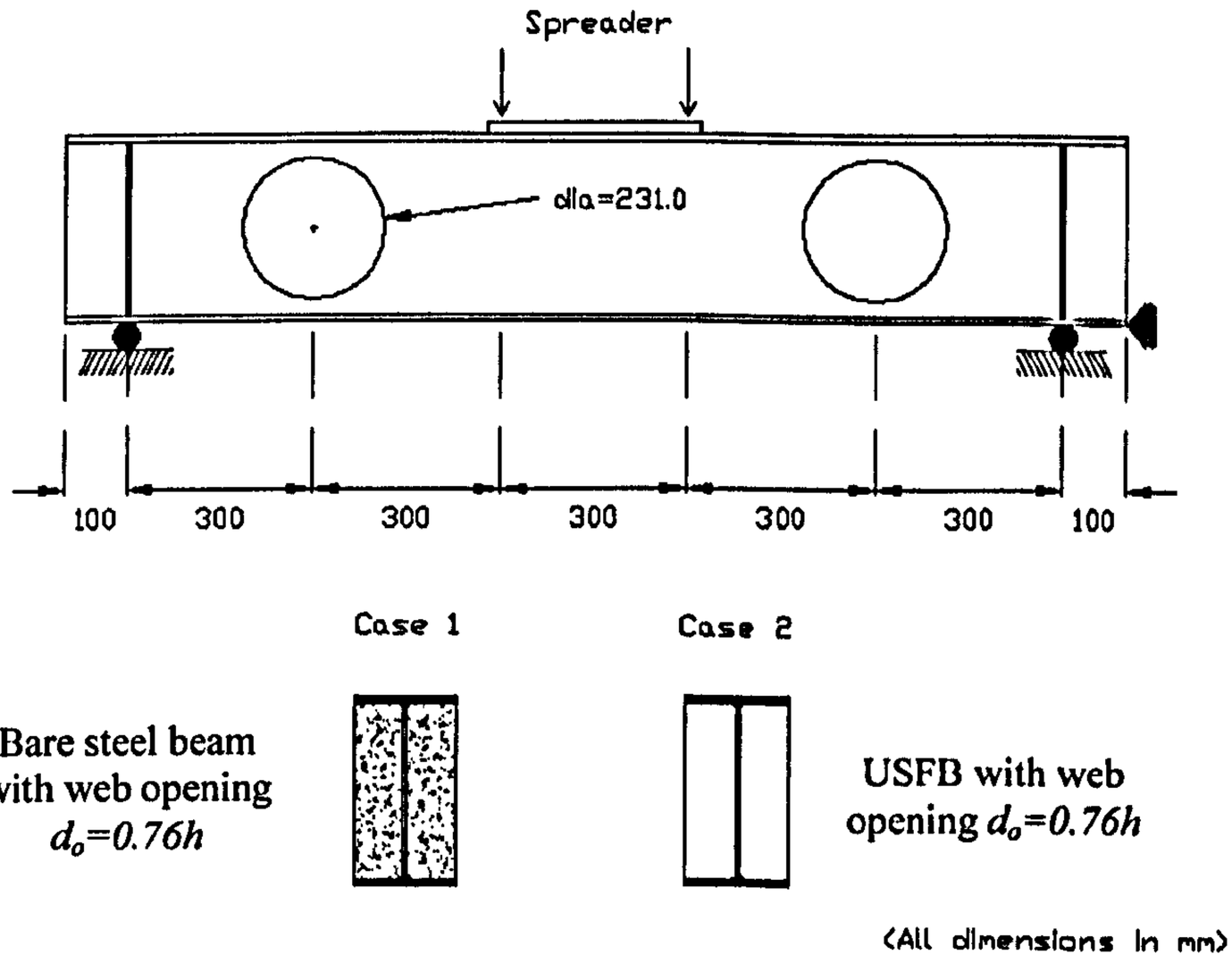

Figure 6.1: Experimental test beam configuration

6.3.2 Rig setup and measurement devices

A three-point bending load arrangement, with simply supported ends, results in a pure bending moment distribution over the mid-span of the beams. The load was applied through two hydraulic jacks and a spreader plate. The applied load and bending moments were obtained from the load cells connected to the jacks. The rig setup and test arrangement is shown in **Figure 4.2**.

To measure vertical deflection, three dial gauges were placed under the tension steel flange and aligned with the edge of the hole. Two dial gauges are applied at the high moment side (HMS) of each web opening (Dial Gauge 1 and 3) and one dial gauge at the mid-span of the test beams (Dial Gauge 2) similarly to **Figure 4.5**. No strain gauges are attached on the USFBs. The rig setup and test arrangement are shown in detail in **Figure 4.4**.

6.3.3 Test cubes procedure

Concrete is the most important construction material which is manufactured at the site. It is usually made outdoors under conditions not conductive to production if a uniform material. Quality control falls logically into two phases, namely, laboratory tests of ingredients sampled at the source and field control tests during and shortly after making the concrete. Quality of concrete is commonly stated in terms of the desired minimum compressive ultimate strength at 28 days. However, it this research programme a desirable maximum compressive strength was required for precautionary reasons (i.e. 35MPa), while the concrete will not be fully dried at the 14^{th} day of curing having the minimum possible compressive strength used by the standards (i.e. 25MPa).

Hence, there are many occasions, on which it is necessary or desirable to go through the process of mix design, where the type of concrete required or the particular criteria specified necessitate careful selection and proportioning of ingredients.

Even when all precautions are taken to test all ingredients inserted into the concrete, in spite the mixing, transporting and placing being properly carried through, follow-up tests are generally considered necessary to determine with certainty the quality of the finished product. These compression tests undertaken on samples, are removed from the forms and allowed to sit for some predetermined period such as 3, 7 and 14 days. The concrete strength tests are standardized and the method of making compressive specimens in the field is covered under **BS EN 197: Part 1**.

6.3.4 Parameters affecting the concrete design

The concrete mix is designed considering the date of the test after the casting (i.e. 14^{th} day), the concrete strength limits (i.e. 25 to 30MPa) and the workability of the concrete, in order to avoid any casting problems (i.e. coarse aggregate of 10mm size). The composite beams

are going to be air-cured in a similar manner to in-situ casting. Although the mixes are designed using a well established method (BRE, 1988), it is found necessary to conduct a trial mix study, as is presented in **Appendix 13**. Based on the guidelines of **BRE**, the fourteen days compressive strength is equal to 85% of the twenty-eight days compressive strength. Moreover, thirteen days of air-cured concrete compressive strength is equal to 70% of the thirteen days water-cured concrete compressive strength.

From the trial mix design in **Appendix 13** it is shown that Mix4 with *w/c* ratio equal to 0.61, conforms to the requirements and this is used for casting the composite beams.

6.3.5 Casting the USFBs

Four composite specimens are produced for testing purposes. The specimens are produced using **Lafarge Blue Circle OPC CEM-I 42.5 N** conforming to **BS EN 197: Part 1**. Sharp sand with a maximum size of 5mm is used as the fine aggregate. River gravel with a maximum size of 10mm is used as the coarse aggregate to overcome the problems associated with having to cast the specimen on one side (**Figure 6.2**). Twenty-four hours (± 4 hours) later, the specimens are de-moulded and left to air-cure in a storage room covered in sheeting for thirteen days. The storage room's temperature was 19 to 23°C at 50% to 60% relative humidity.

The casting of the composite beams is not a routine procedure because the bearing plates at the supports and the web openings make the whole procedure more difficult. This is accomplished by casting the beams as they are lying on the floor, and pouring the concrete through the web openings (**Figure 6.2**). Vibrators are used to ensure that the concrete is well compacted. The compaction of the concrete is also enhanced by the high water-cement ratio (0.61). Also, silicon is used to avoid water leakage between the steel and the framework. In **Figure 6.2** the casting setup used for the composite beams is shown.

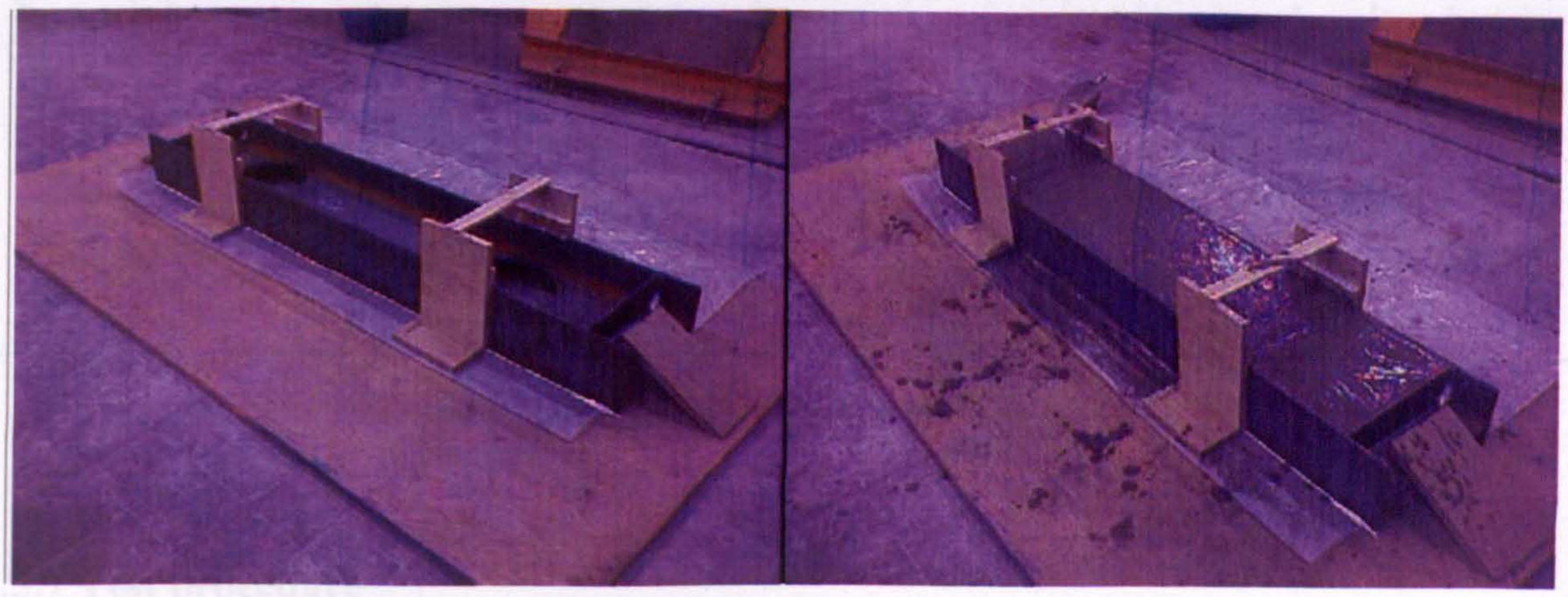

Figure 6.2: Casting procedure of USFBs (i.e. USFB No. 1)

6.3.6 USFB with lower grade concrete

Three USFBs are cast with *w/c* ratio equal to 0.61. Taking into consideration the usual uncertainties caused by human or climate interferences, which occur when the beams are cast in situ, another composite section is also cast with extra water and so lower grade concrete (i.e. higher *w/c* ratio). Segregation phenomenon is observed when the concrete cubes of the latter specimen are tested. An additional aim of this test is to verify the percentage of the shear improvement and the failure mode due to concrete infill (i.e. concrete is a path to the load), and to clarify whether it is the concrete strength or the concrete itself that provides the enhancement to the perforated steel beam.

The compressive cube strength of the USFB No.4 is also shown in **Figure 6.3** (Mix7). The particular specimen is tested after 52 days of curing, as it needed more time to gain strength and reach the required concrete strength limits (25-30MPa). **Appendix 13** also provides the experimental results for all four final mixes.

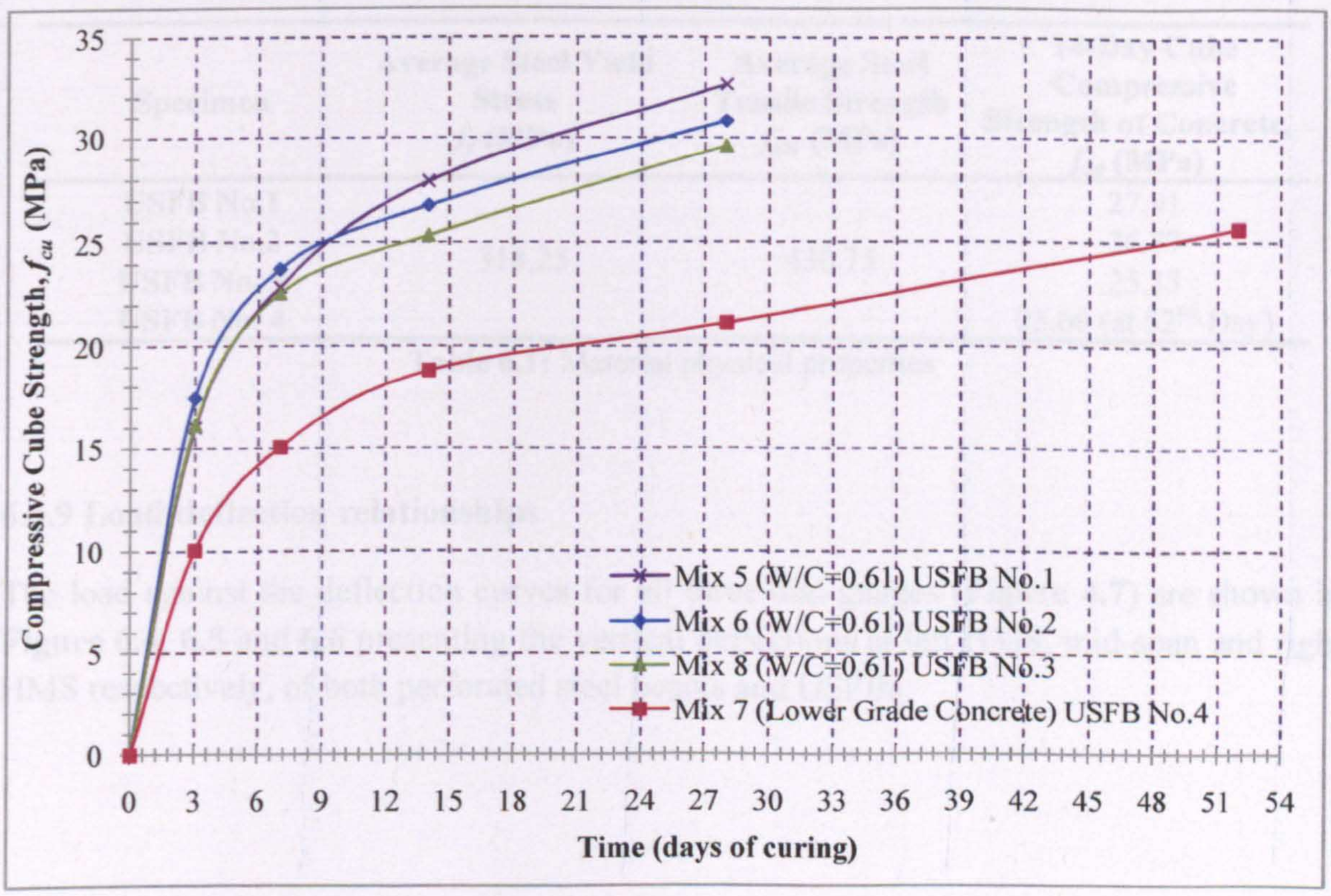

Figure 6.3: Concrete cube compressive strength

6.3.7 Test procedure

After a preloading stage, the load is applied in steps at a low displacement rate, and held at each step to allow load relaxation. All test specimens are loaded past the ultimate load to

obtain a significant part of the post-failure curve. Concrete crack patterns are recorded throughout the tests. Initially the beams are loaded with approximately 10kN and the dial gauges are zeroed. The load is then released and reloaded gradually in 40 to 50kN increments. The loading increments are reduced, after the first diagonal cracking, to approximately 20 to 30kN, up to the point of the beams' ultimate load carrying capacity and then, a further reduction leads the increment to approximately 5 to 10kN per step in the post-elastic region. The tests are performed not only until the maximum load is reached, but also until a sufficient branch of the descending post-failure load deformation curve is recorded. The general test-procedure is summarised in the following four steps: i) preloading, ii) monotonic loading, iii) gradual loading and relaxation and iv) unloading.

6.3.8 Material physical properties

The material properties for the steel coupon tensile tests from **Chapter 4** and concrete cube compressive tests are summarized in **Table 6.1**.

Specimen	Average Steel Yield Stress f_y (MPa)	Average Steel Tensile Strength $f_{ult.}$ (MPa)	14-Day Cube Compressive Strength of Concrete, f_{cu} (MPa)
USFB No.1	318.25	430.75	27.91
USFB No.2			26.77
USFB No. 3			25.33
USFB No. 4			25.60 (at 52nd Day)

Table 6.1: Material physical properties

6.3.9 Load-deflection relationships

The load against the deflection curves for all three dial gauges (**Figure 4.7**) are shown in **Figure 6.4, 6.5** and **6.6** presenting the vertical deflections at left HMS, mid-span and right HMS respectively, of both perforated steel beams and USFBs.

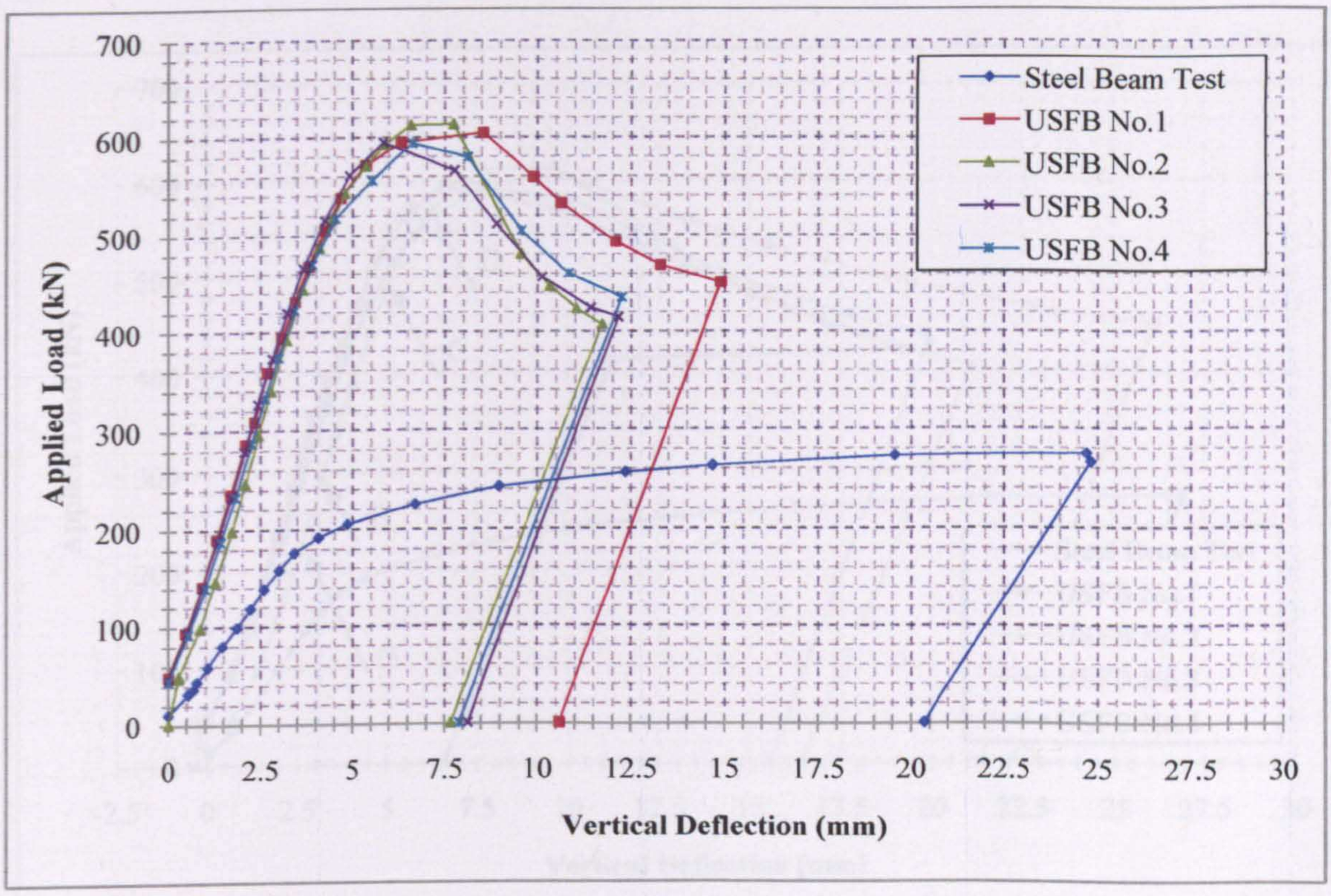

Figure 6.4: Load-deflection curves for non-composite and composite beams for (Dial Gauge 1)

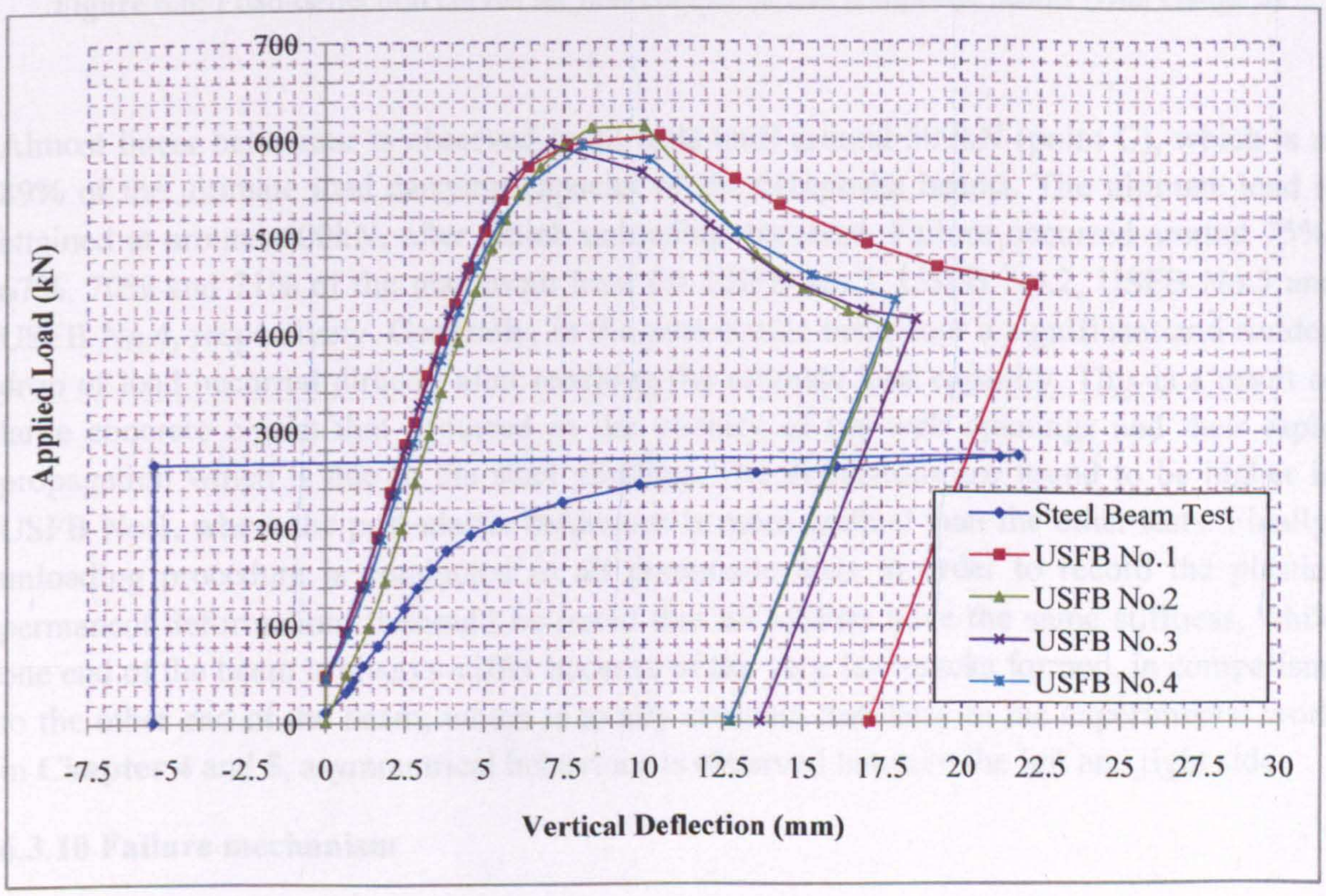

Figure 6.5: Load-deflection curves for non-composite and composite beams for (Dial Gauge 2)

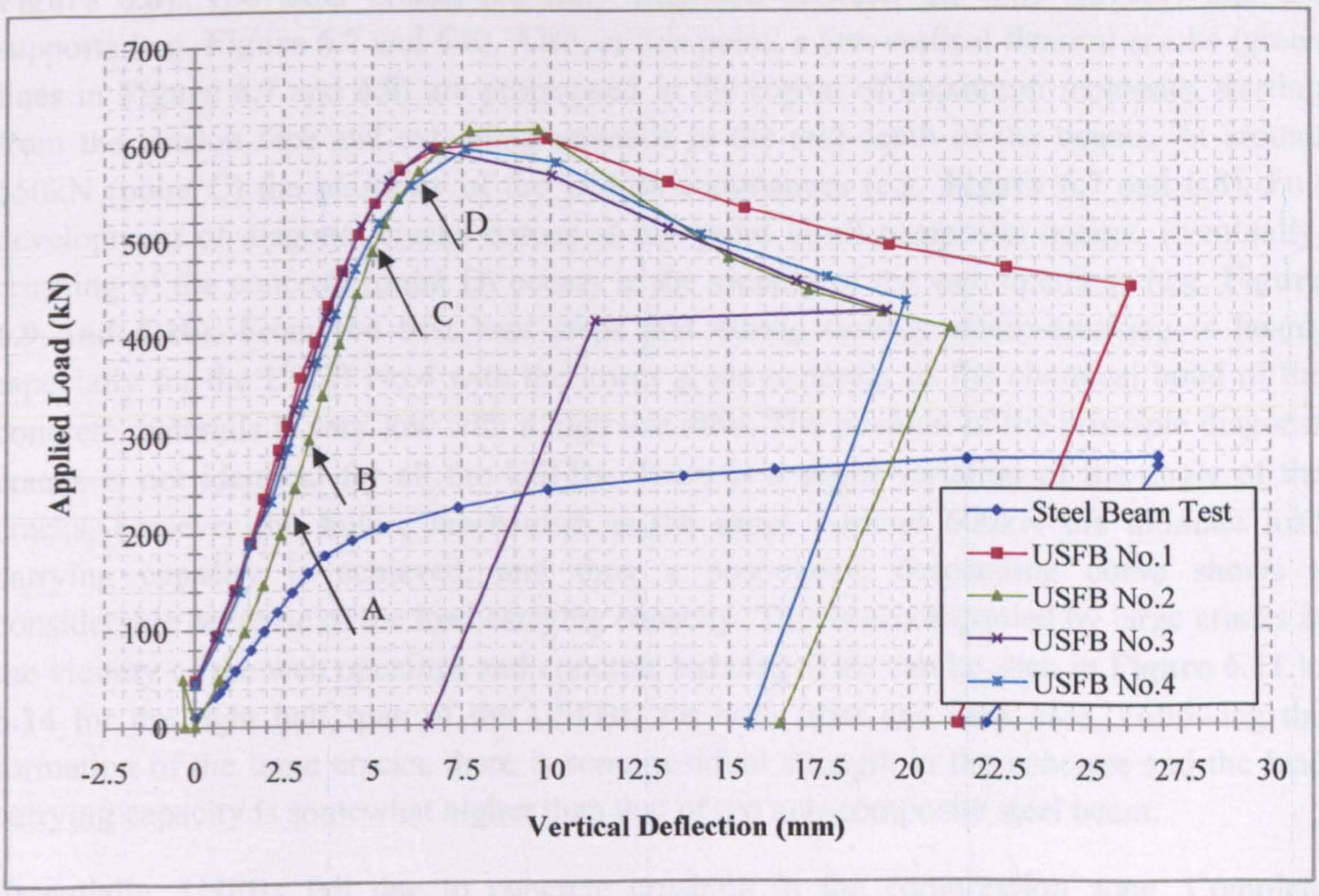

Figure 6.6: Load-deflection curves for non-composite and composite beams (Dial Gauge 3)

Almost linear behaviour is observed in all tests until around 500kN (point C), which is at 89% of the ultimate load carrying capacity of the composite beams. The ultimate load is attained at around 600kN, after which unloading occurred. Failure occurred around 75%, 67%, 70% and 71% of the maximum load for USFB No.1, USFB No.2, USFB No.3 and USFB No.4, respectively. Generally, in the post-elastic behaviour a significant and sudden drop of load occurred directly after reaching the ultimate load capacity. This is a result of large concrete cracks that occurred in the vicinity of the web openings and their rapid propagation which is due to the steel yielding. The deflections are found to be higher in USFB No.1, where the post-elastic behaviour is more gradual than the other tests. Finally, unloading procedure is conducted to all composite tests in order to record the plastic-permanent deformation. It should be noted that all USFBs have the same stiffness, while one end of the beam is always stiffer because of the very few cracks formed, in comparison to the other end of the beam, which is totally crushed. Similarly to the experimental work in **Chapter 4** and **5**, asymmetrical behaviour is observed between the left and right side.

6.3.10 Failure mechanism

Diagonal tension cracks occurred at around 250 to 300kN. Point A indicates the load that the latter diagonal cracking is heard and point B the load that this cracking is seen (e.g.

Figure 6.6). The latter cracks are fully extended between the load spreader and the supports (e.g. **Figure 6.7** and **6.8**). Also, at this point, a few vertical flexural cracks (green lines in **Figure 6.7** and **6.8**) are propagated in the region of maximum moments, starting from the tension face and extending upwards to the mid-depth of the beams. At around 550kN (point C) the plasticity of the USFBs commences (e.g. **Figure 6.7** and **6.8**). Full development of diagonal cracks ensues at this point in all composite beams. Eventually, crushing of the concrete (point D) occurs in the vicinity of the web openings (e.g. **Figure 6.9 and 6.10**). From the first load steps and during testing, micro-cracking is heard, especially for the USFB No.4 with the lower grade concrete, as the chemical bond of the concrete materials is very low with a high *w/c* ratio. The position of the principle diagonal cracks is not identical for all the USFBs. There is a slight variation of the angle of the cracks, however the failure mechanism is the same. Around 600kN the ultimate load carrying capacity is achieved, and then a post-elastic descending curve shows a considerable decrease of the load carrying capacity. This is accompanied by large cracks in the vicinity of the web openings and concrete bursting. This can be seen in **Figure 6.11** to **6.14** for the right half span of the USFBs, for both front and back side. Following the formation of the large cracks, there is some residual strength in the concrete and the load carrying capacity is somewhat higher than that of the non-composite steel beam.

Essentially, USFBs fail due to concrete crushing in the compression zone. Complete composite action up to the ultimate load carrying capacity, is found. Therefore, the proposed system enables the development of sufficient strength and consequently, effective composite behaviour, without causing serviceability problems. Moreover, the longitudinal shear strength of the proposed system consists of the frictional force and the shear-bond strength between the steel and the concrete as well as of the bearing strength of the web opening area. However, in this experimental study the concrete is partially encased since the bearing plates at the supports restrain the longitudinal movement of the concrete. In real life construction the end plate connections will play the same role. Also, it is observed that the plastic behaviour of the composite sections is mainly due to the steel beam's low stiffness and high deformation. In general, the concrete provides a load path from the top to the bottom steel flange; as well as a restraint to the steel web.

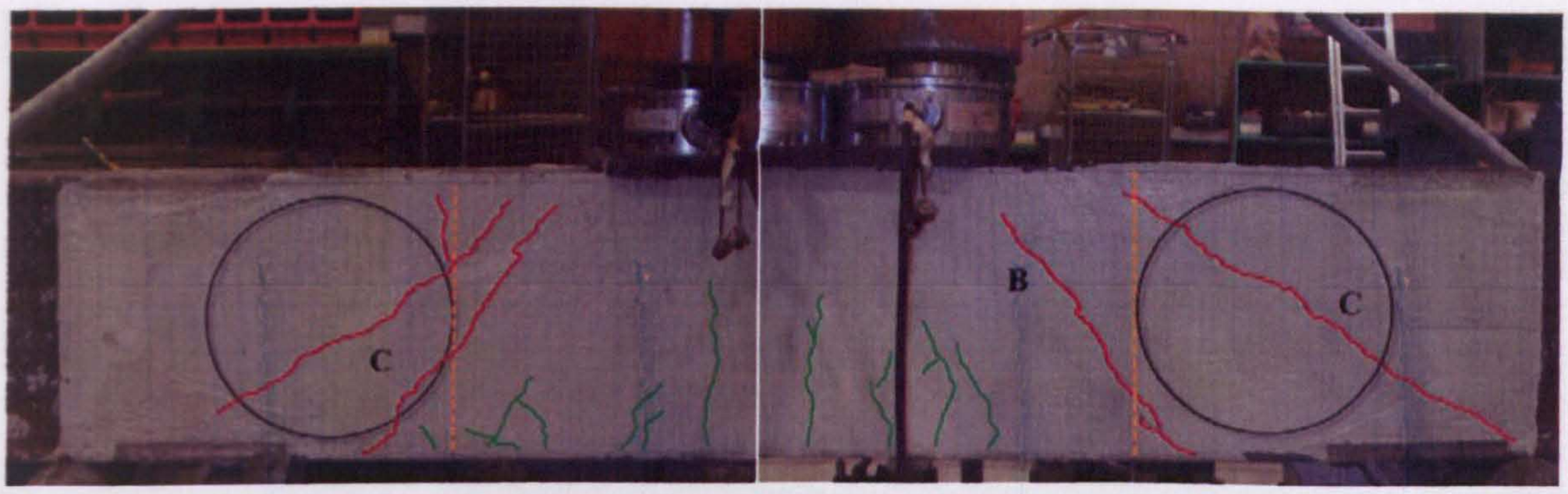

Figure 6.7: USFB No.2

Figure 6.8: USFB No.3

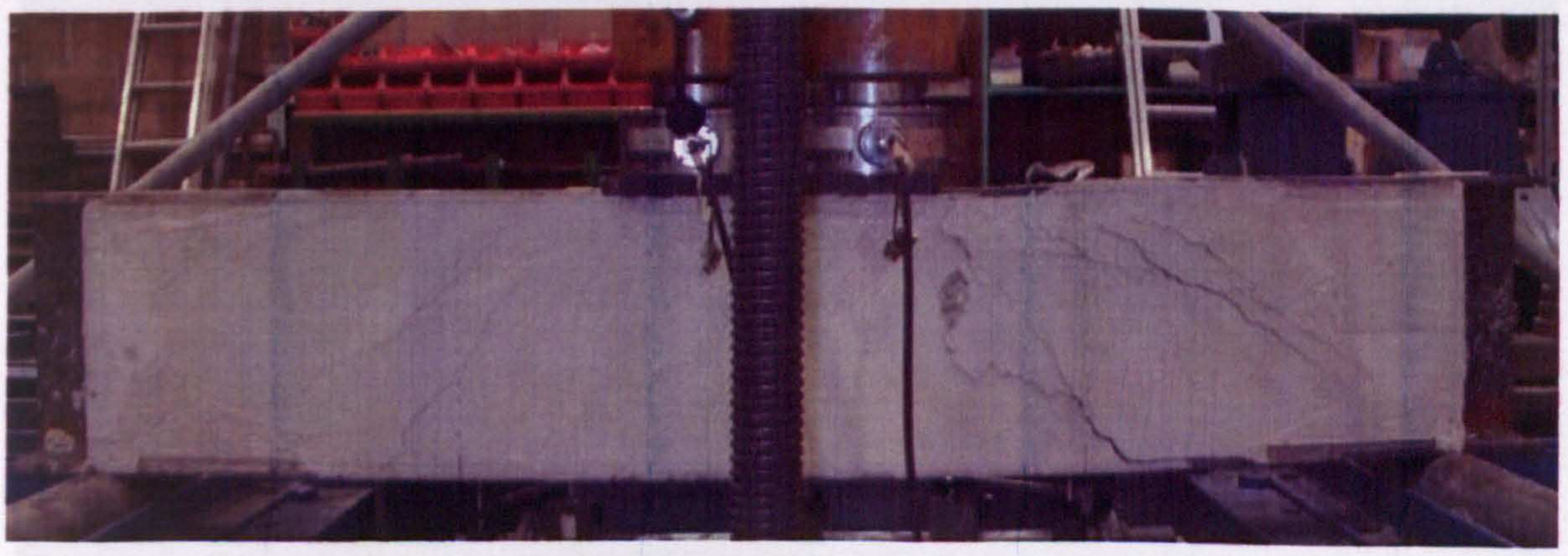

Figure 6.9: USFB No.2 at point D with concrete crushing

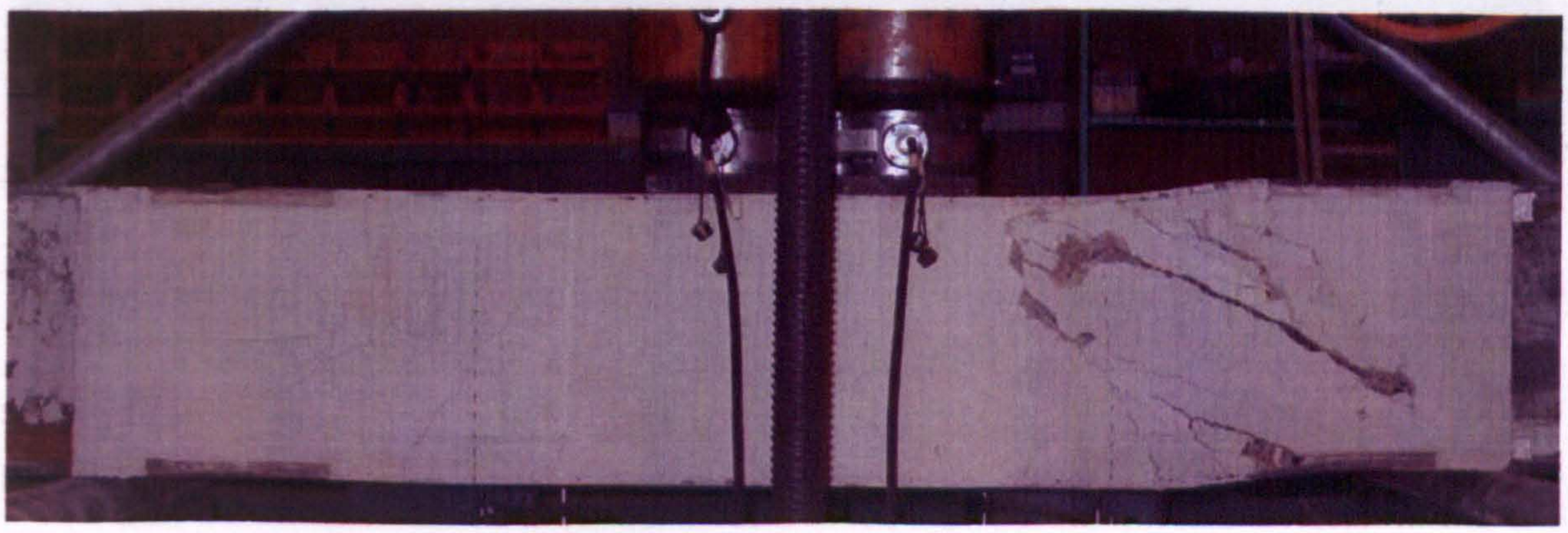

Figure 6.10: USFB No.3 at point D with concrete crushing

Figure 6.11: USFB No.1 with concrete bursting

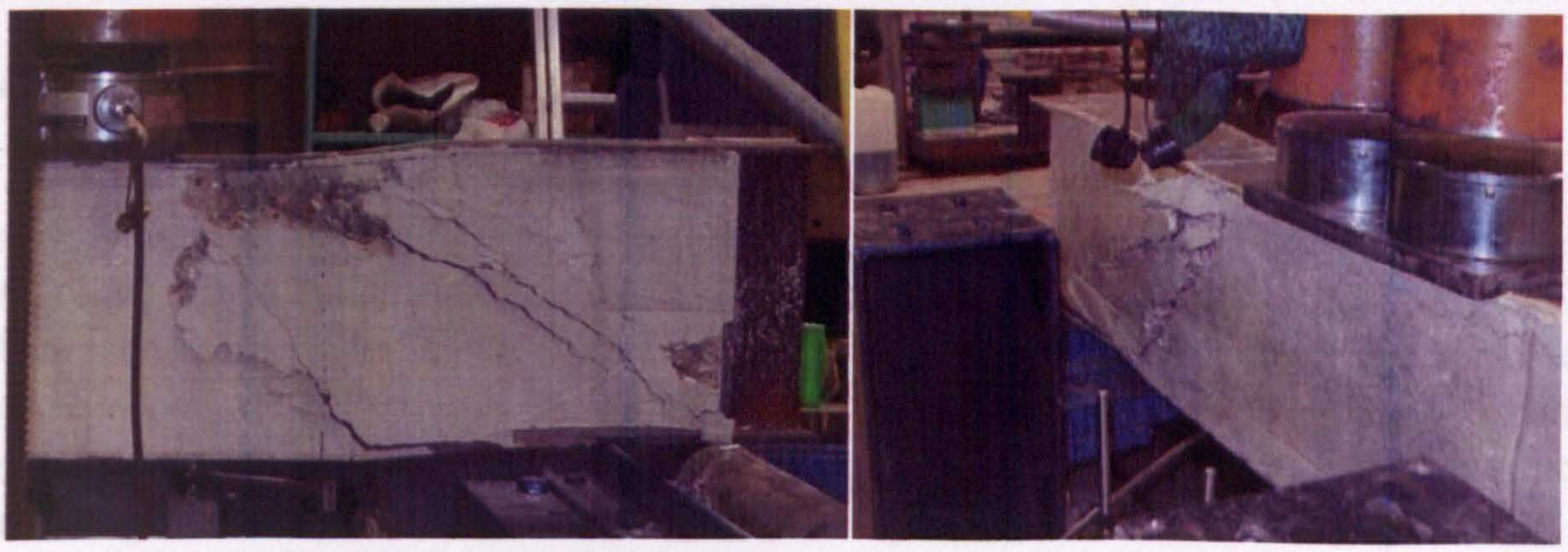

Figure 6.12: USFB No.2 with concrete bursting

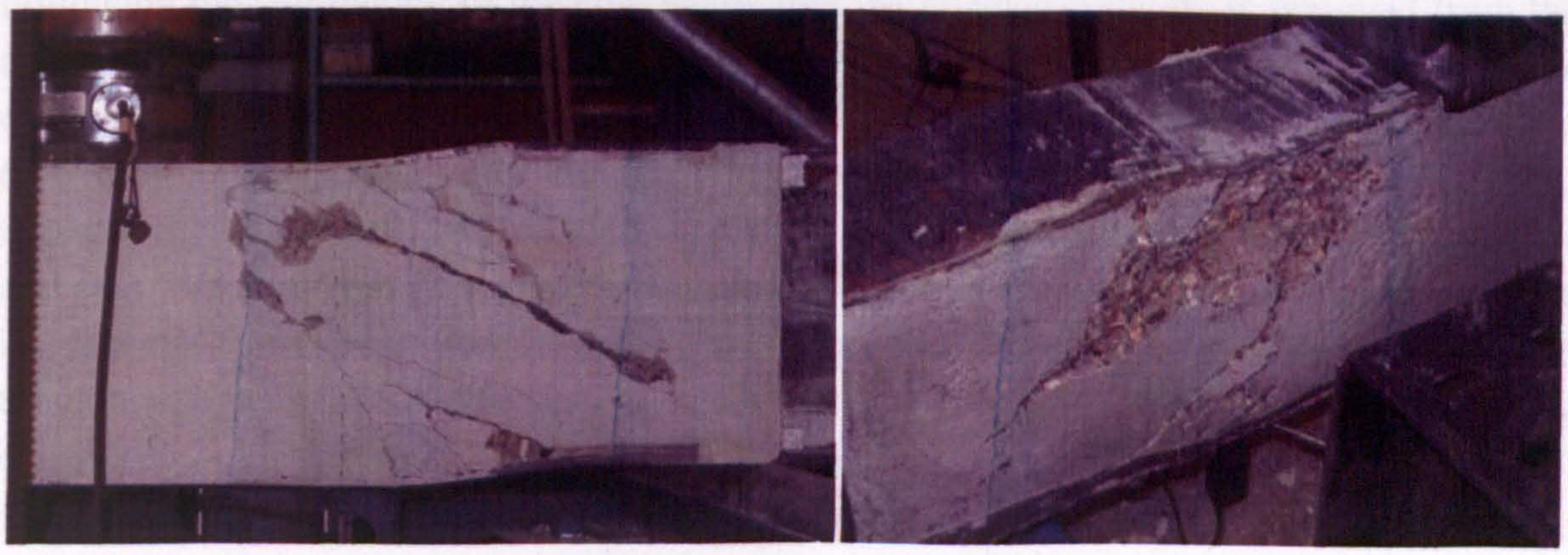

Figure 6.13: USFB No.3 with concrete bursting

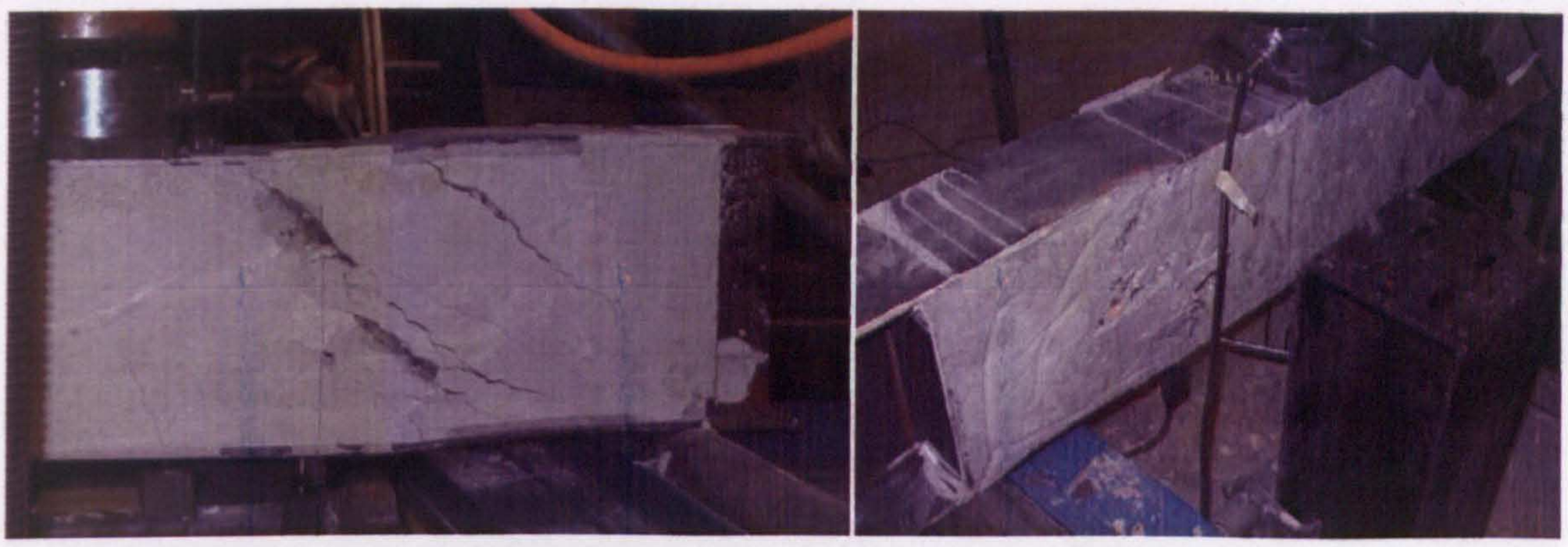

Figure 6.14: USFB No.4 with concrete bursting

6.3.11 Composite action due to partial encasement

The effect of partial encasement on overall flexural action is dependent on the mechanism of shear transfer and the relative slip between the steel section and the concrete. These tests failed by Vierendeel bending at the web openings, as shown in **Figure 6.15** and **6.16**. However, it is apparent that considerable 'arching' action occurred through the concrete encasement, which is resisted by the bearing plates at the supports of the relatively short span beams. Hence, the contribution of the trapped concrete between the steel flanges in resisting vertical shear is achieved.

Following the completion of the composite tests the crushed concrete is removed from the area around the web openings. Removal occurs only in the web opening, where the concrete is catastrophically crushed, in order to look at the steel yielding. **Figure 6.15** and **6.16** show the steel web after the concrete is removed for USFB No.1 and USFB No.2, respectively. It is worth to mention that the concrete is removed only by using a hammer and man force; no heavy equipment was used in trying to remove only the crushed concrete in order not to harm the concrete which is not crushed. This helps to visualize the size of the concrete area around the web opening that is strongly affected by the web opening existence.

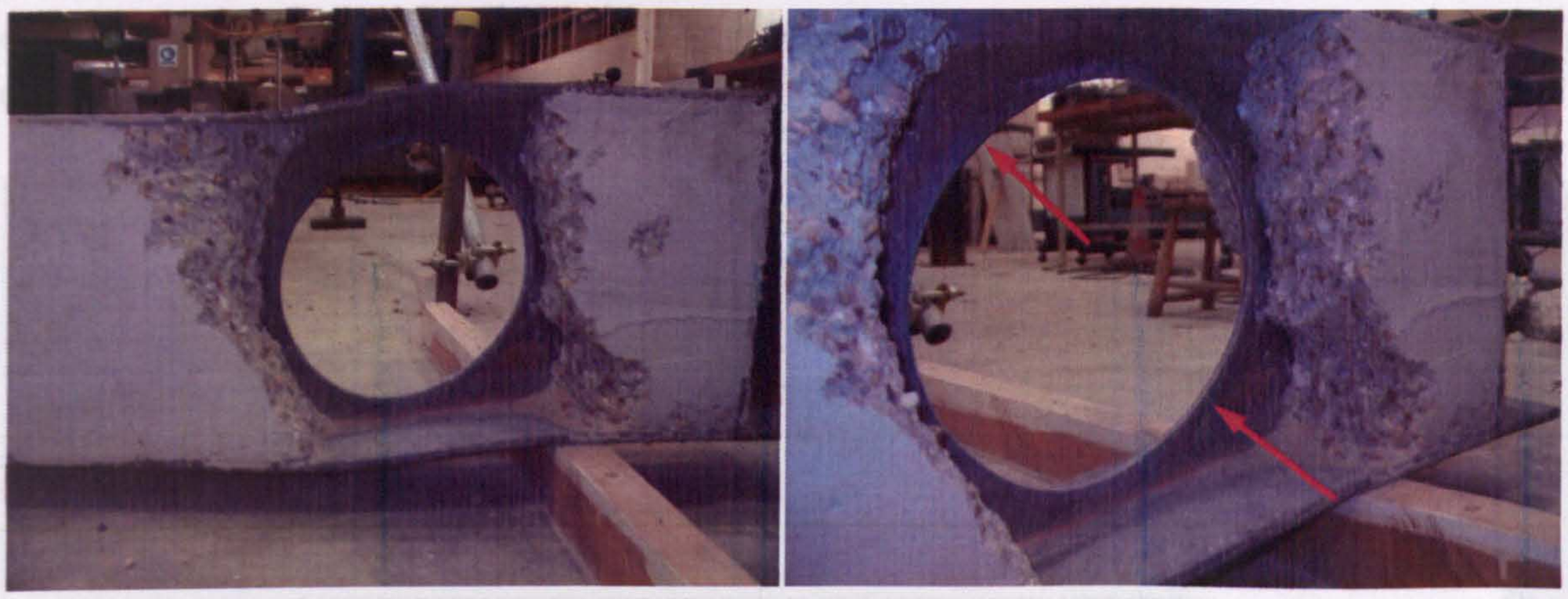

Figure 6.15: USFB No.1 after concrete is removed

Figure 6.16: USFB No.2 after concrete is removed

The steel beam is slightly deformed compared to the non-composite beam, while local web buckling is faintly shown on the diagonal line connecting the load spreader to the supports (red arrows shown in **Figure 6.15** and **6.16**). This implies due to transfer of shear forces across the web openings after the concrete crushed while loading was applied in the post-elastic region. The transfer of shear forces causes local bending moments and therefore local web buckling.

At a web opening, the concrete encasement acts as a strut in compression, which is confined between the flanges and inclined diagonally across the web opening, as illustrated in **Figure 6.17**. The magnitude of this strut action depends on the ability of the flanges to resist the local compression forces by transverse bending. The dimensions of the flanges significantly contribute to the bending and shear resistances of USFBs. The transverse bending moment when the bearing force applies on the flange is drawn in **Figure 6.18**. The horizontal forces act on the bottom flange with a combination of friction, due to the strut force and the shear-bond. The lower bound of the shear-bond strength with the partially

encased flange is given as 0.2MPa in **BS EN1994 1-1**. A coefficient of friction of 0.6 for concrete on steel may be assumed for the local strut action, as in **BS EN 1992-1-1**.

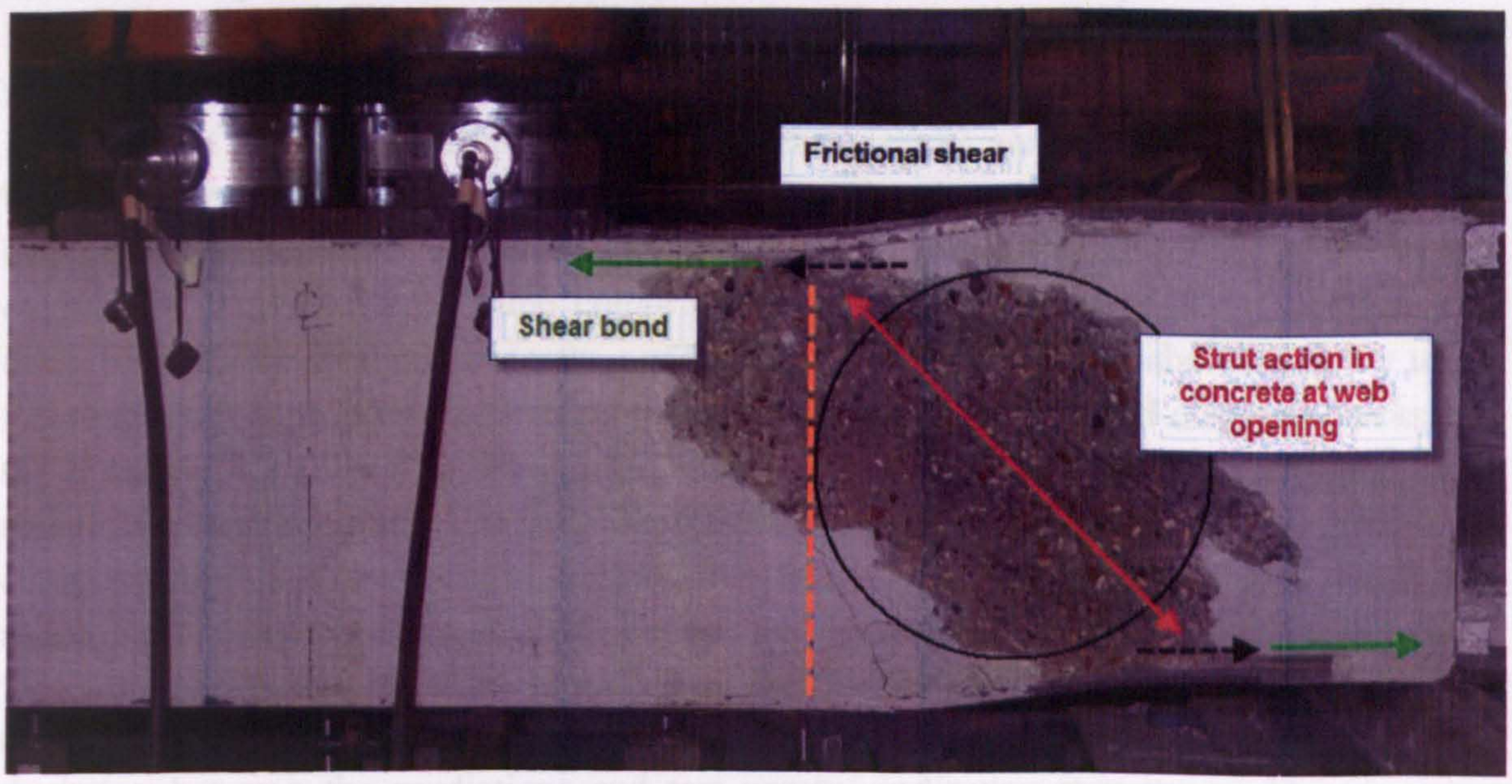

Figure 6.17: Compression force acting in the concrete encasement across the web openings

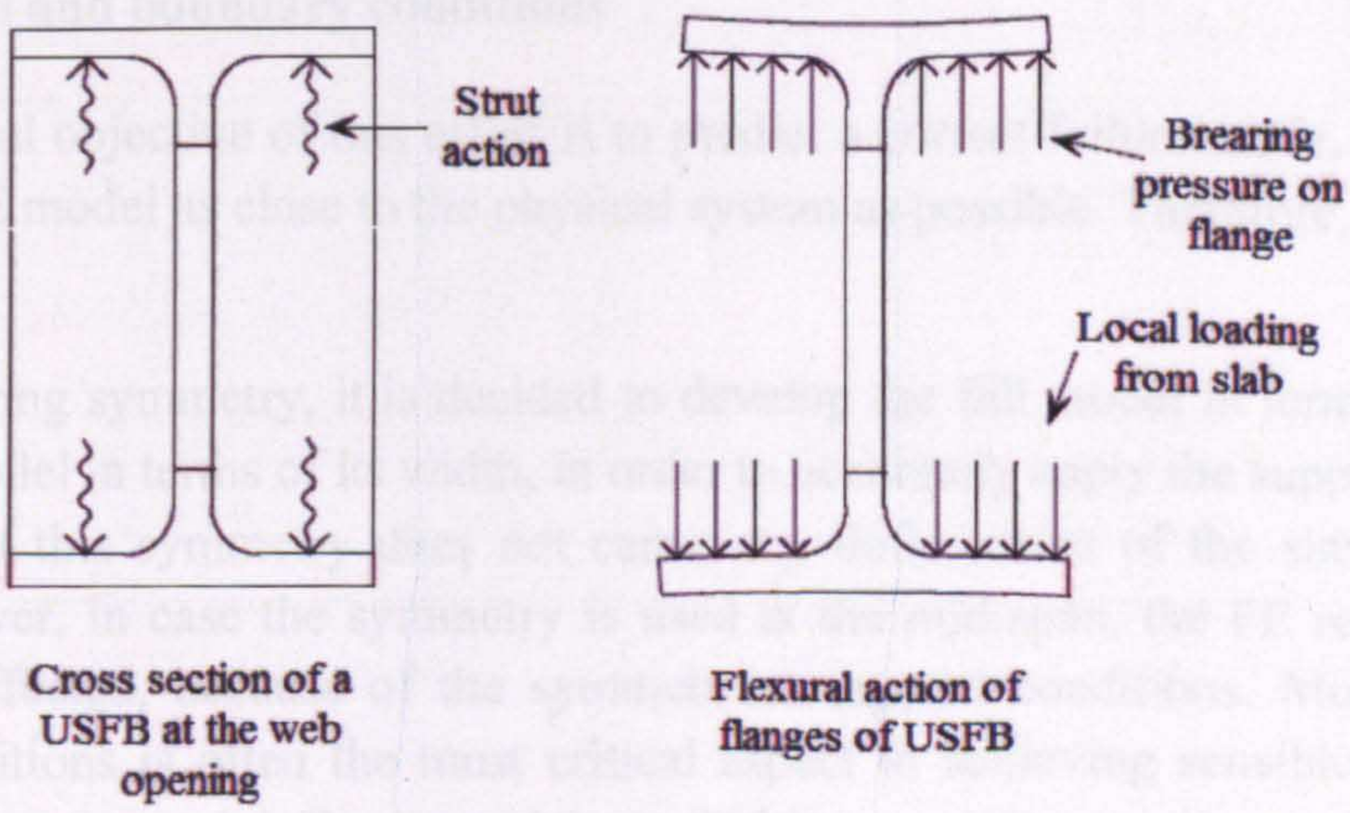

Figure 6.18: Strut action in concrete causing flexural bending

6.4 SENSITIVITY FE STUDY OF THE USFBS

6.4.1 Introduction

A FE model is developed to predict the load-deflection behaviour and failure modes of the composite Ultra Shallow Floor Beams. Due to the introduction of concrete in the FE

models a more complex non-linear analysis is developed. A detailed description of the techniques and tools used to apply the boundary conditions and the material properties is also made. Apart from the geometrical and material non-linearity, the contact surface between the steel and the concrete takes a decisive role in modelling the friction between these two materials when no mechanical connectors are provided. A parametric study is implemented in order to compare the experimental results and examine the sensitivity of these parameters. Interesting observations are made by changing the material properties of both steel and concrete. The characteristics of concrete cracks and contact elements are determined individually by cube compressive tests, and shear-bond tests (i.e. push-out tests) between the steel and concrete, conducted at City University's laboratories. By using FE analysis, it is possible to represent the development of flexural and diagonal cracks and the decrease of USFBs' stiffness after cracking. It is also possible to clarify the shear resistance mechanism of USFBs without reinforcement. The shear resistance of such composite beams is consistent of contributions from the compressive concrete strength, the aggregate interlock and the concrete encasement between the steel flanges (i.e. frictional force and shear-bond resistance), as well as the steel strength. However, it is noteworthy that when deeper beams with a large contact surface are considered, there is a greater deviation between the predictions and test results, indicating that the problem is more complex.

6.4.2 FE model and boundary conditions

Since a principal objective of this effort is to predict a correct failure mode, it is important to develop a FE model as close to the physical system as possible. Therefore, a 3D model is developed.

While considering symmetry, it is decided to develop the full model in terms of its length and the half model in terms of its width, in order to accurately apply the support conditions. It is found that this symmetry does not cause any deficiencies of the simulation of the USFBs. However, in case the symmetry is used at the mid-span, the FE results could be significantly affected, because of the symmetrical support conditions. Modelling of the boundary conditions is often the most critical aspect in achieving sensible, reliable data from a finite element model (Baglin and Scott, 2000).

A 3D model is implemented with a fine mesh of 20mm element size consisting of 68,569 elements (**Figure 6.19**). Regarding the concrete crack modelling with FE software, several researchers have studied the effect of the element size in the nonlinear analysis of reinforced concrete structures (Shayanfar et al., 1997; Choi and Kwak, 1990), and they have shown that the results are indeed dependent on the mesh.

The load and the supports are directly applied on the steel beam and not on the concrete, in order to avoid early local concrete cracking. For better stress distribution, the load is

applied as a pressure on an area and the supports are modelled as restrictions to the degrees of freedom on areas.

Figure 6.19: Symmetric FE model of the USFB

6.4.3 Contact element and contact algorithm

CONTA173 (**Figure 6.20**) is an 4-node element that is intended for flexible-to-flexible contact analysis. In flexible-to-flexible contact, both contact and target surfaces are associated with deformable bodies. CONTA173 is also a surface-to-surface contact element. The contact detection points are the integration points and are located either at nodal points or Gauss points. The contact elements are constrained against penetration into the target surface, at its integration points. However, the target surface can, in principle, penetrate through the contact surface. Nodal contact points are not used, as when a uniform pressure is applied; the kinematical equivalent forces at the nodes are unrepresentative and indicate release at corners (ANSYS manual).

A number of methods are available for modelling friction in contact analyses, however the most commonly used methods are based on a 'Coulomb' friction model. In this model the two contacting surfaces are permitted to carry shear stresses across their interface, up to a defined value, before they begin sliding. The equivalent shear stress at which sliding begins is defined as:

$$\tau_{slide} = \mu P_{Con} + CSR \qquad (6.1)$$

Contact elements offer two models for 'Coulomb' friction: isotropic friction and orthotropic friction. The isotropic friction model is incorporated in this study as it uses a single coefficient of friction, based on the assumption of uniform stick-slip behaviour in all directions. When a penetrating node stays in contact with the target surface, it may either stick to the surface or slip along the surface.

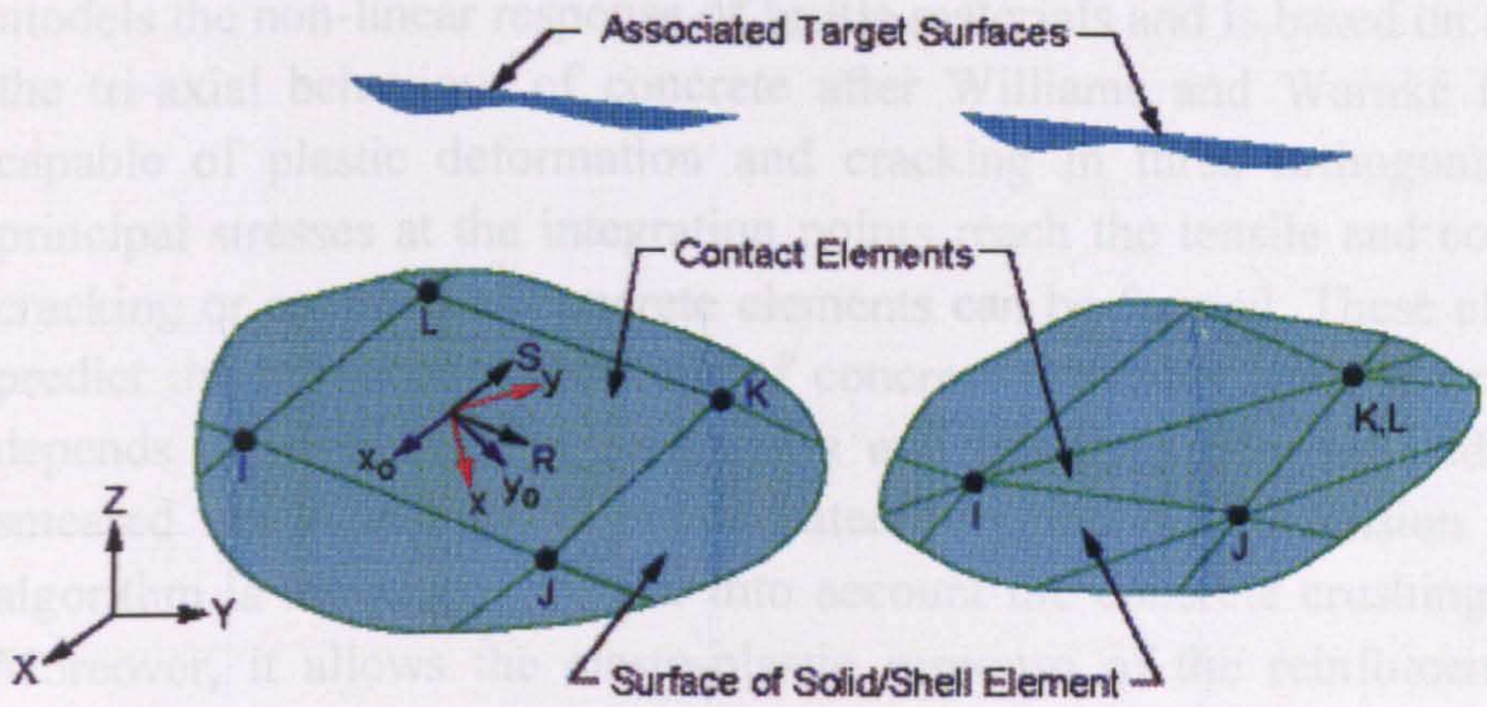

R = Element x-axis for isotropic friction
xo = Element axis for orthotropic friction if element coordinate system is not applied (parallel to global X-axis)
x = Element axis for orthotropic friction if element coordinate system is supplied

Figure 6.20: 3D model of the contact element CONTA173 (ANSYS v11.0)

6.4.4 Element types and material models

Steel: Typical 8-node solid SOLID45 elements are used to model the steel perforated beam with circular web openings. Mainly nominal but also actual material properties are used to model the steel perforated beam. This is for precautionary reasons, as well as for the generalizations of the FE results; a similar methodology followed in the previous chapters. The bi-linear stress-strain curves with strain hardening used in the non-linear FE analyses before, show sufficient agreement with the experimental study of the non-composite steel beam. Hence, the steel material is modelled as an elasto-plastic material with strain hardening and an identical bi-linear stress-strain relationship for both compression and tension (**Figure 6.21(a)**). The Young's Modulus, E, and the Poisson's Ratio, v, of steel are taken as 200GPa and 0.3 respectively. The yield strength, f_y, varies such as: 265, 275, 285 and 355MPa as well as the ultimate strength, $f_{ult.}$, varies such as: 318.25 (average f_y from coupons), 350, 410, 500 and 530MPa. The variation of the material strength applies to the sensitivity study of the material properties. In most analyses, an ultimate strain of around 0.25 is assumed for the structural steel (Liang et al., 2005), hence the Tangent Modulus, E_T, is varied from 540 to 700MPa. It is worth to note that in **Chapter 5**, the Tangent Modulus, E_T, equal to 580MPa is adequately representing the post-elastic behaviour of the steel perforated beams. For the ease of modelling, steel flanges, bearing plates and web consist of the same material properties.

Concrete: 8-node solid iso-parametric SOLID65 elements with the integration points for the cracking and crushing checks are used to model the concrete in ANSYS. SOLID65

models the non-linear response of brittle materials and is based on a constitutive model for the tri-axial behaviour of concrete after Williams and Warnke (1974). The element is capable of plastic deformation and cracking in three orthogonal directions. Once the principal stresses at the integration points reach the tensile and compressive strength, the cracking or crushing of concrete elements can be formed. These elements are also able to predict the non-linear behaviour of concrete materials using a smeared approach, which depends on five material parameters and has been adopted widely in recent years. A smeared crack analogy is incorporated for cracking in tension zones and a plasticity algorithm is introduced to take into account the concrete crushing in compression zones. Moreover, it allows the elasto-plastic response of the reinforcement to be included in simulation. In ANSYS values such as: Material Number, Volume Ratio and Orientation Angles can be entered to define the smeared model. The Material Number refers to the type of the material for the reinforcement. The Volume Ratio of the steel to concrete in the element and the Orientation Angles refer to the orientation of the reinforcement in the smeared model. ANSYS allows the user to enter three re-bar materials in the concrete. Each material corresponds to x, y and z directions in the element. The reinforcement has uni-axial stiffness and the directional orientation is defined by the user. As no reinforcement is provided of the actual experiment in this research programme, default values are kept for smeared reinforcement.

Cracking and crushing are determined by a failure surface. The tensile strength, f_t, is typically 8-15% of the compressive strength, f_c, (Kachlakev, 2002). For research purposes, the ultimate concrete compressive and tensile strengths for every beam model are calculated using various constitutive relationships found in the literature. The concrete in compression is modelled as an elasto-plastic material (**Figure 6.21(b)**) either with or without strain softening. The 'crushing' option is removed and the concrete plasticity (crushing) in the compression zone is modelled using the multi-linear option from ANSYS with Von-Mises plasticity. It is difficult to re-produce shear cracks after bending cracks while the solution diverged. Due to isotropy, the concrete model for tensile stresses is the same as that of the compressive one when this plastic model is adopted. However, as cracking capability has always been kept on, cracking in linear elastic phase should govern the tensile failure in all analyses (Barbosa and Ribeiro, 1998).

Non-linear elastic behaviour of concrete is therefore defined by the multi-linear stress-strain relationships. The compressive cylinder strength, f_c, varies as such: 20, 21.12 (the average cylinder strength from **Figure 6.3** and **Table 6.1**), 26.7 and 32MPa, whereas the other parameters such as Young's Modulus, E_c, and tensile strength of concrete, f_t, are treated as generic data and evaluated by the applying constitutive relationships (**Table 6.2**). In **Table 6.2**, f_c is the stress at any strain ε, f_1 is the stress at strain ε_1 and ε_o is the strain at the ultimate concrete cylinder compressive strength f_c ($f_c = 0.8f_{cu}$).

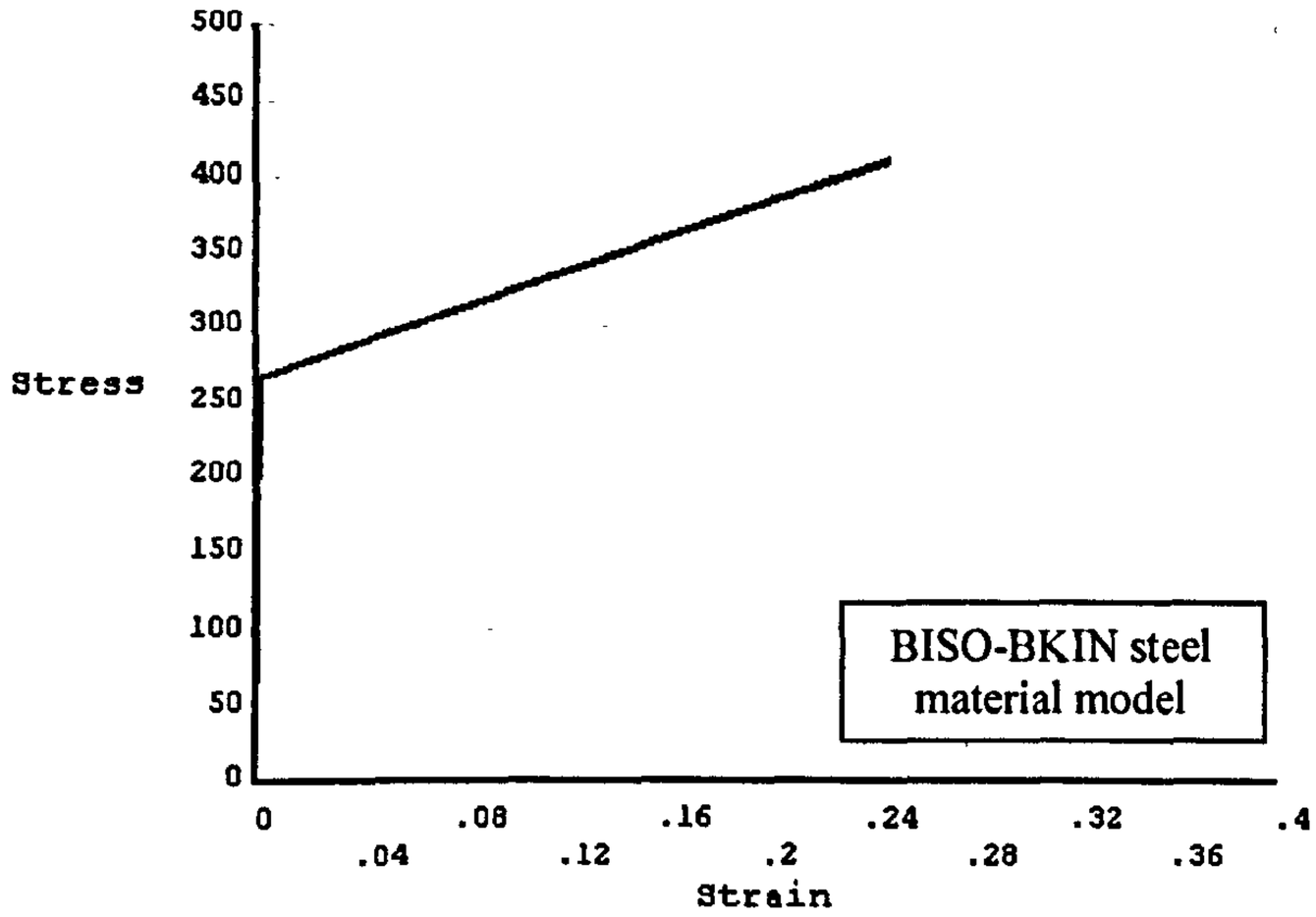

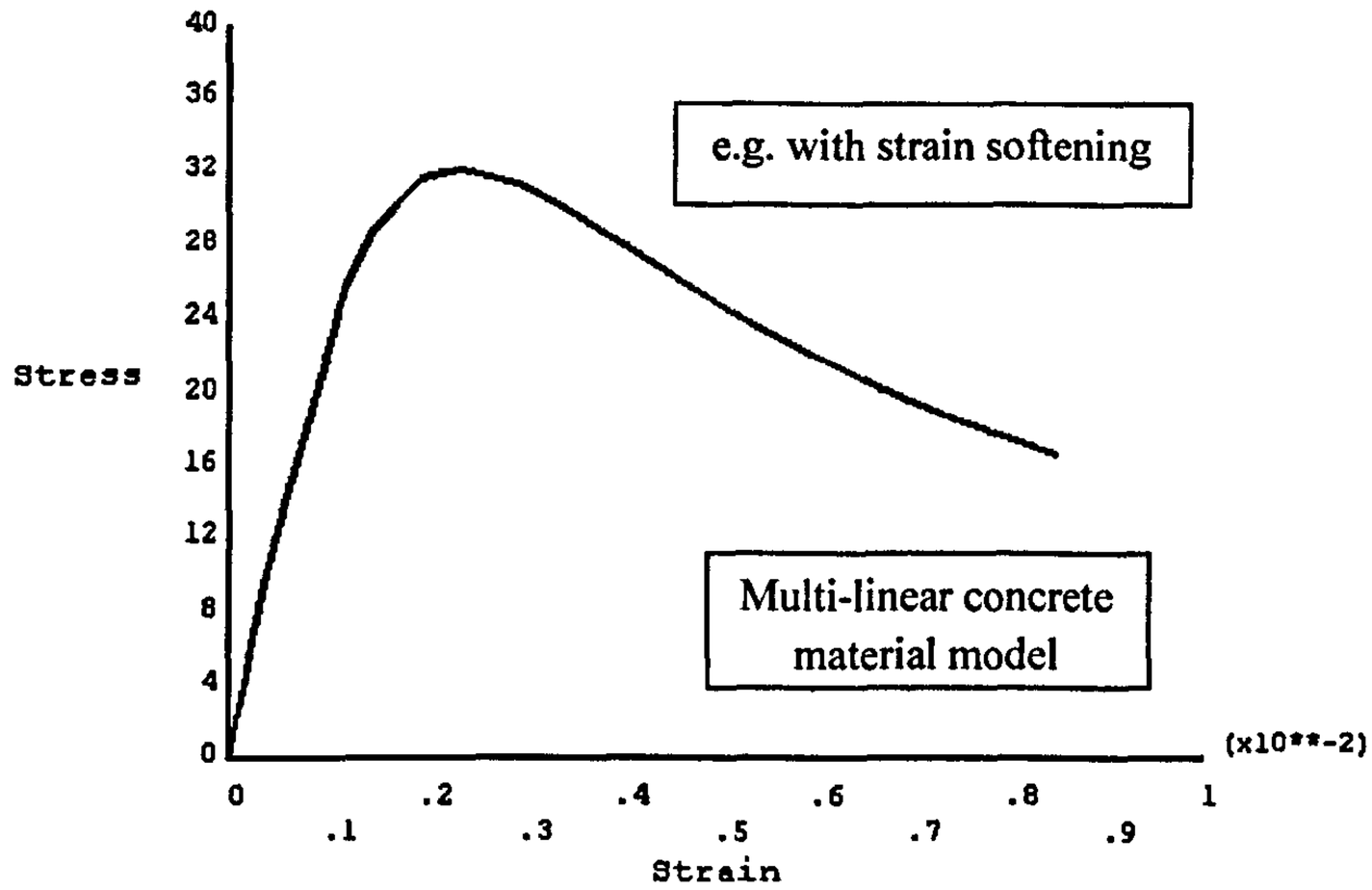

Figure 6.21: (a) Steel material model (Liang and Uy, 2005) and (b) concrete material model (Kachlakev and Miller, 2001)

Reference (in SI)	E_c	f_t and ε_o	f_1 and ε_1	f_c	Coefficients
Ref.: Kachlakev & Miller ***Code:*** ACI 318-99	$E_c = 4730\sqrt{f_c}$	$f_t = 0.623\sqrt{f_c}$	$f_1 = 0.3f_c$	$f_c = \frac{E_c\varepsilon}{1+\left(\frac{\varepsilon}{\varepsilon_o}\right)^2}$	---
	$v = 0.2$	$\varepsilon_o = \frac{2f_c}{E_c}$	$\varepsilon_1 = \frac{f_1}{E_c}$		---
Ref.: Liang & Uy (Carreira & Chu, 1985)	$E_c = 5050\sqrt{f_c}$	$f_t = 0.545\sqrt{f_c}$	$f_1 = 0.4f_c$ (HSC)	$f_c = \frac{\beta\left(\frac{\varepsilon}{\varepsilon_o}\right)f_c}{\beta - 1 + \left(\frac{\varepsilon}{\varepsilon_o}\right)^\beta}$	$\beta = \left[\frac{f_c}{32.4}\right]^3 + 1.55$
	$v = 0.15$	$\varepsilon_o = 0.002$	$\varepsilon_1 = \frac{f_1}{E_c}$		
Ref.: Kaewunruen & Remennikov ***Code:*** AS3600	$E_c = 5050\sqrt{f_c}$	$f_t = 0.4\sqrt{f_c}$	N.A.	$f_c = \frac{E_c\varepsilon}{1+\left(\frac{\varepsilon}{\varepsilon_o}\right)^2}$	---
	$v = 0.3$	$\varepsilon_o = \frac{2p_c}{E_c}$ (apprx. 0.2% proof stress)	$\varepsilon_1 = \frac{f_1}{E_c}$		---
Ref.: Parvanova et al. ***Code:*** BS 8110	$E_c = 9100(f_c)^{1/3}$	$f_t = 0.36\sqrt{f_c}$	N.A.	$f_c = \frac{E_c\varepsilon}{1+\left(\frac{\varepsilon}{\varepsilon_o}\right)^2}$	---
	$v = 0.2$	$\varepsilon_o = \frac{2f_c}{E_c}$	$\varepsilon_1 = \frac{f_1}{E_c}$		---
THE FORMULAS BELOW ARE NOT USED IN THE PARAMETRIC FE STUDY - ONLY FOR REFERENCE					
Ref.: Wang & Chung	$E_c = 5.5\sqrt{f_{cu}}$	$f_t = 0.1f_c$	$f_1 = 0.3f_c$	$f_c = \frac{\beta\left(\frac{\varepsilon}{\varepsilon_o}\right)f_c}{\beta - 1 + \left(\frac{\varepsilon}{\varepsilon_o}\right)^\beta}$	$\beta = \left[\frac{f_c}{32.4}\right]^3 + 1.55$
	N.A.	$\varepsilon_o = 2.4 * 10^{-4}\sqrt{f_{cu}}$	$\varepsilon_1 = \frac{f_1}{E_c}$		
Ref.: Manhmood ***Code:*** ACI318-05	$E_c = 4730\sqrt{f_c}$	$f_t = 0.116f_c$	$f_1 = 0.3f_c$	$f_c = \frac{E_c\varepsilon}{1+\left(\frac{\varepsilon}{\varepsilon_o}\right)^2}$	---
	$v = 0.3$	$\varepsilon_o = \frac{2f_c}{E_c}$	$\varepsilon_1 = \frac{f_1}{E_c}$		---

Table 6.2: Constitutive relationships modelling the concrete material from the literature

Shear Transfer Coefficient, $\beta_{1,2}$: They are also known as "shear retention factors" and can vary between '0' for no aggregate interlock and 1.0 for full aggregate interlock. In opening β_1 or closing β_2 are assumed to take a value of 0.25 and 0.7 respectively, for plain concrete of all grades having no fibres (Barzegor, 1988). Various shear transfer coefficients are used in this study for open cracks and closed cracks. High values entered for the closed crack (e.g. 0.9, 1.0) so as to prevent possible fictitious crushing of the concrete before load transfer occurs through a closed crack. From Bangash (1989) and ACI 318-99 (1999), it is found that when the shear transfer coefficient representing conditions of the crack face, of reinforced concrete structures, varies between 0.05 and 0.25. Moreover, it is worth to note that the lost shear resistance of cracked and/or crushed elements cannot be transferred to the re-bar, which has no shear stiffness. In case the latter phenomenon occurs, care should be taken to apply the load slowly and hence analysis time will significantly increase. Consequently, as the shear capacity plays a significant role in this research study, the smeared approach is more suitable.

Friction Coefficient, μ: Various friction coefficients such as: 0, 0.3, 0.4, 0.6, 0.7, 0.9 and 1.0 are substituted in order to compare the results. By using a friction coefficient equal to 0 or 0.4, a significant decrease of the ultimate load carrying capacity of the USFBs is observed. The results show an increase of the stiffness in the strain of the compressive top flange for beam with higher bond, but in the tensile flange the stiffness is nearly the same. One reason for this behaviour is the cracking of concrete in tensile zone, which starts from the first load steps. In the experiments the bond strength is also different in the compressive zone from the one is the tensile zone of the composite beam, and this is another reason for possible discrepancy between the experimental and the FE results. The local bond strength and the corresponding slip are almost linearly related to the tensile strength of concrete.

Solution Method: The full Newton-Raphson procedure is used, even though this requires the stiffness of the structure to be re-calculated for every iteration. The automatic load control scheme is also employed. A large-displacement and static analysis is used with the maximum number of sub-steps in a load step being 1,000-10,000 in order to apply the load increments very smoothly where it is necessary. Sparse direct equation solvers are used and all values for the non-linear algorithm are set to ANSYS default. A small criterion is used to capture correct response. So, failure of the beam occurs when convergence fails, with a very small load increment. This method is comparable with the experimental data from Buckhouse (1997). The analysis is terminated due to cracking and/or crushing of the concrete through the section as it is expected, due to instability of the stiffness matrices. The vertical deflection at mid-span of the composite beams and the FE divergence load is always monitored.

6.4.5 FE results based on material strengths

**MISO – Multi-linear Isotropic Hardening Plasticity is adopted*
***BISO – Bi-linear Isotropic Hardening Plasticity is adopted*

Steel		*Cont.*	*Concrete*					*Results*	*Run*
f_y *(MPa)*	$f_{ult.}$ *(MPa) or* $E_{Tan.}$	μ	f_c *(MPa)*	ft *(MPa)*	v	$\beta_{1,2}$	*Refer. Theory Based*	F_{FEA} *(kN)*	*Code No.*
265*	410	1.0	26.70	1.86	0.20	0.3,1.0	†	**627**	*59*
265*	410	1.0	26.70	1.86	0.17	0.3,1.0	†	**617**	*3*
265*	410	0.8	26.70	1.86	0.17	0.3,1.0	†	**611**	*7*
265*	410	0.3	26.70	1.86	0.17	0.3,1.0	†	**548**	*8*
265*	410	1.0	26.70	1.86	0.15	0.3,1.0	†	**547**	*58*
265*	410	1.0	26.70	1.86	0.15	0.6,0.6	†	**555**	*16*
265*	410	1.0	26.70	1.86	0.15	0.1,0.9	†	**607**	*18*
265*	410	1.0	26.70	1.86	0.15	1.0,1.0	†	**635**	*19*
265*	410	1.0	26.70	1.86	0.00	1.0,1.0	†	**648**	*20*
275**	$E_{Tan.}$=200	0.8	26.70	1.86	0.15	0.1,0.9	†	**618**	*25*
355*	530	1.0	26.70	1.86	0.20	0.3,1.0	†	**637**	*11*
355*	530	1.0	26.70	1.86	0.17	0.3,1.0	†	**633**	*12*
355*	530	0.0	26.70	1.86	0.17	0.3,1.0	†	**470**	*13*
275*	410	0.9	20.00	2.786	0.2	0.3,1.0	¥	**577**	*B5*
275*	410	0.6	20.00	2.786	0.2	0.3,1.0	¥	**563**	*B6*
355*	499	0.9	20.00	2.786	0.2	0.3,1.0	¥	**730**	*B2*
355*	530	0.9	20.00	2.786	0.2	0.3,1.0	¥	**733**	*B4*
355**	$E_{Tan.}$=20	0.9	20.00	2.786	0.2	0.3,1.0	¥	**734**	*B3*
275*	410	1.0	21.12	2.863	0.2	0.3,1.0	¥	**591**	*B11*
275*	410	0.9	21.12	2.863	0.2	0.3,1.0	¥	**584**	*B10*
275*	410	0.7	21.12	2.863	0.2	0.3,1.0	¥	**578**	*B12*
275*	410	0.4	21.12	2.863	0.2	0.3,1.0	¥	**508**	*C8*
275*	410	1.0	21.12	2.863	0.2	1.0,1.0	¥	**599**	*B13*
318.25*	430	1.0	21.12	2.863	0.2	0.3,1.0	¥	**630**	*D1*
265*	410	0.9	32.00	3.524	0.2	0.3,1.0	¥	**588**	*C1*
275*	410	0.9	32.00	3.524	0.2	0.3,1.0	¥	**611**	*C4*
275*	410	0.6	32.00	3.524	0.2	0.3,1.0	¥	**574**	*C14*
285**	$E_{Tan.}$=20	0.9	32.00	3.524	0.2	0.3,1.0	¥	**622**	*C6*
285*	350	0.9	32.00	3.524	0.2	0.3,1.0	¥	**641**	*C5*
355*	499	0.9	32.00	3.524	0.2	0.3,1.0	¥	**742**	*B1*
275*	410	0.9	21.12	1.839	0.3	0.3,1.0	#	**545**	*B9*
275*	410	0.9	32.00	2.260	0.3	0.3,1.0	#	**621**	*C12*
275*	410	0.6	32.00	2.260	0.3	0.3,1.0	#	**597**	*C13*
275*	410	0.7	21.12	2.505	0.15	0.3,1.0	§	**571**	*C11*
265*	410	1.0	32.00	3.083	0.15	0.3,1.0	§	**629**	*31*
265*	410	0.8	32.00	3.083	0.15	0.3,1.0	§	**610**	*32*
265*	410	0.5	32.00	3.083	0.15	0.3,1.0	§	**565**	*33*
275*	410	0.9	32.00	3.083	0.15	0.3,1.0	§	**615**	*B14*
275*	410	0.9	32.00	3.083	0.15	0.0,1.0	§	**243**	*B15*

Table 6.3: Results of the FE parametric study

Various combinations of all the parameters presented above are conducted, in order to visualize their sensitivity when USFBs are considered. The failure loads obtained from this study are summarised in **Table 6.3** and categorized mainly according to the constitutive relationships used to model the material properties. Sub-categories are also indicated, based on both steel and concrete strength.

The maximum load carrying capacities are reported as failure loads, in the last applied load step before the solution diverges due to numerous cracks and large deflections. Both steel and concrete strength affect the load carrying capacity of the USFBs. In general, it is observed that when the concrete strength is low, the steel strength governs the load carrying capacity of the USFBs.

Various concrete compressive strengths are used in order to examine the percentage of shear enhancement of the USFBs. Also, the concrete tensile strength is varied taking into consideration the mesh size of the concrete elements and the value of fracture energy, G_f. It should be noted that the interfacial fracture energy is almost linearly related to the root of the tensile strength of concrete. Also, various evaluations of concrete Poisson's ratio, v, are examined, as they are related to the condition (i.e. quality) of concrete, while different values of it have been published by researchers. Moreover, it is observed that the numerical solutions are very sensitive to the steel strength in contrast to the concrete strength, and small changes lead to significantly different results. From FE results, it is found that the USFBs with steel yield strength of 265 to 285MPa compare well with the experimental behaviour; there is a reduction of 16.8 to 10.5% to the average steel yield strength (i.e. f_y=*318.25MPa*), as obtained from the coupon tests. This applies to the increased stiffness of the 3D solid elements as well as the complex failure mechanism of the USFBs. Oppositely, in **Chapter 4** where shell elements are used, the material model of f_y=*355MPa* accurately simulates the experimental behaviour. Eventually, it is verified that the ultimate load carrying capacity of the USFBs is governed by the steel strength, as it is also mentioned in the conclusions of the experimental work **(sub-chapter 6.3.10 and 6.3.11)**.

6.4.6 FE results based on the other parameters

Most of the FE results are satisfactorily correlated with the experimental results, while up to the ultimate load level insignificant steel deflection occurs. Thereafter, the steel yields following the large concrete strains and the formation of large cracks, while the load capacity drops considerably. When the USFB with the lower concrete compressive strength is considered, more cracks are developed, even though the capacity of the USFB remains the same. In the experimental tests large steel deflections ensue in the post-elastic curve.

Furthermore, it is apparent that apart from the steel and concrete strength, the shear transfer coefficients and the coefficient of friction play a significant role in modelling the experiment. It is found that the better applicable factors for opened and closed cracks, β_1

and β_2, are 0.3 and 1.0, respectively. Particularly, dramatic change of the divergence load is obtained when the coefficient of friction, μ, is greatly reduced. Observing the real tests it is found that no slip between the steel and the concrete occurs up to the yield point. Subsequently, a value of 1.0 (i.e. perfect bonding) is mainly used at the contact surface modelled in ANSYS. In case $\mu \neq 1.0$, a significant interlocking between the steel and the concrete exists after de-bonding, due to the non-uniform strain across the section of the member.

6.4.7 Load-deflection relationships

Various load-deflection curves at the mid-span are plotted against the experimental test of the USFB No.1 for representation means (**Figure 6.22(a)** and **(b)**). Also, the load-deflection curve of the non-composite perforated beam is plotted for comparison.

There are several effects that might cause the deviation of the stiffness between the FE and the experimental beams. One reason is the concrete micro-cracks in the experimental beams. due to drying shrinkage in the concrete. In addition to that, cracks generated from different elastic modulus of aggregate and cement, thermal coefficient, as well as human interference could cause reduction of the stiffness in the experimental beams. On the other hand, the FE models do not suffer from the above uncertainties and they are usually enough restrained to impose additional constraints on behaviour.

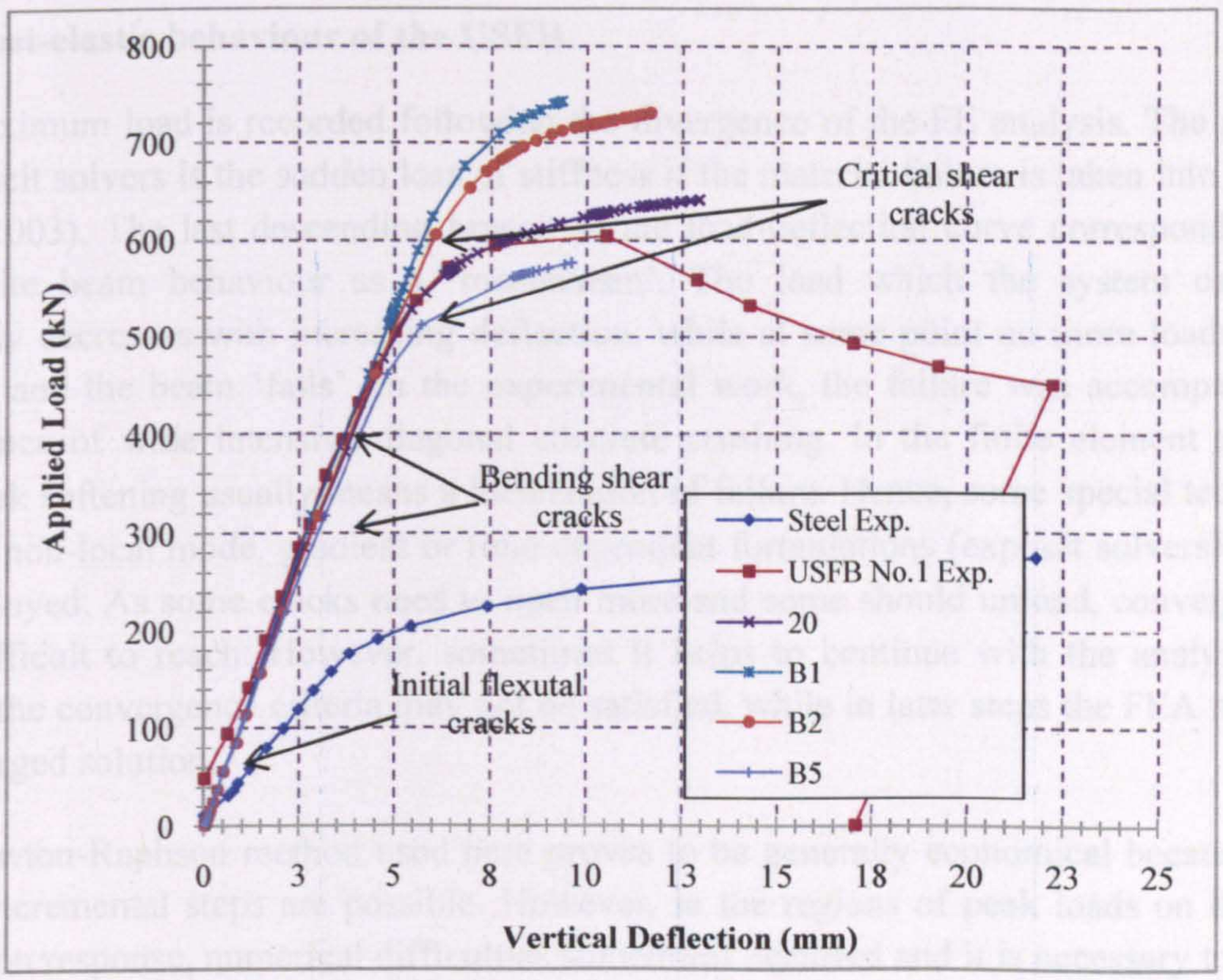

Figure 6.22(a): Load-deflection curves at mid-span against the experimental test (USFB No.1)

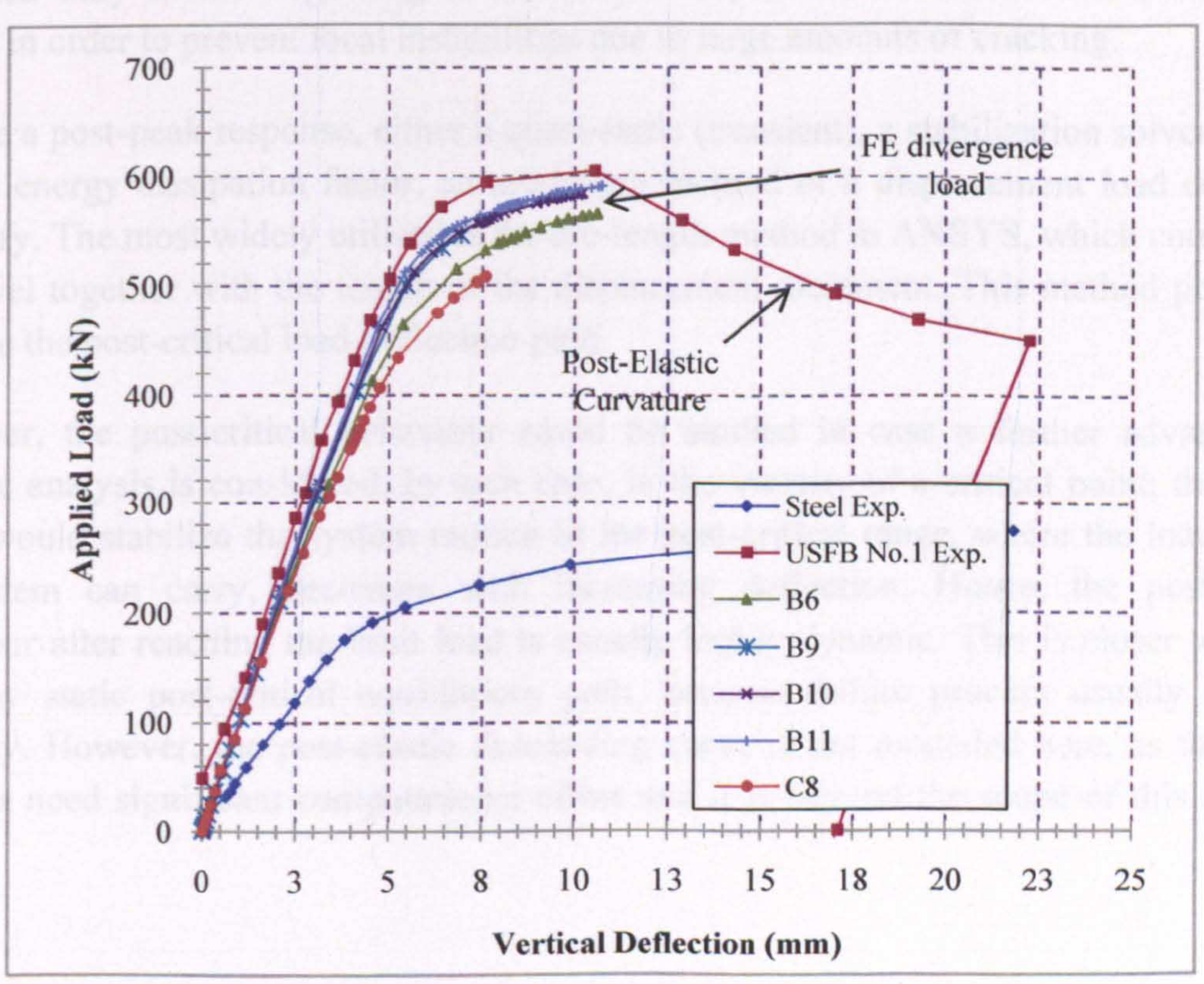

Figure 6.22(b): Load-deflection curves at mid-span against the experimental test (USFB No.1)

6.4.8 Post-elastic behaviour of the USFB

The maximum load is recorded following the divergence of the FE analysis. The problem of implicit solvers is the sudden loss of stiffness if the material failure is taken into account (Rust, 2003). The last descending branch of the load-deflection curve corresponds to the composite beam behaviour as a 'mechanism'. The load which the system can carry gradually decreases with increasing deflection, while at some point no more loads can be resisted and the beam 'fails'. In the experimental work, the failure was accompanied by appearance of wide intensive diagonal concrete crushing. In the finite element analysis, post-peak softening usually means a localization of failure. Hence, some special techniques such as non-local mode, gradient or time dependent formulations (explicit solvers) need to be employed. As some cracks need to open more and some should unload, convergence is very difficult to reach. However, sometimes it helps to continue with the analysis even though the convergence criteria may not be satisfied, while in later steps the FEA may find a converged solution.

The Newton-Raphson method used here proves to be generally economical because much larger incremental steps are possible. However, in the regions of peak loads on the load-deflection response, numerical difficulties sometimes occurred and it is necessary to use the modified Newton-Raphson iteration scheme under which the stiffness of the structure is calculated only at the beginning of the increment, or the modified Riks (Arc-length) method in order to prevent local instabilities due to large amounts of cracking.

To trace a post-peak response, either a quasi-static (transient), a stabilization solver usually with an energy dissipation factor, an arc-length method or a displacement load control is necessary. The most widely utilised is the arc-length method in ANSYS, which controls the load level together with the length of the displacement increment. This method permits to compute the post-critical load-deflection path.

Moreover, the post-critical behaviour could be studied in case a further advantage of dynamic analysis is considered. In such case, in the vicinity of a critical point, the inertia forces would stabilize the system motion in the post-critical range, where the load, which the system can carry, decreases with increasing deflection. Hence, the post-critical behaviour after reaching the limit load is usually highly dynamic. This is closer to reality than any static post-critical equilibrium path, because failure process usually happens suddenly. However, the post-elastic descending curve is not modelled here, as the above methods need significant computational effort and it is beyond the scope of this research study.

6.4.9 Concrete crack patterns and failure mode

Thirty-nine numerical tests are presented simulating the particular USFB configuration using different constitutive relationships and parameters. It can be seen that in all cases the flexural and the diagonal cracks are generated. Characteristic results of concrete cracks, slippage profiles and steel stresses at the contact surface between the steel and the concrete are plotted. By examining the stress distribution, it is revealed that failure occurred due to heavy steel yielding, combined with concrete crushing.

In **Figure 6.23** the crack development is shown at four ideal load steps. Numerous cracks occurred at the mid-span, whereas there are no compressive cracks underneath the loading area. It is now clear that the flexural and shear crack development is of paramount importance for the load carrying capacity and the failure mode of the USFBs.

Nonlinear numerical solutions are capable of replicating the full range cracks including the pure flexural, flexural shear and the critical shear crack. Smeared cracks are spread over the high shear stress region and occur mostly at the ends of the beam between the support and loading area. The path of shear cracks follows the trajectory of the principal stresses and can also be seen in the experimental study. Depending on the geometric as well as the material properties of the USFB, the critical crack might extend to the top of the compression concrete fibres and then stabilize, as it is shown in **Figure 6.23(d)**. At the ultimate load carrying capacity the vertical beam deflections are not very large.

Analytically, diagonal shear failure begins with the development of a few vertical flexural cracks at the mid-span, followed by a destruction of the bond between the bottom steel flange and the concrete. A critical shear diagonal crack develops in the vicinity of the web openings of the steel perforated beam. Very small flexural cracks appear from the beginning of the test, while shear diagonal cracks are not developed up to the load level of approximately 400kN. Similar behaviour is observed at around 250 to 300kN, when the experimental tests are conducted. By looking the inside view of the FE model, it is found that the cracks begin at the mid-width of the beam section, where the concrete passes through the web openings, and more specific cracks are initiated as the steel web tends to deflect **(Figure 6.24)**. These cracks are fully developed in the vicinity of the web openings at approximately 450kN, while cracks move outwards (i.e. transverse to the web). In more detail, the positions of the first cracks are generated where the stress concentration areas in the perforated section (i.e. plastic hinges) are formed. The propagation of such cracks and the high stress in the steel are shown for four ideal load steps in **Figure 6.24**.

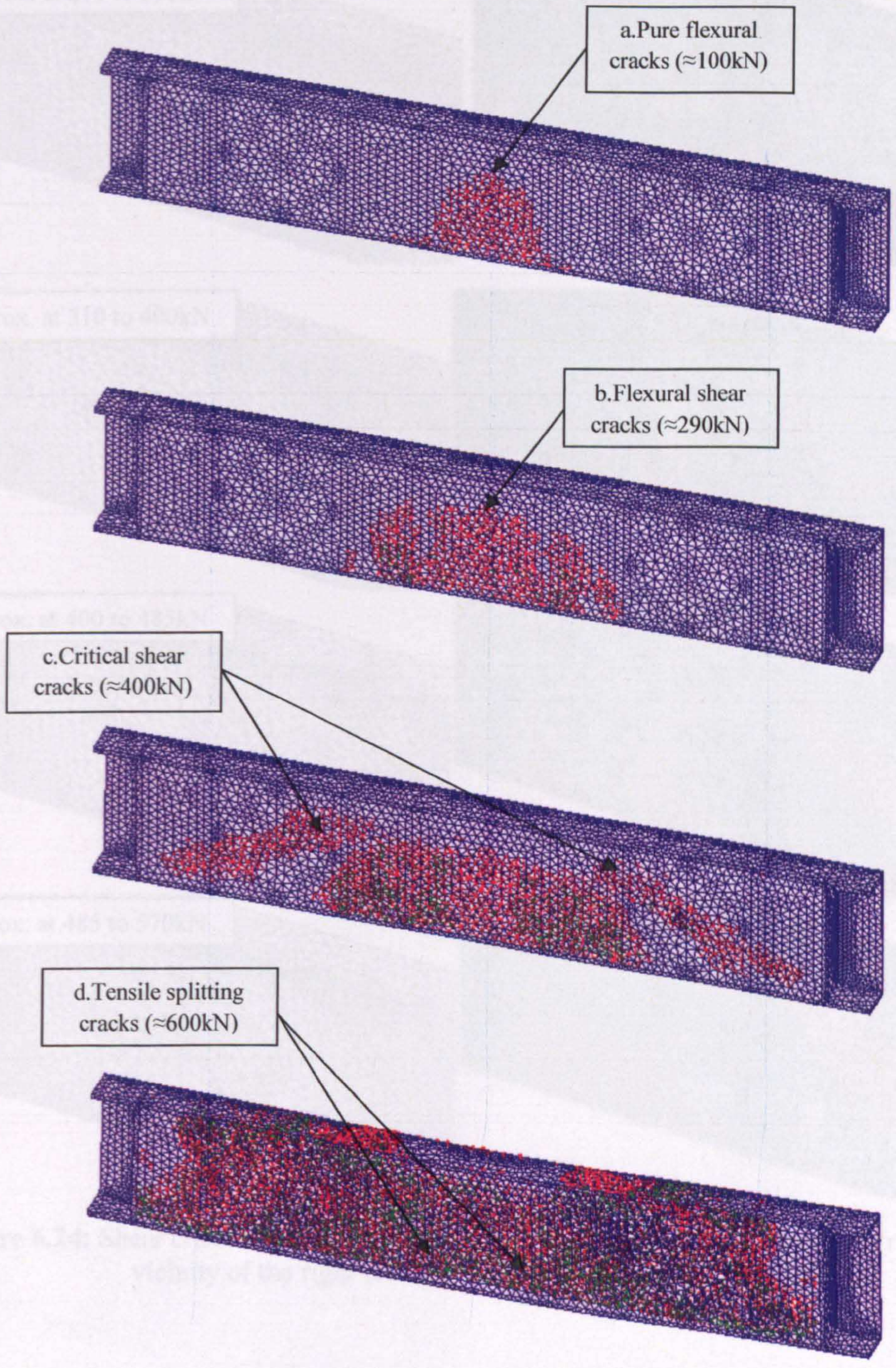

Figure 6.23: Bending and shear crack development at the front side of the beam; (a) Purely flexural (bending) vertical cracks, no yielding in steel, no concrete plasticity (b) Developed flexural cracks, developed flexural/shear cracks, just before initiation of the critical shear cracks (c) Critical shear diagonal cracks are clearly identified and (d) Full cracking state, yielding in steel, concrete plasticity, big displacements increment just before divergence of the FE model, there are splitting cracks at the upper part of the beam due to compression

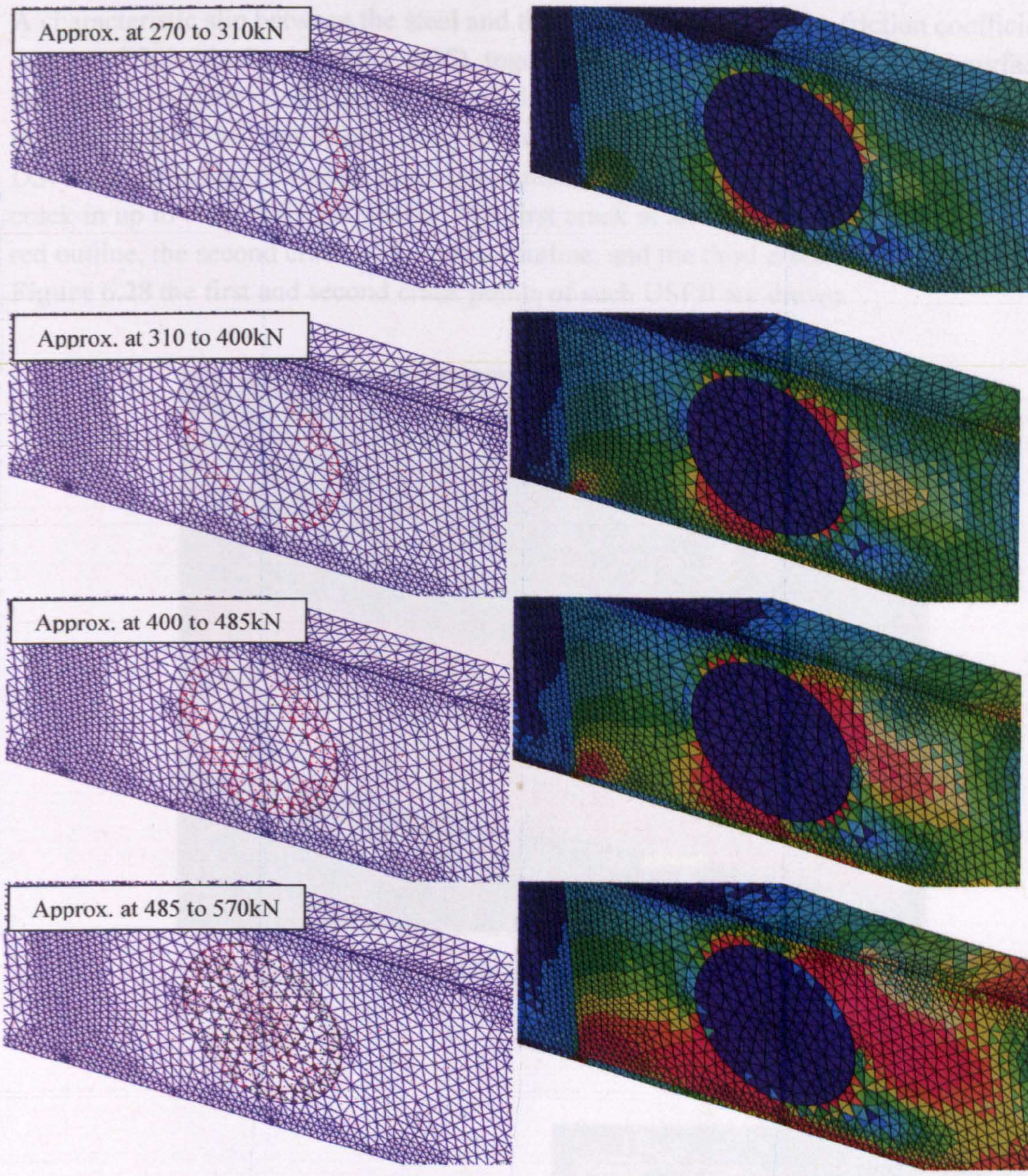

Figure 6.24: Shear crack development (left) and Von-Mises stresses of the steel (right); in the vicinity of the right web opening and mid-width of the USFB

With regards to the extent of the concrete cracks in such composite beams, a close study of the FE results is carried out. The major parameter that determines the number of cracks is the yield strength of the steel. Higher steel grade results in greater loads and so the concrete is fully cracked following the steel deformation. The friction coefficients slightly affect the cracking of the FE models, as the concrete is partially confined and the concrete movement is relatively small. However, the shear transfer coefficients, and especially the open shear crack transfer, could dramatically affect the cracking model.

A characteristic slip between the steel and the concrete, when using a friction coefficient, μ, equal to 0.9, is obtained (**Figure 6.25**), together with the stresses in the contact surface and the contact surface condition for the particular USFB FE model after loading the beam (**Figure 6.26**). The Von-Mises steel stresses are also presented in **Figure 6.27**, while a USFB model is highly loaded. Each integration point of a concrete element (SOLID65) can crack in up to three different planes. The first crack at an integration point is shown with a red outline, the second crack with a green outline, and the third crack with a blue outline. In **Figure 6.28** the first and second crack points of such USFB are drawn.

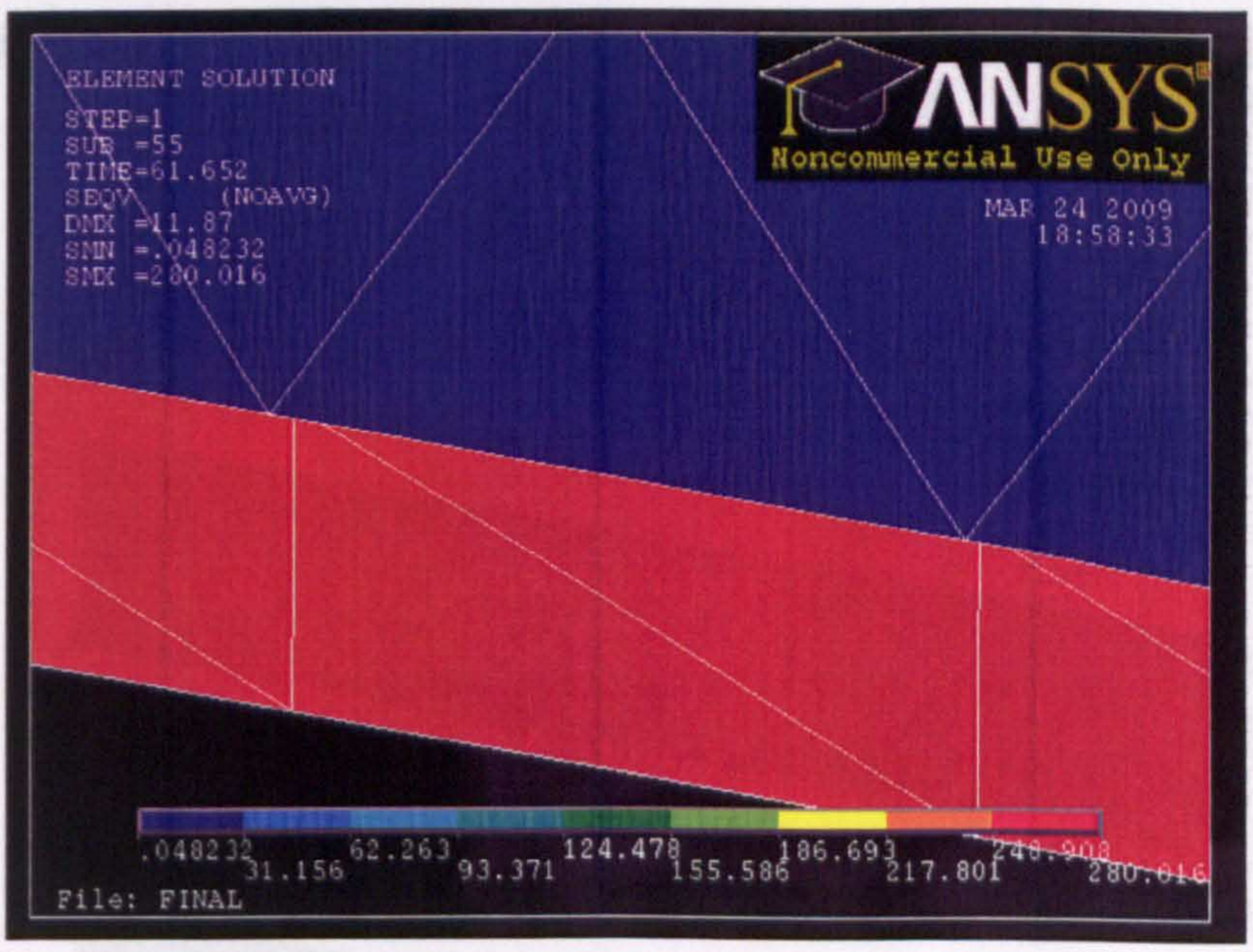

Figure 6.25: Element slip between the steel and the concrete

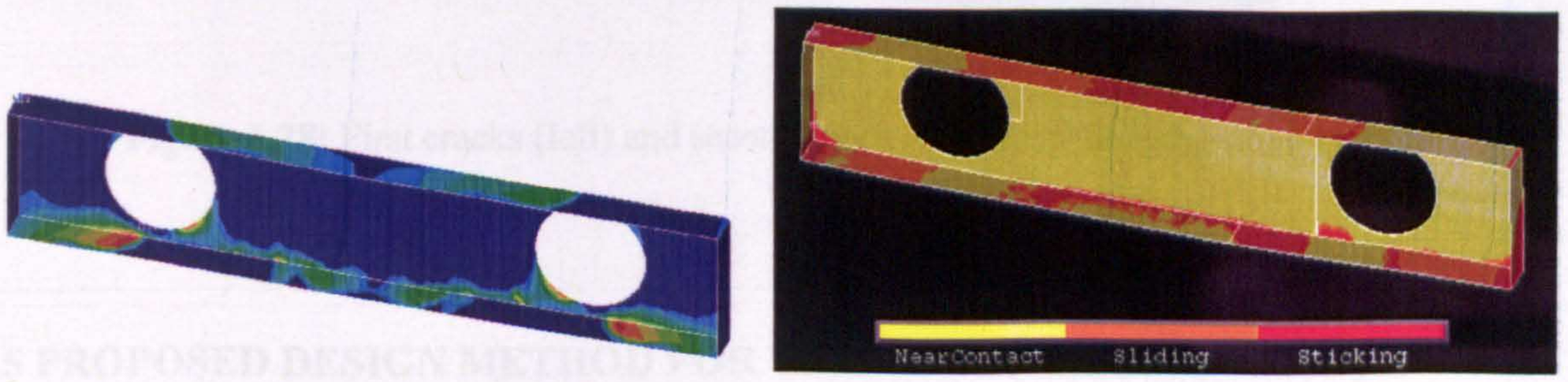

Figure 6.26: Contact stresses (left) and contact surface condition (right) of the USFB

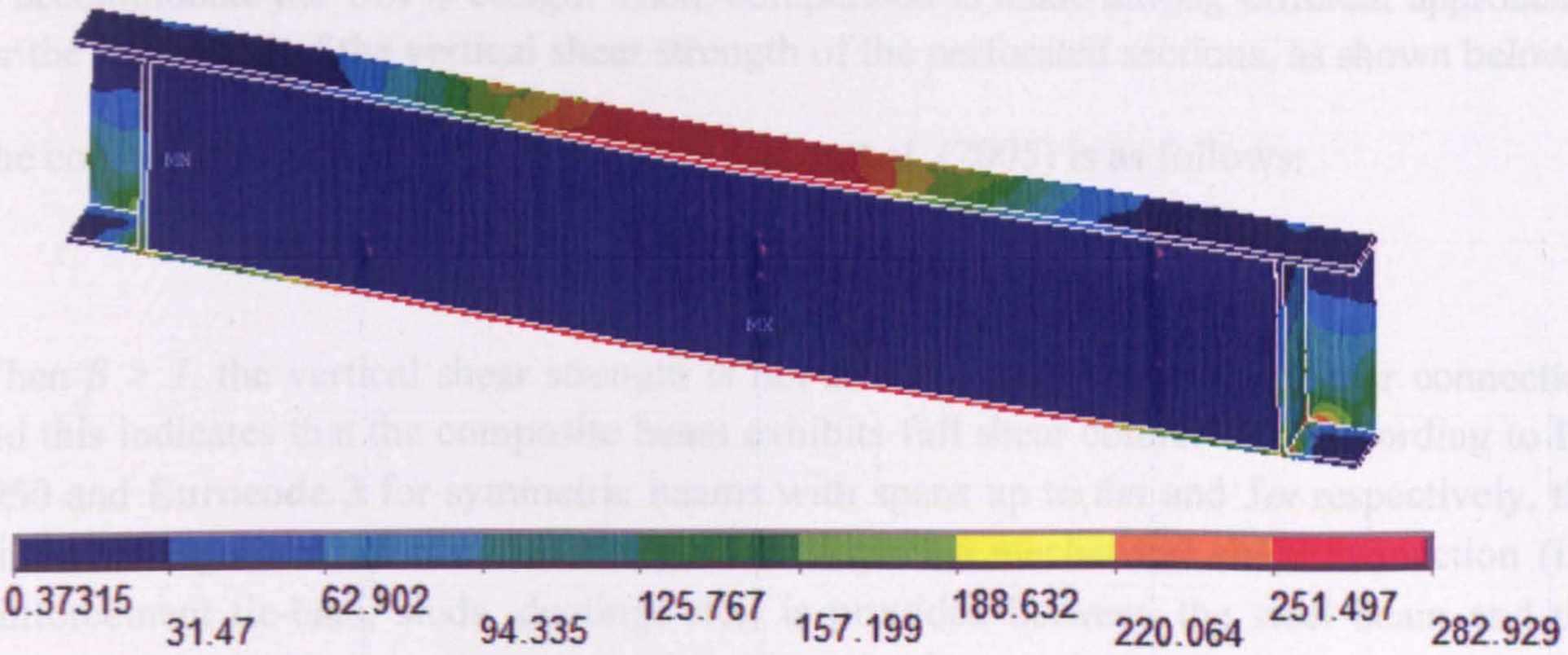

Figure 6.27: Von-Mises stresses in the steel

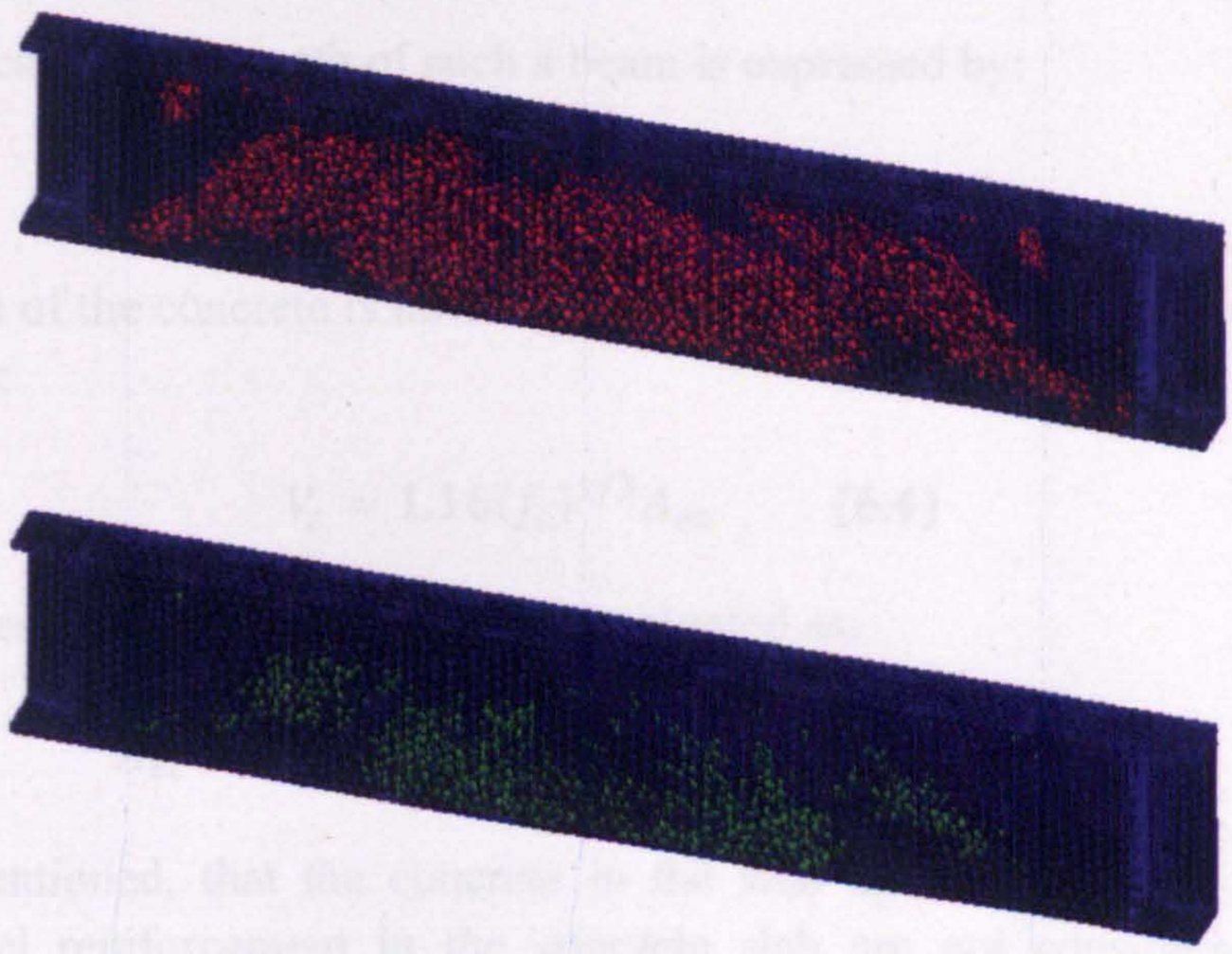

Figure 6.28: First cracks (left) and second cracks (right) at the integration points

6.5 PROPOSED DESIGN METHOD FOR VERTICAL SHEAR STRENGTH

Experiments and non-linear FE analyses show that the concrete in-fill in the perforated sections and the composite action enhance the vertical shear strength of the USFB. Liang et al. (2005) proposed a design method for the vertical shear strength of simply supported un-perforated composite beams (where the concrete slab sits on top of the plain steel beam) with any degree of shear connection. This method is presented herein and adjusted in order

to accommodate the USFB design. Then, comparison is made among different approaches for the evaluation of the vertical shear strength of the perforated sections, as shown below.

The composite action as it is presented by Liang et al. (2005) is as follows:

$$V_{uo} = V_o\left(1 + 1.295\sqrt{\beta}\right) \ (0 \le \beta \le 1) \qquad (6.2)$$

When $\beta > 1$, the vertical shear strength is not affected by the degree of shear connection and this indicates that the composite beam exhibits full shear connection. According to **BS 5950** and **Eurocode 3** for symmetric beams with spans up to *6m* and *5m* respectively, the minimum degree of shear connection is 0.4. When no mechanical shear connection (i.e. reinforcement tie-bars, studs, ducting, etc.) is provided between the steel beam and the concrete slab, the two components work independently to resist vertical shear. However in this particular FE study, the degree of shear connection is assumed equal to the friction coefficient between the steel and the concrete, simulating the frictional force and shear-bond, since no mechanical shear connection is provided.

Hence, the vertical shear strength of such a beam is expressed by:

$$V_o = V_c + V_S \qquad (6.3)$$

The contribution of the concrete is now taken as the shear strength of the concrete infill and it is proposed as:

$$V_c = 1.16(f_c)^{1/3} A_{ec} \qquad (6.4)$$

The effective shear area of concrete and it is evaluated as:

$$A_{ec} = (b_f - t_w)(h - 2t_f) - 0.86\mathrm{r}^2 \qquad (6.5)$$

It should be mentioned, that the concrete in the web opening, as well as the effect of longitudinal steel reinforcement in the concrete slab are not considered in the above equation.

The shear capacity of the steel beam is evaluated with various approaches so as to better correlate the theoretical approach with FE analyses and experiments.

1. The basic shear capacity from **Chapter 3** (Chung et al., 2002) is as follows:

$$V_S = V_{o,Rd} = \frac{0.577 f_y}{\gamma_{Mo}}\left[\left(ht_w + 2\left(0.75{t_f}^2\right)\right) - d_o t_w\right] \qquad (6.6)$$

2. Another approach for the shear resistance for perforated beams (Lawson and Hicks, 2006) is shown below:

$$V_{o,pl,Rd} = \left[V_{pl,Rd} - \frac{d_o t_w f_{yd}}{\sqrt{3}}\right] \qquad (6.7)$$

Where the shear resistance, $V_{pl,Rd}$, for un-perforated beams (**EC3: EN1993-1-5**) is limited by either the plastic shear resistance:

$$V_{pl,Rd} = \frac{A_v\left(\frac{f_y}{\sqrt{3}}\right)}{\gamma_{Mo}} \qquad (6.8(a))$$

or the shear buckling resistance:

$$V_{b,Rd} = \frac{\eta f_{yw} h_w t_w}{\gamma_{M1}\sqrt{3}} \qquad (6.8(b))$$

Where A_v is taken as $A_v = A - 2b_f t_f + (t_w + r)t_f < \eta h_w t_w$, according to **EN 1993-1-5** and the value of γ_{Mo} is equal to 1 and γ_{M1} is equal to 1.1, as well as the value of η is taken as 1.2. It should be noted that, the shear buckling resistance for un-perforated beams with un-stiffened web is considered only if: $h_w/t_w \geq 52\,\varepsilon/\eta$.

3. Moreover, when shear buckling governs the resistance of an un-perforated web, the approach below should be followed for the shear buckling of a perforated beam (Lawson and Hicks, 2006):

$$V_{bw,Rd} = 0.9V_{b,Rd}\left(1 - \frac{\sqrt{d_o l_o}}{h_w}\right) \qquad (6.9)$$

Where l_o is equal to d_o for circular web openings.

4. Lastly, the simple approach for shear capacity of un-perforated steel sections is given by **BS5950 Part 1:2000** and it is modified as below for perforated sections:

$$P_v = 0.6 f_y A_v = 0.6 f_y (h t_w - d_o t_w) \qquad (6.10)$$

In such cases, when $h/t_w \leq 70\varepsilon = 70\sqrt{275/f_y}$ the shear buckling does not need to be checked.

Substituting the material properties from **Table 6.3** in the above theoretical formulas, comparison is carried out between the FE predictions and the theoretical approaches. **Table 6.4** summarizes all the theoretical evaluations as well as the FE prediction over the theoretical evaluation ratios. Comparing the FE results with the results obtained from the theoretical formulas given above, it is found that:

- The basic shear capacity approach given by Chung et al. (2003) for steel perforated beams is the closest approach to the FE analyses, with an average deviation ratio of 0.93.
- The shear resistance approaches given by Lawson and Hicks (2006) and **Formula 6.8(a)**, **6.8(b)** and **6.9**, slightly underestimate the results compared to FE analyses, with average deviation ratios of 0.90, 0.86 and 0.76, respectively. Among the three different approaches, the best approach is always provided when the shear resistance is limited by the plastic shear resistance for the un-perforated section and **Formula 6.8(a) (EN1993-1-5)**. In case of shear buckling resistance, the theoretical approaches are underestimated compared to the FE results.
- Finally, the modified shear capacity approach given by **BS5950 Part 1:2000** for perforated steel sections underestimates the vertical shear strength of the USFBs compared to the FE analyses, with an average deviation ratio of 0.85 and provides some conservatism.

In more detail, the following conclusions can be drawn:

- The smaller the degree of shear connection, β, used in the FE models, the greater the deviation ratio is.
- When steel grade S275 is examined, the FE results are closer to the theoretical ones. In contrast, when steel grade S355 is used, overestimated FE results are obtained because of the increased stiffness of the FE model.

Run Code No.	F_{FEA} *(kN)*	Form. (6.6) F_{theor}/F_{FE}	Form. (6.8(a)) F_{theor}/F_{FE}	Form. (6.8(b)) F_{theor}/F_{FE}	Form. (6.9) F_{theor}/F_{FE}	Form. (6.10) F_{theor}/F_{FE}
59	**617**	0.91	0.88	0.84	0.75	0.83
3	**627**	0.90	0.87	0.83	0.74	0.82
7	**611**	0.87	0.84	0.80	0.71	0.79
8	**548**	0.76	0.74	0.71	0.63	0.70
58	**547**	1.03	0.99	0.95	0.85	0.94
16	**555**	1.01	0.98	0.94	0.84	0.93
18	**607**	0.93	0.89	0.86	0.76	0.85
19	**635**	0.89	0.86	0.82	0.73	0.81
20	**648**	0.87	0.84	0.80	0.72	0.79
25	**618**	0.87	0.84	0.80	0.71	0.79
11	**617**	1.03	0.98	0.93	0.81	0.92
12	**590**	1.07	1.03	0.97	0.85	0.96
13	**470**	0.59	0.56	0.53	0.46	0.53
B5	**577**	0.91	0.87	0.83	0.73	0.82
B6	**563**	0.83	0.80	0.77	0.67	0.76
B2	**730**	0.80	0.76	0.72	0.62	0.71
B4	**733**	0.80	0.76	0.72	0.62	0.71
B3	**734**	0.80	0.76	0.72	0.62	0.71
B11	**591**	0.92	0.88	0.84	0.75	0.84
B10	**584**	0.91	0.87	0.83	0.73	0.82
B12	**578**	0.85	0.82	0.78	0.69	0.78
C8	**508**	0.85	0.82	0.78	0.69	0.77
B13	**583**	0.93	0.90	0.86	0.76	0.85
D1	**630**	0.92	0.88	0.84	0.73	0.82
C1	**588**	0.97	0.93	0.89	0.80	0.89
C4	**611**	0.94	0.91	0.87	0.78	0.86
C14	**574**	0.83	0.80	0.76	0.67	0.75
C6	**622**	0.94	0.91	0.86	0.77	0.86
C5	**641**	0.91	0.88	0.84	0.75	0.83
B1	**742**	0.86	0.82	0.78	0.68	0.77
B9	**545**	0.97	0.93	0.89	0.79	0.88
C12	**621**	0.93	0.90	0.86	0.77	0.85
C13	**597**	0.80	0.76	0.73	0.64	0.72
C11	**571**	0.87	0.83	0.79	0.70	0.78
31	**629**	0.93	0.90	0.86	0.77	0.85
32	**615**	0.90	0.86	0.85	0.74	0.82
33	**565**	0.87	0.84	0.80	0.72	0.79
B14	**610**	0.94	0.91	0.87	0.78	0.86
B15	**243**	2.37	2.29	2.19	1.96	2.17

Table 6.4: Comparison between the FE predictions and the theoretical approaches

6.6 SERVICEABILITY LIMIT STATE (SLS) CHECK

This research programme is an investigation on the failure modes of USFBs, hence only the ultimate limit state (ULS) is under consideration. However, from experimental and FE study, it is found that the contribution of the concrete restrains the steel beams from high deflections. Although large web openings are positioned in the high shear regions, to eliminate the amount of steel and improve the manufacturing procedure of the perforated beam when profile cutting method is adopted, the deflections are negligible compared to the bare steel perforated beam.

6.7 CONCLUSIONS

The results of the FE analyses generally show good agreement with observations and data from the experimental tests of this simple structural form of USFBs. This gives confidence in the use of ANSYS and the developed FE model. A parametric FE study is also conducted to investigate the sensitivity of various factors. These FE models can now be used in further studies to develop design rules for USFBs.

Based on the experimental study presented in this chapter, the following conclusions are drawn:

- All four experimentally studied USFBs show similar behaviour in terms of the failure mode, stiffness and ultimate load carrying capacity.
- The failure mode of the non-composite beam changes when there is concrete in-fill between the flanges. Following the formation of the large crack, there is some residual strength in the concrete preventing local buckling and the load carrying capacity is somewhat higher than that on the non-composite beam.
- For composite beams of the particular configuration, partially concrete encased between the flanges and the bearing plates at the supports, there is a significant and gradual drop in the load-deflection curves but the post-failure loads are above those of the plain steel beam.
- The shear resistance of this USFB, which is composed of perforated steel beam with large web openings and without any mechanical shear connectors, consists of contributions from the concrete in compression and aggregate interlock.
- The ultimate load carrying capacity of the composite beams is dependent on the concrete strength, but appears to be relatively independent of the concrete quality. For the weaker concrete, micro-cracks only occur at an earlier stage of loading.
- Due to the concrete in-fill, the ultimate vertical load carrying capacity of the USFBs is almost doubled, compared to the corresponding non-composite perforated steel beam when under the same load and beam arrangement. This percentage is even higher when

the friction coefficient is closer to 1.0 (i.e. fully bonded). Oppositely, this percentage will be lower when no bearing plates at the supports are used.

- Strut action of the concrete encasement across the web openings reduces the Vierendeel bending effects and improves the vertical shear transfer through the partial concrete encasement.
- The shear force resisted by the concrete at a web opening is dependent on the steel beam dimensions and particularly on the flange dimensions, which contributes to the bending, as well as to the shear resistances. The horizontal component of the strut action is dependent on the frictional force, shear-bond resistance and the bearing strength of the web opening area. The compression resistance of the concrete strut action is mainly dependent on the thickness of the flanges.
- The last descending post-elastic branch of the load-deflection curve corresponds to the composite beam behaviour as a 'mechanism'. Failure is accompanied with the appearance of wide intensive diagonal concrete crushing.

Based on the FE study presented in this chapter, the following conclusions are drawn:

- The particular structural forms of USFBs behave as fully bonded composite elements and this correlates well with the experiments.
- The FE results agree with the experiments in that in composite beams the concrete fails first before any significant distortion of steel web occurs.
- All cracks in the FE analysis seem to develop at a higher load compared to that observed in the experiments. This was probably due to micro-cracks in the experimental specimens.
- Whilst the concrete compressive strength affects the strength of such USFBs, the ultimate load carrying capacity is dominated by the steel strength.
- Moreover, the steel strength mainly affects the concrete crack pattern obtained from ANSYS. The friction coefficient and the shear retention factors can also change the concrete crack pattern in many cases.
- Various researchers have published different constitutive relationships that model the concrete material properties. From the sensitivity study of these constitutive relationships, it is found that they affect the load carrying capacity of USFBs differently.
- As the composite beams contain no confined reinforcement, the concrete tensile strength also played a major role in defining divergence load.
- It is difficult to satisfactorily reproduce the post-elastic curvature of the beams because of the sudden loss of stiffness of the cracking model, especially when the smeared approach is used without steel reinforcement. The maximum load is only interested, while to model the post-elastic behaviour is beyond the scope of this research programme.

- FE results compare well with the design method presented by Liang et al. (2005). The method is modified by different theoretical approaches for the shear resistance of the perforated sections, while the vertical shear strength of simply supported USFBs with any degree of shear connection between the steel and the concrete is also assessed.

6.8 RECOMMENDATIONS AND LIMITATIONS

Although the capacity of the perforated beam is reduced by using large web openings (d_o=*0.76h*), the designer can take advantage of the inherent double shear strength provided by the trapped concrete between the flanges and the bearing plates at the supports. Then, increased flexural strength of the beams, as well as longitudinal shear strength due to the concrete pass through the web openings is provided. Further increased longitudinal shear strength will be obtained in the case mechanical shear connectors are also used. Lower structural depth, inversely to the conventional composite beams, where the concrete slab sits on top of the plain (or perforated) steel beams, is achieved. In addition to that, this new form consists of ultra shallow and usually stocky perforated beams, concluding to lighter construction. Consequently, the decrease of the structural depth for every floor, and the ease of construction for large spans, as long as propping is not necessary for casting the concrete on top of the steel deck which sits on the bottom steel flange, makes the use of USFBs a procedure worth a close study.

USFB floor system is demonstrated in **Figure 2.10**. The steel deck (U- or V-shaped) sits on the wider bottom flange providing clear space for service integration which passes through some of the web openings of the steel beam. There are also web openings which are in-filled by concrete providing the structural enhancement. Various failures modes are incorporated developing a complex failure mode with various parameters and hence there is need for further study. Such overall study of the floor system is not included in this research thesis and it is beyond of the scopes, which are mainly concentrated on the steel point of view and its behaviour when USFBs are used. The above results are applied to another detailed comprehensive study of the global analysis on the overall composite USFB system, isolating the steel and concrete movement under bending and providing information for the percentage of shear enhancement of the steel perforated sections when plain concrete is only used.

The limitations of the present study are that the UB I-section, the web opening shape and size, the loading and the support conditions are kept constant. Consequently, further rigorous research is needed in order to propose reliable formulas, which will accurately model a wide range of typical USFBs. A parametric FE study based on the geometric configuration of the USFBs is equally needed and can be easily used for further advanced research.

CHAPTER 7

CONCLUSIONS
DESIGN GUIDANCE
FUTURE WORK

7.1 INTRODUCTION

The common methods of incorporating services within the structural depth of composite beams and manufacturing long span and light-weight steel beams include: cutting out circular, hexagonal or rectangular openings in the webs of rolled or fabricated beams, or manufacturing cellular or castellated beams with regular circular or hexagonal web openings respectively. The transfer of shear was the dominant effect which gave rise to Vierendeel bending moments that were resisted by local bending of the tee-sections in the vicinity of the web openings. In composite Ultra Shallow Floor Beams, where the concrete was confined by the steel section and passes through the web openings, the local and global bending resistances changed. This applied to the use of larger web openings compared to the traditional flooring systems.

The main objective of this research was to study the failure modes of perforated beams with novel non-standard web openings with particular emphasis on Vierendeel bending and web-post buckling. A theoretical method evaluating formation of plastic mechanisms (hinges) and a theoretical method estimating strut analogy in the web-post were compared with the finite element results.

Finite element models were implemented to accurately simulate and understand the failure modes. Since Vierendeel and especially web buckling usually involved inelastic action the effect of plasticity was considered in conjunction with plastic FEM results, to modify the theoretical models. FE models always correlated with the results of the physical tests either reported in the literature or conducted in the research programme. Approximately 1,600 models were examined in the research programme for a wide range of perforated beam geometries.

The following conclusions on the behaviour of perforated beams are based on several theoretical FE models used, incorporating plastic analyses, and their comparisons with physical test results.

7.2 CONCLUSIONS AND DISCUSSION

This chapter deals with the work carried out in this dissertation against the objectives stated in **Chapter 1**. For convenience each sub-objective is stated prefacing the corresponding conclusions.

Sub-objective: To overview the manufacturing procedures for perforated steel beams with standard and non-standard web openings.
This objective has been successfully achieved. Information regarding the manufacturing procedure of perforated beams has been presented for standard web openings and developed for non-standard web openings. Three manufacturing methods for hot rolled I-sections with a series or isolated (i.e. single) web openings as well as fabricated sections have been obtained and presented.

Sub-objective: To review all the failure modes for perforated beams and study the most significant ones.
This objective has been successfully achieved. Information regarding all the possible failure modes of perforated beams have been obtained and presented. Extensive presentation of the failure modes together with the references initially reported has been made. Moreover, the theoretical background used to approach and analyze the most important failure modes, has been presented.

Sub-objective: To conduct a preliminary FE study of perforated beams with non-standard web opening shapes based on combinations of typical geometrical shapes and to describe their main characteristics.
This objective has been successfully achieved. A preliminary FE investigation has been carried out to present various non-standard web openings on long span perforated beams (20m). Different stresses and deflections were recorded visualizing the effect of the web opening shape to the structural behaviour of such beams. The novel web opening shapes thoroughly examined in this thesis were based on this preliminary study.

Sub-objective: To establish the shear-moment interaction curves based on a current design method and to compare these with the theoretical curves at the low moment side (LMS) and the high moment side (HMS) of a web opening.
This objective has been successfully achieved. The shear-moment interaction curves based on the current design method and the simplified method (i.e. $\varphi=25^o$) were examined and presented. It was found that the 'un-coupled' FEM curves lie between the theoretical LMS and HMS curves. While the 'coupled' FEM curves from this study lie below both LMS and HMS curves, due to the effect of Vierendeel mechanism which is incorporated into shear capacity. Hence, the results are more conservative.

Sub-objective: To investigate the Vierendeel mechanism of unreinforced perforated beams with various standard and non-standard web opening shapes and sizes by using non-linear FE analyses.

This objective has been successfully achieved. Six standard typical and elongated web opening shapes and five non-standard web opening configurations of elliptical shapes have been studied. The global shear capacities allowing for Vierendeel mechanism or the global 'coupled' shear capacities of perforated sections covered in the present study can be obtained directly from the shear-moment FEM interaction curves.

Non-dimensional FEM shear-moment interaction curves were plotted and discussion on the *V/M* ratios of perforated beams with different web opening shapes and sizes was made possible. The UB 457x152x52 sections was mainly used as it produces conservative results (the greater decrease of the 'coupled' shear ratio, $\bar{v}$) among the studied ones. FEM curves of similar trends were obtained for all the various beams with different weight per unit length. However, the shear capacities differ greatly (y-intercept), due to underestimation of the shear capacities of the perforated sections with thick flanges when compared with the FE model.

The flange contributes more to the shear capacity of perforated beams with large web openings. The maximum deviation of the shear capacity ratios is found between the conservative shear area assumption taken from **BS5950 Part 1** and the shear area assumption taken from **Formula 3.3**. On the other hand, shear capacities estimated by using the assumptions from **EC3** and **Formula 3.3**, especially for beams sections UB457x152x52 and UB610x229x101, yielded very close results. It was seen that both the t_f and t_w parameters are considered, although t_f is generally the domain one.

Sub-objective: To evaluate the influence of geometric parameters and investigate the contribution of the web opening shape and particularly the opening length of the top tee-section to the shear capacity of perforated beams.

This objective has been successfully achieved. FEM curves of typical pattern were found for perforated beams with circular and hexagonal web openings. It was concluded that apart from the opening length, *c*, the web opening shape and rotation also controls the performance of a perforated beam due to the movement of the stress concentration points. Regarding the perforated beams with elongated web openings and d_o equal to *0.8h*, considerably reduced moment ratios have been presented when the web openings were located at a high moment region.

Sub-objective: To present the yield patterns of the perforated beams with various web opening shapes and sizes and investigate the location and movement of the plastic hinges as well as the main characteristics of such beams.

This objective has been successfully achieved. The yield patterns at 'failure' (i.e. convergence) point of the perforated beams with different web opening configurations

located at various positions have been analytically plotted. The plastic hinges (i.e. Von-Mises stress concentration points) at the top and bottom tee-sections, stresses in the steel flanges as well as an idea of the beams' local deflections have been obtained. The positions of these plastic hinges were affected by the magnitude of the global shear force and bending moment. It was observed that when web openings with large critical length, *c*, under high *V/M* ratios were considered, the failure came along with the local buckling of the top flange as a result of high axial load in the tee-section. Therefore, both shear and flexural failures of the perforated sections were mainly controlled by the depth of the web openings. The Vierendeel mechanism of the perforated sections was mainly controlled by the opening length, *c*.

It has been verified that φ was increased at perforated sections with web openings close to the supports. However, the shape of the web opening significantly affected the position of the plastic hinges. Moreover, the sequence of the formation of the plastic hinges was not the standard one when the web openings were located very close to the supports.

Sub-objective: To develop a simple design method with generalized shear-moment interaction curves for practical design of steel perforated beams with various standard and non-standard web opening shapes and sizes.

This objective has been successfully achieved. A generalized shear-moment interaction curve has also been presented, based on a design model presented by Chung et al. (2003). The trend of the curves was changed from case to case in order to avoid significant underestimation of the results. It is worth noting that, a conservative design possesses for large non-standard elliptical and elongated web openings.

Sub-objective: To further conduct a parametric FE investigation on perforated beams with large isolated novel non-standard web openings subjected under high shear forces and bending moments.

This objective has been successfully achieved. A parametric FE study of perforated beams with novel non-standard web openings has been conducted and presented. The deflections and Von-Mises stresses against the web opening areas at three 'characteristic' load level points have been extensively plotted for such perforated beams. It was concluded that all perforated beams with novel elliptical web openings, although they have web opening depths of $0.8h$, their stiffness was dramatically increased and their load carrying capacity was even higher than the perforated beams with circular web openings with smaller diameters ($d_o=0.76h$).

Sub-objective: To evaluate the influence of geometric parameters and investigate the contribution of such novel web opening shapes to the structural behaviour of perforated steel beams.

This objective has been successfully achieved. It was concluded that, stresses were affected by both THETA and R of the new elliptical web opening shapes. While deflections were

only affected by the R which is the main factor that determines the web opening area as well as the critical opening length, *c*, at the top and bottom tee-sections. Furthermore, perforated beams with filleted circular web openings of radius, *r*, 15 to 35mm should be utilised as they provide moderate effects. Moreover, from a local FE study of perforated beams with filleted web openings at the sharp-tip points, the critical distance of 15mm was determined by the stress concentration criterion where the strength of the beam, was significantly decreased.

Sub-objective: To investigate the web-post buckling behaviour of unreinforced perforated beams with standard and novel non-standard closely spaced web opening shapes by conducting experimental tests.

This objective has been successfully achieved. Seven short span perforated beams with circular and novel closely spaced web openings have been experimentally tested and presented. Extensive yielding occurred at the web-post of all specimens. Web-post buckling occurred at a load slightly in excess of that at which gross deformations were initially observed. Finally, testing was stopped when either no extra load was able to be withstood or it was considered dangerous as the beam was dramatically distorted. Moreover, it was demonstrated that a similar behaviour dominated for perforated beams with the specific novel web opening shapes.

Sub-objective: To carry out a parametric FE investigation on perforated beams with closely spaced web openings, simulating the experimental structural behaviour, for validation purposes.

This objective has been successfully achieved. A parametric FE study of all seven short span perforated beams with circular and novel closely spaced web openings has been carried out and presented. It was found that all specimens failed in a combination of local buckling and web-post buckling; while the web movement profile was related to the web opening shape. Finally, it was possible to determine the interaction between the two buckling modes and hence to differentiate the area which possessed the failure of the beam (this was mainly shown from stress contour plots). Comparing the experimental with the FE load-deflection curves at the mid-span, it was observed that the FE models provided significant increased stiffness in the elastic region. Particularly, perforated beams with narrow web-posts and sharp-tip points such as the Specimen A-2, A-3 and B-2, were unable to redistribute the stresses and so high stresses were concentrated at these points. Also, the out-of-plane web movement at the yield load level point was negligible in FE analyses in relation to the experimental results. The finite element results provided good prediction of the strength of the beams influenced by web instability, with an overall test-to-predicted ratio of 0.905 and COV of 11.1%. There was some bias in the FEM results, leading to overestimates of strength for very narrow or very wide web-posts, as well as when inclined elliptical web openings were considered.

Sub-objective: To also conduct a parametric local FE investigation on the structural behaviour of the web-posts within two closely and regularly spaced novel web openings.
This objective has been successfully achieved. A parametric local FE study has been carried out for a range of parameters, including the web slenderness on a number of beam sections with various web opening shapes. A parametric study was conducted to investigate the effect of the S/d_o ratio on the resistance of the web-post. Eight S/d_o ratios in the range of 1.1 to 1.8 were studied with five web thicknesses of 3.9mm, 5.0mm, 6.0mm, 7.6mm and 10.5mm. This gave d_o/t_w ratios which varied from 30 to 80.8. The model was extended to examine all web opening shapes of depth d_o, equal to $0.7h$, which were experimentally investigated previously in the web-post study. A new design model for this complex failure mode has been derived for perforated beams with these novel web opening shapes. The latter design model has been developed based on a strut analogy as obtained from FE analyses. The stability of the web was also checked using buckling curves to **BS 5950-1**. The outcome was presented in terms of the effective width of the web opening, and the effective width, b_e, and length, l_e, of the strut, which have been derived from this FE study to give the best fit over the range of web opening parameters.

Sub-objective: To demonstrate the enhancement of the vertical shear capacity of non-composite beams due to the concrete in-fill. To experimentally test an Ultra Shallow Floor Beam (USFB).
This objective has been successfully achieved. An experimental work has been conducted on Ultra Shallow Floor Beams. Also the percentage of the vertical shear capacity enhancement of the perforated beams due to the concrete in-fill has been presented. The test results demonstrated that the concrete significantly contributed to the shear strength of USFBs at the web openings. It was shown that the concrete failed first before any significant distortion of the steel web. Therefore, whilst the concrete compressive strength affected the strength of the USFBs, the ultimate load carrying capacity was dominated by the steel strength. By testing a USFB with lower concrete grade it was found that the ultimate load carrying capacity of the partially encased composite beams was dependent upon its strength but appeared to be relatively independent of the concrete quality. Moreover, it was observed that strut action of the concrete encasement across the web openings reduced the Vierendeel bending effects and improved the vertical shear transfer through the concrete encasement. It was concluded that the shear force resisted by the concrete at a web opening was dependent on the steel beam dimensions and particularly on the flange dimensions, which contributed to the bending as well as the shear resistances. The horizontal component of the strut action was dependent on the frictional force, shear-bond resistance and the bearing strength of the web opening area. The compression resistance of the concrete strut action was mainly dependent on the thickness of the flanges.

Sub-objective: To establish a sensitivity FE study of the USFB model, investigating the effects of the material model parameters. To further examine various constitutive relationships modelling the concrete materials and to compare the results.

This objective has been successfully achieved. A three-dimensional FE model has been developed, in which contact elements were implemented at the interface of the concrete and steel. Various material model parameters were varied such as the steel and concrete strength, the constitutive relationships model, the materials as well as the steel and concrete contact strength. From the sensitivity study of these constitutive relationships it was found that they affected the load carrying capacities of USFBs differently. It was presented that USFBs behave as fully bonded composite elements and this correlated well with the experiments. Whilst the concrete compressive strength affected the strength of the USFBs, the ultimate load carrying capacity was dominated by the steel strength. Moreover, the steel strength mainly affected the concrete crack pattern obtained from ANSYS. The friction coefficient, μ, and the shear retention factors, $\beta_{1,2}$, can also change the concrete crack pattern in many cases. Finally, as the USFBs contained no confined reinforcement, the concrete tensile strength played a major role in defining the divergence load.

Sub-objective: To compare various theoretical approaches based on a modified design method with the FE results and propose a theoretical approach which closely predicts the real behaviour of the USFB.

This objective has been successfully achieved. This FE model could be used in additional studies to develop design rules regarding the vertical shear capacity of the composite USFBs. It was demonstrated that the FE results compared well with the modified design method for typical composite beams that was initially published by Liang et al. (2005). This method was modified by different theoretical approaches for the shear resistance of the perforated sections, to assess the vertical shear strength of simply supported USFBs with any degree of shear connection between the steel and the concrete. It has been presented that the basic shear capacity approach given by Chung et al. (2003) for steel perforated beams was the closest approach to the FE analyses, with an average deviation ratio of 0.93.

7.3 DESIGN STANDARDS USED IN THE THESIS

The necessary codes of practice were considered at all times throughout the thesis, depending on the provisions for conservative design. SCI publication P-355 (2006) refers to codified rules in the Structural Eurocodes such as: **EN 1993-1-1, EN 1994-1-1: 2004** and in the British Standards such as: **BS 5950 Parts 1** and **3**. In relation to the design guidance, it was shown that the differences between the **Eurocodes** and **BS 5950** had little effect.

7.4 REQUIREMENTS OF EC3 ANNEX N: OPENINGS IN WEBS & DESIGN RECOMMENDATIONS

The following requirements of **EC3 Annex N** apply to non-composite cellular beams with multiple circular web openings, and to beams with rectangular or elongated web openings. The relevant clause numbers of **EC3 Annex N** are given. The synopsis of this study was made possible with directions provided by CELLBEAM.

7.4.1 Dimensions of web opening (Clause N 3.1)

- Maximum size of web openings $0.8h_w$
- Minimum depth of tee below flange $0.1h_w$
- Centre-to-centre spacing of the web openings $1.25d_o$ to $1.5d_o$

Where: h_w is the depth of the web

Thesis:

The above requirements were expressed in terms of beam depth rather than the web depth. The centre-to-centre spacing range was increased based on the results of a FE study. The thesis has the following limits:

- Maximum size of web openings $0.8h$
- Minimum depth of tee below flange $0.1h$
- Centre-to-centre spacing of the web openings $1.1d_o$ to $1.8d_o$
  (spacing limits varies for novel elliptical web openings as necessary)

7.4.2 Web classification at web opening (Clause N 1.7.2)

The classification of webs in perforated beams depends on the proportion of the web of the tee-sections and the length of the web opening, especially when the elongated web opening is considered. For long web openings, the limit reduces to the outstand depth of the web in which the limit for Class 2 webs is $11t_w\varepsilon$. The rules for classification of webs are defined below, and the controlling case is normally that of the tee-section. Deeper tee-sections outside limits may be treated as Class 3 by ignoring the ineffective depth of the tee-section outside the Class 3 depth limit. For composite beams, most of the webs are in tension and in this case, the webs may be treated as Class 2.

Webs in perforated beams may be classified in one of two ways:

- By the depth of the web of the top tee-section
- By the total depth of the section

The outstand of the web of the tee-section may be classified, depending on the ratio of the length of the web opening to the outstand depth d_t below the flange, as follows:

$$Class\ 2 \rightarrow\ d_t = \frac{10t_w\varepsilon}{\sqrt{1-\left(\frac{32t_w\varepsilon}{l_o}\right)^2}}\ if\ l_o > 32t_w\varepsilon,\ \ No\ limit\ on\ d_t\ if\ l_o < 32t_w\varepsilon$$

$$Class\ 3 \rightarrow\ d_t = \frac{14t_w\varepsilon}{\sqrt{1-\left(\frac{36t_w\varepsilon}{l_o}\right)^2}}\ if\ l_o > 36t_w\varepsilon,\ \ No\ limit\ on\ d_t\ if\ l_o < 36t_w\varepsilon$$

Webs that satisfy the lower limit of l_o (effective length of the web opening) are classified independently of d_t.

BS 5950 Part 1 considers width to thickness ratios of outstands and depth to thickness ratios of webs in order to classify sections for local buckling. However, for perforated beams, the flange outstands were unchanged, so failed into the same class as the parent steel section.

Thesis:

In this research, classification was not an issue. However, the web classification was based on two requirements:

- Depth of the solid section
- Proportion of the top tee-sections as they have been modified by the critical opening length, c, and presented in **Table 3.8**. (i.e. l_o was taken equal to opening length, c)

7.4.3 Shear resistance (Clause N 3.2.2)

The vertical shear resistance of the beams was checked at the vertical centre-line of each web opening subjected to high shear forces and at LMS. For pure shear checks, the shear was divided between the top and bottom tee-sections in proportion to their shear areas. Each tee-section is then independently checked for the applied shear apportioned to it. Also, according to **BS5950 Part 1:2000**, the shear area of an un-stiffened web outside is not reduced to account for the non-uniform distribution of elastic shear stress. Unlike to **BS5950 Part 1:1990**, where a 10% reduction in shear area was required for tee-sections.

The shear resistance of the tee-sections is determined from **EC3 clause 5.4.6**. For rolled sections, the shear area is conservatively taken as d_T/t_w. However, a more accurate formula is also given in **EC3**. The shear strength of steel is $f_y/\sqrt{3}$ for Class 2 webs. The shear buckling resistance is based on the reduced depth of web.

Thesis:

In **Chapter 3** one new approach was revised for perforated beams with standards and non-standard web openings and their effect was presented in **Table 3.4**. The three different approaches as they have been presented by **BS5950 Part 1:2000, ENV (1993-1-3) EC 3,** and Chung et al. (2003), were compared and important conclusions were drawn. Overall, it was seen that a significant percentage of contribution of the flange was considered in the shear capacity especially when the deep web openings and/or thick flanges existed.

Furthermore, the shear resistance for perforated beams with isolated web openings of various shapes and sizes was investigated with the use of shear-moment interaction curves. **Figure 3.26** presents the results for all specimens and then design formulas were developed evaluating the 'coupled' shear capacities.

7.4.4 Vierendeel bending (Clause N 3.3.3.2.3)

The method in SCI P-100 is used in which shear and axial forces are resolved around the web opening, and the Vierendeel moment is calculated at all angles, φ. The critical angle is usually 20° to 30° from the vertical.

In **BS 5950: Part1 Clause 4.2.6,** the interaction between axial forces (or bending moment) and shear in the webs of beams is based on a linear reduction of axial or bending capacity for shear forces. This interaction may be taken into account by modifying the web thickness depending on the shear force resisted by the web.

Thesis:

The same methodology with SCI P-100 was used while critical angles were presented for standard and non-standard web opening shapes in **Table 3.10** and **Figure 3.36** and **3.37.** The angles, φ_p, were the positions of the initial plastic hinges in the vicinity of the web opening and LMS, when high shear forces were applied. Another notification was given when the web openings were positioned under high shear and moment ratios. In general, the angles, φ_p, were bigger when the web openings were close to the support and decreased when these were moved closer to the mid-span. The distance between the two plastic hinges at LMS and HMS of the top tee-section when high shear forces were considered, was the critical opening length, c. No consideration was provided for the position of the plastic hinges at USFBs, as the Vierendeel bending resistance was significantly increased.

7.4.5 Web-post buckling (Clause N 3.3.3)

The same web-post buckling formulas as in SCI P-100 are used in this clause, except that the following additional limits are introduced:

- Depth of web openings $\leq 60 t_w \varepsilon$

- Bending resistance of web $\leq 0.6M_{el,Rd}$
- Geometric limits as for dimensions of web openings above

The limit $0.6M_{el,Rd}$ was arbitrary, and it was also not clear, what its source was.

Thesis:

The depth of the web openings studied was 70% of the overall beam's depth, based on a preliminary FE study conducted, ensuring that web-post buckling was more critical than Vierendeel-shear failure when circular web openings were regularly spaced. No limit was placed on the elastic bending resistance. Therefore, in **Chapter 5** a similar methodology with SCI P-100 was followed, however this was an extended study covering standard and novel non-standard web openings; with very narrow to wider web-posts, while the web thickness was changed from very low to high values. Design formulas were proposed for six different web opening shapes while the spacing of the web openings and the web thickness varies, complying with web-post buckling and the limiting shear force in the top tee-sections resulting from Vierendeel bending as well as non-linear FE evaluations.

7.2.6 Web-post shear (Clause N 3.3.3)

The shear area is based on the web-post. Its shear strength is $f_y/\sqrt{3}$. In **BS5950 Part 1:2000**, the shear area of an un-stiffened plate is reduced by 10% for cellular beams (i.e. shear area of $0.9A_v$). This is adopted for the web-post to account for the non-uniform distribution of elastic shear stresses in the web-post. **EC3** does not require a 10% reduction, but this conservatism is reasonable because of the possible effects of incomplete welding (if applied) close to the edge of the web opening.

For different steel grades of the top and bottom tee-sections, the horizontal shear resistance is checked separately for each web at their connection (i.e. the minimum multiple of $t_w f_y$ will control). The horizontal shear resistance is determined using similar rules to the vertical shear resistance.

Thesis:

The shear area was reduced according to the web opening shape in order to take account of interactions between shear and in-plane stresses (**Table 5.38**). The in-plane moment acting on the web-post was calculated explicitly, depending on the equilibrium of the top and bottom tee-sections.

The shear strength of the web-post calculating the horizontal shear stress, σ_{hs}, was taken as either $f_y/\sqrt{3}$, by using the vertical shear force obtained from FE analysis at failure, or by using the vertical shear force obtained from the new design model. The results showed some underestimation and overestimation against the nominal shear strength of the web-

post as discussed in **Chapter 5**. The horizontal shear stress, σ_{xy}, from ANSYS at the narrowest point of the web-post was also presented for comparison.

7.4.7 Dimensions of elongated or rectangular web openings (Clause N 2.1.1)

- Maximum size of web openings $0.75h_w$
- Maximum depth of tee below flange $0.1h_w$
- Maximum length of web opening $3.0d_o$
- Maximum eccentricity (above centre-line) $0.125h_w$

Thesis:

The requirements for elongated web openings were taken as the same as for circular web openings given earlier, and generally in this research study were treated similarly.

- Maximum size of web openings $0.8h$
- Maximum depth of tee below flange $0.1h$
- Maximum length of web opening $3.0d_o$

7.4.8 Stiffening of web openings (Clause N 1.6(9))

To prevent the possibility of the compression flange buckling of un-stiffened top tee-sections, this clause required the proportion of the tee-section to satisfy a formula given in this clause, as a function of the length of the web opening. At points of support and concentrated load, the effects of bearing and buckling should be considered. Guidance on web bearing and stiffener design is given in **Section 4.5** of **BS 5950: Part 1**.

Thesis:

Such provision was not considered in this thesis. Hence, highly distorted top tee-sections were obtained from the FE study on perforated beams for instance when elongated web openings.

7.4.9 Anchorage length of stiffeners (Clause N 2.1.5(7))

The anchorage length of the stiffener for elongated web openings is taken as not less than:

- Web opening width / 4
- Tensile resistance of stiffener / strength of fillet per unit length
- Shear resistance of web

Thesis:

Such provision was not considered in this thesis.

7.6 LIST OF PAPERS AND TECHNICAL REPORTS FROM THESIS

Some of the publications produced from this research programme are listed as follows with chronological order:

Tsavdaridis, K.D. and D'Mello, C. (2010) Experimental and Finite Element Investigation on the Vierendeel Bending of Perforated Steel Beams with Various Novel Shapes and Sizes of Web Openings. Will be submitted to the Journal of Constructional Steel Rescarch, Submitted to the Journal of Constructional Steel Research, In review from editors

Yu Huo, B., D'Mello, C. and Tsavdaridis, K.D. (2010) Experimental study and finite element analysis of innovative shear connectors of Ultra Shallow Floor Beam. Submitted to the 34th IABSE Symposium, (Venice Italy September 22-24, 2010) IABSE Press, Venice, Italy

Tsavdaridis, K.D. and D'Mello, C. (2010) Web-Post Buckling Study Investigating the Behaviour and Strength of Perforated Steel Beams with Various Web Opening Shapes. Submitted to the Journal of Structural Engineering – ASCE, In review from editors

Tsavdaridis, K.D. and D'Mello, C. (2009) Finite element investigation of perforated steel beams with different web opening configurations. 6th International Conference on Advances in Steel Structures (Hong Kong China December 16-18, 2009) ICASS'09/IJSSD/IStructE Asia-Pacific Forum, Hong Kong, China, pp. 213-220

Steel Construction Institute (SCI). (2009) Methodology for design of USFB beams with large openings. Proposed model for USFB. Pre-publication draft with incorporation of the tests conducted in this thesis, 25070

Tsavdaridis, K.D., D'Mello, C. and Yu Huo, B. (2009) Computational study modelling the experimental work conducted on the shear capacity of perforated concrete-steel Ultra Shallow Floor Beams (USFB). 16th Concrete Conference (Paphos Cyprus October 21-23, 2009) Conference Press, Paphos, Cyprus, pp. 159

Tsavdaridis, K.D., D'Mello, C. and Hawes, M. (2009) Experimental study of ultra shallow floor beams with perforated steel sections. 11th Nordic Steel Construction Conference (Malmö Sweden September 2-4, 2009) NSCC2009 Press, Malmö, Sweden, pp. 312-319

Tsavdaridis, K.D. (2008) Optimization of web opening shapes in steel perforated beams by using FE analyses, Technical Report Submitted to Westok ltd., Part of the ASD metal services group

Tsavdaridis, K.D. (2008) Innovative web opening configurations for perforated steel sections; studied under high Vierendeel bending, Technical Report Submitted to Westok ltd., Part of the ASD metal services group

Tsavdaridis, K. D. (2010) Failure modes of composite and non-composite perforated beams sections with various shapes and sizes of web openings", 1st Year Report Thesis (supervised by Dr. C. D'Mello), School of Engineering and Mathematical Sciences, City University, London

Tsavdaridis, K.D. (2007) Innovative construction for long spans; Perforated steel sections – Pre-formed web openings, Technical Report Submitted to Westok ltd., Part of the ASD metal services group

7.7 SUGGESTIONS FOR FUTURE RESEARCH WORK

The current research work has contributed to the understanding of the behaviour of non-composite perforated beams with various web opening shapes and sizes as well as partially encased perforated beams with concrete in-fill. New developments were introduced and design procedures were recommended. However, a number of interesting issues were not examined; several topics have been opened for investigation while some proposals require further validation. Furthermore, several suggestions are given:

- Selected novel elliptical web openings can be explored in more depth as they behave positively. Hence, a formula that associates the parameters THETA and R, with the stresses and the load carrying capacities is necessary, in order to make practical this innovation.
- Also, the position (i.e. angle) of the plastic hinges and their movement with different shear-moment interactions can be evaluated and explained by a formula. This can be used to predict the regions of high stresses in the steel and possibly enhance them.
- Wide investigation on numerous web opening shapes should be conducted as they have been found to be practical especially in aeronautical, mechanical and ship building engineering. The parameters defining these shapes can be optimized. Sophisticated formulas can be given, providing a balance between the cost and the performance of such perforated beams with the best application in the structures.
- Regarding the web-post buckling study, more web opening sizes should be analysed similar to the Vierendeel bending study, in order to determine the boundaries of change between two different failure modes mainly due to stress mobilization.
- Different materials other than steel could be reconsidered, exploring the effects of such beams. It is understood that this study could be applied not only to civil engineering but other research areas as well. Hence, the material strength is an important parameter-and the results can be conclusive.
- Mid-range I-section sizes were investigated as the studied perforated beams will be used for normal buildings. There is an interest on examining numerous I-sections sizes and quantifying the results. Therefore, the safety factors could be eliminated saving material costs. Therefore, experimental work as well as FE numerical investigation

should be carried out to cover the wide range of perforated beams subjected under Vierendeel bending and web-post buckling forces.

- Highly asymmetric I-sections were widely applied for various engineering structures. Past research studies have opted to neglect them or assume simple representations that were not adequately calibrated. Also, non-centred web openings have not been examined in the past. This was due to the complexity of the models and the numerous factors that influence the results. Numerous experimental and FE studies could arise by inserting these factors to this research.
- In a more advanced investigation, the web-post buckling study could be conducted while a combination of web openings could be considered. This behaviour is totally unpredictable by physical means or by any empirical formulas established up to date.
- Generally, extensive experimental work should be conducted on the perforated beams with novel web opening shapes, while beams will be tested under different loading conditions and support conditions. Testing is very important, especially for such novel developments.
- Ideally, the introduction of the fillets could also be treated as a 'crack' to the typical circular web openings, which perhaps was created after re-welding of the top and bottom tee-sections. These cracks could cause catastrophic results following a cyclic loading especially when the beams are used in applications such as bridges where fatigue is a dominant factor. Hence, a more advanced study is required, to investigate this uncertainty.
- The contribution of the web to column flange double angle connection usually utilised for perforated beams needs to be examined to determine the actual contribution to torsional and lateral rigidity. The depth of the connection should also be varied to investigate the effect on beam stability.
- The contributions of other connections, such as single plate connections or bottom flange bearing connections, should be investigated to determine what contribution, if any, they have on the stability of perforated beams.
- It would also be interesting to investigate the load carrying capacities of USFBs with different beam arrangements (i.e. span, number and position of web openings, some web openings filled with concrete and some not, etc.). In addition, the web opening shapes could be changed to monitor the longitudinal shear strength of the new proposed system consisting of the bond strength between the steel and the concrete as well as the bearing strength of the new web opening area.
- The effect of various types of mechanical shear connectors (i.e. steel reinforcement tie-bars, shear studs on the web, ducting, etc.) in USFBs is also of interest as such a research programme is taking place at City University at the time of this research programme.
- The manufacturing procedures of perforated beams with various web openings should be thoroughly investigated, especially when novel web opening shapes are utilised. An

economic impact as well as a better product in terms of performance could be the outcome of this study. Information regarding the laser-cut and the welding line should also be given. The length and depth of the beams could be optimized provided that the web opening spacing and the weight of the beams are as required, while the capacity of the beam is not reduced.

Finally, the control of the serviceability limit state in structures with perforated beams is not well defined so far and only a few different representations of this have been adopted in past research studies based on theoretical approaches (i.e. elastic stiffness of the tee-sections due to the web opening existence on non-composite steel beams).

In the absence of field data and adequate existing experimental data, the above future objectives can be met through a series of experimental tests involving composite and non-composite perforated beams of various geometrical and material models. In addition, global and local FE parametric studies are necessary for visualization and understanding of the results as well as to increase the number of examined beam models in saving time and cost.

BIBLIOGRAPHY

Aalborg University Esbjerg. (2008) FEM Lecture Notes and ANSYS Tutorials

ACI 318-99. (1999) American Concrete Institute, Building Code Requirements for Reinforced Concrete. American Concrete Institute, Farmington Hills, Michigan

Adams, V. and Askenazi, A. (2002) Building Better Products with Finite Element Analysis, found in Chalice Engineering Ltd

Allan, R. B. (1997) Elastic-Plastic of a Plate of Strain Hardening Material with a Central Circular Hole – Comparison of experiment with FEA Containing the Unified Constitutive Material Model. Department of Defence

Aloi, N. M., Gross, S.P., Dinehart, D. W. and Yost J. R. (2002) Experimental Tests of Singly and Doubly Symmetric Castellated Beams. SMI-Villanova Research Report No.1

ANSI/AISC 360-05. (2005) Specification for structural steel buildings. American Institute of Steel Construction

ANSYS. (2009) User's Manual Revision 11. ANSYS, Inc., Canonsburg, PA

ASCE. (1973) Suggested design guides for beams with web holes. By the Subcommittee on beams with web openings of the Task Committee on flexural members of the structural division, John E., Bower, Chmn., ASCE Journal of the Structural Division 97:No.ST11 (1971:2707-28; Closure to discussion, 99:No.St.6, pp. 1312-15

ASCE Division. (1980) Proceedings of the American Society of Civil Engineers. Vol. 106, No. ST1

ASCE Standard. (1997) Specification for Structural Steel Beams with Web Openings. American Society of Civil Engineers, SEI/ASCE 23-97

ASD Westok Ltd. (2004) Steel Construction Institute (SCI) Document RT1006. Version 02

Barbosa, A. F. and Ribeiro, G. O. (1998) Analysis of Reinforced Concrete Structures using ANSYS Nonlinear Concrete Model. Computational Mechanics, New Trends and Applications, CIMNE, Barcelona, Spain

Bernuzzi, C., Zandonini, R., In: Buckner, D. and Shahrooz, B.M. editors. (1996) Slim floor steel-concrete composite systems. Composite construction in steel and concrete, vol. III, Germany: ASCE, pp. 486-99

Boresi, A. P., Schmidt, R. J. and Sidebottom, O. M. (1993) Advanced Mechanics of Materials. Fifth Edition, John Wiley and Sons, Inc.

Bower, J. E. (1968) Design of beams with web openings. Journal of the Structural Division, Proceedings of the American Society of Civil Engineers

Brahmachari, K. (1997) Connection and flexural behavior of steel RHS filled with high strength concrete. PhD Thesis, School of Construction and Building Sciences, University of Western Sydney, Hawkesbury

BRE. (1988) Design of normal concrete mixes. BRE report, UK

Brian K. Dougherty. (1980) Elastic Deformation of Beams with Web Openings. ASCE Journal of the Structural Division, 106:No.ST1, pp. 301-312

BS EN 1993-1-1:2005 Eurocode 3. Design of steel structures. General rules and rules for buildings, BSI

BS EN 1994-1-1:2004 Eurocode 4. Design of composite steel and concrete structures. General rules and rules for buildings, BSI

BS EN 197: Part 1: 2000. Cements. Composition, specifications and conformity criteria for common cements. BSI

BS EN 10002-1:2001. Tensile testing of metallic materials. Method of test at ambient temperature, BSI

BS5950 Part 1: 2000. Structural Use of Steelworks in Building. Code of practice for design, Rolled and welded sections, BSI

BS5950-3-1: 1990. Structural Use of Steelworks in Building. Design in composite construction. Code of practice for design of simple and continuous composite beams, BSI

BS5950: 1990. Structural Use of Steelworks in Building. BSI

BS 8110: Part 1: 1985. Structural use of Concrete. Code of Practice for design and construction, BSI

BS5950: 1985. Structural Use of Steelworks in Building. BSI

Buckhouse, E. R. (1997) External Flexural Reinforcement of Existing Reinforced Concrete Beams using Bolted Steel Channels. Master's Thesis, Marquette University, Milwaukee, Wisconsin

Byfield, M. and Nethercot, D. (2001) Safety variations in steel designed using Eurocode 3. JCSS Workshop on Reliability Based Code Calibration

Carlos Graciano and Ove Lagerqvist. (2003) Critical buckling of longitudinally stiffened webs subjected to compressive edge loads. Journal of Constructional Steel Research 59, pp. 1119-1146

Carreira, D. J. and Chu, K. H. (1985) Stress-strain relationship for plain concrete in compression. ACI Struct. J., 82(11), pp. 797-804

Chau, K. T. and Chan, S. L. (2002) Failure of a steel plate containing a circular rivet hole with an emanating crack. Advances in Steel Structures, Vol. II

Cho, S.H. and Redwood, R.G. (1986) The design of composite beams with web openings. Structural Engineering Series, McGill University, Montreal, Quebec, Canada, pp. 86-2

Chung, K. F., Liu, T. C. H. and. Ko, A. C. H. (2003) Steel beams with large web openings of various shapes and sizes: an empirical design method using a generalized moment-shear interaction. Journal of Constructional Steel Research 59, pp. 117-1200

Chung, K. F., Liu, T. C. H. and. Ko, A. C. H. (2001) Investigation on Vierendeel mechanism in steel beams with circular web openings. Journal of Constructional Steel Research 57, pp. 467-490

Clawson, W.C. and Darwin, D. (1982) Tests on composite beams with web openings, Structural Division. Journal of American Society of Civil Engineers 108, P. ST1, pp. 145-162

Clawson, W. C. and Darwin, D. (1980) Composite beams with web openings. SM Report 4. University of Kansas Center for Research

Corus Construction and Industrial. (2006) Advance Sections. CE marked structural sections

Crocetti, R. (2003) Web breathing of full-scale slender I-girders subjected to combined action of bending and shear. Journal of Constructional Steel Research 59, pp. 271-290

Darwin, D. and Donahey, R. C. (1988) LRFD for composite beams with unreinforced web openings. Journal of Structural Engineering, ASCE, 114, 3, pp. 535-552

Darwin, D. and Lucas, W. C. (1990) LRFD for steel and composite beams with web openings. Journal of Structural Engineering, ASCE, 116, 6, pp. 1579-1593

Davies, J. M., Engel, P., Liu, T. C. H. and Morris, L. J. (1990) Realistic modeling of steel portal frame behaviour. The Struct Engr 68, pp. (1): 1-6

Demarco, T. (2003) ProfilARBED – Researches 'Optimization des performances des poutras cellulaires ACB'. 24emes Journees Siderurgiques Interbationales, Paris

Demartino, A., Landolfo, R. and Mazzolani, F. M. (1990) The use of Ramberg-Osgood law for materials of round-house type. Materials and Structures. RILEM Technical Committees, TC 83-CUS Fundamental Mechanical, Properties of Metals, 23, pp. 59-67

Demirdjian, S. (1999) Stability of Castellated beam webs. MEng Thesis, Department of Civil Engineering and Applied Mathematics, McGill University, Montreal, Canada

De Nardin, S. and El Debs. (2009) A.L.H.C. Study of partially encased composite beams with innovative position of stud bolts. Journal of Constructional Steel Research 65, pp. 342-350

Dervinis B. and Kvedaras A. K. (2008) Investigation of rational depth of castellated steel I-beams. Journal of Civil Engineering and Management

Dipaola, V., Prete, F. and Prete, G. (2006) The elasto-plastic behaviour of encased composite beams for slim floors in multi-storey buildings. 2nd International congress-Fib, Naples, FIB, pp. 1-12 (ID 5-24)

Doerk, O., Fricke, W. and Weissenborn, C. (2003) Comparison of different calculation method for structural stresses at welded joints. International journal of fatigue, Vol. 25, pp.359-369

Donahey, R. C. (1987) Deflections of composite beams with web openings. Building Structures, Proceedings, ASCE Structures Congress, D.R. Sherman, ed., Orlando, Florida, pp. 404-417

Donahey, R. C. and Darwin, D. (1988) Web openings in composite beams with ribbed slabs. Journal of Structural Division, ASCE, Vol. 3, No 114 pp. 518-534

Donahey, R. C. and Darwin, D. (1986) Performance and Design of composite beams with web openings. Structural Engineering and Engineering Materials SM Report No.18, University of Kansas Center for Research, Lawrence, Kansas

Donoghue, C. M. (1982) Composite beams with web openings: Design, Journal of Structural Division. ASCE, 108, ST12, pp. 2652-1667

Earls C. J. (2001) Constant moment behavior of high-performance steel I-shaped beams. Journal of Constructional Steel Research 57, pp. 711-728

ECCS. (1995) Multi-storey buildings in steel: Design guide for slim floors with built-in beams. ECCS, Brussels, Belgium

ENV 1993-1-3 Eurocode 3: Design of steel structures: Part1.1. General rules and rules for buildings. 1992, and Amendment A2 of Eurocode 3: Annex N 'Openings in webs'. British Standards Institute

EN 1993-1-8: 1993 Eurocode 3 Part 1.8. 'Design of Steel Structures – Design of Joints'

ENV 1993-1-1:1992/A2:1998 Eurocode 3: Part 1.1 – Amendment A2 CEN, (Pre-Standard)

ENV 1993-1-5:1997 Eurocode 3 Part 1.1. Design of steel structures – General rules; Supplementary rules for planar plated structures without transverse loading

ENV 1993-1-4:1996 Eurocode 3 Part 1.4. Design of steel structures – General rules; Supplementary rules for stainless steels

ENV 1994-1-1:1994 Eurocode 4 Part 1.1. Design of composite steel and concrete structures, General rules and rules for buildings

European Aluminum Association. Good practices in aluminum chassis design and repair, Mass Transport Publication. [Online] Available from: http://www.eaa.net/upl/4/default/doc/GoodPracticesFR.pdf [Accessed March 2008]

European Steel Design Educational Program (ESDEP). (2003) Working Group 12, Fatigue, Teräsrakenneyhdistys. [Online] Available from: http://www.tkk.fi/Units/Civil/Steel/Publications/TKK_TER_series/TKK-TER-29.pdf [Accessed June 2008]

SMI. (2001) Experimental Tests of Non-Composite Castellated and Cellular Beams. Research sponsored by SMI Steel Products under the SMI-Villanova Research Partnership

Fabsec Ltd. (2006) Design of FABSEC Cellular Beams in Non-composite and Composite Applications for both normal temperature and fire engineering conditions

Fanning, P. (2001) Nonlinear Models of Reinforced and Post-tensioned Concrete Beams, Electronic Journal of Structural Engineering, EJSE International, 2

Feldmann, M., Müller, C., Hechler, O., Bureau, A., Cajot, L. G., Vassart, O., Lawson, R. M., Hicks, S., Johansson, B. and Velikovic, M. (2006) Large Web Openings for Service Integration in Composite Floors. Research Fund for Coal and Steel, project carried out with the financial grant of the Research Programme of the Research Fund for Coal and Steel, Coordinator RWTH

Fenner, D. N. (1987) Engineering stress analysis – a finite element approach with FORTRAN 77 software

Fricke, W. (2003) Fatigue of Materials and Structures, Seminar organized by Laboratory for Mechanics of Materials. [Online] Available from: http://www.tuharburg.de/skf/fatiguecourse/ [Accessed April 2008]

Fukumoto, Y., M. ASCE, Itoh, Y. and Kubo, M. (1980) Strength variation of laterally unsupported beams. Journal of the Structural Division

Guillaume, B. and Depaillet S. (2008) Buckling analysis with Ansys – Study of a thin perforated plate in tension and compression. Department of Solid Mechanics, Royal Institute of Technology (KTH), Solid Mechanical Modeling for Design, Project Report in SE2125, Stockholm, Sweden

Harper C. S. (1995) Castellated and Cellular Beams. British Steel Sections, Plates and Commercial Steels, Westok Ltd.

Hearn E. J. Strain Gauges. (1971) Merrow Publishing Co. Ltd.

Hegger, J. and Goralski, C. (2005) Structural behaviour of partially concrete encased composite sections with high strength concrete. 5th International conference in composite construction in steel and concrete, South Africa, pp. 346-55

Hendry A. W. (1977) Elements of Experimental Stress Analysis. Pergamon Press Ltd.

Hertzberg, R. W. (1959) Deformation and Fracture Mechanics of Engineering Materials, John

Wiley and Sons Inc., Toprac A. A. and Cooke B. R. (1959) An experimental investigation of open-web beams

Hirst, M. J. S. and Yeo, M. F. (1980) The analysis of composite beams using standard finite element programs. Comput. Struct., Vol. 3, No 11 pp. 223-237

Hosseini, S. R., Choupani, N. and Gharabaghi, A. R. M. (2008) Experimental Estimation of Mixed-Mode Fracture Properties of Steel Weld. Proceedings of World Academy of Science, Engineering and Technology, Vol. 31

Ito, M., Fujiwara, K. and Okazaki, K. (1991) Ultimate Strength of Beams with U-shaped Holes in Top of Web. Journal of Structural Engineering, ASCE Vol. 117

Ju, Y. K., Chun, S. C. and Kim, S. D. (2009) Flexural test of a composite beam using asymmetric steel section with web openings. Journal of Structural Engineering, ASCE, pp. 448-458

[#]Kaewunruen, S. and Remennikov, A. (2006) Nonlinear finite element modelling of railway prestressed concrete sleeper. Proceedings of the 10th East Asia-Pacific Conference on Structural Engineering and Construction (Bangkok Thailand August 3-5, 2006), Bangkok, Thailand vol.4 Real Structures: Bridges and Tall Buildings, pp. 323-328

[¥]Kachlakev, D. and Miller, T. (2001) FE Modeling of Reinforced Concrete Structures Strengthened with FRP Laminates. Final Report SPR 316, Oregon State University, Department of Transportation

Kala, Z. (2007) Influence of Partial Safety Factors on design reliability of steel structures, probability and fuzzy probability assessments. Brno University of Technology, Faculty of Civil Engineering, Institute of Structural Mechanics, Journal of Civil and Management, Vol XIII, No 4, pp. 291–296

Khuram, S., Sagheer, A. and Himayat, U. (2007) Effect of Geometric Imperfection on Buckling Strength of Cylindrical Shells. UET Taxila - Mechnical Engineering Department, Failure of Engineering Materils & Structures, Code 40

Ko C. H. and Chung K. F. (2000) A comprehensive study on existing design rules for steel beams with circular web openings. Proceedings of the First International Conference on Structural Stability and Dynamics, Taipei, pp. 733-8

Kussman, R. L. and Cooper, P. B. (1976) Design example for beams with web openings. AISC Engineering Journal, 13, 2, pp. 48-56

Lagaros, N. D., Lemonis D., Psarras, Papadrakakis, M. and Panagiotou, G. (2008) Optimum design of steel structures with web openings. Engineering Structures

Larnach, W. J. and Park, R. (1964) The Behaviour under Load of Six Castellated Composite T-Beams. University of Bristol, Civil Engineering and Public Works Review

Lawson, R. M., Chung, K. F. and Price, M. (1992) Tests on composite beams with large web openings to justify existing design methods. The Structural Engineer Journal 1992:70(1)

Lawson, R. M. (1987) Design for openings in the webs of composite beams, CIRIA/Steel Construction Institute. CIRIA Special Publication 51 and SCI Publication 068

Lawson, R. M. and Hicks, S. J. (2006) Design of beams with large openings for services. Published by Steel Construction Institute, SCI Pre-Publication draft pp. 355

[§]Liang, Q. Q., Uy, B., Bradford, M.A. and Ronagh, H. R. (2005) Strength analysis of steel-concrete composite beams in combined bending and shear. ASCE Journal of Structural Engineering, Vol. 131, No 10, pp. 1593-1600

Liu, T. C. H. and Chung, H. F. (2003) Steel beams with large web openings of various shapes and sizes: finite element investigation. Journal of Constructional Steel Rescarch 59, pp. 1150-1176

Liu, T. C. H. and Chung, H. F. (1999) Practical design of Universal steel beams with single web openings of different shapes. Proceeding of the Conference Eurosteel '99, CVUT Praha, pp. 59-62

Liu, T. C. H. and Morris, L. J. (1991) The effect of connection flexibility on portal frame behaviour. In: Int. Workshop on connections in steel structures. Pittsburg: AISC/Eurcom

Lu, W. (2003) Advanced steel structures. Helsinki University of Technology Laboratory of Steel Structures Publications 29, Part 2: Fatigue Design

Lydon F. D. (1982) Concrete Mix Design, Second Edition. Applied Science Publishers

Window A. L., and Holister G. S. (1982) Strain Gauge Technology. Applied Science Publishers Ltd.

MACSTEEL TRADING (PTY) Ltd. (2003) Cellular Beams Design Guide. Publication

Mahmood, M. N. (2007) Nonlinear Analysis of Reinforced Concrete Beams Under Pure Torsion. Journal of Applied Sciences 7 (22): pp. 3524-3529

Marquis, G. and Kähönen, A. (1995) Fatigue Testing and Analysis using the Hot Spot Method. VTT publications, No. 239, Espoo, Finland

Mac Donald B. J. (2007) Practical Stress Analysis with Finite Elements. Glasnevin Publishing

McKenna, P. D. and Lawson, R. M. (2000) Service Integration in Slimdeck. SCI Publication 273, Ascot

McKenna, P. D. and Lawson, R. M. (1997) The design of steel frames buildings for service integration. SCI Publication 166, Ascot

Mehrkar-asl, S, Brookes, C.L. and Duckett, W.G. (2005) Saving half through girder bridges using non-linear Finite Element Analysis

Mitchell, S. A. (1997) Choosing corners of rectangles for mapped meshing. ACM Press, in proc. 13th Annual Symposiumon Computational Geometry, June 4-6 1997, pp. 87-93 Available from: http://sass577.endo.sandia.gov/9225/Personnel/samitch/choosing-corners.html [Accessed July 2008]

Mohri, F., Brouki, A. and Roth, J. C. (2002) Theoretical and numerical stability analyses of unrestrained, mono-symmetric thin-walled beams. Journal of Constructional Steel Research 59, pp. 63-90

Mullett, D. L. (1998) Composite floor systems. Blackwell, Oxford, U.K.

Mullett, D. L. and Lawson, R. M. (1993) Slim floor construction using deep decking. Steel Construction Institute. U.K.

Naeem-ur-Rehman and Khan, M. T. (2007) Sub sea Buckling of Pipes, Department of Solid Mechanics. Royal Institute of Technology (KTH), Solid Mechanical Modeling for Design, Project Report in SE2125, Stockholm, Sweden

Narayanan, R., Al-Amery, R. I. M. and Roberts, T. M. (1989) Shear strength of composite plate girders with rectangular web cut-outs. J. Constr. Steel Res., Vol. 2, No 12 pp. 151-166

Novak, R. and Machacek, J. (1999) Local buckling of undulating webs, Proceeding of the Conference Eurosteel '99, CVUT Praha

Olander, H. C. (1953) A method of calculating stress in rigid frame corners. Journal of the Structural Division, Proceeding of the American Society of Civil Engineers

[†]Parvanova, S. P., Kazakov, K. S., Kerelezova, I. G., Gospodinov, G. K. and Nielsen, M. P. (2004) Modelling the nonlinear behaviour of R/C beams with moderate shear span and without stirrups using ANSYS. Faculty of Civil Eng., Sofia, Research for the National Science Fund under the contract № TH-1406/04, Techical Report

PR NBR 8800. (2007) Design of steel and composite structures for buildings. Brazilian Association of Standard Codes

Psarras, L. D., Lagaros, N. D. and Papadrakakis, M. (2005) Sizing and shape optimization of 3D steel structural structures with web openings. 5th GRACM International Congress on Computational Mechanics, Limassol

Redwood, R. G. (1973) Design of beams with web holes. Canadian Steel Industry Construction Council, Willowdale, Ontario, Canada

Redwood, R. G. (1971) Simplified plastic analysis for reinforced web holes. AISC Engineering Journal, 8, 3, pp. 128-131

Redwood, R. G. (1969) The strength of steel beams with unreinforced web holes. Civil Engineering and Public Works Review

Redwood, R. G. (1968) Plastic behavior and design of beams with web openings. In Proceedings of the First Canadian Structural Engineering Conference, Can. Steel Indust. Const. Council, Toronto, Canada, pp. 127-138

Redwood, R. G. and McCutcheon, J. O. (1968) Beam tests with unreinforced web openings. Journal of the Structural Division, Proceeding of the American Society of Civil Engineers 94, P. (ST1), pp. 1-17

Redwood, R. G. and Poumbouras, G. (1983) Tests of composite beams with web holes. Canadian Journal of Civil Engineering 10

Redwood, R. G. and Shrivastava, S. C. (1980) Design recommendations for steel beams with web holes. Canadian Journal of Civil Engineering, 7, 4, pp. 642-650

Redwood, R. G. and Wong, P. K. (1982) Web holes in composite beams with steel deck. In Proceedings of the Eighth Canadian Structural Engineering Conference, Can, Steel Const. Council, Willowdale, Ontario, Canada

Reiter, M. T., Gross, S. P., Dinehart D.W. and Yost, J. R. (2002) Experimental Tests of Singly and Doubly Symmetric Cellular Beams. SMI-Villanova Research Report No.2

Roberts, T. M. and Al-Amery, R. I. M. (1991) Shear strength of composite plate girders with web cutouts. Journal of Structural Engineering, Vol. 7, No 117 pp. 1897-1910

Rust, W. and Schweizerhof, K. (2003) Finite element limit load analysis of thin-walled structures by ANSYS (implicit), LS-DYNA (explicit) and in combination. Copyright 2002 Elsevier Science Ltd., Thin Walled Structures, Vol.41, Issues 2-3, pp. 227-244

SCI. (2009) Methodology for design of USFB beams with large openings. Pre-publication 25070

SCI. (2008) AD 183: Deflection of composite beams with large web openings. SCI Advisory Desk

SCI. (2007) Part C – Design of Steel Bridges. Simplified bridge design to the Eurocodes for student projects, RT 1156 version 01

Shan, M. Y., Laboube, R. A. and Yu, W. W. (1996) Bending and shear behavior of web elements with openings. Journal of Structural Engineering

Shanmugan, N. E. (1995) Horizontally Curves Steel Beams

Sheldon, I. (2007) Buckling in WB Simulation Eigenvalue Buckling, Nonlinear Buckling, Sheldon's ANSYS, NET Tips and Tricks. STI:07/05

Sherbourne A. N. (1966) The plastic behavior of castellated beams

Sherboune, A. N. and Ostrom, J. V. (1972) Plastic analysis of castellated beams – Interaction of moment, shear and axial force. Journal of Computer and Structures, Vol 2

Standards Australia. (2001) Design of concrete structures. Australian Standard: AS3600-2001

Stephens, H. (2006) Current trends in modern floor construction

Stolarski, T., Nakasone, Y. and Yoshimoto, S. (2006) Engineering Analysis with ANSYS SOFTWARE. Department of Mechanical Engineering Tokyo University of Science, Tokyo Japan

Takabatake, H., Kusumoto, S. and Innoue, T. (1991) Lateral buckling behavior of I-beams stiffened with stiffeners. Journal of Structural Engineering, Vol. 117, No. 11

Tavárez, F. A. (2001) Simulation of behaviour of composite grid reinforced concrete beams using explicit element methods. MSc thesis approved by Dr. Lawrence C. (Bank Date Major Advisor Professor of Civil and Environmental Engineering University of Wisconsin – Madiso, University of Wisconsin, Madison

University of Alberta. (2006) ANSYS Tutorials. [Online] Available from: http://www.mece.ualberta.ca/tutorials/ansys/ [Accessed February 2006]

Unosson, E. (2003) Stainless steel girders – Resistance to concentrated loads and shear. Swedish Institute of Steel Construction

US Department of Housing and Urban Development. (1999) Innovative residential floor construction: Structural evaluation of steel joists with pre-formed web openings

Van de Lindt, J. W. and Ahlborn, T. M. (2005) Development of Steel Beam End Deterioration Guidelines. Michigan Department of Transportation Construction and Technology Division, Research Report RC-1454

Viest, I. M. and Colaco, J. P. (1997) Composite construction design for buildings. ASCE, Reston, Va.

Von Wingerde, A. M., Packer, J. A. and Wardenier, J. (1995) Criteria for the Fatigue Assessment of Hollow Structural Section Connections. Journal of Constructional Steel Research, Vol. 35, No.1, pp. 71-115

Wang, A. J. and Chung, K. F. (2008) Advanced finite element modelling of perforated composite beams with flexural shear connectors. Journal of Structural Engineering, Vol. 30, No 10 pp. 2724-2738

Wang, T. M., Snell, R. R. and Cooper, P. B. (1975) Strength of beams with eccentric reinforced holes. Journal of Structural Division, ASCE, 101, ST9, pp. 1783-1799

Wang, Y., Yang, L.. Shi, Y. and Zhang, R. (2009) Loading capacity of composite slim frame beams. Journal of Steel Constructional Research 65, pp. 650-661

Ward, J. K. (1990) Design of composite and non-composite cellular beams. The Steel Construction Institute, SCI Publication 100

Weber, L. and Cajot, L. Recent developments in the use of quenched and self-tempered hot rolled H-beams. Arcelor Sections Commercial and ProfilARBED Research [Online] Available from: http://www.arcelormittal.com/sheetpiling/ [Accessed April 2009]

William, K. J. and Warnke, E. P. (1974) Constitutive model for triaxial behaviour of concrete. Proceedings of International Association of Bridge and Structural Engineering Conference (Bergamo Italy, 1974) ISMES Press, Bergamo, Italy Vol.19., pp. 174

Wills, J. and Cheung, J. T. (1992) Finite Element Analysis of a Half-Scale Composite Steel and Concrete Bridge Deck. Department of Transport, Research Report 351

Wolanski A. J. (2004) Flexural behavior of reinforced prestressed-concrete beams using Finite Element Analysis. MSc Thesis, Marquette University

Zaarour, W. and Redwood, R. (1996) Web buckling in thin webbed castellated beams. Journal of Structural Engineering

Zahavi, E. and Torbilo. V. (1996) Fatigue Design Life Expectancy of Machine Parts. CRC Press, A Solomon Press Book